SUMMARIES OF VKI'S DOCTORAL CANDIDATE RESEARCH

2010 - 2011



von Karman Institute for
Fluid Dynamics

Covert art : *Pictures come from the article written by Benoît Marinus who won the best presentation Prize during the symposium.*

©2011 by the von Karman Institute for Fluid Dynamics
Waterloosesteenweg 72, B-1640 Sint-Genesius-Rode
To order: https://www.vki.ac.be

ISBN 978-2-87516-018-8

D/2011/0238/581, T. Magin, Editor-in-Chief

The contents of this book are the property of the von Karman Institute for Fluid Dynamics. No part of this book may be reproduced or distributed in any form of by any means, or stored in a database or retrieval system, without the prior written permission from the Publisher.

PREFACE

The second Symposium on the doctoral research took place at the von Karman Institute for Fluid Dynamics during the period March 1 to 3, 2011. The doctoral students have presented the progress of their research work carried out in the three departments: Aeronautics and Aerospace, Environmental and Applied Fluid Dynamics, Turbomachinery and Propulsion. The first year students have presented a poster on their research plans and some preliminary results while candidate in their 2nd and 3rd year proposed a 20 minutes presentation followed by 10 minutes questions.

This event was attended by the faculty of the von Karman Institute as well as some colleagues from other universities and/or industrial partners. The Symposium was totally open to external attendees and the entrance was free of charge. In addition to the presentations of the PhD candidates, we had the pleasure to welcome prominent keynote lecturers for the opening of each day of the Symposium:

- Jean Muylaert director of the von Karman Institute for Fluid Dynamics, as a keynote lecturer on "Review of past-present-future European space projects with emphasis on Critical ATD design issues"
- Dominique Hocquellet from EADS – ASTRIUM, as an invited keynote lecturer on "Challenges in development of thermal protection systems"
- Lorenzo Pons from TURBOMECA, as an invited keynote lecturer on "Current trends in turboengine virtual design"

For the first time this year, the honorary best presentation Prize was organised by the VKI faculty and awarded to **Benoît G. Marinus** for his research entitled: **Towards multidisciplinary optimization of propeller blades.** We would like to congratulate him for this performance. An image illustrating his research is used for the present cover.

The present proceedings volume contains 45 papers which are divided into the following topics: Transition from Laminar to Turbulent Flow, Plasma Flow, CFD and Modeling for Re-entry Flow, Flow during Industrial Hazard, Atmospheric Flow, Multiphase Flow and Heat and Mass Transfer Flow, Aeroacoustics, Flow in Turbines, Flow in Compressors, Engine Analysis and Improvements, Multidisciplinary Optimization in Turbomachinery, Static and Dynamic Stability of Re-entry Vehicle, First year Doctoral Summaries.

We would like to remind here, that this event, is aiming to communicate and to optimize the exchange between the doctoral candidates and the invited guests. The publication of their partial results through proceedings is of crucial importance for the VKI research.

As such, the doctoral candidate students of the VKI play a key role in strengthening the expertise in experimental and numerical/physical modeling of the Institute. Their research deployed at the Institute is often leading to implementation to real life industrial applications that should be strongly congratulated, recognized and acknowledged.

The present proceeding is registered under an ISBN number and may be referred to in any further publication.

We truly hope that this volume with the improved two-column format will have the attention it deserves.

Davide Masutti Sergio Lavagnoli Phd Representatives And Symposium Co-chairman	Patrick Rambaud Symposium Chairman	Jean Muylaert VKI Director

The contribution of all VKI members who helped on this event is deeply acknowledged faculty, library, printing office & secretariat.

TABLE OF CONTENTS

Editorial notes i

Table of contents iii

Transition from Laminar to Turbulent Flow

Davide Masutti 3
Disturbance level characterization of a hypersonic blow-down facility

Fabio Pinna 15
Stability of hypersonic flows in chemical equilibrium

Henny Bottini 21
Design and qualification of a supersonic wind tunnel for transition experiments

Jayson Babajee 31
Modeling and analysis of the laminar to turbulent transition in a low-pressure turbine

Plasma Flow

Francesco Panerai 45
Experimental characterization of the thermal protection system of a lifting reentry vehicle

Damien Le Quang 55
Investigation of high enthalpy plasma flow by means of optical emission spectroscopy

Silvânia Lopes 67
Modeling of inductively coupled plasma reactor for nanoparticles production

Computational Fluid Dynamics & Modeling for Re-entry Flow

Khalil Bensassi 77
Unsteady simulation of hypersonic flow over a heat probe in ground test conditions

Jesús Garicano Mena 87
Residual Distribution methods for atmospheric entry aerothermodynamics

Alessandro Munafo 97
Multiscale models and computational methods for aerothermodynamics

Erik Torres 107
Simulation of rarefied gas flows for aerospace applications

Alessandro Sanna 119
Development of algorithms for multiphysics applications

Stefano D'Angelo 129
Optimal error estimation techniques for Petrov-Galerkin method in linear problems

Martin Vymazal 135
High-order RDS and p-multigrid solution algorithms for compressible flow

Flow during Industrial Hazard

Delphine Laboureur..... 145
Experimental characterization and modeling of hazards: BLEVE and Boilover

Atmospheric Flow

Boris Conan..... 155
Physical modelling of wind in complex terrain: application to wind turbine siting

Domingo Munoz Esparza..... 167
Forecasting of offshore boundary layer conditions using high resolution WRF-PBL schemes for wind energy applications

Antonino Bonanni 177
CFD simulations of atmospheric boundary layer flows over complex terrains

Multiphase Flow & Heat and Mass Transfer Flow

Marcos Lema..... 187
Multi-phase fluid hammer: modeling, experiments and simulations

Evangelos Bacharoudis 193
Experimental investigation of liquid phase detachment and atomization from wall surfaces due to an external air flow field - Application to wiper system

Anthony Delmas..... 205
Shape and temperature field distortions induced by convective effect on hot object in different spectral bands

Tamas Banyai..... 214
Numerical simulation of turbulent incompressible Eulerian-Eulerian two-phase flows

Vasilios Kourakos 225
Experimental study and modeling of single- and two-phase air water flow in singular geometries and safety relief valves

Aeroacoustics

Korcan Kucukcoskun 231
Broadband scattering of the incoming turbulence noise of a stationary airfoil

Peter Toth 241
Beamforming in non-ideal acoustic environments

Lilla Koloszár 251
Numerical prediction of noise production and propagation

Michael Bilka 255
Experimental investigation of rotor broadband self noise by means of rotating controlled diffusion blades

Flow in Turbines

Bayindir H. Saracoğlu 263
Tubine base pressure active control through trailing edge blowing

Beni Cukurel 271
Conjugate heat transfer characterization in a ribbed cooling channel

Sergio Lavagnoli 281
Accurate turbine blade tip clearance measurements in a short-duration wind tunnel

Mehmet Mersinligil 291
A high temperature cooled fast response total pressure probe for measurements in gas turbine combustor and hot gas paths

Flow in Compressors

Balasz Farkas 309
Numerical investigation of secondary flows in low pressure axial compressor stage for contra-rotating turbofan architectures

Nicolas Van der Wyer 319
Experimental investigation of the unsteady flow field in the tip region of a single stage axial compressor with a circumferential groove casing treatment

Fatma Ceyhun Şahin 329
Design of a compressor cascade for flow control tests

Engine Analysis and Improvements

Victor Fernandez Villace 337
Numerical modeling of a combined cycle for high speed propulsion

Laura Villafane..... 345
Aerodynamic characterization of helicoidal fin arrays in transonic flow conditions

Multidisciplinary Optimization in Turbomachinery

Benoît G. Marinus 359
Toward multidisciplinary optimization of propeller blades

Michael Joly 369
Accelerated optimization for multi-disciplinary design of contra-rotating and transonic turbomachinery components

Static and Dynamic Stability of Re-entry Vehicle

Sebastien Paris 381
Experimental investigation of capsule stability in sub-sonic, transonic and supersonic

First year Doctoral Summaries

Leandro Dantas de Santana 395
Innovative noise reduction techniques for airframe noise

Julien De Muelenaere..... 397
Uncertainty quantification for material response of ablators in hypersonic flows

Guillaume Grossir 403
Prediction of natural and forced transition in hypersonic flows - Application to European space vehicles

Bernd Helber 407
Comprehensive experimental characterization of the material response of innovative ablators for the space exploration program

Bart Janssens 411
Numerical modeling and experimental investigation of fine particle coagulation and dispersion in dilute flows

Jérôme Sans..... 415
The effect of solidity on compressor performance and stability

TRANSITION FROM LAMINAR TO TURBULENT FLOW

Disturbance level characterization of a hypersonic blow-down facility

Davide Masutti

Aeronautics and Aerospace Department, masutti@vki.ac.be

Supervisor: Olivier Chazot

Associate Professor, Aeronautics and Aerospace Department, von Karman Institute for Fluid Dynamics, Belgium, chazot@vki.ac.be

Promotor: Fulvio Scarano

Professor, Department of Aerospace Engineering, Kluyverweg 2, Delft, The Netherlands, F.Scarano@TUDelft.nl

Abstract

Free-stream disturbances have a dominant role on boundary layer stability and transition, especially in high speed flows. The assessment of the flow quality in a wind tunnel, therefore is a key issue especially in turbulence studies. With this purpose a detailed characterization of the free-stream disturbance level of the VKI H3 Mach 6 Wind Tunnel at different Reynolds number is carried out by means of classical intrusive measurements techniques (hot-wire anemometry and Pitot pressure probes). Issues concerning the aerodynamic heating of the probes are investigated and a special calibration technique is developed in order to compensate for these problems. Statistical and spectral analyses are compared with the data available in the literature for other hypersonic wind tunnels, working at similar conditions for Mach and Reynolds number. A combined data reduction technique is also developed which allows to extract all flow quantity fluctuations from those directly measurable through the above-mentioned instrumentations. By means of this technique, the validity of some physical hypotheses on the flow can be verified. Moreover, a Kovasznay modal analysis allows to characterize the origin of the disturbances.

Keywords: hypersonic, turbulence, aerodynamic noise, boundary-layer transition, hot-wire anemometry, pressure measurements

1. Introduction

The assessment of the flow quality of a wind tunnel is a key issue, especially in transition studies. Indeed it is well known that freestream disturbances and flow quantities fluctuations have a dominant role on boundary layer stability, especially at high speeds. In Fig. 2 a schematic of the different mechanisms leading to boundary layer transition, according to Morkovin [2] is reported.

It is possible to see that the path to transition is different according to the intensity of the initial disturbance level: some parts of the process may be bypassed or not exist at all. The coupling between model shear layer and free-stream flow disturbances is referred on literature (and also in Fig. 2) as the receptivity problem, and is still largely unsolved. A brief review of boundary layer receptivity issues and their relation to free-stream disturbances is provided by Saric [4] and Pate [12]. The level of disturbance, in a more practical reasoning, also affects the location of the natural boundary layer transition on a vehicle surface. Indeed, in flight conditions, the noise level of the flow is usually very low compared to the wind tunnel environment: this leads to a huge discrepancy between the location of the transition region in ground testing and in flight. Therefore, a knowledge of the disturbance level of the facility is important both in order to build transition models and to extrapolate ground testing results to flight conditions [3].

It is not only important to quantitatively assess the intensity of the disturbances, but also to characterize their nature and their origin. In order to outline the main characteristics of a compressible turbulent flow-field (such as the freestream flow in supersonic or hypersonic wind tunnel) by means of analytical methods, Kovasznay [5] developed a simpli-

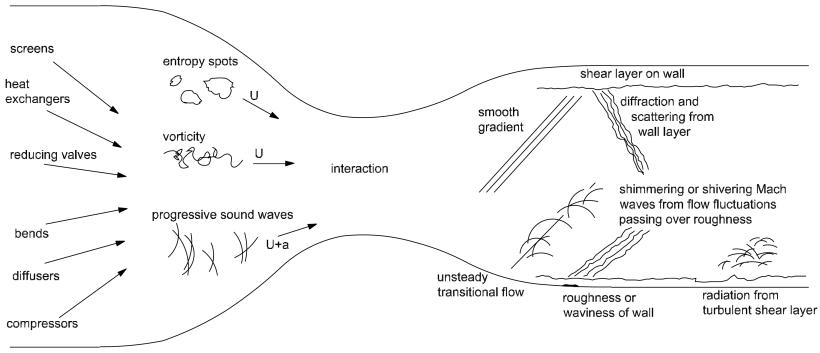

Figure 1: Freestream disturbances in supersonic/hypersonic wind tunnels [7]

fied analysis. According to this analysis, the fluctuations of a gas moving at a supersonic speed, at any point, by means of a small perturbation analysis can be considered as a superposition of three modes of covarying physical properties: a sound-wave mode (variation of pressure, density and temperature and of the coupled irrotational field at constant entropy, also referred to as the acoustic mode), an entropy mode (variation of entropy, density and temperature at constant pressure, also mentioned as entropy spottiness or temperature spottiness mode), and a vorticity mode (variation of the solenoidal component of the velocity field, which is known as simple "'turbulence"' at low speeds). In the case of a freestream flow in a supersonic/hypersonic wind tunnel, the entropy and vorticity modes are convected essentially along streamlines

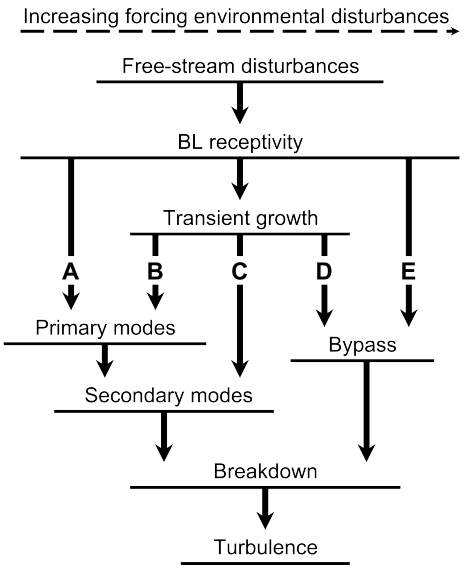

Figure 2: Paths to Transition

and may be related to the conditions of the settling chamber: sound-wave disturbances can travel across the streamlines and they may arise from both the settling chamber and the test section / nozzle boundaries. Morkovin [6] provided a further classification of sound-wave mode disturbances, also reported in Schneider [7]: eddy Mach wave radiation, that is a quadrupole and dipole radiation from the turbulent boundary layers, developing in the nozzle and in the test section of a supersonic wind tunnel, and shivering Mach waves, generated at flaws in the nozzle contour, that fluctuate in position when turbulence passes over them (Fig. 1). Eddy Mach wave radiation finds its theoretical basis on an extension of Lighthill analogy (for the aeroacoustic production of sound) to supersonic field. This extension was carried out by Philips [9] and by Ffocks-Williams [10]. At supersonic speeds indeed, the relative velocity of quadrupole sources, responsible for sound generation according to Lighthill, is greater than the speed of sound. In this way a mutual cancellation of waves cannot take place along the Mach wave direction, along which (much more than the other directions) a monopole-type sound radiation results. Shivering Mach waves are described in more detail in Morkovin [11] and result in lower frequency fluctuations than the eddy Mach waves fluctuations.
These considerations were experimentally confirmed by Laufer [8], who showed that the disturbance field in a supersonic Mach 5 wind tunnel located at the Jet Propulsion Laboratory (Pasadena) was dominated by sound waves, having an orientation slightly different from the Mach angle. Moreover, he showed that this sound pressure field was radiated by the turbulent boundary layers of the nozzle walls. These results can be generalized for all the supersonic and hypersonic wind tunnels, and constitute the starting point of the following analyses.

The knowledge of the physical origin of the disturbances can lead the way to some engineering solutions. This is the case of the so-called quiet wind tunnels. The objective of these wind tunnels is to produce a uniform flow in the test section. Since the disturbances are essentially originated at the boundary layer on the nozzle walls, most of these wind tunnel operate boundary layer suction in those regions, maintaining a laminar boundary layer and therefore reducing the disturbance level. This allows to reproduce ground testing flow conditions much closer to flight and to carry out transition studies in a low-noise environment, that allows to observe better the physics of the transition process itself.
The objective of this work is to carry out an investigation of the free-stream disturbance environment of the VKI H3 test section jet by means of classical intrusive measurements techniques such as hot-wire anemometry and Pitot pressure probes, provided with fast response pressure transducers. Another important objective is the implementation of these technique for this facility and an evaluation of their effectiveness in measuring the unsteady properties of the flow.

2. Experimental Setup

2.1. VHI H3 Mach 6 Hypersonic Wind Tunnel

All experiments have been performed in the H3 Hypersonic Wind Tunnel of the von Karman Institute for Fluid Dynamics (Fig. 3).

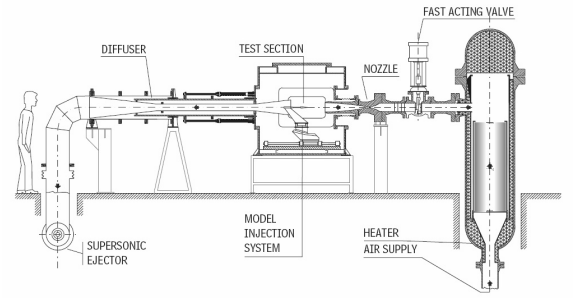

Figure 3: VKI H3 Hypersonic Wind Tunnel schematics

The VKI H3 test facility is a blow-down to vacuum type wind tunnel. It can provide a uniform axisymmetric jet with a diameter of 12 cm at Mach 6. Dried air is supplied from a 40 bar reservoir, which can provide stagnation pressures ranging from 7 to 35 bar. Air is heated up to a total temperature of 500 K to avoid condensation in the test section. The Reynolds number of the flow can be varied between $3 \cdot 10^6$ and $30 \cdot 10^6$ m^{-1}. The wind tunnel is provided with a model injection mechanism to avoid blockage of the wind tunnel and also to avoid excessive heating of the model itself during the start-up. The test chamber is vacuumed prior to the test using a supersonic ejector. The wind tunnel model is injected once the Mach 6 free-jet is fully established.

2.2. Dual Hot-Wire Anemometry Setup

As reported extensively in literature [13; 14; 15], a hot-wire in supersonic/hypersonic flow is sensitive to two flow variables: mass-flow (ρu) and total temperature (T_0). In order to separate the contribution of these two variables in the hot-wire output, a simple probe containing a single wire is not sufficient: a special setup needs to be used. A good paper comparing two typical setups for hot-wire measurements in high speed flows is by Walker and Walker [15]. In the present work the use of a dual hot-wire probe is chosen. A picture of the probe setup is reported in Fig. 4.

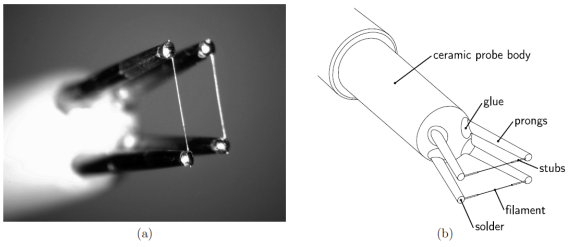

Figure 4: Hot-wire Probe Picture

In the dual hot-wire anemometry technique, the two hot-wires are heated at a different overheat ratios: in the present case, two tungsten 6.7% platinum plated wires are used. Due to the oxidation problems, it was not possible to set the overhat ratio to a value higher than 1.4. In order to have a certain difference between the two overheat ratios, the lower overheat is set to 1.1.
The static calibration procedure of the dual wire probe is an essential feature of the hot-wire anemometry procedure. For low overheat ratios, Smits [13] suggests to use the following relation among the hot-wire voltage, the mass flow and the total temperature:

$$E^2 = C_1\, T_0^{a+1} + C_2\, T_0^{a} + C_3\, T_0^{a-1} + (\rho\, u)^n \left(C_4\, T_0^{a-n\,b+1} + C_5\, T_0^{a-n\,b} + C_6 T_0^{a-n\,b-1}\right). \quad (1)$$

For the present problem it is assumed that a=b=0.768 and n=0.55. Chosen the form of the calibration relation, the calibration procedure provides the coefficients $C_1, C_2 ... C_6$, present in Eq. 1. The procedure is schematized in Fig. 5. The determination of the coefficients is carried out for each single wire and exploits a solution in the least-squares sense. The calibration tests are performed "in situ", since it is very difficult to reproduce in a pilot facility the extreme conditions encountered both for mass-flow and total temperature during a test in the VKI H3 Wind Tunnel. An example of the calibration routine is synthesized in Fig. 5.

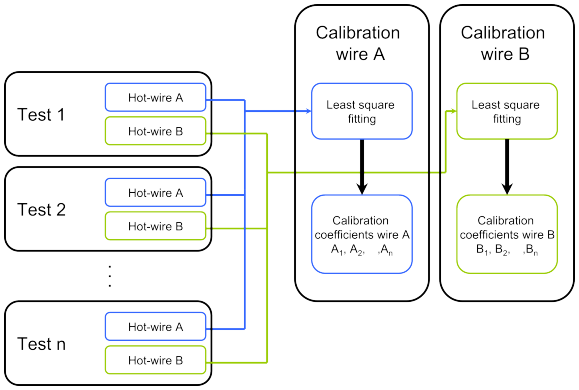

Figure 5: Schematic of the Hot-Wire Calibration Procedure, by means of the approach developed by Smits [13]

Once the calibration coefficients are determined, it is possible to reconstruct the instantaneous mass-flow and total temperature signals from the direct hot-wire outputs by means of the procedure schematized in Fig. 6. As it is possible to see, this procedure involves the solution of a non-linear system of equations, for each instant, i.e. for each time series sample.
A dynamic calibration for each anemometer system is carried out at ambient conditions, reproducing the condition for mass-flow encountered during a test in the VKI H3 Wind Tunnel. This procedure reveals a frequency response of 25 kHz for the system with overheat ratio 1.4 and 10 kHz for the system with overheat ratio 1.1. More details are reported in Spinosa [1].

2.3. Pitot Pressure Measurement Setup

Pitot pressure measurements are carried out by means of a classical Pitot tube, incorporating a fast response pressure transducer, flush mounted on its upstream extremity. The used transducer is a Kulite

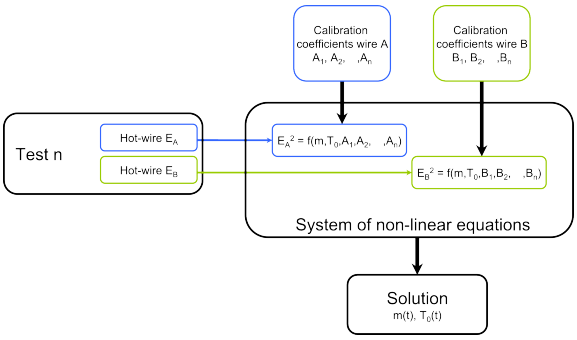

Figure 6: Schematic of the Hot-Wire Variable Contribution Separation, by means of the approach developed by Smits [13]

XCE-093-50A (B screen) made for harsh environment and with a wide temperature capability. The pressure sensing principle is based on an active four-arm strain gage bridge diffused into a sculptured diaphragm for maximum sensitivity and wide-band frequency response. The Pitot pressure probes are placed in the Pitot rake support, also used for placing the hot-wire. In Fig. 7 a sketch of this support mounted in front of the VKI H3 nozzle.

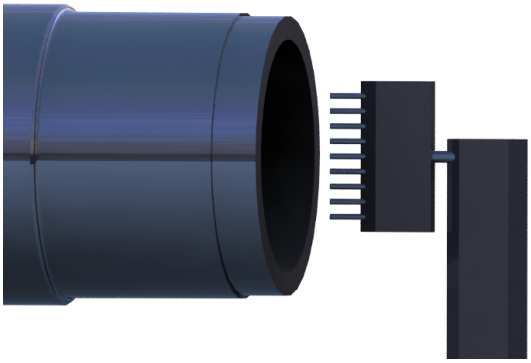

Figure 7: Pitot rake in front of the VKI H3 nozzle

During a test in the VKI H3 Wind Tunnel, the Pitot probe undergoes an important effect of aerothermodynamic heating, due to the stagnation point downstream the normal shock. Since the miniature pressure transducer is directly facing the stagnation point, the temperature of its electronic chip changes during a test, and can differ about 50-100K from the ambient temperature. Therefore a static calibration of the transducer at ambient conditions is not valid, since it is well known that the transducer response strongly depends on temperature. This dependence can be explained by the differing thermal coefficients of the resistive components on the Kulite diaphragm that lead

to an unbalancing of the sensor bridge[1]. These effects result in an offset (zero drift) of the pressure transducer calibration law derived at ambient conditions, as well as a change of the sensitivity (scale or span drift), leading to a substantial under or over-estimation of the measured pressure. This change in sensitivity can be corrected and compensated by means of an adapted calibration technique, developed at Oxford University [20] and at VKI [18; 17]. The technique is based on the assumption that the coefficients of the linear calibration law for a pressure transducer (slope and offset) depend also linearly on the temperature of the transducer chip; this assumption has also been verified by the Oxford University group [20]. Keeping this into account, calibration tests can be performed during a transient, in which both pressure and temperature change. In particular, in the present work, the calibration tests are carried out in transient phase before, during and after the injection of the probe in the hypersonic jet. In order to monitor the variations of the chip temperature during this transient, an electronic circuit developed by the Turbomachinery and Propulsion Department and built at the VKI Electronic Laboratory is used. A conceptual schematic of the circuit is reported in Fig. 8. As it is possible to see, in this circuit a resistor is placed in series after the Wheatstone bridge circuit: this particular design provide two output:

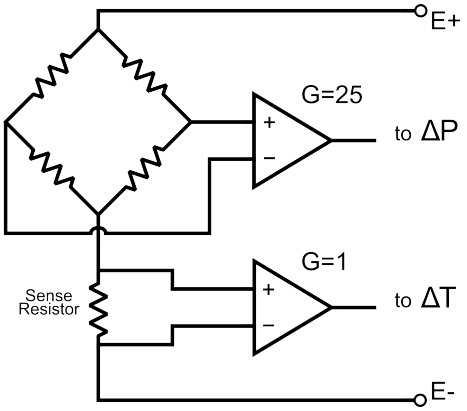

Figure 8: Compensation circuit for piezoresistive pressure transducer calibration and tests [17]

- the first one (indicated with ΔP in Fig. 8) is the standard fast-response transducer voltage output, referred to as V_P;
- the second signal (indicated with ΔT in Fig. 8) is proportional to the chip temperature: this voltage signal is also low-pass filtered, since due to the thermal capacity of the chip, oscillations greater than 10Hz are not expected to be significant: it is referred to as V_T;

Together with the fast-pressure probe flush mounted on a Pitot tube, a second Pitot tube, closely placed to the first one, has been used. This second Pitot tube is simply connected with a pneumatic to an absolute pressure transducer located outside of the test section. The latter is not affected by any temperature effect and can be used as an 'in situ' reference for the Pitot pressure.

Assuming the coefficients of calibration linearly dependent on temperature, it is possible to search for a calibration relation for the fast-response pressure transducer of the form:

$$P_{Ku} = (\mathrm{AA}\, V_T + \mathrm{AB})\; V_P + (\mathrm{BA}\, V_T + \mathrm{BB})\,. \qquad (2)$$

These coefficient are computed by means of an optimization routine,which minimizes the following objective function, representing a non-dimensional form of the quadratic deviation of the fast-response pressure from the target pressure:

$$\text{Objective Function} = \sum^{N} \left[\frac{(P_{Ku} - P_{PZ})^2}{P_{PZ}^2} \right] \qquad (3)$$

where N is the number of points for which the routine is applied (usually a subset of the original signal data points). The minimization is carried out using a Nelder-Mead Simplex Direct Search method.

3. Experimental Results

Freestream disturbance measurements are carried out along the centerline of the VKI H3 Wind Tunnel. The fluctuations of the flow quantities are supposed to be uniform in the potential core of the test section jet: this hypothesis has not been proven yet for the VKI H3 Wind Tunnel, but similar results are found in literature, for example in Wagner [21] for a hypersonic Mach 5 jet and therefore can be considered valid also for the present case. Tests are repeated for different unit Reynolds numbers.

3.1. Hot-wire Anemometer Measurements

Hot-wire measurements are conducted along the centerline of the hypersonic free-jet st 10mm downstream of the nozzle exit. As specified in section 2.2,

[1] moreover, temperature entails a non-linear expansion of the transducer housing and the generation of other non-symmetrical forces.

tests are both used for the calibration and for the disturbance characterization: data are acquired simultaneously by means of the Data Acquisition System, at a sampling frequency of 500 kHz during an observation time of 0.5 seconds. The frequency response of the two systems is different, but in any case, no anti-aliasing filter is needed, since the frequency response of the wires is much lower than one half of the sampling frequency used. In the present paper, only results obtained by means of the calibration law proposed by Smits for each wire are reported (see section 2.2), indeed this method is considered the most reliable, since its derivation starts from physical arguments, unlike other empirical approaches. The application of other methods for the calibration of the hot-wire probe is reported in Spinosa [1]. Disturbance analyses are conducted on tests for which the reconstructed mean values for mass-flow and total temperature do not depart much from the actual values measured by means of the instrumentation placed in the VKI H3 settling chamber. Since the low overheat ratio wire system has a frequency response of 10 kHz, before processing each signal, a digital low-pass filter with 10 kHz band-width is applied to both direct output signals: so, the information above 10kHz are not used.
Statistical analyses are carried out on the mass-flow and total temperature signals in order to provide information about the intensity of the fluctuations of the two flow quantities. In Fig. 9 the normalized RMS of the mass-flow and total temperature fluctuations measured with the hot-wire probe are reported as a function of the freestream unit Reynolds number.

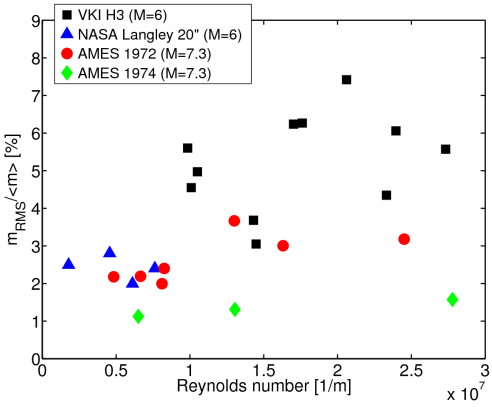

(a) Normalized RMS value of the mass-flow

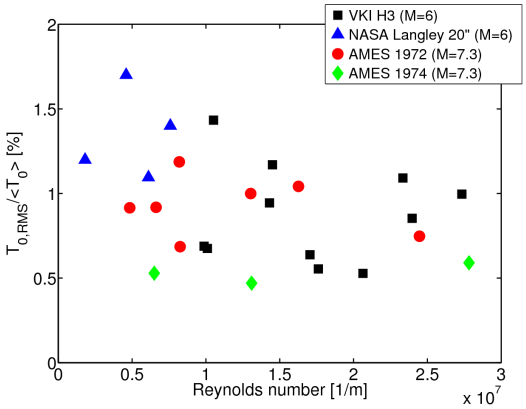

(b) Normalized RMS value of the total temperature

Figure 9: Normalized RMS value of the mass-flow and total temperature, measured by means of the double Hot-Wire probe as function of the Unit Reynolds number: Smits calibration law

The values of the normalized mass-flow RMS are around 5%, while the values of the normalized total temperature RMS are around 1%. It is possible also to see that the mass-flow fluctuations and the total temperature fluctuation do not show a definite trend, therefore do not have any dependency on the Reynolds number. As reported in Stainback [23], for supersonic/hypersonic wind tunnels the low level of total temperature fluctation is generally based on the hypothesis that the predominant fluctations are coming from radiated sound. At a Mach number of 6, this assumption leads to the conclusion that the total temperature fluctuations are around 3% and 4% of the mass-flow fluctuation. In this case their value is around 15% of the mass-flow fluctuations. Just as in the study carried out by Stainback on the Mach 6 Langley Research Center 20-Inch Wind Tunnel, there can be two possible explanations:

- there is a systematic error in the computation of the total temperature fluctuations;
- the total temperature fluctuations are not only related to the radiated sound disturbance mode.

The fact that the flow is heated in the reservoir upstream and that there is no thermal equalizer system in the wind tunnel suggests that the 'high' value (compared with Stainback results) of the total temperature fluctuation can be related to the entropy spottiness mode. Similar results are already been observed [23]. In Fig. 10 and 11 are shown the power spectral density for the hot-wire direct output signals not yet filtered. The power spectral density is computed by means of the Welch Periodogram Method with intervals of 2^{16} points and an overlapping of 25%. The term 'noise' refers to an acquisition carried out just before the test itself, without flow but with hot-wire

conditioner turned on: this acquisition gives information about the electronic and environmental noise sensed by the electronics.

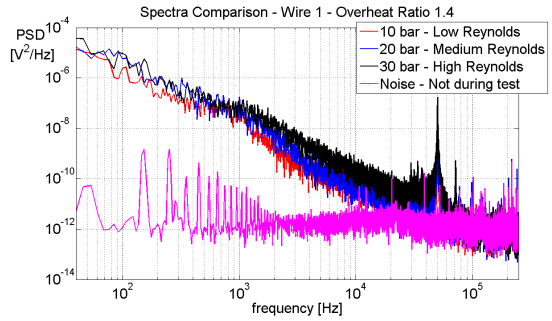

Figure 10: Power Spectral Density for noise and signal coming from the high overheat wire, for the three fundamental Reynolds number cases

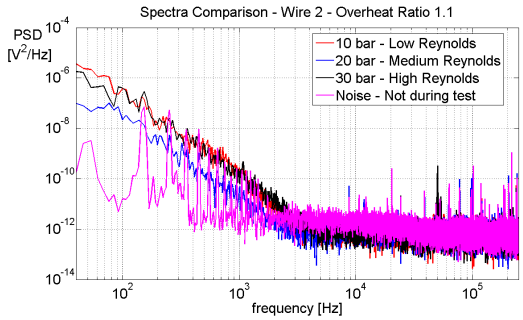

Figure 11: Power Spectral Density for noise and signal coming from the low overheat wire, for the three fundamental Reynolds number cases

The graph in Fig. 11 immediately shows the different frequency response of the two hot-wire systems: in particular the power spectral density of the low overheat ratio wire system shows a flattening of the PSD around 5 kHz, a lower value than expected from the dynamic calibration. This consideration has to be taken into account as another source of error in the disturbance measurements. It is interesting to observe how the power spectral density levels are much lower for the second wire than for the first wire. In the low overheat case, the background noise is likely to disturb the frequency content of the signal in a more important way, in other words the signal to noise ratio is lower for the low overheat ratio wire than for the high overheat ratio wire. This consideration is important since a higher signal to noise ratio may affect the measurement procedure. Indeed, it is possible to see how some peaks in the noise spectrum, being representative of the electronic and environmental noise of various nature have the same intensity as the voltage frequency content.

In Fig.s 12 and 13 the power spectral density distributions for the the mass-flow and total temperature fluctuations are reported, up to 10 kHz.

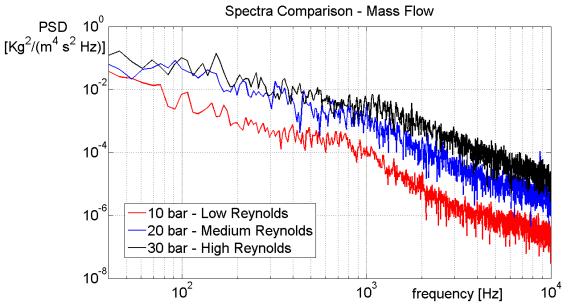

Figure 12: Power Spectral Density for Mass-flow signal, for the three fundamental Reynolds number cases

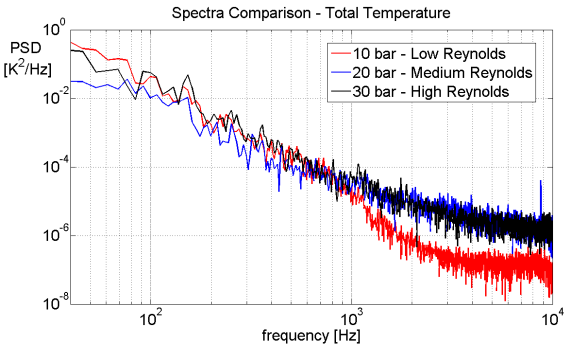

Figure 13: Power Spectral Density for Total Temperature flow signal, for the three fundamental Reynolds number cases

From the spectral analysis it is possible to verify the observations already done in the statistical analysis: indeed, for the mass-flow spectra it is possible to see a difference both in the frequency content and in the frequency band of the disturbances between the low Reynolds case and the medium and high Reynolds case; for the latter case also high NRMS values are observed. No particular trend appears as far as the total temperature fluctuations are concerned. It is possible anyway to see how the frequency contents tends to extend in this case as the Reynolds number increases, due to the the presence of a turbulent boundary layer on the nozzle wall.

3.2. Pitot Pressure Measurements

Pitot pressure measurements are carried out by means of the instrumentation described in section 2.3.

For each test, two active probes are inserted in the rake; the one incorporating the Kulite pressure transducer is mounted on the probe placed along the centerline of the nozzle and of the test section. The streamwise distance between the probe tip and the nozzle exit is about 10mm. The pneumatic reference Pitot probe is displaced spanwise of 12mm respect to the centerline [2]. During each test, the two outputs are recorded by means of a National Instrument PXI System and sampled at 1MHz during an observation time of 5 sec. Since the natural frequency of the Kulite pressure transducer is much lower than the the half of the sampling frequency, no anti-aliasing filter is needed.

In Fig. 14(a) the normalized RMS, briefly indicated as NRMS is plotted against the Unit Reynolds number of the flow, computed from the VKI H3 settling chamber measurements. NRMS values are around 1.6 %. As it possible to see, the NRMS have a linear inverse dependency from the unit Reynolds number which is coherent with the theory of the stabilizing effect of the incresing Reynolds number. Similar results were also obtained by Stainback et al. [22; 21; 30] for the NASA Langley Mach 5 Wind Tunnel and more recently by Lafferty et al. [31] in the AEDC Hypervelocity Wind Tunnel. In Fig. 14(b) the Pitot pressure fluctuation of the VKI H3 Wind Tunnel are compared with the amplitute of fluctuation measured by Stainback in the Langley Mach 5 Wind Tunnel, as can be seen the level of pressure fluctuations are very well matching as well as the decreasing trend of the amplitude caused by the Reynolds number stabilizing effect. A similar comparison can be done between the VKI H3 and the AEDC Hypervelocity Wind Tunnel in Fig. 14(c), where again the level of pressure fluctuations are very well comparable and in particular they are lower (in the order of 60%) respect to the fluctuations obtain in AEDC at higher Mach numbers. Stainback [30] stress the point that the disturbance field of a hypersonic wind tunnel is mainly dominated by the sound radiated from the boundary layer developing on the nozzle walls, it consequently has a preferred orientation, that is very close to the Mach angle direction. Therefore, the probe in the flow-field is sensitive mostly to the disturbances that originate from the turbulent boundary layer on the nozzle walls. In Fig. 15 the power spectral density of the signals is reported

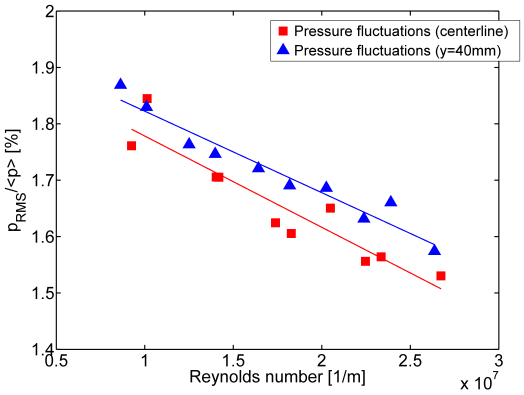

(a) Unit Reynolds number dependency

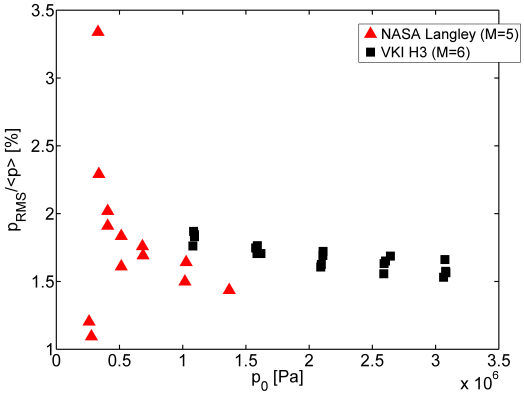

(b) Comparison with results from Stainback et al. [30]

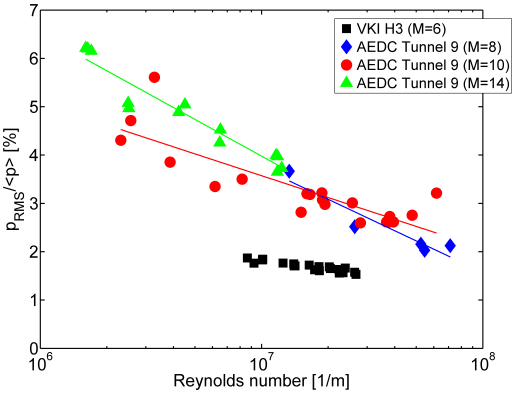

(c) Comparison with results from Lafferty et al. [31]

Figure 14: Pitot pressure fluctuations

[2] as mentioned before, is possible to assume that the mean values and the fluctuating values of the flow quantities do not vary in the potential core of the jet itself [21], consequently the two measurements should provide equivalent results.

against the wavenumber in double logarithmic scale. The power spectral density (PSD) is computed by using the Welch Modified Periodogram Method, with a number of points per interval equal to $2^{16} = 65536$ and with an overlapping of 25% in each interval.

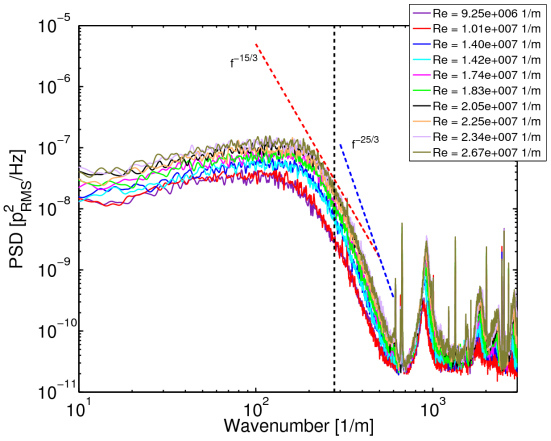

Figure 15: Power Spectral Density of the Pitot pressure signal

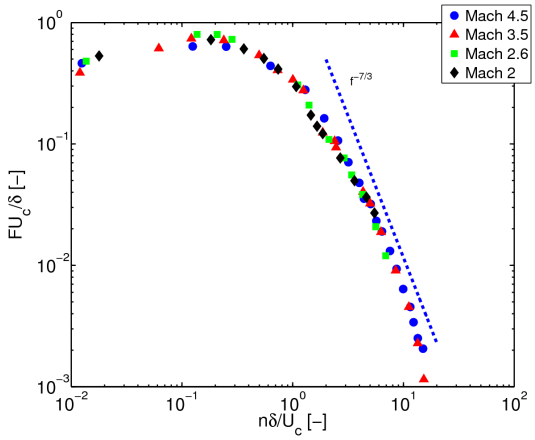

Figure 16: Energy spectrum of pressure fluctuation for various supersonic Mach numbers (from Laufer [32])

Peaks in the PSD are clearly present around a wavenumber[3] of $900m^{-1}$, corresponding to a frequency of about 135kHz. These peak are possibly related to the Helmholtz resonance of the cavity between the external screen, that shields the transducer, and the actual sensor membrane. Some preliminary calculations have shown that the order of magnitude of the resonance frequency is the same as the frequency of these peaks. However, the Helmholtz frequency depends strongly on the local speed of sound and therefore on the local temperature of the cavity: this temperature depends on the viscous effects, and this may be the reason why the small shift in frequency of the peaks is directly related to the Reynolds number. To correctly analyze the PSD in Fig. 15 we have also to take into account the transducer's size effect. The pressure transducer output is proportional to the integrated pressure force on its active area, effectively averaging out fluctuations with characteristic wave length smaller or comparable to the probe tip size. A simplified hypothesis can be applied, yielding a first-hand estimation of the probe high frequency response. Supposing an active probe diameter of about 1.8mm which yield a wavenumber of about $560m^{-1}$, assuming that the Nyquist theorem is also applicable to the wavenumber, the probe high wavenumber (frequency) response is $280m^{-1}$ (42kHz).

For every Unit Reynolds case, the PSD shows an almost flat response until about 150-200m^{-1}, after which it starts to decrease, as it is expected in a freestream turbulence. Considering the high wavenumber response limit of the probe (vertical black line in Fig. 15), the energy decay for wave numbers between 200-300m^{-1} follows a trend around $f^{-15/3}$, while for wavenumbers between 300-600m^{-1} the energy decay is steeper (around $f^{-25/3}$). In any case the energy decay $f^{-15/3}$ of the pressure fluctuations in the VKI H3 Wind Tunnel is above the classical Kolmogorov's $k^{-7/3}$ law for pressure fluctuations decay (see George et al. [33]). Considering the results obtain by Laufer [32] and reported in Fig. 16, he obtain after a suitable normalization, a decay of the energy spectrum for pressure fluctuation under supersonic flows which follows a trend of $f^{-7/3}$ and he proved that such a decay is typical for a noisy supersonic wind tunnel which is dominated by eddy Mach waves. Comparing the initial decay (before the transducer high frequency response) of the pressure energy spectra in the VKI H3 with the ones reported by Laufer for his supersonic wind tunnel, the VKI H3 Wind Tunnel provide a slightly turbulent hypersonic free-jet core, with a less important influence of the eddy Mach waves. Nevertheless, the VKI H3 Wind Tunnel is still a conventional noisy wind tunnel affected by disturbances with relatively wide range of frequencies (up to 200m^{-1} or 30KHz); this broadband frequency content is typical of the acoustic disturbances in the flow and provide a verification of their dominant sound-wave nature.

[3] recalling the wavenumber as $k = 2\pi f/v_p$, where v_p is equal to the freestream velocity (≈940m/s)

4. Combined Data Reduction Methodology

In the framework of this work a combined data reduction methodology has been developed. This technique can allow to estimate the level of fluctuation of all the flow quantities, from those directly measurable through the above mentioned instrumentation. Indeed in the compressible case the turbulence description of a flow at a point is more complicated than in the incompressible case: all the flow variables show a certain degree of fluctuation, usually non predictable a priori. The characterization of all variable fluctuations is a difficult task, but it can be performed under certain hypothesis. This procedure is also outlined in Owen and Owen [3; 26] and it has been also revisited in Spinosa[1]. The developed combined methodology is valid under the following hypothesis:

- the hypersonic free jet is locally isoentropic;
- the measurements are done in a steady state flow so the statistical properties of the fluid variables are not time dependent, whereas time-series analysis does;
- the pressure fluctuations measured by the Pitot probe downstream the normal shock wave can be directly related to the static pressure fluctuations of the freestream.

With these hypothesis, the following equations are used:

$$\begin{aligned} m &= \rho\, u \\ p &= \rho\, R\, T \\ C_P\, T_0 &= C_P\, T + u^2/2 \end{aligned} \tag{4}$$

introducing the Reynolds decomposition for all the variables involved and neglecting higher order terms[4] we obtain the following set of equations:

$$\begin{aligned} \frac{m'}{\overline{m}} &= \frac{\rho'}{\overline{\rho}} + \frac{u'}{\overline{u}} \\ \frac{p'}{\overline{p}} &= \frac{\rho'}{\overline{\rho}} + \frac{T'}{\overline{T}} \\ \frac{T_0'}{\overline{T}_0} &= \alpha\, \frac{T'}{\overline{T}} + \beta\, \frac{u'}{\overline{u}} \end{aligned} \tag{5}$$

[4]the same results can be easily obtained by using the so-called logarithm derivative approach, used in Morkovin [25]: in this approach the logarithmic derivative of each side of the equation is taken and the differential terms are interpreted as a small disturbance: results are analogous to Reynolds decomposition and elaboration

where

$$\begin{aligned} \alpha &= \left(1 + \frac{\gamma - 1}{2}\, M^2\right)^{-1} \\ \beta &= (\gamma - 1)\, M^2\, \alpha \\ M &= \frac{\overline{u}}{\sqrt{\gamma\, R\, \overline{T}}} \end{aligned} \tag{6}$$

The system of equations (5) has six unknowns, if $\frac{m'}{\overline{m}}$ and $\frac{T_0'}{\overline{T}_0}$ are measured in the core of the wind tunnel jet by means of the hot-wire anemometer and $\frac{p'}{\overline{p}}$ are measured by a pressure probe, then it is possible to compute all the other fluctuation variables by solving the linear system (5) (3 equations and 3 unknowns). To successfully apply the combined data reduction methodology, the pressure measurements coming from the Pitot probe have to be manipulated. Using the Pitot-Rayleigh equation (see Anderson [29]),the Pitot pressure can be directly related to the freestream static pressure with the following:

$$p = \frac{2\, p_{pitot}}{C_p \gamma M^2 + 2} \tag{7}$$

where

$$\begin{aligned} C_p \;=\; & \frac{2}{\gamma\, M^2}\left[\frac{(\gamma+1)^2\, M^2}{4\,\gamma\, M^2 - 2(\gamma - 1)}\right]^{\gamma/(\gamma-1)} \\ & \left[\frac{1 - \gamma + 2\,\gamma\, M^2}{\gamma + 1}\right] - 1 \end{aligned} \tag{8}$$

The results from the combined data reduction process are shown in Fig. 17.

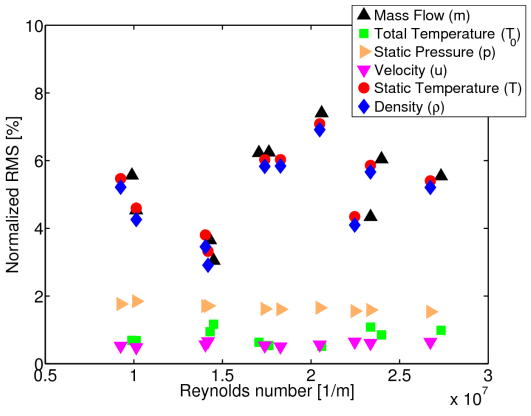

Figure 17: Combined data reduction methodology results

Fluctuations of the static temperature and density are closely related to the fluctuations of mass flow

(between 3% and 7%), while velocity fluctuations are stable around 0.6% for the increasing unit Reynolds number. Indeed, if we consider the manipulated continuity equation 5 and that $\frac{u'}{\bar{u}} < 1$, than $\frac{m'}{\bar{m}} \approx \frac{\rho'}{\bar{\rho}}$, for the same reason, considering the law of the perfect gas, the density is function of the static pressure and the static temperature, therefore if $\frac{p'}{\bar{p}} \approx 1$ than $\frac{m'}{\bar{m}} \approx \frac{\rho'}{\bar{\rho}} \approx \frac{T'}{\bar{T}}$. Resuming, mass flow fluctuations, total temperature fluctuations and pressure fluctuations in the freestream are respectively in the order of 5.2%, 0.8% and 1.7%; while derived quantities like density fluctuations, static temperature fluctuations and velocity fluctuations are in the order of 4.9%, 5.2% and 0.6%.

5. Conclusions

An experimental characterization of the freestream jet of the VKI H3 Wind Tunnel was carried out by means of classical intrusive techniques: for this propose, mass flow, total temperature and pressure fluctuations are measured using a double hot-wire probe and Pitot pressure probe in combination with data reduction technique.

Mass-flow fluctuations show larger values respect to the total temperature fluctuations, respectively around 5.2% and 0.8%. As far as the total temperature fluctuations are concerned, it is possible to notice that their values are smaller than the mass-flow fluctuations, but they are not as small as they would be if the radiated sound was the only dominant characteristic of the disturbance field. This consideration, together with the fact that the VKI H3 Wind Tunnel does not have any thermal equalizing system, leads to think that also the entropy spottiness mode can have an important role in the freestream disturbance of the freestream jet. Mass flow fluctuations show a bigger amplitude compared with other hypersonic facilities in the same Mach number range, the reason is also associated with entropy fluctuations in the flow.

Pitot measurements have shown the classical trend expected for the supersonic-hypersonic wind tunnel facilities. Since the disturbance field is dominated by sound waves radiated by the turbulent boundary layers on the nozzle wall, this sound has a preferred orientation, that is close to the Mach wave direction. The normalized Pitot pressure fluctuations are around 1.7% and show a decreasing trend with the increasing unit Reynolds number (stabilizing effect of the Reynolds number). Regarding the energy content in the spectra, a peak due to Helmholtz resonance is present around 135 kHz which is slightly increasing frequency with the increasing Reynolds number. After an almost flat energy content up to 30kHz, the energy start decaying with a slope close to $f^{-15/3}$, above the Kolmogorov's $k^{-7/3}$ law for pressure decay, this decaying is than becoming steeper ($f^{-25/3}$) after the high frequency response of the probe around 42kHz, which proves the impossibility for the setup used to resolve smaller wavelength. This energy decay is a sign of a slightly turbulent flow, or a laminar flow which strongly affected by nozzle wall generated noise (eddy Mach waves), as presented by Laufer [32]. Moreover the wide frequency content up to 30kHz in the power spectral density, is an indirect confirmation of the sound predominant disturbance mode in the flow, which is characterized by high frequencies.

The combined data reduction brings more information regarding the fluctuation of the fluid dynamic variables in the jet core. Fluctuations of the static temperature and density are laying between the 3% and 7%, while velocity fluctuations are in the order of 0.6%. The latter is a demonstration of the turbulent nature of the freestream flow, but its very low value of turbulence intensity suggest a slightly turbulent flow. Resuming, the VKI H3 Wind Tunnel is a conventional noisy wind tunnel with a very low turbulence intensity, however affected by sound-wave disturbances (eddy Mach waves) with a relatively wide range of frequencies and a bigger amplitude if compared with entropy and vorticity fluctuations.

References

[1] Spinosa E. - *Experimental Characterization of the Disturbance Level of the VKI H3 Wind Tunnel*, VKI Project Report 2010-32

[2] Morkovin M.V., Reshotko E., Herbert T. - *Transition in open flow systems* - APS, Volume 39, Issue 9, 1994

[3] Owen F.K, Owen A.K. - *Measurements and Assessment of Wind Tunnel Flow Quality*, Progress in Aerospace Sciences, Vol 44, pp. 315-348, 2008

[4] Saric W., White E.B., Reed H. - *Boundary Layer Receptivity to Freestream Disturbances and Its Role in Transition*, AIAA Paper 1999 - 3788

[5] Kovasznay L.S.G. - *Turbulence in Supersonic Flow*, Journal of Aeronautical Sciences, Volume 20, N.10, October 1953

[6] Morkovin M.V. - *On Transition Experiments at Moderate Supersonic Speeds*, Journal of the Aeronautical Sciences, 1957

[7] Schneider S.P. - *Development of Hypersonic Quiet Wind Tunnels*, Journal of Spacecrafts and Rockets, Vol. 45, No. 4, July-August 2008

[8] Laufer J. - *Aerodynamic Noise in Supersonic Wind Tunnels*, Journal of the Aerospace Sciences, Vol. 28, No. 9, September 1961, pp. 685 - 692

[9] Phillips O. M. - *On the generation of sound by supersonic turbulent shear layers*, Journal of Fluid Mechanics, Vol. 9, pp 1-28, 1960

[10] Ffocks-Williams J.E. , Maidanik G. - *The Mach wave field radiated by supersonic turbulent shear flows*, Journal of Fluid Mechanics, Vol. 21, pp. 641-657, 1965

[11] Morkovin M.V. - On Supersonic Wind Tunnels With Low Free-Stream Disturbances, Journal of Applied Mechanics, Vol. 26, pp. 319-323, 1959.

[12] Pate S. R. , *Effect on Wind Tunnel Disturbances on Boundary Layer Transition, with Emphasis on Radiated Noise: a Review*, ARO INC ARNOLD AFS TN, available at http://handle.dtic.mil/100.2/ADA384962

[13] Smits A.J., Hayakawa K., Muck K.C. - *Constant Temperature Hot-Wire Anemometer Practice in Supersonic Flow*, Experiments in Fluids, Vol 1, pp. 83 - 92, 1983

[14] Spina E.F. , McGinley C.B. - *Constant Temperature Anemometry in Hypersonic Flow: Critical Issues and Sample Results*, Experiments in Fluids, Vol 17, pp. 365 - 375, 1994

[15] Walker D.A., Ng W.F., Walker N.D. - *Experimental Comparison of Two Hot Wire Techniques in Supersonic Flow*, AIAA Journal, Vol 27, N.8, pp. 1074 - 1080

[16] Smith D.R., Smits A.J. - *Simultaneous Measurement of Velocity and Temperature Fluctuations in the Boundary Layer of a Supersonic Flow*, Experimental Thermal and Fluid Sciences, Vol 7, pp. 221-229, 1993

[17] Arts T., Sieverding C. H., Denos R., Brouckaert J.F. *Measurement techniques for unsteady flows in turbomachines*, Experiments in Fluids Vol. 28, pp. 285-321, 2000

[18] Denos R. - *Influence of temperature transients and centrifugal force on fast response pressure transducers* - Experiments in Fluids Vol 33, pp. 256-264, 2002

[19] Ainsworth R.W., Miller R.J. , Moss R.W. and Thorpe S.J. - U*nsteady pressure measurement Measurement Science and Technology*, 11 (7). pp. 1055-1076. ISSN 0957-0233

[20] Ainsworth R. - *Recent Development in Fast Response Aerodynamic Technology* - VKI LS 1995-01, Measurement Techniques, Von Karman Institute for Fluid Dynamics, 1995

[21] Wagner R.D. *Mean Flow and Turbulence Measurements in a Mach 5 Free Shear Layer*, NASA Technical Note N-D-7366, Langley Research Center, Virginia, U.S., 1973

[22] Stainback P.C., Anders J.B., Keefe L.R., Beckwith I.E. - *Sound and Fluctuating Disturbance Measurements in the Settling Chamber and Test Section of a Small, Mach 5 Wind Tunnel*, 6th ICIASF (International Congress on Instrumentation in Aerospace Simulation Facilities)

[23] Stainback P.C., Kubendran L.R. - *The Measurement of Disturbance Levels in the Langley Research Center 20-Inch Mach 6 Tunnel*, NASA CR 4571, 1994

[24] Logan P. - *Modal Analysis of Hot-Wire Measurements in Supersonic Turbulence*, AIAA-Paper 1988-423, 26th Aerospace Sciences Meeting, Reno, NV, Jan 11-14, 1988

[25] Morkovin M.V. - *Fluctuations and Hot-Wire Anemometry in Compressible Flow*, AGARDograph 24, Nov. 1956

[26] F.K. Owen - *Transition and Turbulence Measurements in Hypersonic Flows*, AIAA Second International Aerospace Planes Conference, 29-31 October 1990/Orlando, FL, AIAA Paper 90-5231

[27] Biagioni L., d'Agostino L. - *A Pressure Based Method for Turbulence Measurements in Hypersonic Flow*, 18th ICIASF International Congress on Instrumentation in Aerospace Simulation Facilities, Toulouse France, 1999

[28] Biagioni L., d'Agostino L. - *Measurement of Energy Spectra in Weakly Compressible Turbulence*, AIAA Paper 99-3516, 30th AIAA Fluid Dynamics Conference, 1999

[29] Anderson J.D. - *Hypersonic and Hugh Temperature Gas Dynamics*, 2nd edition, McGraw Hill, 1990

[30] Stainback P.C., Wagner R.D. - *A Comparison of Disturbance Levels Measured in Hypersonic Tunnels using a Hot-wires Anemometer and a Pitot Pressure Probe*, AIAA Paper 72-1003, 1972

[31] Lafferty John F., Norris Joseph D. - *Measurements of Fluctuating Pitot Pressure, Tunnel Noise, in the AEDC Hypervelocity Wind Tunnel No. 9*, US Air Force T&E Days, 2007

[32] Laufer John - *Sound Radiation From a Turbulent Boundary Layer*, Mecanique de la Turbulence, Colloques Internationaux du CNRS, No. 108, 1962

[33] William K. George, Paul D. Beuther, Roger E.A. Arndt - *Pressure spectra in turbulent free shear flows*, Journal of Fluid Mechanics, 148, pp. 155-191, 1984

Stability of hypersonic flows in chemical equilibrium

Fabio Pinna

Aeronautics and Aerospace Department, fabio.pinna@vki.ac.be

Supervisor: Patrick Rambaud

Professor, Aeronautics and Aerospace Department, Belgium, rambaud@vki.ac.be

Promotor: Paolo Orlandi

Professor, Dipartimento Meccanica e Aeronautica, Via Eudossiana 18, 00184, Roma, Italy, paolo.orlandi@uniroma1.it

Promotor: Renato Paciorri

Professor, Dipartimento Meccanica e Aeronautica, Via Eudossiana 18, 00184, Roma, Italy, renato.paciorri@uniroma1.it

Abstract

Space vehicles flying at very high speed suffer from extreme aerodynamic heating, which is further increased in case of turbulent flow. A correct estimation of the laminar to turbulent transition help to understand where the heating peaks will be produced. In this regard a stability study is strongly related to the transition prediction. In this report the problem of high speed flow stability is addressed showing the influence of chemical reaction in the stability of high Mach number flows.

Keywords: hypersonics, transition, stability, chemical equilibrium

1. Introduction

Following the renewed interested in hypersonic vehicles and the recent European challenge of the EXPERT flying test bed, the transition community is more and more involved in the study of stability of flows at hypersonic speeds. A number of effects should be considered when treating a real vehicle aerodynamics such as shocks, geometry, catalicity at the wall, chemical reactions. Of course the relative weight of one aspect with respect to the others depends on the particular conditions to be studied. When temperature exceeds 2000K air can not be considered as a single gas any longer because at that temperature oxygen starts dissociating and at 4000K nitrogen dissociates too. It is evident that neither calorically perfect gas model (i.e. constant specific heat) nor a thermally perfect gas (i.e internal energy, enthalpy, and specific heats are functions of temperature only) are realistic models of those situations. Owing to the typical temperatures of an hypersonic flows it is then recommendable to treat air as a mixture of the single dissociated species. As the flow energy increases air could be described as in chemical equilibrium, where reaction are fast enough to adapt to the thermodynamic conditions, chemical non equilibrium where reaction are slower and therefore far from the equilibrium composition and in thermo-chemical non equilibrium where molecules are highly excited and their internal energy state cannot be described anymore by a single temperature. This modelings are correlated with the altitude as the higher the vehicle is flying the faster it goes. Because of this, transition is more likely to happen where only chemical equilibrium is valid and therefore only this aspect will be considered in this report.

2. Governing equations

Linear stability theory for compressible flow with chemistry is not qualitatively different from what is done usually to compute the stability of compressible flows. Anyway when the flow is in chemical equilibrium thermodynamic and transport properties de-

pend on two thermodynamic variables. Because of this, once the usual decomposition has been applied to the Navier-Stokes equation

$$Q(x,y,z,t) = \overline{Q}(x,y,z) + q'(x,y,z,t); \qquad (1)$$

the result is linearized with respect to the mean flow and finally perturbations are represented by:

$$q'(x,y,z,t) = \tilde{q} \cdot \exp(i\alpha x + i\beta z - i\omega t) + c.c.\ ; \qquad (2)$$

the amplitude function of the thermodynamic and transport variables are written as depending on pressure and temperature perturbations following what is done hereafter for the viscosity.

$$\mu' = \frac{\mathrm{d}\mu}{\mathrm{d}T}T' + \frac{\mathrm{d}\mu}{\mathrm{d}p}p'. \qquad (3)$$

An air-5 mixture (N_2,O_2,N,O,NO) is used in the present work to compute the rates and the flow properties, and the gas state equation is re-written as

$$p = \rho r T \zeta; \qquad (4)$$

where r is the gas constant for the undissociated gas $N_2 - O_2$ mixture and $\zeta = M_{und}/M_{dis}$ is the so called compressibility factor.
Navier-Stokes equations have been non-dimensionalized using reference quantities: length is scaled by $l = \sqrt{\nu_e x_e / U_e}$, velocity by U_e, density by ρ_e, pressure by $\rho_e U_e^2$, time by l/U_e, and temperature by T_e. The reference viscosity (both first and second coefficient) is, for sake of consistency, the value corresponding to T_e and p_e. The final equation could be find in [1]. As in the caloricaly perfect gas counterpart these system of equations could be represented as

$$\left[AD^2 + BD + C\right]\phi = 0 \qquad (5)$$

being $\phi = [\tilde{u}, \tilde{v}, \tilde{p}, \tilde{T}, \tilde{w}]$ and $D = \mathrm{d}/\,\mathrm{d}y$ the derivative operator.

2.1. thermodynamic and transport properties

In order to solve the stability equations the thermodynamic and transport properties are needed. For this purpose the MUTATION library is used [2]. This library could run interactively or inside a shell script thanks to its front-end (called MUTATION code). As the flow computed is in chemical equilibrium all the desired properties could be computed once and for all as their value is depending only on p and T
Partial derivatives with respect to temperature and/or pressure are obtained by computing first the selected property on a range of p and T spaced according to Chebyshev spacing

$$y = \cos\left(\frac{\pi(2j+1)}{2(N+1)}\right); \qquad (6)$$

where N is the total number of points, and in a second step by deriving the interpolants

$$u(x)'_{interp} = \sum_{n=0}^{N-1} a_n^{(1)} T_n(x) \qquad (7)$$

where

$$a_n^{(1)} = \frac{2}{c_n} \sum_{\substack{p=n+1 \\ p+n \text{ odd}}}^{N} p a_p \quad \text{where} \qquad c_n = \begin{cases} 2 & n = 0 \\ 1 & n > 0 \end{cases}. \qquad (8)$$

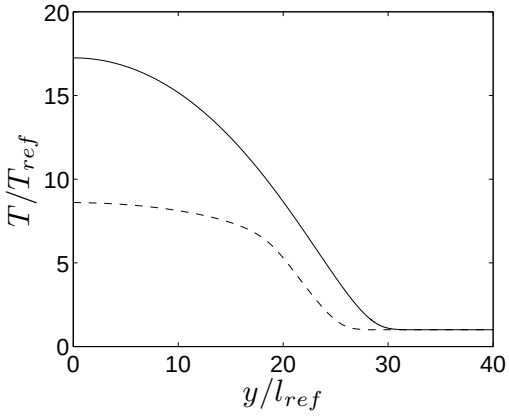

Figure 1: non-dimensional temperature profile for Mach 10 flow at $Re_l = 2000$ T_e 350K: ---- LTE, —— CPG

3. Stability of a compressible flow on a flat plate at Mach 10

For comparison purposes a hypersonic flat plate case is presented at the same conditions as the one reported in [3]. This is a simple flat plate at Mach 10 $Pr_\infty = 0.69$ with $Re_{c_\infty} = \frac{\rho_\infty c_\infty L_{ref}}{\mu_\infty} = 10^4$, $T_\infty = 350K$, $p_\infty = 3596Pa$. The mean flow has been computed by a shooting method and the main difference between the two cases are displayed in Fig. 1 and Fig. 2.

In the LTE case the boundary layer is thinner and looking at the temperature profile the maximum temperature is about half of the calorically perfect gas.

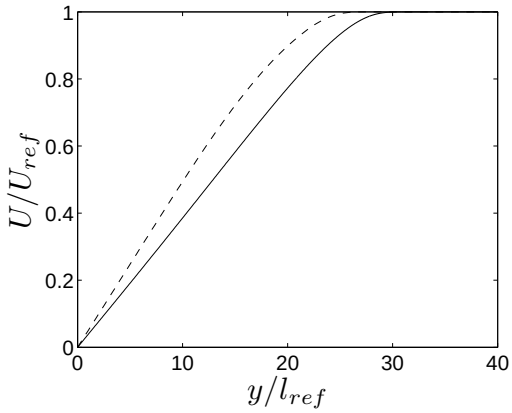

Figure 2: non-dimensional profiles for Mach 10 flow at $Re_l = 2000$ T_e 350K: - - - - LTE, ——— CPG

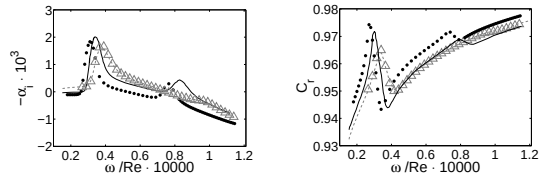

(a) growth rate (b) phase velocity

Figure 3: $Re_l = 2000$, $\omega = 0.068$, $\beta = 0$, Mach 10, comparison with Malik's computation: present LTE •, Malik's LTE ——— , present CPG △, Malik's CPG - - - -

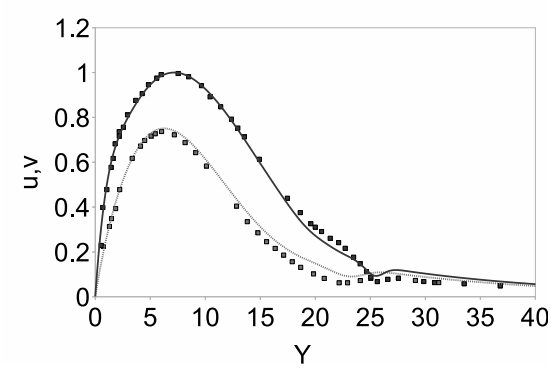

Figure 4: stream wise and wall normal velocity perturbation profiles referred to the most unstable mode for a Mach 10 flow at $Re_l = 2000$ and $\omega = 0.068$: ■ DNS, ——— LST

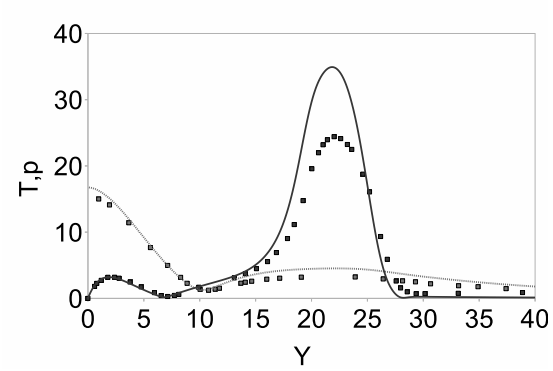

Figure 5: temperature and pressure perturbation profiles referred to the most unstable mode for a Mach 10 flow at $Re_l = 2000$ and $\omega = 0.068$: ■ DNS, ——— LST

This is due to the increase of specific heat with temperature. Summarizing, chemical equilibrium properties act a first time on the velocity and temperature profile modifying their shape. As we already explained they also affect the stability equations as it is possible to see in Fig. 3.
The perfect gas computations match perfectly with the one performed in [3] while the LTE calculations show a slight shift toward lower frequencies. This is probably due to the differences in the transport and thermodynamic properties. It should also be noted that the overall behavior is recovered with the appearance of the third mode (not showing in the CPG cases) and a higher peak in the growth rate due to the second mode. The same test case has been proposed in [4] and a comparison taken from [1] is shown in Fig. 5. The DNS and LST computation use the same properties provided by the library MUTATION and therefore it is an interesting case as usually researchers cannot access the same data and the same libraries. The overall agreement for pressure, and velocity is very good while the temperature shows a little overshoot with respect to the DNS computation.

3.1. Effect of pressure

The effect of temperature is evident and intuitive, furthermore, looking at Fig. 8 and Fig. 9, it could seem that the increase in temperature is overruling any other effect. This is not true and any intention of dropping the derivatives with respect to temperature to simplify the equations would not generally hold. Fixing the external temperature at $350K$ with $Re = 2000$ and spanning the pressure from $3596Pa$ to $8000Pa$ shows how the temperature profiles change. The Fig. 7, as expected, shows almost no influence of pressure on

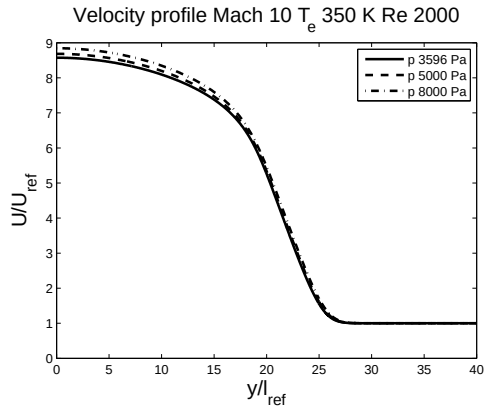

Figure 6: non-dimensional temperature profiles Mach 10 flow at $Re_l = 2000$ and T_e 350K

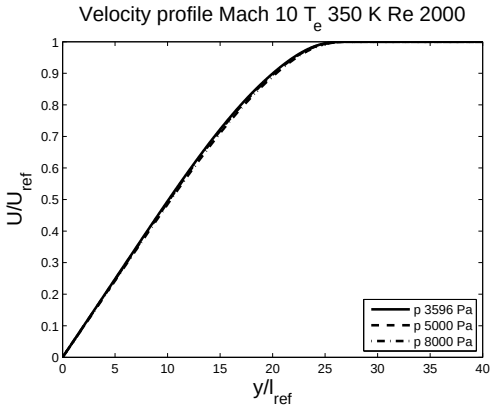

Figure 7: non-dimensional velocity profiles for Mach 10 flow at $Re_l = 2000$ and T_e 350K

the velocity profile. This is consistent with the comparison carried out in the previous section. In Fig. 6 the profiles are not superimposed one on top of the other clearly assessing that pressure plays a non negligible role. This justify *a posteriori* the splitting done in Eq. (3) and the statement that no further simplifications could be done. The unstable eigenvalues are displayed in Table 1

4. Neutral curves at hypersonic speeds

It is clear that by considering chemical reactions stability properties of the flow will change and this is reflected also in the neutral stability curve. Nevertheless these changes are strongly depending on the value of the thermodynamic variables. If, for instance, one takes the case of an hypersonic flow with an external

pressure Pa	ω
3596	1.15872e-1 +i3.91503e-4
5000	1.15849e-1 +i3.88952e-4
8000	1.17399e-1 +i1.72125e-3

Table 1: eigenvalues varying with pressure

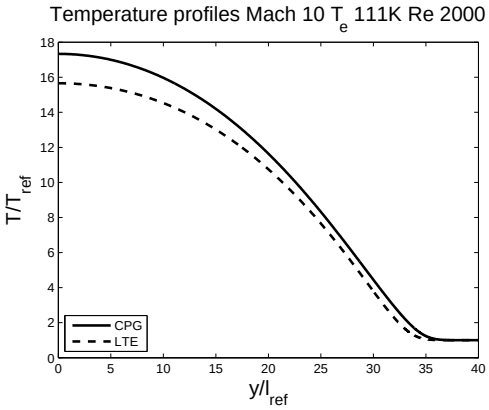

Figure 8: non-dimensional temperature profiles Mach 10 flow at $Re_l = 2000$ and T_e 111K

temperature of $111K$ profile variations are not as dramatic as the one in Fig. 1 and they are displayed in Fig. 8 and in Fig. 9 . Because of this we do not expect to see big variations on the neutral stability curve plot and as matter of fact only few differences can be spotted in the Fig. 10 and Fig. 11. Nevertheless it is possible to note a lower critical Reynolds number and an overall more stable lower branch. The last statement is an agreement with the general effect attributed to chemical reaction while the lower Re_{cr} is totally contrasting with that. Anyway this does not represent a paradox as chemistry could play different roles with different modes.

5. Conclusion

In this short paper the new capabilities of the VKI Expandable Stability and Transition Analysis toolkit (VESTA) for hypersonic flow in chemical equilibrium are presented. A brief outline about the effects that chemical reactions induce on the stability of hypersonic flow is shown with a comparison with DNS and previous LST codes.
The most important effect is due to the high temperature of these kind of flow; when the temperature is low, stability features of the flow differ only slightly

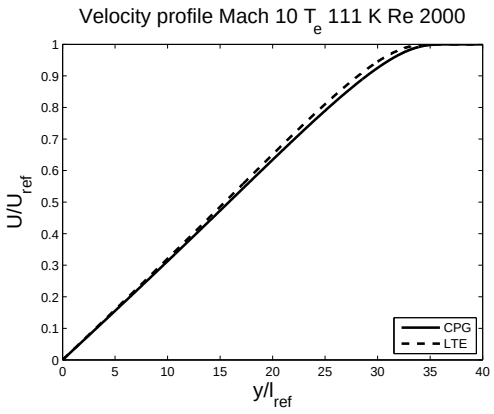

Figure 9: non-dimensional velocity profiles for Mach 10 flow at $Re_l = 2000$ and T_e 111K

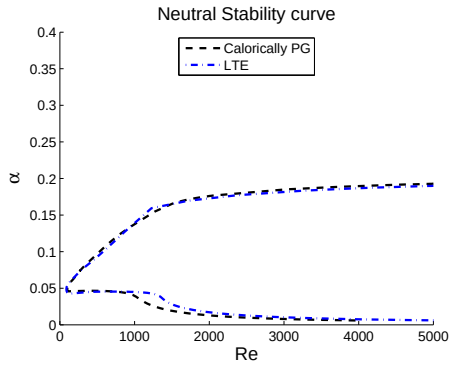

Figure 10: Neutral stability curve for Mach 10 at T_e 111K:

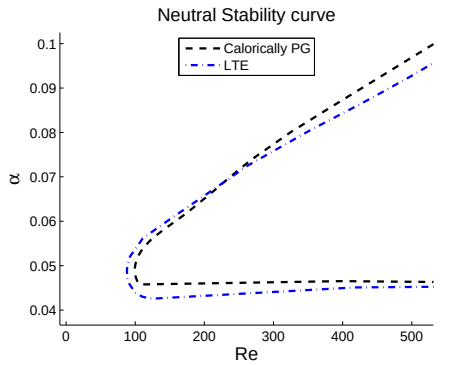

Figure 11: Neutral stability curve for Mach 10 at T_e 111K: zoom in the critical region

form the calorically perfect gas behavior.
At high temperature chemistry modifies substantially the temperature profile and this causes the instability to shift toward lower frequencies. On the other hand pressure plays a minor role with respect to temperature but it is not negligible.
Similarly to what happens in a supersonic flow where the so-called second mode pops up, becoming dominant in specific conditions, chemistry enhances the third mode allowing it to appear and eventually to be unstable, thus modifying the overall stability properties of the flow.

References

[1] F. Pinna, K. Bensassi, P. Rambaud, O. Chazot, A. Lani, O. Marxen, Development of an integrated methodology for the post-flight analysis of the transition payload on the expert mission, in: CTR Summer Program, proceedings, 2010.

[2] T. Magin, G. Degrez, Transport algorithms for partially ionized and unmagnetized plasmas., Journal of Computational Physics 198.

[3] M. R. Malik, E. C. Anderson, Real gas effects on hypersonic boundary-layer stability, Physics of Fluids A 3 (5) (1991) 803–820.

[4] O. Marxen, T. Magin, G. Iaccarino, E. S. Shaqfeh, Hypersonic boundary-layer instability with chemical reactions, in: AIAA (Ed.), 48th AIAA Aerospace Sciences Meeting, no. AIAA 2010-707, AIAA, AIAA, 2010.

Design and qualification of a supersonic wind tunnel for transition experiments

Henny Bottini

Turbomachinery and Propulsion Department, bottini@vki.ac.be

Supervisor: Guillermo Paniagua

Associate Professor, Turbomachinery and Propulsion Department, von Karman Institute for Fluid Dynamics, Belgium, paniagua@vki.ac.be.

Abstract

The design of a quiet wind tunnel for supersonic transition experiments at different Mach numbers is presented. Its features for attaining a low-disturbances environment are described.The design and the instrumentation of two test models are presented. The qualification procedure to assess its performance in terms of Mach and Reynolds numbers and in terms of quietness is illustrated.

Keywords: transition, turbulence, supersonic flow, wind tunnels, design

1. Introduction

The present paper describes a wind tunnel designed for supersonic boundary-layer transition experiments. The transition process should be both natural and enhanced by the presence of a single squared roughness element located along the centerline of the test article. The Mach number range for these experiments will be $1.8 \div 3$, a range within which there is a particular dearth of data on transition. The data from the single roughness experiments will serve to validate DNS computations and to provide physical understanding.

Boundary layer prediction and control are vital for any hypersonic aircraft intake. In particular, at the intake where pressure gradients and shocks appear the boundary layer should be kept attached. A turbulent boundary layer is more robust than a laminar one, but the higher aerothermal losses must be properly accounted for in the combined vehicle-engines design. Consequently, transition experiments are needed to show the location and the mechanisms to establish the turbulent boundary layer tripped by the single roughness. Experiments are focused on the understanding of the turbulence onset, specifically on the birth, growth, and evolution of turbulent spots, and for this reason a basic test article, a flat plate, has been selected.

This kind of experiments, however, requires a facility that does not interfere with the transition process on the test article. At the considered supersonic Mach numbers, the facility must not produce strong pressure fluctuations. Namely, the RMS in pressure should be less than 1% of p_∞ [1]; additionally the velocity fluctuations should be bounded [2]. Otherwise, their influence on the transition process would be so heavy that the experimental data could not be extrapolated to real-flight conditions [3]. It has been proven [3] that the main cause of pressure fluctuations inside the test section of a supersonic wind tunnel is the turbulent boundary layer on the test section walls, which radiates pressure disturbances onto the test article. Therefore, the solution for having meaningful transition experiments is to keep the boundary layer laminar on those walls, that is, to have a "quiet wind tunnel". More than one feature must be implemented to reach quietness, and the present paper describes those selected for our wind tunnel. The paper also describes how the test articles have been instrumented to perform the transition experiments, and the planned way to qualify the wind tunnel and assess its quietness.

2. Compression-tube facility

The linear cascade compression-tube of the Von Karman Institute, CT-2, is an isentropic, short-duration blow-down facility, designed to test turbomachinery airfoils.

The heated pressurized air is supplied to the test section by a 5-m long, 1-m diameter compression

tube. The process by which the high-pressure-driven light-weight piston compresses and thus heats the air is nearly isentropic. As soon as the operating conditions are established, a fast-acting shutter valve is opened and the air is discharged through the test section. If the volumetric flow rate which is supplied by a high pressure reservoir is equal to that leaving through the test section, a constant pressure can be maintained in the test section (typically with a running time of $\Delta t \in [0.1 - 0.8]\ s$).

The general arrangement has been partially modified for the present experiments. Notably, air is vented out to atmosphere through a low-noise device instead of collected into a dump tank. Additionally, a new 2D nozzle with a straight divergent geometry has been designed. The dump tank is used as a component of the bleed system at the throat of the nozzle that is one of the new features of this wind tunnel expressively conceived to make it "quiet". The 2D nozzle has been placed in the existing casing whose overall dimensions were fixed. This has yielded a series of constraints on its design (fixed width) and on the design of the test models (maximum length) (Figure 1).

Total temperature and total pressure are measured and recorded just before the beginning of the test, as well as the pressure in the dump tank. The latter values will track the good functioning of the bleed system.

2.1. The aspiration system

The bleed system will work thanks to the presence of an aspiration system that assures the required mass flow. This system is comprised of a large tank beneath the test section of the wind tunnel linked to the bleed slots through tubes and the void part of the casing downstream of the slots throat. The tank will be evacuated of air just before the test and isolated from the slots as long as the test starts. At that moment the connection will be established and air will be automatically sucked in from the slots by pressure difference. To check the correct function of this system, the tank and the tube will be instrumented as to measure the mass flow through the slots.

3. Test section for supersonic experiments

3.1. Design

The requirement of operations at different Mach numbers has imposed the design of movable ramps to select the angle of the divergent part of the nozzle, keeping the throat area practically unchanged. A further constraint was the inability to modify the existing casing of the test section, hence a mechanism for vertical movements had to be used (Figure 1).

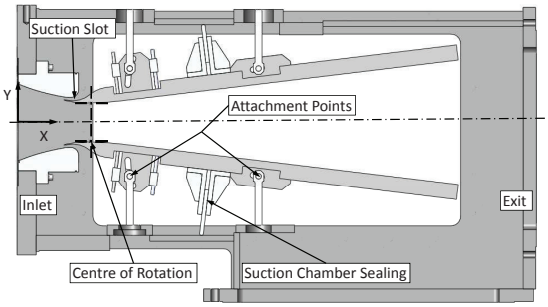

Figure 1: The test section and the mechanical arrangement of its movable ramps

Wind tunnels for transition experiments should assure a rather limited amount of disturbances to the boundary-layer flow along the test article not to alter its natural transition process. In case of supersonic flows [2; 3], the most dangerous of these disturbances are pressure fluctuations (noise) radiated by the turbulent boundary layer developing on the walls of the wind tunnel. Then the most straightforward method to avoid these pressure disturbances is to keep the boundary layer laminar on those parts of the wind tunnel from where it could radiate noise onto the test article. This is achieved by using, chiefly, bleed slots just upstream of the throat of the nozzle and fine wall polishing. Both solutions have been implemented in the present research and are complemented by the use of straight walls for the nozzle divergent.

3.2. Straight nozzle-walls selection

Straight nozzle walls have a positive effect on the quietness of the wind tunnel. In fact, if the bleed slots just upstream the nozzle throat serve to hinder disturbances from the convergent to travel and contaminate the boundary layer in the divergent, straight walls in this part of the nozzle avoid altogether the birth of disturbances in the laminar boundary layer. These disturbances are of a special kind and are called Taylor-Görtler vortices.They are counter-rotating vortices created by centrifugal instabilities in viscous regions.

Taylor, first discovered this effect in 1923, investigating the flow in the sept between two rotating cylinders. As regard as wind-tunnel flows then, in supersonic nozzles (De Laval nozzles) the uniform test region is customarily achieved by concave walls,

so that the laminar boundary layer there experiences centrifugal forces as it flows along. Therefore, the Taylor-Görtler instability is found in supersonic nozzles, showing up in their boundary layer as illustrated by Figure 2. Furthermore, it has been shown in [4]

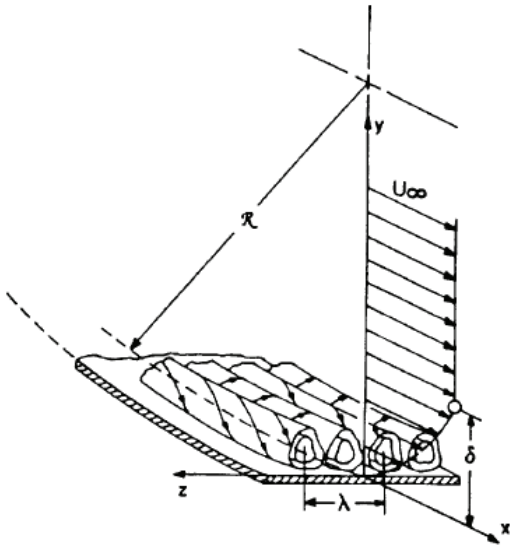

Figure 2: The Taylor-Görtler vortices on a concave wall

that boundary-layer transition on the walls of nozzles is due mainly to the Taylor-Görtler instability rather than Tollmien-Schlichting waves, so delaying and/or limiting the growth of the Taylor-Görtler vortices become essential to prevent the boundary layer from becoming turbulent.

If one wanted to keep the concave shape, the delaying could be achieved by using a straight contour for the initial part of the diverging supersonic section (no curvature, no instability), and the mitigation by lengthening the divergent section of the nozzle. The result is called the "quiet rhombus" (Figure 3)

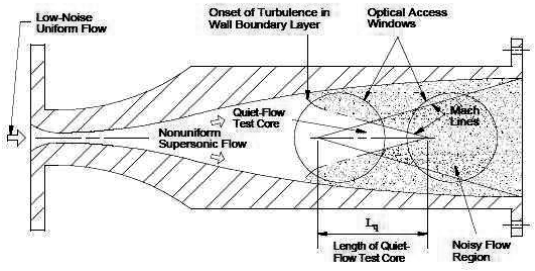

Figure 3: The quiet rhombus

i.e. a quiet region in the test section where the test article will not experience any perturbation from the turbulent boundary layer on the nozzle wall, while the flow still features constant Mach number. This rhombus is drawn by two Mach lines starting from the exit edges and the Mach lines traced from the location on the nozzle where turbulence sets on, as well as the lateral boundaries that are found with Mach lines originating from the sidewalls transition-onset locations.

In the present case, instead, the Taylor-Görtler instability does not appear at all because of the use of straight walls (ramps) for the nozzle. This solution, as said in the preceding, was dictated by the need of operating at different Mach numbers, and offers as side effect this important advantage in terms of "quietness". Of course, the draw back of this solution is that the test article cannot be in a region of uniform and constant Mach number: this will vary (increase) along it. And the quantification of this increase is to be made to assess the importance of its effects.

3.2.1. Pressure gradient along the test article and its effects on the boundary layer flow

The flat plates to be used in the experiments will be placed between the ramps that constitute the divergent part of the nozzle. This means that the flow along them will experience a positive pressure gradient, i.e. an acceleration. Now, the main purpose of the experiments to be performed in the quiet wind tunnel is the study of turbulent spots evolution, so it is mandatory to understand what effects, and in what extent, this positive pressure gradient will have on the generation and evolution of turbulent spots.

Turbulent spots are the manifestation of the last stage of turbulence onset in a laminar boundary layer, thus their occurrence depends on how, and on whether, the preceding stages occur. The first of these stages is instabilities growth within the laminar boundary layer, and, even if more work is in need for the full understanding of it, some of its key mechanisms have been set clear, at least about its initial linear part. Among these mechanisms there is the benevolent effect of a positive pressure gradient on the stability of the boundary layer (e.g. [5]). That is a positive pressure gradient delay transition, so, for what concerns here, it delays the appearance of turbulent spots.

But a second effect of a positive pressure gradient, directly on the length of the zone where the spots evolve, has experimentally been observed as well. This appears in the fashion of a lengthening of

this zone respect to the case of pressure gradient absence. These observations concerned low- and high-speed flows ([6; 7]), while hypersonic flows on cones featured the opposite effects, i.e. the evolution zone shortened ([8]).

Jacks in [6] offers a criterion for the evaluation of this lengthening for flows on axial-symmetric bodies and, for want of a better suited criterion, this has been used here to evaluate the effect of the positive pressure gradient on the flat plate as well. The parameter to be computed for this criterion is the pressure gradient along the length of the body expressed as $\frac{d}{dx}(\frac{p}{p_0})$, which in this case has been approximated as $\frac{p_{back}-p_{LE}}{p_{LE}\cdot L}$, with p_{back} the pressure at the back end of the plate, p_{LE} the pressure at the plate leading edge, and L the plate length. The following Figure 4 shows this parameter evaluated at different Mach numbers. The parameter value for which the transition-zone length increases of 54% respect to the case without pressure gradient is reported in [6], to be $-3.94m^{-1}$, so that the values in Figure 4 should mean a much milder effect for the present case. As complementary information, the Mach number increase along the flat plate is as maximum as +12% from the leading edge to the back end. In conclusion, the straight nozzle walls will have an effect on the phenomenon to be studied in the wind tunnel, but this effect should not be very heavy, and, perhaps, the avoidance of Görtler instability can well compensate it.

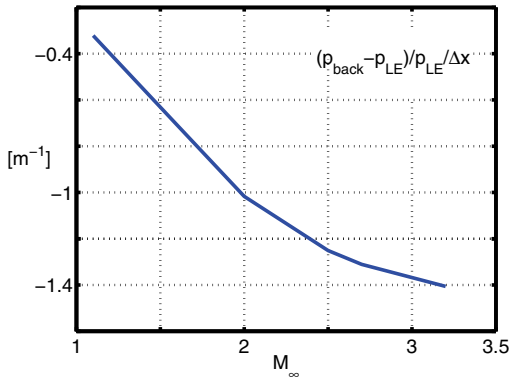

Figure 4: Jack's parameter at different Mach numbers for a flat plate

3.3. The bleed slots

Boundary-layer bleed slots are located upstream of the nozzle throat to ingest the boundary layer developed in the nozzle convergent with all the disturbances that may have developed in it. In so doing these disturbances do not endanger the laminar boundary layer along the divergent, which, in fact, starts anew from just downstream of the slots [4]. An example of bleed slots is in Figure 5. It is clear, then, that the slots



Figure 5: Example of bleed slots

should not produce disturbances in this new laminar boundary layer. The possible sources for these disturbances are recirculation bubbles on the slots surface and/or the suction system that makes the slots work. For the latter, the remedy is to assure a sonic throat in the duct downstream of the slot entrance so that no disturbances generated in the suction system cam move up into the wind tunnel flow. For the former, a special contour of the slot lip must be designed.

A recirculation bubble can be generated by two different suction regimes: strong and weak (Figure 6) [9]. For strong suction, a stagnation point will occur

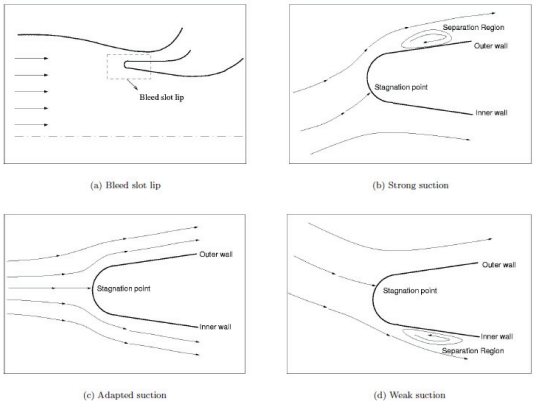

Figure 6: Typical flows around the lip of a bleeding slot

on the side of the bleed-slot lip toward the wind tun-

nel center-line (inner wall). Thus the subsonic boundary layer flow to be ingested by the slot experiences an acceleration around the lip tip just followed by a deceleration flowing downstream along the straight surface. This is the typical situation in which a recirculation bubble appears. For weak suction, however, the stagnation point moves to the outer surface of the lip, leading to a recirculation bubble on the inner wall. Both of these configurations can cause dangerous perturbations in the boundary layer flow heading to the test-section. The latter design may be particularly harmful because it creates noise directly in the downstream flow increasing the risk of early transition of the boundary layer on the tunnel walls. The case of strong suction could also cause perturbations in the main flow, if the mass flow through the slot becomes unsteady, causing flow oscillations on the stagnation point on the bleed lip. The adapted suction is the optimal design by which no separation due to bleed slot installation is observed [9]. Figure 6 shows a perfectly round lip, one of the first configurations to be used–and the simplest, but it was too prone to form highly unsteady recirculation bubbles. Therefore, it has been preferred to it a *modified super ellipse* contour described as

$$\left(\frac{y}{b}\right)^2 + \left(\frac{a-x}{a}\right)^m = 1$$
$$m = 2 + \left(\frac{x}{a}\right)^2$$

where, the origin is at the stagnation line and a and b are the major and minor axes of the ellipse. With this profile, the curvature goes continuously to zero as $x \longrightarrow a$ [10]. A fully semi-elliptical leading edge was eventually introduced in the Purdue University Mach-6 wind tunnel and its higher radius of curvature reduced effectively the adverse pressure gradient just aft of the lip tip. However,a discontinuity in curvature at the point of intersection between the fully semi-elliptical and the straight parts of the bleed occurs, and to avoid it the modified super ellipse contour has been proposed.

Figure 7 shows the streamlines and the pressure contours around the modified super-elliptical tip implemented in the pressent design of the slots lips as computed by CoolFLUID, our in-house Navier-Stokes solver. The simulation is for a flow at M_∞ = 2.8 at the model leading edge. This Figure shows that no laminar recirculation bubble is caused by the elliptical bleed tip. Figure 8 instead shows the velocity

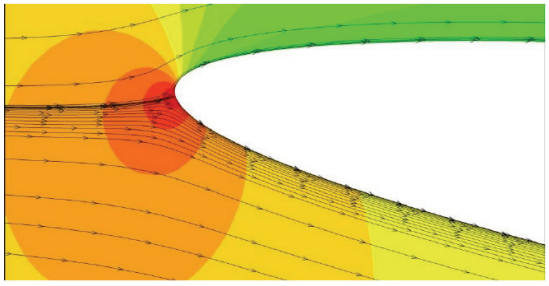

Figure 7: Streamlines and pressure contours around the lip tip for M_∞ = 2.8

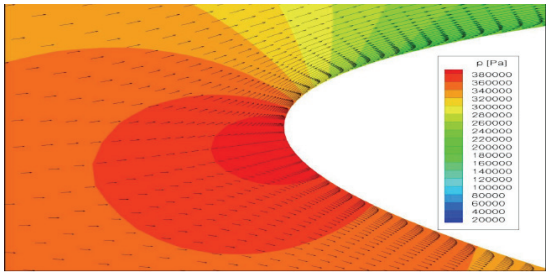

Figure 8: Velocity vectors and pressure contours at the lip tip for M_∞ = 2.8

vectors around the ellipse tip, together with the pressure contours. As can be seen, the stagnation point is slightly below the geometric tip. Finally, Figure 9 shows streamlines and pressure contours for M_∞ = 1.95 and this time a recirculation bubble is present on the upper side of the lip. The bubble extends for about 0.6 *mm* and its maximum height is about 0.05 *mm*.This bubble is due to the adverse pressure gradient experienced by the flow past the tip on the upper side of the lip. This gradient, in turn, is just caused by the angle of attack of the lip respect to the main flow as evident by the comparison of Figure 7 with Figure 9. For the reasons exposed in the preceding, this recirculation bubble may not endanger the quietness of the as long as it is not strongly unsteady. Only a verification of the nozzle performance can shed light on this matter.

3.4. Polishing of nozzle walls

Even the most sophisticated and performing boundary layer removal technique can result useless if not complemented by very highly polished nozzle surfaces. In fact tests showed that the wall and free-stream pressure fluctuations were found to scale with the mean wall shear for all Mach numbers [11]. Refining the smoothness of the nozzle from a RMS of 2-10

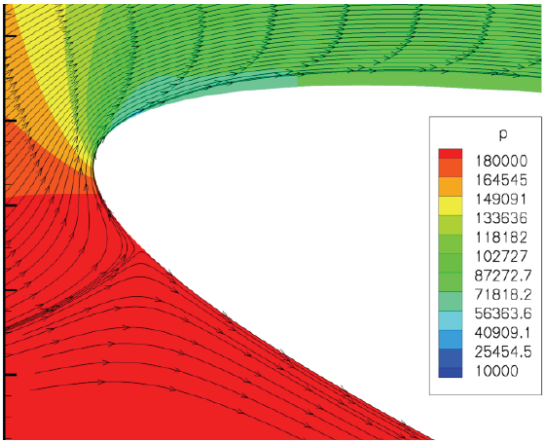

Figure 9: Streamlines and pressure contours showing a recirculation bubble on the upper side of the lip for $M_\infty = 1.95$

in. to a RMS of 1-3 in. improved the Reynolds number at which the NASA- Langley Mach-3.5 tunnel is quiet by a factor of two. High smoothness is deemed important especially for the throat surface.

The "aerodynamic smoothness" of a surface can be judged taking as reference height the thickness of the laminar sub-layer of a hypothetical turbulent boundary layer at the location of interest. (Of course, the hypothetical turbulent boundary layer has to be compatible with the properties of the flow under exam.) Then, a surface can be considered smooth if The RMS in the roughness height is less than the thickness of that laminar sub-layer [12].

Usually the thickness of the laminar sub-layer is $y^+ = 5 - 6$ (OlivariBenocciCN157) with

$$\begin{aligned} y^+ &= \frac{y \cdot u_\tau}{\nu} \\ u_\tau &= \sqrt{\frac{\tau_w}{\rho}} \\ \tau_w &= \frac{\rho_\infty u_\infty^2}{2} C_f \end{aligned}$$

Now the approximate maximum value for the C_f to be expected for $M_\infty \in [1 \div 3]$ can be evaluated as $5 \cdot 10^{-3}$, taking account of the expected total temperature, thus the expected Reynolds number. Then the height of the laminar sub-layer results in the range $6 - 11\ \mu m$.

The smoothness of the ramps was measured by a roughness-meter Mitutoyo SJ-201P in five different locations across its entire width (see Figure 10). This device works with an extremely thin pinpoint that passes along a predefined length on the surface whose smoothness has to be measured. As it passes,

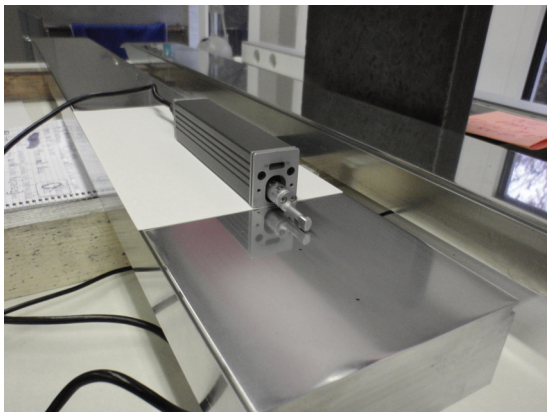

Figure 10: The roughness meter Mitutoyo SJ-201P on one of the nozzle ramps

the roughness displaces it vertically and this displacement is recorded and converted in the roughness measurement. In the present case, the measurements were repeated as to check repeatability, and two quantities, considered the most meaningful, have been recorded: the RMS, R_q, and the average value, R_a, of the roughness height. The roughness standard selected was ISO. The results are $R_a \in [0.06 \div 0.11]\,\mu m$ and $R_q \in [0.08 \div 0.14]\,\mu m$, i.e. two orders of magnitude less than the laminar sub-layer thickness. Therefore, one can judge the ramps surfaces smooth enough to prevent turbulence onset due to distributed roughness produced by the machining of the pieces.

The vertical side walls have been polished as well, but no quantification of the roughness height has been possible because the roughness-meter works only on horizontal surfaces, while these walls were kept vertical during the polishing. Their finishing is shown in Figure 11

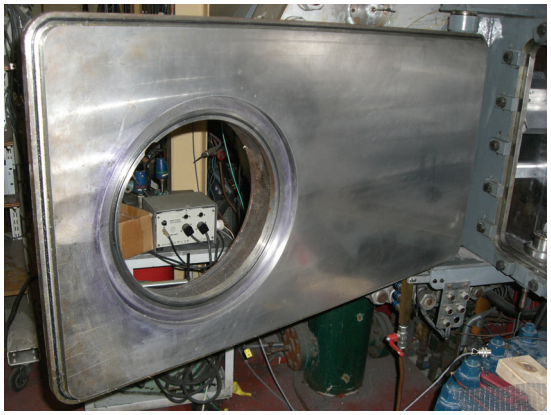

Figure 11: One of the wind-tunnel side walls after the polishing

4. Flat-plate test model

The boundary layer flow to be experimentally investigated is plane and supersonic, thus the test article for the experiments is a flat plate. Different techniques have been selected for these experiments and they will need a dedicated plate. Nevertheless all these plates feature the same round leading edge of 0.5 *mm* of radius and the same overall dimensions of 30 *cm* in length per 9 *cm* of width and 0.8 *cm* in thickness. The round leading edge has been chosen of that size as to be uniformly machined; in fact, there are experimental evidences[1] that a leading edge with nonuniform radius can trip transition in the boundary layer. The plate width is narrow enough to prevent the spreading on the plate of the boundary layer developing on the wind tunnel lateral walls. The thickness has been reduced as much as possible to avoid any possibility of wind tunnel blockage.

The plate will be hosted on a cantilever support along the center-line of the wind tunnel, with the possibility of adjusting its longitudinal and vertical position, as well as its angle of attack (Figure 12).

This cantilever solution was considered the cleanest possible from the point of view of blockage, but it could have posed a vibrations problem. This is because the facility to be used works impulsively and so are applied the aerodynamic loads on the test article. During this impulse the ensemble support plus plate may feature a transient response in which it can vibrate at its natural frequencies [13]. If these frequencies were in the range of the frequencies of the instabilities developing in the boundary layer, then they would alter the natural process of transition to turbulence.

In fact, according to Gedney [14], the effect of test article vibrations on the boundary layer flow developed on it can be dramatic. Depending on their phase they can sensibly amplify (in phase) or damp (out of phase) the TS waves evolving in the laminar boundary layer. This would be a major issue for the experiments, so that the possibility of its occurrence had to be analyzed.

The ensemble cantilever-plate-support has been idealized as a beam clamped on one end and with a weight on the free end. This weight simulated the weight of the plate and its support plus the aerodynamic load expected from the interaction of the entire

[1] M. Carbonaro personal communication

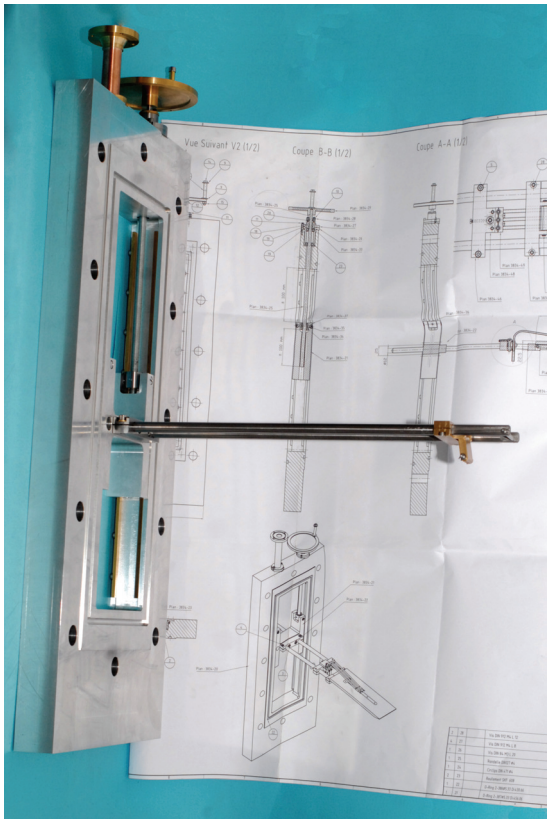

Figure 12: The plate support

plate with the flow. Then the natural frequency of vibration was calculated according to the formula [15]

$$f_n = \frac{1}{2\pi} \cdot \sqrt{\frac{3EI}{l^3(m_{free} + 0.23m_{beam})}}$$

The result is that the frequency of vibration to be expected is about 29 Hz. This value has been checked against linear-stability calculations found in literature [5], and resulted too low to interfere with the evolution of the TS waves. Therefore, the plate vibration should not vitiate the transition experiments. As a further precaution, one plate will be instrumented with an accelerometer to measure its vibrations, so to be aware of their real amplitude and frequencies.

4.1. The thin-films plate

The evolution of turbulent spots will be mainly tracked by the use of thirty thin-films on the surface of one flat plate. These devices have already been validated for this purpose and gave important results [16; 17]. In the present case, as said in the preceding, they have to be used for two plate configurations,

with and without a single roughness element. And the presence of this roughness has influenced heavily the location of the thin-films on the plate (Figure 13).

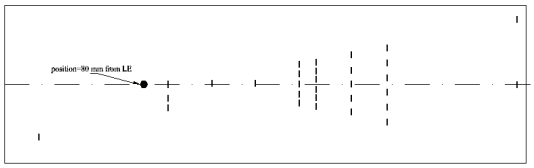

Figure 13: The arrangements of thin-films on the plate

Here we see that: one thin-film, just downstream of the leading edge, will be used as reference for the laminar condition; three thin-films will be used to estimate the lateral extent of the horse-shoe vortices developing from the roughness; two thin-films are located at the very back of the plate to sense the possible turbulent boundary layer; the majority of the sensors are arranged in four rows. These rows and the sensors in them are differently spaced to better track turbulent spots evolutions as from considerations about spots possible size at different Mach numbers and during their evolution (e.g., [18]).

4.2. The PCB plate

PCB are piezoelectric transducers capable of measuring pressure fluctuations up to frequencies of 1 MHz (Figure 14). These transducers work according to the piezoelectric effect, for which a crystal of a specific material produces electricity when under stress. This stress to the crystal is the pressure to be sensed. Since this electricity production is an ephemeral phenomenon, piezoelectric transducers will sense only pressure fluctuations and not the steady value. The electricity produced is then measured and the pressure value found by the use of a calibration curve.

The calibration curve is obtained by sensing with the transducer different single "pressure impulses". These are obtained by putting the transducer into a closed volume, a rubber ballon, whose internal pressure, p_{in}, can be adjusted by inflation with more or less air. Then the ballon is popped and the transducer senses the sudden pressure difference $\Delta p = p_{atm} - p_{in}$. The value of p_{in} is measured by a Kulite pressure transducer coaxial with the PCB.

Figure 15 shows the arrangement of the height PCB on the test article. They are hosted in an thermally-insulating insert as to be protected from the high wall



Figure 14: One of the eighth piezoelectric transducers PCB 132A3

temperatures to be set when testing the effects of different wall temperatures. This type of PCB can stand a maximum temperature of 80° Celsius.

This sensors arrangement is also dictated by the need of measuring pressure fluctuations in the wake of the single roughness as well as in the case of the clean plate. Here six out of eighth PCBs are located on the plate center-line to investigate the downstream evolution of the pressure fluctuations. And the remaining two form a three-sensor row at the end of the insert to provide a minimal spanwise resolution. Thus, spanwise resolution is somewhat sacrificed to streamwise resolution because of the total number of sensors available.

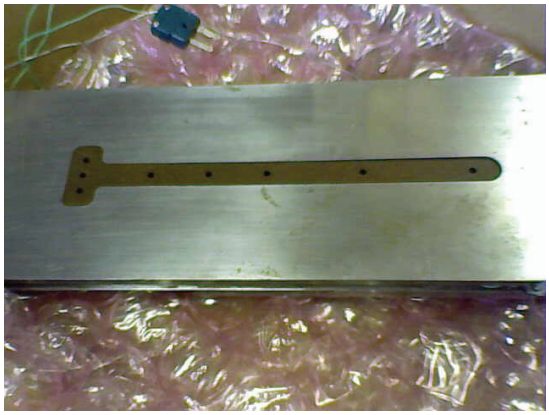

Figure 15: Arrangement of eighth piezoelectric transducers PCB 132A3 on the test article

5. Wind Tunnel Qualification

The qualification of the wind tunnel will start by assessing the achievable Mach range, and will be followed by the assessment of its degree of quietness.

For this second purpose the flat plate machined for PSP measurements has been modified as to be used as noise probe. The sensor of this probe is again a single PCB, whose location had to be estimated conveniently. In fact, a sensor flush-mounted on a flat plate can be used to measure noise, provided that the boundary layer on the plate at the sensor location is laminar, and that there is not a strong shock wave between the sensor and the noise source [19; 3]. The reason for the first condition is obvious: if a turbulent boundary layer flows above the sensor, the sensor will record its fluctuations and not those coming from the environment. The reason for the second is that a pressure fluctuation is altered in passing through a shock wave so to induce as a more biased noise measurements as stronger is the shock wave [20].

Both these issues can be dealt with by adjusting the sensor position on the plate as to have it close enough to the leading edge to be below a laminar boundary layer and far enough from it to be away from the strongest part of the bow shock. Figure 16 shows the shape of the bow shocks generated by the plate with a leading-edge radius of 0.5 *mm* for the lowest and highest Mach number of the range considered for the experiments. For each shock shape the Mach line corresponding to the given Mach number is also shown. The Mach line serves as a reference to estimate at what height from the plate surface the shock wave approaches intensity zero. This height is useful because as a shock wave fades into a Mach line its intensity goes to zero so its effect on the fluctuations passing through it becomes negligibly small.

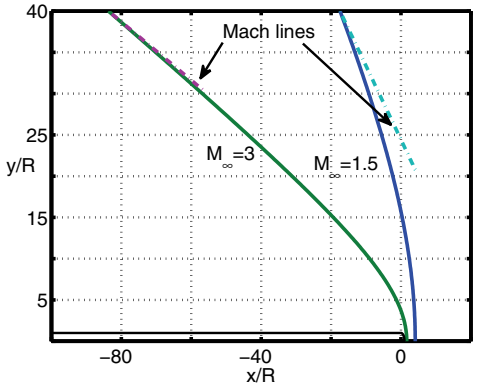

Figure 16: Bow-shock shapes from M_∞ 1.5 and 3; abscissa and ordinate expressed as relative to the leading edge radius R

Considering that one expects the most dangerous noise to be radiated onto the plate from the upper ramp, so from above the plate, an axial position of 4 *cm* downstream of the leading edge has been judged sufficient to have the noise passing through the weakest part of the shock waves at all the Mach numbers considered. This position then is still close enough to the leading edge for the boundary layer to be still fully laminar at supersonic velocities. The final arrangement of the single PCB on the plate to be used for noise assessment is shown in Figure 17.

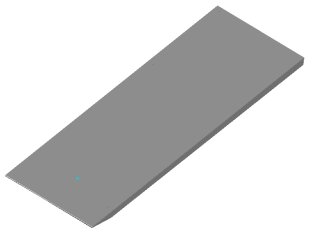

Figure 17: The plate for the noise assessment with the PCB hosting

6. Conclusions

The design of this supersonic wind tunnel has been intended since the beginning to comprise solutions for the reduction of the facility-generated interferences on transition experiments. Nevertheless, the design and construction of an effective quiet wind tunnel has proven so far a slow and difficult process to those who have undertaken it. The proof is the scarcity of wind tunnels of this type in the world, despite the general importance of transition experiments.

The solutions adopted for the present project were those found in the open literature and the ways and means used to implement them have came from the Von Karman Institute know-how of, chiefly, flows experiments on turbo-machinery. But the authors are aware that a specific know-how, often based on trial-and-error experience, is a key factor for the design, construction, and operation of an effective quiet wind tunnel, so they do not expect to fully succeed at their first attempt. It is likely that the wind tunnel will not behave quietly throughout the entire Mach range for which has been build. And the probability that it will not at any Mach number may well be not small.

But the authors are confident that, at least, the arrays of measurements techniques that they can use in the facility (not only noise measurements but also, e.g., Schlieren visualization of portions of the ramps) will permit to single out the deficiencies of this first attempt, and highlight the problems that have been so far unseen. In this way, that trial-and-error process toward a better and better design can start and, perhaps, end up in another operative supersonic quiet windtunnel to add to the few available.

References

[1] S. V. Murthy, F. W. Steinle, On boundary layer transition in high subsonic and transonic flow under the influence of acoustic disturbances and free-stream turbulence, in: AIAA 85-0082, 1985.

[2] S. R. Pate, Effects of wind tunnel disturbances on boundary-layer transition with emphasis on radiated noise: A review, in: 11th Aerodynamic Testing Conference, Colorado Springs, Colorado/March 18-20, 1980.

[3] W. Harvey, Influence of free-stream disturbances on boundary-layer transition, Tech. rep., NASA (1978).

[4] I. E. Beckwith, Aerothermodynamics and transition in high-speed wind tunnels at nasa langley, Annual Review of Fluid Mechanics 22 (1990) 419–439.

[5] L. M. Mack, Boundary-layer linear stability theory, Tech. Rep. R 709, AGARD (1984).

[6] J. R. Jack, Effect of favorable pressure gradients on transition for several body of revolution at mach 3.12, Tech. Rep. 4313, NACA (1958).

[7] H. Schlichting, Boundary Layer Theory, McGraw-Hill Book Company, Inc., USA, 1987.

[8] R. L. Kimmel, The effect of pressure gradients on transition zone length in hypersonic boundary layers, Tech. rep., Wright Laboratory (1993).

[9] S. P. Schneider, Numerical analysis of the bleed slot design of the purdue mach 6 wind tunnel, in: AIAA-2005-91, 2005.

[10] N. Lin, H. Reed, W. Saric, Effect of leading edge geometry on boundary-layer receptivity to freestream sound, in: Stability, Transition and Turbulence, Springer-Verlag, New York, 1991.

[11] S. R. Pate, Radiated aerodynamic noise effects on boundary-layer transition in supersonic and hypersonic wind tunnels, AIAA Journal 7 (1969) Nr. 3.

[12] E. Reshotko, Roughness-induced transition, transient growth in 3-d and supersonic flow, in: AVT 151 Lecture Series on Advances in laminar-turbulent transition modelling, RTO-AVT-VKI, 2008.

[13] C. M. Harris, C. E. Crede, Shock and Vibration Handbook, McGraw-Hill Book Company, Inc., USA, 1976.

[14] C. J. Gedney, The cancellation of a sound-excited tollmiend-schlichting wave with plate vibration, Physics of Fluids 26 (1983) 1158–1160.

[15] R. J. Roark, W. C. Young, Formulas for Stress and Strain, McGraw-Hill Book Company, Inc., USA, 1976.

[16] D. J. Mee, C. P. Goyne, Turbulent spots in boundary layers in a free-piston shock-tunnel flow, Shock Waves 6 (1996) 337–343.

[17] J. P. Clark, T. V. Jones, J. E. LaGraff, On the propagation of naturally-occurring turbulent spots, Journal of Engineering Mathematics 28 (1994) 1–19.

[18] L. Krishnan, N. D. Sandham, Effect of mach number on the structure of turbulent spots, Journal of Fluid Mechanics 566 (2006) 225–234.

[19] I. E. Beckwith, M. H. Bertram, A survey of nasa langley studies on high-speed transition and the quiet tunnel, Tech. Rep. NASA-TM-X-2566, NASA (1972).

[20] J. F. McKenzie, K. O. Westphal, Interaction of linear waves with oblique shock waves, The Physics of Fluids II (1968) 2350–2363.

Modeling and analysis of the laminar to turbulent transition in a low-pressure turbine

Jayson Babajee

Turbomachinery and Propulsion Department, jayson.babajee@vki.ac.be

Supervisor: Tony Arts

Professor, Head of Turbomachinery and Propulsion Department, von Karman Institute for Fluid Dynamics, Belgium, arts@vki.ac.be.

Promotor: Francis Leboeuf

Professor, LMFA (Laboratoire de Mécanique des Fluides et d'Acoustique), 36 avenue Guy de Collongue - 69134 Ecully Cedex - France, Francis.Leboeuf@ec-lyon.fr

Abstract

This paper focuses on the analysis of the laminar to turbulent transition mechanisms occurring in new Low-Pressure Turbine (LPT) designs. For that, a first investigation of several test campaigns on different LPT rotor blades will be highlighted in order to assess their behavior on boundary layer characteristics. The aim is to find a correlation between the LPT environmental parameters and the ones of the boundary layer. Those issues will be mainly addressed numerically (by using the ONERA code elsA).

Keywords: Low-Pressure Turbine, Separation-Induced Transition, Wake-Induced Transition, Reynolds number, Turbulence, Correlation

Nomenclature

Acronyms

AGS	= Abu-Ghannam and Shaw
AMDCKO	= Ainley and Mathieson/Dunham and Came/Kacker and Okapuu
CFD	= Computational Fluid Dynamics
K-H	= Kelvin-Helmholtz
LPT	= Low-Pressure Turbine
RANS	= Reynolds-Averaged Navier-Stokes
T-S	= Tollmien-Schlichting
HL	= High-Lift
HLLPT	= High-Lift Low-Pressure Turbine

Symbols

c	= Chord, m
c_{ax}	= Axial chord, m
f_{bar}	= Bar passing frequency, s^{-1}
f_r	= Reduced frequency = $(f_{bar} \cdot c) / U_{TE}$
g	= Pitch, m
h	= Heat transfer coefficient, W m^{-2} K^{-1}
k	= Turbulent kinetic energy, m^2 s^{-2}
$l.e.$	= Leading edge
R	= Radius, m
Re	= Reynolds number
s	= Curvilinear abscissa, m
s_0	= Curvilinear length of the blade suction side, m
t	= Time, s
T	= Period, s
$t.e.$	= Trailing edge
Tu	= Turbulence intensity in %
U_{TE}	= Trailing edge freestream velocity, m s^{-1}
U_∞	= Freestream velocity, m s^{-1}
V_x	= Axial velocity, m s^{-1}
β	= Angle with respect to the axial direction, degree
γ	= Intermittency coefficient
ν	= Kinematic viscosity, m^2 s^{-1}
ρ	= Density, kg m^{-3}
ω	= Specific turbulence dissipation rate, s^{-1}
ζ	= Kinetic losses in %
ΔH	= Total enthalpy variation across the rotor blade, J kg^{-1}

ΔV_θ = Tangential velocity variation across the rotor blade, m s^{-1}
Ω = Rotational speed, rad s^{-1}
Ψ_{inc} = Incompressible Zweifel loading coef.
Ψ = Compressible Zweifel loading coef.

Subscripts
1 = Inlet condition
2 = Outlet condition
cr = Critical value for AGS correlation
is = Isentropic condition
MD = Maximum of Displacement
reat = Reattachment
sep = Separation
TE = Trailing Edge
θ = Momentum thickness, m

1. Introduction

In the years following the World War II, the aircraft manufacturers were conscious of the advantages of the jet engine over the piston engine. Those are the possibility to fly at higher speeds, climb faster and fly at higher altitudes in a vibration-free and quiet environment. Nowadays, the aircraft engine designs are still based on Turbojets but characterized by High By-Pass ratio (8:1 to 10:1) in order to fulfill more severe consumption, performance and noise constraints. Then, they are called Turbofans where more than 80% of the flow entering the nacelle is passing through the by-pass duct. That is why the fan is a critical part of the design. Considering it is driven by the LPT via a shaft, it seems quite obvious that this latter component is of interest in order to get the maximum efficiency.

The main topic of this study is to analyze the laminar to turbulent transition mechanisms that occur in a LPT. For this purpose, one can evaluate the work done by the rotor with the turning of the flow from the Euler's momentum equation in pure axial flow:

$$\Delta H = \Omega \cdot R \cdot \Delta V_\theta \quad (1)$$

A standard LPT is usually made of several stages (4 stages in the case of the CFM56-7B). LPTs commonly operate at an outlet Mach number in the range of 0.6 to 0.9 and above all weight 20% to 30% of the overall mass of the engine [1]. Thus, the aim is not to manufacture more powerful and heavy engines like the industrial gas turbine but to get the most efficient one in terms of power with respect to the weight and the drag mainly. At a first sight, one solution is inevitably to reduce the weight of the LPT components by reducing the number of blades. Then, this would imply an increase of the pitch-to-chord ratio (g/c). In the meantime, this entails a more important loading per blade in order to compensate for the lower number of working blades for a given stage loading. As a consequence, the velocity suction peak would be higher as well as the diffusion over the rear part of the suction side. Nevertheless, one has to be aware for this study of the separation and transition phenomena. Those latter points shows the importance of the Reynolds number (Re) since the current LPT operating Reynolds number is below 100000 at cruise conditions and more than 400000 at take-off. This shows the wide operating conditions of a LPT and above all the changing flow conditions as highlighted by Hourmouziadis in [2]. In figure 1, one can see the different flow topologies encountered in a LPT. Then, at high Reynolds number (case b), the flow stays attached to the wall and the flow turning is as expected (case a is not really encountered in nowadays LPT). While reducing the Reynolds number (case c), a short separation bubble appears. A bubble is defined as a zone where the flow separates from the wall and reattaches further aft. It is characterized by a dead air region followed by a recirculation area. Basically, this type of bubble does not affect the losses. Case d is representative of a long separation bubble. At last, case e illustrates the bursting of the bubble. It leads to an open separation which is detrimental in terms of turning and consequently of losses (cf. Equation 1). That is why the study of the transition mechanisms is of interest because in the case of open separation, the flow does not behave like it should and the turning is less than expected.

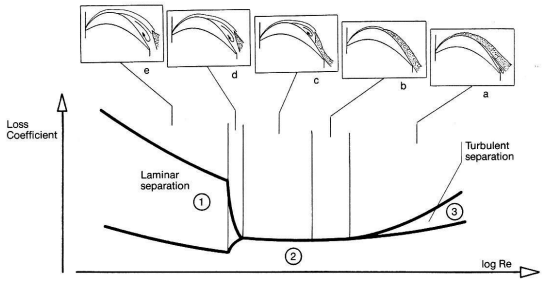

Figure 1: Turbine Cascade Performance - After Hourmouziadis [2]

It is a matter of dealing with some economical and environmental concerns that leads to a reduction of the

number of blades per row and then to consider what is called “High-Lift blade (HL)”.

That is why one can focus on the internal environment of the turbojet to cope with this separation phenomenon. Thus, the interactions between a blade and the upstream row of blades are still the most promising factor due to the unsteady environment of a turbojet. Consequently, one can manage to take advantage of the “calming effect”. It is defined by the so-called calmed regions which present the advantages of the laminar and turbulent regions without their respective drawbacks [3]. Moreover, the turbulence intensity as well as the turbulence global scales are also important factors to keep in mind.

Therefore, the main aim of this work will be to find a solution to keep the flow attached over the suction side by triggering the transition.

2. Transition and Separation Phenomena in LPT

Transition occurs due to the amplification of instabilities in the boundary layer. The main factors affecting it are the Reynolds number, the turbulence intensity, the turbulence scales and the pressure gradient.

2.1. Steady Transition

Even though a LPT environment is rather unsteady, one still needs to define the basics of the physics behind steady transition since most of cascade investigations in wind tunnel are carried out at steady condition. There are four kinds of transition. The natural transition, the by-pass transition, the separation-induced transition and the reverse transition (relaminarization).

In LPT cases, the last three cases are of interest since only natural transition occurs at really low turbulence level. In the by-pass transition, the transition occurs due to disturbances that lead directly to the formation of turbulent spots by by-passing the growth of Tollmien-Schlichting (T-S) waves. Basically, those disturbances are defined by a high turbulence level. Considering the separation-induced transition, the flow is subjected to a separation bubble which is caused mainly by an adverse pressure gradient and depending on the Reynolds number as well. Then, at low Reynolds numbers and with a strong diffusion (which is the case of HLLPT), the laminar boundary layer separates and the transition process occurs in the free shear layer. However, depending on the turbulence intensity and scales, the reattachment process may not happen, leading to an open separation which is the worst case in terms of losses. There are three separated flow modes according to the work of Hatman and Wang [4]. Those are the transitional separation mode, the laminar separation/short bubble mode and the laminar separation/long bubble mode.At last, the reverse transition is typically a way back from a turbulent flow to a laminar flow which occurs in region of very strong acceleration like in the rear part of the blade pressure side.

2.2. Multimode Transition

This type of transition is an unsteady transition. It is a realistic illustration of the turbomachinery environment where the wakes from a blade row impinge on the following blade row while triggering the transition or inhibiting separation. Actually, the growth of turbulent spots, after the impingement of a wake on the suction side of a blade, implies the apparition of calmed regions which are less sensible to disturbances. The effectiveness of this calmed region was illustrated in [5] and [6]. This region follows the turbulent region at a lower velocity based on the work of Schubauer and Klebanoff [7]. They highlighted that the flow starts to be very stable and no breakdown seems to occur from the spot tail. Moreover, one can see the interest of this calmed region by looking at the distance-time diagram (cf. Fig. 2). The difference between the leading edge and the trailing edge velocities of this region insures the development of a laminar look-alike region.

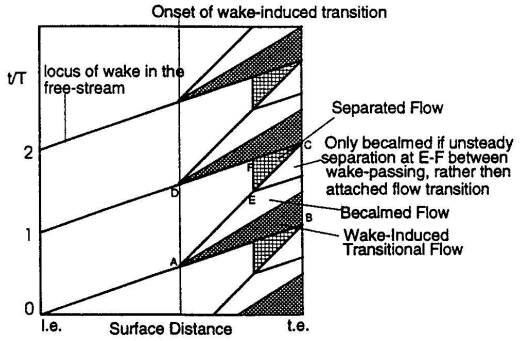

Figure 2: Time-space diagram of the turbulent spots - After Schulte and Hodson [8]

Indeed, this setting of the incoming wakes frequency (blade passing frequency) is of importance since it will condition the nature of the flow after the impinging of the wakes. In fact, if the frequency is too high, it will lead to the coalescence of the turbulent areas corresponding to the black regions in Fig. 2. Then, the point is to have the largest calmed region (white area after the onset of wake-induced transition).

Those conclusions are corroborated by the work of Coull et al. [9]. In their study, they investigated the effects of the velocity peak location, the diffusion factor and the reduced frequency (f_r) on the performance and the boundary layer development for low-speed conditions over a flat plate. A moving bar mechanism was set up in order to reproduce typical turbomachinery unsteady wakes. Then, three reduced frequencies were chosen: 0.314, 0.628 and 0.942. This reduced frequency is a ratio between the convection time scale of a fluid particle over the disturbance time scale of the upstream rotating bars simulating the upstream blade row. Concerning the Reynolds number range for this experiment, it is between 50000 and 220000. The turbulence intensity was set at 3% by means of a turbulence grid. Thus, the effect of the incoming wakes is visible in Fig. 3 and illustrates this trade-off in the choice of the blade passing frequency.

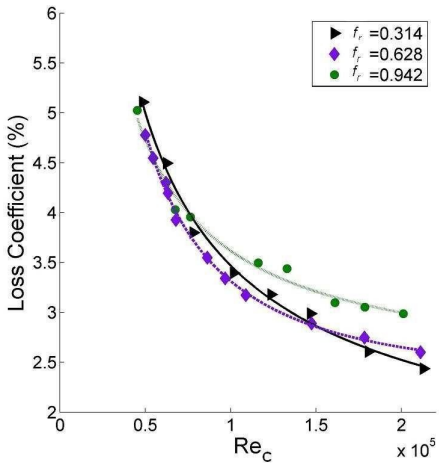

Figure 3: Reduced frequency study - After Coull et al. [9]

2.3. *Parameters affecting Transition and Separation*

At this point of the review, the most important factors affecting transition are the Reynolds number, the turbulence intensity, the pressure gradient and the unsteady feature of the incoming wakes. However, Mayle depicted the existence of other factors which are less significative in terms of turbulent spot production rate than the pressure gradient [10]. Among them, the surface roughness and the surface curvature might be of interest in a LPT environment.

To illustrate the most important factors (Reynolds number and pressure gradient), Prakash et al. studied the effect of the loading level distribution on LPT performance [11]. Their experiments were carried out in a stationary linear cascade at an exit Mach number of 0.64. To vary the loading level, they change the solidity (chord-to-pitch ratio), the stagger angle and the unguided turning angle. Then, the incompressible Zweifel loading coefficient Ψ_{inc} ranges between 1 and 1.27 and the Reynolds number ranges between 70000 and 350000.

$$\Psi_{inc} = 2 \cdot \frac{g}{c_{ax}} \cdot \cos^2\beta_2 \left(\tan\beta_1 - \tan\beta_2\right) \qquad (2)$$

Concerning the geometries tested, they chose two groups of blade, the nominal-lift (NL) and the high-lift (HL) groups. Then, for each group, they tested three different geometries (nominal-B, aft-A and front-F loaded blades) even though they have the same inlet (46.7 deg.) and outlet angles (-62.7 deg.) with the same pressure ratio. Their conclusions lead to an increase of the suction side separation and consequent high losses as the loading level is increased and moved aft as well as the Reynolds number is reduced. Indeed, one can see in Fig. 4 that the front-loaded case has a beneficial effect on the losses and particularly at low Reynolds numbers although the improvement is not so obvious at mid and high Reynolds numbers.

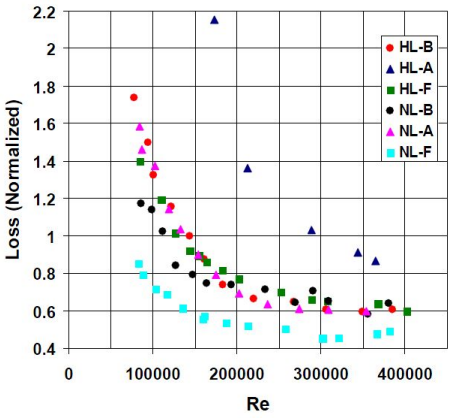

Figure 4: Kinetic Losses normalized by the HL-B loss at Re~146000 - After Prakash et al. [11]

This trend is confirmed by the work of Coull et al. [9] described previously where they concluded that moving the peak velocity forward has a beneficial effect when the bubble generated losses are high, that is to say at low Reynolds numbers, low reduced frequencies and high levels of diffusion.

2.4. *Control Devices to trigger Transition and/or remove Separation*

Even though the calming effect introduced before showed a promising solution to overcome the com-

plex separation-induced transition, it exists other ways to cope with it. Those are essentially of two kinds - passive and active control devices. The effort to implement and set the passive ones up is less important compared to the active ones. There are mainly geometrical extensions such as transition wire, roughness strip or other kinds of disturbance generator. In contrary to those, the active control devices are still promising despite an actuation for some of them or a complicated geometrical shape. In general, all those devices are intended for promoting turbulence production from their location in order to increase the momentum of the fluid in the near wall region. That is why the goal is to set those devices before the separation location or typically after the peak velocity location at least.

To illustrate the passive control device, a study led at the University of Cambridge highlights the effectiveness of simple geometries such as a spanwise rectangular groove coupled with the calming effect [12]. The experiments were carried out in the Cambridge Low-Speed LPT linear cascade facility equipped with a moving bar mechanism on a Low-Speed version of the T106C. In fact, this element seems promising for further implementation since it does not have the detrimental blockage effect encounter in the case of an elevated control device.

In addition to this depression-type roughness strip, Himmel and Hodson described their work on another kind of passive flow control device [13]. This investigation introduced blowing channels connecting the pressure side and the suction side of a blade. The aim is to take advantage of the large pressure difference between the pressure side and the suction side of High-Lift Low-Pressure turbine blades. Typically, it reproduces a forced jet (like an active control device where the blowing mechanism is embedded in the blade) but without any actuation. It is a self-maintained mechanism. The experiments were carried in the same facility described before on a modified T106C blade. They concluded on the effectiveness of those passive jets in reducing the separation bubble at low Reynolds numbers. Then, the interaction between the incoming wakes, the turbulence level and the passive jets seems to be beneficial and particularly at high Reynolds numbers where usually wakes have the tendency to increase the losses.

About active control devices, they are still not as simple as the passive ones since they will need to be implemented inside an engine with extremely harsh working conditions. In fact, one example which seems viable is described in the work of Volino et al. [14]. They assessed the effect of Vortex Generator Jets on the boundary layer separation occurring in Very High-Lift Low-Pressure Turbine airfoils. Their experiments were done under low freestream turbulence intensity and in a low-speed cascade. Then, it was feasible to reach very low Reynolds number (25000 to 100000). Basically, their jet pulsing design was defined by a cavity in the central of all the blades, connected to a compressed air line. By setting the pulsing jet frequency, they could blow air via small orifices on the suction side of the blade. Their orifice design leads to the creation of streamwise vortices which brings high momentum fluid into the near wall region. However, this study does not take into account the effect of the upstream blade row incoming wakes. According to their results, the effectiveness of the pulsed jet in the suction side boundary layer was proven in reducing the separation length and consequently promoting the reattachment of the flow in the case of very low Reynolds number where open separation occurs generally. Moreover, they highlighted the fact that pulsed jets were more effective than steady jets in their configuration.

Otherwise, there are in the literature other examples of active control devices. The case of plasma actuators seems very promising in the sense it could be switched on only when needed and is not intrusive. Huang et al. investigated the ability of this actuator to ionize the air [15]. From that, this ionized air produce a body force on the ambient air. Since, the configuration of the electrodes is asymmetric, it makes possible to create a wall jet, first towards the wall then in the downstream direction.

3. Correlations

The search for performance models in axial turbines is still relatively tricky. The need for loss prediction models is critical when designing a new turbine. In fact, this process starts with the mean line model of the velocity triangles. However, one has to incorporate the standard expected losses into his mean line prediction in order to get an estimation of the efficiency of the blade design. Those main losses are generally referred as profile losses (contribution of the boundary layer shear), secondary losses (which corresponds to the development of vortices due to the presence of the end walls), trailing edge losses (or base pressure losses), shock losses and some others. Relevant studies about those correlated models dates back six decades with the work of Ainley and Mathieson [16]. They described the losses as a summation of the

individual effect of each class of losses. They incorporated the influences of the flow deviation and the Reynolds number. However, this study is still considered as a basis for axial turbine prediction model. Thus, other groups improved it and added some correction factors and this is referred as the AMDCKO correlation ([17] and [18]).

$$\zeta_{cascade} = \zeta_{profile} \cdot f\,(Re) \;+\; \zeta_{TE} \;+\; \zeta_{secondary} \quad (3)$$

In the present study, a comparison of some available test cases of LPT blades was done. Actually, since those kinds of design were not really part of the study of the AMDCKO correlation, one does not expect to match the predictions. However, as expected, the blade designs, which do not face open separation, fit the prediction or at least the trend with a difference of almost 0.5 point in terms of losses. Thus, one can see that some additions to this AMDCKO could be performed and particularly by taking into account the coupling of different parameters that contribute to the degradation of the losses such as the Reynolds number, the diffusion factor, the velocity peak in order to add a correction to the outlet flow angle.

After describing correlations based on heuristic, data-driven and mean line models, one can focus on more data-driven physical models. An illustration of this kind of model is the correlation made by Hatman and Wang [4] during their study of the separation bubble types on a low free-stream turbulence flat plate with an imposed adverse pressure gradient and at low speed conditions. This study highlights the different transition processes of those separated bubble types. Instead of establishing their correlation on standard integral thicknesses, they preferred to use the streamwise positions of the separation (sep), the maximum displacement of the bubble (MD), the reattachment (reat), the transition onset and the transition exit. According to their findings, the position of the maximum displacement is the key of their correlation since it quantifies the length scale of the K-H instabilities to develop since they do not take into account the presence of the wall. As the authors stated in the article, this semi-empirical study for predicting some of the separated-flow properties is appropriate for flat plates. However, since it constitutes a step forward in the understanding of separated-flow transition, it should be of interest to compare their "academic" correlation to a set of data from the LPT environment.

Indeed, a couple of LPT blades are at disposal and were studied in a cascade environment at high-speed conditions. The Reynolds number range covers the one of standard HLPPT blades. About, the turbulence intensity, it corresponds to the one of the wind tunnel freestream condition which is around 1%. They form a panel of different kinds of LPT blades from aft-loaded to front-loaded, from normal-lift to HL designs. The compressible Zweifel loading coefficient Ψ ranges from 1.07 to 1.50.

$$\Psi = 2 \cdot \frac{g}{c_{ax}} \cdot \frac{|\rho V_\theta V_x|_2 - |\rho V_\theta V_x|_1}{\rho_2 V_2^2} \quad (4)$$

The correlation between the reattachment Reynolds number and the separation Reynolds number is shown in Fig. 5. Likewise, one can display the correlation

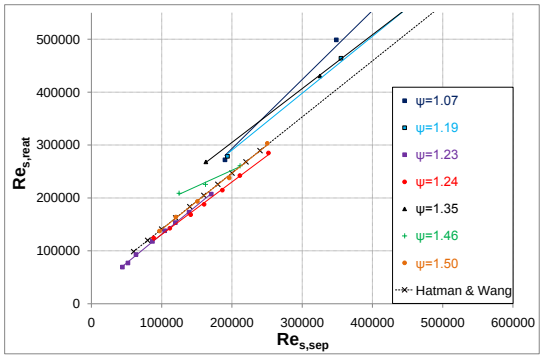

Figure 5: Investigation of Hatman and Wang $Re_{s,reat} = f\left(Re_{s,sep}\right)$ correlation for LPT blades

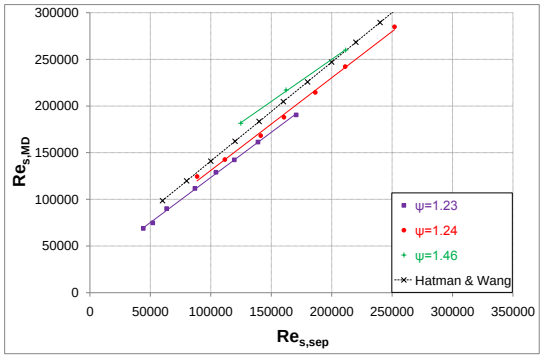

Figure 6: Investigation of Hatman and Wang $Re_{s,MD} = f\left(Re_{s,sep}\right)$ correlation for LPT blades

between the maximum displacement Reynolds number and the separation Reynolds number (cf. Fig. 6). However, the maximum displacement of the boundary layer induced by the separation bubble is not directly measurable in the wind tunnel with the instruments at

disposal. That is why one can consider that the divergence of the streamlines from the bubble maximum height to the reattachment defines the pressure recovery increase according to Houtermans et al. [19]. This pressure recovery increase process is visible in the static pressure distribution. Basically, it ends the pressure plateau and defines this divergence by the important pressure gradient in order to reattach on the wall. According to this investigation, one can conclude that the LPT database shows a very good agreement with the separated-flow transition modes study of Hatman and Wang [4].

To end this review of separation-induced transition correlations, the most popular correlation used in the field of turbomachinery is the one done by Abu-Ghannam and Shaw [20]. Their investigation was carried out on a flat plate in a low-speed wind tunnel with a turbulence intensity ranging from 0.3 to 5%. Moreover, the configuration reproduced the typical pressure gradient encountered in turbomachinery blades without separation. This correlation is based on the turbulence intensity and the pressure gradient. It gives the designer the value of the momentum thickness Reynolds number from which the transition process starts according to the following set of equations:

$$Re_{\theta,cr} = 163 + \exp\left[F\left(\Lambda_{cr}\right) - \frac{F\left(\Lambda_{cr}\right)\cdot Tu}{6.91}\right] \quad (5)$$

$$F\left(\Lambda\right) = 6.91 + 12.75\Lambda + 63.64\Lambda^2 : \Lambda < 0 \quad (6)$$

$$F\left(\Lambda\right) = 6.91 + 2.48\Lambda - 12.27\Lambda^2 : \Lambda > 0 \quad (7)$$

$$\Lambda = \left(\frac{\theta^2}{\nu}\right)\left(\frac{dU_\infty}{ds}\right) \quad (8)$$

Moreover, they derived a couple of boundary layer parameters during transition in function of a non-dimensional distance η from the start of transition over the transition length.

$$\eta = \frac{s - s_{onset}}{s_{end} - s_{onset}} \quad (9)$$

Here is the relationship between the intermittency coefficient γ, which defines the fraction of time during transition for which the flow is turbulent, and η.

$$\gamma = 1 - \exp\left(-5\eta^3\right) \quad (10)$$

4. Numerical Approach

To understand the phenomenon of separated-flow transition, one should get a large database in order to assess the findings on each configuration in the aim of making a universal model. However, it could demand a lot of effort since each configuration may be one of a kind and consequently will not infer the principle of universality. That is why data-driven correlations are still useful in predicting models based on trends. Concerning the momentum thickness Reynolds number, it is based on the momentum thickness θ which quantifies the portion (in terms of distance away from the wall) of momentum flux loss due to the presence of the wall and consequently the viscous dissipation through viscous stress tensor. Moreover, in the case of turbulent flow, the instabilities are more important due to the presence of large eddies which interact and break down into smaller eddies. Then, knowing that eddies are really efficient in the mixing process, it means that the momentum thickness will behave differently according to the nature of the flow in the boundary layer. That might be an explanation for the perpetual use of this parameter in the correlations. However, one drawback is its complicated assessment in a cascade configuration. Then, one sees the interest of the numerical approach to get more information about this critical parameter.

For this approach, three-dimensional CFD simulations are carried out with the ONERA in-house code elsA (ensemble logiciel de simulation en Aérodynamique). The elsA software package is based on a cell-centered finite volume method for solving the Navier-Stokes equations. The space discretization is carried out by multi-block structured meshes. It allows the simulation of steady or unsteady flows, of inviscid or viscous fluids, in fixed or moving frame. Many turbulence models are available with elsA, from simple mixing length approach to Reynolds Stress Models. However, in this study, only RANS simulations with k-ω turbulence models are considered since they are robust, have a good modeling of turbulence in the near-wall region, show superior performance for low Reynolds number flows and above all are suitable for adverse pressure gradient and separation. Then, the turbulence model is coupled with a transition criterion in order to trigger the turbulent production at the transition onset and consequently take into account the laminar part of the boundary layer ahead of this position. The use of the particular single-step case of the Runge-Kutta method for time integration, known as the "Backward Euler" time integration scheme is used. This scheme is coupled with a LU implicit phase technique. There are two space discretization schemes available in elsA. The Jameson scheme is a centered scheme which is stabilized by the addition of

numerical dissipation. The second one is a second order Roe scheme with the Harten entropic correction. The mesh topology is a standard O4H with High Staggered corrections since the geometries are defined by high value of deviation (cf. Fig. 7). The central O-mesh is around the blade and has at least 25 points in the perpendicular direction away from the blade surface. In the streamwise direction around the blade, the number of nodes is above 225 in order to get a good discretization of the suction side of the blade. However, the extension of the mesh in the spanwise direction is restricted to 5 layers. It is of interest to save a lot of computation time by focusing on the middle of the blade in order to apply convergence acceleration methodologies. Moreover, to avoid the calculation of the endwall regions, the study focuses on LPT blades which have high aspect-ratios. This is to mimic the experimental configuration where the measurements were taken at midspan. This methodology is referred as "2.5D".

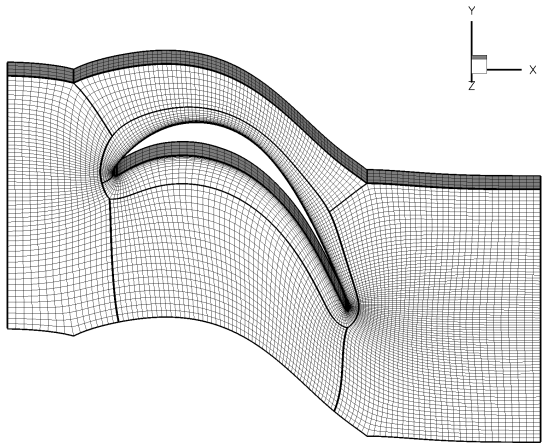

Figure 7: Mesh Topology of T106C (Ψ = 1.24)

The available transition criteria are all based upon empirical correlations such as the formulations of Abu-Ghannam and Shaw (AGS) described in Section 3, Drela, Mayle and many others. Those criteria are made non-local in the sense they take into account the history of the boundary layer with the freestream information (turbulence intensity and pressure gradient). When the transition criterion is met, the so-called "intermittency weighting function" is switched on from 0 to 1 (like a step) and consequently triggers the production of the turbulent kinetic energy. However, despite its numerical definition, it still keeps the same qualitative meaning of the intermittency coefficient defined in Section 3. Besides, this kind of methodology implies the need of the boundary layer thickness calculation from the integration of the velocity profiles.

To overcome these properties of those correlation-based methodologies, new methods for the computation of transition founded on transport equations are of interest such the $\gamma - Re_\theta$ model of Menter and coworkers [21]. This model uses a relationship between the transition onset momentum thickness Reynolds number derived from empirical correlations and local boundary layer quantities via the vorticity Reynolds number. Then, an equation for the transport of intermittency permits to trigger locally the transition by switching on the production term of the turbulent kinetic energy of the k-ω Menter SST model. Moreover, another equation for the transport of the transition onset momentum thickness Reynolds number is needed in order to take into account the non-local influence of the turbulence and the pressure gradient. In contrast, a full local approach based on the laminar kinetic energy concept described by Mayle and Schulz [22] is illustrated in Pacciani et al. [23]. They carried out the coupling of a transport equation for the laminar kinetic energy with the k-ω Wilcox model. This model enables to take into account the pre-transitional rise of the fluctuating kinetic energy and its breakdown to turbulence. They provided results from High-Speed HLLPT configuration and they are in good agreement with the experimental since they adapted their model for the transition induced by separation.

5. Results

In this section, some results of the assessment of the transition criterion as well as the turbulence models available in the CFD code elsA are presented. "2.5" RANS calculations were carried out with the Roe scheme associated to the k-ω Wilcox model. The transition criterion used is the AGS correlation described in Section 3). This investigation will focus only on the suction side because the flow on the pressure side is subjected to a separation after the leading edge but experiences a reverse transition process over the aft part. Thus, it is assumed the profile losses contribution of the pressure side is negligible in comparison to the ones of the suction side.

First of all, the "baseline" methodology which is the coupling of the k-ω Wilcox model with the AGS transition criterion was carried out. Three Reynolds numbers (190000, 350000 and 650000) are investigated over a HLLPT rotor blade which compressible

Zweifel loading coefficient is 1.35. The experimental investigation was carried out in a short duration isentropic compression tube cascade facility, where the isentropic exit Mach number was maintained at 0.8 and the turbulence level was fixed at 0.8%, that is to say the natural turbulence level of the facility. According to the experimental data, one would expect a transitional separation mode for the high Reynolds number, a laminar separation/short bubble mode for the medium Reynolds number and a laminar separation/long bubble mode and/or even an open separation for the low Reynolds number. Those findings are based on the experimental mass-averaged profiles losses (not presented here) and the suction side heat transfer coefficient normalized with the leading edge experimental value at the lowest Reynolds number. While looking at the high Reynolds number case (cf. Fig. 8), one can see that the "baseline" simulation does not predict any separation (this is corroborated by the shear stress distribution which is not presented here). In fact, the expected rapid and monotonic decrease of the heat transfer coefficient is not visible. This is characteristic of the separation process according to Rivir et al. [24]. At this Reynolds number, the losses prediction will not be so affected because the flow reattaches. However, the prediction of the boundary layer thicknesses might be false. Moreover, at all Reynolds numbers (cf. Fig. 8 to Fig. 10), one can see that the positions of separation are predicted downstream of the experimental ones. About the low Reynolds number (Fig. 10), the "baseline" case predicts a reattachment which is not the case in the experiment. This reattachment location is defined by the maximum value of the heat transfer coefficient, downstream of its minimum value, and followed by a second decrease of the heat transfer coefficient due to the thickening of the boundary layer. The explanation could be the strong pressure gradient encounters in those HLLPT designs which might not be suited for the AGS transition criterion.

In order to match with the experiments, it is possible to "force" the transition process by imposing an "intermittency weighting function" on the blade wall. An explanation of the non-prediction of the separation bubble in the high Reynolds number case might be the too sudden production of turbulent kinetic energy due to the step of the intermittency weighting function. Likewise, this conclusion applies to the low Reynolds number case. An attempt to remedy to this issue is a more progressive intermittency function. Basically, according to the literature, one can find some relevant works about the modeling of this intermittency

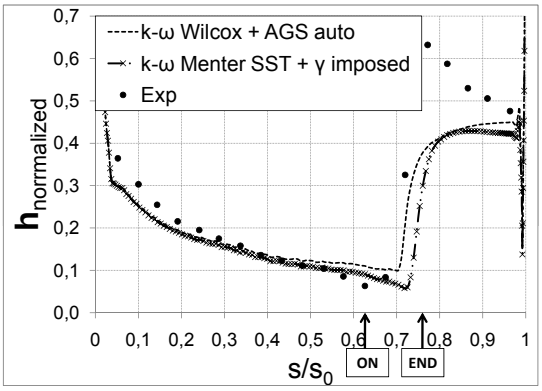

Figure 8: $\Psi = 1.35 - Re_{2,is} = 650000$

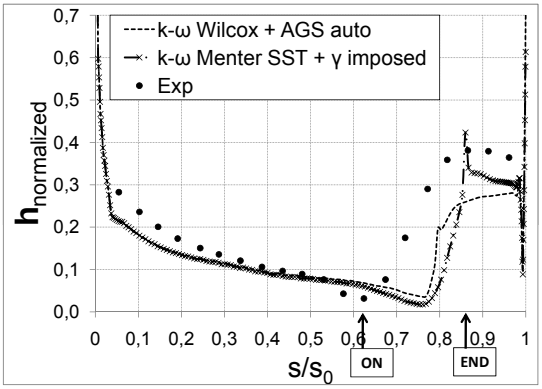

Figure 9: $\Psi = 1.35 - Re_{2,is} = 350000$

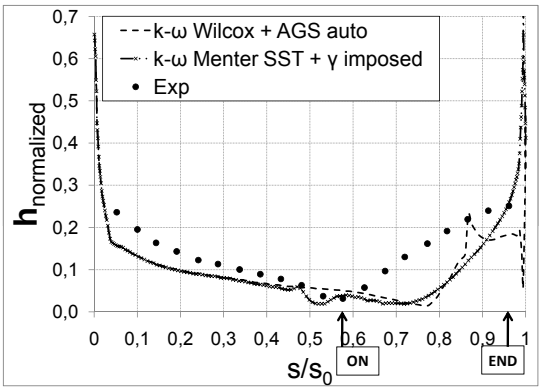

Figure 10: $\Psi = 1.35 - Re_{2,is} = 190000$

coefficient (a review of some of them is described in Narasimha [25]). Then, the choice went on the function derived from Abu-Ghannam and Shaw [20] described in Eq.9 and 10. The simplicity of this formulation relies on the relationship between γ and the positions of onset and end of transition (these positions are indicated on the curvilinear abscissa axis of Fig. 8 to Fig. 10 by ON for transition onset and END for end of transition). Moreover, the transition criterion is not needed any more. Besides, an investigation of the k-ω Menter SST model was carried out when coupled to this intermittency function and revealed to be more robust than the k-ω Wilcox in predicting separation. It turned out that the introduction of this intermittency function allows to predict a small separation bubble in the high Reynolds number case and a massive separation in the low Reynolds number case. Moreover, one can see a slight improvement of the heat transfer coefficient gradient after the transition onset.

6. Conclusion

The transition processes in LPT rotor blade have been reviewed in order to set the issues that should be tackled. Then, it came out that a new LPT design known as HLLPT design is the trend adopted by the aircraft engine designers for reducing the weight of their machine and consequently tends to improve their competitiveness for a given stage loading. However, the main issue to tackle remains the transition induced by flow separation or even worst a total separation of the flow since those components work at severe Reynolds conditions.

There are some control devices that showed a great interest in promoting transition and/or removing flow separation. Some of them are still under developments whereas the others are already implemented but need some tuning. Many studies dating from the middle of the second half of the past century focused already on the topic of separated-flow transition but still did not solve the complete problem. Based on their own experimental database, people were able to build reliable correlation models to predict the transition of a boundary layer. That is why some of those models are implemented in CFD codes. However, they lack information in the case of separated-flow transition.

Thus, it is suggested to tackle this topic by correlating information (geometrical characteristics) extracted from a database of a range of LPT rotor blades with influent parameters of the boundary layer such as the momentum thickness Reynolds number used by previous workers for its ability to take into account the nature of the flow locally. Some aspects of the LPT database were assessed on a recent general flat plate model of separated-flow transition. It turned out to show good agreements with this general model. In order to investigate in more details the flow patterns of LPT environment, the ONERA in-house CFD code is used. A first investigation on a HLLPT with the criteria available in this code did not predict the experimental behavior. An intermittency weighting function was suggested. It gave some improvements but is still not able to catch the experimental predictions.

However, a promising transport equation model for transition has been implemented in this CFD code and shows good agreements with other studies. Hopefully, the LPT database will be investigated with it soon. Moreover, since the separated-flow transition was shown to be unsteady, some Unsteady-RANS simulations will be of interest.

Acknowledgments

The author thanks SNECMA for the appreciated financial support and the permission to publish this article.

References

[1] H. P. Hodson, R. J. Howell, The Role of Transition in High Lift Low Pressure Turbines, von Karman Institute for Fluid Dynamics Lecture Series 2005-03 (2005).

[2] J. Hourmouziadis, Aerodynamic Design of Low Pressure Turbines, AGARD Lecture Series 167 (1989).

[3] T. Coton, Unsteady Wake-Boundary Layer Interaction on Advanced High Lift Low Pressure Turbine Airfoils, Ph.D. thesis, Université Libre de Liège (2003).

[4] A. Hatman, T. Wang, A Prediction Model for Separated-Flow Transition, ASME Journal of Turbomachinery 121 (3) (1999) 594–602.

[5] H. Pfeil, R. Herbst, Transition Procedure of Instationary Boundary Layers, in: ASME Gas Turbine Conference and Exhibit and Solar Energy Conference, no. 79-GT-128, San Diego, California, USA, 1979.

[6] H. Pfeil, R. Herbst, T. Schröder, Investigation of the Laminar-Turbulent Transition of Boundary Layers Disturbed by Wakes, ASME Journal of Engineering for Power 105 (1) (1983) 130–137.

[7] G. B. Schubauer, P. S. Klebanoff, Contributions on the Mechanics of Boundary-Layer Transition, Technical Note 3489, National Advisory Commitee for Aeronautics (1955).

[8] V. Schulte, H. P. Hodson, Prediction of the Becalmed Region for LP Turbine Profile Design, ASME Journal of Turbomachinery 120 (4) (1998) 839–846.

[9] J. D. Coull, R. L. Thomas, H. P. Hodson, Velocity Distributions for Low Pressure Turbines, in: ASME Turbo Expo 2008: Power for Land, Sea and Air, no. GT2008-50589, Berlin, Germany, 2008.

[10] R. E. Mayle, The Role of Laminar-Turbulent Transition in Gas Turbine Engines, ASME Journal of Turbomachinery 113 (4) (1991) 509–537.

[11] C. Prakash, D. G. Cherry, H. W. Shin, J. Machnaim, L. Dailey, R. Beacock, D. Halstead, A. R. Wadia, S. Guillot, Effect of Loading Level and Distribution on LPT Losses, in: ASME Turbo Expo 2008: Power for Land, Sea and Air, no. GT2008-50052, Berlin, Germany, 2008.

[12] C. G. Himmel, H. P. Hodson, Modifying Ultra-High Lift Low Pressure Turbine Blades for Low Reynolds Number Applications, in: 12th International Symposium on Unsteady Aerodynamics, Aeroacoustics & Aeroelasticity of Turbomachines (ISUAAAT12), no. I12-S7-3, Imperial College London, UK, 2009.

[13] C. G. Himmel, H. P. Hodson, Passive Air Jets for Loss Reductions in High Lift Low Pressure Turbines, in: ISABE, no. 1295, 2009.

[14] R. J. Volino, O. Kartuzova, M. B. Ibrahim, Experimental and Computational Investigations of Low-Pressure Turbine Separation Control Using Vortex Generator Jets, in: ASME Turbo Expo 2009: Power for Land, Sea and Air, no. GT2009-59983, Orlando, Florida, USA, 2009.

[15] J. Huang, T. C. Corke, F. O. Thomas, Plasma Actuators for Separation Control of Low-Pressure Turbine Blades, AIAA Journal 44 (1) (2006) 51–57.

[16] D. G. Ainley, G. C. R. Mathieson, A Method of Performance Estimation for Axial-Flows Turbines, Reports and Memoranda 2974, British Aeronautical Research Council (1957).

[17] J. Dunham, P. M. Came, Improvements to the Ainley-Mathieson Method of Turbine Performance Prediction, ASME Journal of Engineering for Power 92 (3) (1970) 252–256.

[18] S. C. Kacker, U. Okapuu, A Mean Line Prediction Method for Axial Flow Turbine Efficiency, ASME Journal of Engineering for Power 104 (1) (1982) 111–119.

[19] R. Houtermans, T. Coton, T. Arts, Aerodynamic Performance of a Very High Lift LP Turbine Blade with Emphasis on Separation Prediction, in: ASME Turbo Expo 2003: Power for Land, Sea and Air, no. GT2003-38802, Atlanta, Georgia, USA, 2003.

[20] B. J. Abu-Ghannam, R. Shaw, Natural Transition of Boundary Layers - The Effects of Turbulence, Pressure Gradient and Flow History, Journal Mechanical Engineering Science 22 (5) (1980) 213–228.

[21] R. B. Langtry, F. R. Menter, Correlation-Based Transition Modeling for Unstructured Parallelized Computational Fluid Dynamics Codes, AIAA Journal 47 (12) (2009) 2894–2906.

[22] R. E. Mayle, A. Schulz, The Path to Predicting Bypass Transition, ASME Journal of Turbomachinery 119 (3) (1997) 405–411.

[23] R. Pacciani, M. Marconcini, A. Fadai-Ghotbi, S. Lardeau, M. A. Leschziner, Calculation of High-Lift Cascades in Low Pressure Turbine Conditions using a Three-equation model, in: ASME Turbo Expo 2009: Power for Land, Sea and Air, no. GT2009-59557, Orlando, Florida, USA, 2009.

[24] R. B. Rivir, J. P. Johnston, J. K. Eaton, Heat Transfer on a Flat Surface Under a Region of Turbulent Separation, ASME Journal of Turbomachinery 116 (1) (1994) 57–62.

[25] R. Narasimha, The Dynamics of the Transition Zone and its Modelling, von Karman Institute for Fluid Dynamics Lecture Series 1991-06 (1991).

PLASMA FLOW

Experimental characterization of the thermal protection system of a lifting reentry vehicle

Francesco Panerai

Aeronautics and Aerospace Department, panerai@vki.ac.be.

Supervisor: Olivier Chazot

Associate Professor, Aeronautics and Aerospace Department, von Karman Institute for Fluid Dynamics, Belgium, chazot@vki.ac.be.

Promotor: Gianluca Rossi

Professor, Dipartimento di Ingegneria Industriale, Università degli Studi di Perugia, Via Duranti 67, 06125 Perugia, Italy, gianluca@unipg.it.

Abstract

An experimental campaign dedicated to the characterization of Intermediate eXperimental Vehicle thermal protection system is performed at the VKI Plasmatron wind tunnel. Emissivity and catalycity properties for representative ceramic specimens are determined under a wide set of operating conditions in order to reproduce the reentry flight trajectory. Intrusive measurements for flow characterization are used together with optical infrared techniques that provide diagnostic of the test articles surface. Experimental data are postprocessed by means of numerical simulations that allow flow enthalpy rebuilding and the characterization the chemical environment for the different conditions investigated.

Keywords: Thermal Protection System, Catalysis, Emissivity, Plasma, Ground Testing

Nomenclature

A = surface, m^2
C = heat capacity, J kg^{-1} K^{-1}
h = enthalpy per unit mass, J kg^{-1}
L = radiance, W m^{-2} sr^{-1} μm^{-1}
$\dot{m}$ = mass flow rate, kg s^{-1}
p = pressure, Pa
PW = power, W
q = heat flux, W m^{-2}
r = reflectivity
R = radius, m
T = temperature, T
x = surface parallel coordinate, m
y = surface normal coordinate, m
u = velocity x-component, m s^{-1}
v = velocity y-component, m s^{-1}
V = freestream velocity , m s^{-1}

Greek
γ = catalycity
β = velocity gradient, s^{-1}
ε = emissivity
λ = wavelength, m
ρ = density, kg m^{-3}

Subscript
cond = conductive
cw = cold wall
d = dynamic
diff = diffusive
e = boundary layer edge
f = flight
i = chemical species
in = inlet
out = outlet
O = oxygen
N = nitrogen
p = at constant pressure
s = static
sp = stagnation point
tot = total
w = wall

Superscript
exp = experimental

Acronyms

CMC = Ceramic Matrix Composite
IXV = Intermediate eXperimental Vehicle
LEO = Low Earth Orbit
$LHTS$= Local Heat Transfer Simulation
ICP = Inductively Coupled Plasma
IPM = Institute for Problems in Mechanics
TPS = Thermal Protection System
TPM = Thermal Protection Material
VKI = von Karman Institute

1. Introduction

Space vehicles that enter a planetary atmosphere require the use of a thermal protection system (TPS) to protect them from aerodynamic heating generated at the surface due to compression and surface friction of the atmospheric gas. Materials with a high temperature capability are required to ensure that the aerodynamic heating is radiated back into space by virtue of the high surface temperature. For the design of a heat shield catalytic and radiative properties of the thermal protection material (TPM) must be determined, since they are necessary inputs aerothermodynamic loads computations.

The catalytic nature of a TPS describes the behavior of the material to act as a catalyst for recombination reactions of the atomic species in the surrounding gas mixture. Their exothermic nature makes surface reactions responsible for a considerable quota of the heat flux transferred to the wall. As a rule of thumb one can state that the heat flux can be halved by choosing an ideal non catalytic material. In the scientific community several experimental approaches exist in order to determine the catalytic behavior of TPS materials. Usually they are strictly associated with a specific type of facility like diffusion reactors [1], arc-jets [2] and inductively coupled plasma generators [3]. The outcome of experimental methods is a macroscopic catalycity value γ applicable for a specific pair of gas and surface material and environmental conditions.

Radiative phenomena are the only cooling process for passive reusable TPS. This capability depends on the TPM emissivity, i.e. the ratio of the actual radiated energy per unit time over the theoretical maximum limit. Together with catalycity, emissivity becomes therefore a driving factor in the TPS design. Several experimental arrangements exist for emissivity determination: one mainly distinguish between facility where the material is measured at high temperature and setups based on room temperature reflectivity measurements from which ε can be extrapolated at high temperatures.

This paper describes the results of an experimental campaign on ceramic matrix composites (CMC) specimens carried out at the VKI Plasmatron facility, aimed to characterize the TPS of the Intermediate eXperimental Vehicle (IXV), under development at the European Space Agency [4]. A carbon-silicon carbide based TPS is chosen for the nose and the windward of IXV, which are the areas that undergo the harshest conditions during its LEO lifting re-entry.

Details on the experimental setup and the related methodology are firstly provided. The results present the outcome of in-situ measurements of emissivity and the numerical rebuilding of flow properties and catalycity values. A comparison between the experimental data and the IXV trajectory is given to assess the reproduction of the real flight.

2. Experimental setup

The experimental measurements are conducted in the VKI Plasmatron. This is a high enthalpy wind tunnel in which plasma is generated by electromagnetic induction and blown in the form of a subsonic jet inside a test chamber at sub-atmospheric pressure (between 5 and 200 mbar). The facility, which is the most powerful induction-coupled plasma (ICP) wind tunnel in the world, uses a high frequency, high power, high voltage (400 kHz, 1.2 MW, 2 kV) solid state (MOS technology) generator, feeding the single-turn inductor of the 160 mm diameter plasma torch. The torch is mounted on a 1.4 m diameter, 2.5 m long, water-cooled test chamber, fitted with different portholes that allow unrestricted optical access to the test section.

A copper water cooled probe is used for the calibration of the plasma flow conditions. A copper calorimeter placed in the center of the front face is able to measure the cold wall (~350 K) heat flux at the stagnation point. This is determined by the mass flow (controlled by a calibrated rotameter) and the temperature difference in the cooling water supply and return lines measured by two type E thermocouples also calibrated prior to the test, by means of a uniform temperature oil bath and a reference mercury thermometer. In order to have correct measurements, the sidewalls of the calorimeter have to be adiabatic, therefore a Teflon insulator is installed between the calorimeter and the wall of the probe for this purpose. Both the probe and calorimeter have polished copper surfaces

which are assumed to be high catalytic to nitrogen and oxygen atom surface recombination[1]. The heat flux is given by:

$$q_{cw} = \frac{\dot{m} \cdot C_p \cdot (T_{out} - T_{in})}{A} \tag{1}$$

The error on this measurements is estimated to be ±10% by means of the following formula:

$$\frac{\delta q_{cw}}{q_{cw}} = \left[\left(\frac{\partial \dot{m}}{\dot{m}} \right)^2 + \left(\frac{\partial C_p}{C_p} \right)^2 + \left(\frac{\partial \left(T_{out} - T_{in} \right)}{T_{out} - T_{in}} \right)^2 + \left(\frac{\partial A}{A} \right)^2 \right]^{1/2} \tag{2}$$

A Pitot probe with the same geometry of the heat flux probe is used to measure dynamic pressure. The pressure line is connected to a pressure transducer, which is calibrated prior to the test. Such measurements are 7% accurate.

The sample holder is composed of two coaxial tubes in which water circulates for cooling. At the extremity, a support for the sample made of SiC is attached to the holder body by three metallic pins. A thick insulation layer of Procelit® 180 is placed as back support for the sample in order to limit the heat flux dispersion by conduction.

Two Raytek Marathon Series pyrometers record the front surface temperature of the sample. They are chosen alternatively according to the target and the measurement range (700-1800 °C for the MR1SB and 1000-3000 °C for the MR1SC). As two-color pyrometers they measure over two overlapping narrow waveband around 1 m, providing an output value independent on emissivity. These are two-color pyrometers, pointed and focused in the stagnation point of the sample, look through a quartz window of 1 cm thickness. The pyrometers are calibrated by a LANDCAL R1500T blackbody reference source together with the quartz window. The overall uncertainty of pyrometer measurements is estimated to be 10 °C. The pyrometer records the signal at 1 Hz.

The probes are mounted inside the Plasmatron test chamber at a standard distance of 0.445 m from the probe stagnation point to the exit of the nozzle. The placement ensures that the axis of the probe and the axis of the nozzle coincide.

[1] It as been shown that cold copper is not fully catalytic to N- and O-atom recombination [5]. It is considered here as "high reference catalytic".

3. Methodology

The reproduction of flight conditions in the Plasmatron facility relies on the Local Heat Transfer Simulation (LHTS) concept. The methodology, developed at the Institute for Problems in Mechanics of Moscow (IPM) [6] and adopted at the VKI [7], is a derivation of the theory of stagnation-point heat transfer in chemically reacting flows developed by Fay and Riddell [8] and Goulard [9] in the late fifties. It has been shown that a complete duplication of the real hypersonic flight can be achieved in a ground subsonic facility if the flight total enthalpy H_f, the total pressure P_f and the velocity gradient du_f/dx are locally matched on the test article.

3.1. Catalycity determination

Based on LHTS, the process of catalycity prediction by Plasmatron testing in stagnation point configuration combines experimental measurements and CFD data. Simulations of the subsonic Plasmatron flowfield, under Local Thermochemical Equilibrium (LTE) and axisymmetric flow assumptions, are performed by means of the VKI ICP Code [10]. The VKI Boundary Layer Code [11] solves the equations of the reacting boundary layer over a catalytic surface, under the assumption of Chemical Non-EQuilibrium (CNEQ) and axisymmetric flow, providing computations of the stagnation point heat flux as a function of wall temperature T_w, catalycity γ and boundary layer properties. The thermodynamic and transport properties of air are determined by means of the PEGASE library [12]. The VKI Rebuilding Code iterates on the boundary layer outer edge temperature T_e, until experimental and numerical heat flux are matched, so that the Boundary Layer Code provides outer edge enthalpy h_e and velocity v_e as outputs. Catalycity values can be finally identified by intersecting the experimental conditions q_w^{exp} and T_w^{exp} on an heat flux abacus $q_w = q_w(T_w, \gamma)$, built by the Boundary Layer Code. It is remarked that the hot wall experimental heat flux is calculated by radiative equilibrium wall assumption. The contribution coming from the conduction term is neglected ($q_{cond} = 0$), so that the heat flux is slightly underestimated. The error induced by this assumption is negligible with respect to the uncertainty in the cold wall heat flux. Still, the assumption is conservative.

3.2. Emissivity measurements

Directional emissivity values can be determined in-situ from Plasmatron infrared measurements. By definition the total emissivity is the ratio between the object radiance L and the blackbody radiance L^0 at the

same conditions of temperature and wavelength. The blackbody radiance at a given temperature is know if the temperature is known and can therefore be calculated by means of 2-color pyrometer measurements (which is indeed emissivity independent). The infrared radiance of the sample is instead measured by the radiometer in the 0.6-39 μm infrared range. Therefore the total emissivity at a certain temperature can be determined as:

$$\varepsilon = \frac{L}{L^0} \tag{3}$$

Emissivities can be also estimated by spectral reflectivity room-temperature measurements on virgin samples prior to plasma exposure. A Cary-500 VARIAN spectrophotometer working from the ultraviolet to the near infrared waveband (0.25 to 2.5 μm) is used together with Bruker IFS66v Fourier Transform Infrared Spectrometer operating from near infrared to medium infrared (2.5 to 40 μm). Correcting the measured reflectivity by Kirchhoff's law and weighting by the Planck's radiation distribution function $E(\lambda, T)$ the total emissivity as a function of the wall temperature reads:

$$\varepsilon(T) = \frac{\int_{0.25\mu m}^{40\mu m} (1 - r(\lambda)) E(\lambda, T)\, d\lambda}{\int_{0.25\mu m}^{40\mu m} E(\lambda, T)\, d\lambda} \tag{4}$$

4. Results

4.1. Operating conditions

The measurements are performed under standard air plasma (80% N_2 and 20% O_2) at a mass flow of 16 g/s. Table 1 describes the test conditions: surface temperature and chamber static pressure are chosen as target conditions accoriding to the IXV flight trajectory.

The reference temperature is measured at the center of the sample, on the surface exposed to the plasma flow, by the 2-color pyrometer. The generator power is adjusted in order to have the desired temperature target and pressure values specified are maintained constant thanks to air by-pass and vacuum pumps regulation. At steady state conditions, the samples are exposed to the plasma stream for the total test time specified. Flow conditions are calibrated right after the plasma exposure by means of the calorimetric and pressure probes which are maintained into the plasma stream until steady state conditions are well established.

Table 1: Test conditions matrix

Test	P_s	PW	T_w	q_{cw}	P_d	t
	[Pa]	[kW]	[K]	[kW/m2]	[Pa]	300
1	1300	99	1400	360	83	300
2	2000	104	1400	385	60	300
3	3000	133	1400	410	60	300
4	4000	124	1400	375	35	300
5	5000	130	1400	390	27	300
6	1300	152	1600	745	160	300
7	2000	158	1600	735	115	300
8	3000	158	1600	810	75	300
9	4000	178	1600	745	75	300
10	5000	189	1600	700	55	300
11	1300	235	1800	1150	235	300
12	2000	242	1800	1250	175	300
13	3000	253	1800	1280	130	300
14	4000	230	1800	1300	80	300
15	5000	236	1800	1215	80	300
16	1300	287	2000	1510	305	300
17	2000	292	2000	1490	220	300
18	3000	312	2000	1570	170	300
19	4000	331	2000	1655	150	300
20	5000	300	2000	1775	105	300
21	1300	84	1200	195	75	300
22	2000	93	1200	185	65	300
23	3000	95	1200	180	45	300
24	4000	99	1200	175	32	300
25	5000	105	1200	160	25	300

4.2. Enthalpy rebuilding and extrapolation to flight

The boundary layer environment for each test case was numerically rebuilt following the methodology explained in Sec. 3, through which enthalpy, temperature and velocity at the boundary layer outer edge can be determined. Enthalpy versus pressure conditions are compared with the IXV flight trajectory in Fig. 1. The flight data are computed as:

$$H^f_{tot} = h^f_\infty + \frac{1}{2} V^{2f}_\infty \tag{5}$$

$$p^f_{tot} = p^f_\infty + \rho^f_\infty V^{2f}_\infty \tag{6}$$

considering that at hypersonic speeds the first terms of the two formulas are negligible.

One can see that the test conditions cover the relevant part of the reentry. Particularly the cases at 1600 K and 1800 K offer the best reproducibility of the real case.

4.3. Emissivity

Emissivity values are calculated according to Eq. 3. These are shown in Fig. 2 which highlights the high radiative nature of the material, given by an ε that is

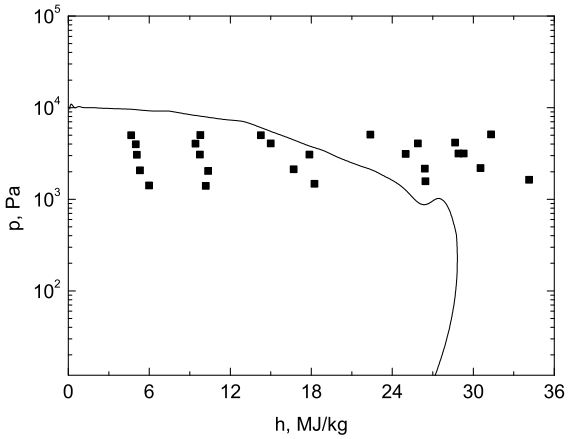

Figure 1: Comparison between the IXV flight trajectory and the rebuilt test conditions.

overall higher that 0.7 at high temperatures. One can observe an improvement of radiative properties of the TPS as the temperature raises from 1200 to 1600 K. For higher temperatures this trend is inverted and the emissivity decreases to lower values as a consequence of surface optical properties degradation. Minor differences can be instead noticed with pressure conditions.

Different statuses of the test environment in terms of pressure and temperature lead to different oxidations of the samples surface, which correspond to different optical properties, i.e. different emissivities. The diverse surface oxidation can be clearly noticed observing the samples surface in Fig. 3. Typically at low temperatures the material undergoes passive oxidation, that is an SiO_2 layer is formed over the surface. The thickness of the such layer increases from the order of Ångström (brownish color, sample 3a) to few microns (yellowish color, sample 3c), which corresponds to an improvement of emissivity from ~ 0.75 to ~ 0.85. It can be reasonably assumed that at higher temperatures the sample start to undergo into an active oxidation process (first a dark gray, sample 3d, and then light gray, sample 3e, color is observed), where the mention layers are removed from the surface with consequent degradation of emissivity. The variation of the processes described depends also on pressure, even though such variation are less evident and regular.

The results of in-situ measurements are also compared with total emissivity values extracted for room temperature reflectivity measurements after plasma exposure (the extrapolated value at the plasma test temperature is chosen for comparison). The agreement between the two techniques is excellent.

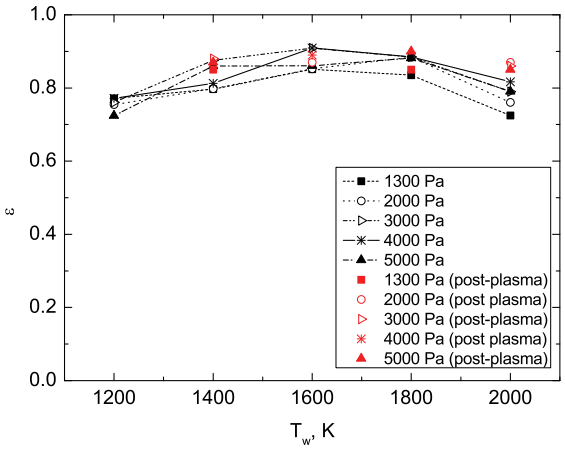

Figure 2: In-situ emissivity measurements and comparison with post-plasma room temperature measurements.

A temperature-dependent model of emissivity is built fitting the experimental data. The data available for flight condition cover the range 1200-2000 K. Additionally, room temperature measurements performed on virgin samples provide emissivity values at 300 K and 400 K. A 4th order polynomial curve is chosen to fit both Plasmatron data at reentry conditions and room temperature values. The result is shown in Fig. 4 together with the correspondent error bands. The fitting law predicts that the emissivity does not vary in the range 400-1100 K (where no experimental data at temperature are available). This can be considered reasonable, as only negligible surface changes due to oxidation processes are expected for such low temperatures. 2100 K is assumed as the upper applicability limit as for higher temperatures strong active oxidation phenomena become the leading processes, implying radical surface modification that cannot be handled by the present model.

If the fitting law is compared with the emissivity extrapolation obtained from room temperature measurements, as shown in Fig. 5, one can notice that the model underestimates emissivity values in the 400-1100 K range and above 2000 K, which is conservative for design calculations.

4.4. Catalycity

Catalycity values calculated by data processing of Plasmatron measurements are illustrated in Fig. 6 where γ is plotted as a function of wall temperature



(a) T_w = 1200 K (b) T_w = 1400 K (c) T_w = 1600 K (d) T_w = 1800 K (e) T_w = 2000 K

Figure 3: Change of surface appearance for different test conditions.

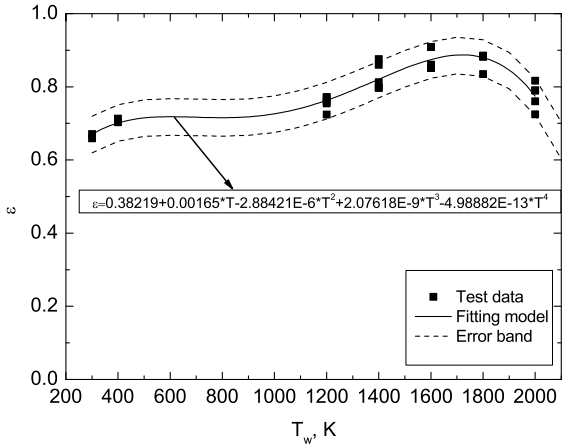

Figure 4: Emissivity model for the IXV thermal protection system.

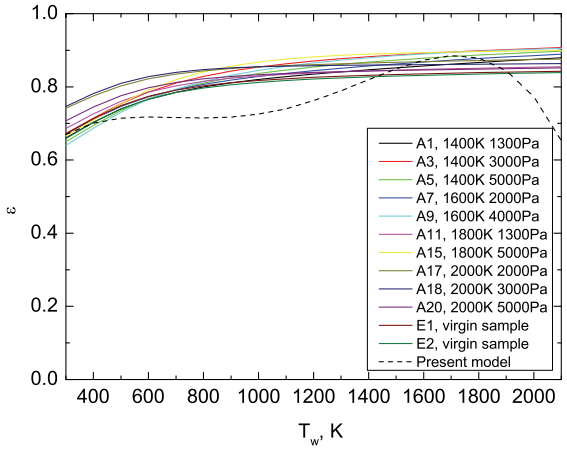

Figure 5: Comparison of the model with room-temperature measurements.

for different pressures imposed. One can notice that catalycity decreases with temperature from 1200 K to 1400 K and increases for temperatures higher that 1400 K up to 2000 K. Lower values of pressure yield higher catalycity and vice versa.

The results summarized for the effective recombination coefficients for the CMC TPS samples have been obtained from experimental measurements and a data processing taking into account a chemistry model for the chemical non-equilibrium in the boundary layer and a model for the wall recombination assuming $\gamma_O = \gamma_N = 1$. The results exhibit some trends that could be interpreted in the frame of the models used considering classical stagnation point heat-transfer expression for dissociated gases. Nevertheless it has to be noted that many phenomena happen together , even considering the macroscopic quantities, so the remarks given are illustrative and cannot stand for a final explanations or demonstrations.

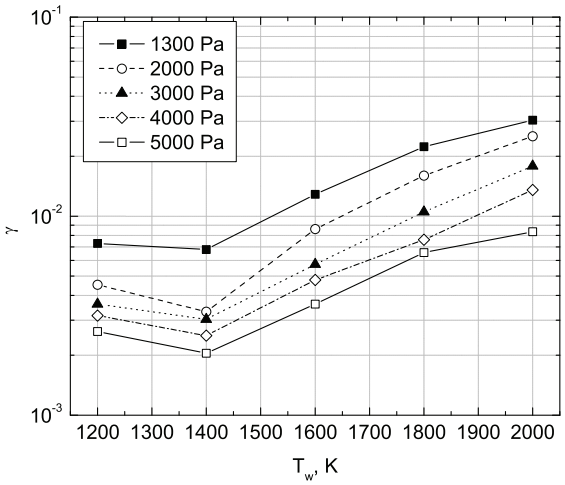

Figure 6: Calculated catalycity values for the different plasma conditions.

It appears that γ decreases when the static pressure increases, for all the temperature range considered. This feature is commonly observed from experimental characterization of surface recombination probabilities in plasma wind tunnels [13]. Considering a constant wall temperature, it implies a constant total heat flux. In a dissociated gas this heat flux corresponds to a conductive heat flux q_{cond} plus a diffusion heat flux due to the recombination at the wall q_{diff}. When the pressure rises, more chemistry is enhanced in the boundary layer, and in reference to Fay and Riddell equation for stagnation point heat transfer [8] q_{cond} becomes higher. Since q_{tot} is constant the remaining q_{diff} becomes smaller and in consequence γ which is directly related to the diffusion heat flux, decreases.

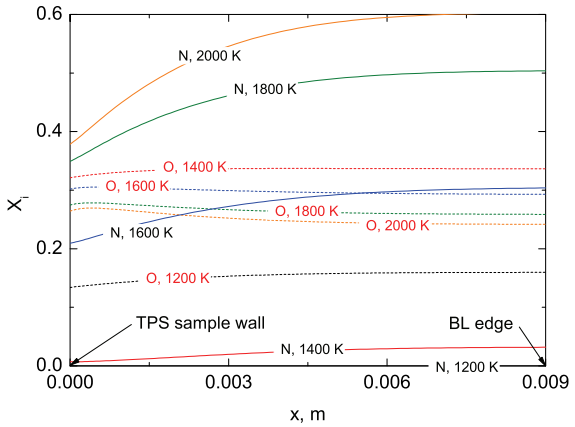

Figure 7: Atomic oxygen and nitrogen concentrations at 3000 Pa for different temperatures.

The variation of γ with the wall temperature presents two different behaviors as it decreases from 1200 to 1400 K and it increases at higher temperatures. Considering first the behavior between 1400 and 2000 K, some comments can be given once again from the stagnation point heat transfer expression, derived by Goulard [9]. This formula strictly applies for frozen boundary layer, which can be considered valid for the different tests cases analyzed. When T_{w} rises, q_{tot} increases, q_{NC} increases also (taking $\Phi = 0$ in the Goulard's formula). This trend is also clearly visible from the abaci plotted in Fig. 8. Looking at the a particular pressure (3000 Pa) one could see that the sum of the mass fraction of O and N ($X_{\text{O}} + X_{\text{N}}$) increases at the wall (see Fig. 7), which indicates that the contribution of the diffusion heat-flux increase as well. This last feature manifests that γ increases with T_{w} in this range of temperature. It appears through the velocity gradient β_{e} and the term $h_{\text{D,e}} y_{\text{e}}$ in Goulard's formula.

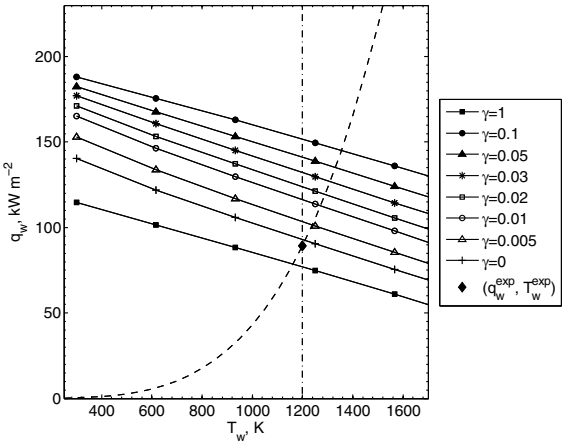

(a) T_{w} = 1200 K.

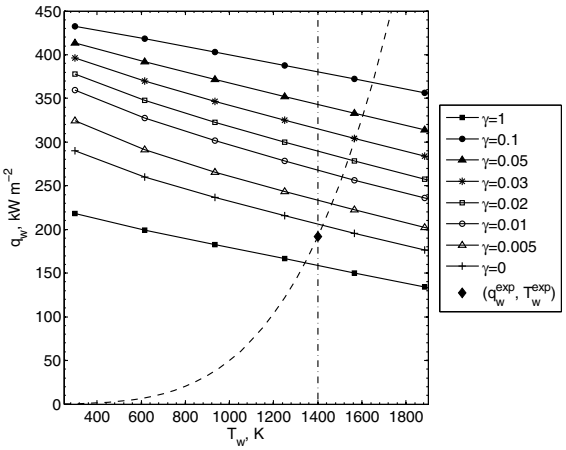

(b) T_{w} = 1400 K.

Figure 8: Abaci for case B3 (top) and case A3 (bottom) at 3000 Pa.

The decrease of γ between 1200 K and 1400 K is a direct consequence of the model which consider γ constant for O and N atoms reaching the wall. For T_w = 1200 K only O atoms recombine at the wall and release their formation energy. At T_w = 1400 K some N atoms start to diffuse to the wall as well and release a formation energy which is almost twice the one corresponding to O_2 formation. The same reasoning could be made for the different heat fluxes when T_w increases from 1200 K to 1400 K: q_{tot} increases, q_{NC} increases as well as q_{diff} (see Fig. 8). However since q_{diff} is constituted by two species (for T_w = 1400 K), O and N, and because N atoms which reach the surface carry much more energy to be released at the wall it results on a slight decrease for the global recombination coefficient.

Based on the results illustrated, a catalycity model is built fitting the experimental data. We look for a $\gamma = \mathbb{P}^n(p,T)$ polynomial surface by means of the MATLAB computational toolbox. A preliminary grid is necessary for data interpolation. We fit then the data with a 4th order polynomial function that reads:

$$\begin{aligned}\gamma = \mathbb{P}^4(p,T) = &C_1 \cdot T^4 + C_2 \cdot T^3 \cdot p + \\ &+ C_3 \cdot T^3 + C_4 \cdot T^2 \cdot p^2 + C_5 \cdot T^2 \cdot p + \\ &+ C_6 \cdot T^2 + C_7 \cdot T \cdot p^3 + C_8 \cdot T \cdot p^2 + \\ &+ C_9 \cdot T \cdot p + C_{10} \cdot T + \cdot C_{11} \cdot p^4 + \\ &+ C_{12} \cdot p^3 + C_{13} \cdot p^2 + C_{14} \cdot p + C_{15}\end{aligned} \tag{7}$$

The calculated coefficient are reported in Table 2 and the results is plot in Fig. 9 over the experiments data point.

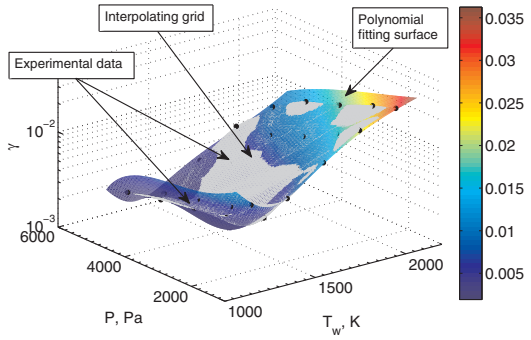

Figure 9: Catalycity model for the IXV thermal protection system.

Table 2: Coefficients for the catalycity polynomial surface

Coefficient	Value
C_1	3.79E-14
C_2	1.52E-14
C_3	-3.24E-10
C_4	-2.47E-15
C_5	-6.49E-11
C_6	9.96E-07
C_7	2.48E-16
C_8	6.08E-12
C_9	8.57E-08
C_{10}	-0.001274151
C_{11}	3.05E-17
C_{12}	-1.06E-12
C_{13}	1.86E-09
C_{14}	-5.21E-05
C_{15}	0.595900508

5. Conclusions

We have presented a summary of the experimental activities carried out at VKI Plasmatron facility in the framework of IXV mission, for the characterization of the ceramic Thermal Protection Material on the vehicle nose and windward side. The material has showed high emissivity and low catalytic nature which are ideal properties for thermal protection.

Catalycity and emissivity models have been built for the complete range of temperatures expected during flight which can be easily coupled in the well known radiative equilibrium wall boundary condition for CFD implementation. The validity of the models is strictly bounded to the range of flow conditions and particularly to the temperature/pressure levels imposed. The catalycity model provided takes into account a law depending on pressure and temperature. A future extension of the model should take into account additional parameters characterizing the specific testing conditions, in order to consider other relevant features for the ground-to-flight extrapolation.

Acknowledgments

The experimental campaign was performed under Snecma Propulsion Solide contract. The derivation of the models was performed under Dassault Aviation contract. The author is grateful to Mr. Pascal Collin for the operation of the experimental campaign. The European Space Agency and Thales Alenia Space are acknowledge for the constant support during the activities.l to Mr. Pascal Collin for the operation of the experimental campaign. The European Space Agency

and Thales Alenia Space are acknowledge for the constant support during the activities.

References

[1] M. J. H. Balat, M. Czerniak, J. M. Badie, Ceramics Catalysis Evaluation at High Temperature Using Thermal and CHemical Approaches, Journal of Spacecraft and Rockets 36 (2) (1999) 273–279.

[2] D. A. Stewart, Determination of Surface Catalytic Efficiency for Thermal Protection Materials - Room Temperature to Their Upper Use Limit, in: 31st AIAA Thermophysics Conference, AIAA 96-1863, New Orleans, LA,USA, 1996.

[3] A. F. Kolesnikov, A. N. Gordeev, S. A. Vasil'evsky, Simulation of Stagnation Point Heating and Predicting Surface Catalyisty for the EXPERT Re-Entry Conditions, in: The 6th European Symposium on Aerothermodynamics for Space Vehicles, ESA SP-659, Versailles, France, 2008.

[4] G. Tumino, IXV: the Intermadiate eXperimental Vehicle, ESA Bulletin 128 (November 2006).

[5] H. W. Krassilchikoff, O. Chazot, J. Thoemel, Procedure for the Determination of Cold Copper Recombination Efficiency, in: 2nd European Conference for Aero-Space Sciences, Bruxelles, Belgium, 2007.

[6] A. F. Kolesnikov, Conditions of Simulation of Stagnation Point Heat Transfer from a High-enthalpy Flow, Fluid Dynamics 28 (1) (1993) 131–137.

[7] P. F. Barbante, O. Chazot, Flight Extrapolation of Plasma Wind Tunnel Stagnation Region Flowfield, Journal of Thermophysics and Heat Transfer 20 (3) (2006) 493–499.

[8] J. A. Fay, F. R. Riddell, Theory of Stagnation Point Heat Transfer in Dissociated Air, Journal of Aeronautical Science 25 (2) (1958) 73–85.

[9] R. Goulard, On Catalytic Recombination Rates in Hypersonic Stagnation Heat Transfer, Jet Propulsion 28 (11) (1958) 737–745.

[10] G. Degrez, D. P. Vanden Abeele, P. F. Barbante, B. Bottin, Numerical Simulation of Inductively Coupled Plasma Flows under Chemical Non-equilibrium, International Journal of Numerical Methods for Heat & Fluid Flow 14 (4) (2004) 538–558.

[11] P. F. Barbante, G. Degrez, G. S. R. Sarma, Computation of Nonequilibrium High Temperature Axisymmetric Boundary-Layer Flows, Journal of Thermophysics and Heat Transfer 16 (4) (2002) 490–497.

[12] B. Bottin, D. P. Vanden Abeele, M. Carbonaro, G. Degrez, G. S. R. Sarma, Thermodynamic and Transport Properties for Inductively Plasma Modeling, Journal of Thermophysics and Heat Transfer 13 (3) (1999) 343–350.

[13] O. Chazot, J. Thoemel, M. Balat-Pichelin, Air Catalycity Determination in Plasma Wind Tunnels and Diffusion Reactors, in: Sixth European Symposium on Aerothermodynamics for Space Vehicles, ESA, Versailles, 2008.

Investigation of high enthalpy plasma flow by means of optical emission spectroscopy

Damien Le Quang

Aeronautics and Aerospace Department, lequang@vki.ac.be

Supervisor: Yacine Babou

Research engineer, Aeronautics and Aerospace Department, von Karman Institute for Fluid Dynamics, Belgium, babou@vki.ac.be

Pascal Andre

Professor, Electric arc and thermal plasmas, 24 avenue des Landais Aubière - France,Pascal.ANDRE@univ-bpclermont.fr

Abstract

The radiation of high enthalpy plasma jets produced by both Plasmatron and Microwave Plasma Torch (MPT) VKI facilities has been investigated by means of Optical Emission Spectroscopy (OES) in the visible and UV spectral ranges for various plasmagene gas (Air, N_2 and CO_2) . Appropriate diagnostics have been employed to characterize plasma properties for relevant operating conditions evidencing molecular and atomic radiative contribution. Proximity to equilibrium situation was evidenced and additional investigation on plasma optical thickness was executed by performing calculations accounting for radiative transfer.

Keywords: Plasma, Optical Emission Spectroscopy

1. Introduction

Plasma jets are used in various applications ([1], [2]) involving number of plasma generation technologies. Plasma produced using electromagnetic fields are classified as DC and AC discharges. Depending on the type of energy supplied and the amounts of energy transferred to the plasma, the properties of the plasma change in terms of electronic density and temperature [3]. In the present contribution, the analysis of the plasma thermodynamic state is carried out by means of Optical Emission Spectroscopy (OES) in the UV and visible spectral ranges. Focus is made on plasma jets produced by two different technologies. RF inductively coupled and microwave surface waves driven discharges, namely the Plasmatron and the new Microwave Plasma Torch (MPT) VKI facilities have been investigated. Typical temperatures achieved in the Plasmatron (resp. MPT) are about 5000 to 10 000 K (resp. 3000 to 6000 K). According to Griem criterion [4], plasmas described in this paper are expected to be close to LTE situation. Indeed, efficient energy exchange processes through collisions tend to promote the achievement of equilibrium. However, possible nonequilibrium arising from various causes detailed in [5] might occur in the investigated plasmas.

Conventional OES was performed to record the spectral radiance of the plasma. Emission was collected through an aperture and then focused with a fused silica converging lens onto the entrance slit of a spectrometer (1200 g/mm grating), combined with a CCD camera. This arrangement enabled to capture spatial emission in either radial or axial direction of the jet. Radial measurements were performed in the plasma jet generated by the Plasmatron at 21 cm from the exit. Axial measurements were also performed in the centerline of the jet generated by MPT. In both cases, the magnification was chosen in order to image 20 cm, which gives an estimated spatial resolution of about 800 μm. The slit was set to 10 μm leading to a measured spectral resolution of 0.066 nm. Calibration procedure was executed to characterize the optical response of the whole bench. Absolute calibration was performed in the visible spectral range using a ribbon tungsten lamp and its documented radiance. Relative

calibrations in the UV and visible spectral ranges were performed using deuterium and halogen sources (DH-2000 Mikropack). Abel inversion, completed with spatial filtering procedure has been applied to spectral radiance recorded during Plasmatron experiments in order to rebuild the local emission. In the case of MPT measurements, the local emission has been evaluated in the frame of the homogeneous isotherm column approximation. Methods adopted to examine the equilibrium situation taking place in the plasma are described in section 2. The resulting rebuilt temperatures are discussed in section 3 for Plasmatron measurements. Plasmatron facility will not be detailed in the following as it exists numerous sources available in the literature [6],[7]. MPT facility will be briefly described in section 4 before introducing the rebuilt properties of the jet.

2. Spectroscopic plasma diagnostics

In our situations, the main contribution to plasma emission are the atomic and molecular bound-bound radiative transitions. OES performed in the UV and visible spectral range enables to detect electronic transitions of about 1 to 6 eV. It enables to probe electronic population of the upper energy levels involved in emission process. Well suited methods coupled with plausible assumptions need to be adopted pending on the transition examined (atomic or diatomic) in order to identify relevant plasma jet properties (gas temperature T_g, excitation temperature T_{exc}, electronic density N_e) and assess possible departure from equilibrium. Methods are specified hereafter for atomic 2.1 and molecular 2.2 contribution.

2.1. Plasma diagnostics using atomic lines

2.1.1. Absolute population probing of a single electronic emitting level

The knowledge of the local radiance ϵ_{ul} allows a straight probing of the upper (emitting) level u population density through the relation:

$$\epsilon_{ul} = n_u \frac{A_{ul}}{4\pi} \frac{hc}{\lambda_{ul}} \quad (W.m^{-3}.sr^{-1}), \qquad (1)$$

where A_{ul} (s^{-1}) is the Einstein coefficient associated to spontaneous emission from level u to level l respectively of energy E_u and E_l (m^{-1}) and $\lambda_{ul} = \frac{1}{(E_u - E_l)}$ (m) designates the line position. At LTE, for a given atomic species, the internal level population density of a level u of energy E_u and degeneracy g_u follows the Boltzmann distribution at well defined temperature T_{LTE} given by:

$$n_u(T_{LTE}) = N(T_{LTE}) \frac{g_u exp\left(-\frac{hcE_u}{k_B T_{LTE}}\right)}{Q_{int}(T_{LTE})} \quad (m^{-3}), \quad (2)$$

where computed species concentration N (m^{-3}) and internal partition function Q_{int} are calculated at equilibrium using common tool [8]. The emission associated to a single transition (or to a group of transitions) is determined after subtracting a baseline (obtained through a linear fit on the edge of the lineshape) to the spectral line profile. It enables to remove molecular emission contribution which becomes stringent at plasma edges consequently to a weaker temperature. The local radiance is then obtained as the spectrally integrated profile corrected by the baseline. Equilibrium temperature T_{LTE} profiles are obtained solving equation 1 with population density given by equation 2. This approach might introduce errors due to uncertainty on molecular emission contribution which rise away from the center and becomes significant at the edge of the jet.

2.1.2. Population distribution of electronic emitting levels

Assuming that populations of excited states obey Boltzmann distribution (and without any assumption on chemical equilibrium situation), the excitation temperature T_{exc} is evaluated on the basis of the Boltzmann diagram method. This approach consists in plotting population densities n_u of probed emitting levels u versus energy E_u. Upper level density being straightly related to emission through relation 1, it might be expressed in terms of T_{exc} combining equations (1) and (2) in the form:

$$ln\left(\frac{n_u}{g_u}\right) = -\left(\frac{hc}{k_b T ex}\right) E_u + ln\left(\frac{N}{Q_{int}}\right). \qquad (3)$$

Excitation temperature T_{exc} of high lying states is then straightly obtained from the slope of a straight line fitted on the set of experimental emission logarithm values (left term of Equation 3).

2.1.3. Line broadening of hydrogen atom

The evaluation of electron density is performed through the measurement of the hydrogen line broadening due to Stark effect. Balmer transition (4-2) of atomic hydrogen line undergoes important broadening which is determined in a straight manner. The maximum of measured H_β line is obtained by subtracting a linear baseline intensity fitted on the edge of

the spectral line as illustrated in figure 1. Instrumental broadening (W_I) and to a lesser extent Doppler broadening (W_D) effects are the most important competing broadening mechanism occurring in the plasma. They are accounted through the following relations in order to get the Stark broadening contribution W_S from the measured Half Width at Half Maximum (HWHM) W_m:

$$\begin{aligned} W_D &= 3.58 \times 10^{-7} \lambda \left(\frac{T_g}{M}\right)^{0.5} \\ W_{DI} &= (W_D^2 + W_I^2)^{0.5} \\ W_S &= (W_m^{1.4} - W_{DI}^{1.4})^{\frac{1}{1.4}} \end{aligned} \tag{4}$$

M is the hydrogen weight (1.008 atomic mass unit) and lambda is the H_β center line position (486.13 nm). The gas temperature T_g is assumed to be equal to T_{LTE}. Electron densities were determined from an approximate experimental formula equation 5 using several assumptions detailed in [4].

$$N_e = 10^{22} \left(\frac{W_S}{4.7333}\right)^{1.49} \quad (m^{-3}) \tag{5}$$

Electron densities are also evaluated using up-to-date computed data offering higher accuracy than equation 5 proposed in [4]. Various sources provide tabulated H_β theoretical line profile for a wide set of validity domains in terms of electron densities, electronic temperatures and perturbing species. Stark width computations are proposed in [9] for electron densities between $10^{20} m^{-3}$ and $4 \times 10^{23} m^{-3}$. Supplied HWHM values in [9] correspond to W_{SD} defined as the broadening resulting from Stark and Doppler effects and approximated by $W_{SD} = (W_m^{1.4} - W_I^{1.4})^{\frac{1}{1.4}}$. Electron densities were determined using these data reported in Appendix A, assuming that electron temperature T_{el} is equal to the excitation temperature T_{exc}. Electron densities were calculated applying adequate interpolation on the measured T_{exc} and W_{SD}.

Experimentally, the investigated plasmas needs to be seeded with a small amount of water ($\approx 1\%$ mole fraction) in order to detect hydrogen line. We insure that the major contribution to plasma emission is not affected by the addition of water.

2.2. Plasma diagnostics using molecular spectra

The characterization in terms of temperature and concentration is made on the basis of molecular spectra fitting procedure. It consists on the minimization of the functional defined by the Root Mean Square Error between the experimental spectrum and the spectrum calculated under various equilibrium assumptions. In practice, the fitting algorithm for the minimization of the functional F, also designated by RMSE, was developed in Fortran environment, employing the EO4JYF so-called routine, based on quasi-Newton method well suited for our single and two variables fitting application.

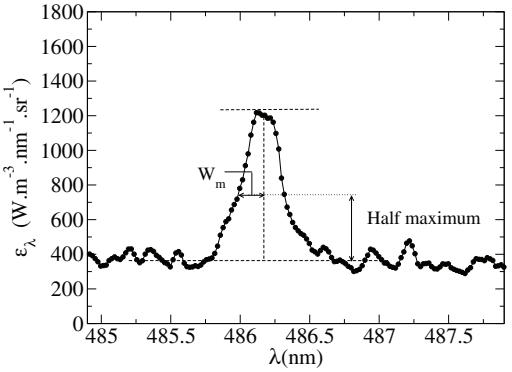

Figure 1: Spectral emission profile of H_β transition

The theoretical spectra required to determine the RMSE, have been calculated on the basis of the advanced tool developed and available at the EM2C laboratory, partially presented in various contributions [10] and so-called High Temperature Gas Radiation (HTGR) code. This computational tool enable to determine for non equilibrium C-N-O-Ar mixture plasmas at high temperature, high resolution emission and absorption spectra due to bound-bound, bound-free and free-free transitions over a wide spectral range from the VUV to the far infrared. This tool includes an exhaustive and reliable spectroscopic data base presented in [11]. In particular for diatomic bound-bound transitions the radiative properties are calculated combining up-to-date selected Electronic Transition Moment Function (ETMF) with vibrational wave functions obtained by means of the RKR method. HTGR code can support various assumption concerning the distribution of absorbing and emitting levels from the most basic (LTE assumption) to the detailed description of the internal levels populations.

Following the recommendations of [10] appropriate corrections should be applied to the theoretical emission spectra generated at high resolution, in order to elaborate simulated spectra compliant with the experimental data features. The effect of the instrumental broadening is taken into account by convoluting the theoretical spectra with the apparatus function experimentally which can be assessed as Gaussian profile shape in our experiments. Correction on calculated

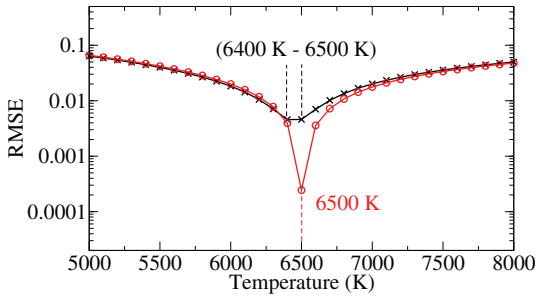

Figure 2: RMSE resulting from the fitting of a reference spectrum calculated at 6500 K (circles) and adding noise contribution (crosses)

lines spectral position is applied to account for the optical refractive index of air. Possible decrease of spectral resolution to improve the quality of the fitting procedure by fading the slight discrepancies between calculated and measured rotational line positions can be performed.

In order to assess the robustness of adopted approaches, several tests have been carried out using a reference spectrum. Additional background and noise have been added to a reference spectrum elaborated at T_{LTE}=6500 K and the fitting procedure was applied. We evidence deterioration of the accuracy on the RMSE minimum (as illustrated figure 2) due to superimposed random noise of 10% of the spectral intensity value. Nevertheless, best fit are obtained with a good approximation on the temperature (less than 1%). The examination of the equilibrium situation taking place in plasma jets is conducted using the minimization procedure under three distinct assumptions in order to yield reliable indications about the actual situation through resulting temperature profiles cross comparisons. These assumptions are specified in the followings.

2.2.1. *Temperature determination assuming thermal equilibrium*

Assuming that the plasma is at thermal equilibrium, a unique temperature is defined in the plasma T_{gas}, meaning that the overall internal levels (electronic vibrational and rotational) are populated following the Boltzmann distribution at T_{gas}. The fitting is then performed on the basis of elaborated spectra calculated with a single temperature T_{gas}. The temperature is obtained applying the fitting procedure on experimental spectrum normalized to unity, which consist in the minimization of the functional:

$$F\left(T_{gas}\right) = \sqrt{\frac{1}{N}\sum_{i=1}^{N}\left(\bar{S}_{\lambda_i}^{exp} - \bar{S}_{\lambda i}^{theo}(T_{gas})\right)^2} \qquad (6)$$

where $\bar{S}_{\lambda_i}^{exp}$ (resp. $\bar{S}_{\lambda_i}^{theo}$) designates the normalized experimental spectrum (resp. calculated spectrum) and spectrum and N is the number of experimental points in the considered spectral range.

2.2.2. *Thermal non equilibrium assessment using two temperatures approach*

The common two temperatures description of the plasma is considered, assuming that electronic and vibrational population levels follow a Boltzmann distribution ruled by a well determined temperature T_{vib}, and rotational levels are assumed to be in equilibrium with the translational mode of heavy species at the temperature T_{rot}. The determination of the couple of temperatures (T_{rot},T_{vib}) consists in the minimization of the functional defined as:

$$F\left(T_{rot}, T_{vib}\right) = \sqrt{\frac{1}{N}\sum_{i=1}^{N}\left(\bar{S}_{\lambda_i}^{exp} - \bar{S}_{\lambda_i}^{theo}(T_{rot}, T_{vib})\right)^2} \qquad (7)$$

2.2.3. *Chemical non equilibrium assessment assuming thermal equilibrium*

In addition to the two previous approaches, which can be applied to emission spectra measured in relative units, spectra available in absolute intensity are useful to estimate departure to chemical equilibrium assumption. In the frame of this approach the thermal equilibrium is admitted to be achieved at the unique temperature defined by T_{gas} . However, no assumption is made concerning the total amount of the excited molecular species N_{mol}. The couple of data (T_{gas}, N_{mol}) are determined minimizing the functional expressed as follows:

$$F\left(T_{mol}, N_{mol}\right) = \sqrt{\frac{1}{N}\sum_{i=1}^{N}\left(S_{\lambda_i}^{exp} - S_{\lambda_i}^{theo}(T_{gas}, N_{mol})\right)^2} \qquad (8)$$

where $S_{\lambda_i}^{exp}$ (resp. $S_{\lambda_i}^{theo}$) is related to the emission of the absolute intensity of the experimental spectrum (resp. calculated spectrum)

3. Plasma flow characterization in VKI Plasmatron facility

3.1. *Air plasma jet*

Air plasma jet produced by VKI Plasmatron facility operating at 273 mbar, 500 kW and 16 g/s was investigated. The radial characterization of air plasma

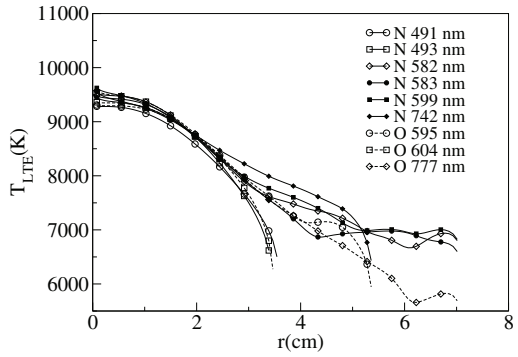

Figure 3: Equilibrium temperature profiles using N and O atomic lines in air Plasma jet

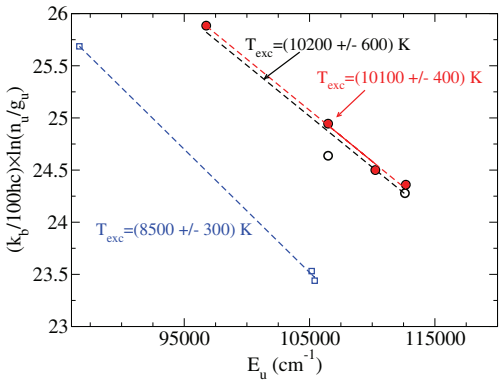

Figure 4: Boltzmann plots at the center of the jet using 6 N lines (black circles), 4 N lines (red filled circles) and 3 O lines (blue squares)

in terms of temperature was performed using measured local radiance ϵ_{ul} associated to radiative transitions due to spontaneous emission of N and O excited species. Required spectroscopic data with associated references are given in Appendix B. LTE temperature profiles are then obtained solving equation 1 at each radial position, with population density given by equation 2. Admitting a severe error of 20% on rebuilt emission, uncertainties on T_{LTE} were estimated on the basis of the logarithm of equation 1 to be less than 2 %:

$$\left|\frac{\Delta T_{LTE}}{T_{LTE}}\right| = \frac{k_b T_{LTE}}{hcE_u}\left|\frac{\Delta\epsilon_{ul}}{\epsilon_{ul}}\right| \tag{9}$$

Selected lines offer strong and distinct peaks allowing an accurate determination on line intensities over a large radial extent. Discrepancies starting to rise beyond 2.5 cm are attributed to higher errors on rebuilt total emission of the lines due to lower signal over noise ratio of weak transitions. Strong emission line of Oxygen at 777 nm allows reliable total emission rebuilding until 6 cm radial distance. LTE temperature profiles plotted in figure 3 show excellent agreement with a temperature of about 9500 K at the centerline of the plasma and about 8000 K 2.5 cm further. Within this temperature range, O and N equilibrium concentrations remains nearly constant with the temperature ($\approx 1.8 \times 10^{23} m^{-3}$ for N and $5 \times 10^{22} m^{-3}$ for O). In this case, temperature determination is mostly driven by the exponential term equation 2 . Good agreement between temperature profiles suggests for the proximity to LTE.

In the implemented procedure, the number of lines taken into account for the excitation temperature determination is ruled by an intensity threshold that excludes weak lines drown in the noisy background. For the calculation accounting 6 N lines at the center of the jet, only two lines (599 nm with $E_u = 110245$ cm^{-1} and 742 nm with $E_u = 96750$ cm^{-1}) are remaining at 3 cm radial distance. For the calculation using 4 N lines at the center of the jet, we excluded both the line at 583 nm ($E_u = 112609$ cm^{-1}) vanishing rapidly and the line at 599 nm which deviates slightly from the linear regression performed using 6 N lines, as shown figure 4. Although the number of accessible Oxygen lines is small, it covers a large energy range allowing a high reliability in temperature determination. Boltzmann diagrams obtained at the centerline, displayed in figure 4, allows straight determination of excitation temperature using linear regression. This method presents a considerable sensitivity to the number of lines taken into account and their corresponding upper energy levels that affects greatly the estimated error on the linear regression. Uncertainties associated to this approach are evaluated by the standard deviation of the slope associated to the linear regression. The small dispersion of experimental points compared to linear regressions ensured an uncertainty of less than 6%. On figure 5, excitation temperature profiles T_{exc} are plotted with the averaged equilibrium temperature profile T_{LTE} resulting from atomic lines displayed in figure 3. Confrontation between equilibrium T_{LTE} and excitation T_{exc} temperatures shows an overall good agreement and would confirm the LTE establishment.

The electron number density profiles resulting from Stark broadening investigation for air plasma at 273 mbar seeded with small amount of water are plotted in figure 6. A good agreement is observed between profiles rebuilt from empirical relation 5 and using tables in Appendix A taken from [9]. Calculations with $W_I = 0.03$ nm remains in good agreement with

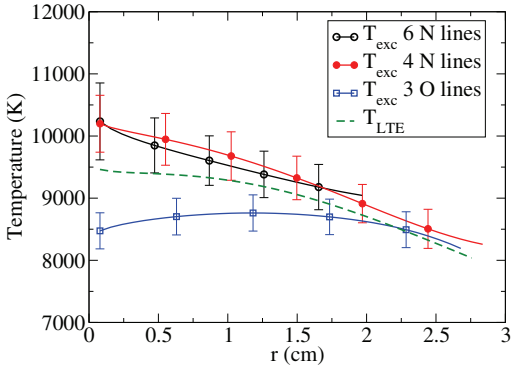

Figure 5: Excitation temperature profiles using 6 N lines (black circles), 4 N lines (red filled circles) and 3 O lines (blue squares) and mean equilibrium temperature profile derived from N and O lines (dashed line)

calculations using actual value of 0.066 nm. The weak sensitivity to possible experimental uncertainty on the instrumental broadening W_I points out the good robustness of both approaches. Electron density profile calculated at equilibrium with measured T_{LTE} exhibits a considerable departure to measurements which is kept along the radius. Equilibrium temperature associated to measured electron densities was estimated to be

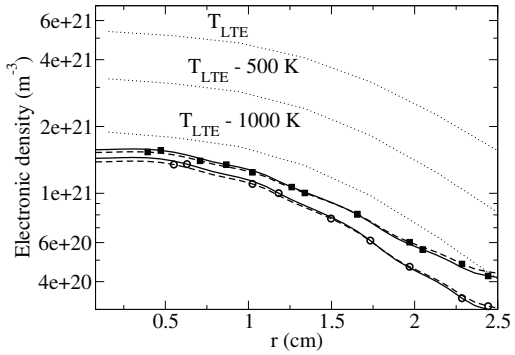

Figure 6: Electronic density profiles derived from approximate formula 5 (solid lines), computed data from [9] (dashed lines; circles:W_I=0.03 nm, squares:W_I=0.066 nm), and corresponding equilibrium calculation (dot line) at mean T_{LTE}, T_{LTE}-500 K and T_{LTE}-1000 K

Although measured electron densities and those rebuilt at equilibrium remains of same order of magnitude (10^{21} m^{-3}), observed differences give evidence for a significant departure of the plasma from equilibrium resulting from some electronic reactions ruled by improper balance. This peculiarity is typical of plasma undergoing recombination where measured electron densities are lower than equilibrium values [12], conversely to ionizing plasma characterized by electron densities higher than equilibrium values. This recombining situation was not evidenced with Boltzmann diagrams plotted using observed atomic lines. However, such situation would be possibly pointed out if lines involving energy levels close to the ionization energy E_i (117225 cm^{-1} for N and 109837 cm^{-1} for O species) would have been measured.

3.2. CO_2 plasma jet

The investigation of the thermodynamic state of the CO_2 plasma jet produced at 200 mbar, 300 kW and 16 g/s was carried out using the C_2 Swan vibrational bands Δ v=0 and -1. We check that the contribution of CO^+ Comet Tail system was not significant in the spectral range of interest and therefore fittings are performed only accounting C_2 Swan molecular system. Fitting procedures were applied radially using various methods described in 2.2 until the drop of the signal at about 2.5 cm away from the jet center line. Results were compared with an equilibrium temperature profile issued from O and C atomic lines (777 nm, 833 nm and 844 nm Appendix B) and giving a temperature of about 6700 K at the jet centerline. All temperature profiles are gathered in figure 10.
Equilibrium temperature T_{gas} was determined using the vibrational band sequence Δv=0, lying in the spectral range 490-520 nm for two spectral resolutions (0.1 and 1 nm) higher lower than the experimental one. Best fits are displayed in figure 7. Whatever the adopted resolution the best fits present an excellent agreement with the experimental spectrum. The intensity of the three main vibrational bands (0-0, 1-1 and 2-2) does not present any particular departure to the LTE calculation. Both temperature profiles are in excellent agreement over the considered radial domain. The agreement is less good with the atomic temperature profile at LTE but however reasonable enough ($\sim$ 7 % at the center) to admit the achievement of equilibrium.

The vibrational and rotational temperatures have been rebuilt with a fitting applied to the C_2 Swan emission in the spectral range 490-565 nm (at 0.1 nm resolution), including the contribution of vibrational sequences Δ v=0 and -1 to consider a large number of emitting vibrational levels. The resulting best fit are given in figure 8. The temperature profiles are found to be in good agreement indicating for a medium close the thermal equilibrium. Nevertheless, at the center, T_{vib} and T_{rot} are found to be about 800 K lower than the atomic temperature at LTE. The difference ($\sim$ 15 % at the center) is reduced toward the edges.

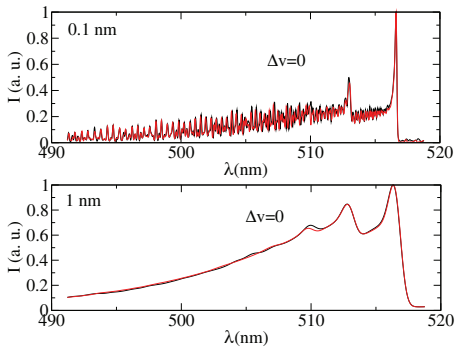

Figure 7: Experimental spectra (black) and best fits (red) using Δ v=0 C_2 Swan system with 1 nm (top) and 0.1 nm (bottom) spectral resolutions

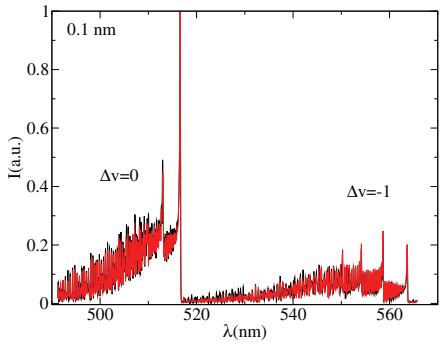

Figure 8: Experimental spectra (black) and best fits (red) using Δ v=0 and Δ v=-1 C_2 Swan systems with 0.1 nm spectral resolution

In the frame of the approach accounting for species concentration, the absolute emission associated to vibrational bands Δv=0 have been used to determine the equilibrium temperature T_{gas} and the C_2 species concentration N_{C_2}. The fitting was applied for two resolutions 0.1 and 1 nm. The best fits are compared to the experimental spectra in figure 9. As in the previous cases a very good agreement was obtained. The temperatures present a fair agreement with the atomic temperature confirming the above considerations. In figure 9, deviation between the measured concentration of C_2 and the calculated calculated concentration at atomic T_{LTE} is observed. It emphasis a departure to chemical equilibrium situation. The C_2 concentration profiles are slightly affected by the selected resolution. The overall temperature profiles resulting from the various fitting methods are displayed in figure 10. Profiles exhibit an important dispersion however limited to 1000 K leading to difference of ($\sim$ 15 % along the radius). The observed discrepancies can be reasonably attributed to quality of the experimental data. Nevertheless the general good agreement would indicate for a situation close to LTE situation.

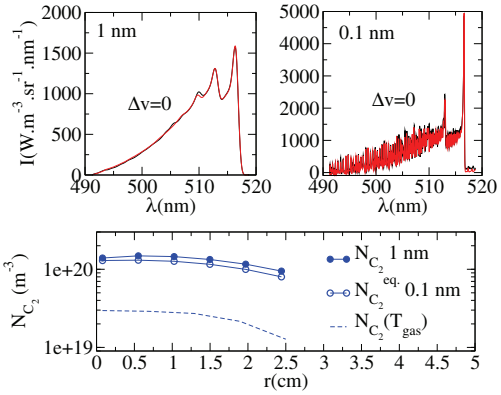

Figure 9: [*TOP*] Experimental spectra (black) and best fits (red) using Δ v=0 C_2 Swan system with 1 nm and 0.1 nm spectral resolutions.[*BOTTOM*] Corresponding measured C_2 concentration and calculated concentration at T_{LTE} derived from atomic lines

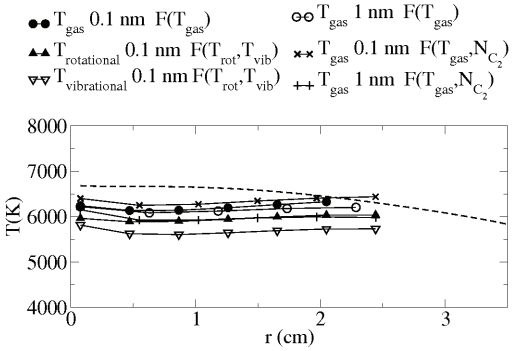

Figure 10: Overall temperature profiles of CO_2 plasma jet at 200 mbar (solid lines) and T_{LTE} temperature profile calculated using atomic lines

Also to assess the identified equilibrium situations, a comparison between measured spectra and calculations accounting radiative transfer inside the jet is proposed. Starting from a reference temperature profile based on atomic LTE temperature will be used to perform radiative transfer calculation. The line of sight spectral radiance ($W.m^{-2}.sr^{-1}.nm^{-1}$) is rebuilt. The spectral radiance ϵ_λ recorded experimentally is rebuilt solving the Radiative Transfer Equation (RTE) along the plasma jet diameter. Simple 1D geometry can be investigated as the collected light travels on the optical

axis. The RTE can then be written as:

$$\frac{d\epsilon_\lambda}{dx} = \eta_\lambda(x) - \kappa_\lambda\epsilon_\lambda(x) \qquad (10)$$

where η_λ (resp. κ_λ) designates the emission (resp. absorption) coefficient calculated with the HTGR computational tool. A finite difference method was used to solve equation 10. An appropriate spatial step, corresponding to the experimental spatial resolution (800μm) in the radial direction of the jet, was used for the calculation. Boundary condition was set to $\epsilon_\lambda(0)$=0. For each radiative transition HTGR code gives the coefficients of emission and absorption corrected by induced emission. Calculations have been performed considering optically thin (no absorption) and optically thick (absorption) cases for the emission of C_2 Swan Δv=0,+1 and -1. Calculated spectra were convoluted with an apparatus function of 0.066 nm to match experimental resolution. A very good agreement is observed with less than 10% discrepancy on the total intensity from the three bands Δv=0,+1 and -1 of C_2 Swan system (figure 11), evidencing for negligible self absorption in the visible spectral region. Also, the good agreement between associated cumulated intensities, depicted in figure 11, allow to rely on the radiative properties determination and suggests that the plasma can be reasonably described using the Local Thermodynamic Equilibrium assumption.

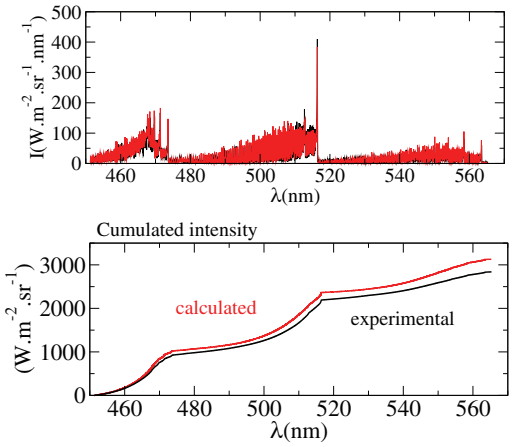

Figure 11: Experimental spectrum (black) and HTGR rebuilt spectrum convoluted with 0.066 nm apparatus function (red)

4. Investigation of a new microwave plasma source

A new plasma source was built on the basis of a magnetron operating at 2.45 GHz to produce microwave power in the kilowatt range transmitted through a rectangular waveguide to the gas flowing in a quartz tube of 30 mm inner diameter, figure 12. As described in [13], different types of microwave induced plasma can be distinguished. The VKI MPT facility produced what is called surface waves sustained discharges. Microwaves that sustain the plasma are launched into a quartz tube, electromagnetic waves propagate along the quartz-plasma boundary and ionize the gas. The power ranges achieved allow to sustain molecular plasmas suitable to perform OES.

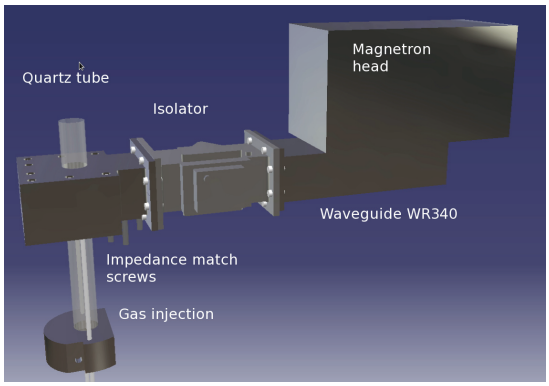

Figure 12: Representation of the Microwave Plasma Torch

4.1. *Plasma flow regimes for various operating conditions*

Various configuration of the torch have been preliminary investigated for a wide range of operating flow rates (0 - 1 g/s), injected power ($\geq$ 1 kW - 3 kW), geometrical configurations (injection strategies, additional nozzle, quartz tube length) and impedance matching. It allows to determine ideal configurations of the torch which involves both optimized electrical coupling and steady flow behavior. An isolator is placed between the magnetron head an the waveguide preventing from any reflection occurring onto the magnetron head and allowing power monitoring. Reflected power monitoring offers a good indication on electrical coupling and flow dynamic unsteadiness. Indeed, the electrical coupling between microwave energy and plasma flow in the quartz tube is strongly depending on the dynamical behavior of the flow which changes the impedance as it fluctuates. As an example, figure 13 shows the reflected power in time or frequency domain representation at different mas flow rate, in the case of an air plasma with a forwarded power of 1500 W. Amplitudes of the signals are greatly affected by the plasma flow behavior. Fourier transformation reveals important fluctua-

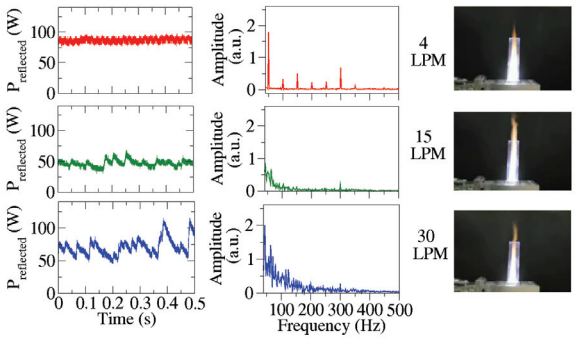

Figure 13: Reflected power in time and frequency domain for several mass flow rates and associated picture of the jet

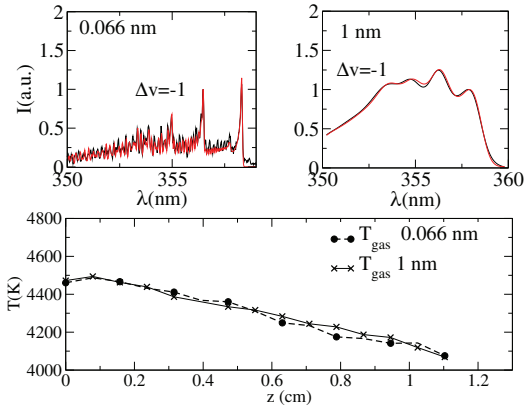

Figure 14: [*TOP*]Experimental spectra (black) and best fits (red). [*BOTTOM*]Equilibrium temperature axial profiles determined from N_2^+ Δv=-1 system using 1 nm and 0.066 nm spectral resolution

tion of the jet in a frequency domain lower than 200 Hz as the mass flow rate is increased. For low mass flow rate, only fluctuations corresponding to electrical frequency of 50 Hz and its harmonics are observed. A mass flow rate of 5 LPM was chosen to perform OES on nitrogen plasma jet in the following.

4.2. N_2 plasma flow in the VKI MPT facility

OES was performed in the UV spectral range to record axial profile of both N_2 2nd Positive and N_2^+ First Negative molecular emission occurring in a pure N_2 plasma. As some nitrogen lines are overlapping the molecular emission in this spectral range, we carefully investigated the emission between 350 and 360 nm where only molecular emission is observed. In order to perform optical diagnostics of the jet, some assumptions on the nature of the jet are required, as the spatial direction investigated does not present any symmetry. We assume that the radial distribution of the emission is flat. In this case, we are straightly obtaining the local emission from the measured emission, allowing a direct comparison with calculated spectra. Figure 14 shows molecular equilibrium temperature profiles using approach detailed in 2.2 for 1 nm and 0.066 nm spectral resolution. On figure 14, best fits (red) present an excellent agreement with the experimental spectrum (black). The spectral resolution does not affect temperature determination. Calculated spectra using a single temperature fit with experimental spectra, which assess the proximity to thermal equilibrium.

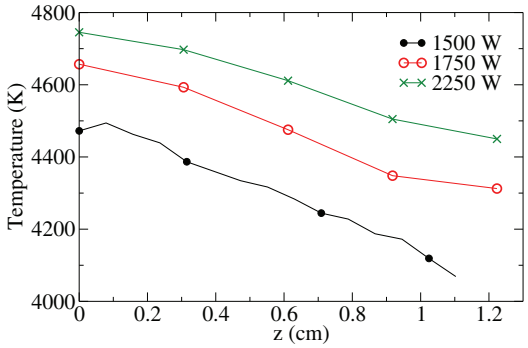

Figure 15: Equilibrium temperature axial profiles determined from N_2^+ Δv=-1 system using 1 nm spectral resolution for several forwarded power

Increasing the power leads to an increase of the temperature over a larger extent as shown figure 15. The temperature at the centerline of the jet is about 4550 K, 4650 K and 4750 K for the respective forwarded powers of 1500 W, 1750 W and 2250 W.

5. Conclusion

Conventional optical diagnostics by mean of OES have been performed for both VKI Plasmatron and MPT facilities. It allows to assess the thermodynamical state of the plasma using non intrusive technique. Confrontation between equilibrium and excitation temperatures from N and O atomic lines have suggested that air plasma produced at 273 mbar by Plasmatron facility is close to thermal equilibrium with a temperature of about 9500 K in the centerline of the jet. Analysis of electronic density emphasis a slight

departure from chemical equilibrium similar to the situation encountered in plasma undergoing recombination. CO_2 plasma jet at 200 mbar has been characterized in terms of temperature using the emission of C_2 Swan vibrational bands. The overall satisfactory agreement between measured temperatures using several kind of equilibrium assumptions indicates that the plasma is close to thermal equilibrium ($\approx$ 6700 K at the jet centerline), while measured C_2 concentration indicates a slight departure to chemical equilibrium. Optically thin CO_2 plasma assumption has been confirmed in the visible spectral range. Preliminary investigations of surface waves sustained discharge created by the MPT was performed to determine ideal configuration of the torch to perform spectroscopic measurements. Emission of pure N_2 plasma jet was recorded in the UV spectral range. Typical equilibrium temperature of about 4600 K were found at the jet centerline. Several improvements will be made concerning the analysis of spectra, in particular with the probing of vibrational levels using molecular fitting procedure. Plasma facilities will be employed to produce supersonic plasma jet that exhibits strong departures to equilibrium in order to validated kinetic models.

Appendix

Appendix A. Tabulated electron density

T_{el} (K)	5000	10000	15000
N_e (m^{-3})			
1.00×10^{20}	0.444	0.424	0.409
2.14×10^{20}	0.764	0.741	0.722
4.68×10^{20}	1.260	1.290	1.280
1.21×10^{21}	2.110	2.170	2.180
2.14×10^{21}	3.480	3.610	3.660
4.68×10^{21}	5.760	6.010	6.100
1.00×10^{22}	9.560	9.990	10.200

Table A.1: Stark and Doppler broadening W_{SD} full width at half maximum (Å) supplied in [9] versus electron temperature T_{el} and electron density N_e.

Appendix B. Spectroscopic data

Table B.2: Spectroscopic data of the considered O and N emission lines used for air plasma. [14] and [15] (indicated by a star).

λ_{air}(nm)	A_{ji} (s^{-1})	E_i (cm^{-1})	E_j (cm^{-1})	g_i	g_j
N lines			$D_e = 117225.7 cm^{-1}$		
491.494*	8.08 10^5	86137.350	106477.800	2	2
493.512*	1.76 10^6	86220.510	106477.800	4	2
582.954	6.375 10^5	95532.150	112681.389	6	6
583.462	3.800 10^5	95475.310	112609.612	2	4
599.943	3.64 10^6	93581.550	110245.183	2	2
742.3641	5.95 10^6	83284.070.550	96750.840	2	4
O lines			$D_e = 109837.02 cm^{-1}$		
595.839	3.78 10^5	88630.587	105409.008	3	3
595.839	6.80 10^5	88630.587	105409.008	3	5
595.858	2.27 10^5	88631.146	105409.008	5	5
595.858	2.52 10^4	88631.146	105409.008	5	3
595.858	9.06 10^5	88631.146	105409.008	5	7
595.864	5.04 10^5	88631.303	105409.008	1	3
604.623	1.05 10^6	88630.587	105165.232	3	3
604.644	1.75 10^6	88631.146	105165.232	5	3
604.649	3.50 10^5	88631.303	105165.232	1	3
777.194	3.69 10^7	73768.200	86631.454	5	7
777.417	3.69 10^7	73768.200	86627.778	5	5
777.539	3.69 10^7	73768.200	86625.757	5	3

Table B.3: Spectroscopic data of the considered C and O emission lines used for CO_2 plasma. [14].

λ_{air}(nm)	A_{ji} (s^{-1})	E_i (cm^{-1})	E_j (cm^{-1})	g_i	g_j
C lines			$D_e = 90820.42 cm^{-1}$		
833.515	3.51 10^7	61981.82	73975.91	3	1
O lines			$D_e = 109837.02 cm^{-1}$		
777.194	3.69 10^7	73768.200	86631.454	5	7
777.417	3.69 10^7	73768.200	86627.778	5	5
777.539	3.69 10^7	73768.200	86625.757	5	3
844.625	3.22 10^7	76794.978	88631.303	3	1
844.636	3.22 10^7	76794.978	88631.146	3	5
844.676	3.22 10^7	76794.978	88630.587	3	3

Acknowledgments

Results concerning VKI Plasmatron high enthalpy flow characterization were produced within the frame of AMOD and VAEC contract supported by ESA.

References

[1] H. Conrads, M. Schmidt, Plasma generation and plasma sources, Plasma Sources Sci. Technol. Vol.9 (2000) pp.441–454.

[2] A. Ganguli, R. D. Tarey, Understanding plasma sources, Current Science Vol.83-NO.3.

[3] C. Tendero, C. Tixier, P. tristan, J. Desmaison and P. Leprince, Atmospheric pressure plasmas: A review, Spectrochimica Acta Part B 61 (2006) 2 30.

[4] H. Griem, Plasma spectroscopy, Mcgraw-Hill, New York.

[5] C. H. Kruger, T. Owano, M. Gordon, C. Laux, Nonequilibrium effects in thermal plasmas, Pure and Appl. Chem. Vol. 64, No. 5, pp. 607-61.

[6] B. Bottin, M. Carbonaro , S. Zemsch and G. Degrez, Aerothermodynamic design of an inductively coupled plasma wind tunnel, 32nd AIAA Thermophysics Conference, Atlanta, USA AIAA paper 97-2498.

[7] B. Bottin, O. Chazot, M. Carbonaro, V. Van Der Haagen and S. Paris, Measurement techniques for high enthalpy and plasma flows, RTO-EN-8 AC/323(AVT)TP/23,8.

[8] B. J. McBride, S. Gordon, Computer program for calculation of complex chemical equilibrium compositions and application. II User manual and program description., NASA Lewis Research Center, Cleveland, OH Reference publication 1311.

[9] M. A. Gigosos, V. Cardenoso, New plasma diagnosis tables of hydrogen Stark broadening including ions dynamics, J. Phys. B:At. Mol. Opt. Phys. 29 (1996) 4795–4838.

[10] Y. Babou, Transferts radiatifs dans les plasmas de mélange CO_2-N_2: base de données spectroscopiques, étude expérimentale et application aux rentrées atmosphèriques, Laboratoire d'Enèrgétique Moléculaire et Macroscopique, Combustion (EM2C) du CNRS et de l'ECP, Paris.

[11] M. Y. Perrin, P. Rivière, A. Soufiani, Radiation database for Earth and Mars entry, Von Karman Lecture Series RTO-EN-AVT-162.

[12] C. O. Laux, T. G. Spence, C. H. Kruger, R. N. Zare, Optical diagnostics of atmospheric pressure air plasmas, Plasma Sources Sci. Technol. 12, 124-138.

[13] N. de Vries, Spectroscopic study of microwave induced plasma: Exploration of active and passive method, Technische Universiteit Eindhoven.

[14] NIST atomic spectra database , http://physics.nist.gov/PhysRefData/ASD/index.html.

[15] P. L. Smith, C. Heise, J. R. Esmond, R. L. Kurucz, KURUTZ atomic spectra database , http://www.pmp.uni-hannover.de/cgi-bin/ssi/test/kurucz/sekur.html.

Modeling of inductively coupled plasma reactor for nanoparticles production

Silvânia Lopes

Aeronautics and Aerospace Department, lopes@vki.ac.be

Supervisor: Patrick Rambaud

Assistant Professor, Aeronautics and Aerospace, Environmental and Applied Fluid Dynamics Department, von Karman Institute for Fluid Dynamics, Belgium, rambaud@vki.ac.be.

Promotor: Jean-Marie Buchlin

Professor, Faculté des science appliquées, Université Libre de Bruxelles B – 1050, Belgium, buchlin@vki.ac.be.

Abstract

The general purpose of this thesis is to design a inductively coupled plasma (ICP) reactor for efficient production of nanoparticles and to model the nanoparticle synthesis in the ICP reactor. In the present work, a mathematical model has been developed for simulating the behavior of ICP torches, using a Computational Fluid Dynamic open (CFD) source code OpenFoam. Preliminary experimental characterization of ICP jet has been also performed, using the VKI plasma Minitorch.

Keywords: CFD modeling,ICP reactor, pressure measurement.

1. Introduction

Nanotechnologies, especially nanoparticles related applications, have recently received tremendous interest due the numerous innovative potential they offer. Nanomaterials are usually produced by compaction of a powder of nanoparticles. They are characterized by a large number of grain boundary interfaces in which the local atomic arrangements are different from those of the crystal lattice [1]. The small size of the nanoparticles is responsible for many changes in the thermo-physical properties compared with the bulk materials, which makes them suitable for novel applications. Examples of these new properties include lower melting temperature, improved hardness and ductility, high self-diffusion coefficient, catalytic activity, and intriguing optical and electronic properties. However, the processes used for generating the nanoparticles play an important role in terms of controlling the size, morphology, crystalline phase, and composition, which ultimately determine the properties of the nanostructure material.

Inductively couples thermal plasma (ICTP), and in general thermal plasma processing present several distinctive advantages over other synthesis routes for nanoparticles, due mainly to their high temperature and energy density, large plasma volume and long residence/reaction time by virtue of its low velocity. Additionally, an ICTP is inherently contamination-free because it is generated without any internal electrodes and it offers the possibility to work under a controlled atmosphere [2]. It is relatively easy, in principle, to evaporate all input materials and then to condensate the vapors and obtain nanoparticles of the desired morphology and size distribution. Although several methods have been developed to produce nanoparticles, neither the precise control of the particle size nor mass production has been successful in practice. The final particle size and distributions, chemical compositions, shape and phase of the synthesized nanoparticles, are heavily influenced by the thermal history of the formed particles.

To master and optimize the thermal plasma technologies is it necessary to understand not only the mechanisms of generation, growth, and deposition of nanoparticles, but also the fundamental nature of the transport phenomena occurring in the plasma during the synthesis.

Modeling studies can play an important role in the

development and improvement of the nanoparticles synthesis process, providing an insight into the phenomena involved and helping to identify the right process operations to employ. However, a full theoretical description of the aerosol dynamics in plasma processing, within actual industrial environment is very complex [3]. A complete model of such a system requires the solution of the coupled system of the fluid mechanical equations of continuity, momentum, and energy, and the vector potential formulation of the Maxwell's equations, that are used to describe the generation of the plasma. The description of the micrometer particles injected in the plasma as a precursor and the equation describing the aerosol dynamics are added to the plasma model. Beside the complexity related to the modeling of such production, the calculation of the transport properties and the effects of the plasma and quenching parameters, including torch design and configuration, on the flow and on the formation of the nanoparticles are of enormous importance. Thus, the overall purpose of this thesis is to develop a plasma process for efficient producing of high-purity nanoparticles with narrow size distribution, controlled composition and morphology. The investigated is carried out in both computational and experimental way, in order to better understand the physical mechanism of this process.

In the present study, an extended-field model for simulating the behavior of inductively coupled plasma torches (ICPTS) has been developed using a Computational Fluid Dynamic (CFD) open source code, OpenFOAM. One of the key advantages of OpenFOAM is its extensibility: the source code is accessible, and the architecture of OpenFoam makes it relatively easy to write new solvers for new applications. Therefore, this code can be at some point optimized and adapted for complete prediction of nanoparticles formation, i.e. starting from heat and mass transfer between plasma and particles (particle evaporation) to nucleation and condensation (growth of nano scale particle).

2. Mathematical model of the ICP

Mathematical modeling of the effect of the coupling of the electromagnetic and aerodynamic field has been studies, aimed at obtaining a description of the gas flow and temperature field in the induction zone, on the assumption of a local thermal equilibrium (LTE) condition. The LTE assumption dictates an infinite reaction rate for any reaction, no convection and no diffusion effects for density distributions. It assumes that the electron temperature is in equilibrium with the heavy particles temperature. Therefore, is it possible to reduce the full set of non-equilibrium equations to a system formally equivalent to the conventional Navier-Stokes equations (continuity, momentum, energy), complemented by a modified equation of state ρ(p,T) computed from statistical mechanics assuming a fixed elemental composition in the flow.

The motion of the plasma is described using a system of Navier-Stokes equations and the solution of the electromagnetic field is derived from Maxwell equations. The coupling between these two systems of equations is realized by the Lorentz force acting on the charged particles, Joule dissipation which heats up the plasma and through the dependence of electrical conductivity on temperature and pressure.

2.1. Hypothesis

The basic assumptions on the development of the present model are:

- Steady state, axisymetric and laminar pure argon plasma flow at atmospheric pressure.
- Two dimensional electromagnetic, velocity and temperature field.
- Local thermodynamic equilibrium conditions (LTE).
- Radiative heat transfer based on the net emission coefficient approach.
- Negligible displacement current.

2.2. Governing equation for the LTE model

The ICP behavior can be described by the governing equations:

Mass conservation:

$$\nabla \cdot (\rho \mathbf{u}) = 0 \tag{1}$$

Momentum:

$$\nabla\cdot(\rho\mathbf{uu}) = -\nabla p+\nabla\cdot\left[\mu\left(\nabla\mathbf{u} + \nabla u^T\right) - \frac{2}{3}\mu\nabla\cdot(\mathbf{u}I)\right]+F_{lz} \tag{2}$$

Energy:

$$\rho c_P \mathbf{u}\cdot\nabla(T) - \mathrm{k}\nabla^2(T) = P_J + R \tag{3}$$

where $\mathbf{u}$ is the flow velocity. ρ, μ, k, c_P, are the fluid density, dynamic viscosity, thermal conductivity, specific heat at constant pressure, respectively. T is

the temperature, p is the pressure, and P_J and R are the Joule heating and the radiation loss, respectively.

The Lorentz forces and the Joule heating are expressed as:

$$F_{lz} = -\frac{1}{2}\mu_0\sigma\omega\mathrm{Re}[\mathbf{A}\times\mathbf{H}] \tag{4}$$

$$P_J = \frac{1}{2}\sigma\mathrm{Re}\left[E_\theta E_\theta^*\right]. \tag{5}$$

Vector potential:
The vector potential formulation is used, where

$$\nabla^2\mathbf{A} = -\mu_0\left(j_{coil} + j_{ind}\right). \tag{6}$$

For the standard induction plasma torch, if the coil is assumed to be composed of parallel rings, the vector has only an azimuthal component $\mathbf{A} = (0, A_\theta, 0)$ [4].

The electromagnetic fields can be obtained by the following relation after solving the vector potential equation:

$$E_\theta = -i\omega A_\theta. \tag{7}$$

$$\mathbf{H} = -\frac{1}{\mu_0}\nabla\times\mathbf{A}. \tag{8}$$

where μ_0 is the magnetic permeability of free space, σ is the electrical conductivity. The superscript $*$ represent the conjugate and Re the real part of a complex number.

3. Computatinal methodology

The ICP torch modeling using OpenFoam source code is done by extending the calculating domain of the electromagnetic field, induced by the induction coil, well outside of the plasma discharge region.

In OpenFOAM as in any other CFD code, the flow equations are described by a system of linked partial differential equations. The code itself is a collection of object-oriented routines developed for the manipulation of the tensor fields found in fluid mechanics equations. Coupling between equations is treated using a segregated approach, in which equations are formulated for each dependent variable and solve sequentially, with the possibility of iteration over the system of equation until convergence is achieved.

The characteristics of the torch, identified in Fig. 1 and the operating conditions used for the numerical simulations of the plasma flow are summarized in Table 1.

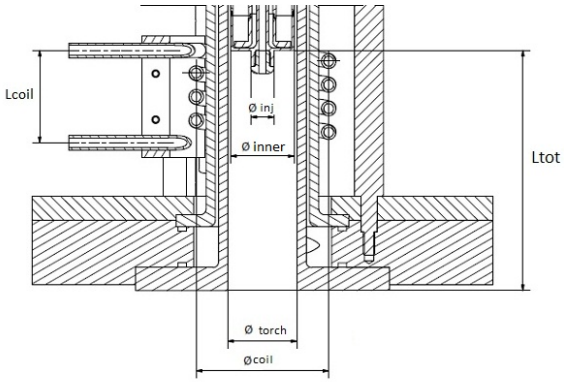

Figure 1: Torch geometry used for simulations

Table 1: Torch geometry and operating conditions

Power=5KW	Pressure = 1atm	f =13.56 MHz
D_{torch} = 30mm	D_{inner} = 27.6mm	D_{coil} = 57.5mm
D_{inj} = 10mm	L_{inj} = 15mm	L_{torch} = 104.5mm
L_{coil} = 40.2mm	Q_1 = 0.9g/s	Q_2 = 0.045g/s
Δ_{coil}=12.88mm	D_{ext} = 140mm	

3.1. Grid structure and boundary condition

OpenFOAM has been designed from the start for 3-dimensional space and defines all geometrical grids or meshes as such. However, two dimensional and axisymmetric problems can be simulated by generating a mesh in 3 dimensions and applying special boundary conditions on any patch in the plane normal to direction of interest. More especially for axisymmetric problems, the geometry is specified as a wedge of 5 degree angle and one cell thick running along the plane of symmetry (Fig. 2) .

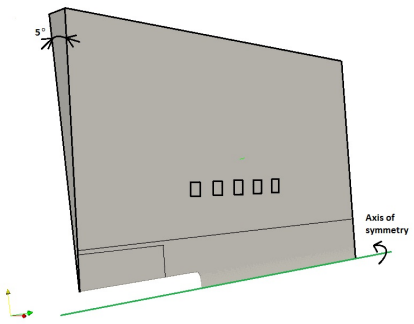

Figure 2: Axisymetric geometry using the wedge patch type

The boundary conditions of the vector potential, because of the distance from the carrying current coil, are set as zero. At the interfaces between the zones is assumed continuity of the vector potential cross the interfaces with jumping. That is done by creating for each wall an adjacent wall separated by an arbitrary small distance (1 m not meshed). The mass flux is described at the inlets and from it is computed the inlet velocity. Zero gradient of the variables are used for the outlet boundary condition and no-slip wall condition for the walls with fixed temperature of 300K.

3.2. Numerical Procedure

The mathematical model including the governing equations for mass conservation (Eq. 1), momentum (Eq. 2) and energy (Eq. 3) is solved by the OpenFoam solver inside the torch region, while the electromagnetic field equation (Eq. 6) is solved in a domain extending outside the torch region, in order to apply the vanishing boundary conditions for the vector potential.

In order to obtain satisfactory convergence and stability, since there is a very strong coupling of the physical phenomena involved in the model, the following model solution procedure was used:

- A set of initial values are given including the gas specie mixture ate LTE with corresponding pressure and temperature.
- Only the mass conservation and momentum equations are solved with a $k - \epsilon$ turbulence model and without sources term, for few iterations.
- The electromagnetic field equation is solved until convergence.
- All governing equation are solved with sources term for energy and momentum with a constant profile of electrical conductivity, for few iteration.
- At the end, all governing equation are solved with the sources term, electrical conductivity as a function of temperature and for a laminar condition, until convergence.

4. Results and Discussion

4.1. Thermofluid fields in the ICTP

In this section, computational results of the extended-field model are presented and a basic parametric study has been performed to find the range of operation conditions for which the new torch model could be operated. The model is applied to an pure argon inductively coupled plasma torch with the input power varied from 2.22 kW to 6.35 kW and a axial mass flow rate of 0.9 g/s to 1.2 g/s.

Solution of the flow field equations for the axial velocity and temperature are shown in Fig. 3. The dissipated power is set to 5kW, the axial mass flow rate to 0.9 g/s and the injector carrying gas to 0.045g/s. In the right side of the Fig. 3, the high temperature zone is generated near the coil region, where argon gas partially ionized and where many electrons are produced. The high temperature zone has a large electrical conductivity and because of the electrical field induced near the coil, the flow is Joule heated as expressed by Eq. 5, which maintains the ICP flow.

The left side of the Fig. 3 presents the axial velocity field in the plasma torch region. We may expect that the Lorenz forces have an important influence on the flow due to the high pressure [5]. The effect of the Lorentz force on the flow is proportional to the operating pressure. Also, according to [5] the Lorentz force actually *destabilize* the plasma in situation where they strongly dominate the flow.

Fig. 4 show the flow when recalculating the argon case of figure Fig. 3, but setting Lorentz force to zero. Clearly we still obtain a well-behaved vortex but it appears to have an important effect on the observed velocity downstream, at the outlet of the torch. The velocity profile at the outlet presents a M-shape along the diameter when taking into account the Lorentz forces.

4.1.1. Basic parametric study on the plasma jet- Effects of power input and mass flow

First, a short study has been made of the effect of the dissipated power and mass flow rate on the numerical model. To illustrate the effect of the power input and mass flow on the ICP torch, the profiles of axial velocity for different condition is shown is Fig. 5. It can be observed that for the same mass flow, by increasing the the input power the axial velocity rises close to the wall border and remains the same close to jet center. On the other hand, when only the mass flow increases, the axial velocity remains close to the wall and increases at the jet center. The extreme of these two variables leads to a plasma solution in *ring mode*, mean the plasma core attached to the torch wall in from of the coil or a fluctuating plasma solution which extinguish. When the mass flow is too low or the power is too high the numerical plasma solution obtained is the *ring mode* and when the mass flow is

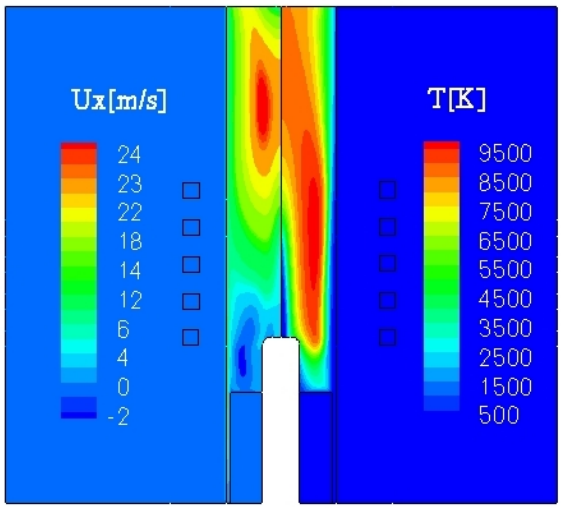

Figure 3: Axial velocity(left) and temperature field(right): $5kW$; $0.9g/s$

too high or the power is too low the solution obtained is the extinguish solution. This fact is in agreement with the feeling that one obtain while operating a real inductively coupled plasma in a laboratory.

4.2. *Experimental investigation an Air plasma jet*

Currently experimental investigations are being carried out using the VKI inductively coupled plasma *Minitorch*. It is a small facility, operating at mass flow rate of order 1 $g7s$, and using a 30 mm diameter torch, supplied by a high frequency (27 MHz) which delivers up to 15 kW anode power at anode voltage up to 6 kV.

Dynamic pressure measurements are very important for a first potential comparison simulation-experiment. In the *Minitorch* facility dynamic pressure measurement are performed by means of a water-cooled Pitot probe. The reference static pressure tap is placed at the upper part of the chamber. The difference between these two pressure is then recorded.

The experimental results are obtained at the exit of the torch and divided in three categories with respect to the working condition of the ICP torch. The first ones the static pressure and the mass flow is maintained constant wile the power is varying. In the second category of measurement, the power and static pressure ire fixed, and the mass flow is increased to see the evolution f the dynamic pressure.

The evolution of the dynamic pressure profile with the anode power is shown in Fig. 6. Varying the input power at constant mass flow, one vary the average temperature of the plasma and therefore on the gas properties. Consequently, increasing the dissipated power(the temperature) of the plasma , the density decreases and the viscosity increases, which dictate a decrease on the Reynolds number. Moreover the dynamic pressure increases because the velocity increases to satisfy the continuity condition. As can seen in Fig. 6 both conditions has the same tendencies of the curve, both present an *M shape* behavior, but for higher anode power the *M shape* is more accentuated with higher dynamic pressure.

The evolution of the dynamic pressure profile with the mass flow is shown in Fig. 7. Contrary to the anode power, mass flow variation do not impose variation on the properties of the gas because temperature and pressure remind constant. The velocity in-

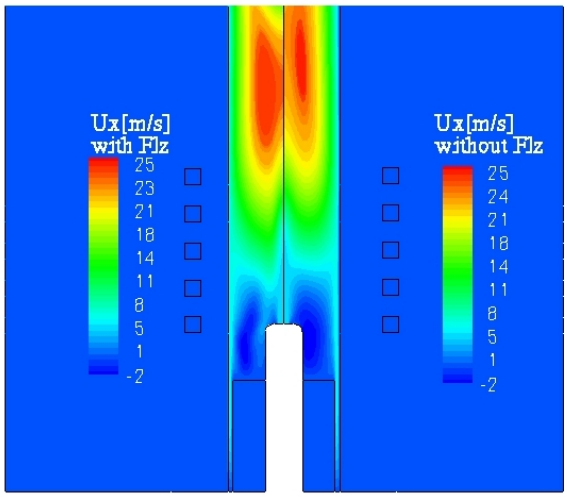

Figure 4: Axial velocity: $5kW$; $0.9g/s$; left-with Lorentz forces; right-with Lorentz force set to zero

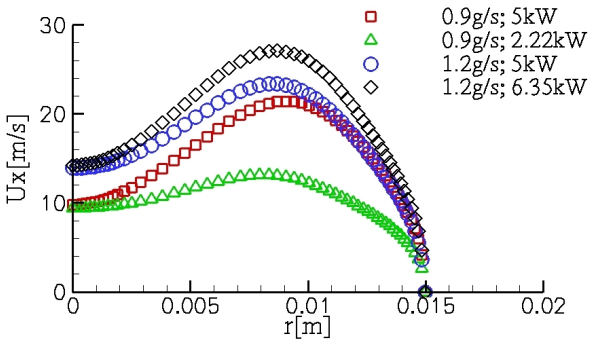

Figure 5: Axial velocity profile at the exit of the torch

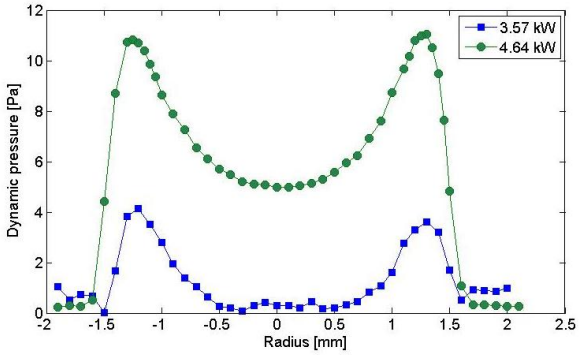

Figure 6: Dynamic pressure profile for 0.85 g/s air, 35 *mbar*

creases directly proportional to the injected mass flow and therefor the dynamic pressure also increases.

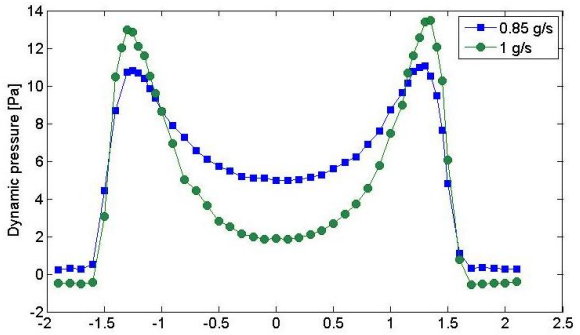

Figure 7: Dynamic pressure profile for 4.64 *kW*, 35 *mbar*, air

The effect of static pressure variation on the dynamic pressure is show in Fig. 8. Contrarily to the previous cases, the dynamic pressure decreases, increasing static pressure. In this case, at constant mass flow and power, the viscosity remains almost constant while density increases with pressure. Because of the velocity effect the Reynold number does not change.

Also in the work of O.Chazot [6] they extensively investigate the behavior of the plasma jet with respect to anode power, mass flow and static pressure. In their work was demonstrated that the behavior of the jet can be explained by considering the mean Reynolds number of the jet:

$$Re = \frac{\rho V D}{\mu} = \frac{4\dot{m}}{\Pi D \mu} \tag{9}$$

where $\dot{m}$ is the mass flow, D the torch diameter and μ the viscosity. Assuming as a first approximation that the specific enthalpy(power) defines the temperature of the jet, while the mass flow rate and static pressure defines the velocity and the density respectively.

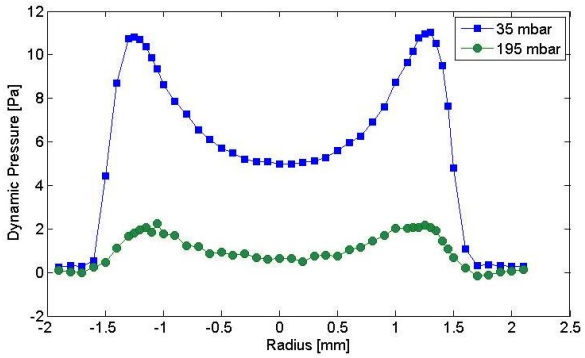

Figure 8: Dynamic pressure profile for 0.85 g/s air, 4.64 *kW*

When only the mass flow increases the Reynolds number grows and the dynamic pressure profile tend to have a *M-Shape*, which indicates that the viscous effect are not strong enough to damp the effect of annular injection. On the other hand, when only the enthalpy increases, the temperature increases in the jet and the viscosity rises, increasing the role of the viscous effect. Thus, the Re number decreases and the initial *M-shape* tend to disappear. For different pressure the main Re number does not change significantly, because the mass flow remains constant and the viscosity remains,a s referred before, almost constant. Therefor the shape of the dynamic pressure profile remains similar.

5. Conclusion

The model for inductively coupled plasma developed with the open source code, OpenFoam, seems to provide solutions that are very much similar to the ones found at literature, and moreover with a behavior similar to what is expected experimentally . On the other hand, the thermodynamic and transport properties of high temperature gases being so important in the prediction of the plasma fields and that could affect the calculations, are easily formulated in OpenFoam and in much more flexible manner. For the future the code is going to be optimized and adapted to nanoparticles formation in inductively coupled plasma. Concerning to the experimental work, further experimental investigation with namely spectroscopy measurement, heat flux exchange and wall pressure measurement are pretended o be used to have better description of the flow and temperature field of the plasma flow, so significant on quality of the finale nanoparicle product.

Acknowledgments

I would like to thank my supervisor Patrick Rambaud, co-supervisor Oliver Chazot and all the VKI Nano Group for all their help and support on this project.

References

[1] S. L. Girshick, C. P. Chiu, R. Muno, C. Y. Wu, L. yang, S. Singh, P. McMurry, Thermal plasma synthesis of ultrafine iron particles, J. Aerosol Sci. 24 (3) (1993) 367–382.

[2] Brushan (Ed.), Springer Handbook of Nanotechnology, Springer, 2007.

[3] N. Mendoza-Gonzalez, B. Goortani, P. Proulx, Numerical simulation of silica nanoparticles production in an rf plasma reactor: Effect of quench, Materials Science and Engineering C 27 (2007) 12651269.

[4] S. Pai, Magneto-gasdynamics and Plasma dynamics, Springer-Verlag, 1962.

[5] D. V. Abeele, An efficient computational model for inductively coupled air plasma flows under thermal and chemical non-equilibrium, Ph.D. thesis, Phd thesis, VKI (2000).

[6] O. Chazot, D. vanden Abeele, M. Carbonaro, Comparison of experimental and numerical result for the dynamic pressure in an inductive plasma flow.

COMPUTATIONAL FLUID DYNAMICS & MODELING FOR RE-ENTRY FLOW

Unsteady simulation of hypersonic flow over a heat probe in ground test conditions

Khalil Bensassi

Aeronautics and Aerospace Department, bensassi@vki.ac.be

Supervisor: Patrick Rambaud

Assistant Professor, Aeronautics and Aerospace Department, von Karman Institute for Fluid Dynamics, Belgium, rambaud@vki.ac.be.

Promotor: Herman Deconinck

Professor, Aeronautics and Aerospace Department, von Karman Institute for Fluid Dynamics, Belgium, deconinck@vki.ac.be.

Abstract

In order to asses the rebuilding procedure used to determine the free stream conditions and the total enthalpy in VKI-Longshot facility, numerical simulations of hypersonic flow over a heat probe have been done. The free stream conditions provided by experiments as function of time were used as unsteady inlet boundary conditions for these simulations. Three test conditions corresponding to high, medium and low Reynolds number are considered. The full 20 ms of the test are simulated by means of unsteady second order time accurate finite volume solver. Numerical methods and time integration procedure used during this investigation are described. The computational results are compared with experimental data and the limitation of the current rebuilding procedure is discussed.

Keywords: Unsteady Hyperonic flow, VKI-Longshot facility, Blunt body, Heat flux.

1. Introduction

The free stream conditions in most hypersonic wind tunnels are very difficult to assess and the uncertainties on their values could reach 20%. It's mostly due to a lack of experimental data on some part of the facility like inside the nozzle or the driven tube and also to some technical difficulties to measure some main flow parameters. The usual method to overcome this limitation is to rebuild those missing data using one dimensional solver based on shock relations and/or isentropic assumptions. In the VKI-Longshot wind tunnel which is is a short duration facility, the measured data are the pressure in the reservoir, the stagnation pressure and the heat flux in the chamber. Fay-Riddell [5] formulae is used to compute the total enthalpy from the measured heat flux. The free stream conditions are computed using normal shock relations and assuming isentropic expansion in the nozzle. The accuracy and the reliability of the free stream conditions depend on this rebuilding procedure. A good knowledge of the free stream conditions is necessary for CFD validation purpose. In this work we focus on the validation of this rebuilding process using a time accurate finite volume solver.

2. Experimental setup

2.1. The VKI-Longshot facility

The VKI-Longshot free piston tunnel is a short duration facility (Fig.1) that can be operated with either nitrogen or carbon dioxide and it is designed to reach very high Reynolds number hypersonic flows. It is essentially based on two tubes (driver and driven tubes) and a nozzle which discharges into a test chamber. It has a Mach 14 contoured nozzle [22] of 0.42 m exit diameter and a 6° conical nozzle of 0.60 m exit diameter which can be used throughout a Mach number range from 15 to 20.

Due to the very high pressure levels achieved into the reservoir, the Reynolds numbers simulated are very high (up to 14 millions per meter). Therefore, this facility is particularly well suited for the study of

Table 1: VKI-Longshot hypersonic nozzle dimensions

Inlet radius [mm]	38.1
Throat radius [mm]	3.225
Exit radius [mm]	213.34
Length [mm]	3067

high Mach and Reynolds number flows and provides a good duplication of spacecraft re-entry trajectories with respect to these two non dimensional parameters.

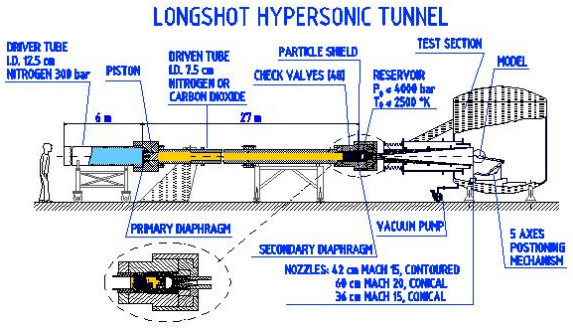

Figure 1: Schematic online of the Longshot tunnel

The driver gas, usually nitrogen operates at a pressure between 300 and 1000 bars at room temperature, in a 12.5 cm diameter tube which is 6 m long. Before the shot, the driven tube is closed by the piston on the upstream side and on the downstream side by a system of 48 valves followed by the reservoir and finally closed by a diaphragm. The initial pressure of the gas in the driven tube can vary from 1 to 15 bars and its temperature is the room temperature. The nozzle and chamber are evacuated down to about 1 Pa pressure.The piston, weighting is between 1.5 to 9 kg, it is maintained by a diaphragm made in aluminum at the end of the driver tube. In order to release the piston, a valve opens and applies the initial pressure on an extra surface of the piston front which is enough to break the diaphragm. The piston, then moves in the driven tube and it is accelerated at speeds of the order of 600 m/s, compressing the gas through a shock wave standing ahead. In front of the piston, the shock wave reflects when it hits the end of the driver tube leading to an increasing of reservoir pressure, then it strikes the piston and reflects again. A series of reflection occur between the piston head and the driver tube end which finally stops the piston. A decompression wave appears at the rear of the piston due to the rarefaction of the gas. It travels from the driver tube to eventually reach the rear part of the piston and causes the piston rebound. When the piston moves back in the driven tube, the pressure ahead of the piston decreases and finally becomes lower than in the reservoir. Therefore, in order to trap the gas in the $320cm^3$ reservoir, a plate check valves is installed at the end of the piston course which causes the closure of the 48 check valves. Once the gas is trapped, the second diaphragm breaks and this allows the gas to expand through the nozzle into a $16m^3$ vacuum vessel. In order to prevent the biggest particles caused by the rupture of the diaphragm from obstructing the nozzle or destroying the model, a particle shield has been placed just upstream the diaphragm.

2.2. *Experimental data*

The experimental data during the test are the reservoir pressure, the stagnation pressure in the chamber and the stagnation heat flux obtained with a spherical heat probe of 12.7 [mm] radius. Detailed description of VKI-Longshot instrumentation could found in Ref [23].

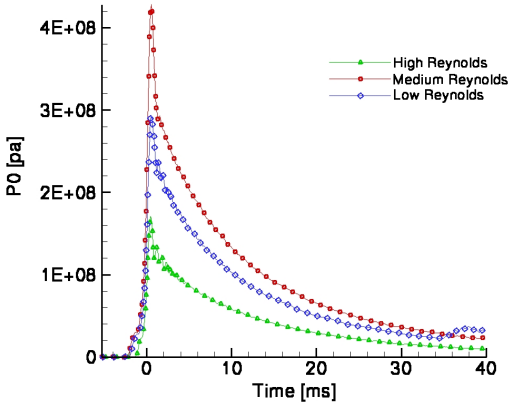

Figure 2: Measured pressure in the reservoir.

Figure 2 shows the total pressure in the reservoir along time corresponding to three different Reynolds numbers (high, medium and low Reynolds number). Figure 3 and figure 4 show respectively the stagnation pressure and the heat flux in the chamber. The useful test time is 20 ms and the reference free stream conditions are taken at 10 ms. The total temperature in the reservoir is computed together with the free stream conditions using a rebuilding process as

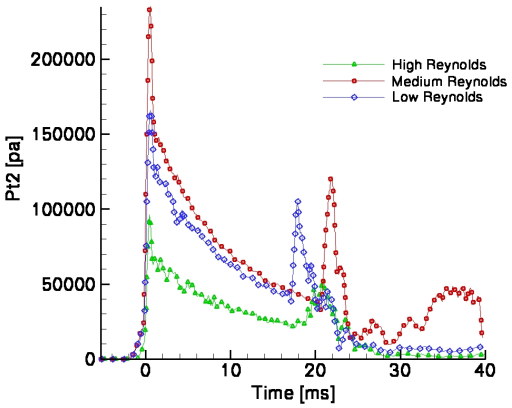

Figure 3: Measured stagnation heat flux in the chamber.

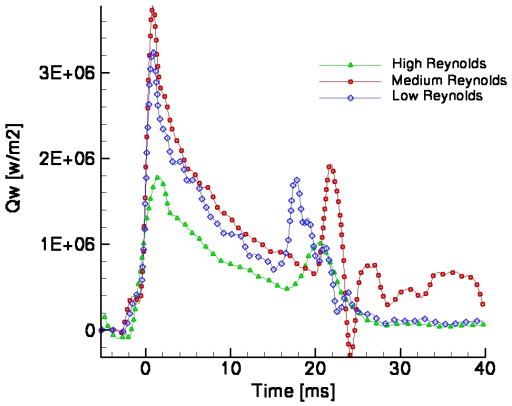

Figure 4: Measured stagnation pressure in the chamber.

described in the next section.

2.3. The rebuilding Process

In order to rebuild the free stream condition, One need first to determine the total temperature. Figure 5 shows the algorithm used for this purpose.

t

The procedure starts with a first guess of total temperature in the reservoir, the heat flux predicted by Fay-Riddell formulae is compared to the one measured experimentally, if there is matching the time step is incremented otherwise the total temperature is incremented. Once the total temperature is computed, knowing the stagnation pressure in the chamber and the total pressure in the reservoir, using normal shock relations the free steam conditions could be computed.

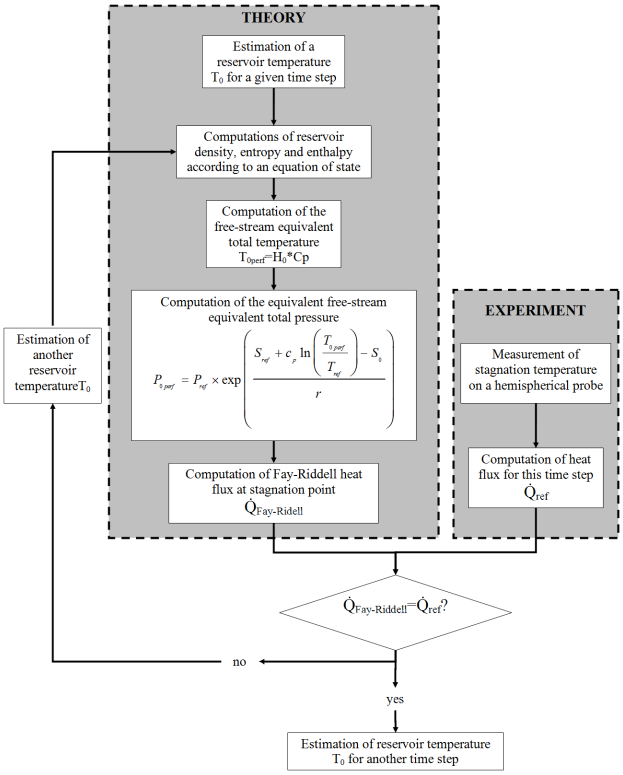

Figure 5: VKI-Longshot rebuilding process.

More details on the rebuilding process could found in [6].

3. Governing equations

The sets of governing PDE's (Navier-Stokes) describing a 2D axisymmetric flow in a continuum regime can be expressed in conservative and hyper-vectorial form as:

$$\frac{\partial \mathbf{U}}{\partial \mathbf{P}} \frac{\partial r\mathbf{P}}{\partial t} + \frac{\partial r\mathbf{F}_x^c}{\partial x} + \frac{\partial r\mathbf{F}_r^c}{\partial r} = \frac{\partial r\mathbf{F}_x^d}{\partial x} + \frac{\partial r\mathbf{F}_r^d}{\partial r} + \mathbf{S} \quad (1)$$

where x and r are the axial and radial directions. Herein, $\mathbf{U}$ are the conservative variables, $\mathbf{P}$ the variables used for the solution update, $\mathbf{F}^c$ and $\mathbf{F}^d$ respectively the convective and diffusive fluxes, $\mathbf{S}$ the source term.

In the most comprehensive case here considered, namely that of a gas mixture in thermal and chemical non-equilibrium, the conservative and natural variables corresponding to a 2-temperature model for neutral mixtures [7; 18] can be expressed as follows:

$$\mathbf{U} = (\rho_s, \rho\mathbf{u}, \rho E, \rho e_v)^T, \quad \mathbf{P} = (\rho_s, \mathbf{u}, T, T_v)^T \tag{2}$$

where, in particular, ρ_s represents the partial densities, e_v is the vibrational energy per unit mass and T_v stands for the vibrational temperature.

3.1. Convective and diffusive fluxes

In this case, the convective and diffusive fluxes are defined by:

$$\mathbf{F}^c = \begin{pmatrix} \rho_s\mathbf{u} \\ \rho\mathbf{u}\mathbf{u} + p\hat{I} \\ \rho\mathbf{u}H \\ \rho\mathbf{u}e^v \end{pmatrix}, \ \mathbf{F}^d = \begin{pmatrix} -\rho_s\mathbf{u}_s^d \\ \bar{\bar{\tau}} \\ (\bar{\bar{\tau}}\cdot\mathbf{u})^T - \mathbf{q} \\ -\mathbf{q}_v \end{pmatrix}. \tag{3}$$

The tensor of viscous stresses $\bar{\bar{\tau}}$ appearing in Eq. 3 is defined as

$$\tau_{ij} = \mu\left[\left(\frac{\partial u_j}{\partial x_i} + \frac{\partial u_i}{\partial x_j}\right) - \frac{2}{3}\nabla\cdot\mathbf{u}\ \delta_{ij}\right] - \delta_{ij}\frac{2}{3}\mu\frac{v}{r} \tag{4}$$

and it is computed using Stokes' hypothesis of negligible bulk viscosity effects. Herein, the dynamic viscosity μ is computed rigorously from kinetic theory by using the transport algorithms described in [13].
The mass diffusion fluxes $\rho_s\mathbf{u}_s^d$ are computed by solving the Stefan-Maxwell system [1; 2] of equations which consist of a linear system (in the diffusion fluxes) of as many equations as the chemical species are present in the mixture. The roto-translational and vibrational heat fluxes $\mathbf{q}$ and $\mathbf{q}_v$ are defined as

$$\mathbf{q} = -\lambda\nabla T - \lambda_v\nabla T_v - \sum_s \rho_s\mathbf{u}_s h_s \tag{5}$$

$$\mathbf{q}_V = -\lambda_v\nabla T_v - \sum_s \rho_s\mathbf{u}_s h_s^v \tag{6}$$

where the λ is the roto-translational thermal conductivity, λ_v is the vibrational thermal conductivity and the species enthalpies h_s include translational, rotational, vibrational and formation contributions.

3.2. Source terms

The source terms in Eq. 2 can be expressed as

$$\mathbf{S} = \begin{pmatrix} \mathbf{0} \\ 0 \\ p - \tau_{\theta\theta} \\ 0 \\ 0 \end{pmatrix} + \frac{1}{r}\begin{pmatrix} \dot{\omega}_s \\ 0 \\ 0 \\ 0 \\ \dot{\omega}^v \end{pmatrix} \tag{7}$$

where, in particular, $\tau_{\theta\theta}$ represents the following additional viscous stress component in the circumferential direction θ, due the axisymmetric formulation:

$$\tau_{\theta\theta} = -\frac{2}{3}\mu\left(\frac{\partial u}{\partial x} + \frac{\partial v}{\partial r} - 2\frac{v}{r}\right) \tag{8}$$

The mass production/destruction term $\dot{\omega}_s$ for chemical species with partial densities ρ_s which appears in Eq. 7 is formulated as follows:

$$\frac{\dot{\omega}_s}{M_s} = \sum_{r=1}^{Nr}\left(\nu_{sr}^{''} - \nu_{sr}^{'}\right) * \left\{k_{fr}\prod_{j=1}^{Ns}\left(\frac{\rho_j}{M_j}\right)^{\nu_{jr}^{'}} - k_{br}\prod_{j=1}^{Ns}\left(\frac{\rho_j}{M_j}\right)^{\nu_{jr}^{''}}\right\} \tag{9}$$

where the forward reaction rates k_{fr} corresponding to a 2-species nitrogen mixture used in this work are taken from [15].
The term $\dot{\omega}^v$ expresses the energy exchange (relaxation) between vibrational and translational modes and the vibrational energy lost or gained due to molecular depletion (dissociation) or production (recombination):

$$\dot{\omega}^v = \sum_s \rho_s\frac{(e_{v,s}^* - e_{v,s})}{\tau_s} + \sum_s \tilde{D}_s\dot{\omega}_s \tag{10}$$

where the relaxation time τ_s is given by Millikan and White [14] with Park's correction for high temperatures [17]. More details about the thermo-chemical model can be found in [16].

4. Numerical methods

4.1. Finite Volume method

All the results to be presented have been obtained by means of the parallel FV solver for unstructured grids [10] provided by the COOLFluiD framework [11; 19]. The FV discretization is applied to the system of governing equations written in integral conservation form:

$$\frac{\partial}{\partial t}\int_\Omega \mathbf{U}\, d\Omega + \oint_{d\partial\Omega} \mathbf{F}^c\cdot\mathbf{n}\, d\partial\Omega = \oint_{d\partial\Omega} \mathbf{F}^d\cdot\mathbf{n}\, d\partial\Omega + \int_\Omega \mathbf{S}\, d\Omega \tag{11}$$

We apply a conventional cell centered approximation, which assumes solution vectors located at the centroid of each computational cell. Inverse-distance weighted least square reconstruction [3] is utilized to yield second order accuracy. Oscillation free solutions are obtained with the multidimensional limiter

of Venkatakhrisnan [24]. In particular, a version of the Roe scheme [20] which combines the consistent linearization described in [18] and an entropy fix from [21] has been utilized for discretizing the convective fluxes in all our computations, as described hereafter [10].

4.1.1. Convective Flux discretization

In its general formulation [20] Roe's scheme reads:

$$\mathbf{F}^{Roe} = \frac{1}{2}\left[\mathbf{F}_n(\mathbf{P}^L) + \mathbf{F}_n(\mathbf{P}^R)\right] - \frac{1}{2} \mid \mathbf{A}(\bar{\mathbf{Z}}) \mid \left[\mathbf{U}(\mathbf{P}^R) - \mathbf{U}(\mathbf{P}^L)\right] \tag{12}$$

with

$$\mathbf{A} = \frac{\partial \mathbf{F}_n}{\partial \mathbf{U}}, \quad \mid \mathbf{A} \mid = \mathbf{R} \mid \mathbf{\Lambda} \mid \mathbf{R^{-1}}, \quad \mid \mathbf{\Lambda} \mid_{ij} = \mid \lambda \mid_i \delta_{ij} \tag{13}$$

where $\mathbf{R}$ is the matrix of right eigenvectors, $\mathbf{\Lambda}$ the diagonal matrix of eigenvalues,$\mathbf{U}$ are the conservative variables and $\mathbf{P}$ are the natural variables in our case. A key ingredient of the method is the linearization of the flux jacobian matrix $\mid \mathbf{A} \mid$, projected onto the direction of the face normal $\mathbf{n}$. However, for the system of equations describing a mixture of perfect gases in thermo-chemical non equilibrium such a linearization is not readily available. As recalled in [18], one of the properties that the matrix $\bar{\mathbf{A}}$ has to satisfy is:

$$\Delta(\mathbf{F}_n) = \bar{\mathbf{A}}\Delta(\mathbf{U}) \tag{14}$$

where $\Delta(.) = (.)_R - (.)_L$. Eq.14 is rigorously valid for all the flux components which are homogeneous quadratic functions in the components of Z, except for the pressure flux. In the case of a neutral gas mixture with N_s chemical species, the momentum components of Eq. 14 are satisfied if the following condition holds:

$$\Delta(p) = \sum_{s=1}^{N_s} \bar{\alpha_s}\Delta(\rho_s) + \bar{\beta}\Delta\rho(e_{tr}) \tag{15}$$

where

$$\beta = \frac{\partial p}{\partial \rho E}, \quad \alpha_s = RT/M_s - \beta e_{tr,s} \tag{16}$$

$$e_{tr,s} = (f_s RT + \Delta h_{f,s})/M_s \tag{17}$$

with $f_s = 2.5$ for molecules and $f_s = 1.5$ for atoms. Different methods have been proposed in order to satisfy Eq.15, like the approximate and relatively complex solution in [12], the recipe based on computational experience in [8], the choice of a simple average of left and right states in conservative variables as in [21]. In our case, following the simple and yet accurate approach presented in [18], requiring that $\bar{\alpha_s}$ and $\bar{\beta}$ form a consistent set of thermodynamic variables together with the other Roe-average variables, we define $a = \sqrt{\rho_L}/(\sqrt{\rho_L} + \sqrt{\rho_R})$ and $b = (1-a)$. Consequently, the following relations hold:

$$\bar{y}_s = a(y_s)_L + b(y_R)_R, \qquad s = 1, ..., N_s \tag{18}$$

$$\bar{\mathbf{u}} = a\mathbf{u}_L + b\mathbf{u}_R, \quad \bar{H} = aH_L + bH_R, \tag{19}$$

$$\bar{e}_V = a(e_V)_L + b(e_V)_R \tag{20}$$

Moreover, if we choose the following definitions for $\bar{\beta}$, $\bar{\alpha_s}$,$\bar{e}_{tr,s}$ and $\bar{a}^2$:

$$\bar{\beta} = \left[\sum_{s=1}^{N_s} \bar{y}_s/M_s\right] / \left[\sum_{s=1}^{N_s} f_s\bar{y}_s/M_s\right] \tag{21}$$

$$\bar{\alpha_s} = R\bar{T}/M_s - \beta\bar{e_{tr,s}} \tag{22}$$

$$\bar{e}_{tr,s} = (f_s R\bar{T} + \Delta h_{f,s})/M_s \tag{23}$$

$$\bar{a}^2 = \sum_{s=1}^{N_s} \bar{\alpha_s}\bar{y}_s + \bar{\beta}(\bar{H} - \bar{q} - \bar{e}_V) \tag{24}$$

As shown in [18], those relations lead to some remarkably simple results like

$$\bar{T} = aT_L + bT_R, \quad \bar{e}_{tr} = a(e_{tr})_L + b(e_{tr})_R, \tag{25}$$

$$\overline{p/\rho} = a(p/\rho)_L + b(p/\rho)_R \tag{26}$$

which allow us to perform a consistent linearization $\mid \mathbf{A} \mid$.

In order to prevent the appearance of unphysical expansion shocks in the rapidly accelerating flow, we apply one of the entropy fixes proposed in [21] to correct the linearized eigenvalues:

$$\mid \tilde{\lambda}_l \mid = max(\mid \lambda_l(\bar{\mathbf{Z}} \mid, \eta) \tag{27}$$

4.2. Implicit Time integration

The time integration scheme proposed by Wuilbaut [25] which is a blending between a first-order positive time integration scheme (Backward Euler) and the 2nd order accurate Backward Differentiation scheme.

$$\frac{\mathbf{U}(\mathbf{P^{n+1}}) - \mathbf{U}(\mathbf{P}^n)}{\Delta t} + \theta\left(\frac{\mathbf{U}(\mathbf{P^{n+)}}) - 2\mathbf{U}(\mathbf{P}^n) + \mathbf{U}(\mathbf{P}^{n-1})}{\Delta t}\right) = -\mathbf{R}(\mathbf{P}^{n+1}) \tag{28}$$

where θ is a blending coefficient $\theta \in [0, 1]$. This blending is defined such that when $\theta = 1.$, the scheme is the 2nd order Backward Differentiation scheme while when $\theta = 0.$, the scheme transforms into a 1st order Backward Euler scheme. The resulting scheme is of order two in smooth flows ($\theta = 1.$) while reducing to 1st order at discontinuities ($\theta = 0$).

At each timestep, the system (28) is solved implicitly until convergence through a Newton iteration. At each of the inner timestep iterations, the value of θ is updated using the solution $U^{n+1,k}$ where k is the inner iterations index. The GMRES algorithm with an Additive Schwartz preconditioner provided by the PETSC library [9] serves to solve in parallel the corresponding linear systems arising from Newton linearizations. The solution update is also performed in natural variables.

5. Computational procedure

The aim this of investigation is to simulate the flow around the heat probe during the first 20 ms of the test, taking as input for the computations the free stream data provided by the rebuilding process. Those inlet conditions [$P_{info}(t)$, $U_{info}(t)$, $T_{info}(t)$] are given as a function of time. The computational procedure is completed in two steps. The first step is to perform a steady state computations taking as input the free stream conditions corresponding to the test pic conditions (ie at time of 0 ms). [$P_{info}(t = 0)$, $U_{info}(t = 0)$, $T_{info}(t = 0)$]. Table 2 summarize the free steam conditions for the steady state computations that were performed for three different Reynolds numbers. Figure 6 shows the grid used for all the computation. It's structured grid of 20000 elements where the first distance to the wall is 0.1 [μm].

Table 2: The free stream conditions at time of 0 ms.

Reynolds numbers	P [pa]	U [m/s]	T [K]
1.58702E+07	590.928	2445.4	67.0117
3.47548E+06	495.129	2402.78	66.6898
1.78469E+06	210.878	2153.04	53.19415

T-bonehe second step is to start the unsteady computation from the converged steady solution and taking into account the variation in time of the free steam conditions. For this purpose, a curve fit of the rebuilt experimental data has been used. Figure 7, 8 and 9

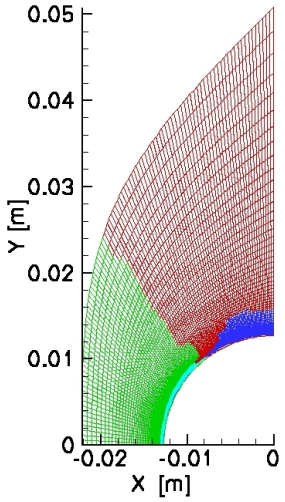

Figure 6: Heat Probe grid

show respectively the profile along time of the free stream pressure, velocity and temperature and the corresponding curve fit used as inlet conditions for the unsteady computations. A boundary condition has been implemented in order to take a polynomial fit of the free stream conditions as a functions of time as input for the Finite Volume solver.

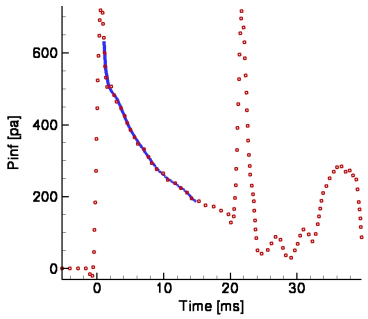

Figure 7: Rebuilt free stream pressure and its curve fit.

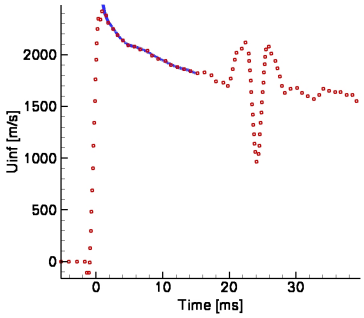

Figure 8: Rebuilt free stream velocity and its curve fit.

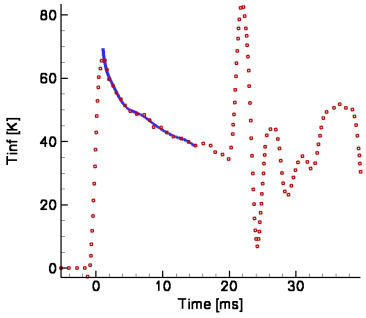

Figure 9: Rebuilt free stream temperature and its curve fit.

6. Results

The computed heat flux and the stagnation pressure are compared with the experimental data given by a heat prode and a pitot probe. Figures 10, 11 and 12 show the comparison between the numerical and the experimental result respectively for high, medium and low Reynolds numbers.

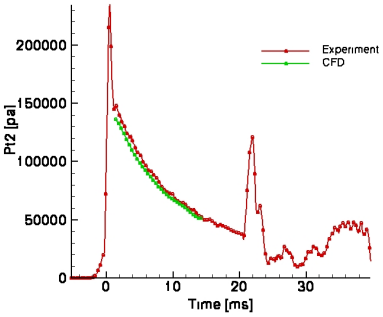

Figure 10: Numerical and Experimental stagnation pressure : High Reynolds condition

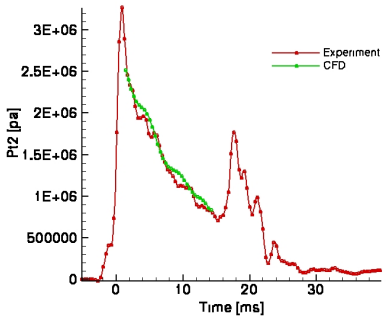

Figure 11: Numerical and Experimental stagnation pressure : Medium Reynolds condition

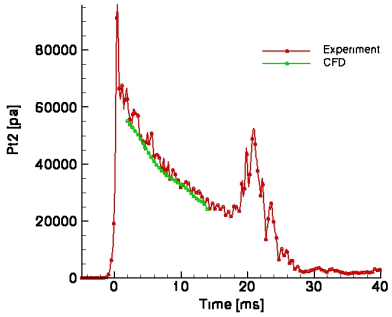

Figure 12: Numerical and Experimental stagnation pressure : Low Reynolds condition.

The CFD results concerning the stagnation pressure in the chamber match generally well with the experimental data. The computed stagnation pressure is slightly lower than the experimental data for the three Reynolds number conditions, however the differences remain less than 2 % during the full test.

The results concerning the heat flux are shown in figures 13, 14 and 15.

The predicted CFD heat flux is pretty close to the experimental data during the full 20 ms test. It is lightly over-predicted for the three Reynolds conditions, nevertheless, the difference with the experiments is less that 6 % which is acceptable compared to the uncertainty on the measured heat flux estimated above 10 %.

The rebuilding process is based on Fay-Riddel formulae which is valid for steady state flows close to equilibrium. Therefore, the agreement between the numerics and experiments indicates that the flow is quasi-steady during the range of time simulated (ie

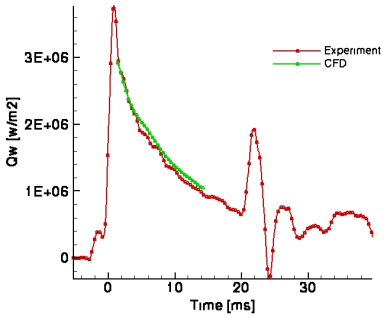

Figure 13: Numerical and Experimental heat flux : High Reynolds condition.

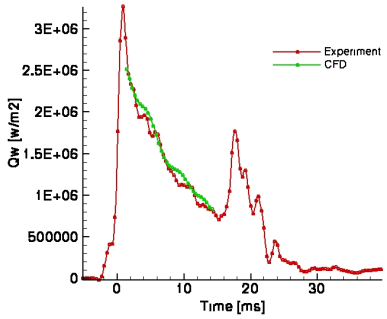

Figure 14: Numerical and Experimental heat flux : Medium Reynolds condition.

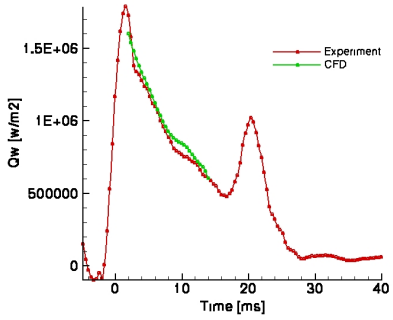

Figure 15: Numerical and Experimental heat flux: Low Reynolds condition.

20 ms), and the modified Fay-Riddel formulae used in this rebuilding process is still valid for this range of applications. However, if the the total enthalpy is a unique solution to a given heat flux, different free stream conditions could lead to the same heat flux. Therefore the uniqueness of the free stream conditions provided by the rebuilding code for a given heat flux is not proven. In addition to this, it has been shown by [4] that the flow at the exit of the nozzle is thermal nonequilibirium state and it affects the free stream condition, which is not taken into account in the current rebuilding procedure.

7. Conclusion

Numerical simulations are carried out in order to assess the VKI-Longshot rebuilding code by means of a second order time accurate finite volume solver. The free stream data provided by the rebuilding process were used as inlet conditions. Good agreement is obtained between the numerical results and the measured data for both the stagnation pressure and the heat flux during the useful test time of 20 ms. This indicates that the rebuilding code does provide the correct free stream conditions for the given stagnation experimental data. However, the current procedure does not take into account the themal nonequilibrium effect in the nozzle and fails to provide a unique free steam conditions. A new rebuilding procedure based on coupling CFD and experimental is needed.

References

[1] D. Vanden Abeele, P. Barbante, G. Degrez, and J.-P. Mellado González. Numerical simulation of multi-component inductive plasma flows under chemical non-equilibrium. In *Heat and Mass Transfer under Plasma Conditions (Ed. P. Fauchais, J. van der Mullen, J. Heberlein)*, volume 891, pages 340–347, New York, 1999. Annals of the New York Academy of Sciences.

[2] P. F. Barbante, G. Degrez, and G. S. R. Sarma. Computation of Nonequilibrium High-Temperature Axisymmetric Boundary-Layer Flows. *Journal of Thermophysics and Heat Transfer*, 16(4):490–497, 2002.

[3] Timothy Barth. Aspects of unstructured grids and finite volume solvers for the euler and navier-stokes equations. 25th Computational Fluid Dynamics Lecture Series. Von Karman Institute, March 1994.

[4] Khalil Bensassi, Andrea Lani, Olivier Chazot, and Patrick Rambaud. Numerical simulation of hypersonic flow in vki-longshot contoured nozzle. In *AIAA-2010-4857*, Chicago,Illinois, June 2010. 40th Fluid Dynamics Conference and Exhibit, Chicago, Illinois, June 28-1, 2010.

[5] J. Fay and F. R. Riddell. Theory of Stagnation Point Hheat Transfert in Dissociated Air. *Journal of the Aeronautical Sciences*, 121:73–85, 1958.

[6] G.Grossir. User guide longshot post-processing v2.1. VKI report 2011-04, von Karman Institute, St. Genesius-Rode, Belgium, 2011.

[7] P. A. Gnoffo, R. N. Gupta, and J. L. Shinn. Conservation equations and physical models for hypersonic air flows in thermal and chemical non-equilibrium. Technical Paper 2867, NASA, 1989.

[8] Peter A. Gnoffo. Upwind-biased, point-implicit relaxation strategies for viscous hypersonic flows. *AIAA Paper*, (89-1972-CP), 1989.

[9] Argonne National Laboratory. Petsc: Portable, extensible toolkit for scientific computation, 2007.

[10] A. Lani. *An Object Oriented and High Performance Platform for Aerothermodynamics Simulation*. PhD thesis, Von Karman Institute for Fluid Dynamics, 2009.

[11] A. Lani, T. Quintino, D. Kimpe, H. Deconinck, S. Vandewalle, and S. Poedts. The COOLFluiD framework: Design solutions for high-performance object oriented scientific computing software. In P. M. A. Sloot V. S. Sunderan, G. D. van Albada and J. J. Dongarra, editors, *Computational Science ICCS 2005*, volume 1 of *LNCS 3514*, pages 281–286, Atlanta, GA, USA, May 2005. Emory University, Springer.

[12] Yen Liu and Marcel Vinokur. Upwind algorithms for general thermo-chemical nonequilibrium flows. In *27th AIAA Aerospace Sciences Meeting*, Reno, Nevada (US), Jan 1989. AIAA 89-0201.

[13] T. Magin and G. Degrez. Transport algorithms for partially ionized and unmagnetized plasmas. *Journal of Computational Physics*, 198:424, 2004.

[14] R. C. Millikan and D. R. White. Systematics of vibrational relaxation. *Journal of Chemical Physics*, 39(12):3209–3213, 1963.

[15] I. Nompelis. *Computational Study of Hypersonic Double-Cone Experiments for Code Validation*. PhD thesis, University of Minnesota, May 2004.

[16] M. Panesi, A. Lani, T. Magin, F. Pinna, O. Chazot, and H. Deconinck. Numerical investigation of the non equilibrium shock-layer around the expert vehicle. In *AIAA Paper 2007-4317*, Miami (Florida), Jun 2007. 38th AIAA Plasmadynamics and Lasers Conference.

[17] C. Park. Review of chemical-kinetic problems of future nasa mission, I: Earth entries. *Journal of Thermophysics an Transfer*, 7:385–398, July-Sept 1993.

[18] Ramadas K. Prabhu. An implementation of a chemical and thermal nonequilibrium flow solver on unstructured meshes and application to blunt bodies. Technical Report NASA-CR-194967, NASA Langley Center, Aug 1994.

[19] T. Quintino. *A Component Environment for High-Performance Scientific Computing. Design and Implementation*. PhD thesis, Katholieke Universiteit Leuven, 2008.

[20] P. Roe. Approximate riemann solvers, parameters vectors and difference schemes. *Journal of Computational Physics*, 43:357–372, 1981.

[21] Richard Sanders, Eric Morano, and Marie-Claude Druguet. Multidimensional dissipation for upwind schemes: stability and applications to gas dynamics. *Journal of Computational Physics*, 145(CP986047):511–537, 1998.

[22] G. Simeonides. The vki contoured mach 15 longshot nozzle: final design parameters and construction. VKI IN 87/AR, von Karman Institute for Fluid Dynamics, St. Genesius-Rode, Belgium, 1989.

[23] G. Simeonides. The vki hypersonic wind tunnels and associated measurement techniques. VKI TM 46, von Karman Institute for Fluid Dynamics, St. Genesius-Rode, Belgium, 1990.

[24] V. Venkatakrishnan. Convergence to steady state solutions of the euler equations on unstructured grids with limiters. *Journal of Computational Physics*, 118:120–130, 1995.

[25] T. Wuilbaut. *Multi-Physics*. PhD thesis, Université Libre de Bruxelles, 2008.

Residual Distribution methods for atmospheric entry aerothermodynamics

Jesús Garicano Mena

Aeronautics and Aerospace Department, jesus.garicano.mena@vki.ac.be

Supervisor: Herman Deconinck

Professor, Aeronautics and Aerospace Department, von Karman Institute for Fluid Dynamics, Belgium, deconinck@vki.ac.be

Co-Supervisor: Andrea Lani

Research Engineer, Aeronautics and Aerospace Department, von Karman Institute for Fluid Dynamics, Belgium, lani@vki.ac.be

Promotor: Gérard Degrez

Professor, Service Aéro-Thermo-Mécanique, ULB, Avenue F. D. Roosevelt 50, 1050 Bruxelles, Belgium, Gerard.Degrez@ulb.ac.be

Abstract

In the present contribution the issue of simulating hypersonic flows by means of Residual Distribution Schemes is discussed. In particular, this discretization technique is briefly presented and its current capabilities reviewed. It turns out that certain aspects of the technique need some adjustments to deal with the very particular characteristics of the hypersonic regime. These elements are addressed, and among them, extensive attention is given to the subject of the *carbuncle* phenomenon and the known remedies for it.

Keywords: Residual distribution schemes, Carbuncle phenomenon, Hypersonic flow, Compressible Flow, Shock waves, Artificial diffusion

1. Introduction

Numerical simulation of hypersonic flows is a challenging activity, since the complexities of compressible flow aerodynamics have to be dealt together with additional high-temperature effects due to chemical and thermal non equilibrium phenomena (further details in [1]).

In the present contribution, we propose to use the Residual Distribution [1] (**RD**) framework for the discretization of the equations that govern the non-equilibrium hypersonic flow of air, as presented in [2]. The system of equations presented there expresses the conservation of mass, momentum and energy and can be cast in compact, vector form as:

$$\frac{\partial \vec{U}}{\partial t} + \nabla \cdot \bar{\bar{F}}^c = \nabla \cdot \bar{\bar{F}}^d + \vec{S} \tag{1}$$

where $\vec{U}$ stands for the vector of conserved variables. For a two temperatures, N chemical species model, $\vec{U}$ includes the species densities ρ_s, the momentum ρu_j and the total ρE and electronic-vibrational energies ρe_v:

$$\vec{U} = \left[\rho_s, \quad \rho u_j, \quad \rho E, \quad \rho e_v\right]^t \tag{2}$$

Tensors $\bar{\bar{F}}^c$ and $\bar{\bar{F}}^d$ describe the convective and diffusive fluxes of the conserved quantities, while vector $\vec{S}$ contains the chemical and internal energy modes source terms.

In the following, we review the characteristics of **RD** schemes as used nowadays and discuss its suitability for the simulation of aerothermodynamics of hypersonic flows. The **RD** formalism has been already applied to systems of equations structurally alike to that in (1) (*e.g.* the Navier-Stokes equations with turbulence model source terms, in [3] and [4]). Nevertheless, a critical difference between the reported cases and the current one is the lack of a con-

[1] Sometimes **RD** methods are called fluctuation splitting (**FS**) as well.

servative linearization for the Jacobian of the advective fluxes. This does not compromise, though, the conservation requirement, since a reformulation of the basic **RD** approach, known as Conservative Residual Distribution scheme (**CRD**), can handle this situation. The **CRD**, presented in [5], enforces conservation by computing the flux balance by numerical integration of the advective fluxes.

Another advantage of some **RD** (N, LDA) schemes is its true multidimensional nature (see [3]), which results in lower cross-diffusion effects than those of Finite Volume **FV** schemes based on one-dimensional Riemann solvers.

Conditions for monotonicity (including the effect of the time operator discretization) of the **RD** numerical solutions are examined in [6].

The method employs a nodal based, finite element method like space discretization. The flow domain is discretized into simplex elements, resulting in an unstructured grid topology, which eases the meshing of complex geometries.

Regarding the accuracy of the method, when the simplest $P1$ basis functions (piecewise linear) are employed, 2nd order of accuracy at steady state is retrieved. As proven in [7], this property carries on up to $(k+1)^{th}$ order of accuracy if Pk elements are employed[2]. However, extension of the positivity properties to higher order schemes seems not to be straightforward and further investigation on this issue is being carried at the moment.

Regarding the efficiency, two opposed tendencies should be pointed out. On the one hand, the framework relies on the factorization of nodal Jacobian matrices. On the other hand, the compact closest neighboring cells stencil allows easy and efficient parallelizability. For the large system of equations (1) (Jacobian matrices of $N+6$-th order) even parallelizing might be of little use when N is too big; nevertheless, by reformulating the cell residual distribution in symmetrizing variables [8], the $N+6$-th order nodal Jacobians are reduced to a $N+1$ diagonal submatrix and a 5-th order symmetric submatrix. In conclusion, **RD** schemes can be competitive with other numerical methods in terms of computational effort; in fact, Lani reports in [9] to have achieved equivalent resolution of a $M = 11.5$ flow field over a double cone configuration with one quarter of the DOF's needed in a Finite Volume computation.

[2] And this, even if solution independent source terms are present[6].

Finally, the **RD** method has a formulation general enough to accommodate different thermochemical models. The `COOLFluiD` platform, a *VKI* in-house CFD tool (see [10] and [11]), includes at the moment of writing this document, a **CRD** solver, which has been designed to accommodate a variety of thermochemical non-equilibrium models provided by the MUTATION library ([12]).

All the reasons presented before support the application of **CRD** schemes to the simulation of atmospheric entry flow problems. Nevertheless, the particular features of hypersonic flows prevent straightforward application of the method in its present form, since some details are not properly understood or still missing. Among these, we find:

- shock instability fix, to avoid the so called *carbuncle* that appear when simulating hypersonic flows around blunted geometries;
- source terms treatment;
- higher order extensions.

In this document, the focus is on the carbuncle fix. Given the technological advantages of blunt configurations for atmospheric entry applications (lower heat fluxes at the wall), having an effective way of dealing with this spurious instability is an essential element for the application of the **CRD** solver to simulate high Mach number flows.

In the following section, the carbuncle phenomenon is described and its causes pointed out. After that, in the third section we present the shock fix proposed in [4] and analyze its behavior in detail: a sensitivity analysis is performed and its effect on the iterative convergence of time marching schemes are discussed. In the fourth section we present a generalized formulation of the carbuncle fix that allows to treat the energy equation consistently. The last section summarizes our conclusions and present several propositions to continue our work. A brief appendix with the minimal generalities of **RD** schemes, closes the contribution.

2. The carbuncle phenomenon

In the shock capturing methods community, the numerical instability that appears recurring when simulating high Ma number flows around blunted geometries with flux difference splitting (or Godunov type) schemes and shock surface aligned meshes is known as *carbuncle*. The name comes from the appearance

of the computed shock profile, a *blister* growing upstream of the normal region of the bow shock (where the fluid is undergoing a supersonic to subsonic compression), as in Figure 2-a. The flow structure is what would result if a nail were placed in the stagnation point of the body: two oblique shock waves attached to the nail projecting backwards, that at some point interact with the bow shock profile of the blunt body. Since this happens when no spike is present, the post shock conditions are unphysical and the computed heat flux is wrong.

Throughout the bibliography regarding this subject ([13], [14], [15], [16], [17],...), carbuncle is observed *mainly*[3] when using schemes with the desirable property of preserving steady contact waves -*e.g.* the **RD** N-scheme [3], and other well established **FV** schemes (Godunov, Roe and Osher schemes). Whether carbuncle appears or not is very dependent on the mesh employed; the bibliography agrees on that cells elongated across the shock profile favors the apparition of the instability [16]. Another fact observed is that the higher the Ma number is, the more likely is to obtain a carbuncle, with $Ma = 6$ as the threshold traditionally accepted for a well developed carbuncle. However, some weaker forms of instability (shock profile thickening) can observed at Ma as low as 1.5 [17].

The first analysis of the carbuncle phenomenon was carried out by Quirk in [13]. There, he realized that the **FV** Roe scheme, typically affected by carbuncle for blunt body simulations, is as well unable to preserve the shock profile flatness of a normal shock wave propagating along a straight channel uniformly meshed but with the central grid line being a small sawtooth profile (amplitude of 1^{-6} over 1.)[4]. This subtle modification is enough to induce sawtooth perturbations in the pressure and density profiles along the shock wave. In short, this implies that different sections of the shock profile propagate at different speeds (since the local sound speed is different). Under some conditions, these perturbations will not damp out but amplify, and the shock profile will break down. Quirk observed an equivalent behavior (confirmed theoretically in later studies [15] and [17]) in flow simulations around blunted geometries, that could be triggered even by round-off errors in any trivial manipulation of the numerical flow field.

Since it is Roe scheme's property of preserving steady contact waves what prevents the crosswind perturbations to damp out, Quirk proposed as a remedy to increase locally the crosswind dissipation in the numerical solution, by flagging the cells crossed by a shock wave using a tunable pressure based detector and using there a more diffusive scheme (in his case, Einfeldt's **HLLE**). This remedy solves the problem for the $1D$ shock wave propagation, and applied to flow over blunt bodies, prevents carbuncle to show up. This is the first known *cure* for the carbuncle phenomenon.

Dissatisfied with the constrains of Quirk's carbuncle fix formulation (tunable shock detector, two different schemes involved, dimension by dimension extension of $1D$ ideas), Sanders *et al.* proposed another fix in [14], of multidimensional nature and using a single scheme (either Roe's or Godunov's), which they applied to a structured grid **FV** solver. This fix increases locally the crosswind dissipation as well, by applying an entropy fix correction [19] to the flux function computed at every cell interface. Multidimensionality comes from considering the maximum entropy correction among a given cell interface and all others that intersect it. For $2D$ structured, regular grids the stencil is H-shaped, and hence the name of H-correction. Later on, Pandolfi and D'Ambrosio reported in [16] the appearance of carbuncle in viscous computations; H-correction algorithm was able to prevent shock instabilities for Navier-Stokes computations as well, but with a tendency to over diffuse boundary layers. Thus they refined the H-correction algorithm by removing from its stencil the current interface where the flux function is to be computed. In this way, the fix is not activated when in presence of a transverse density gradient, what avoids erroneously diffusing boundary layers.

In [20], its author, after extensive study of many Quirk's tests, identified a correlation between spurious post-shock vorticity and the crosswind perturbations characteristic of carbuncle flawed solutions. From this observation, the author proposes techniques to control vorticity. However, he finds that acting on vorticity does not suffice to avoid carbuncle. The author suggests then to ensure that entropy is effectively

[3] We stress the *mainly* because [18] disproves the widespread belief that dissipative schemes as Van Leer or H'anel do not present shock instabilities. It is true that they don't present protruding carbuncle as contact wave preserving schemes do, but some [18, multidimensional shock anomalies for a mesh either with a large number of cells in the shock parallel direction or a large cell AR] can be observed.

[4] This configuration (and variations of it) is now known as Quirk's test. These Quirk's tests, that replicate somehow the normal region of a bow shock wave, are an important research tool regarding carbuncle phenomena, since they allow characterize a scheme behavior face to numerical instabilities in multidimensional situations studying these simpler $1D$ problems (see for example [16] and [18]).

produced at shock waves; he finds that if the flux functions are evaluated at a particular averaged intercell state (depending on a single parameter), then no carbuncle appear for a wide range of test conditions.

3. A carbuncle fix for Residual Distribution Schemes

The N scheme [3], a 1st order accurate, positive, multidimensional upwind scheme, is the building block of **RD** schemes. According to [21], it is a generalization of the classical Roe scheme, and as such, is subject to generate carbuncle, as shown in Figure 2-a.

The eventual objective for avoiding the shock instability is to damp out the perturbations along the normal region of the shock wave and prevent them to grow up to form a carbuncle; doing so by adding dissipation through an artificial diffusive term can, in principle, be as effective as any of the strategies in Section 2. This approach avoids modifying the advective Jacobian eigenvalues through an entropy fix physically unrelated to carbuncle, and saves some of the computational complexity of mixing two differently behaved schemes. On top of that, discretizing a dissipative term is simpler than extending H-stencil fixes tailored to structured, cell centered meshes to the unstructured, nodal based grids **RD** discretization employs. Of course, then the question arises of what should be the form and the relative importance of this artificial dissipative term.

3.1. Original formulation

Sermeus, in [4], used this strategy to derive a remedy against carbuncle in the framework of **RD** schemes. He proposed to add an artificial diffusion term $\vec{\Delta}$ to the momentum conservation equation projected along the streamlines, and applied it to the $2D$, non-viscous, non-reacting version of (1):

$$\frac{\partial \vec{U}}{\partial t} + \frac{\partial \vec{F}^c_x}{\partial x} + \frac{\partial \vec{F}^c_y}{\partial y} = \vec{\Delta} \text{ with } \vec{\Delta} = \frac{\partial}{\partial \eta}\left(\mu_s \frac{\partial u_\xi}{\partial \eta}\right) \vec{1}_{\rho u_\xi}$$

where η is the dimension parallel to the numerical shock surface and u_ξ is the projection of the velocity across the shock wave surface, as in Figure 1.

With $\vec{1}_{\rho u_\xi}$ we stress that the fix only affects the momentum conservation equation along streamlines. The influence in the global system of reference is obtained through the following relation:

$$\vec{1}_{\rho u_\xi} = \cos\theta \, \vec{1}_{\rho u} + \sin\theta \, \vec{1}_{\rho v}, \tag{3}$$

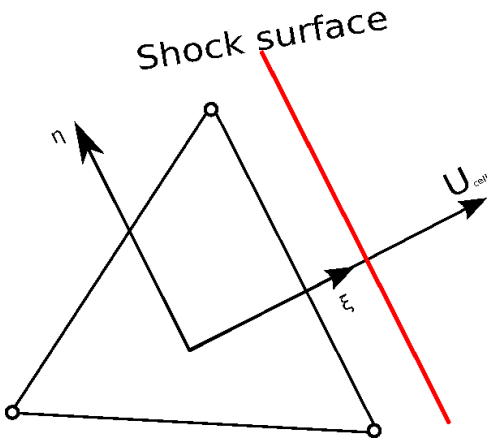

Figure 1: Sonic cell.

with θ the angle of the local streamline with the x axis of the global system of reference.

The contribution to the j-th nodal residual (see the appendix on **RD** for cell/nodal residual definition) is obtained by discretizing it with the Galerkin method, that in the case of using $P1$ elements results in:

$$\vec{\Phi}^{ad}_j = \int_\Omega \omega_j \, \vec{\Delta} \, dV = -\mu_s \frac{n_{\eta,j}}{4\Omega} \sum_{k=1}^{3} n_{\eta,k} \, u_{\xi,k} \, \vec{1}_{\rho u_\xi} \tag{4}$$

All the quantities in Equation (4) are known in the global system of reference:

$$\begin{aligned} n_{\eta,k} &= -\sin\theta \, n_{x,k} + \cos\theta \, n_{y,k}, \\ u_{\xi,k} &= \cos\theta \, u_k + \sin\theta \, v_k, \end{aligned} \tag{5}$$

This artificial dissipation is applied only in those cells where the flow undergoes a supersonic to subsonic compression. To detect them, let I be the set of vertices of element Ω, and call I_{super} and I_{sub} the subsets of vertices where Ma number is supersonic and subsonic respectively. If for a given cell both I_{super}, I_{sub} are not empty and the cross product of Ma number gradient with the cell speed is negative, the fix is applied:

$$\begin{aligned} \Omega / I = I_{super} \cup I_{sub}, \; I_{super}, I_{sub} \neq \emptyset, \\ \nabla M|_{cell} \cdot \vec{1}_\xi < 0. \end{aligned} \tag{6}$$

The fix depends on the parameter μ_s, estimated as:

$$\mu_s = \epsilon_s \, h \, \lambda_{max} \left[L^2 \, T^{-1}\right] \tag{7}$$

where h characterizes the size of the cell, λ_{max} is the maximum eigenvalue in absolute terms and ϵ_s is a tunable parameter. In the original formulation it is adviced to set it to 0.1. But, for a closer resemblance to a physical dissipative term, we have preferred to define it as:

$$\mu_s = \epsilon_s \, h \, \rho_{cell} \, \lambda_{max} \left[M \, L^{-1} \, T^{-1}\right] \tag{8}$$

With this interpretation, the adviced ϵ_s of 0.1, implies that in all cells where the fix is active, the Peclet number is 10. Indeed:

$$Pe_{cell} = \frac{\frac{\rho_{cell}\, A^2_{max}}{h}}{\frac{\mu_s\, \lambda_{max}}{h^2}} = \frac{1}{\epsilon_s}, \tag{9}$$

We defer the discussion about the choice of ϵ_s to the following Subsection.

3.1.1. Results

A sensitivity analysis of the fix has been performed with respect to its only controlling parameter, ϵ_s. As test case, the hypersonic inviscid flow field over an infinite cylinder of 50.8 *mm* in diameter has been simulated. The free stream conditions, chosen to match those in [22], are given in Table 1. Several simulations have been performed on a 400×30 nodes triangulated mesh (400 nodes over the wall and 30 along the radial direction), each time with a different value of ϵ_s.

Table 1: Free stream conditions.

M_∞	$\rho_\infty\,[kg/m^3]$	$U_\infty\,[m/s]$	$T_\infty\,[K]$	$p_\infty\,[Pa]$
15.0	0.00922	4688.15	241.0	640.53

A Newton method time stepping procedure was employed, with the CFL number given at every iteration I by:

$$CFL_I = \begin{cases} 1.0, \text{ if } I \leq 1000, \\ max\,(1.01 \cdot CFL_{I-1}, 50.0) \text{ otherwise.} \end{cases} \tag{10}$$

The convergence history shown in Figure 2 was obtained by *freezing* the value of μ_s once the main flow features reached its final position, in the spirit of what it is done for the flux limiter values in **FV** methods.

Table 2: Carbuncle fix sensitivity to ϵ_s.

ϵ_s	Pe_{cell}	Result
0.01	100.0	Carbuncle
0.05	20.0	Carbuncle
0.1	10.0	No carbuncle
0.5	2.0	Diverges
1.0	1.0	Diverges

Results of this study are summarized in Table 2 and in Figure 2. At the sight of Table 2, the value of 0.1 advised in [4] proves to be optimal: values below 0.1 (thus $Pe_{cell} > 10.0$) do not introduce enough dissipation to prevent the carbuncle (see Figure 2-a), while larger values ($Pe_{cell} < 10.0$) prevent the simulation to converge. In this sense it is not surprising that the optimal ϵ_s is such that $Pe_{cell} = 10.0$ since this Pe number offers the maximum dissipation while staying on the advection dominated regime, where **RD** schemes are known to work better (see [7]).

Regarding the Ma sensitivity, we have used this value of $\epsilon_s = 0.1$ for Ma number as high as 20.0 and no trace of carbuncle has been observed.

Then we decided to apply the fix to a $400x20$ nodes mesh. With less nodes along the radial direction, and thus more stretched elements across the shock wave, this mesh is more prone to induce the carbuncle instability. The fix was effective in preventing the carbuncle to appear, but the convergence history degraded from the one in 2-c to that in 3-a: convergence is never achieved, even though we apply the μ_s freezing strategy that worked for the 400×30 nodes mesh.

4. Extended formulation

Once the principles under which the carbuncle fix of the preceding section operates were understood, we realized that it is possible to extend it in order to control better the artificial dissipation: since a dissipation of momentum implies some dissipation in energy as well, we wondered whether including explicitly this contribution would have any effect on the result or on the convergence history.

We considered the general form of the physical dissipative tensor $\bar{\bar{F}}^d$ in (1), and compared its structure with the artificial dissipative term proposed by Sermeus. We explain in what follows the path followed, for the $2D$, non viscous, non reacting version of (1). The reasoning carries on straightforwardly to the $3D$ case.

To start with, we consider the form of the physical dissipative tensor $\bar{\bar{F}}^d$, in a Cartesian frame of reference. It is:

$$\begin{aligned} \bar{\bar{F}}^d = & \left(A_{xx} \frac{\partial \vec{P}}{\partial x} + A_{xy} \frac{\partial \vec{P}}{\partial y} \right) \vec{1}^t_x \\ & + \left(A_{yx} \frac{\partial \vec{P}}{\partial x} + A_{yy} \frac{\partial \vec{P}}{\partial y} \right) \vec{1}^t_y \end{aligned} \tag{11}$$

where vector $\vec{P}$ is the vector of the primitive variable set:

$$\vec{P} = (\rho, \vec{v}, T)^t \tag{12}$$

and the matrices $A_{x_i\, x_j}$ are 4×4 square matrices whose rows tell how the dissipative phenomena affect each of the conservation equations: with 1st row being for the mass conservation equation, 2nd and 3rd for the two components of the momentum conservation equation, and the 4th one for the total energy conservation equation. For Newtonian fluids, $A_{yx} = A^t_{xy}$, what implies that they describe an isotropic behavior.

The structure of Equation (11) is conserved if the diffusive tensor is expressed in any Cartesian, right handed system of reference. If we were to write the original carbuncle fix in [4] as in Equation (11), we would find that only $A_{\eta\eta}$ is

non zero, and that it has the following form:

$$A_{\eta\eta}^{Original} = \begin{bmatrix} 0 & 0 & 0 & 0 \\ 0 & \mu_s & 0 & 0 \\ 0 & 0 & 0 & 0 \\ 0 & 0 & 0 & 0 \end{bmatrix} \tag{13}$$

Equation (13) respects the consensus throughout the carbuncle bibliography of the connection between transverse perturbations, their variations along the shock surface and the shock instability. Comparing Equation (13) with matrix A_{yy} in (11) (once expressed in the shock wave system of reference, and with the assumption $\mu_v = -\frac{2}{3}\mu$ for the bulk viscosity coefficient):

$$A_{\eta\eta} = \begin{bmatrix} 0 & 0 & 0 & 0 \\ 0 & \mu & 0 & 0 \\ 0 & 0 & \frac{4}{3}\mu & 0 \\ 0 & \mu\, u_\xi & \frac{4}{3}\mu\, u_\eta & \kappa \end{bmatrix} \tag{14}$$

we observe that the main differences are the inclusion of transversal variations of u_η (that might be non zero at the numerical level) and T, and the fact that the *dissipation* of momentum is accompanied by a consistent dissipation of energy. Notice also that all the eigenvalues of $A_{\eta\eta}$ are either positive or zero, what is in line with the proper entropy dissipation advocated in [20].

We can employ matrix (14) (denoted from now on as $A_{\eta\eta}^{New}$) to construct a carbuncle fix just by applying the associated diffusive tensor in the cells containing a supersonic to subsonic compression, given by (6).

$$\bar{\bar{F}}^{ad} = A_{\eta\eta}^{New} \frac{\partial \vec{P}}{\partial \eta}\, \vec{1}_\eta^t \tag{15}$$

At the sight of Equation (14), we realize that we have gained full control of the way our artificial diffusion acts. For example we could choose to keep only the terms affecting variations of u_ξ (the second column), obtaining a carbuncle fix with the consistent energy dissipation. Or we could decide to consider contributions from the variations of T to the energy conservation equation, since variations in energy affect the pressure field. Or... Thus, more than a carbuncle fix, we have run into a full family of them.

Any of the fixes can be discretized using Galerkin method, exactly as in (4). As an example, we present the discretization of the carbuncle fix obtained considering contributions from u_ξ and T variations:

$$\begin{aligned} \vec{\Phi}_j^{ad} = -\mu_s \frac{n_{\eta,j}}{2} \frac{\partial u_\xi}{\partial \eta}|^h \left(\vec{1}_{\rho u_\xi} + \bar{u}_\xi\, \vec{1}_{\rho E} \right) \\ -\kappa_s \frac{n_{\eta,j}}{2} \frac{\partial T}{\partial \eta}|^h\, \vec{1}_{\rho E} \end{aligned} \tag{16}$$

where $\frac{\partial}{\partial \eta}|^h$ and $\bar{u}_\sigma$ stand, respectively, for the discretization of derivative $\frac{\partial m}{\partial \eta}$ for any magnitude m and for an average of u_σ ($\sigma = \xi, \eta$) over the sonic cell where the fix is applied.They are given by:

$$\frac{\partial m}{\partial \eta}|^h = \frac{1}{2\,\Omega} \sum_{k=1}^{3} n_{\eta,k}\, m_k, \quad \bar{u}_\sigma = \tfrac{1}{3} \textstyle\sum_{k=1}^{3} u_{\sigma,k}. \tag{17}$$

The different vectors and nodal quantities needed are given by expressions similar to those in Equation (5).

In order not to increase the number of parameters controlling the fix performance, we have decided to relate κ_s with μ_s by considering a fixed Prandtl number of $Pr = 0.7$, as:

$$Pr = \frac{\mu_s\, c_p}{\kappa_s}, \tag{18}$$

where c_p is the specific heat capacity at constant pressure of the gas at hand, assuming a perfect gas behavior. This very crude assumption has sufficed to obtain the results presented hereafter and prove the feasibility of the carbuncle fixes described. However, one should keep in mind that improved coupling (considering high temperature effects) will certainly be necessary for dealing with real life applications.

4.1. Results

We have tested the modified fix (16) on the same mesh where the standard fix (4) was unable of reaching a converged solution. The modified fix, with the following CFL ramping procedure:

$$CFL_I = \begin{cases} 1.0, \text{ if } I \leq 500, \\ max\,(1.01 \cdot CFL_{I-1}, 50.0) \text{ otherwise,} \end{cases} \tag{19}$$

and together with the freezing strategy described in Section 3.1.1 prevent the carbuncle to appear as well (Figure 3-c) with the convergence history shown in Fig.3-b.

So, the beneficial effect of *more* consistent dissipative term as carbuncle fix has been proven.

5. Conclusions

In the present contribution, we have argued the convenience of applying the **RD** schemes to the atmospheric entry problem, reviewing the present capabilities of the method and pointing out those elements that have to be improved or developed. Among the current shortcomings of the method we have focused on the known cures for the carbuncle phenomenon. We have studied different remedies appearing in the bibliography, all of them applied in the **FV** context. We have analyzed in depth the only carbuncle fix tailored to the **RD** framework, presented in [4]: a sensitivity analysis with respect to its only controlling parameter ϵ_s has been performed. We have been able to justify the optimality of ϵ_s given in the aforementioned reference. We have also addressed the problem of lack of convergence when the fix is applied in the form presented in the bibliography. We have been able to extend the fix in such a way that the choice of using energy consistent forms is available. A beneficial effect of the energy consistency in the iterative converge process has been proven. The fixes presented are general enough to be applied to other discretization techniques, *e.g.* **FV**.

At the moment of finishing this document, work to extend the fixes discussed to the Chemical and Thermal non equilibrium cases is currently in progress.

Residual Distribution Schemes: the basics.

A very short review of **RD** for the discretization of (1) is presented in this appendix. The interested reader will find extensive explanations in [3], [6] and [7].
The solution is expressed by means of a finite element representation on P1 linear triangles.

$$\vec{U}^h(\vec{x},t) = \sum_{j=1}^{\#DOF} \vec{U}_j(t)\, N_j(\vec{x}) \tag{20}$$

where the following property holds:

$$N_j(\vec{x}_k) = \delta_{jk} \tag{21}$$

The steady state residual for cell Ω is defined as:

$$\vec{\Phi}^{\Omega} = \int_V \left(\frac{\partial \vec{F}_j^c}{\partial x_j} - \frac{\partial \vec{F}_j^d}{\partial x_j} - \vec{S}^U \right) dV = \vec{\Phi}^{c,U} - \vec{\Phi}^{d,U} - \vec{\Phi}^{S,U} \tag{22}$$

with contributions from the convective, dissipative and source terms.

The nodal system of equations is obtained by distributing fractions of the cell residuals $\vec{\Phi}^{\Omega}$ to the nodes forming part of the cell. The convective contribution to the nodal equation of the cell residual is expressed generically as:

$$\vec{\Phi}_l^{c,U} = \sum_{\Omega_i \in \Xi_l} B_l^{\Omega_i,U}(K^{\pm}) \cdot \vec{\Phi}_{\Omega_i}^{c,U}$$

in terms of the so called distribution matrices $B_l^{\Omega_i,U}$, which depend on the nodal upwind parameters:

$$K_j = A_{j,x}\, n_{j,x} + A_{j,y}\, n_{j,y} + A_{j,z}\, n_{j,z} \tag{23}$$

where A_{j,x_d} is the Jacobian of the advective flux along direction x_d, and n_{j,x_d} are the components of the vectors normal to the element faces.

Different forms of the $B_l^{\Omega_i,U}$ matrices define different schemes. In this work, multidimensional, positive matrix N-scheme, in its conservative formulation Nc (further details in [6]) has been employed.

Distribution of diffusive contributions to the cell residual is done, when a $P1$ element mesh is used, by Galerkin discretization:

$$\vec{\Phi}_j^{d,U} = \int_{\Omega} \omega_j \nabla \cdot \bar{\bar{F}}^v\, dV \tag{24}$$

while source terms can be distributed either with the Galerkin method or together with the advective residual.

From the distribution process introduced before results a system of differential equation controlling the time evolution of the solution at the grid nodes. For l-th node, it is:

$$\Xi_l \frac{d\vec{U}_l}{dt} + \vec{\Phi}_l^{c,U} - \vec{\Phi}_l^{d,U} - \vec{\Phi}_l^{S,U} = \vec{0}, \tag{25}$$

where Ξ_l stands for the volume of the median dual cell around l-th node.

Acknowledgment

The author wants to express his gratitude, first of all, to Prof. Deconinck for providing him with the opportunity of joining the Von Kármán Institute as a Ph.D. candidate. Its advices at critical moments are always very appreciated. The help of Dr. Lani and Dr. Villedieu regarding `COOLFluiD` related issues has been essential for achieving the results presented in this contribution. Other developers of the `COOLFluiD` community are acknowledged as well for their patience in asking many questions. Thanks goes to K. Sermeus for information about the original **RD** carbuncle fix as well. Finally, the author kindly acknowledges the financial support provided by the Von Kármán Institute, without which nothing of this could have been possible.

References

[1] J. Anderson, Hypersonic and high temperature gas dynamics, McGraw-Hill, New York, 1989.

[2] Gnoffo, P., Gupta, R. and Shinn, J., Conservation equations and physical models for hypersonic air flows in thermal and chemical non-equilibrium, TP 2867, NASA (1989).

[3] van der Weide, E., Compressible flow simulation on unstructured grids using multi-dimensiona upwind schemes, Ph.D. thesis, Technische Universitet Delft (1998).

[4] Sermeus, K. and Deconinck, H., Solution of steady euler and navier-stokes equations using residual distribution schemes, LS 2003-05, VKI (2003).

[5] Csik, A., Ricchiuto, M. and Deconinck, H., Conservative formulation of the multidimensional upwind residual distribution schemes for general nonlinear conservation laws, Journal of Computational Physics 179 (1) (2002) 286–312.

[6] Ricchiuto, M., Construction and analysis of compact residual distribution discretizations for conservation laws on unstructured meshes, Ph.D. thesis, Université Libre de Bruxelles (2005).

[7] Villedieu, N., High order discretisation by residual distribution schemes, Ph.D. thesis, Université Libre de Bruxelles (2009).

[8] Garicano Mena, J., Lani, A., Degrez, G. and Deconinck, H., A symmetrizing variables formulation for hypersonic thermochemical non-equilibrium flow, with application to residual distribution schemes, in: V European Conference on Computational Fluid Dynamics, 2010.

[9] Lani, A. and Deconick, H., Conservative residual distribution method for hypersonic flows in thermochemical nonequilibrium, AIAA.

[10] Lani, A., An object oriented and high-performance platform for aerothermodynamic simulations, Ph.D. thesis, Université Libre de Bruxelles (2008).

[11] Quintino, T., A component enviroment for high-performance scientific computing. Design and implementation, Ph.D. thesis, Katholieke Universiteit Leuven (2008).

[12] Panesi, M., Physical models for nonequilibrium plasma flow , Ph.D. thesis, Universit degli studi di Pisa (2009).

[13] Quirk, J.J., A contribution to the great Riemann solver debate, International Journal for Numerical Methods in Fluids 18 (6) (1994) 555–574.

[14] Sanders, R., Morano, E. and Druguet, M.-C., Multidimensional dissipation for upwind schemes: stability and applications to gas dynamics, Journal of Computational Physics 145 (1998) 511–537.

[15] Robinet, J.-Ch., Gressier, J., Casalis, G. and Moschetta, J.-M., Shock wave instability and carbuncle phenomenon: same intrinsic origin?, Journal of Fluid Mechanics 417 (2000) 237–263.

[16] Pandolfi, M. and D'Ambrosio, D., Numerical instabilities in upwind methods: analysis and cures for the carbuncle phenomenon, Journal of Computational Physics 166 (2) (2001) 217–301.

[17] Dumbser, M., Moschetta, J.-M. and Gressier,J., A matrix stability analysis of the carbuncle phenomenon, Journal of Computational Physics 197 (2) (2004) 647–670.

[18] Kitamura, K., Shima, E., Nakamura, Y. and Roe, P.L., Evaluation of Euler fluxes for hypersonic flow computations, AIAA Journal 48 (4) (2010) 763–776.

[19] Harten, A., High resolution schemes for hyperbolic conservation laws, Journal of Computational Physics 135 (2) (1994) 555–574.

[20] Ismail, F., Towards a reliable prediction of shocks in hypersonic flow: resolving carbuncles with entropy and vorticity control, Ph.D. thesis, University of Michigan (2006).

[21] Deconinck, H., Roe, P.L. and Struijs, R., A multidimensional generalization of Roe's flux difference splitter for the euler equations, Computers and Fluids 22 (2-3) (1993) 215–222.

[22] R. Prabhu, An implementation of a chemical and thermal nonequilibrium flow solver on unstructured meshes and applications to blunt bodies, CR 194967, NASA (1994).

Figure 2: *Nc* scheme, Roe linearization, standard fix (4). 400×30 nodes, splitted mesh. Newton method time stepping.

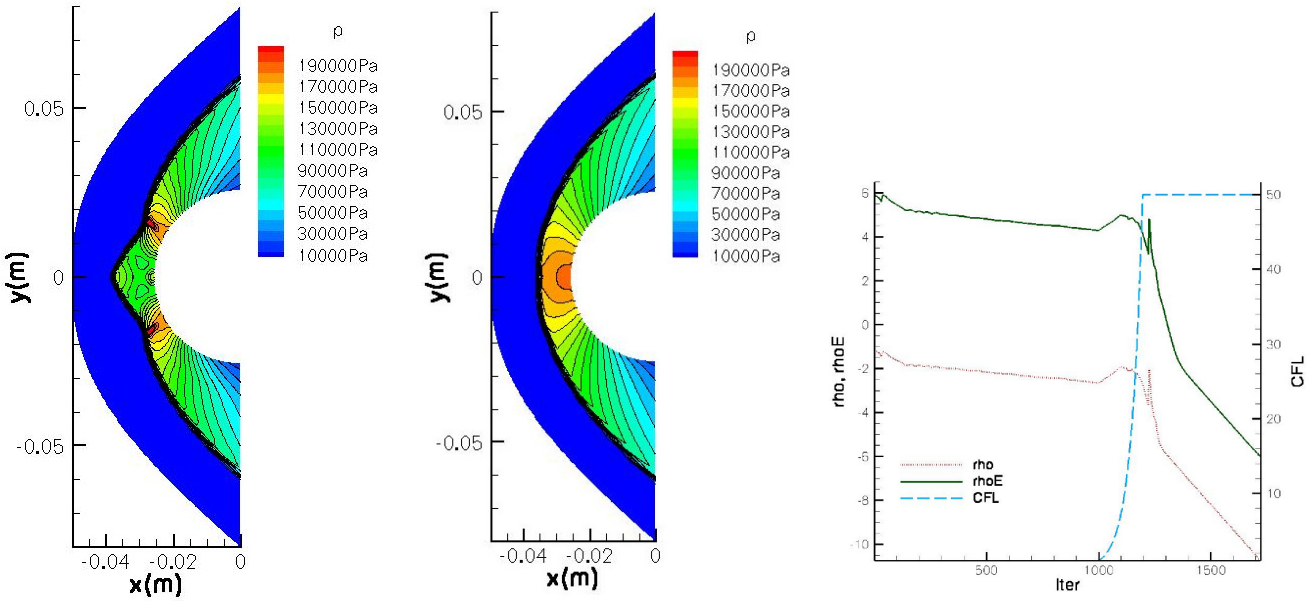

(a) Pressure isocontours, $\epsilon_s = 0.05$. (b) Pressure isocontours, $\epsilon_s = 0.1$. (c) Convergence history for standard fix, $\epsilon_s = 0.1$.

Figure 3: *Nc* scheme, Roe linearization, standard (4) *vs* modified (16) fix. 400×20 nodes, splitted mesh. Newton method time stepping.

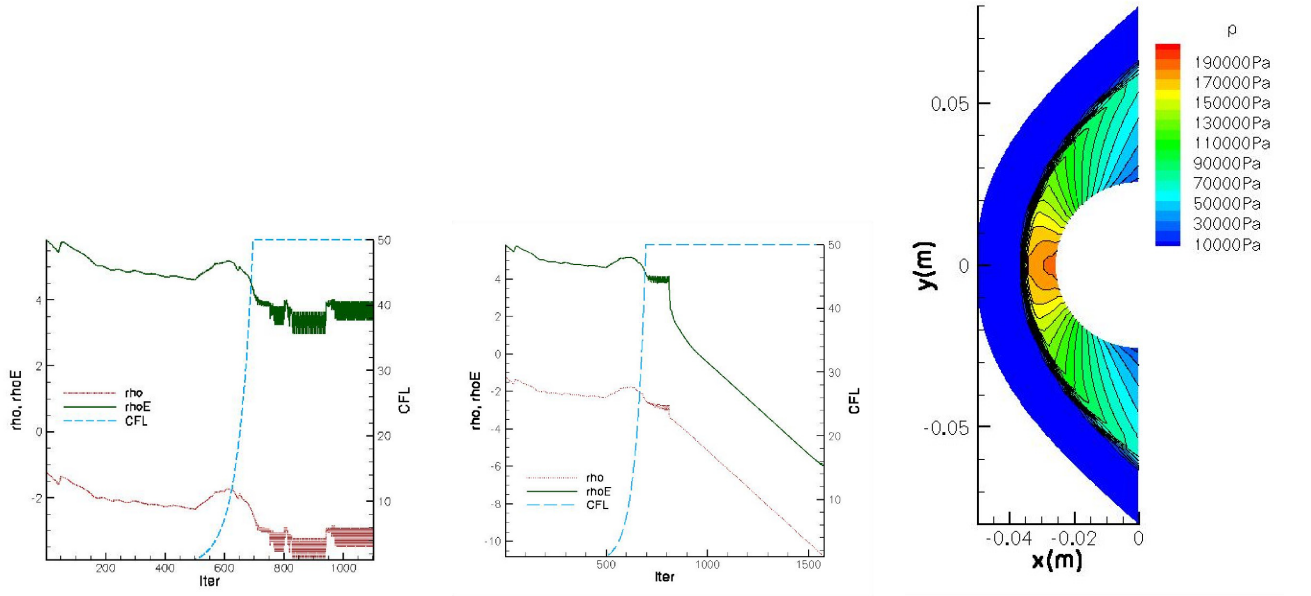

(a) Convergence history, standard fix (4),$\epsilon_s = 0.1$. (b) Convergence history, modified (16), $\epsilon_s = 0.1$. (c) Pressure isocontours, $\epsilon_s = 0.1$.

Multiscale models and computational methods for aerothermodynamics

Alessandro Munafó

Aeronautics and Aerospace Department, munafo@vki.ac.be

Supervisor: Thierry Magin

Assistant Professor, Aeronautics and Aerospace Department, von Karman Institute for Fluid Dynamics, Belgium, magin@vki.ac.be

Promoter: Anne Bourdon

Chargée de recherche CNRS, Laboratoire EM2C CNRS UPR 288, École Central Paris, Grande Voie des Vignes, 92290, Châtenay-Malabry, France, anne.bourdon@em2c.ecp.fr

Abstract

We propose to develop physical models and numerical methods for an accurate description of nonequilibrium physico-chemical phenomena in aerothermodynamics flows. Applications in aerospace range from space vehicle heat shield design to interpretation of experimental diagnostic measurements in high enthalpy facilities. In this work, we focus on the development of reduced collisional-radiative models.

Keywords: Nonequilibrium flows, Boltzmann equation, Collisional radiative models, Finite volume method.

1. Introduction

Understanding nonequilibrium phenomena occurring in aerothermodynamic flows (such as the one around a spacecraft entering a planetary atmosphere) is of fundamental importance for many applications. Typical examples, taken from the aerospace domain, are the design of heat shields for space vehicles and interpretation of experiments carried out in high enthalpy wind tunnels. Nonequilibrium phenomena are also present in industrial processes making use of lasers, discharges and plasma torches. Progresses made in developing physical models and computational methods for aerospace applications, on which we focus here, could also be used in other areas (such as plasma enhanced combustion and electric propulsion) where the occurrence of nonequilibrium must be taken into account as well.

Before proceeding further, it is necessary to explain nonequilibrium. The concept can be introduced by recalling what occurs around a spacecraft entering a planetary atmosphere at hypersonic speeds. A strong bow shock (actually one should say a thin compression region) is formed in front of the vehicle. The flow experiences a sudden compression. Pressure and density increase and, at the same time, most of the flow macroscopic kinetic energy is converted into thermal energy, leading therefore to a steep temperature increase. The combined effects of pressure and temperature lead to higher values of collision frequencies between atoms and molecules and to more energetic collisions. These cause excitation of internal energy degrees of freedom and, if the collision is energetic enough, breaking of chemical bonds can occur (molecular dissociation). If the entry speed is high enough ionization may also occur, and the gas becomes in this case a partially ionized plasma.

The flowfield is strongly coupled with the radiation field. Radiative transitions become more and more important with increasing degree of ionization. This induces a coupling between flow motion and radiative field that must taken into account if a correct estimation of surface heat flux is wished. As an example, we can mention that for Earth re-entry at speeds higher than 11 km/s, more than one half of surface heat flux is due to radiation (see Figure 1).

The description of this kind of flows is extremely complicated because all processes (both collisional and radiative) within the gas flow need a finite time to occur. If this time is very small compared to some macroscopic characteristic time scale (such as

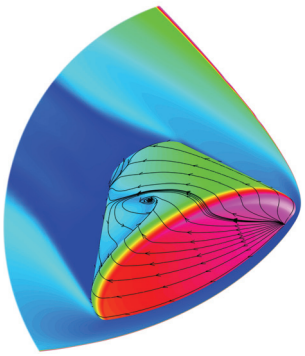

Figure 1: Computed temperature field for the ORION Crew Exploration Vehicle reentry at 10.15, km/s (peak radiative heating point). Courtesy NASA Ames Research Center.

the time needed for a fluid particle to pass across a shock wave or the boundary layer), the flow can immediately adapt to the varying conditions of pressure and temperature without any lag. One then talks of *equilibrium* flow. If the inverse situation occurs the flow is said to be *frozen*. In an intermediate situation, a certain lag will be always present and a correct description of the flowfield can be achieved only if the *finite rate* nature of collisional and radiative processes is taken into account in the governing equations expressing conservation of mass, momentum and energy. Flows in such a condition are labeled as *nonequilibrium* flows. They are usually described (especially for CFD applications) by means of the well known Navier-Stokes equations where nonequilibrium effects can be taken into account by means of different approaches (see Section 3.3).

A further complication in nonequilibrium flows is that the Navier-Stokes equations cannot be applied everywhere in the flowfield. An example of that is the zone around the bow shock in front of the entry vehicle. In those regions Newton and Fourier laws for shear stress tensor and heat flux vector, respectively, no longer hold. If a detailed study is wished, one should refer to the *Boltzmann* equation (always valid for dilute gases).

We conclude this introduction by mentioning that nonequilibrium is also present in recombining flows such as those occurring in boundary layers and nozzles. The latter are adopted in high enthalpy wind tunnels where understanding nonequilibrium is of crucial importance for a correct interpretation of experimental measurements.

2. Motivations and goals of the research activity.

Despite the research efforts performed nowadays and in the past years and the increasing available computational power and resources, the computation of nonequilibrium aerothermodynamic flows still poses problems. This is mainly due to the lack of accurate physical models (within a wide range of conditions) for collisional and radiative processes and transport phenomena in gas phase.

For the present doctoral period, we have decided to concentrate the research activity on the following topics:

- Development of reduced collisional-radiative models for CFD applications. This activity will be performed within an innovative context at the interface between computational quantum chemistry and computational fluid dynamics.
- Exploitation of recent developments in the field of kinetic theory of gases, providing the macroscopic equations for plasmas together with the expressions for transport fluxes and chemical production rates, accounting for chemical reactions and excitation of internal energy modes of atoms and molecules.
- Development of computational methods for the direct solution of the Boltzmann equation with chemical reactions and internal energy excitation. Applications will focus on flows out of the range of applicability of the Navier-Stokes equations (such as shock waves).

The paper focuses on the first item of the previous list and is structured as follows. In Section 3 the fundamental Boltzmann equation of kinetic theory of gases is briefly recalled, together with the solution method leading to the Navier-Stokes equations. Then, the existing approaches used for the quantitative description of collisional and radiative processes involving internal energy are presented. After this introductory discussion, first results concerning the development of reduced collisional-radiative models are shown in Section 4.

3. Mathematical and physical description of nonequilibrium flows.

3.1. The Boltzmann equation.

The starting point for the mathematical description of nonequilibrium gas flows is the Boltzmann equa-

tion for a mixture of perfect gases [7]:

$$\frac{\partial f_s}{\partial t} + c_{s_i}\frac{\partial f_s}{\partial x_i} + F_{si}\frac{\partial f_s}{\partial c_{s_i}} = \sum_r^{n_s} J_{sr}^{\text{el}} + \sum_r^{n_s} J_{sr}^{\text{in}} \qquad (1)$$

In eq. (1) f_s is the velocity distribution function that is nothing but a phase space density. It is defined such that the quantity $f_s(c_{s_i}, x_i, t)\, d^3c_s\, d^3x$ represents the *expected* number of particles of species s that at time t are contained within the volume d^3x around x_i and with velocity lying within the volume d^3c_s around c_{s_i}. The two terms on the right-hand-side of the same equation represents the effects of elastic and inelastic collisions (such as chemical reactions) also known as elastic and inelastic collision operators, respectively. The complete description of the flowfield can be obtained once eq. (1) is solved for the species velocity distribution function f_s. All flow macroscopic quantities can be computed by means of suitable integral averages over the velocity space. As an example, the mass density, mass flux and total energy per unit volume read:

$$\rho = \sum_s^{n_s} m_s \int f_s\, d^3c_s \qquad (2)$$

$$\rho u_i = \sum_s^{n_s} m_s \int c_{s_i} f_s\, d^3c_s\ ,\ i = 1,2,3 \qquad (3)$$

$$\rho E = \sum_s^{n_s} \frac{1}{2} m_s \int c_s^2 f_s\, d^3c_s \qquad (4)$$

In general, due to the complex mathematical structure of the elastic and inelastic collision operators, eq. (1) is very difficult to solve explicitly for f_s. A situation for which this becomes possible is for a gas (or mixture of) in *thermodynamic equilibrium* (left-hand-side of eq. (1) equal to zero). The velocity distribution function (if there is no external force field) in this case reads:

$$f_s = f_s^0 = n_s \left(\frac{m_s}{2\pi kT}\right)^{3/2} e^{-\frac{m_s(c_s-u)^2}{2kT}} \qquad (5)$$

Eq. (5) is also known as *Maxwellian* velocity distribution function. For sake of completeness, it must be said that eq. (5) is valid only for a gas mixture without considering species internal structure. In this last case, it can be shown that eq. (5) generalizes to the *Boltzmann* distribution.

3.2. The Navier-Stokes equations.

In case of small values of the Knudsen number Kn ($Kn < 0.01$), one way to tackle the problem of solving eq. (1), is to seek for a series solution:

$$f_s = \sum_i^n f_s^0 \phi_{s_i}^i = f_s^0 \left(1 + \phi_{s_1} + \phi_{s_2}^2 + \phi_{s_3}^3 \ldots\right) \qquad (6)$$

If one considers eq. (6) and neglects second and higher order terms, that is:

$$f_s = f_s^0 \left(1 + \phi_{s_1}\right) \qquad (7)$$

and plugs eq. (7) in eq. (1) and finally take moments of the expression obtained with respect to the *collisional invariants* (mass, momentum and energy), the Navier-Stokes equations for a chemically reacting gas are obtained:

$$\frac{\partial \rho_s}{\partial t} + \frac{\partial \rho_s u_i}{\partial x_i} = \omega_s - \frac{\partial \rho_s V_{s_i}}{\partial x_i} \qquad (8)$$

$$\frac{\partial \rho u_i}{\partial t} + \frac{\partial \rho u_i u_j}{\partial x_j} = \frac{\partial \tau_{ij}}{\partial x_j} - \frac{\partial p}{\partial x_i} \qquad (9)$$

$$\frac{\partial \rho E}{\partial t} + \frac{\partial \rho u_i H}{\partial x_i} = \frac{\partial \tau_{ij} u_j}{\partial x_i} - \frac{\partial q_i}{\partial x_i} \qquad (10)$$

It can be shown that, in eqs. (8) - (10), the expressions for the viscous stress tensor τ_{ij}, heat flux vector q_i and species diffusion velocities V_{s_i} are linear functions of macroscopic quantity gradients. The proportionality factors are the so called *transport properties* (such as dynamic viscosity and thermal conductivity). Kinetic theory of gases allows to obtain analytical expressions for transport properties in terms of the so called *reduced collision integrals* (that are in turn functions of atom and molecule interaction potentials). It can be also shown that, in view of the choice done for the expression of the perturbation parameter ϕ_{s_1}, the computation of macroscopic properties (such as mass density and energy per unit mass) only depends on the *local Maxwellian* or *zero order distribution function* f_0^s. In this case one speaks of flows in *small translational nonequilibrium*, since the velocity distribution function is a slightly perturbed Maxwellian.

Eqs. (8) (and related boundary and initial conditions) are sufficient for the description of the flow of a mixture of monoatomic gases without internal structure. However, when its presence is taken into account, additional considerations must be addressed. Two different methods have been proposed for this. Namely, multi-temperature and collisional radiative models. In both cases, the effects of transport phenomena is neglected and only chemical reactions are considered.

3.3. Multi-temperature and collisional-radiative models.

The multi-temperature approach [1] is of macroscopic kind. There, as shown in Figure (2), a given internal energy mode j (such as rotation, vibration or excited electronic states) is supposed to be populated according to a Boltzmann distribution at its own temperature T_j.

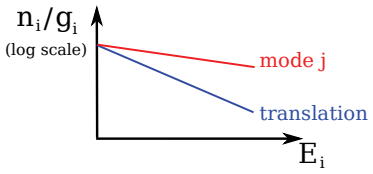

Figure 2: Energy level population in a multi-temperature approach.

Its value is obtained as an outcome from the solution of eqs. (8) - (10) coupled with a separated energy equation for the mode j:

$$\frac{\partial \rho_j e_j}{\partial t} + \frac{\partial \rho_j e_j u_k}{\partial x_k} = \Omega_j - \frac{\partial \rho_j e_j V_{j_k}}{\partial x_k} \qquad (11)$$

The source term Ω_j in eq. (11) takes into account for the *thermal nonequilibrium* between the mode j and the other modes. Its expression can be obtained by means of theoretical, empirical or semi-empirical models and the related literature is quite vast. However all these models are always based on adjustable and non physical tuning parameters. Moreover, the assumption of pseudo-Boltzmann fails dramatically for strong departure from equilibrium (see Section 4.2).

In order to overcome the deficiencies of the multi-temperature approach, collisional-radiative models were formulated. When only collisional interactions are considered, this is known in literature as *State-to-state* approach. Each internal energy level i is now treated as a separated *pseudo-species* and all *replenishing* and *depleting* transitions involving it are taken into account (see Figure 3).

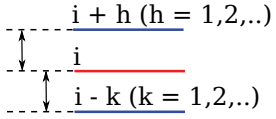

Figure 3: Energy levels in a state-to-state approach.

Once this done, a species continuity equation is written for the internal energy level i:

$$\frac{\partial \rho_i}{\partial t} + \frac{\partial \rho_i u_k}{\partial x_k} = \overbrace{\sum_{k \neq i} (\ )}^{\textbf{repl.}} - \overbrace{\sum_{k \neq i} (\ )}^{\textbf{depl.}} - \frac{\partial \rho_i V_{i_k}}{\partial x_k} \qquad (12)$$

Eq. (12) is then written for all species internal energy levels and must be coupled to the global momentum and energy conservations equations (eqs. (9) and eqs. (10), respectively). This approach is for sure more complete than the previous one. However, some drawbacks arise. First, expensive and lengthly quantum mechanics and molecular dynamics computations are needed in order to obtain *rate coefficients* for each *elementary process* (collisional or radiative). Second, the number of equations to be solved rapidly increases, leading to expensive computations even for 1D flows (such as normal shock wave and nozzle flows).

4. First steps towards mechanism reduction

We will focus here on one of the objectives of the research activity mentioned in Section 2, that is, seeking for a *reduction* of collisional-radiative models to be used within CFD codes.

When performing 2D/3D computations, there is the need for physical models that must both properly describe nonequilibrium in the flow and be not too expensive in terms of CPU time. If one refers to the entry of a spacecraft (see Figure 1), there is a primary interest in understanding internal energy excitation and dissociation across and after the bow shock (compressing flow) and recombination in the boundary layer (expanding flow). On the other hand, it is true that the study of these *key zones* could be performed by considering simple 1D testcases, such as the flow across and after a normal shock wave and the quasi 1D flow trough a nozzle of given area distribution (see Figures 4(a) and 4(b)).

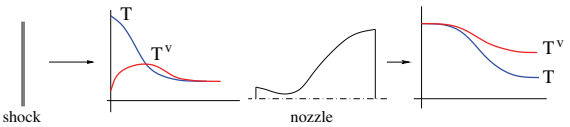

(a) Normal shock flow. (b) Nozzle flow.

Figure 4: 1D computational benchmarks.

The advantage of this approach is that, being the problems essentially 1D, collisional-radiative models can be used without limits of detail. Moreover, the computations performed (and the analysis of the related results) can be used as starting point for obtaining *physics based reduced* models that could be easily plugged in CFD codes. The final goal is therefore to formulate a *macroscopic* and *simplified* description of the physics of the flowfield.

The starting point for the application of above approach, is a rigorous description of collisional and radiative processes. This can be achieved by applying methods of quantum chemistry. In this way, numerical values for collision *cross sections* are obtained. After that, rate coefficients are computed by averaging over a *Maxwellian* velocity distribution function for translational degree of freedom of collision partners.

Within the context of the present work, the research activity has focused on the internal energy excitation and dissociation/recombination of the $N + N_2$ system. The set of rate coefficients used have been provided by the NASA Ames Computational Quantum Chemistry Group.

4.1. The NASA Ames database for the $N + N_2$ *system*

The NASA Ames database [4] [5] [6] comprises 9390 (v, J) ro-vibrational levels for the electronic ground state of nitrogen. These levels can also be denoted by means of a global index i, sorting them as a function of their vibrational quantum number v and then considering their rotational quantum number J. The relation between both i and (v, J) notations is expressed as:

$$i = i(v, J), \quad v = 0, \ldots, v_{\max}, \quad J = 0, \ldots, J_{\max}(v) \tag{13}$$

Conversely, the relation between the (v, J) and i notations is given by the relations

$$v = v(i), \quad J = J(i), \quad i \in \mathrm{I_{BP}} \tag{14}$$

where $\mathrm{I_{BP}}$ is the set of global indices for the nitrogen energy levels. Hence, for the vibrational state-to-state collisional model the energy of a level i can be written as:

$$E_i = \tilde{E}_v + \Delta\tilde{E}(v, J) \tag{15}$$

with $\tilde{E}_v = E_{i(v,0)}$, while $\Delta\tilde{E}(v, J)$ stands for the rotational contribution.

The NASA Ames database comprises more than 23 million reaction rate coefficients for dissociation of truly bound states and quasi-bound states and excitation between all states for nine values of the gas translational temperature (7500; 10000; 12500; 15000; 20000; 25000 30000; 40000 and 50000 K). It is important to mention that not only mono-quantum but also multi-quantum processes are accounted for.

4.2. Mechanism Reduction: Vibrational State-to-State Collisional Model

A vibrational state-to-state collisional model is developed as a first step towards a more tractable and simplified description of the energy excitation and dissociation in nitrogen flows. The 61 vibrational energy levels of N_2 of the NASA Ames database are taken into account, as well as all the averaged elementary rate coefficients for excitation and dissociation. Predissociation is not accounted for. Therefore, the collisional processes considered are:

$$\mathrm{N_2}(v) + \mathrm{N} \quad \leftrightarrows \quad 2\mathrm{N} + \mathrm{N}, \quad v = 0, \ldots, v_{\max} \tag{16}$$

$$\mathrm{N_2}(v) + \mathrm{N} \quad \leftrightarrows \quad \mathrm{N_2}(v') + \mathrm{N}, \quad v' > v \tag{17}$$

The vibrationally averaged rate coefficients are obtained by assuming that the rotational levels of a given vibrational quantum state v follow a Boltzmann distribution at the temperature T:

$$\frac{n_i}{\tilde{n}_v} = \frac{1}{\tilde{Q}_v} g_i \, e^{-\dfrac{\Delta\tilde{E}(v, J)}{kT}}, \quad i \in \mathrm{I_{BP}} \tag{18}$$

$$\tilde{Q}_v = \sum_{J=0}^{J_{\max}(v)} g_i \, e^{-\dfrac{\Delta\tilde{E}(v, J)}{kT}} \tag{19}$$

$$\tilde{n}_v = \sum_{J=0}^{J_{\max}(v)} n_i \tag{20}$$

are read [2]:

$$\tilde{k}_v^{Df} = \frac{1}{\tilde{Q}_v} \sum_{J=0}^{J_{\max}(v)} g_i \, e^{-\dfrac{\Delta\tilde{E}(v, J)}{kT}} k_i^{Df} \tag{21}$$

$$\tilde{k}_{vv'}^{E} = \frac{1}{\tilde{Q}_v} \sum_{J=0}^{J_{\max}(v)} g_i \, e^{-\dfrac{\Delta\tilde{E}(v, J)}{kT}} \sum_{J'=0}^{J_{\max}(v')} k_{ij}^{E} \tag{22}$$

with $v' > v$. Their numerical values (computed at discrete temperatures) have been fitted by applying least square method. An example is shown in Figures 5 and 6, where vibrationally specific rate coefficients for dissociation and excitation from the ground state ($v = 0$, $J = 0$) from 3000 to 50000 K are plotted. Values below 7500 K are obtained by extrapolating the result of the least square fit.

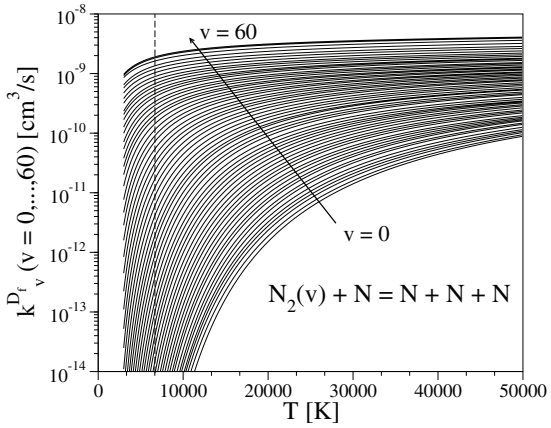

Figure 5: Dissociation rate coefficients for all vibrational levels.

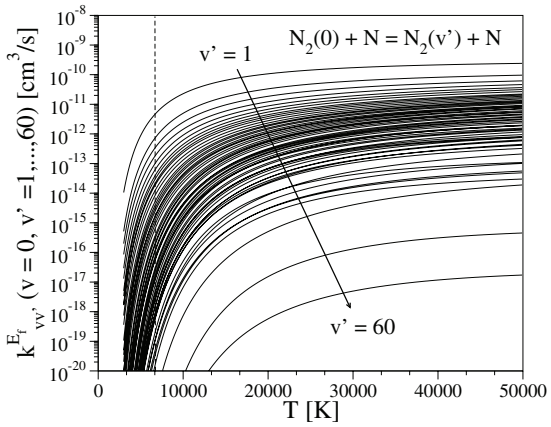

Figure 6: Excitation rate coefficients for vibrational ground state.

4.3. Governing equations in conservation law form

The governing equations (in conservation law form) describing the quasi-one dimensional non-equilibrium flow of a chemically reacting gas in a duct of given cross sectional area distribution A ($A = 1$ for a shock wave) are written in conservation law form:

$$\frac{\partial \mathbf{U}}{\partial t} + \frac{\partial \mathbf{F}}{\partial x} = \frac{\partial \mathbf{D}}{\partial x} + \mathbf{S} \tag{23}$$

where $\mathbf{U}$ is the conservative variable vector, $\mathbf{F}$ is the inviscid flux vector, $\mathbf{D}$ is the diffusive flux vector and $\mathbf{S}$ is the source term that takes account both for kinetics and cross-sectional area variation:

$$\mathbf{S} = \mathbf{S}_{\text{kin}} + \mathbf{S}_{\text{area}} \tag{24}$$

The last term on the right hand side of eq. (24) is obviously zero for a normal shock wave. Moreover transport phenomena are not taken into account for expanding flows within nozzles. The vectors in eq. (23) are:

$$\mathbf{U} = \left[\begin{array}{cccc} \rho_{\text{N}} & \rho_v & \rho u & \rho E \end{array} \right]^{\text{T}} \tag{25}$$

$$\mathbf{F} = \left[\begin{array}{cccc} \rho_{\text{N}} u & \rho_v u & p + \rho u^2 & \rho u H \end{array} \right]^{\text{T}} \tag{26}$$

$$\mathbf{D} = \left[\begin{array}{cccc} -\rho_{\text{N}} V_{\text{N}} & -\rho_v V_v & \tau & \tau u - q \end{array} \right]^{\text{T}} \tag{27}$$

$$\mathbf{S}_{\text{kin}} = \left[\begin{array}{cccc} \omega_{\text{N}} & \omega_v & 0 & 0 \end{array} \right]^{\text{T}} \tag{28}$$

$$\mathbf{S}_{\text{area}} = -\frac{\partial \ln A}{\partial x} \left[\begin{array}{cccc} \rho_{\text{N}} u & \rho_v u & \rho u^2 & \rho u H \end{array} \right]^{\text{T}} \tag{29}$$

with $v = 0, \ldots, v_{\max}$. The expressions of each single vector component in eqs. 25 - 29 are given in [3] and, for sake of brevity, will not be detailed here.

4.4. Numerical method

The governing equations in conservation law form (eqs. (23)) are solved numerically by means of Finite volume method. The method of lines is applied. Hence, the spatial discretization is first performed. Then, the resulting system of ODE's is integrated in time. In the present work, semi-implicit and implicit methods were considered because of the stiffness typical of problems involving kinetics.

For the semi-implicit case, the discretized equation for the cell i reads:

$$\left[\frac{\mathbf{I}}{\Delta t} - \left(\frac{\partial \mathbf{S}_i}{\partial \mathbf{U}_i} \right)^n \right] \delta \mathbf{U}_i^n = \mathbf{R}_i^n \tag{30}$$

with:

$$\mathbf{R}_i^n = \mathbf{S}_i^n - \frac{1}{V_i} \left[\left(\tilde{\mathbf{F}}_{i+\frac{1}{2}}^n - \tilde{\mathbf{F}}_{i-\frac{1}{2}}^n \right) - \left(\tilde{\mathbf{D}}_{i+\frac{1}{2}}^n - \tilde{\mathbf{D}}_{i-\frac{1}{2}}^n \right) \right] \tag{31}$$

In eq. (31) the tilde symbol indicates that fluxes (both convective and diffusive) at cell interfaces must be estimated in some manner since the solution is discontinuous at cell interfaces. Eq. (30) can be easily solved for $\delta \mathbf{U}_i^n$ and after that the solution can be advanced in time:

$$\mathbf{U}_i^{n+1} = \mathbf{U}_i^n + \delta \mathbf{U}_i^n \tag{32}$$

Eq. (32) shows that the update of the solution in a given cell is performed independently from the others. No algebraic system has to be solved (as required instead for implicit methods). This choice is therefore computationally efficient and should be therefore the favorite one (especially at initial stages of computations) when the flowfield presents some features (i.e

shock waves) inducing strong limitations on the maximum allowable time-step in order to maintain stability.

In case of an implicit method, the discretized equation for cell i is:

$$\mathbf{A}_i^n \delta\mathbf{U}_{i-1}^n + \mathbf{B}_i^n \delta\mathbf{U}_i^n + \mathbf{C}_i^n \delta\mathbf{U}_{i+1}^n = \mathbf{R}_i^n \tag{33}$$

where:

$$\mathbf{A}_i^n = \frac{1}{V_i}\left(\frac{\partial\tilde{\mathbf{D}}_{i-1/2}}{\partial\mathbf{U}_{i-1}} - \frac{\partial\tilde{\mathbf{F}}_{i-1/2}}{\partial\mathbf{U}_{i-1}}\right)^n \tag{34}$$

$$\mathbf{B}_i^n = \frac{\mathbf{I}}{\Delta t} - \left(\frac{\partial\mathbf{S}_i}{\partial\mathbf{U}_i}\right)^n + \frac{1}{V_i}\left[\left(\frac{\partial\tilde{\mathbf{F}}_{i+1/2}}{\partial\mathbf{U}_i} - \frac{\partial\tilde{\mathbf{F}}_{i-1/2}}{\partial\mathbf{U}_i}\right) + \right.$$
$$\left. - \left(\frac{\partial\tilde{\mathbf{D}}_{i+1/2}}{\partial\mathbf{U}_i} - \frac{\partial\tilde{\mathbf{D}}_{i-1/2}}{\partial\mathbf{U}_i}\right)\right]^n \tag{35}$$

$$\mathbf{C}_i^n = \frac{1}{V_i}\left(\frac{\partial\tilde{\mathbf{F}}_{i+1/2}}{\partial\mathbf{U}_{i+1}} - \frac{\partial\tilde{\mathbf{D}}_{i+1/2}}{\partial\mathbf{U}_{i+1}}\right)^n \tag{36}$$

This time, the solution variation within the cell i is coupled to that of its neighbors $i-1$, $i+1$. Therefore, the update can be performed by solving the set on linear equations obtained by writing eq. (33) for each cell. Within the context of the present work, the COOLFluiD framework [8] has been used in order to advance the solution in time when considering a fully implicit method.

The AUSM flux splitter [9], [10] or the Roe approximate Riemann solver (with the linearization proposed in [11]) are used for the estimation of convective fluxes, while diffusive fluxes are computed by means of a simple central finite difference formula (for more details the interested reader is referred to [3]). Finally, the WMUSCL reconstruction [3], [8] is applied in order to achieve second order accuracy in space.

4.5. Computational results

We present here computational results obtained by applying the vibrational state-to-state collisional model for the N + N_2 system (VSTS in what follows) described in Section 4.2 in compressing and expanding flows. In both cases, a comparison against the classical Park multi-temperature model [1] (Park 2 species in what follows) is considered in order to show the lack of accuracy of multi-temperature models in strong nonequilibrium conditions.

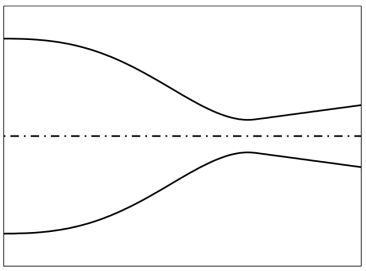

Figure 7: VKI minitorch nozzle geometry. Throat position x_t = 2.85 cm, throat radius r_t = 2.5 mm.

4.5.1. Expanding flow

The expansion within the nozzle of the VKI minitorch facility (see Figure 7) was studied.
The N + N_2 mixture was supposed to be in thermodynamic equilibrium in the reservoir. A subsonic inlet and supersonic outlet boundary conditions were applied at nozzle inlet and outlet, respectively. The AUSM flux splitter (together with the Van Leer limiter [12] [13]) was used for convective fluxes. In this case, before running computations, the problem of choosing right and meaningful reservoir conditions was faced. All this was caused by the lack of data regarding N_2 + N_2 collisions. As explained in detail in [3], after preliminary computations performed by means of the classical multi-temperature models (considering also processes involving free electrons), it was decided to set reservoir stagnation pressure p_0 and temperature T_0 to 101325 Pa and 10000 K respectively. As a matter of fact, it was shown in [3] that the effect of N_2 + N_2 collisions and the presence of free electrons (and related collisional processes) did not have a big influence on the flow behavior.

Once the choice made, computations were performed by using the VSTS and Park 2 species models. A first comparison on the variation of velocity and temperatures is shown in Figures 8(a) and 8(b). For the VSTS model the vibrational temperature T^v was computed according to the following equation:

$$T^v = \frac{\tilde{E}_1 - \tilde{E}_0}{k \ln\left(\frac{\rho_0 \tilde{Q}_1}{\rho_1 \tilde{Q}_0}\right)} \tag{37}$$

Differences arise in the diverging part of the nozzle for the vibrational temperature, while velocity and translational temperature are basically the same (a part some very little differences at nozzle outlet). In both cases, the flow remains in thermal equilibrium for the first part of the converging portion. Then, as the rate of expansion increases, the characteristic macroscopic

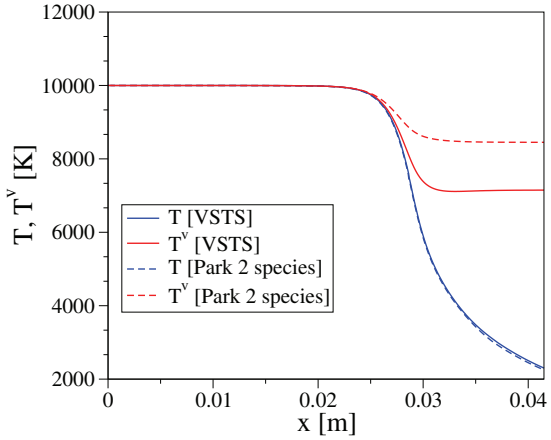

(a) Temperature.

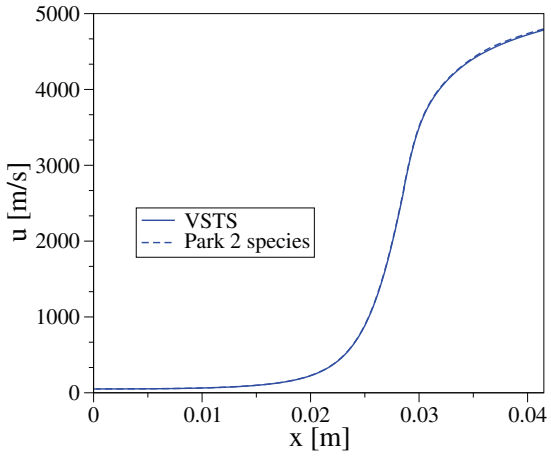

(b) Velocity.

Figure 8: Temperature and velocity profiles for the VKI minitorch based on the VSTS and Park 2 species models.

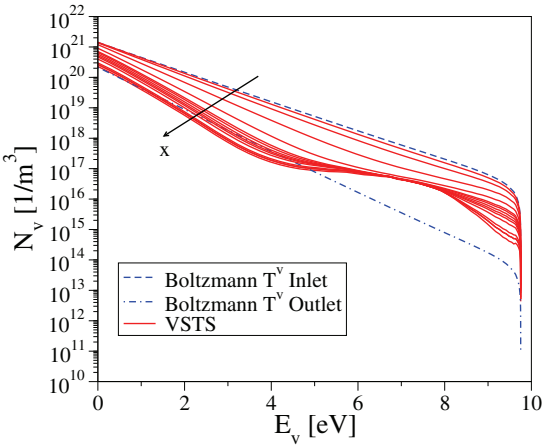

(a) Population at different locations along nozzle axis.

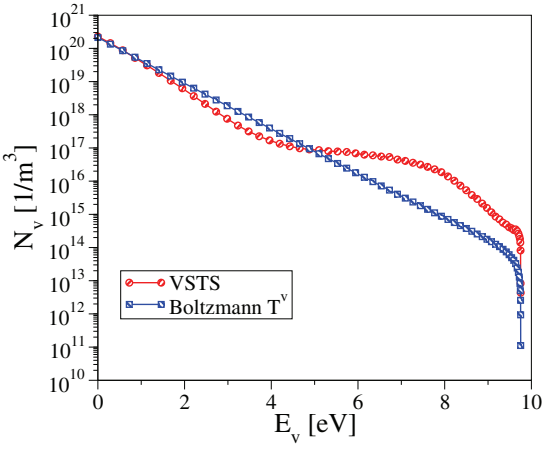

(b) Population at nozzle outlet.

Figure 9: Evolution of vibrational energy level population at different locations for the VKI minitorch nozzle.

time scale decreases (the velocity increases) and becomes closer and closer to that of collisional processes. This induces thermal and chemical nonequilibrium to occur even before the throat is reached ($x \simeq 0.0285$ m). Once this location passed, the further reduction of flow macroscopic time scale due to high velocity gradients and the increase of that of collisional processes as a consequence of temperature decrease (quenching effect), leads to the freezing of vibrational temperature for both models under use.

The different behavior of the vibrational temperature between the two models does not assure that the hypothesis at the base of the multi-temperature approach (pseudo Boltzmann distribution) is wrong. In order to be sure of that one has to investigate the population distribution of all the vibrational ladder.

Figure 9(a) shows its complete evolution while Figure 9(b) focuses on nozzle outlet. As it can be seen, deviations from Boltzmann distribution at temperature T^v appear at the outlet (even though not so strong). In particular the first 4-5 levels follow a straight line. Intermediate ones exhibit little under population, while high lying levels are overpopulated and the over population is always less than two orders of magnitude.

The variation of population distribution with space (fig. 9(a)) allows to obtain information about the dynamics of de-excitation and recombination during the expansion. The population distribution experiences at the beginning just an increase of its slope (remaining substantially Boltzmann). Despite not indicated in the plot, this part refers to the converging portion of the nozzle, where gradients are small and temperature remains at values such that all vibrational levels are able

to immediately adapt to the varying flow conditions. Then, as soon as the flow approaches the throat, high gradients starts to occur. The temperature experiences a strong decrease and this induces a lag of collisional de-excitation from high lying vibrational levels. As a consequence of that, overpopulation starts to appear in high lying vibrational levels and the amount of that remains almost constant for all the expansion because of the freezing of de-excitation due temperature decrease. On the other hand, low lying vibrational levels adapt to varying flow conditions much faster. As a matter of fact, for almost all the expansion they seem to follow a Boltzmann like distribution at the vibrational temperature T^v. However, in the final part they experience under population with respect to the previous distribution.

4.5.2. Compressing flow

The compressing flow across and past a normal shock wave was studied by means of both VSTS and Park 2 species models. Transport phenomena were considered and their influence on relaxation towards equilibrium was analyzed as well.

From a mathematical point of view (even when the set of governing equations is written for the steady state), one has to deal with a two point boundary problem. On the other hand, when the hypothesis of inviscid flow is introduced, one ends up with an initial value problem whose initial state is provided by some suitable *jump relations* giving the state of the flow immediately after the shock. This method has been successfully used for many years and it has been recently applied to the model under investigation [2] where the set of ordinary differential equations was solved by means of the LSODE package [14]. However, the drawback is that the influence of dissipation phenomena on the relaxation is totally neglected.

In order to include their presence, it was decided to use the Finite volume method. Eqs. 23 were again discretized by means of the method of lines and the numerical solution was marched in time till steady state convergence. Despite bigger programming efforts required than when using any package for *stiff* initial value problems, this approach is very convenient. As a matter of fact, it allows to compute both inviscid and viscous flows. The only problem encountered is that related to the treatment of the outlet boundary (downstream of the shock) whose location is initially unknown. The solution suggested in [3] was here considered.

In order to overcome the problem of lacking of data for $N_2 + N_2$ collisions, a little amount of atomic nitrogen was added in the freestream ($X_N = 0.1$). Table 1 shows the freestream and post-shock conditions for both VSTS and Park 2 species models.

State	1	2 (VSTS)	2 (Park 2 species)
p [Pa]	40	29067	29071
T [K]	300	7415	7394
u [m/s]	8500	498	497

Table 1: Freestream (1) and equilibrium post-shock (2) conditions for VSTS and Park 2 species models.

The numerical solution was obtained by using the semi-implicit method described in Section 4.4. Convective fluxes were estimated by means of Roe scheme together with Van Leer limiter for second order accuracy.

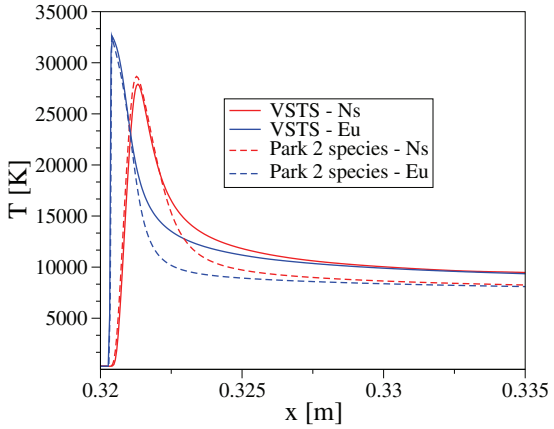

(a) Translational temperature.

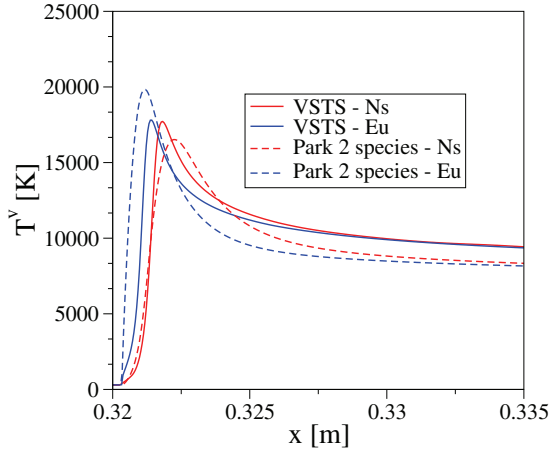

(b) Vibrational temperature.

Figure 10: Translational and vibrational temperature profiles for VSTS and Park 2 species models in case of viscous (Ns) and inviscid (Eu) 1D shock flow.

As one can appreciate, the Park 2 species model gives a faster relaxation towards equilibrium. This result should be expected, since, as mentioned before, the multi-temperature approach performs well only in cases of low departure from equilibrium. The results show that, also for compressing flows, the use of multi-temperature models can lead to erroneous results. Therefore, they should not be used for CFD applications. Another important and interesting aspect to observe is that, for both models, the presence of viscous effects plays an important role in the relaxation process. In particular:

- The shock is strongly smeared (as it should be) with respect to the inviscid case.
- Post shock temperature is lower when dissipative phenomena are added.
- The vibrational excitation and the related relaxation takes place in lag with respect to the inviscid case. This leads in turn to a longer distance needed to achieve equilibrium.

5. Conclusions and Future Work

After introducing the problems related to the accurate computation of nonequilibrium flows for entry applications, a brief description of the state of art physical models has been given. After that, attention has been put on the study of internal energy excitation and dissociation/recombination of molecular nitrogen by means of multi-temperature and collisional-radiative models in compressing and expanding flows. Simple 1D testcases have been computed by employing a mechanism reduction approach (vibrational collisional model in this case) in order to study in a simplified and tractable way the dynamics of internal energy level population. The comparison against results obtained by means of classical multi-temperature models have shown all drawbacks and lack of accuracy of the latter.

Future work will focus on seeking for an alternative and more accurate mechanism reduction approach. In particular, the hypothesis of rotational equilibrium will be rejected. At the same time, efforts will be devoted to the derivation of physics based macroscopic models that will be used in CFD applications.

Acknowledgments

I would like to thank Dr. Richard Jaffe and Dr. David Schwenke (from the NASA Ames Computational Quantum Chemistry Group) for the collaboration on the database for the $N + N_2$ system.

A sincere thank also to Dr. Marco Panesi (from The University of Texas at Austin) for his continuous help during this last year.

References

[1] Park, C. 1990 Nonequilibrium hypersonic aerothermodynamics. Wiley, New York.

[2] Magin, T. E., Panesi, M., Bourdon, A., Jaffe, R. and Schwenke D. 2009 Internal excitation and dissociation of molecular nitrogen in a compressing flow. AIAA 2009-3837, 41st AIAA Thermophysics Conference, San Antonio, Texas.

[3] Munafó, A., Panesi, M. , Jaffe, R., Lani, A. and Magin, T. E. 2010 Vibrational state to state kinetics in expanding and compressing nitrogen flows. AIAA 2010-4335, 42nd AIAA Thermophysics Conference, Chicago, Illinois.

[4] Jaffe, R., Schwenke, D., Chaban G. Huo., W. 2008 Vibrational and rotational excitation and relaxation of nitrogen from accurate theoretical calculations. AIAA 2008-1208, 46th AIAA Aerospace Sciences Meeting and Exhibit, Reno, Nevada.

[5] Jaffe, R., Schwenke, D. Chaban G. 2008 Theoretical analysis of N collisional dissociation and rotation-vibration energy transfer. AIAA 2009-1569, 47th AIAA Aerospace Sciences Meeting and Exhibit, Orlando, Florida.

[6] Schwenke, D. 2008 Dissociation cross-sections and rates for nitrogen. VKI LS 2008, Non-equilibrium Gas Dynamics, from Physical Models to Hypersonic Flights, Rhode-Saint-Genèse, Belgium.

[7] Chapman, S., Cowling, T. G. 1970 The Mathematical theory of non-uniform Gases. Cambridge University Press, UK, Third Edition.

[8] Lani, A. 2008 An object oriented and high-performance platform for areothermodynamics simulations. PhD. thesis, ULB, Belgium.

[9] Liou, M. S. 1996 A sequel to AUSM: AUSM$^+$. Journal of Computational Physics, No. 129, pp. 364-382.

[10] Liou, M. S. 2006 A sequel to AUSM, Part II: AUSM$^+$-up for all speeds. Journal of Computational Physics, No. 214, pp. 137-170.

[11] R. K. Prabhu 1994 An implementation of a chemical and thermal nonequilibrium flow solver on unstructured meshes and application to blunt bodies. Technical Report, NASA CR 194967, NASA Langley Center.

[12] Hirsch, C. 2006 Numerical computation of internal and external flow, Part I. Butterworth-Heinemann, Oxford.

[13] Hirsch C. 1990 Numerical computation of internal and external flow, Part II. Butterworth-Heinemann, Oxford.

[14] Radhakrishnan, K and Hindmarsh, A. C. 1993 Description and use of LSODE, the livermore solver for ordinary differential equations. NASA RP 1327.

Simulation of rarefied gas flows for aerospace applications

Erik Torres

Aeronautics and Aerospace Department, torres@vki.ac.be

Supervisor: Thierry Magin

Assistant Professor, Aeronautics and Aerospace Department, von Karman Institute for Fluid Dynamics, Belgium, magin@vki.ac.be

Promotor: Stefanos Fasoulas

Professor, Institute of Space Systems (IRS), Universität Stuttgart, Pfaffenwaldring 31, 70569 Stuttgart, fasoulas@irs.uni-stuttgart.de

Abstract

Rarefied gas effects are of importance when predicting the behavior of space vehicles entering a planetary atmosphere. A major factor in the success of such a mission is the correct determination of aerodynamic forces and moments affecting the stability of the vehicle. The flight envelope of the next generation of airbreathing hypersonic cruise vehicles is also expected to include extended periods at relatively high altitudes. Under rarefied conditions the continuum description of the gas is no longer valid and traditional CFD techniques based on solving the Navier-Stokes equations produce inaccurate results. Nowadays, the preferred technique for the numerical simulation of rarefied flows is direct simulation Monte Carlo (DSMC). This is a particle-based method capable of describing the flow at a molecular level. It is very flexible in the sense that it can incorporate complex physical phenomena, such as excitation of internal energy modes and non-equilibrium chemistry directly into the collision algorithm. The goal of this PhD is to improve those parts of the DSMC method, that are of special relevance for reentry flows, i.e. models for internal energy excitation and models for non-equilibrium chemical reactions in DSMC. Additionally, it is planned to investigate possible techniques for extending the applicability of DSMC to near-continuum flows.

Keywords: rarefied gas dynamics, RGD, reentry, hypersonics, direct simulation Monte Carlo, DSMC, non-equilibrium phenomena

1. Introduction

When a space vehicle returns from orbit, it passes through a region of the upper atmosphere with extremely low gas density. In this residual atmosphere, the average distance traveled by molecules between collisions (i.e. the mean free path λ) can reach the order of several meters, a distance comparable to the size of the vehicle itself. Fluid flows under such conditions, are commonly referred to as rarefied flows. There exists a dimensionless parameter, the Knudsen number, which is used to quantify the degree of rarefaction in a flow. It is defined as the ratio of the mean free path of the gas to some characteristic length:

$$\mathrm{Kn} = \frac{\lambda}{L} \tag{1}$$

The Knudsen number can either be defined as a single, global quantity representing the flow as a whole, or as a local flow field parameter. In the first case, it is natural to use a well-defined mean free path (e.g. the one of the incoming free-stream gas) and a particular physical dimension representative of the problem (e.g. vehicle diameter) to calculate a global Knudsen number. In the second case, the Knudsen number can be defined a product of the local mean free path and the dimensionless gradient of a local flow quantity (such as density, temperature, etc.):

$$\mathrm{Kn}_\rho = \lambda \cdot \frac{\nabla \rho}{\rho} \tag{2}$$

This quantity is useful to characterize flows, in which rarefied effects only play a role in some parts

of the flow field. Figure 1 sketches an overview of the different flow regimes as a function of Knudsen number. The Knudsen number increases from left to right, along with the degree of rarefaction. At the lower end, when Kn $\rightarrow$ 0, the collision rate between gas molecules is so high that they tend towards a state of equilibrium. This situation corresponds to inviscid flow, which can be described by the Euler equations. As the Knudsen number increases slightly, some diffusive effects associated to gradients of macroscopic quantities start to become relevant. In this regime, the diffusive fluxes of momentum, energy and mass can be expressed as linear functions of velocity, temperature and species concentration gradients. The flow can thus be described by means of the Navier-Stokes equations. If the Knudsen number is increased even further (to values above Kn $\approx$ 0.1), these linear relations no longer hold and a closed form of the macroscopic conservation equations can not be formulated without going to higher order systems (Burnett equations, Grad 13 equations). Continuum breakdown is said to occur and the flow can only be accurately described via a statistical treatment of the molecules based on kinetic theory. The Boltzmann equation provides an adequate description of the flow under these circumstances. Finally, at the other extreme, when Kn $\rightarrow \infty$, the limiting case of free molecular flow is reached. At this point, the mean free path is so large, that the effect of molecular collisions on the flow as a whole becomes negligible. This means that a body immersed in such a flow is in direct contact with the free-stream molecules. They will collide with the body surface, but not with other molecules in their vicinity.

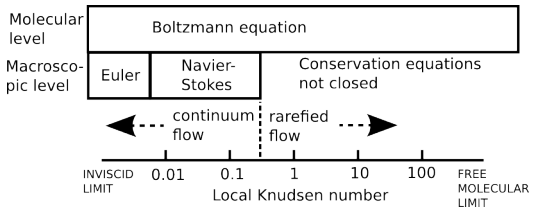

Figure 1: Classification of flow regimes according to Knudsen number

This summary is structured as follows: Section 2 introduces some basic concepts from the kinetic theory of gases. This includes the velocity distribution function, the concept of phase space and the Boltzmann equation. Section 3 gives a brief introduction into the DSMC method and the algorithm behind it. Then, in section 4 two test cases from literature are reproduced with RGDAS, the DSMC software used at VKI. Finally, section 5 provides some conclusions and outlines steps to be taken in the next year of research.

2. Molecular description of the gas and the Boltzmann equation

As indicated in figure 1, the Boltzmann equation allows to provide a mathematical description of dilute gas flows for all Knudsen numbers. This is possible because it takes into account statistical information on the state of the gas at the molecular level. The most detailed representation of this microscopic state can be obtained if one determines the velocity (and internal energy) of each molecule and its location in space at a given time. In practical situations however, such detailed information is not needed and it is enough to know how the molecules located in a given volume are distributed among possible energy states. For a mixture of monoatomic gases, this information can be expressed in terms of the so-called velocity distribution function (VDF). This distribution function is generally written as $f_i(\vec{c}, \vec{x})$ and its value provides information about the relative frequency of occurrence of a given molecular velocity $\vec{c}$ among all the molecules of species i located in the vicinity of coordinate $\vec{x}$.

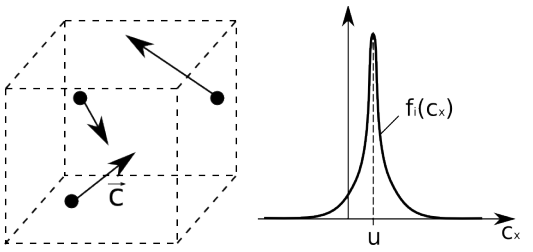

(a) Individual molecules around $\vec{x}$ (b) VDF for the x-component of molecular velocities for species i

Figure 2: The molecules in a small volume centered around coordinate $\vec{x}$ have molecular velocities distributed over the whole range ($-\infty < \vec{c} < \infty$). In near-equilibrium situations, the majority of molecular velocities is clustered around the average velocity.

The VDF is therefore not only a function of the three spatial coordinates (and time, for unsteady flows), but also of the components of molecular velocity. In analogy to physical space, where the $\vec{x}$ vector points to the position of a given molecule (or collection of molecules close to $\vec{x}$), one can also imagine a "velocity space", in which each molecule is located at a given velocity coordinate $\vec{c}$. The combination of

both the physical and velocity spaces is called phase space.

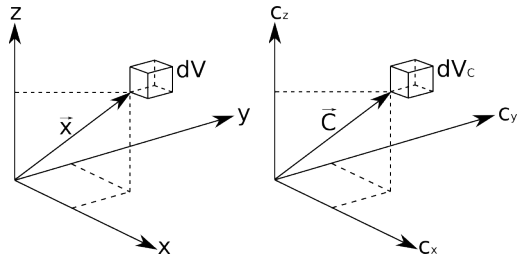

(a) Volume element in physical space (b) Volume element in velocity space

Figure 3: Phase space is the union of both physical and velocity space. The VDF, $f_i(\vec{x},\vec{c})$ has to be understood as providing information about a collection of molecules of species i in a small volume dV, dV_C.

2.1. Moments of the velocity distribution function

There exists a connection between the velocity distribution function and those field variables describing the flow at a macroscopic level. All of them are obtained by weighting a property of the molecules (i.e. molecular mass, velocity, etc.) by f_i and then averaging the product over the whole range of molecular velocities. The integration over the complete velocity space is necessary, since a collection of molecules located around a particular position $\vec{x}$, will generally be spread over the whole range of velocity space. For example, averaging the molecular mass m_i, one obtains the partial density of species i:

$$\rho_i = n_i \int f_i \, m_i \, dV_c. \tag{3}$$

Summing the partial densities over all species will result in the total density: $\sum_{i=1..N} \rho_i = \rho$. Here, the integration operator should be understood as $\int (\cdot)\, dV_c = \int_{-\infty}^{\infty}\int_{-\infty}^{\infty}\int_{-\infty}^{\infty} (\cdot)\, dc_x\, dc_y\, dc_z$. The quantity n is called the number density. It it is related to the mass density via the molecular mass and Avogadro's number. Adding up

When averaging the momentum of individual molecules, after integration and summation over all species, one obtains the average momentum per unit volume in the gas:

$$\rho\,\vec{u} = n_i \sum_i^N \int f_i \, m_i \, \vec{c}\, dV_c. \tag{4}$$

Analogously, averaging the kinetic energy of the molecules produces the total energy, i.e. the sum of macroscopic kinetic and thermal energy:

$$\rho\, e = \sum_i^N n_i \int f_i \, \frac{1}{2}\, m_i \, \vec{c}\cdot\vec{c}\, dV_c. \tag{5}$$

The quantities on the left hand side are called "moments" of the velocity distribution function. They allow for a macroscopic description of the system.

2.2. The Boltzmann equation

The Boltzmann equation itself takes on different forms, depending on the physical effects being considered. References [1] and [2] provide details on its derivation. For a mixture of inert particles, only taking into account their translational energy, it can be written as:

$$\begin{aligned}&\frac{\partial}{\partial t}(n_i f_i) + \vec{c}_i \cdot \frac{\partial}{\partial \vec{x}}(n_i f_i) + \vec{F}_i \cdot \frac{\partial}{\partial \vec{c}}(n_i f_i) = \\ &\sum_{j=1}^{N} \int_{-\infty}^{\infty}\int_0^{4\pi} n_i\, n_j \left(f_i'(\vec{c})\, f_j'\left(\vec{\zeta}\right) - f_i(\vec{c})\, f_j\left(\vec{\zeta}\right)\right) \times \\ &\times\, g_{ij}\, \sigma_{ij} d\omega\, dV_\zeta.\end{aligned} \tag{6}$$

The left-hand side of equation (6) is called the streaming operator. It expresses the time evolution of the velocity distribution function due to advective motion of molecules in phase space. The first and second term together represent the time rate of change of the VDF at a given location, plus its advection in physical space. The third term is only relevant if external forces $\vec{F}_i$ (e.g. due to electromagnetic or gravitational fields) influence the molecular trajectories. It may be viewed as representing advection of f in velocity space. The streaming operator can be thought of as a "substantial derivative" of f_i in the phase space.

The right-hand side of equation (6) is called the collision operator. It expresses the time rate of change of f_i due to collisions between molecules of class $\vec{c}$ with molecules j of all velocities $\vec{\zeta}$. For a mixture, the collision term consists of a sum of N integrals. The outer integral is computed over all velocity classes $\vec{\zeta}$. The inner integral, taken over the solid angle ω, represents the full range of possible post-collision deflection angles between the two molecules (see figure 4). The collision rate itself is proportional to the relative speed between collision partners g_{ij} and the collision cross section σ_{ij}. It comprises a term with negative sign, proportional to $f_i(\vec{c})\cdot f_j\left(\vec{\zeta}\right)$, due to collisions scattering particles out of velocity class $\vec{c}$ (i.e. direct collisions, see figure 5(a)) and another term with positive sign, proportional to $f_i'(\vec{c})\cdot f_j'\left(\vec{\zeta}\right)$, responsible for bringing

particles back into class $\vec{c}$ via inverse collisions (see figure 5(b)).

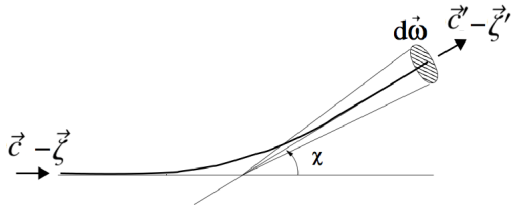

Figure 4: Dynamics of a binary collision: In the collision plane, χ is called the deflection angle

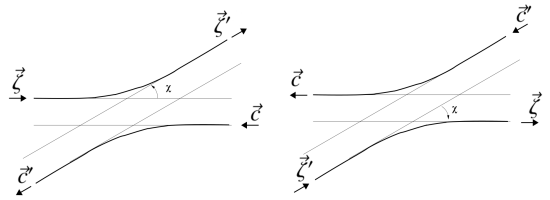

(a) Direct collisions (b) Inverse collisions

Figure 5: A direct collision is one in which molecules belonging to velocity classes $(\vec{c}_i, \vec{\zeta}_j)$ transition to velocity classes $(\vec{c}'_i, \vec{\zeta}'_j)$. The corresponding inverse collision occurs when particles with initial velocities $(\vec{c}'_i, \vec{\zeta}'_j)$ transition to velocities $(\vec{c}_i, \vec{\zeta}_j)$ after the collision.

3. The DSMC method

The direct simulation Monte Carlo (DSMC) method is a numerical technique developed to simulate dilute gas flows. It is a particle-based method emulating gas behavior at the molecular level. In a DSMC calculation, the gas molecules are represented by a relatively small number of simulation particles. During the course of the computation, these particles move through the flow domain, colliding with each other and with solid surfaces in a manner that emulates the behavior of the real molecules. The position of each particle is tracked over discrete time steps and is updated according to its instantaneous velocity. When particles leave the flow domain, they are removed from the simulation, whereas new particles are injected at flow inlets. By counting the number of particles and averaging their velocities over small volume elements, one is able to obtain macroscopic quantities of interest, such as density, velocity and temperature.

The most distinctive feature of the DSMC method is that collisions between particles are computed in a stochastic manner, as opposed to a deterministic approach. This means that particles selected for collision do not necessarily have intersecting trajectories, but need only be relatively close to one another just before the moment of collision. Collision partners are selected at random from a small group of neighboring particles and the probability of them colliding increases the smaller the distance between them becomes. The selection of collision partners, as well as the determination of their post-collision velocities, is accomplished with the aid of random numbers. Every individual collision event represents only one possible realization among many. However, for a large number of such simulated events, the collection of particles will behave in the physically correct manner. Mathematical algorithms which rely on such stochastic procedures are called Monte Carlo methods, thus giving the DSMC method its name.

The development history of DSMC reaches back several decades. The most important early work can be attributed to G.A. Bird, who also wrote the most widely known reference on the subject [2]. The method is commonly used to simulate flows where Knudsen numbers are relatively high and has been applied to problems in aerospace, e.g. early stages of atmospheric entry, thruster performance in near-vacuum, hypersonic cruise vehicles, electric propulsion, etc. Another branch where it has come into use, is in simulating flow in microscopic systems such as Micro Electro Mechanical devices, or MEMS (e.g. mechanical parts in computer hard drives), as well as for simulating material deposition processes in near-vacuum conditions.

Nowadays, there exist only a few DSMC codes capable of simulating the physics of reentry problems. The most noteworthy implementations are: The "DSMC Analysis code" (DAC) developed by LeBeau et al [3], the SMILE code developed at the institute of Theoretical and Applied Mechanics (ITAM) in Novosibirsk, Russia by the team of Ivanov [4; 5], as well as the MONACO code developed by Boyd's group[6; 7]. Finally, G.A. Bird has also developed a 2D/3D DSMC code for hypersonic flow applications [8].

3.1. The DSMC algorithm

The basic DSMC algorithm is presented in the flow chart of figure 6. A central assumption inherent to the DSMC method is that the continuous process of molecular motion and collisions can be decoupled into two separate phases for sufficiently small time steps Δt. This means that all particles in the flow may be

simultaneously displaced from their initial positions $\vec{x}_{p,i}$, according to their initial velocities $\vec{c}_{p,i}$ without interacting with each other. For the case where no external forces act on the molecules:

$$\vec{x}_{p,f} = \vec{x}_{p,i} + \vec{c}_{p,i} \cdot \Delta t \tag{7}$$

After the movement phase has been completed for all particles, collisions will be simulated. In order to limit the number of possible collision partners for a given particle, the flow domain is divided into a grid of cells. Only particles located within the same cell may be selected for collision. At the beginning of the collision phase, the number of collisions in each cell has to be determined. Following Bird's NTC method[2]:

$$N_{coll} = \frac{1}{2} N (N-1) \; F_N \, (\sigma_T \, g)_{\max} \; \Delta t / V_C \tag{8}$$

In this equation N stands for the number of particles in the cell. The factor F_N represents the ratio of real molecules to simulation particles. Its value is set as a user defined parameter a the beginning of the simulation and remains constant. The term in brackets $(\sigma_T \, g)_{\max}$ is the maximum value of the product of collision cross section and the relative speed between any two molecules in the cell. Finally, Δt represents the length of the time step and V_C the cell volume.

The next step is to select two particles at random from within the cell and to compute their probability of colliding with one another according to the expression:

$$P_{coll} = \frac{\sigma_T \, g}{(\sigma_T \, g)_{\max}} \tag{9}$$

The result of this expression will give a value between zero and one. This value is compared to a randomly generated number R_f, also from within the interval $[0, 1]$. If $P_{coll} > R_f$, the collision is "accepted" and post-collision velocities are computed according to the laws of conservation for momentum and energy of the collision pair. Otherwise, if $P_{coll} < R_f$, a different pair of particles is tested for collision. This process is repeated until the number of collisions N_{coll} for the cell has been reached. No more collisions are computed for the given time step and the particle movement phase of the next time step can begin with the updated particle velocities.

In most situations of practical interest, the boundary conditions are set up in such a way that, after an initial transient period, a steady flow field will be established at the macroscopic level. Once this has happened, the sampling of macroscopic flow fields is started. The sampling of macroscopic variables is accomplished by averaging molecular quantities of all particles in a given cell. This is analogous to the procedure described in section 2.2. However, since DSMC naturally provides molecular velocities as part of the algorithm, there is no need to determine the velocity distribution function before computing the moments.

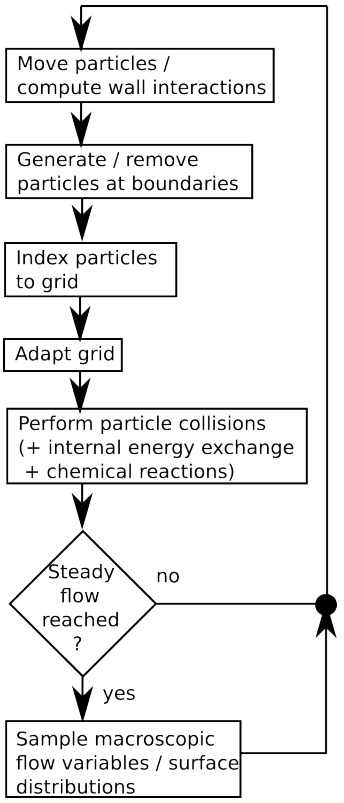

Figure 6: Sequence of a typical DSMC time step

4. DSMC at VKI

Thanks to a cooperation agreement with ITAM, the VKI has access to the "Rarefied Gas Dynamics Analysis System" (RGDAS), a software package based on the SMILE code[4; 5]. RGDAS is in fact a combination of DSMC solver, the pre-processing tools necessary for setting up a simulation and the post-processing utilities needed for analyzing the results. Two distinct DSMC solvers, one for 2D/axisymmetric and another for arbitrary 3D flows form the basis of RGDAS. RGDAS may make use of either the Variable Hard Sphere (VHS) [2], or the Variable Soft Sphere

(VSS) [9] model for collision cross sections. Excitation of internal energy degrees of freedom for polyatomic gases is handled using the standard model proposed by Borgnakke and Larsen[10]. Chemical reactions in the gas phase are modeled using the total collision energy model (TCE) [11]. One feature, which makes RGDAS especially useful for inexperienced users is its graphical user interface (GUI). The whole process of preparing, running and post-processing a calculation can be performed from this GUI.

SMILE/RGDAS is a mature code and is one of the references in DSMC. However, at the beginning of this PhD project, there was little expertise available at VKI on the use of RGDAS, or on the DSMC method in general. For this reason, a major part of the first year of the PhD was spent on gaining familiarity with the code and on assessing its performance. Two test cases were selected from literature and attempts were made to reproduce the published results.

4.1. Cylinder in cross-flow

The first test case, taken from a paper by Lofthouse[12], is studied using the 2D version of RGDAS. The setup consists of a cylinder of infinite length immersed in a uniform flow of pure Argon. The incoming flow direction is perpendicular to the cylinder axis (see figure 7). The incoming flow is supersonic, with $M_\infty = 10$ and $T_\infty = 200\,K$. The cylinder itself has a diameter of 0.3048 m and the surface temperature is assumed to be constant at $T_w = 500\,K$. In the original study, the flow was simulated for four different free-stream Knudsen numbers, ranging from rarefied to near-continuum conditions (Kn = 0.25, 0.05, 0.01 and 0.002). In the present study, only the first three Knudsen numbers were simulated with RGDAS. All calculations were run on the SGI cluster of VKI. The simulations at Kn = 0.25 and Kn = 0.05 were run on 32 processing cores each, while the one at Kn = 0.01 had to be run on 64 cores due to increased memory requirements. Lofthouse used 32 cores for the three equivalent simulations. Table 1 compares the number of particles used in the reference to those used in the present case. The number of particles is a good indicator for computational cost in a DSMC simulation. The reason for the significant deviations between the two codes is not known at present. One reason for the discrepancy might be that domains of very different sizes were used in both cases. Unfortunately, the original article does not provide such information. In a paper by Bird [13], the same test case is used for comparing several popular DSMC implementations. He also makes the observation that the number of particles needed may vary several orders of magnitude depending on the code.

Kn_∞	Particles (M)	Particles (R)
0.01	26.8×10^6	348.8×10^6 !
0.05	7.1×10^6	2.25×10^6
0.25	16.5×10^6	0.16×10^6

Table 1: Number of particles used by Lofthouse with MONACO (M) and present simulations with RGDAS (R)

In addition to giving precise inflow conditions, Lofthouse's paper also provides the parameters needed to compute the VHS collision cross sections: $d_{ref} = 3.595 \times 10^{-10}\,m$ at $T_{ref} = 1000$ K and $\omega = 0.734$ The same values were used for the present simulations.

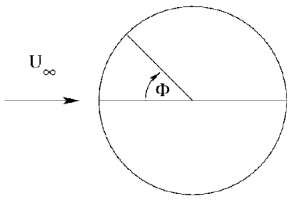

Figure 7: Cylinder flow geometry

The first simulation results available for comparison with Lofthouse are distributions of pressure, friction and heat transfer coefficients along the cylinder surface. They are plotted as function of the angle Φ measured from the forward stagnation point (see figure 7). Figures 8, 9 and 10 show plots of the pressure, friction and heat transfer coefficients along the cylinder surface for Kn = 0.01. The solid black curves labeled "DSMC" are the reference results generated with MONACO, while the small circles represent the results obtained with RGDAS. The agreement is very good for all three cases. Only the friction coefficient predicted with RGDAS lies slightly below the reference curve.

The same set of curves can also be generated for the other two Knudsen numbers considered. The discrepancies between RGDAS and the reference are even less pronounced in these cases. Figures 11, 12 and 13 show the curves corresponding to Kn = 0.25.

Figures 14 and 15 show contour plots of the overall temperature and the density ratio ρ/ρ_∞ at Kn = 0.01. The top half of the picture shows the flow field as reported by Lofthouse, the lower half is the corresponding result obtained with RGDAS. Small discrepancies

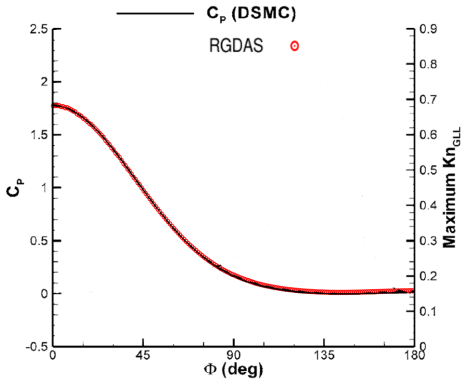

Figure 8: c_p at $Kn = 0.01$

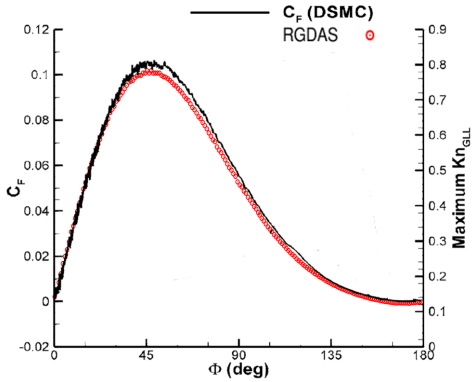

Figure 9: c_f at $Kn = 0.01$

in the contours are visible, especially when comparing the two density plots in figure 14. These may be attributed to the different sampling grids used in both simulations. Figures 17 and 16 show the comparison plots of density ratio and temperature for Kn = 0.25.

Lofthouse reports numerical values for the heat flux at the forward stagnation point. Table 2 lists values obtained with RGDAS and the reference quantities for all three Knudsen numbers considered. As can be seen, the relative difference does not exceed 3%. Another numerical quantity for comparison is the drag force per unit length given in table 3. Here the differences are even smaller and it can be said that both DSMC implementations essentially provide the same results.

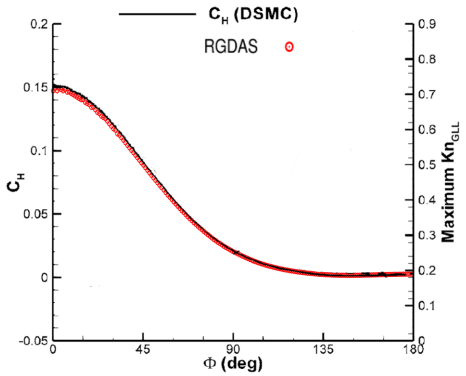

Figure 10: c_h at $Kn = 0.01$

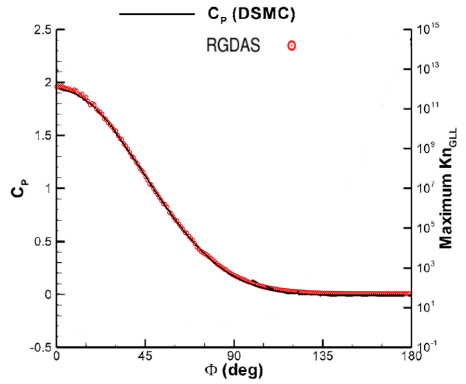

Figure 11: c_p at $Kn = 0.25$

Kn_∞	MONACO	RGDAS	diff. (%)
0.01	39319	38112	−3.0
0.05	16067	15966	−0.6
0.25	5984	5963	−0.4

Table 2: Peak heat flux $[W/m^2]$

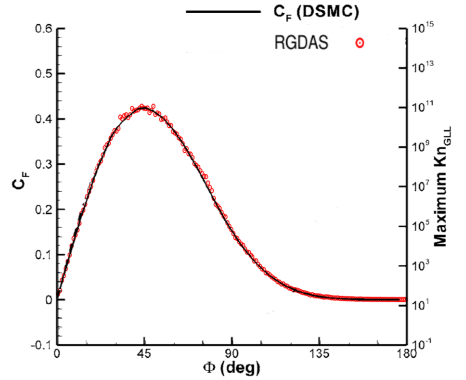

Figure 12: c_f at $Kn = 0.25$

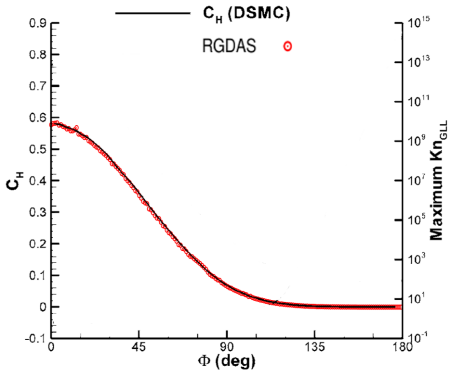

Figure 13: c_h at $Kn = 0.25$

Kn_∞	MONACO	RGDAS	diff. (%)
0.01	40.0	39.91	−0.23
0.05	8.91	8.91	0.0
0.25	2.08	2.10	−0.96

Table 3: Drag per unit length $[N/m]$

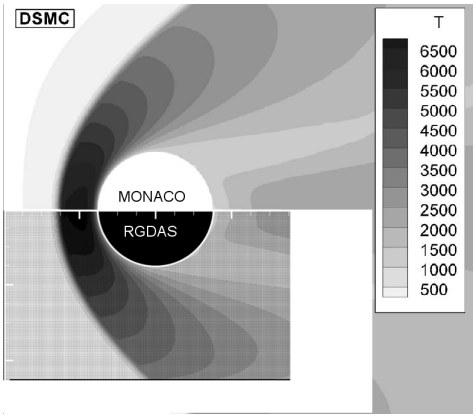

Figure 14: Temperature (K) at Kn = 0.01

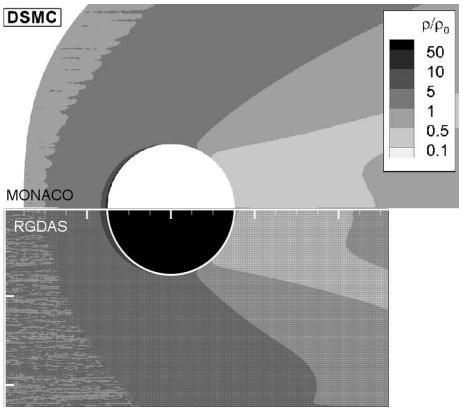

Figure 15: Density ratio ρ/ρ_∞ at Kn = 0.01

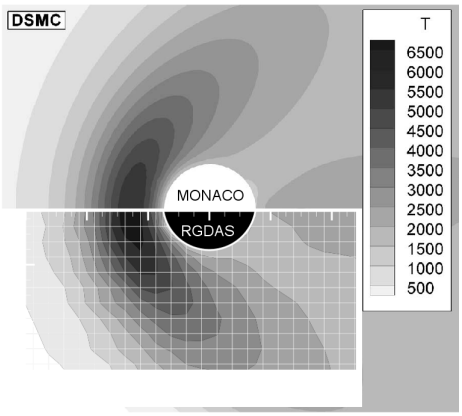

Figure 16: Temperature (K) at Kn = 0.25

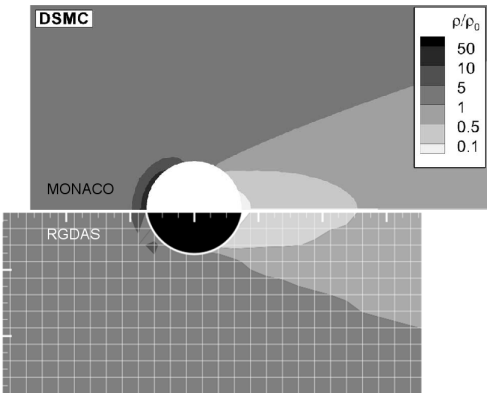

Figure 17: Density ratio ρ/ρ_∞ at Kn = 0.25

4.2. Apollo capsule

The second test case deals with a classic reentry flow configuration. A study by Moss[14] on the aerodynamic behavior of the Apollo command module is used as a reference. This source reports aerodynamic coefficients (lift, drag, pitching moment) for a range of altitudes from 200 km down to 65 km. For altitudes above 85 km, Moss used Bird's DS3V[8] code is used to calculate the coefficients, whereas the results for lower altitudes were obtained with a continuum CFD code. The reference only provides aerodynamic coefficients, thus no comparisons of flow field variables or surface distributions can be made. This test case, however is more representative of a real-world application of DSMC, since it includes high temperature gas effects such as rotational and vibrational energy excitation, as well as dissociation reactions.

For this test case the 3D version of RGDAS was used. Five species (N_2, O_2, N, O and NO) were considered to represent Earth's atmosphere. For molecular collisions, the VHS model was used. The capsule surface was modeled as diffusely reflecting with full energy accommodation. Figure 18 shows the surface mesh used to represent the capsule in the RGDAS software.

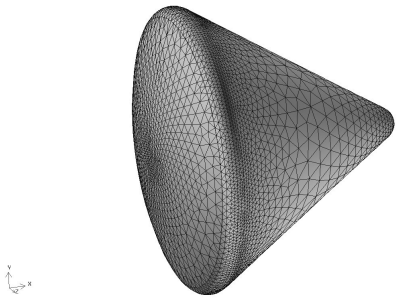

Figure 18: Surface mesh of Apollo geometry

The first set of calculations was conducted at a constant angle of attack of -25 degrees (see figure 19) and a free-stream speed of 9600 meters per second, while only varying the flight altitude. Moss's paper provides the composition of the free-stream gas mixture at the particular altitudes considered in this study. The increasing computational cost of DSMC at lower Knudsen numbers limits altitudes which can be simulated on the available hardware. In the present case, results were obtained only for altitudes between 95 and 200 km.

Figures 20, 21 and 22 respectively show the dependence of drag, lift and pitching moment coefficients

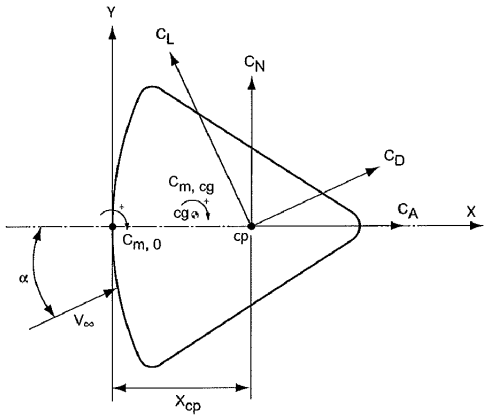

Figure 19: Nomenclature for aerodynamic coefficients in the pitch plane

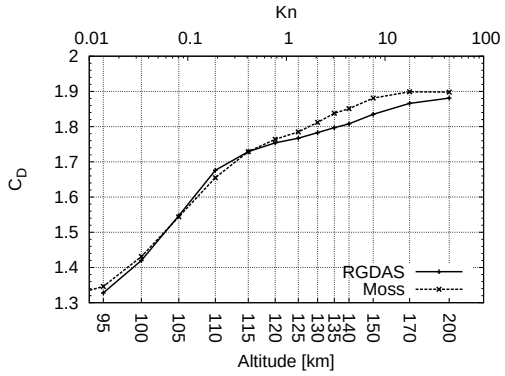

Figure 20: Drag coefficient as function of Knudsen number

on the Knudsen number (and altitude). Two curves are plotted in each diagram, the solid lines represent the results obtained with RGDAS, while the dashed lines show the reference values given by Moss. A strong dependence of aerodynamic coefficients on Knudsen number is noticeable. Looking at figure 22 one may notice that the pitching moment around the center of gravity of the capsule remains negative for all altitudes considered. This means that the capsule flying at an angle of attack of -25 degrees is in a statically unstable configuration for much of its initial reentry trajectory. Only at much lower altitudes, not covered in these plots, does the pitching moment become positive. For lower altitudes, up until 115 km, the agreement between the two data sets is quite good and the deviations do not exceed 5%. However, starting at about 120 km, there is a noticeable gap between the two sets of curves in all three plots. It is believed that these deviations come about due to differences in the VHS parameters used by RGDAS and DS3V to cal-

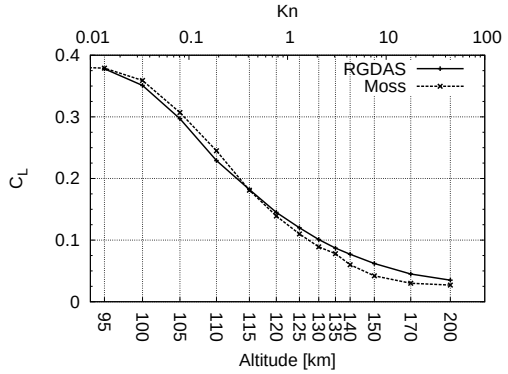

Figure 21: Lift coefficient as function of Knudsen number

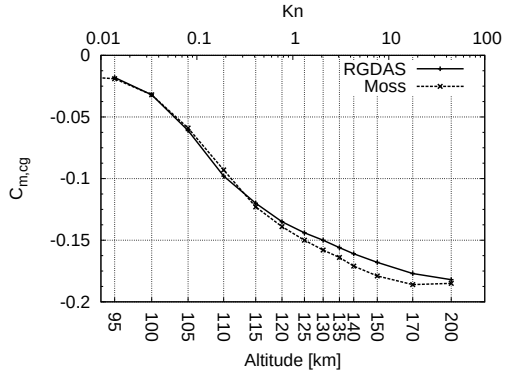

Figure 22: Pitching moment coefficient around CG as function of Knudsen number

culate the collision cross sections.

A second series of coefficients was calculated for a constant altitude of 105 km and the same free-stream velocity of 9600 meters per second as before. Now however, the angle of attack of the incoming flow was varied from -180 to 180 degrees. The results are presented in figures 23 to 25. At this altitude, the results of both RGDAS and Moss's calculations lie very close to one another. In figure 25 it can be seen that the only stable trim angles for the apollo capsule (i.e. where $C_{m,cg} = 0$ and at the same time $\partial C_{m,cg}/\partial\alpha < 0$) is at $-165°$.

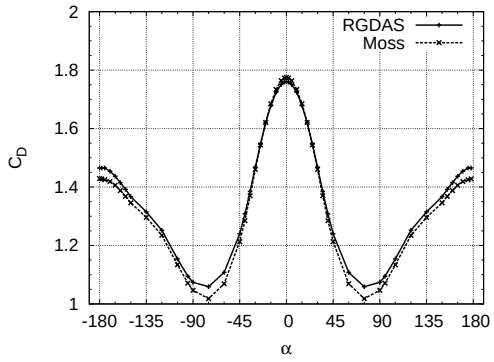

Figure 23: Drag coefficient as function of the angle of attack

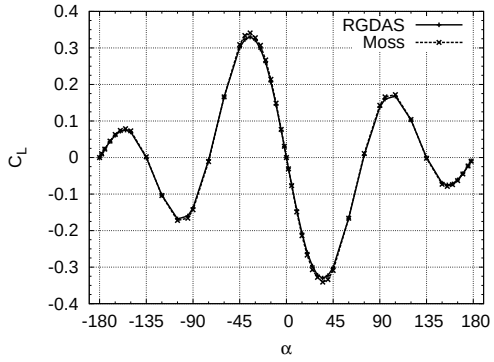

Figure 24: Lift coefficient as function of the angle of attack

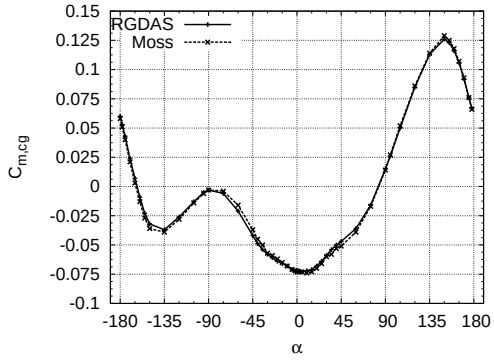

Figure 25: Pitching moment coefficient around CG as function of the angle of attack

5. Conclusion and future work

In the first year of this PhD project, work was focused on gaining insight into both the theoretical aspects of rarefied flows, as well as the numerical methods used to simulate such flows. DSMC simulations were performed on different test cases using the RGDAS software in order to gain familiarity with the method. Along the way, valuable knowlede was gained on the parameters to judge the quality of a DSMC simulation.

Work in the next year will concentrate on the models used for internal energy exchange in inelastic collisons. It is intended to find and implement improvements over the current standard Larsen-Borgnakke method, which will take into account the quantized nature of molecular internal energy states. For the purpose of studying the internal energy excitation and dissociation, a one-dimensional test case will be used: Supersonic flow of nitrogen is decelerated through a standing shock wave, causing the internal energy modes of the N_2 molecules to be excited and leading to partial dissociation of N_2. Downstream of the shock, the evolution of the translational, rotational and vibrational temperatures, as well as the fraction of atomic nitrogen will be monitored. Another configuration that will be studied with DSMC is the flow of nitrogen gas through a divergent nozzle and the subsequent expansion plume. The results from the DSMC calculations will be compared to continuum CFD calculations based on the Navier-Stokes equations. These simulations will rely on the same physical assumptions and incorporate the same multi-temperature models as the DSMC code.

Acknowledgments

The author wishes to thank Prof. M. Ivanov and his co-workers from the Institute of Theoretical and Applied Mechanics, Siberian branch of the Russian Academy of Sciences, for making the RGDAS software available.

References

[1] W. Vincenti, C. Kruger, Introduction to Physical Gas Dynamics, Wiley, New York, 1965.

[2] G. Bird, Molecular Gas Dynamics and the Direct Simulation of Gas Flows, Oxford University Press, 1994.

[3] G. LeBeau, A parallel implementation of the direct simulation monte carlo method, Computer methods in applied mechanics and engineering 174 (1999) 319–337.

[4] M. Ivanov, G. Markelov, A. Kashkovsky, S. Gimelshein, Statistical simulation of high-altitude aerodynamic problems, in: Third European Symposium on Aerothermodynamics for Space Vehicles, ESTEC, Noordwijk, The Netherlands, 1998.

[5] M. Ivanov, G. Markelov, S. Gimelshein, Statistical simulation of reactive rarefied flows: numerical approach and applications, in: 7th AIAA/ASME Joint Thermophysics and Heat Transfer Conference, 1998.

[6] S. Dietrich, I. Boyd, Parallel implementation on the ibm sp-2 of the direct simulation monte carlo method, in: 29th AlAA Thermophysics Conference, 1995.

[7] S. Dietrich, I. Boyd, Scalar and parallel optimized implementation of the direct simulation monte carlo, Journal of Computational Physics 126 (1996) 328–342.

[8] B. G.A., The ds2v/3v program suite for dsmc calculations, in: 24th International Symposium on Rarefied Gas Dynamics, 2005.

[9] K. Koura, H. Matsumoto, Variable soft sphere molecular model for inverse-power-law or lennard-jones potential, Physics of Fluids A 3(10) (1991) 2459–2465.

[10] C. Borgnakke, P. Larsen, Statistical collision model for monte carlo simulation of polyatomic gas mixture, Journal of Computational Physics 18 (1975) 405–420.

[11] I. Boyd, Chemical dynamics in extreme environments, World Scientific, 2001, Ch. 3, pp. 81–137.

[12] A. Lofthouse, I. Boyd, M. Wright, Effects of continuum breakdown on hypersonic aerothermodynamics, Physics of Fluids 19 (2007) Article 027105.

[13] G. Bird, Sophisticated dsmc, in: DSMC07 meeting, Santa Fe, 2007.

[14] J. Moss, C. Glass, F. Greene, Dsmc simulations of apollo capsule aerodynamics for hypersonic rarefied conditions, in: 9th AIAA/ASME Joint Thermophysics and Heat Transfer Conference, 2006.

Development of algorithms for multiphysics applications

Alessandro Sanna

Aeronautics and Aerospace Department, sanna@vki.ac.be

Supervisor: Herman Deconinck

Professor, Aeronautics and Aerospace Department, von Karman Institute for Fluid Dynamics, Belgium, deconinck@vki.ac.be.

Promotor: Gérard Degrez

Professor, Université Libre de Bruxelles, Belgium

Abstract

During this first year and half of my PhD I have dealt with many different topics concerning the development of algorithms for multiphysics applications. In order not to be too short and not very clear in providing explanations, I decided to bring in this article only the description of that part of my work on develop and implement the Monte Carlo Method for Radiative Heat Transfer.
The work of develop and implement the Monte Carlo Method for Radiative Heat Transfer is not straightforward. It consist of three tasks: the random number generation, the particle tracking and the solution method. Many choices can be done in order to accomplish each of these tasks; these several choices lead to different implemented solutions that can differ in performance and accuracy.

Keywords: CFD, Radiative Heat Transfer, Monte Carlo Method, Finite Volume Method, Particle Tracking, Parallel Algorithms, Discontinuous Galerkin Methods, Moving Boundary, Software Developments.

1. Introduction

Energy transfer by radiation through translucent media with high entalpy can be significant. Media can emit, absorb or scatter radiation, giving rise to a complex phenomenon of heat transfer. The importance of this phenomenon rises with high temperature. It has received incresed attention in the past fifty years and many authors have ventured in its study [1]. Some important applications are hot gases in furnaces, engine combustion chamber at high pressure and temperature, rocket propulsion, glass manufacturing, fibrous insulating layers, nuclear explosion, hypersonic shock layer, plasma generators, ablating thermal protection systems, translucent ceramics at high temperature, and heat transfer in porous regions.
Two difficulties make it challenging to study radiation in absorbng, emitting and scattering media. One is that absorption, emission, and scattering can occur at all locations within the medium. A complete solution for energy exchange requires knowing the radiation intensity, temperature, and physical properties throughout the medium. The mathematics describing the radiative field is inherently complex. A second difficulty is that spectral effects are often much more pronounced in gasses than for solid surfaces, and detailed spectrally dependent analysis may be required.
In the present report is shown the development and the implementation of the Monte Carlo Method for Radiative Transfer [1],[2],[11], that we made. This implementation allow us to deal with radiative transfer simulations with both 2D or 3D case, and structured or unstructured grids. This is to be possible through the development of algorithms able to perform the different tasks efficiently.
This article is structured in the following way. Section 2 starts explaining the physics of radiation, than it illustrates the Monte Carlo method used here to solve the radiation transport. Section 3 speaks on the algorithm employed for particle tracking. Section 4 describes how we implemented the methods. Finally in

section 5 some validation results are shown.

2. Radiative Transfer

2.1. Energy Equation

The energy balance equation for an infinitesimal element reads [1]:

$$\rho C_p \frac{DT}{D\tau} \equiv \frac{\partial T}{\partial t} + \mathbf{v} \cdot \nabla T = \frac{Dp}{D\tau} + \nabla \cdot (k \nabla T - \mathbf{q}_r) + q_h + \Phi \quad (1)$$

where ρ indicates density; C_p, specific heat under constant pressure; T, temperature; τ, time; p, pressure; k, thermal conductivity; $\mathbf{q}_r$, radiant heat flux vector; q_h, chemical heat generation rate; and Φ, viscous heat dissipation rate.
The $\nabla \cdot \mathbf{q}_r$ term in eq. (1) signifies the divergence of radiative heat flux, that is the difference between total radiation incident from all solid angles ω_i that is locally absorbed, and the locally emitted radiation.

2.2. Radiative Transport Equation (RTE)

Radiative Transport Equation (RTE) is the equation that describes the radiation intensity, $i_\lambda(\lambda, \omega_i)$, along a path in a fixed direction through an absorbing, emitting and scattering medium.
The classical form of the equation of radiative transfer is:

$$\frac{di_\lambda}{dk_\lambda} + i_\lambda(k_\lambda) = I_\lambda(K_\lambda, \omega) \quad (2)$$

An integrated form of the transfer equation is obtained by using an integrating factor. Multiplying eq. (2) by e^{k_λ} gives:

$$\frac{di_\lambda}{dk_\lambda} e^{k_\lambda} + i_\lambda(k_\lambda) e^{k_\lambda} = I_\lambda(K_\lambda, \omega) e^{k_\lambda} \quad (3)$$

Integrating over an optical thickness from $k_\lambda = 0$ to $k_\lambda(S)$ and rearranging it gives:

$$i_\lambda(k_\lambda, \omega) = i_\lambda(0, \omega) e^{-k_\lambda} + \int_0^{k_\lambda} I_\lambda(k_\lambda, \omega) e^{-(k_\lambda - k_\lambda^*)} dk_\lambda^* \quad (4)$$

where k_λ^* is a dummy optical variable of integration along S, and $i_\lambda(0, \omega)$ is the intensity in the direction of S at location where $S = 0$. Eq. (4) is the integrated form of the equation of transfer. It is physically interpreted as the intensity at optical depth k_λ, being composed of two terms. The first is the attenuated initial intensity that arrives at k_λ. The second is the intensity at k_λ resulting from emission and incoming scattering in the S direction by all thickness elements along the path from 0 to S, reduced by exponential attenuation between each location of emission and incoming scattering k_λ^* and the location k_λ.

2.3. Solution Procedures

In order to solve the RTE several methods have been developed in the last 50 years. These methods can be grouped in two types, depending if they are solving the differential or the integral form of the RTE.
Among the differential solution we can cite: the *Milne-Eddington method*, *Diffusion method*, *Taylor series expansion*, and the *Two-flux method*. But the most popular solutions are the integral ones. These can be further classified in:

- *Angular discretization about a volume element*. Like the *Multi-flux method* and the *Discrete transfer metod*.
- *Direct transfer among volume elements*. Like the *Zonal method*, the *Finite Volume, Element or Difference method*.
- *Approximate methods*. Like the *Cold medium and emission approximations*, or the *Mean beam length*.
- *Stochastic solution method*. Like the *Monte Carlo method* or the *Markov chain* method.

2.4. Monte Carlo Method

The Monte Carlo method is a stochastic method for numerical integration [6]. There is no single Monte Carlo method, instead there are many different approaches. The common pattern of all of these approaches tends to have the following steps:

1. Define a domain of possible inputs or problem space.
2. Generate N random points x_i in the problem space using a certain specified probability distribution.
3. Perform a deterministic computation of the score $f_i = f(x_i)$ for the N points.
4. Aggregate the results of the individual computations, f_i, into the final result g: $g = g(f_i)\ \forall i$.
5. According to the Central Limit Theorem, for large N g will approach the true value $\hat{g}$.

In this way we avoid to compute all the points (or basic processes) of the problem space (domain of the overall process). This would be computationally too expensive. Instead we compute only a certain number of points, randomly chosen, and relying on the central limit theorem, to ensure the consistency, we can get a good estimation of the value of the global variable that we are looking for.
These concepts are applied in the radiation transfer problem in the following way. The global or whole process are the set of radiative heat transfer phenomena inside the computational domain. Instead the basic process consists in a energy particle emitted from an atom or molecule and absorbed by another atom or molecule. Not being able to simulate, for obvious reasons, the atomic scale, one implements a discretization where the units that emit or absorb the energy particle are no longer infinitesimal size entities such as atoms or molecules, but cells of finite size. These cells can be the same used to discretize the fluid domain (like the finite volume or element cells). Obviously the consistency between finite cells and atoms scales has to worth. For each cell the problem space is the set of energy particles emitted from that cell, therefore each energy particle is a point in the Monte Carlo explanation above. Then, what Monte Carlo method does, is to trace the behavior of a randomly selected finite number of energy particles. Some authors refer to energy particles as rays or beams or virtual photons; hereafter we will use these terms interchangeably.

2.4.1. Simulation of Radiative Heat Transfer

For each cell of the computational domain a heat balance equation is written, [5]. For a gas cell we have:

$$q_{r,NET,Gas} = q_{r,IN,Gas} - q_{r,OUT,Gas} \tag{5}$$

and for a wall face:

$$q_{r,NET,Wall} = q_{r,IN,Wall} - q_{r,OUT,Wall} \tag{6}$$

Where $q_{r,NET,Gas}$ $q_{r,NET,Wall}$ mean, respectively, the net radiative heat flow for a gas cell and for a wall face.

The tricky part now is how to compute the absorbed terms of the balance equations: $q_{r,IN,Gas}$ and $q_{r,IN,Wall}$. The task of simulating radiative transfer consists of six steps, [4],[3]:

1. determine number and energy of the energy particles;
2. simulation of Gas and Wall Emission;
3. ray tracing;
4. simulation of Gas Absorption;
5. simulation of Wall Absorption and Reflection;
6. solution Method.

In the next sections we will briefly discuss each of these parts.

2.4.2. Determine number and energy of the energy particles

The first task is the computation of the energy emitted from each cell; then you'll need to assign this energy to a certain number of photons.

2.4.3. Simulation of Gas and Wall Emission

According to the explanation of the Monte Carlo method given above, in this step we have to send in random directions **d** the energy particles emitted from each cell. The direction vector **d** is computed from a set of evenly distributed random numbers, R_i: one for each dimension of the physical domain.

In order to accomplish this task we have to generate evenly distributed random number. This has to be done carefully. In fact, in order to properly use the Monte Carlo method it is necessary that the random number generator is powerful enough, that is: the numbers generated have to be able to pass sophisticated tests of randomness. This is a key point for the success of the method. For this reason we decided to implement the Mersenne-Twister random numbers generator, [7], that is the most powerful known.

2.4.4. Ray Tracing

Once the energy particle is calculated for each direction, one must trace his path within the computational domain until one of the following three things happen:

- the energy particle is absorbed into a gas cell;
- the energy particle is absorbed on a wall face;
- the energy particle disappears in another boundary.

In order to accomplish this task we develop and implement a particle tracking algorithm, this will be explained in section (3).

2.4.5. Simulation of Gas Absorption

It can be shown that integrating the absorption equation and considering some suitable assumptions, one can get the so called BEER's Law. It expresses the attenuation of radiant energy inside a volume of thickness S as:

$$I = I_0 e^{-a_\lambda S} \tag{7}$$

Here, the physical units of a_λ and S are inverse meters and meters, respectively. Their product $a_\lambda S$ becomes dimensionless, and is named absorptive distance or optical length.
Equation (7) treats the radiative energy as a continuous as it has to be in a macroscopic point of view. But with the Monte Carlo method we are no longer modeling the macroscopic phenomena because of their laws, but as a superposition of the basic microscopic processes. This procedure is called distributed approach and no longer needs the use of a continuous variable as the intensity of the radiation. But what the distributed approach has to ensure is that with an adequate number of simulated energy particles we get the behavior described by macroscopic laws. In the case of absorption we have to ensure that from the laws used to describe the individual energy particles naturally follows the Beer's law.
It can be shown that to achieve this purpose it is sufficient that the individual energy particles yield obedience to the two following postulates:

1. all radiative energy of each particle will eventually be absorbed by gas atoms or molecules at a certain location x;
2. the energy possessed by each particle remains unchanged during its flight.

This is precisely the same concept as the transfer of radiative energy by "real" photon.

2.4.6. Simulation of Wall Absorption and Reflection

In the continuous approach, when a beam impacts against a wall it happens that some of its energy is absorbed by the wall and another part remains in the beam that is reflected. Unlike in the distributed approach of Monte Carlo the impacting energy particle can be: or completely absorbed or completely reflected. In both cases all the energy possessed by the energy particle go or to the wall or to the reflected energy particle, respectively. The criterion that discriminates the two cases is the following:

$$R_r \begin{cases} \leq \varepsilon & \text{then the energy particle is absorbed;} \\ \geq \varepsilon & \text{then the energy particle is reflected.} \end{cases} \tag{8}$$

Where ε is the emissivity of the wall. If reflection happens, the energy particle is reflected with the distributed counterpart of the Lambert's cosine law.

2.4.7. Solution Method

Each time a particle is absorbed by a wall face or the gas cell we have to store the informations related to: energy possessed, cell or face that emitted it and cell or face that has absorbed it. Once for each cell or face, all particles have been traced we can compute the heat flux entering in each element. Two methods are available to do that: the energy method and the radiative energy absorption distribution (READ) method, [2]. We will briefly discuss both of them.

Energy method . In this method the energy e_0 possessed by every energy particle is the same for all cell. Therefore what change between different cells is only the number N_a of energy particles emitted. Then we have:

$$q_{r,IN} = N_a e_0 \tag{9}$$

From this equation it is clear that N_a is a function of the leaving radiative heat flux and then it is in function of the temperature. This means that the Monte Carlo procedure has to be applied for each iteration in the temperature convergence loop. Obviously this is not the best approach from a computational time consuming point of view.

READ method . In order to avoid that the Monte Carlo procedure is applied for each iteration, some authors developed the READ method. Here we developed a particular version of the READ method in which the incoming radiative heat flux is computed as:

$$q_{r,IN,i,b} = \sum_{gas} R_d(a,b) \cdot q_{r,OUT,Gas,a} + \sum_{wall} R_d(a,b) \cdot q_{r,OUT,Wall,a} \tag{10}$$

$for\ i = gas,\ wall$. Here, $R_d(a,b)$ is the fraction of radiative energy emitted from a gas or wall element a, that is absorbed by the element b. Elements a and b should not coincide.
This method relies on the fact that the magnitude of $R_d(a,b)$ depends only on the system geometry and the distribution of radiative physical properties and not on the temperature. It follows that we can perform the computation of $R_d(a,b)$ by means of Monte Carlo method just once at pre temperature iteration step.

3. Particle Tracking

3.1. General Introduction

Monte Carlo Radiative Transfer is not the only frame that need a particle tracking tool. Indeed, in many applications of computational physics, particles entities are involved. These particles can represent different physical entities, like

- bubbles
- beams
- small solid particles
- virtual entities used to define the flow field

All these entities are moving in the fluid domain in accordance with their laws. Whatever is the laws that moves the particle, the CFD code needs, for its computations, to know the cells that a particle crossed. In other words: the code need to locate the particles. Several alternative techniques have been proposed in the literature to efficiently locate particles within unstructured grids, [8],[9],[10].
Among others we can mention the use of:

- A Cartesian background grid.
- A tree structures.
- The successive neighbor searches.

In the Cartesian background grid the idea is to superimpose the irregular foreground grid on a regular background grid. The elements of the foreground mesh that cover each cell of the Cartesian mesh are stored in a linked list. Given a new particle position x_p, the cell of the Cartesian background grid is obtained from:

$$i_c = INT\left(\frac{(x_p - x_{min})}{(x_{max} - x_{min})}N_x\right) + 1$$
$$j_c = INT\left(\frac{(y_p - y_{min})}{(y_{max} - y_{min})}N_y\right) + 1$$

The main shortcoming of this approach is the inefficiency and inaccuracy that arises when meshes with large variations in element size are employed.
In order to circumvent the problem encountered by the previous method, the tree Structure Method attempts to use a hierarchy of Cartesian meshes. The shortcoming now is the additional complexity in coding.
Instead the successive Neighbor Searches Method have the following facilities.

- The idea is to exploit as a judicious guess the host element before the particle was moved.
- Then, should the particle no longer be found in that element, the immediate neighbor most likely to contain the particle is searched next.
- This procedure is repeated until the new host element is found.
- The algorithm is relatively easy to implement and fast.
- The number of neighbor-element searches required is typically small.
- This method has no problems related to mesh with large variations in element size.

The idea commonly used, to search the neighbor element that host the particle, is based on the shape functions. A possible algorithm that implements this idea follows these steps:

1. Initial conditions: start point, $\vec{P}$, direction, $\vec{d}$, spatial increment, h.
2. Determine target point T with: $\vec{T} = \vec{P} + h\vec{d}$.
3. Transform the start cell into unit space.
4. Determine if the target point lies in the same cell, if yes, double the spatial increment, h, and restart with step 2, if not proceed with step 5.
5. Determine the cell face through which the particle will leave the current cell using the transformation in unit space.
6. Given the exit face find the next cell.
7. Use the same method to determine if the target point lies within the adjacent cell, if no halve h and restart at step 2.
8. Now the particle has traveled from the initial cell to a immediate neighbor

However the neighbor search methods based on shape functions have some shortcomings:

- first of all we note that in order to find the host cell, one should goes from the physical space to the unit space, makes all the task needed to find the host cell and came back to the physical space;
- many different variants of this approach do exist for 2D case, while few robust suggestions have been proposed for 3D case;
- there is the lack of a general implementation valid for both 2D and 3D cases, and for whatever kind of cells employed;

- therefore in order to deal with every possible mesh, both 2D and 3D, one must deal with a program that implements methods for all possible cases, thus making things more complicated.

On the contrary one would like a general method which is able to deal with:

- 2D case;
- 3D case, without loosing simplicity than if 2D;
- all types of cells, treating them all equally.

A method that meets all these demands is the proposed one. This method employee only vector operations and vector properties in order to accomplish its tasks.

3.2. *Particle Tracking Algorithm*

In figure (1) is shown a typical case where to apply the particle tracking. Here we have the point $x(t)$ where particle is at time t, and the point $x(t+\Delta t)$ where the particle is at time $t + \Delta t$. The goal of the particle tracking algorithm is to find all and only the cells that are crossed by a straight line connecting point $x(t)$ and $x(t + \Delta t)$.

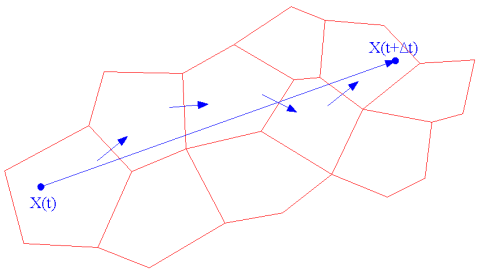

Figure 1: Particle Tracking Goal

3.3. *Ray Tracing*

The problem of tracking the trajectory of a particle within the computational domain can occur in two ways:

1. The first case is when the end point could be calculated based on the state of the fluid at the point where the particle was at time before. This is the case of a solid particle that moves according to the resultant of forces acting on it at a given instant of time. The tracing algorithm will then find which is the cell that hosts the endpoint of the particle given the coordinates.
2. The second case is when the endpoint is derived from the value of a function that integrates gradually along the route. This is the case of a energy particle (in the Monte Carlo Method for Radiative Heat Transfer) that travels in one direction and will stop (it will be absorbed) when its optical length (integral function of the path) reaches a threshold value. Starting from the cell that currently houses the particle, the tracking algorithm has to find the immediately neighboring cell where the particle is going.

For the ray tracing we are interested only in the second case, however we decided to develop a program that was general enough to be able to deal with any type of particle; not only energy particle, but also solid particle, bubble, etc. Therefore we implemented both the two possible cases of particle tracking. This has been done adapting the above particle tracking algorithm in order to have an optimized implementation for both of the two different cases.
The parallelization of the algorithm has been implemented using the double level approach. In this approach we have two programs: the slave and the master. The slave works in serial, while the master performs the parallel tasks. In our implementation the slave perform in serial all the particle tracking algorithm, while the master performs the physical implementation stuff and the inter-process communications. We found that this approach was the most general, and the most computationally efficient: since it is carrying less communications. When the slave program during the tracing of the path of a particle reaches the boundary of two processors sub-domains, it stops computing that particle and tells what has found to the master program. The master collects this information and once all particles have been traced within the different sub domains processor, it performs a communication for exchanging data between processors.
Moreover as we said the master program performs also the physical computations by the RayTracing function. In the radiation transfer the energy particles are traced by the slave cell by cell, and each time the slave tells to the master which is the new hosting cell or the face that the particle trajectory crosses. With these information the master check the following possibilities:

1. if the particle is absorbed by the new hosting cell;
2. if the particle has impacted to the wall, and in case if it is reflected or absorbed;
3. if the particle has crossed a boundary (different from wall) and then it disappears;

4. if the particle has crossed a partition boundary, and then it will have to be sent to the processor that compute the new hosting cell;
5. it continues to flight within the same processor subdomain.

We have called the master function that compute the physical stuff and act as interface with the slave as *Ray Tracing*.

4. Monte Carlo Implementation

As solution method I have formulated and used a modified READ method, for the advantages that this method appears to have compared to the Energy method. Therefore the program is divided into two broad parts. The first part is computed before the iteration loop on temperature and is involved in calculating the coefficients $R(a, b)$ of the modified READ method. The second part takes care of calculating the radiative heat flux and is computed each time the temperature field changes, that is: for each time step. Here we will briefly discuss how these two parts have been implemented.

4.1. READ method implementation

The modified READ method is implemented in the READ function that acts as the master program for the parallelization of the particle tracking. The modified READ method has ultimately the purpose of associating to each element i (cell or face) a set of other elements j's (cells and / or faces) which individually absorb a number, $N_{i,j}$, of its energy particles. Therefore we have to implement a function f_{READ} defined as:

$$f_{READ} : \; i \rightarrow \; (j_i \times N_{i,j})^d \qquad i, j, N_{i,j}, d \in \mathbb{Z} \quad (11)$$

The number of entity d that absorb the energy particles emitted by element i is never greater than the number N_i of particle that i emits. In the modified READ method N_i is equal for all elements. This fact greatly facilitates the manipulation of vectors that store the collected data. A priori, one can not know how many of these n particles are absorbed in the same processor that computes their emission and how many others are absorbed by the various other processors. We know however that with a high probability a good percentage of particles are absorbed within the sub domain of the same processor that emits them. In general it can also happen that before a particle is absorbed it has crossed the sub domains of N_p processors. Obviously a priori we do not know the N_p number of each particle of each element.
In order to have an implementation which, taking into account these comments, is as general as possible we have formulated a suitable algorithm. The implementation solution is composed of two modules: in the first one the processors compute the energy particle emitted inside their sub domains; while in the second module the processes compute the energy particle that came in their sub domains from other partition sub domains.
The first module does a loop along all the energy particles emitted from all the elements inside the sub domains. It accomplish this task calling the function *RayTracing* which can provide three different output depending on whether the particle is:

1. absorbed by a gas cell;
2. absorbed by a wall face;
3. end up in another sub domain;

or it can not provide output if the particle is dispersed. In the first two cases, the acquired information are stored in the vector R. In the third case instead the information on the particle are stored in another vector P. Only for all energy particles already absorbed, the vector R stores information about the quantities i, j_i and $N_{i,j}$. Instead for all the energy particles that go to another partition sub domain, the vector P stores information on i and on the actual optical length. Once this loop is finished, the second module can start its procedure. First of all the vector P is reorganized in a send buffer vector suitable to perform a total exchange with *MPI Alltoallv*. This reorganization is possible because based on the ID of the partition face we already know, thanks to *boundaryKnowledge* function (see below), to which process a particle as to be communicated. Let's observe that if all processors have null sendbuffer size, then all particles have been computed till their absorption or dispersion; in this case the READ function has finished its job. If this is not the case then each processor has to compute, with the *RayTracing* function, the new energy particles that came from its partition sub domain border. Again the possibility are: or that the energy particles are absorbed into this sub domain or they go to another sub domain. In the first case the acquired information are stored in a vector R_p which similar to R. Instead in the second possibility we rebuild the vector P with the new energy particles that go to another partition and we iterate the second module procedure. The loop of

this procedure will stop when all processors have null sendbuffer size. In this case then the last task will be to do a total exchange of vector R_p and then merge the received R_p with R. Therefore at the end the vector R realizes the function (11).
One of the task of *BoundaryKnowledge* function is to build a map for each processor that has as key the partition face ID and as value the ID of the other processor that share the partition face. This task is accomplished in a elegant way using the *MPI sendrecv* function to make a ring communication protocol between all the processors.

4.2. *Implementing the computation of radiative heat flux*

Once one uses the read method, the part of the calculation of the radiative heat flux becomes simple. The steps are:

1. compute the energy emitted by each element;
2. compute the energy carried by each element particle;
3. thanks to vector R build the sendbuffer with the fractions of energy absorbed by the various elements;
4. perform a total exchange of send buffer;
5. use the receive buffer to calculate the net radiative heat flux entering in each element;
6. and finally compute the net radiative heat flux in each element.

5. Monte Carlo Validation

In this section the entire algorithm is validated against some analytical solution of 1D and 1D axisymmetric problems. For the former we use the infinite slab model testcase, while for the latter we use the infinite cylinder testcase.

5.1. *Slab Testcase*

For an infinite slab there exists an analytical solution to compute the radiative heat flux. In [11] the analytical solution is derived.

It has been simulated a parallelepiped of dimensions: height ($H = 1$), depth ($D = 1$), length ($L = 10m$). The temperature distribution is linear along the height, from 0 K ($H = 0$) to 10000 K ($H = 1$). The absorption coefficient is constant throughout the volume equal to 1 m^{-1}. The discretization consists of 100 grid points along L, 100 along H, and a long D. In fact, the slab are considered stacked along H. The boundary surfaces that are coplanar with H, are considered walls that reflect the photons. The other two surfaces allow photons to escape out of the computational domain. Each cell emitted 300 particles.

In fig. (2) are shown the analytical and Monte Carlo results for this problem. We can see a good agreement between the two results. We can also observe a bit of "noise" in the Monte Carlo one, probably due to the low number of particles per cell used and the low number of cell along the height: that is slabs.

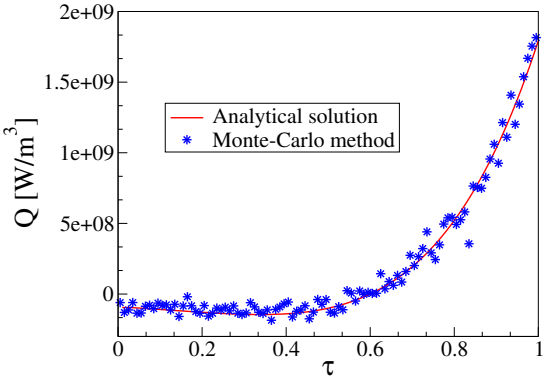

Figure 2: Slab testcase: Radiative source term (divergence of heat flux): analytical result (continuous line), Monte Carlo result (dotted line with points)

5.2. *Cylinder Testcase*

For the infinite cylinder an analytical solution is given in [12], where a general expression for axial symmetric geometry is presented.

It has been simulated the radiative heat flux along the radius of a cylinder of radius $r = 1$ and length $l = 10$. The temperature and absorption coefficient were constant along the radius and equal to 10000 K and 1 m^{-1} respectively. The reflective surfaces were those circular section. the external cylindrical surface, allowed the photons to escape out of the computational domain.
The computing grid used had the same number, N, of grid points across the radius, length and a quarter of circumference. The discretization of the circular section was performed with a radial mesh. Two simulations were performed, one with N = 8 and 16 emitted particles per cell, and the second with N = 16 and 32 particles per cell.

In Fig.s (3) and (4) are shown the results for the cylinder with a mesh of $N = 8$ and $N = 16$, respectively.

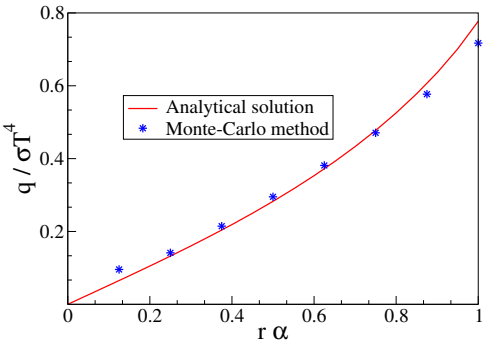

Figure 3: Cylinder testcase: Radiative Heat Souce from Monte Carlo (a) and radiative heat flux from Monte Carlo and Analytic solution (b) with $N = 8$.

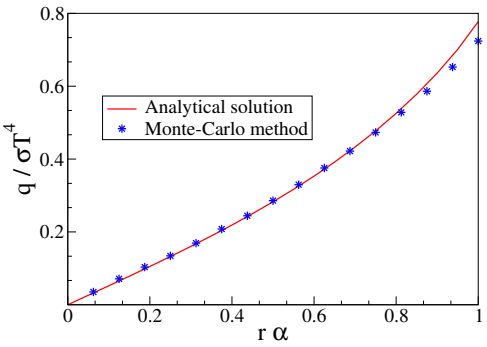

Figure 4: Cylinder testcase: Radiative Heat Souce from Monte Carlo (a) and radiative heat flux from Monte Carlo and Analytic solution (b) with $N = 16$.

We can see a good agreement between the analytical and numerical solutions. Moreover we see that increasing the number N the error between the two decreases.

6. Conclusions

In this work a new Monte Carlo algorithm for radiative heat transfer is developed and implemented. This algorithm work for every computational case: 2D and 3D domain, structured or unstructured mesh, serial or parallel computation. For each task in which the Monte Carlo method consists, a particular solution has been found. The result is an algorithm that, according to the testcases, works well and manages to approximate the analytical solution with a moderately low number of particles per cell.
Future work could be to couple this implementation with a radiation code that compute the spectral features of the gases and a CFD code that compute the temperature. After this, a validation is required in order to test the whole machine. This could be done with a simulation of the reentry of a space capsule.

Acknowledgment

I want to thank Andrea Lani, my real CFD master, to have introduced me in the CFD and programming world .

References

[1] M.F. Modest, Radiative Heat Transfer, 2003.
[2] W.J. Yang, H. Taniguchi, K. Kudo, Radiative Heat Transfer by the Monte Carlo Method, Academic Press, 1995.
[3] S. Karl, Simulation of Radiative effects in Plasma Flows, VKI Project Report 2001-18, June 2001.
[4] D. Potter, S. Karl, Validation of Aerothermo-Chemistry Models for Re-Entry Applications, AMOD Technical Note TN 3.2, 30 June 2009.
[5] Y. Wu, M.F. Modest, D.C. Haworth, A high-order photon Monte Carlo method for radiative transfer in direct numerical simulation, Journal of Computational Physics 223 (2007) 898-922.
[6] M.F. Modest, Backward Monte Carlo Simulations in Radiative Heat Transfer, Journal of Heat Transfer, February 2003, Vol. 125.
[7] M. Matsumoto, T. Nishimura, Mersenne Twister: A 623-Dimensionally Equidistributed Uniform Pseudo-Random Number Generator, ACM Transactions on Modeling and Computer Simulation, Vol. 8, No. 1, January 1998, Pages 3-30.
[8] R. Lohner, J. Ambrosiano, A Vectorized Particle Tracer for Unstructured Grids, Journal of Computational Physics, 91, 22-31 (1990).
[9] M. Widhalm, C. Bartels, J.Meyer, N. Kroll, Lagrangian Particle Tracking on Large Unstructured Three-Dimensional Meshes, AIAA 2008-472, 46th AIAA Aerospace Science Meeting and Exhibit, Reno, 2008.
[10] G. Li, M.F. Modest, An Effective Particle Tracing Scheme on Structure/Unstructured Grids in Hybrid Finite Volume/PDF Monte Carlo Methods, Journal of Computational Physics 173, 187-207 (2001).
[11] H. Lee, R.O. Buckius, Reducing scattering to nonscattering problems in radiation heat transfer, International Journal of Heat and Mass Transfer, 26(7) (1983) 1055-1062.
[12] K. Sawada, T. Sakai, M. Mitsuda, Application of Planck-Rosseland-gray model for high entalpy arc heaters, AIAA Paper, 98-0861, Jan. 1998.

Optimal error estimation techniques for Petrov-Galerkin method in linear problems

Stefano D'Angelo

Aeronautics and Aerospace Department, dangelo@vki.ac.be

Supervisor: Hermann Deconinck

Professor, Aeronautics and Aerospace Department, von Karman Institute for Fluid Dynamics, Belgium, deconinck@vki.ac.be.

Promotor: Mario Ricchiuto

Research Engineer, INRIA Bordeaux - Sud-Ouest, 351 cours de la Liberation, Bat. A29 bis, mario.ricchiuto@inria.fr.

Abstract

The current work concerns the study and the implementation of a modern algorithm for error estimation in CFD computations. This estimate involves the dealing of the adjoint argument. By solving the adjoint problem, it is possible to obtain important information about the transport of the error towards the quantity of interest. The aim is to apply for the first time this procedure into Petrov-Galerkin (PG) method. Streamline Upwind Petrov-Galerkin, stabilised Residual Distribution and bubble method are involved for the implementation. Scalar hyperbolic problems are firstly used as test cases.

Keywords: Error Estimation, adjoint problem, Petrov-Galerkin method, Residual Distribution scheme, advection-reaction problem

1. Introduction

Over the last decade, much progress has been made in the area of Error Estimation. This theory provides a way to construct error indicators for CFD computations of PDE's. These error indicators can be used to drive automatic mesh adaptation algorithms. By adapting the mesh, we optimize the mesh spacings or reduce memory usage.
In this field, the *a posteriori* error analysis is one of the most used procedures to compute numerical error indicators. The relevance and generality of this estimation has been powerfully argued in the work of Johnson and his collaborators [1]. The *a posteriori* error bounds resulting from this analysis involve the numerical residual, obtained by inserting the computed solution into the current problem equations; this residual measures the extent to which the numerical approximation to the analytical solution fails to satisfy the current problem. From this study, the *Type II a posteriori* error bounds have been defined.
Becker and Rannacher worked also on this issue and they developed the so-called weighted-residual-based, or *Type I*, *a posteriori* error estimation ([2] and [3]). Here, the error representation formula defines the error in the target functional with the numerical residual, weighted by the solution of an adjoint problem. The key ingredient is this auxiliary problem, involving the formal adjoint of the current partial differential operator. For computing this product, also this adjoint problem will have to be implemented and solved numerically. The data for the adjoint problem is a quantity of interest depending on the application. In engineering applications, this is typically a functional of the analitical solution such as a mean, point value, boundary flux. In fluid dynamics, it may be the pression at the stagnation point, the pressure-drop between inflow and outflow or the drag or lift coefficients of a body immersed into the fluid.
For solving the adjoint problem, added cost rises. However, it is paid back by important information which helps us to identify where the real source of the error comes from. An example is given by Hartmann ([4]) who shows the relevance and the advent-

ages of *Type I* indicators over the *Type II* for the adaptive mesh design for a supersonic flow past an airfoil.

Definition in continuous

Primal problem model. Let Ω be a bounded open domain R^d with boundary Γ. Given the *primal problem*

$$Lu = f \quad \text{in} \quad \Omega \qquad Bu = g \quad \text{on} \quad \Gamma \tag{1}$$

where $f \in L^2(\Omega)$ and $g \in L^2(\Gamma)$, L denotes a linear differential operator on Ω and B denotes a linear boundary operator on Γ.
To solve this problem a numerical discretization is given and an approximated solution, u_h, is sought in the place of u, by using a discrete numerical method. We consider the numerical solution as a linear combination of piecewise polynomial functions of degree p on a partition $\mathcal{T}_h$ of the domain Ω. For this reason we can write $u_h \in V_{h,p}$.

The functional $J(\cdot)$. In many problems of physical interest the quantity of interest for the current problem is an output or target functional of the solution rather the solution itself. This target functional is defined as $J(\cdot)$. Depending on the problem, it can be a different quantity, for example the drag or the lift coefficient or a point value of the solution.
This functional will be computed numerically and evaluated by the numerical solution, $J_h(u_h)$. The final purpose is to compute as good as possible this quantity, trying to estimate the order of error that the numerical approximations generate. Given a tolerance $\mathsf{TOL} > 0$, then the problem might be defined as finding $u_h \in V_{h,p}$ such that

$$|J(u) - J_h(u_h)| \leq \mathsf{TOL} \tag{2}$$

On this paper, we neglet the approximation of the functional $J_h(\cdot)$ and we simply assume to compute the exact functional by the numerical solution $J(u_h)$.

Associated adjoint problem. Mathematical theory tells us that, by the (continuous) *compatibility condition*

$$(Lu, v)_\Omega + (Bu, C^* v)_\Gamma = (u, L^* v)_\Omega + (Cu, B^* v)_\Gamma \tag{3}$$

for each operator appearing in the primal problem, L, B and C, there exists a corresponding adjoint one, L^*, B^* and C^*. By these so-called *adjoint operators*, we build the adjoint problem associated to (1)

$$L^* z = \hat{j}_\Omega \quad \text{in} \quad \Omega, \qquad B^* z = \hat{j}_\Gamma \quad \text{on} \quad \Gamma. \tag{4}$$

Terms $\hat{j}_\Omega$ and $\hat{j}_\Gamma$ on the right-hand side depend on the target quantity that we want to investigate and that, according to the theory, it is defined as follows

$$J(\omega) = (\omega, \hat{j}_\Omega)_\Omega + (C\omega, \hat{j}_\Gamma)_\Gamma \tag{5}$$

where $\hat{j}_\Omega \in L^2(\Omega)$ and $\hat{j}_\Gamma \in L^2(\Gamma)$ and C is a differential boundary operator on Γ.
The associated adjoint problem is hugely important. It provides how the information is transported towards the current quantity of interest. This property is extremely useful to derive where and how the source of the error of the target quantity is carried over the domain. The error indicator derived by this further information will be able to refine only the terms that really affect the error of the quantity of interest.

Numerical discretization

Let Ω be subdivided into shape-regular mesh $\mathcal{K} = \{\kappa\}$ consisting of elements κ. Let $\mathcal{V}_{h,p}$ be the standard finite element space of piecewise polynomials of complete degree p with C^0 continuity between elements

$$\mathcal{V}_{h,p} = \{v : v \in C^0(\Omega), v|_\kappa \in \mathcal{P}_p(\kappa), \forall \kappa \in \mathcal{K}\} \tag{6}$$

with $\mathcal{P}(\kappa)$ the space of polynomials of degree $\leq p$ defined on an element κ. Let then define a second space $\mathcal{V}^B_{h,q}$ which is the mesh dependent broken space of piecewise polynomials of complete degree q in each κ with no continuity between elements

$$\mathcal{V}^B_{h,q} = \{v : v|_\kappa \in \mathcal{P}_q(\kappa), \forall \kappa \in \mathcal{K}\} \tag{7}$$

Now, let discretize and numerically solve both problems (1) and (4) by using a *Petrov-Galerkin* (PG) method, where trial and test functions belong to $\mathcal{V}_{h,p}$ and $\mathcal{V}^B_{h,q}$, depending on the current problem.
According to (6) and (7), the boundary conditions are not included in the functional spaces and then, they are added and solved thorough the current problem. The approch with a strong formulation for the boundary conditions is hint in Appendix A.
Then following (3), the (discrete) compatibility condition holds as follows

$$\begin{gathered}(Lu_h, v_B)_\Omega + (Bu_h, C^* v_B)_\Gamma \\ = \\ (u_h, L^* v_B)_\Omega + (Cu_h, B^* v_B)_\Gamma + \sum_k (H(u_h, \boldsymbol{n}), v_B^+)_{\partial\kappa \setminus \Gamma}\end{gathered} \tag{8}$$

where $H(w_h, \boldsymbol{n})$ is the numerical flux over $\partial\kappa$, which is continuous because the $w_h \in \mathcal{V}_{h,p}$, $\boldsymbol{n}$ is the outward normal along the element boundary and v_B^+ the outward traces of v_B over $\partial\kappa$.
We can so define a bilinear operator $\mathcal{B}(\cdot,\cdot)$ as

$$\mathcal{B}(u_h, v_B) = (u_h, L^* v_B)_\Omega + (C u_h, B^* v_B)_\Gamma + \sum_k (H(u_h, \boldsymbol{n}), v_B^+)_{\partial\kappa\setminus\Gamma} \quad (9)$$

By the identity (8), we state that this operator is *adjoint consistent*. The latter property is very important as it provides that using it into the numerical adjoint problem, this will be a consistent discretization of the continuous problem.
The (discrete) primal problem is then defined as

PRIMAL PROBLEM Find $u_h \in \mathcal{V}_{h,p}$ such that

$$\mathcal{B}(u_h, v_B) = F(v_B) \qquad \forall v \in \mathcal{V}^B_{h,q} \quad (10)$$

while the corresponding adjoint problem is given by

ADJOINT PROBLEM Find $z_B \in \mathcal{V}^B_{h,q}$ such that

$$\mathcal{B}(w_h, z_B) = J(w_h) \qquad \forall w_h \in \mathcal{V}_{h,p} \quad (11)$$

As we see, both problems use the same operator $\mathcal{B}(\cdot,\cdot)$ but in the primal one, the solution $u_h \in \mathcal{V}_{h,p}$ and the test function belongs to $\mathcal{V}^B_{h,q}$, while for the adjoint problem, the solution $z_B \in \mathcal{V}^B_{h,q}$ and the test function is taken from $\mathcal{V}_{h,p}$.
Let now remember that

$$u_h = \sum_{\kappa\in\mathcal{K}} \sum_{j\in\kappa} \varphi_j u_j \quad \text{and} \quad z_B = \sum_{\kappa\in\mathcal{K}} \sum_{i\in\kappa} \Psi_i z_i$$

Gathering all the coefficients u_j, into a vector, $\boldsymbol{u} = \{u_1, u_2, \ldots, u_N\}$, let write the primal problem in the following matrix form

$$\boldsymbol{B}\,\boldsymbol{u} = \boldsymbol{F} \quad (12)$$

Then, we can prove that since the bilinear operator $\mathcal{B}(\cdot,\cdot)$ is symmetrical and adjoint consistent, the adjoint problem can be written in a matrix form as

$$\boldsymbol{B}^T\,\boldsymbol{z} = \boldsymbol{J} \quad (13)$$

where the vector $\boldsymbol{z} = \{z_1, z_2, \ldots, z_N\}$ and $\boldsymbol{B}^T$ is simply the transpose of the matrix used in the primal problem. Besides the matrix approach, we also deal with an alternative solver by using the iterative explicit method in Appendix B.

Broken space $\mathcal{V}^B_{h,q}$

A pletora of possible Broken spaces $\mathcal{V}^B_{h,q}$ are available. Herebelow let list the three Petrov-Galerkin spaces that will be taken into account for the next computations. Therefore, let remind that for a PG method, all of the broken spaces $\mathcal{V}^B_{h,q}$ can be always defined by a sum of two contributions

$$\mathcal{V}^B_{h,q} = \text{span}\{\Psi^0 + \Psi^1\}$$

where Ψ^0 is the "main" shape function of the space and Ψ^1 is a element stabilizer term.

Streamline Upwind Petrov-Galerkin method. In case of a Stremline Upwind Petrov-Galerkin (SUPG) method, the broken space $\mathcal{V}^B_{h,q}$ is the same than $\mathcal{V}_{h,p}$ with still the addition of a stabilizer term

$$\mathcal{V}^B_{h,q} = \text{span}\{\varphi_i^q + \tau_\kappa \boldsymbol{b}\cdot\nabla\varphi_i^q\} \quad (14)$$

where τ_κ is usually the size of the element κ and φ_i^q the Lagrange interpolant polynomial of the degree of freedom, i, and order q. So for this functional space $\Psi_j^0 = \varphi_j^q$ and $\Psi_j^1 = \tau_\kappa \boldsymbol{b}\cdot\nabla\varphi_j^q$.

Residual-Distribution Method. If the stabilised Residual Distribution (RD) space is chosen, the broken space, $\mathcal{V}^B_{h,q}$, is defined as

$$\begin{aligned} \mathcal{V}^B_{h,q} &= \text{span}\{\chi^\kappa \beta_i^\kappa\} && \text{for} \quad q = 1 \\ \mathcal{V}^B_{h,q} &= \text{span}\{\chi^\kappa \beta_i^\kappa + \tau_\kappa \boldsymbol{b}\cdot\nabla\varphi_i^q\} && \text{for} \quad q > 1 \end{aligned} \quad (15)$$

where $\beta_i^\kappa \in C^0$, χ^κ is 1 in κ and 0 everywhere else, while τ_κ is usually the size of the element κ and φ_i^q the Lagrange interpolant polynomial of the degree of freedom, i, and order q. So $\Psi_j^0 = \chi^\kappa\beta_j^\kappa$ and $\Psi_j^1 = 0$ or $\tau_\kappa \boldsymbol{b}\cdot\nabla\varphi_j^q$.

"Bubble" method. The "bubble" method comes out from the equivalence of the RD and SUPG method. Indeed, it takes the following broken space $\mathcal{V}^B_{h,q}$

$$\mathcal{V}^B_{h,q} = \text{span}\{\varphi_i^q + S^\kappa \alpha_i^\kappa\} \quad (16)$$

where φ_i^q the Lagrange interpolant polynomial of the degree of freedom, i, and order q, while S^κ is a bubble function null along $\partial\kappa$. In this case, it is either a linear bubble, unary in the baricentric point $\boldsymbol{x}_g$, or a cubic one, coming out from the product of the three vertex

linear functions. Finally α_i^κ is given by solving the equivalence

$$\int_\kappa \varphi_i^q + S^\kappa \alpha_i^\kappa d\boldsymbol{x} = \int_\kappa \beta_i^\kappa d\boldsymbol{x}$$

Then here $\Psi_j^0 = \varphi_j^q$ and $\Psi_j^1 = S^\kappa \alpha_i^\kappa$.

Superconvergence of Functionals

Let now examinate the convergence rates for functionals. Barth proved that functionals show a superconvergence property when the Galerkin orthogonality of the error $u - u_h$ holds with respect to the all test functions of the bilinear operator ([5]). So even if the convergence rates for the global error measures might be not affected, the convergence rates for the functionals can be quite different with or without this orthogonality property. Barth showed in fact that for finite volumes with reconstruction, because of this orthogonality loss the superconvergence for the functionals is not attained.

In the setting of linear advection problems, this superconvergence theory for functionals has been treated as well by Süli and Houston for streamline diffusion discretization ([6]). For problems with sufficiently smooth primal and adjoint solutions, the basic theoretical result states that if the primal method converges at the rate $O(h^{p+1/2})$ then functionals converge at the rate $O(h^{2p+1})$.

This theory comes from by using the classic definition of streamline diffusion method where the stabilizer term appears in the bilinear operator and not in the projected functional space, $\mathcal{V}_{h,q}^B$ like in the current approach. Both being the same method simply rewritten in two different ways, the same convergence ratio is expected. So now, to prove it, let use this alternative approach with the SUPG as broken space and numerically verify the convergence rate of functionals.

The simple channel case is then taken, where the advection is unary and parallel to the walls and with g=sin$^2(y)$ and $\hat{j}_\Gamma$=sin$^2(y)$. Table 1 tabulates values of the global solution error and the error in the funtional using a sequence of four nested meshes. The numerical results using p=1 and p=2 approximation confirm the theoretically order convergence in the global L^2 error norm and in the weighted outflow functional. The superconvergence of functionals, here verified for SUPG method, will later have to be done also for the RD and bubble broken space.

Method	dofs	p	$\|u - u_h\|_{L^2}$		$\|J(u) - J(u_h)\|$	
SUPG	524	1	.134e-1		.120e-2	
SUPG	2013	1	.256e-2	(2.39)	.161e-3	(2.90)
SUPG	7841	1	.490e-3	(2.38)	.203e-4	(2.99)
SUPG	31233	1	.104e-3	(2.24)	.253e-5	(3.00)
SUPG	2013	2	.829e-3		.190e-2	
SUPG	7889	2	.882e-4	(3.23)	.243e-3	(4.64)
SUPG	31041	2	.109e-4	(3.02)	.301e-4	(4.84)
SUPG	124289	2	.148e-5	(2.89)	.370e-5	(4.91)

Table 1: Convergence rates of SUPG method for channel problem. Tabulated data for the global $L^2(\Omega)$ error and error in the outflow flux functional.

Error Reppresentation Formula

Let consider the primal numerical problem (10) and that holds the *Galerkin orthogonality condition*

$$\mathcal{B}(u - u_h, v_B) = 0 \qquad \forall v \in \mathcal{V}_{h,p} \tag{17}$$

Let then notice that by the *compatibility condition* (3), using infinite-dimentional trial and test space, the adjoint problem can be redefined as

$$\mathcal{B}(w, z) = J(w) \qquad \forall w \in \mathcal{V}$$

So, an exact error reppresentation formula for a given functional $J(\cdot)$ results from the following steps, where π_B denotes any suitable projection operator (i.e. interpolation, L_2 projection) into $\mathcal{V}_{h,p}^B$,

$$\begin{aligned} J(u) - J(u_h) &= J(u - u_h) \\ &= \mathcal{B}(u - u_h, z) \\ &= \mathcal{B}(u - u_h, z - \pi_B z) \\ &= \mathcal{B}(u, z - \pi_B z) - \mathcal{B}(u_h, z - \pi_B z) \\ &= F(z - \pi_B z) - \mathcal{B}(u_h, z - \pi_B z) \end{aligned} \tag{18}$$

so in summary

$$J(u) - J(u_h) = F(z - \pi_B z) - \mathcal{B}(u_h, z - \pi_B z) \tag{19}$$

where no dependence on the exact solution u appears. Comptutationally, this error representation formula is not suitable for obtaing computable *a posteriori* error estimation unless the function $z - \pi_B z$ is unknown, since $z \in \mathcal{V}^B$ is a solution of the infinite-dimensional adjoint problem. So z has to be computed by the discrete adjoint problem (11). Since the (8), we can solve the adjoint problem by using the same bilinear operator, $\mathcal{B}(w_h, z)$, used for the primal problem. However, due to the Galerkin orthogonality, the adjoint numerical problem must be approximated in a larger space

of functions than that utilized in the primal numerical problem. Here, this is achieved by solving the adjoint problem using a polynomial space that is one polynomial degree higher than the primal numerical problem, i.e. if $v_B \in \mathcal{V}^B_{h,q}$ then $z \approx z_{B'} \in \mathcal{V}^B_{h,q+1}$.
Besides, the error reppresentation formula written in the global abstract form of the (19) does not indicate which elements in the mesh should be refined to reduce the measured error in a functional. So, now the goal is to estimate the *local* contribution of each element in the mesh to the functional error. This local cell contribution will then be used as an error indicator for choosing which elements to refine or coarsen in the adaptive mesh procedure. By applying the *triangle inequality*, indeed, we have

$$\begin{aligned}\left|J(u) - J(u_h)\right| &= \left|F(z - \pi_B z) - \mathcal{B}(u_h, z - \pi_B z)\right| \\ &= \Big|\sum_{\kappa\in\mathcal{K}} F_\kappa(z - \pi_B z) - \mathcal{B}_\kappa(u_h, z - \pi_B z)\Big| \\ &\le \sum_{\kappa\in\mathcal{K}} \left|F_\kappa(z - \pi_B z) - \mathcal{B}_\kappa(u_h, z - \pi_B z)\right|\end{aligned} \tag{20}$$

This direct estimate let us define for each partition element κ the *adaptation element indicator* η_κ

$$|\eta_\kappa| \equiv \left|\mathcal{R}_\kappa(u_h, z - \pi z)\right| \tag{21}$$

with

$$\mathcal{R}_\kappa(u, v) = (R(u), v)_\kappa + (r(u), C^* v)_{\partial\kappa\cap\Gamma}$$

where $R(u) = f - Lu$ and $r(u) = g - Bu$. Such that the simplest adaptation stopping criteria will be

$$|J(u) - J(u_h)| = \Big|\sum_\kappa \eta_\kappa\Big|$$

and according to a particular adaptive meshing strategy the element will be refine or coarse depening on the corresponding η_κ.

Projection Operation π_B. As seen, the unkonwn function $z - \pi_B z$ is computed by approximating $z \approx z_{B'} \in \mathcal{V}^B_{h,q+1}$, such that seeking the adjoint solution in a larger space than the trial one used for the primal problem and later it is projected onto $\mathcal{V}^B_{h,q}$. Let

$$z = \sum_i^N \Psi_i z_i \qquad \text{and} \qquad \pi z = \sum_i^{N^\pi} \Psi^\pi_i \pi z_i$$

Because $\Psi_i(\boldsymbol{x}_i) = 1$ but $\Psi_i(\boldsymbol{x}_j) \neq 0$, then both $z(\boldsymbol{x}_i) \neq z_i$ and $\pi z(\boldsymbol{x}_i) \neq \pi z_i$. So, to get the coefficients πz_i we need to solve the following identity

$$\int_\Omega \Psi^\pi_{i_B} z \, d\boldsymbol{x} = \int_\Omega \Psi^\pi_{i_B} \pi z \, d\boldsymbol{x} \tag{22}$$

According to the z and πz definitions and because of the local element support of the shape functions, we end up to a local element linear system as follows

$$\boldsymbol{P}_\kappa \, \boldsymbol{z}_\kappa = \boldsymbol{M}_\kappa \, \pi\boldsymbol{z}_\kappa \tag{23}$$

where the pedex κ means by the current κ-element and

$$\boldsymbol{M}_\kappa = \int_\kappa \Psi^\pi_i \Psi^\pi_j, \; \boldsymbol{P}_\kappa = \int_\kappa \Psi^\pi_i \Psi_j, \qquad \boldsymbol{z}_\kappa = z^\kappa_i, \; \pi\boldsymbol{z}_\kappa = \pi z^\kappa_i$$

so finally,

$$\pi\boldsymbol{z}_\kappa = \boldsymbol{M}^{-1}_\kappa (\boldsymbol{P}_\kappa \, \boldsymbol{z}_\kappa)$$

The projected solution πz is then computed and hence, we can obtain the local error indicator defined in (21).

Conclusions

Among different types of error representation formula, we interested in Type I error indicator. Unlike Type II error bounds where the only local residual is taken into account, Type I involves also the solution of the associated adjoint problem. By it, we are able to obtain further information concerning the trasport of the error of computing the quantity of interest.
For the first time, we want to develop this error analysis applied a Petrov-Galerkin numerical discretization by using methods like Streamline Upwind PG, stabilised Residual Distribution and bubble method.
In the current PG discretization, the asymmetry of both function spaces, $\mathcal{V}_{h,p}$ and $\mathcal{V}^B_{h,q}$, is kept into their own definitions, so without affecting the bilinear operator terms. This and the (discrete) compatibility condition let us define a unique adjoint consistent $\mathcal{B}(\cdot,\cdot)$ as in the Galerkin form.
By now, we are implementing this error estimation theory on a code. We start by simple scalar first-order hyperbolic problem (using for the primal solution both p=1 and p=2) to pass later to more complicated problems like the 2D compressible Euler equations.

Appendix A. Strong boundary conditions

Strong boundary conditions are realized by considering an appropriate function (sub)space $\mathcal{V}_{h,p,0} \subset \mathcal{V}_{h,p}$ (or $\mathcal{V}_{B,q,0} \subset \mathcal{V}_{B,q}$) which incorportates directly the conditions on the boundary Γ. Then, the function spaces to search the primal and adjoint solutions that

also include homogenous boundary conditions are, respectively,

$$\begin{aligned}\mathcal{V}_{h,p,0} &= \{v : v \in C^0(\Omega), v|_\kappa \in \mathcal{P}_p(\kappa), \forall \kappa \in \mathcal{K},\ Bv = 0 \text{ on } \Gamma\} \\ \mathcal{V}^B_{h,q,0} &= \{v : v|_\kappa \in \mathcal{P}_q(\kappa), \forall \kappa \in \mathcal{K},\ B^* v = 0 \text{ on } \Gamma\}\end{aligned} \tag{A.1}$$

and so the corresponding bilinear operator is given by

$$\mathcal{B}_0(u_{h,0}, v_B) = (u_{h,0}, L^* v_B)_\Omega + \sum_k (H(u_{h,0}, \boldsymbol{n}), v_B^+)_{\partial\kappa\setminus\Gamma}$$

For the realization of the inhomogeneous inflow boundary conditions, assume that $u_h = u_{h,0} + u_g$ with $u_g \in \mathcal{V}_{h,p}$ and such that $Bu_h = g$ on Γ; since $Bu_{h,0}\big|_\Gamma = 0$, by definition, then $Bu_g = g$ on Γ. The same approch is taken for $z_B = z_{B,0} + z_{\hat{J}_\Gamma}$, with $z_{\hat{J}_\Gamma} \in \mathcal{V}_{h,q}$ and where $B^* z_B = \hat{J}_\Gamma$ and $B^* z_{B,0} = 0$ on Γ such that $B^* z_{\hat{J}_\Gamma} = \hat{J}_\Gamma$ on Γ.

Appendix B. Iterative explicit Method

Let remember the bilinear operator definition

$$\begin{aligned}\mathcal{B}(u_h, v_B) = (u_h, L^* v_B)_\Omega + (Cu_h, B^* v_B)_\Gamma \\ + \sum_k (H(u_h, \boldsymbol{n}), v_B^+)_{\partial\kappa\setminus\Gamma}\end{aligned}$$

and the definitions of both solutions

$$u_h = \sum_{\kappa\in\mathcal{K}} \sum_{j\in\kappa} \varphi_j u_j \quad \text{and} \quad z_B = \sum_{\kappa\in\mathcal{K}} \sum_{i\in\kappa} \Psi_i z_i$$

Hence, we could solve both problems by computing the coefficients u_i and z_j througth the explicit iterative method

$$\begin{aligned}u_i^{n+1} &= u_i^n - \omega \Phi_i^u \qquad \text{with} \qquad \Phi_i^u = \mathcal{B}(u_h, \Psi_i) - F(\Psi_i) \\ z_j^{n+1} &= z_j^n - \omega \Phi_j^z \qquad \text{with} \qquad \Phi_j^z = \mathcal{B}(w_j, z_B) - J(w_j)\end{aligned} \tag{B.1}$$

where $\Psi_i \in \mathcal{V}_{h,p}$ and $w_j \in \mathcal{V}_{h,q}$ and u_i^0 and z_j^0 are given initial solutions.

References

[1] P. H. K. Eriksson, D. Estep, C. Johnson, Introduction to adaptive methods for different equations, Acta Numerica (1995) 105–158.

[2] R. Becker, R. Rannacher, A feed-back approach to error control in finite element methods: basis analysis and examples, Journal Numerical Mathematics 4 (1996) 237–264.

[3] R. Becker, R. Rannacher, An optimal control approach to a-posteriori error estimation in finite element methods, Acta Numerica 10 (2001) 1–102.

[4] R. Hartmann, Adaptive finite element methods for the compressible euler equations, Ph.D. thesis, Universität Heidelberg (2002).

[5] T. Barth, *A Posteriori* error estimation and mesh adaptivity for finite volume and finite element methods, Tech. rep., NASA Ames Research Center (2002).

[6] P. H. E. Süli, Adaptive Finite Element Approximation of Hyperbolic Problems, Barth & Deconinck, 2002.

High–order RDS and p-multigrid solution algorithms for compressible flow

Martin Vymazal

Aeronautics and Aerospace Department, martin.vymazal@vki.ac.be

Supervisor: Herman Deconinck

Professor, Aeronautics and Aerospace Department, von Karman Institute for Fluid Dynamics, Belgium, deconinck@vki.ac.be.

Co-supervisor: Tiago Quintino

Research engineer, Aeronautics and Aerospace Department, von Karman Institute for Fluid Dynamics, Belgium, quintino@vki.ac.be.

Promotor: Chris Lacor

Professor, Department of Mechanical Engineering, Faculty of Applied Sciences, Vrije Universiteit Brussel, Chris.Lacor@vub.ac.be

Abstract

Residual distribution schemes are discussed in the context of higher order spatial discretization for hyperbolic conservation laws. The discrete solution is approximated by a finite element space based on triangular Lagrangian P_k elements. A natural subtriangulation of these elements allows the reuse of simple distribution formula previously developed for linear P_1 triangles. Curved elements with piecewise quadratic and cubic approximation of the boundaries of the domain are considered.

In the second part, a new variant of RD scheme is proposed. This particular formulation avoids the sub–triangulation procedure.

Keywords: residual distribution, multidimensional upwind, high order, curvilinear geometry

1. Introduction

The present work follows a Residual Distribution approach (1; 2; 3), which is close to continuous finite element methods, but allows the use of a maximum principle to construct nonlinear monotonicity preserving and truely multidimensional stabilizations. In previous papers (4) we have exploited the close relation with continuous finite element discretizations to present a class of higher order residual distribution methods defined on P_k Lagrangian triangular finite elements. Here we focus on the use of curved elements to allow for a higher order representation of the boundaries of the domain, using sub- or isoparametric transformation from physical space to a Cartesian parent element.

2. Notations

We consider the steady state solution of a conservation law on a two–dimensional spatial domain Ω:

$$\frac{\partial \boldsymbol{u}}{\partial t} + \nabla \cdot \boldsymbol{\mathcal{F}} = 0 \quad \forall (x, y) \in \Omega \subset \mathbb{R}^2, \quad \forall t \geq 0, \quad (1)$$

where $\boldsymbol{u}$ is the vector of conserved variables and $\boldsymbol{\mathcal{F}}$ is the inviscid flux vector, $\boldsymbol{\mathcal{F}}(\boldsymbol{u}) = (\mathbf{f}(\boldsymbol{u}), \mathbf{g}(\boldsymbol{u}))$. We denote by $\mathcal{T}_{h,k}$ a triangulation of the domain Ω, whereby each triangular element T of the triangulation $\mathcal{T}_{h,k}$ is a Lagrangian P_k finite element equipped with $K = \frac{(k+1)(k+2)}{2}$ degrees of freedom.

In the simplest case the geometry of the P_k triangle is considered to be linear, defined by its three corner nodes. Hence, the intermediate nodes on the boundary of the element are all located on the straight edges and therefore the boundary of the domain Ω is approximated by a polygone. Such a discretization will be denoted as a P_1P_k discretization (P_1 for geometry and P_k for the solution).

We work with elements whose edges are described by second- and third- order polynomials. Elements with quadratic geometry will be denoted as P_2P_k elements (P_2 for geometry and P_k for the solution). P_2P_2 elements are called isoparametric, while P_2P_k with $k > 2$ are called subparametric elements. The notation for P_3 elements is analogous.

The geometry of the curvilinear P_2 (P_3) element is transformed to a parent element in ξ–η space. In our

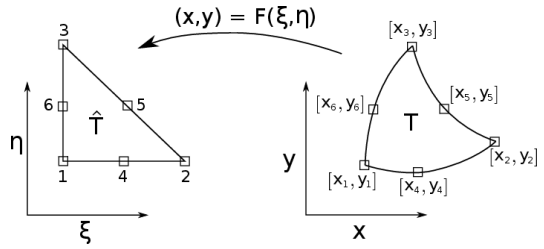

Figure 1: Transformation of triangle geometry from physical to reference space using Lagrange shape functions

case, we define $\mathbf{F}(\xi, \eta)$ from figure (1) as isoparametric mapping

$$\begin{bmatrix} x(\xi,\eta) \\ y(\xi,\eta) \end{bmatrix} = \sum_{i=1}^{N} \varphi_i^{h,k}(\xi,\eta) \cdot \begin{bmatrix} x_i \\ y_i \end{bmatrix} \tag{2}$$

where N is the number of degrees of freedom of P_2 or P_3 triangle, respectively. The number k refers to the order of shape functions φ_i and x_i, y_i denote the nodal coordinates of the triangle.

3. Residual Distribution method

For any triangulation $\mathcal{T}^{h,k}$ the cell residual for a given triangle is defined as the integral over the triangle of the spatial operator:

$$\begin{aligned} \phi^T &= \int_T \nabla \mathcal{F}(u^{h,k})\, d\Omega = \oint_{\partial T} \mathcal{F}(u^{h,k}) \cdot \vec{n}\, dl \\ &= \sum_{s=0}^{N_s} \int_{T_s} \vec{a}(u^{h,k}) \cdot \nabla u^{h,k}\, dx\, dy \\ &\quad (N_s \ldots \text{number of sub–elements}) \end{aligned} \tag{3}$$

where we have used the expression for the Jacobian of the flux $\mathcal{F}(u)$ in (1),

$$\vec{a}(u) = \frac{\partial \mathcal{F}(u)}{\partial u} = \left(\frac{\partial f_1(u)}{\partial u}, \frac{\partial f_2(u)}{\partial u} \right) \tag{4}$$

We can also construct the residual over each P_1 sub-element of $\mathcal{T}^{h,k}$

$$\phi^{T_s} = \oint_{\partial T_s} \mathcal{F}(u^{h,k}) \cdot \vec{n}\, dl \tag{5a}$$

$$= \int_{T_s} \vec{a}(u^{h,k}) \cdot \nabla u^{h,k}\, dx\, dy \equiv \vec{a}^* \cdot \int_{T_s} \nabla u^{h,k}\, dx\, dy \tag{5b}$$

with $\vec{a}^*$ a properly defined local average of $\vec{a}(u)$ over the sub-triangle such that conservation is preserved (5). The existence of such local average for general nonlinear conservation law is not guaranteed, but in case of the conservation law (1) applied to the Euler equations considered in this work, a conservative linearisation is possible under the assumption that the vector of Roe variables changes linearly in each cell.

The basic idea of the residual distribution (RD) method consists of distributing fractions of this cell residual to the three nodes of the element T. The fraction sent to node $i \in T$ is denoted ϕ_i and we require

$$\sum_{i \in T} \phi_i = \phi^T \tag{6}$$

This requirement can be written in terms of *distribution coefficients* β_i which for consistency sum to unity

$$\sum_{i \in T} \beta_i = 1, \qquad \beta_i = \frac{\phi_i}{\phi^T} \tag{7}$$

After assembling all contributions in the nodes, the nodal equation for node i reads, with $\mathcal{D}_i$ the set of all triangles that share node i:

$$\sum_{T \in \mathcal{D}_i} \phi_i = 0 \tag{8}$$

Since the distribution is restricted to the nodes of the triangle itself, the stencil of the scheme remains compact. This equation can be solved by embedding in a pseudo–time iteration, i.e. by finding a steady state solution of

$$|S_i| \frac{du_i}{d\tau} + \sum_{T \in \mathcal{D}_i} \phi_i^T = 0, \tag{9}$$

where $|S_i|$ is the area of median dual cell.

3.1. Residual Distribution schemes on P_1 elements

For a given P_1 (both solution and geometry) triangle we consider the set of normal vectors $\{\vec{n}_j\}_{j \in T}$, defined by the inward normals to the edges of T facing each node $j \in T$ (see figure 2 left). The norm of $\vec{n}_i$

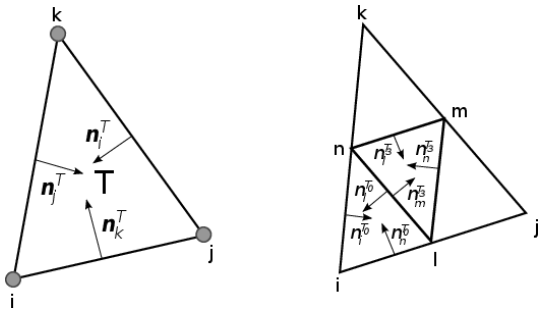

Figure 2: Definition of the normal vectors $\vec{n}_i$ in P_1 and P_2 elements

is equal to the length of the edge. Let us define the upwind parameter

$$k_j = \frac{1}{2}\vec{a}^* \cdot \vec{n}_j \quad \text{implying} \quad \sum_{i \in T_s} k_i = 0 \tag{10}$$

In this case, using a conservative linearisation (eq. 5b, 10), we can express the cell residual as follows:

$$\phi^T = \oint_{\partial T} \mathcal{F}(u^{h,1}) \cdot \vec{n}\, dl = \int_T \nabla \mathcal{F}(u^{h,1})\, d\Omega = \sum_{i \in T} k_i u_i \tag{11}$$

When all contributions for a given node are assembled, we end up with the following system of nodal equations, similar to equation (9), to be solved using explicit or implicit pseudo-time iterations. For example, using forward Euler method, we get:

$$|S_i| \frac{u_i^{n+1} - u_i^n}{\Delta\tau} + \sum_{T_s,\, i \in T_s} \phi_{i,n}^{T_s} = 0 \tag{12}$$

Many distribution schemes (defining the split residuals ϕ_i) for P_1 elements have been developed in the past (4; 6; 7). A particular class satisfies a multidimensional upwinding property (MU). Such distributions satisfy the requirement that a node in a triangle does not receive a contribution if its opposed face is an outflow face. The condition is easily imposed by requiring $\phi_i = 0$ whenever $k_i < 0$. Within this work, we limited ourselves to the use of the LDA (Low Diffusion A) scheme. Denoting by k_i^+ and k_i^- the positive and negative part of the upwind parameter, $k^\pm = \frac{k \pm |k|}{2}$, the distribution coefficients of the LDA scheme can be written as

$$\beta_i^{LDA} = \frac{k_i^+}{\sum_{m=1}^3 k_m^+} \tag{13}$$

This scheme is of order $O(k+1)$ (k being the order of interpolating polynomial), but not strictly monotone. We refer the reader interested in detailed description of the LDA scheme to other literature (1; 8; 4; 6; 9).

3.2. Residual distribution schemes on P_1P_k elements

Consider now the extension of multidimensional upwind (MU) schemes to high order P_1P_k elements. We will assume that the inward normals $\vec{n}_j$'s are defined on the local P_1 sub-elements $T_s \in T$, as shown on figure 2 (right) for $k = 2$. Note that if we consider a P_1P_k element (P_k element for the solution but only P_1 triangles for the geometry, defined by the 3 corner nodes), the inward normals of the sub-elements can be deduced easily from the ones of the parent element by a simple rescaling. We compute the residual on each sub-element:

$$\phi^{T_s} = \int_{T_s} \nabla \mathcal{F}(u^{h,k})\, d\Omega = \oint_{\partial T_s} \mathcal{F}(u^{h,k}) \cdot \hat{n}\, dl \tag{14}$$

Then, this residual is distributed to the 3 nodes of the sub-element, using the LDA distribution scheme (13) developed for P_1 triangles:

$$\phi_i^{T_s,LDA} = \beta_i \phi^{T_s} \tag{15}$$

The linearization used to compute the parameters k_i can be based on any linearized state over the sub-triangle, without affecting accuracy nor conservation.

Remark. *This is not the only strategy to achieve residual distribution schemes on P_k elements. In particular, we refer to Lax Friedrichs distribution schemes of Abgrall and collaborators (10), (11). In this case the residual is computed on the complete P_k element and then distributed to the N nodes of the element without making use of a sub-triangulation.*

3.3. Curvilinear P_2P_k and P_3P_k elements

We consider elements where the geometry is either piecewise quadratic or cubic. The geometry and numerical solution can be discretized independently so in general the solution can have any order k. However, we focus on isoparametric (P_2P_2 or P_3P_3) high–order elements.

To ensure conservation of fluxes, we compute the sub-element residual from equation (14) as a contour integral:

$$\phi^{T_s} = \oint_{\partial T_s} \mathcal{F}(u^{h,k}) \cdot \vec{n}\, dl \tag{16}$$

The boundary ∂T_s is described by transformation (2). For every face on ∂T_s, this transformation is a function of only one parameter ζ:

$$\begin{aligned} x &= x(\zeta) \\ y &= y(\zeta) \end{aligned} \tag{17}$$

We integrate numerical the fluxes of (16) using Gauss quadrature: 3 points per face f of the sub–element for P_2 and 5 points for P_3:

$$\oint_f \mathcal{F}(u^{h,k}) \cdot \vec{n}\, dl \simeq \sum_{q=1}^{N} w_q [\mathcal{F}(u_q) \cdot \vec{n}_q] J_q, \qquad (18)$$

$$J_q = \sqrt{\dot{x}^2(\zeta_q) + \dot{y}^2(\zeta_q)} \qquad (19)$$

where J_q is the Jacobian of transformation (17) at quadrature point q. We use the transformation also to compute the normal $\vec{n}_q$.

The integral over f in equation (18) is approximated:

- by three-point Gauss quadrature for each face of P_1P_1 triangle
- by the same quadrature for each face of each *sub–triangle* in the case of P_1P_2 and P_2P_2 elements
- by five–point Gauss quadrature on each sub–face of the P_3P_3 element

The quadrature nodes and weights on the biunit interval are given in table 1.

	Quadrature points	*Weights*
P_1P_1, $P_{1(2)}P_2$	0.0	$\frac{8}{9}$
	$\pm\sqrt{\frac{3}{5}}$	$\frac{5}{9}$
P_3P_3	0.0	0.5688888889
	±0.5384693101	0.4786286705
	±0.9061798459	0.2369268850

Table 1: Gauss quadrature used to approximate the residuals $\phi^{T,in}$.

3.4. Subsonic flow around a cylinder

We present results for a test case with stagnation point, namely the flow around a circular cylinder at $M_\infty = 0.38$. We consider four O–meshes with 16×5 (M1), 32×9 (M2), 64×17 (M3) and 128×33 (M4) points as described in (12). The first number indicates the number of nodes in the circular direction of the mesh, the second number refers to the number of nodes in the radial direction (figure 3). The radii of the circles in each mesh follow a geometric series

$$r_j = r_0 \left(1 + \frac{2\pi}{128} \sum_{k=0}^{j-1} \alpha^k\right),\ j = 1, 2, \ldots 32, \qquad (20)$$

where $\alpha = 1.1648336$ and $r_0 = 0.5$ is the radius of the cylinder. The farfield boundary is located at 20 diameters from the center. To have the same number of degrees of freedom and make a fair comparison between the P_1P_1 and P_2P_2 schemes, we create a P_1 sub-triangulation of each P_2 triangle. The P_3P_3 meshes were created independently such that the number of *elements* is equal for P_1P_2, P_2P_2 and P_3P_3 meshes. We plot the P_1 solutions on all four meshes

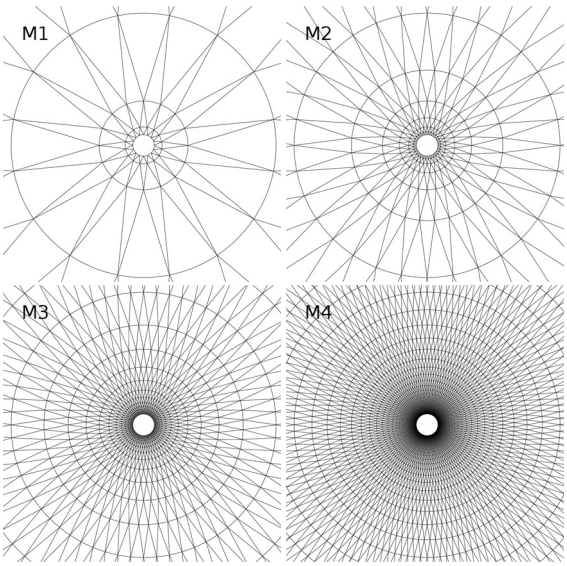

Figure 3: 16×5, 32×9, 64×17 and 128×33 meshes for subsonic cylinder test case.

(figure 4). Higher–order solution is shown in figure 5 for M2 and M3. Figure 6 presents the pressure coefficient on the cylinder wall and the entropy deviation on mesh M1. We measure the rate of convergence again by computing the relative decrease of the L_2 norm of entropy error Σ as the mesh is refined. The measured order is reported in figure 7. We did not include the entropy error on M1 in the computation of the convergence order of P_1P_2 discretization, since this error is very large (all values are listed table 2). As a result, the convergence rate measured on all four meshes seems to be very high due to rapid decrease of the entropy error as the element size becomes small compared to the curvature of the cylinder.

4. Residual distribution schemes with variable distribution coefficient

We consider a linear differential problem

$$Lu = f,$$

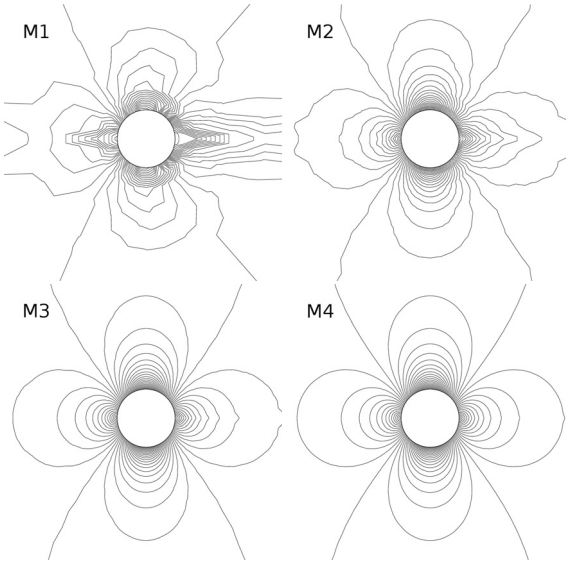

Figure 4: Mach isolines plotted for Ma $\in \langle 0, 1\rangle$, $\Delta Ma = 0.025$ on mesh with P_1P_1 elements.

		P_1P_1	P_1P_2
Mesh	NDOF	$\|\Sigma\|_{L_2}$	$\|\Sigma\|_{L_2}$
M1	288	4.87E -02	6.03E-02
M2	1088	7.64E -03	1.78E-03
M3	4224	1.13E -03	1.57E-04
M4	16640	1.78E -04	2.04E-05
Order		*1.99*	*3.05*

		P_2P_2	P_3P_3
Mesh	NDOF	$\|\Sigma\|_{L_2}$	$\|\Sigma\|_{L_2}$
M1	624	1.00E-02	1.46E-03
M2	2400	1.78E-03	5.62E-05
M3	9408	1.27E-04	5.35E-06
M4	37248	2.76E-05	5.33E-07
Order		*2.98*	*3.84*

Table 2: L_2 norm of entropy error (Σ): subsonic cylinder test case.

with for example $L = \boldsymbol{\lambda} \cdot \nabla$ or $L = \boldsymbol{\lambda} \cdot \nabla - \nu\Delta$. The numerical solution $u^{h,k}$, is again a FE representation polynomial of the discrete solution:

$$u_h = \sum_{T \in \text{mesh}} \sum_{j \in T} \varphi_j u_j^{h,k}$$

When $k = 1$ ($u^{h,k}$ is a linear polynomial), RDS proceeds as follows

1. *Compute residual:*

$$\Phi^T = \int_T Lu^h dX = \sum_{j \in T} \left(\int_T L\varphi_j \, dX \right) u_j \qquad (21)$$
$$= \sum_{j \in T} u_j \int_T k_j \, dX$$

   defining k_j as

$$k_j = L\varphi_j$$

2. *Distribution:* achieved eventually via the definition of coefficients $\beta_i^T = \beta_i^T(\{k_j\}_{j \in T}, u_h, \boldsymbol{\lambda}, h, \Phi^T)$
3. *Assembly/resolution:* obtain the values $\{u_j\}_{j \in \text{mesh}}$ as a solution of $\sum_{T | j \in T} \beta_j^T \Phi^T = 0$

In the linear case the derivatives of the basis functions are constants. This allows the following reinterpretation of the above scheme as a Petrov–Galerkin scheme.

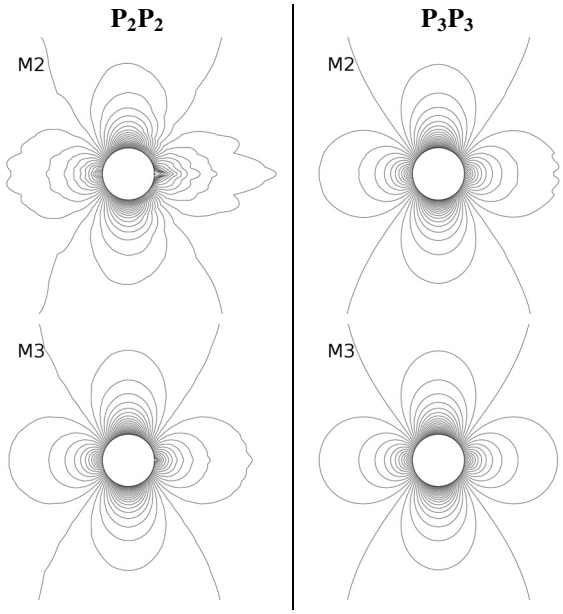

Figure 5: Mach number isolines plotted for $Ma \in \langle 0, 1\rangle$, $\Delta Ma = 0.025$ on meshes M_2 and M_3. Left: P_2 elements, right: P_3 elements.

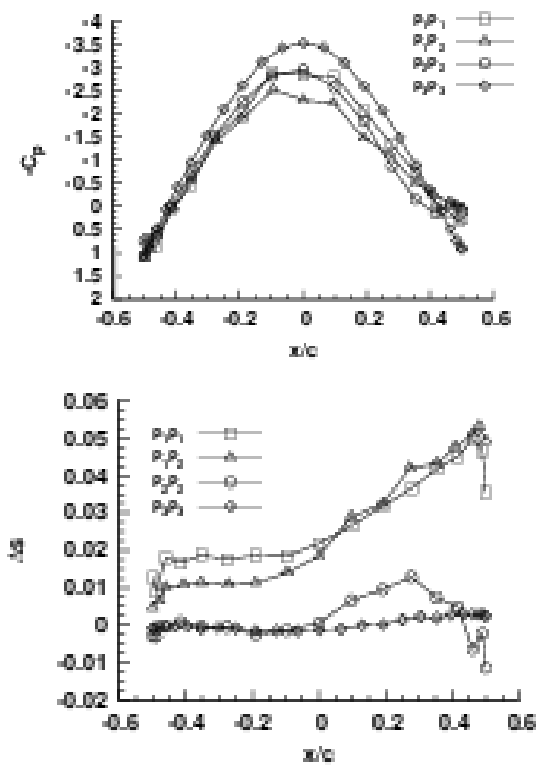

Figure 6: Pressure coefficient (left) and entropy deviation $s - s_{in}$ (right) on the cylinder wall on mesh M1

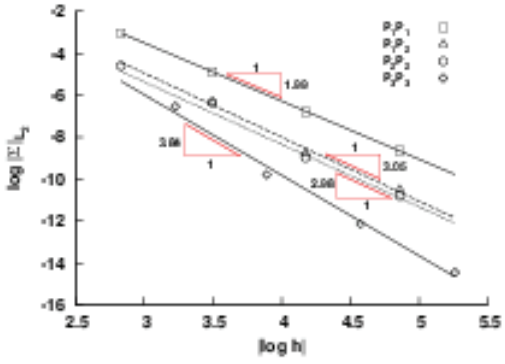

Figure 7: Subsonic cylinder test case; L_2 norm of the entropy error as a function of the mesh size h.

1. Definition of the test function β:

$$k_j = L\varphi_j, \quad \beta_j(x) = \beta_j^T(\{k_j\}_{j\in T}, u_h, \boldsymbol{\lambda}, h, r^T)$$
$$\text{with } r^T = Lu_h|_T$$

2. Integrate: $\Phi_i^T = \int_T \beta_i(x) r^T$
3. Assembly/resolution: get the values $\{u_j\}_{j\in\text{mesh}}$ by solving $0 = \sum_{T|j\in T} \Phi_i^T = \sum_{T|j\in T} \int_T \beta_i(x) r^K$

Since all the known definitions ob β_i^T depend on the definition of k_j (i.e. on the derivatives of the shape functions), the two schemes are identical in the P^1 case. The schemes are not the same anymore for P^k interpolation, $k > 1$.

4.1. Advantages of RD formulation with variable β

The RD schemes with variable distribution coefficient β work without any substantial modification not only on simplex elements, but also on tensor-product elements (quadrilaterals in 2D). The construction of sub–elements for the RD method described in section 3.1 becomes an important issue as the polynomial order of the underlying FE interpolation space becomes high (number of quadrature points per element quickly increases) and as we go to three dimensions (division into sub–elements becomes rather complex to implement in computer codes).

The generic formulation (21) avoids these problems and at the same time, it preserves the upwind nature of the original formulation of the RD schemes.

4.2. LDA scheme

For the LDA scheme, we set

$$\beta_i^T = \frac{k_i^+}{\sum_{j\in T} k_j^+}$$

and the nodal residual becomes

$$\Phi_i^T = \int_T \frac{(L\varphi_i)^+}{\sum_{j\in T}(L\varphi_j)^+} Lu_h \, dX$$

4.3. Scalar advection test case

Given a rectangular domain, we consider a steady advection equation

$$\lambda \cdot \nabla u = 0 \text{ with } \boldsymbol{\lambda} = (y, -x)$$

A cosinus profile is imposed at the inlet. The advection field is supposed to rotate this profile in the direction indicated in figure 8. The solution on a mesh consisting of linear triangles and quadrilaterals is depicted in figure 9.

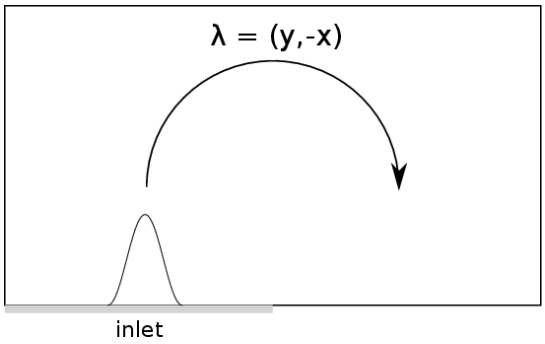

Figure 8: Setup for linear advection test case

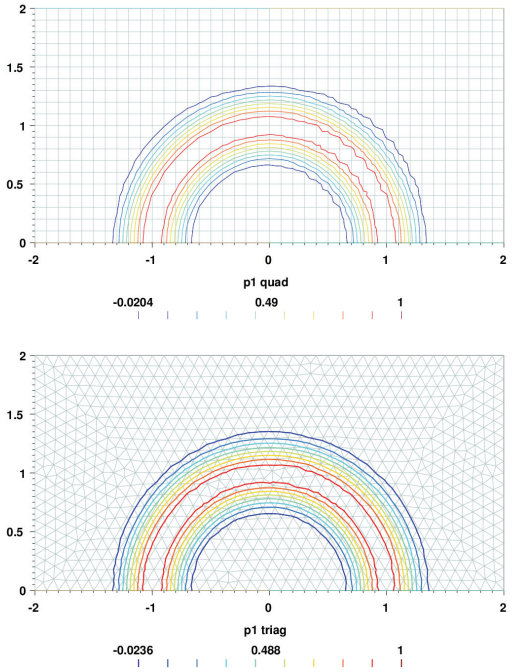

Figure 9: Linear advection test case

Acknowledgments

The presented results were obtained in collaboration with Tiago Quintino, Mario Ricchiuto and Nadège Villedieu. The construction of residual distribution schemes with variable β-coefficients as described in section 4 is due to an original idea of Mario Ricchiuto. No papers on this topic have been published so far.

References

[1] H. Deconinck, R. Abgrall, Introduction to residual distribution methods, VKI Lecture Series, Comput. Fluid Dynam., 2005.

[2] M. Ricchiuto, N. Villedieu, R. Abgrall, H. Deconinck, On uniformly high–order accurate residual distribution schemes for advection-diffusion, J. Comput. Appl. Math. 215 (2008) 547–556.

[3] H. Deconinck, K. Sermeus, R. Abgrall, Status of multidimensional upwind residual distribution schemes and applications in aeronautics, AIAA paper 2000-2328, AIAA CFD Conference, Denver (USA), June 2000.

[4] M. Ricchiuto, N. Villedieu, R. Abgrall, H. Deconinck, High–order residual distribution schemes: discontinuity capturing crosswind and extension to advection–diffusion, VKI Lecture Series, Comput. Fluid Dynam., 2005.

[5] H. Deconinck, P. L. Roe, R. Struijs, A multidimensional generalization of Roe's difference splitter for the Euler equations, Computers and Fluids 22(2/3) (1993) 215–222.

[6] H. Paillere, Multidimensional upwind residual distribution schemes for the Euler and Navier–Stokes equations on unstructured grids, Ph.D. thesis, Von Karman Institute for Fluid Dynamics and Université Libre de Bruxelles, Faculté des Sciences Appliquées (1995).

[7] E. van der Weide, H. Deconinck, Positive matrix distribution schemes for hyperbolic systems, with application to the Euler equations, Computational Fluid Dynamics (1996) 747–753.

[8] E. van der Weide, Compressible flow simulation on unstructured grids using multi–dimensional upwind schemes, Ph.D. thesis, Von Karman Institute for Fluid Dynamics and TU Delft (1998).

[9] N. Villedieu, T. Quintino, M. Vymazal, H. Deconinck, High-order residual distribution schemes: Unsteady and viscous terms, 35th Computational Fluid Dynamics Lecture Series, VKI/ADIGMA Course on High order Discretization Methods, Von Karman Institute for Fluid Dynamics, 2008.

[10] R. Abgrall, A. Lerat, M. Ricchiuto, C. Tavé, A simple construction of very high order non-oscillatory compact schemes on unstructured meshes, Computers and Fluids 38(7) (2009) 1314–1323.

[11] R. Abgrall, Residual distribution schemes: Current status and future trends, Computers and Fluids 35(7) (2006) 641–669.

[12] F. Bassi, S. Rebay, High–order accurate discontinuous finite element solution of the 2D Euler equations, J. Comput. Phys. 138 (1997) 251–285.

FLOW DURING INDUSTRIAL HAZARD

Experimental characterization and modeling of hazards: BLEVE and Boilover

Delphine Laboureur

Environmental and Applied Fluid Dynamics Department, laboureu@vki.ac.be

Supervisor and Promotor: Jean-Marie Buchlin

Professor, Environmental and Applied Fluid Dynamics Department, von Karman Institute for Fluid Dynamics, Belgium, buchlin@vki.ac.be.

Co-supervisor: Patrick Rambaud

Associate Professor, Environmental and Applied Fluid Dynamics Department, von Karman Institute for Fluid Dynamics, Belgium, rambaud@vki.ac.be.

Abstract

BLEVE and Boilover are two types of devastating accidents, involving pressure liquefied reservoir and atmospheric vessels respectively. This paper provides first results of small scale experiments performed in the BABELs facility. BLEVE experiments using 42g propane reservoirs pointed the influence of the reservoir strength on the release phenomenon. Boilover visualizations with 80mm diameter glass reservoirs helped to understand the phenomenology of water boiling at Boilover apparition.

Keywords: BLEVE, Boilover, shadowgraphy, visualization, LEDAR

1. Introduction

Nowadays, more and more chemical process plant sites include storage sites based on pressure liquefied reservoir and/or atmospheric vessels, depending on the industrial activity. These sites can suffer from two types of devastating accidents: BLEVE and Boilover. The BLEVE is defined by Walls [1] as an explosion resulting from the catastrophic failure of a vessel containing a liquid at a temperature significantly above its boiling point at normal atmospheric pressure (i.e. superheated liquid). The Boilover is a violent ejection of fuel due to the vaporization of a water sub-layer, resulting in an enormous fire enlargement and formation of fireball and ground fire.
The objective of the thesis is twofold: to understand the occurrence factors and consequences of these two phenomena, and to model them. The methodology involves extensive literature survey, laboratory and medium field tests experiments as well as CFD simulations. This paper provides a synthetic review of the work done so far on the two topics, focused on laboratory experiments performed in the new BABELs facility.

2. Experimental setup

BLEVE and Boilover experiments include important flame dimensions, fuel or fragment projections, pressure wave,... Therefore, a dedicated facility called **BABELs** has been built and is available since beginning 2010 at the von Karman Institute, to guarantee secure small scale experiments in a calm and uniform environment. A general view of this facility is displayed in Fig. 1. BABELs is an acronym for **B**leve **A**nd **B**oilover **E**xperimenta**L** **s**etup and consists of a cylindrical chamber of 2m diameter, and 3m high, with round-shaped flanges, made out of steel with a rated pressure of $0.5MPa$. It has 3 series of 7 optical accesses of 0.15m in diameter, separated by 90°, and a door of $0.57mx0.77m$. The setup allows air venting through openings in its bottom and upper parts, the last one being ended by a exhaust vent that can be used after each test to remove smoke or gas from the chamber. A ladder and a circumferential walking area are located at mid-height for better accessibility of the upper optical accesses. All the experimental results presented in this paper have been carried out in BABELs.



Figure 1: BABELs experimental facility

3. BLEVE research

3.1. Experimental apparatus and technique

According to literature, the most important cause of BLEVE is fire. The typical scenario involves a reservoir engulfed in flames, causing an increase in liquid temperature and therefore in internal pressure, until rupture.

This BLEVE scenario is performed at small scale using horizontal cylindrical reservoirs of 40mm diameter, 138mm long and 2mm thick, filled with 86% volume of propane (mass: 42g), provided by Nippon Tansan Gas Co (NTG), as Fig. 2. This reservoir is layed on a spiral microheater GA-XP from Micropyretics Heaters International. This resistor can be supplied with varying electrical power, changing the heat flux applied to the reservoir by Joule effect. In the experiments presented here, the electrical power is about 460W. To protect the resistor from the reservoir rupture, a metal plate is added on the resistance. The reservoir is positionned on the plate, and inside a cradle for a better heat distibution and stability on the resistor.

Temperature is monitored by type K thermocouples located between the plate and the cradle, at the top and the bottom of the reservoir, and sampled at 3Hz. The pressure wave generated at rupture is recorded by two PCB 106B50, filtered at 25kHz (to remove the influence of the 50kHz resonance frequency, determined by shock tube experiments) and sampled at 250kHz. One of the reservoir is also connected to a Validyne pressure sensor that monitors the internal pressure at 100Hz. This sensor is calibrated thanks

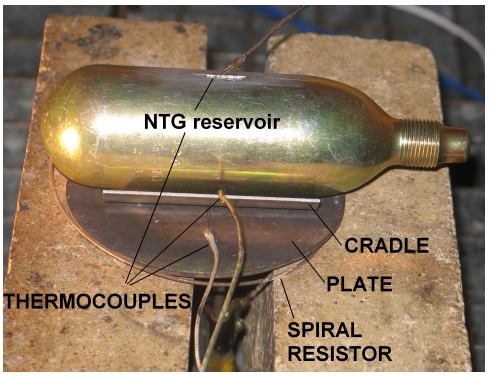

Figure 2: NTG reservoir

to a dead weight tester 5020SMPR by Desgranges & Huot. All these measurements are recorded by National Instrument Compact DAQ and LabView acquisition software.

For visualization purposes, a Phantom V7.1 high

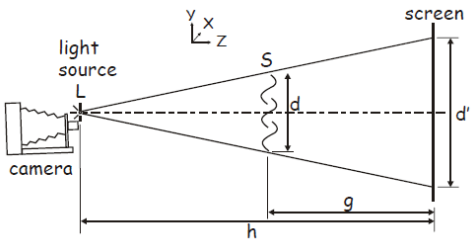

Figure 3: Diagram of Edgerton direct shadowgraph technique [2]

speed camera is used, combined with a 12mm focal length objective. The images are recorded at 14035Hz. First, simple visualization of the vapor cloud generated by the rupture is performed with the help of two halogen lamps.

For observation of the pressure wave generated by the rupture, an Edgerton's direct shadowgraph technique is used. As showed in Fig. 3, the purpose is to illuminate an object S with a point source L (Elix 4W LED coolwhite, 180 lumen) and to look simultaneously at the object and its shadow on a screen (Oralite retroreflective film 5300). The slight offset between the light source and the camera positions causes double imaging that should be corrected in further measurements.

3.2. Results and discussion

As the reservoir fragmentation during rupture is a phenomenon difficult to predict, the reservoirs are weakened prior the experiment. A scratch of 0.6mm deep (corresponding to 30% of thickness removed)

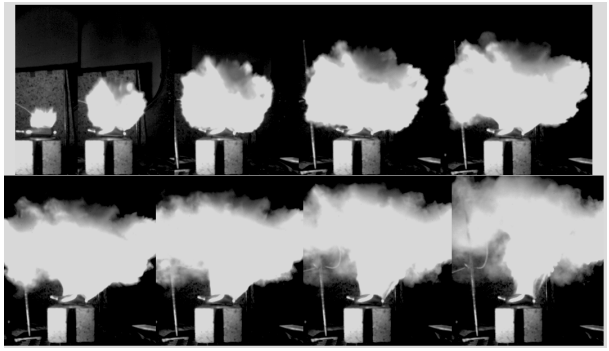

Figure 4: NTG bottle rupture with 77mm long weakness. Δt between images: $0.28ms$

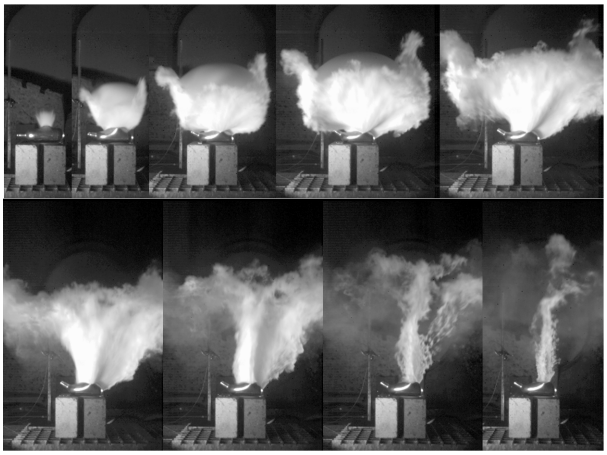

Figure 5: NTG bottle rupture with 15mm long weakness. Δt between images: $0.28ms$

and 15 or 77mm long is made along the length of the reservoir, and is located on top of it during the experiment. After analysis of several BLEVE experiments performed in the same configuration, the size of the weakness is changing completely the rupture phenomenon.

3.2.1. Rupture visualization

A strongly weakened reservoir (77mm long) burst can be observed in Fig. 4. At rupture, the rapid vaporization and expansion of propane results in a spherical cloud of vapor and small droplets. With time, the cloud rises and the two-phase ejection decreases (as the jet release angle decreases). Once the reservoir is empty, the cloud is diffusing and the droplets are evaporating until complete visual disappearance. In this type of rupture, the propane is not ignited and no fireball can be observed.

If the weak spot is smaller (15mm), the release is completely different (Fig. 5). In this case, the cloud experiences a perfectly round-shaped curve on the upper part. During ejection, the cloud ignites at first from the outside and propagates inward. The propane ejection is faster in this configuration than the strongly weakened reservoir.

The rupture pattern is similar for both sizes of scratch (Fig. 6). But the less the reservoir is weakened, the larger will be the opening. Following the nomenclature of Fig. 6, a reservoir with a 77mm long scratch ends up with an opening of $A = 81mm$ and $B = 135mm$. If the reservoir has a smaller scratch (15mm), the breach size increases up to respectively $A = 95mm$ and $B = 145mm$. In addition, the time for BLEVE apparition is decreasing with the reservoir strength. In average of several tests performed in the same configuration, a large weakness induces a rupture after 615.5sec of heat and a small weakness after 927.8sec.

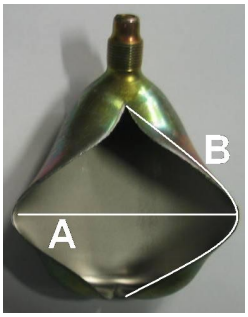

Figure 6: NTG reservoir after rupture

3.2.2. Pressure wave

One physical effect of a BLEVE explosion is the generation of a blast wave. The Fig. 7 shows pressure measurements taken at two distances from the reservoir, and for the two weak spot sizes. Overpressure signals experiences a single peak, generated by the combination of the top space vapor expansion and the liquid flash vaporization. The value of the peak is decreasing with distance from the reservoir, and is increasing for a less weakened reservoir. In overpressure modeling (see [3; 4; 5]), if all other variables stay constant (like the type of liquid, the fill level, the reservoir size, etc...), the overpressure at a given distance depends directly on the pressure inside the tank during the explosion. Therefore, when the reservoir is less weakened, the rupture happens at a higher internal pressure, and generates a higher blast wave.

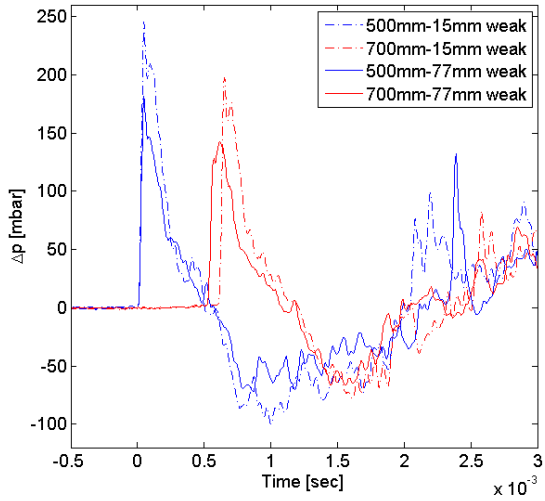

Figure 7: Overpressure measured at 500mm and 700mm from the reservoir center

The time difference in the apparition of the pressure peak at 700mm from the reservoir is probably due to a slight modification of the position of the reservoir between the two tests.

The blast wave generated by the vessel burst can also

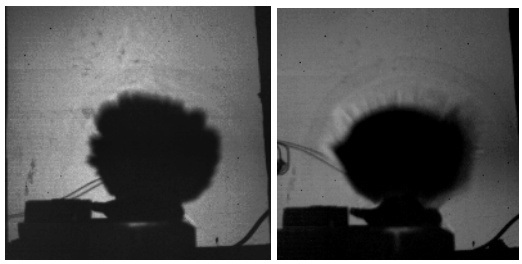

Figure 8: Shadowgrams showing the blast wave generated by the explosion. Left image: 77mm weakness, Right image: 15mm weakness

be observed in the shadowgrams (Fig. 8). The wave appears perfectly spherical. Its thickness is linked to a too long exposition time (55μs) that was imposed by the light source intensity and the camera objective. In further experiments, a shorter exposition time should be used for a clearer visualization. A difference in contrast of the wave compared to the background can be observed between the two images: the blast generated by the small weakness appears more clearly. This can be linked to the overpressure signals: a higher contrast in the shadowgram is representative of a stronger blast wave.

3.2.3. Internal pressure measurement

One of the BLEVE experiments has been performed with a small weak point (15mm) and a pressure transducer that monitor the internal pressure. The Fig. 9 shows the internal pressure evolution, plotted against the temperature of the top of the reservoir. This measurement is compared with the saturation curve of propane, and with the experiment of Stawczyk [6] that generated a BLEVE with a 5kg reservoir of propane, filled at 70%.

At first, the pressure is following the saturation

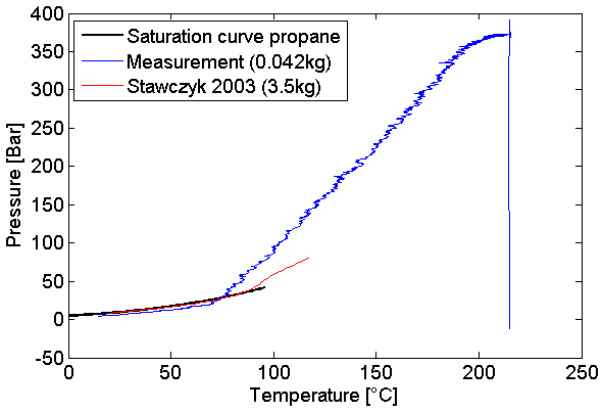

Figure 9: Vapor pressure vs. temperature

line (the small deviation from the line is probably due to the temperature difference inside and outside the reservoir). At one point below the critical point, the measurement deviates from the saturation line and shows a higher increase in pressure. This phenomenon is also observed by Stawczyk that relates it to the change from one to two-phase medium. Finally, the BLEVE happens at a pressure of 372bar. The rupture temperature is then well above the superheat limit temperature, and according to Birk [7], is defining a hot BLEVE. In the specifications of the reservoir, they set the minimum burst pressure around 441bar, which means that the weakness and/or the heat is influencing the rupture pressure. The strong difference between the burst pressure of this measurement and Stawczyk is propably due to a difference in the theoretical burst pressure even if the one of the 5kg reservoir is not specified.

3.2.4. Hot and cold BLEVE

In all the different aspects of the BLEVE measured, the phenomenon following the reservoir rupture is dependent on the strength of the reservoir. In 1993, Birk [7] listed a series of criteria that describe a hot or cold

BLEVE. In first papers dedicated to BLEVE [1; 8; 3], authors link the BLEVE apparition only if the liquid temperature at rupture is higher than the superheat limit temperature. But Birk showed that a BLEVE can happen also at lower temperature, and defines the two types of BLEVE as hot or cold.
A cold BLEVE is a reservoir that fails before reaching the superheat limit temperature; this happens mostly because the tank is too weak and fails at lower pressure. The result is a rupture where part of the liquid flashes to vapor and the remaining liquid is dispersed as droplets. A hot BLEVE happens in a reservoir that fails at a temperature higher than the superheat limit temperature. A hot liquid and a local failure are necessary but the tank can be very strong. Almost all liquid flashes to vapor. If ignited, a classic rising fireball can be observed, and the overpressure generated is stronger than for the cold BLEVE.
All these differences between hot and cold BLEVE can be linked to the two types of rupture experienced in this measurement campaign. The size of the scratch would then modify the rupture pressure and therefore the type of BLEVE. This will be confirmed in later measurements by measuring the internal pressure in a strongly weakened reservoir.

4. Boilover research

On the way to a complete understanding of the Boilover phenomenon, one important step is the characterization of the boiling water influence on the Boilover apparition.
In literature, it is commonly accepted that the Boilover starts with the vaporization of the water sub-layer that induces a piston effect due to the enormous volume increase of the vapor phase compared to liquid. Garo [9] and Hua [10] performed visualizations of the fuel and water layers, and show that bubbles appear at the fuel - water interface, and increase in scale and in generation rate with time up to Boilover apparition. But both experiments use a thick water layer, non representative of the real industrial Boilover accidents, and they do not present results about the exact starting moment of Boilover.

4.1. Experimental apparatus and technique

In order to perform clear visualizations of the liquids behavior, in BABELs, small cylindrical reservoirs made of DURAN glass, of 80mm diameter and 45mm height are used to generate a Boilover, with a water layer of 6mm and 16mm of fuel, ignited with a butane torch. The fuel used is a mixture of lamp oil and Valvata Shell 460 oil. The lamp oil generates less carbon residues compared to diesel, and therefore stays more transparent during the test. A Phantom V7.1 high-speed camera records the Boilover phenomenon in series of 2048 images, with an acquisition frequency of 1 kHz. Two angles of view are chosen (Fig. 10) : sideview to have a visualization of the evolution of water and fuel layers and a bottom view to observe the evolution of both layers along the whole reservoir diameter. To improve the visualization quality, tracing paper is placed in front of the two halogen lamps, giving a better light diffusion.

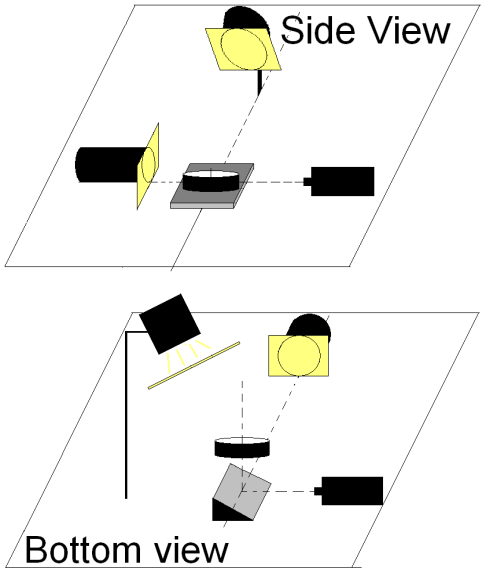

Figure 10: Camera and lighting disposition

4.2. Phenomenology

Typical pictures extracted from the high-speed visualizations are presented in Fig. 11, to illustrate each step of the phenomenon. At first, some bubbles appear on the fuel surface close to the walls (Fig. 11.A). After about a third of Boilover time, water vapor bubbles start to grow from the fuel-water interface and reach the top fuel surface with a size around 5% of tank diameter (Fig. 11.B). The bubble generation rate accelerates with time and bubbles in cluster can be observed at fuel surface (Fig. 11.C). At that time, the initial bubble size at the fuel-water interface is big enough to be visible, showing columns of bubbles through the fuel thickness (Fig. 11.D). Coming closer to the Boilover occurrence, the fuel-water interface experiences a fast growth of bubbles of bigger size

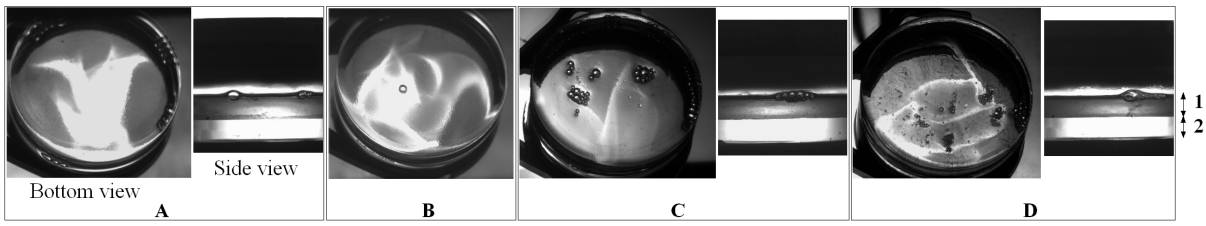

Figure 11: Fuel ($n°1$) & water ($n°2$) visualization during period prior Boilover apparition (bottom and side view): A: $t \approx 0.1 - 0.2t_{bo}$, B: $t \approx 0.2 - 0.3t_{bo}$, C: $t \approx 0.5 - 0.6t_{bo}$ and D: $t \approx 0.7 - 0.8t_{bo}$.

(15 to 20% of tank diameter), that create waves at the interface and accelerate even more the water boiling. This period of strong boiling prior Boilover event can be linked to the premonitory period of Boilover, as defined by Hua [10] and characterized by a crackling noise, due to water bubbles wrapped in a layer of fuel, that are projected into the flame zone.

Finally, at Boilover onset (see Fig. 12), the growth of

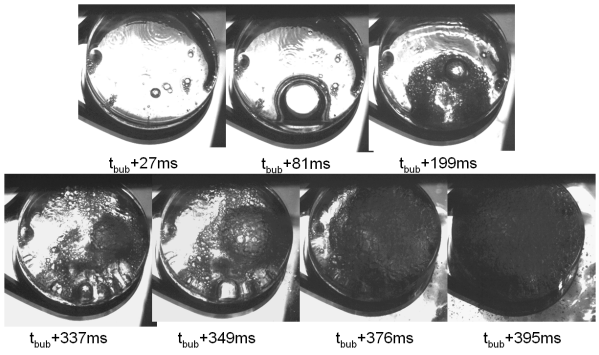

Figure 12: Bottom visualization of evaporation front at Boilover onset for lamp oil experiment

one big bubble induces a boiling front that propagates radially all along the fuel-water interface, ejecting the upper fuel layer and leading to the increase of flame size, as observed during Boilover phenomenon. This gives a first visualization of the piston effect as described in previous literature, showing in addition that the vaporization of the water layer is homogeneous.

The Boilover behavior can also be quantified from side view image analysis. The fuel - flame interface and the fuel - water interface positions are monitored by an edge detection technique based on Forward Step filter algorithm, implemented in the LEDAR software (Level Detection and Recording) developed by Planquart [11]. The tracking of the two interfaces leads to the same conclusions drawn from the visualizations. First, a big bubble appears at the fuel-water layer interface, that disturbs the fuel layer as shown in Fig. 13 for t=0s. This flow perturbation lasts until a two-phase (boiling) front is propagating in the entire reservoir (around t=0.12s in Fig. 13). Among the 10 tests performed for visualization purposes, in the same configuration, the average Boilover onset duration, estimated from the apparition of the first big bubble to the complete propagation of the boiling front is about 278.5msec, with a large standard deviation of 154.5msec. That poor reproducibility in time is not yet explained.

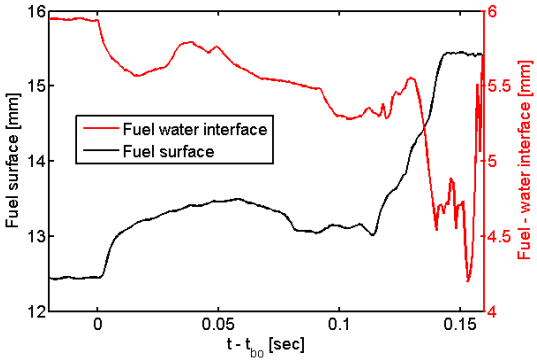

Figure 13: Time evolution of fuel-water interface & fuel surface position compared to the reservoir bottom, at Boilover apparition

5. Conclusion

Small scale experiments of BLEVE and Boilover are performed, in the new BABELs facility, builded to guarantee secure measurements in a calm and uniform environment.

Cylindrical metal reservoirs with 42g of propane are used in the modeling of the most common BLEVE scenario: reservoir engulfed in flames. High speed and shadowgraph visualizations, temperature, overpressure and internal pressure measurements help to identify two types of BLEVE rupture, depending on the weakness size performed on the reservoir. A small

weakening experiences a faster rupture, with a higher blast wave generated, leading to ignition of the two-phase mixture ejected. A stronger weakness shows no fire and a slower ejection of a two-phase cloud. These differences can be linked to the two types of BLEVE defined by Birk [7]. In future experiments, internal pressure will be measured in every reservoir to better understand the relation between weakness size, rupture pattern and rupture pressure. The Edgerton direct shadowgraphy technique will be improved to better characterize the blast wave.

Small scale Boilover experiments using glass reservoir and a mixture of lamp oil and Valvata oil are performed using high-speed visualization, allowing a first clear understanding of the Boilover onset. They show that bubbles appear at the fuel - water interface and as time come closer to Boilover apparition, grow in size and in generation rate. At Boilover apparition, the growth of a bigger size bubble is disturbing the fuel water interface, enhancing the water boiling. This leads to the creation of a two-phase boiling front that propagates along the whole reservoir and causes the fuel expulsion, significative of the flame enlargment observed during Boilover. In future experiments, measurements of the temperature of fuel and water layers, radiation from the flames, mass loss caused by fuel combustion will be performed to better characterize all the Boilover aspects. In addition, flame visualizations and edge detection technique will quantify the flame enlargment.

Acknowledgments

The authors wish to thank the CEA of Gramat which is supporting this study and collaborating with the von Karman Institute and the École des Mines d'Alès in this joint research project about source term characterization in major hazards.

References

[1] W. Walls, The bleve - part 1, Fire Command (1979) 22–24.

[2] G. Settles, T. Grumstrup, J. Miller, M. Hargather, L. Dodson, J. Gatto, Full-scale high-speed 'edgerton' retroreflective shadowgraphy of explosions and gunshots, 5th Pacific Symposium on Flow Visualisation and Image Processing, Australia PSFVIP (2005) 5–251.

[3] R. Prugh, Quantitative evaluation of bleve hazards, J. of Fire Prot. Engr. 3 (1) (1991) 9–24.

[4] E. Planas-Cuchi, J. Salla, J. Casal, Calculating overpressure from bleve explosions, J. of Loss Prev. in Process Ind 17 (6) (2004) 431–436.

[5] B. Genova, M. Silvestrini, F. L. Trujillo, Evaluation of the blast wave overpressure and fragment initial velocity for a bleve event via empirical correlations derived by a simplified model of released energy, J. of Loss Prev. in the Process Ind. 21 (1) (2008) 110–117.

[6] J. Stawczyk, Experimentl evaluation of lpg tank explosion hazards, J. of hazardous materials 93 (2-3) (2003) 189–200.

[7] A. Birk., Z. Ye, J. Maillette, M. Cunningham, Hot and cold bleves: Observation and discussion of two different kinds of bleves, AiChE Heat Transfer Conference, AiChE Symposium Serie 89 (1993) 119–130.

[8] R. Reid, Possible mechanism for pressurized-liquid tank explosions or bleve's, Science 203 (23) (1979) 1263–1265.

[9] J. Garo, J. Vantelon, Effect of the fuel boiling point on the boilover burning of liquid fuels spilled on water, 26th Int. Symp. on Combustion (1996) 1461–1467.

[10] J. Hua, W. Fan, G. Liao, Study and prediction of boilover in liquid pool fires with a water sublayer using micro-explosion noise phenomena, Fire Safety Journal 30 (3) (1998) 269–291.

[11] P. Planquart, M. Riethmuller, A. Joly, J. Detry, Real time optical detection and characterisation of water model free surfaces application to the study of mold, 4th European Continuous Casting Conference, Birmingham, UK (October 2002) 14–16.

ATMOSPHERIC FLOW

Physical modelling of wind in complex terrain: application to wind turbine siting

Boris Conan

Environmental and Applied Fluid Dynamics Department, boris.conan@vki.ac.be

Supervisor: Jeroen van Beeck

Professor, Environmental and Applied Fluid Dynamics Department, von Karman Institute for Fluid Dynamics, Belgium, jeroen.vanbeeck@vki.ac.be

Supervisor: Sandrine Aubrun

Institut PRISME, Polytech'Orléans, 8, rue Léonard de Vinci, Orléans FRANCE, sandrine.aubrun@univ-orleans.fr

Promotor: Philippe Devinant

Professor, Institut PRISME, Polytech'Orléans, 8, rue Léonard de Vinci, Orléans FRANCE, philippe.devinant@univ-orleans.fr

Abstract

Wind resource assessment is crucial to predict the potential wind power production at given site. In mountainous terrain, where linear models fails and numerical models are in development, wind tunnel physical modelling is an option. The paper proposes to discuss advances in the physical modelling: similarity parameters, inlet conditions, model roughness, area of interest and measurement techniques.

Keywords: atmospheric boundary layer, wind resource assessment, atmospheric turbulence, complex terrain, physical modelling, PIV, triple hot-wire,

1. Introduction

In the fast development of wind energy, wind resource assessment is a major concern for the prediction of the annual energy production and the profitability of wind turbines. The choice of the wind turbine design depends also on the characteristics of the wind at a given site. European targets are ambitious for wind turbine siting: to have, regardless the complexity of the terrain, an uncertainty of 3% on long-term annual energy production forecasting and 3% on local wind conditions forecasting. [1]
This challenge comes in addition to the fact that lots of high wind potential sites with good accessibility are exploited or under project. Therefore, the expansion of wind energy capacity goes through the development of reliable tools for wind assessment in complex terrains like hills, mountains, forests, ridges, cliffs or even cities.
For the prediction of the flow over very complex terrain, slopes greater than 15%, linear models fail and CFD is at the research state. Wind tunnel is a complementary tool to study the flow over complex sites. The physical modelling is commonly used in pollution dispersion, for the study of the wind over forests [2; 3], or on simplified geometry [4; 5] but it is still a confined tool in wind resource assessment [6].
As for numerical modelling, the physical modelling needs to satisfy modelling assumptions, to meet similarity requirements, and to reproduce inflow conditions.

The aim of this work is to demonstrate the suitability of wind tunnel tests for wind assessment in mountainous terrains and to discuss important modelling issues encountered. The paper is focused on the general aspects of the simulation with physical models and on the description of the flow field over mountainous terrain.

In the first part of the paper, the modelling of atmospheric flows in the wind tunnel is discussed. In the second part, the reproduction of inflow conditions in the wind tunnel of the von Karman Institute is presented. Then, PIV is implemented and the flow over a mountainous terrain is described in mean and fluctuating quantities. Modelling parameters like the scaling of the terrain, the choice of the modelled area and the reproduction of the inlet boundary layer are discussed.

2. Physical modelling of atmospheric flows

2.1. Similarity criteria

The modelling of atmospheric flows in the wind tunnel needs to satisfy a number of similarity requirements. In the ideal case, geometrical similarity, kinematic similarity, dynamic similarity, thermal similarity and boundary conditions (section 2.2) have to be fulfilled [7; 8; 9].

The geometrical similarity and the kinematic energy similarity are completed providing that the same scaling factor is applied in the three directions, see Cermak [7].

The dynamic similarity, coming from the momentum conservation equation, leads to three dimensionless numbers: Reynolds number (Re), Richardson number (Ri) and Rossby number (Ro).
Due to the large dimensions of the characteristic lengths of atmospheric flows, the conservation of the Reynolds number is usually impossible in air; it would require very high velocities in the wind tunnel: $U_{model} = U_{real} \times (scaling factor)$. The assumption made is that above $Re \geqslant 10\ 000$, the flow is fully turbulent and Re independent. A minimum roughness Reynolds number can also be defined in the wind tunnel to ensure the turbulence state close to the wall [8]:

$$Re_{critical} = \frac{u_*.(z_0)_{wt}}{\nu} > 5 \qquad (1)$$

with u_*: wall friction velocity [m/s]; $(z_0)_{wt}$: roughness length in the wind tunnel [m]; ν: kinetic viscosity [m/s].

The Reynolds independence is verified (but not reported here) by varying the inlet velocity from 5 m/s to 20 m/s. Notice that with the Reynolds number relaxation, dissipation scales are not respected.
The wind tunnel works at ambient temperature, the Richardson number (ratio of the Buoyancy forces over inertial forces) equals zero: $Ri = 0$. Only neutral atmospheric boundary layer conditions can be simulated.
The Rossby number, taking into account the Coriolis force, is here neglected. Even if the area modelled is of the order of 10 km, the effect is neglected compared to topographic perturbation.

From the conservation of the energy equation, thermal similarities bring two new dimensionless numbers: the Prandtl number (Pr) and the Eckert number (Ec). These similarities are easily fulfilled: the first depends on the fluid properties and the second is considered constant while $U << c$, c being the velocity of sound in air.

2.2. Inlet conditions

Additionally to the above mentioned similarity criteria, inlet boundary conditions has to be reproduced. The atmospheric wind presents different characteristics in terms of mean velocity, turbulence, roughness length, turbulent scale and friction velocity that depend on the real roughness of the terrain: sea, landscape, city, forest. These characteristics have to be reproduced in the wind tunnel.

Norms, like the Eurocode, ESDU and VDI guidelines [10; 9; 8] are classifying different classes of terrain by their roughness length. Smooth terrains like sea or lakes are represented by a very small roughness length $z_0 \approx 0.0005$ and very rough terrains like city centres or forests are represented by higher values $z_0 \geqslant 1$.
The atmospheric velocity profile of a neutral boundary layer is often described by a log law, coming from the integration of the flux-gradient relation of the local closure scheme [11]. The roughness length is a key parameter:

$$\frac{U}{u_*} = \frac{1}{\kappa}.ln\frac{Z}{z_0} \qquad (2)$$

with Z: altitude [m]; U: mean velocity [m/s] at the altitude Z; κ: von Karman constant (= 0.4); z_0: roughness length [m]; u_*: friction velocity [m/s].

The friction velocity is usually determined from its definition: ${u_*}^2 = -(\overline{u'w'})_0$ with u' and w' the longitudinal and vertical velocity fluctuation. If only the vertical velocity profile is available, other techniques like the "slope" method can be used. In this case, u_* is determined by plotting u versus $ln(z)$,

the slope of the linear curve in the logarithmic layer is proportional to the friction velocity: $u_* = \kappa.slope$, see Fig. 8 b-.
This very same plot is used to determine the roughness length of the wind profile simulated in the wind tunnel: z_0 is the intersection of the linear part of the logarithmic layer with the Z axis (U= 0 leads to $Z = z_0$ in Eq. 2).

To be consistent with the roughness terrain, the turbulence intensity profile in the three directions has to follow classification [8; 9; 10]. VDI guidelines and ESDU norms are plotted in Fig 1.

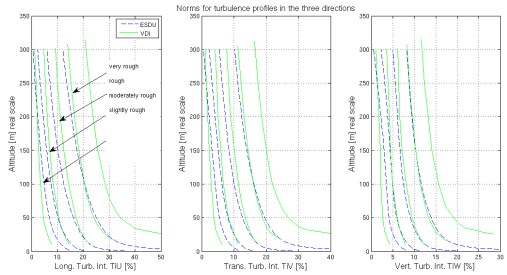

Figure 1: VDI guidelines and ESDU norms for the simulation of the turbulent intensity profile in function of the roughness length.

Two additional conditions are necessary to model atmospheric flows in a wind tunnel: the fully developed state: $\frac{dU}{dX} = 0$, and the constant pressure gradient: $\frac{dP}{dX} = 0$. The fully developed state is confirmed by comparing two profiles taken at different longitudinal positions. For the pressure gradient, a commonly accepted condition[8] is :

$$\frac{\left(\frac{dP}{dX}.\delta\right)}{\left(\frac{\rho_a}{2}.{U_\delta}^2\right)} \leq 0.05 \qquad (3)$$

where P: pressure [Pa]; X: longitudinal coordinate of the wind tunnel; δ height of the simulated boundary layer [m]; ρ_a ambient air density [kg/m3]; U_δ : velocity at the top edge of the boundary layer [m/s].

2.3. Flow over complex terrain

For every natural area that is not a flat terrain, another effect is to add to the roughness: the effect of the orography. Indeed, the presence of an obstacle disturbs the flow. In case of a low-slopped terrain, the flow is accelerated due to the obstacle blockage (Bernoulli). This acceleration is mainly linked to the height and the slope of the hill. The speed-up at the hill's top can be a very profitable phenomenon for wind turbine siting.

For more slopped terrains, above 10% to 17%, flow separation can occur at the hill's top or on the lee side. The over-speed is still present at the hill's top, but high shear layers and turbulent levels are appearing due to the separation of the flow. If the flow perturbation is too high, the possibility of placing wind turbines can be compromised. In addition, a high perturbation influences the downstream flow characteristics for a long distance: reduction of the speed, increase of the turbulence intensity.

The reproduction of these flow behaviours in a wind tunnel, especially the flow detachment, involves not only the reproduction of the geometry but also several other parameters like the surface roughness, the Reynolds number and inlet conditions.

2.4. Recurring topics

Lots of topics are under investigation for the modelling of a complex terrain in a wind tunnel. The main parameters to consider are: inlet flow conditions, model roughness, Reynolds number dependency and far upwind relief (area of influence).
All parameters can have an impact on the right reproduction of the flow behaviour, but their relative importance are unknown.
The reproduction of inlet conditions is a classical topic, several norms and guidelines exist to model the ABL with the appropriate flow features. But what if the area modelled does not take into account an upstream relief? On the other hand, enlarging the modelled area leads to increase the scaling factor, so going worst for the Reynolds number similarity, and including the possibility to change the flow behaviour.
This study aims at contributing to the understanding in these topics.

3. Modelling of inlet conditions

The reproduction of atmospheric inflow conditions is a major task in the simulation of a flow over a complex terrain. A very deep knowledge is requested on the mean and fluctuating quantities of the wind simulated. The wind tunnel inlet as to reproduce, at the right scale, the roughness conditions of the real profile.
For this topic, still under investigation, the objective is to characterize deeply the flow in the wind tunnel

and to find the best way to model different roughness lengths at different scales.

3.1. Wind tunnel facility

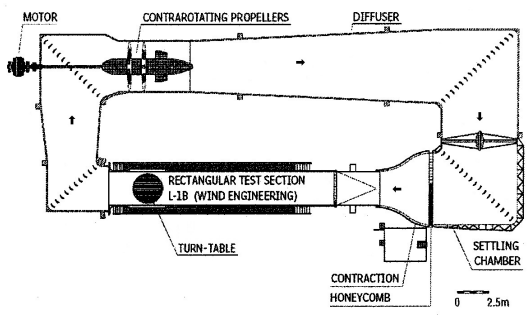

Figure 2: Wind tunnel in the wind engineering configuration.

The von Karman Institute is equipped with a large low-speed closed-looped wind tunnel: VKI-L1. The closed test section of the facility is 2 m high, 3 m wide and 15 m long (Fig. 2). Two contra-rotating fans driven by 580 kW DC motor allow a maximum speed of 60 m/s. For wind engineering applications, the velocity is often limited to 20 m/s and the length of the test section is used to model the neutral atmospheric boundary layer. To simulate the wind coming from all directions, mock-ups are placed on a 2.8 m diameter turn-table (foreground of Fig. 4). If necessary, the ceiling of the wind tunnel can be adjusted to control the pressure-losses over the tunnel. This particularity can also overcome a blockage effect.

3.2. Atmospheric boundary layer generation technique

To archive the development of a neutral atmospheric boundary layer (ABL), a set of obstacles is placed inside the test section of the wind tunnel in order to create velocity and turbulence gradients. In the literature, a common practice is to have a castellated fence and elliptical vortex generators at the beginning of the test section. Then the length of the test section, usually around 10 m, is covered with roughness elements. Different shapes can be find in the literature [12; 13; 14; 15].

In the wind tunnel of the von Karman Institute, a grid and a fence are placed at the very beginning of the test section. These items are starting the development of the boundary layer by giving a strong initial perturbation (Fig. 3). Then, over 12 m, conical elements are distributed on the floor. These elements are organised in 6 transversal rows of 24 elements and 23 rows of 12 elements (Fig. 5). The roughness element height can be adapted to the roughness classification to the scale desired. It is possible to change the roughness elements next to the model to have a smooth transition with it.

The different elements used for the generation of the ABL are summarized in Table 1.

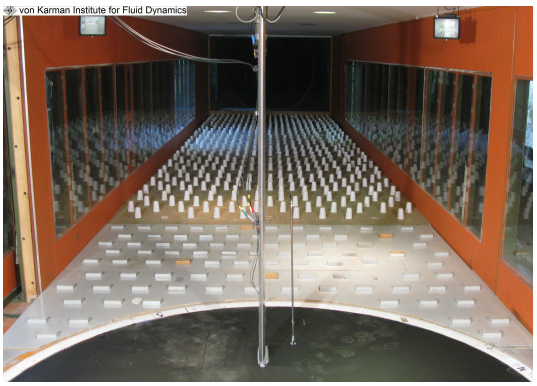

Figure 4: Wind tunnel in the wind engineering configuration.

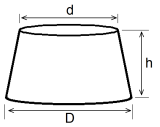

Figure 5: Roughness element geometry.

Farell [12] proposes a roughness distribution classification and defines the roughness density $\lambda = A_g/S_G$ and the frontal roughness density $\lambda_f = A_f/S_G$. A_g is the projected area of a roughness element to the ground, A_f the projected frontal area of a roughness element and S_G the ground area per roughness element. For example, a configuration with "Cup 1" as boundary layer generators and transition elements, gives $S_G = (3 \times 12)/504$ and a roughness distribution ratio of $\lambda = 1.71\%$ and $\lambda_f = 1.57\%$. With "Cup 2" elements, $\lambda = 4.5\%$ and $\lambda_f = 8\%$.
This is relatively low compared to other studies presented.

3.3. Triple hot-wire measurements

In order to provide a sufficiently deep knowledge of the mean and fluctuating quantities of the inlet profile, vertical traverses are performed with a triple hot-wire placed at the future position of the model (Dantec

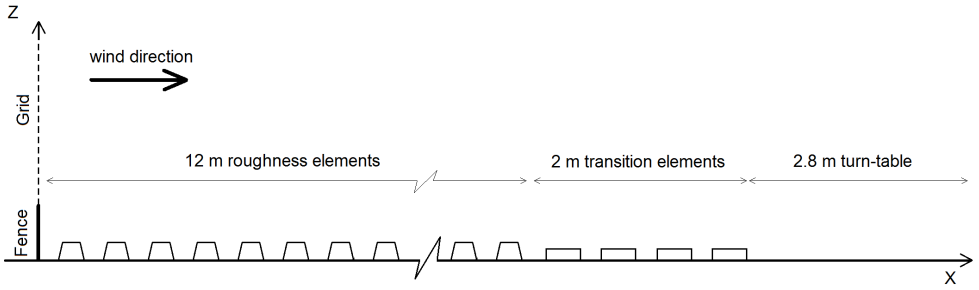

Figure 3: Atmospheric boundary layer generation technique.

Element	Number	Description	Size (L x W x H) [mm]
Fence	1	wooden board	- x 3 000 x 150
Grid	1	metal mesh	- x 3 000 x 2 000
Roughness el.: Cup 1	6 rows of 24 el. + 23 rows of 12 el. [420]	plastic, conical shape	30-40 x 30-40 x 32
Roughness el.: Cup 2	6 rows of 24 el. + 23 rows of 12 el. [420]	plastic, conical shape	45-70 x 45-70 x 100
Transition elements	7 row of 12 elements [84]	wooden cubes	50 x 120 x 20

Table 1: Description of boundary layer generators.



Figure 6: Triple hot-wire probe.

55P91: [16; 17], Fig. 6).
The probe has three orthogonal wires; they define a frame (X1, X2, X3) that is rotated in two directions from the test section frame (U,V,W) (or (X, Y, Z)). A rotation matrix R can therefore be defined with two angles $\theta = 45°$ and $\phi = 35.3°$ such as:

$$R = \begin{pmatrix} cos\,\phi \times cos\,\theta & cos\,\phi \times sin\,\theta & sin\,\theta \\ -sin\,\theta & cos\,\theta & 0 \\ -sin\,\phi \times cos\,\theta & -sin\,\phi \times sin\,\theta & cos\,\theta \end{pmatrix} \quad (4)$$

Foe the velocity calibration, the output voltage(E) of each wire is related to the effective cooling velocity U_{eff} by a 4th order polynomial curve:

$$U_{eff} = P_0 + P_1.E + P_2.E^2 + P_3.E^3 + P_4.E^4 \quad (5)$$

with P_i: coefficients of the polynomial fit.

Each effective cooling velocity is then related to the three components of the velocity in the frame of the wires (X1, X2, X3) using the Jørgensen law:

$$U_{eff}{}^2 = U_N{}^2 + U_B{}^2.k^2 + U_T{}^2.h^2 \quad (6)$$

with U_N: velocity component normal to the wire; U_B: velocity component bi-normal to the wire; U_T: velocity component tangential to the wire; h: yaw angle coefficient and k: pitch angle coefficient.

For this particular probe, the three wires are orthogonal, then, the normal direction of the first wire is the tangential direction of the second wire as well as the bi-normal direction of the third wire. This relationship is maintained in a cylindrical order. The resolution of the Jørgensen law is then simplified to:

$$\begin{pmatrix} U_{eff_I}{}^2 \\ U_{eff_{II}}{}^2 \\ U_{eff_{III}}{}^2 \end{pmatrix} = \begin{pmatrix} k_I{}^2 & 1 & h_I{}^2 \\ h_{II}{}^2 & k_{II}{}^2 & 1 \\ 1 & h_{III}{}^2 & k_{III}{}^2 \end{pmatrix} . \begin{pmatrix} X_1{}^2 \\ X_2{}^2 \\ X_3{}^2 \end{pmatrix} \quad (7)$$

with U_{eff_i}: effective cooling velocity of the wire (i); X_i: velocity in the frame of the wires and (h_i, k_i): yaw and pitch coefficients of the wire (i).

The values of the pitch and yaw coefficients are determined by aerodynamic (angular) calibration.
This calibration depends only on geometrical considerations and has to be performed only once. For this study, as commonly done in the literature, these coefficients are considered as constants ($h_I = h_{II} = h_{III}$) and equal to the default value given by the manufacturer.
A precise calibration is nevertheless planned in the future.

The volume of the probe is rather important (6 mm diameter), therefore, measurements are taken

only at a few positions in the vertical profile.
For this study, the acquisition time is 120 seconds at a sampling frequency of 3 kHz. The signal is filtered with a 1 kHz low-pass filter.

The measurement of the three components at a high sampling frequency is necessary to compute, in the three directions, the turbulent intensity, shear stresses, integral length scales and power spectra.

3.4. Preliminary results

The use of the triple hot-wire allows a deep characterization of the wind tunnel profile in mean and fluctuating quantities. Measurement are performed to determine the rule of each of the ABL generation devices in the modelling of atmospheric inflows.
Other measurements, like transversal profiles, are performed to assess the quality of the flow.
These data are under post-processing and will be compared with a numerical work performed at the wind tunnel scale in different configurations.

4. Test on a real complex terrain

4.1. Test case

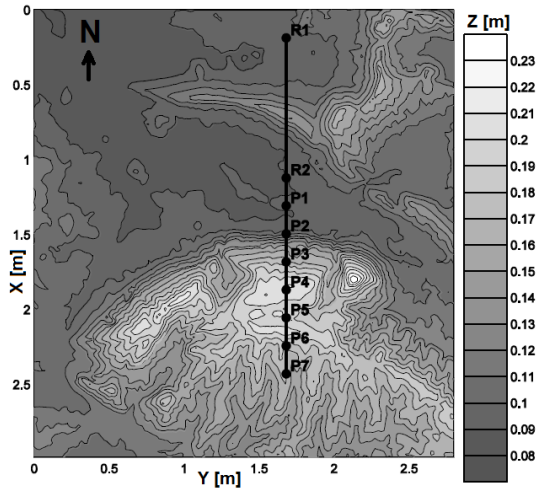

Figure 7: View of the area simulated around Alaiz mountain.

The test case selected for this study is the Alaiz mountain (Fig. 7). This is a very complex terrain with steep slopes situated in Navarra, South from Pamplona, in the North of Spain [18; 19]. The terrain is a mountain 1130 m high surrounded by sloping terrain in the North and very complex topography in the South. It is more than 12 km long in the W-E direction. Wind turbines farms are already installed on site in the Southern part. The test case, selected for its complexity, is also being studied by 2D numerical simulations at the wind tunnel scale [20].
One of the most probable wind direction indicated by the wind rose is North, it is the one chosen for the wind tunnel tests.
The choice of the modelled area is supported by the will to include the 200 m high (with respect to the local height) transversal ridge situated upstream of the mountain. This ridge is approximately 1/3 of the mountain height and situated 4 km to the North, however, its influence on the mountain is expected to be non-negligible. The area chosen is then 16 km long in the wind direction and 15 km in the W-E direction (Fig. 7). To fit in the wind tunnel, the mock-up is 2.8 m wide x 3 m long. That leads to a scaling factor of 1/5357. This choice implies non-quantified effects due to the high scaling factor. The blockage in the wind tunnel is approximately 7.8%.

The mock-up is made out of blocks of Necuron directly drilled from the same 3D numerical mesh used by numerical modellers provided by CENER [1]. The model was fabricated at UPM [2] on a numerical tool with 1/10 mm precision. The final surface roughness is approximately = 10 m. This first mock-up does not take into account the real surface roughness and the roughness changes of the terrain. The surface finishing can be considered smooth. It is a baseline for future studies where roughness elements can be added.

For this simulation, the boundary layer is generated by a fence, a grid and 30 mm high cups roughness elements. Figure 8 describes the inlet velocity profiles obtained. The inlet conditions are simulating an aerodynamic roughness length of z_0 = 2.2 m in the real scale. The friction velocity is u_* = 0.68 m/s.
Comparing to the VDI guidelines and ESDU classification [8; 9], the turbulence intensity in the three directions models a ”rough” to ”very rough” terrain (Fig. 8). This is consistent with the high aerodynamic roughness length in the wind tunnel. The inflow reproduction has to be confirmed with field data.

A spectrum analysis is performed to evaluate the energy distribution in the three directions at 500

[1] National Renewable Energy Center of Spain
[2] Universidad Politecnica de Madrid, Spain

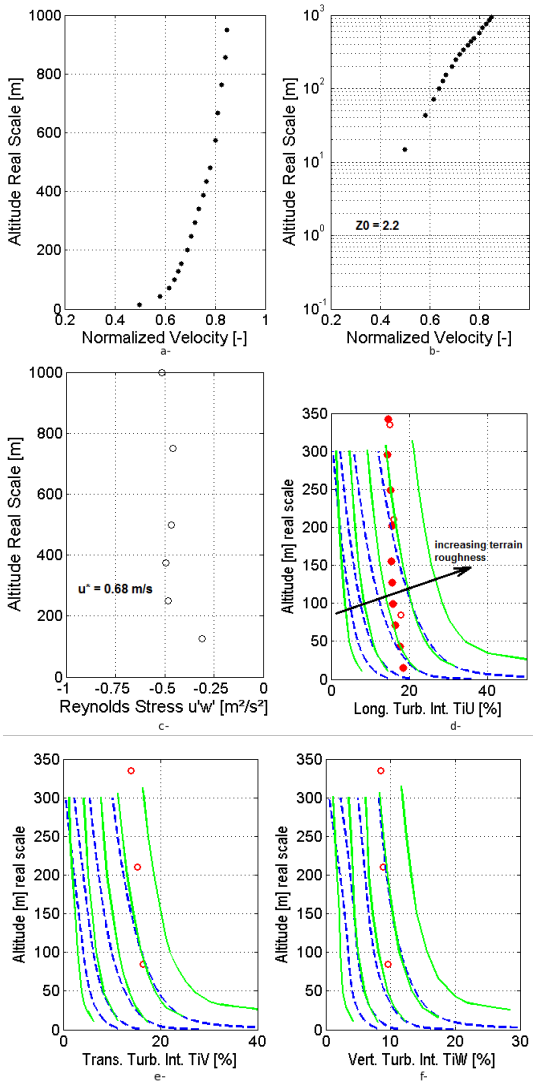

Figure 8: Description of the inlet conditions. (a-): inlet velocity profile; (b-): determination of he roughness length z_0; (c-): Reynolds stress and determination of the friction velocity u_*; (d-), (e-) and (f-): comparison of turbulent levels with norms. Legend: (•) single hot-wire measurement; (○) triple hot-wire measurements; (-) VDI guidelines and (- -) ESDU.

m height (Z = 100 mm at wind tunnel scale) at the position R1 (Figure 7). The measured spectra are compared with the Kaimal [21] spectra in Figure 9. Current studies are trying to improve the spectrum quality along the profile.

Due to the very large scaling factor, inlet conditions are difficult to fit with the guidelines close to the wall. The model being rather smooth, an inner boundary layer is growing at the link between roughness elements and the model itself, the production of kinetic energy is decreased next to the wall. That may be the explanation for the decrease of the wall shear stress and the low turbulent levels next to the ground (Fig. 8). Further investigation are planned to improve the modelling of inlet conditions at very large scale. The model roughness is also an area of research.

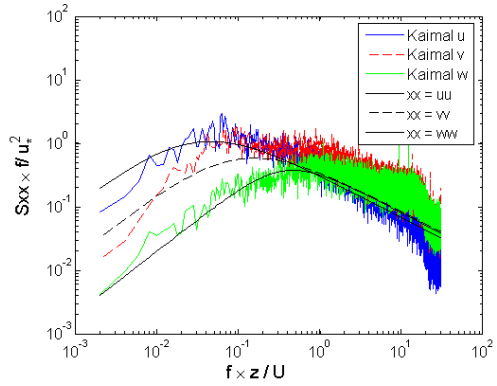

Figure 9: Comparison of Kaimal spectra with measured data at Z=500 m real scale.

4.2. *Measurement techniques*

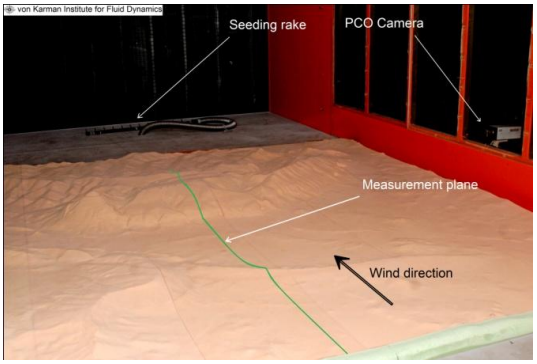

Figure 10: PIV set-up.

4.2.1. *PIV implementation in the wind tunnel*

To measure the wind over the modelled mountain, the Particle Image Velocimetry technique (PIV) is implemented in the wind tunnel [22]. It is performed in a 2D vertical plane aligned with the wind direction to allow an easy comparison with 2D numerical simulation (Fig. 7 from R2 to P6). This non-intrusive technique is able to provide instantaneous 2D velocity vector fields with both longitudinal and vertical components (U, W).

In the wind tunnel, a double pulsed mini-Yag laser is placed on the ceiling of the test section and lights the model from the top with a laser sheet. The 3D shape of the terrain leads to important light scatter, the major part is avoided by painting the mock-up in mat black.
A PIV camera is placed outside the test section and takes images through the side window of the tunnel (Fig. 10).
Due to the close return circuit, the seeding rake placed downstream of the model ensures a homogeneous distribution of the particles and prevents perturbations in the incoming flow. Seeding problems found by Siddiqui [6] are not encountered here.
The complete system is synchronised to record images at 3 Hz. This rate does not allow the resolution of the flow in time but it provides statistics of the most important flow quantities. In this study, the number of images is chosen as 500 to have enough images for the convergence of the mean value.
The area of interest is larger than the field of view of the camera. Therefore, it is divided in six overlapping planes. Image recording is performed at different times and the final plane is reconstructed in post-processing. Some discrepancies may occur at the link between two planes, they can be reduced by increasing the number of samples.
The post-processing is done by an in-house code [23]. The choice of the final interrogation windows size leads to a longitudinal and vertical resolution of around 10 m at real scale, that is 10 velocity vectors for a 100 m profile.

4.2.2. Single wire measurements

In addition to PIV, traverses are performed on the mountain, at discrete points (R2 to P7 in Fig. 7) with a single wire hot-wire probe (CTA). The aim is to validate PIV data and to get missing information such as the integral turbulence length and the turbulent spectra.
This technique is preferred to triple hot-wire anemometry because it is simpler to use and it is able to perform measurements at high spatial resolution next to the wall.
The probe, orientated in the vertical direction is calibrated in-situ with a static Pitot probe, the calibration curve is fitted with a 4th order polynomial. The acquisition time is 120 s with a frequency set to 1 kHz and 300 Hz low pass filter.

4.2.3. Comparison of measurement techniques and error analysis

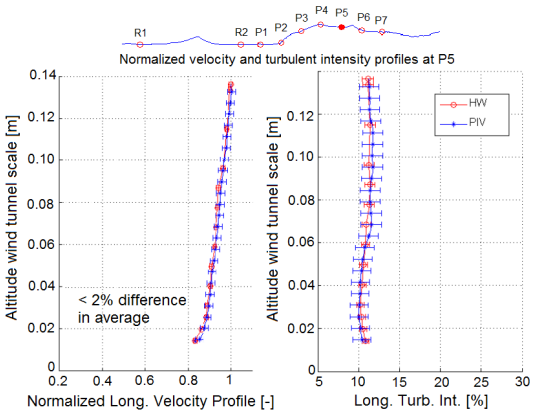

Figure 13: Comparison PIV and single hot-wire measurements.

From Figure 13, the PIV and hot-wire anemometry techniques give very similar results for the wind speed over the topography. To make a fair comparison, each profile is normalized by the velocity at the same height. In the comparison between measurement techniques at position P5, differences are less than 1% for averaged quantities and around 2% for fluctuating quantities. At all tested positions both techniques agree very well.
The measurement error of the PIV data is 1.5% approximately and 2% for the hot-wire anemometry. The statistical uncertainty analysis is performed by taking into account only independents samples. For the PIV the uncertainty leads to 1.5% at 95% confidence level for the mean quantities in the free-flow and 8% uncertainty for fluctuating quantities at the same confidence level. For hot-wire, the uncertainty analysis gives 1% error for the mean value and 5.7% for the fluctuating values at 95% confidence level. Results are reported in Figure 13 with the statistic uncertainty.
The two techniques are comparable in terms of error. In literature, errors reported are of the same order of magnitude or higher [6]. In both techniques this uncertainty can be decreased by increasing the number of samples.

In the wind tunnel, the hot-wire technique has the advantage of providing a time resolution two orders of magnitude higher than PIV. This information is essential for the characterization of the atmospheric modelling in terms of length scales and turbulent spectra. However, the measurement with single

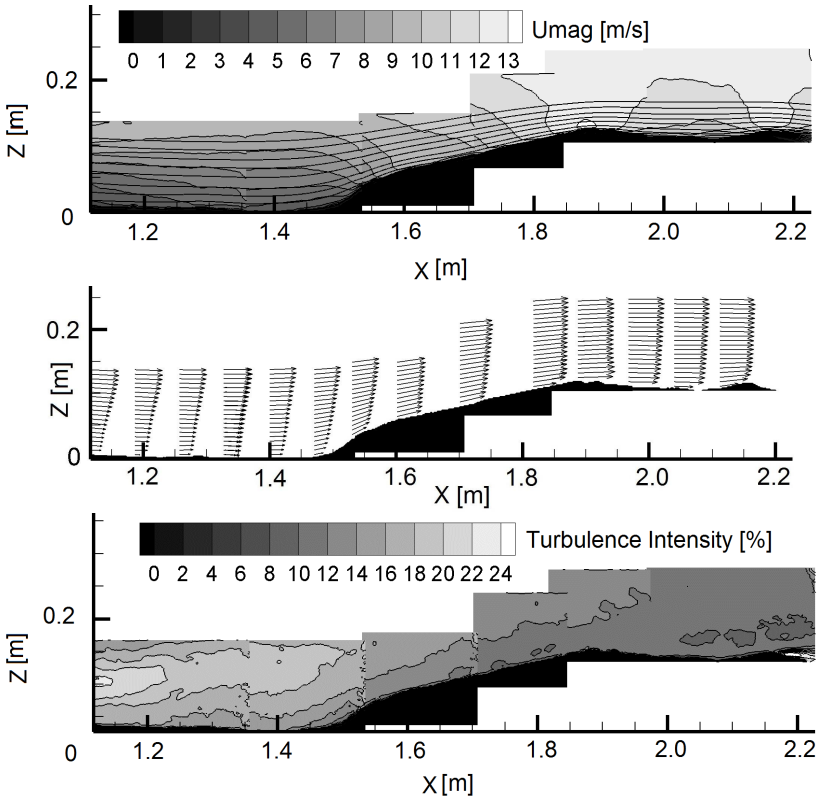

Figure 11: Mean velocity, vector field and turbulence level extracted from PIV measurements.

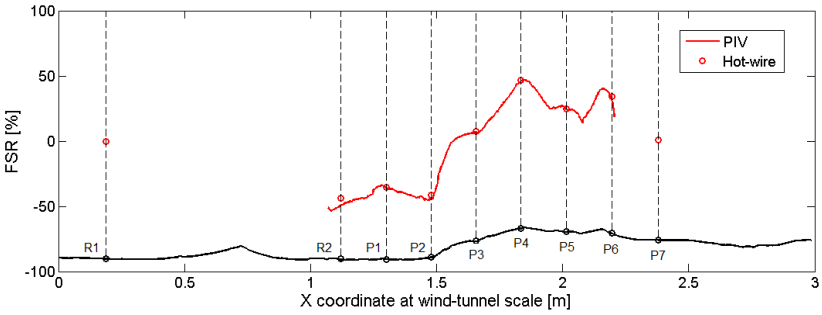

Figure 12: FRS at 90m real scale.

hot-wire is punctual, unidirectional and intrusive.
On the other hand, despite its lack of time resolution, Particle Image Velocimetry provides very high space resolution. Instantaneously, a 2D field of vector is measured. This feature has the advantage of providing the instantaneous information on the velocity profile over the model.

4.3. Results discussions

The average velocity field is reconstructed from the six PIV planes in Figure 11. As expected from literature [4; 5; 24; 25], the mountain creates a blockage effect leading to an over-speed at the top of it. On the figure, converging streamlines are showing this effect.
The turbulence intensity upstream the mountain is important, a peak, not present in the inlet profile, is clearly appearing in the contour plot at Z $\approx$ 0.08 m, this is approximately the front ridge height at the wind tunnel scale. This may be the sign of a flow separation after the front ridge. The disturbed velocity profile shown in the vector plot reinforces

this hypothesis.

Additionally the Fractional Speed-up Ratio (FSR) is computed, it is defined as the ratio of change of the wind speed due to the terrain:

$$FSR_P = \frac{U_P - U_{ref}}{U_{ref}} \quad (8)$$

with FSR_P: Fractional Speed-up Ratio at the position P; U_{ref} :velocity at the reference upstream position; U_P: velocity at the position P.

The FSR is equal to zero at the reference point, here it is the inlet profile (position R1 in Fig. 8) at 90 m a.g.l.. The FSR is giving the ratio of change of the velocity with respect to this reference point.

From Figure 8, the FSR at position R2 is negative. That means that the front ridge (X = 0.75 m) induces a wind speed reduction of almost 50% at the position R2 compared with R1. The FSR curve is then increasing until P1, the flow recovers from the upstream perturbation. Between P1 and P2, the FSR decreases again, this is a velocity reduction due to the presence of the mountain creating a blockage, so a speed-down at the mountain foot.

Compared to the reference R1, the wind is still under perturbation when it reaches the main mountain at P2 (X = 1.5).
Along the slope, the wind dramatically increases to reach a maximum at the top of the mountain. Next to the position P4, the over-speed is almost 100% compared to the bottom of the hill (P1). This phenomenon is very often used to increase the profitability of a wind farm.

However, due to the perturbation of the front ridge, this over-speed is damped and leads to only 50% increase compared to R1. The upstream ridge influences a lot the turbulence intensity, its perturbation is still visible on the main mountain. This important effect with a probable separation justifies the extension of the area modelled until the upstream ridge.

Numerical simulations performed on this test case are matching quite well with experimental results [20]. A comparison with field data is the next step.

The study underlines the marked influence of an upstream minor topography on a mountain. In this case, the choice of a very high scaling factor is justified by the large influence of the upstream ridge on the mountain in terms of wind speed and turbulence intensity.

5. Conclusions and Future investigations

The study of wind on mountainous terrain performed with wind tunnel physical modelling is giving promising results.

The ongoing research on the characterization of the flow in the wind tunnel will allow to find the best way to model different roughness lengths at different scales.
The study of the mountain shown that, for very high scaling factors, the reproduction of the atmospheric inflow is a challenge because the production of turbulence in the near-wall region is too low. The boundary layer generators necessary to model the inlet flow are not in adequacy with the model surface roughness. The inlet boundary layer is therefore adapting to the model roughness and it is not sufficient to maintain enough turbulence next to the wall.
At very high scales, the model roughness may be oversized to reproduce the production of turbulent kinetic energy. In the future, attention will be paid to have the same order of roughness between the inlet flow and the model.

In this work, PIV appears to be a very suitable tool for micro siting studies in a wind tunnel. Measurements can provide field of average and fluctuating information with a fairly good spatial resolution and accuracy.
Complementary to PIV, hot-wire measurements have the advantage of a very high temporal resolution that enables spectral and integral scales studies.
Tests can therefore be conducted first by PIV, to scan the model and to detect high wind resource areas. Then, fine characterization with time resolved information in the three directions can be performed at the most interesting zones using hot-wire anemometry.
In the future, to fill the need for three component measurements (shear stresses, turbulence intensities, integral length scales...), the possibility of scanning the terrain with 2D-3C PIV together with time resolved multi-component hot-wire measurements has all arguments to be a very fast, accurate and powerful tool for the assessment of wind in very complex terrain. The technique will be first implemented in a

smaller wind tunnel.

The Alaiz mountain is creating a very important speed-up, almost 100% compared to its foot. However, due to the presence of the upstream ridge, this speed-up is reduced to 50% compared with inlet conditions. The turbulence intensity is very affected as well.
This study underlines the important influence that an upstream topography can have on a three times higher mountain situated 4 km downstream.
This statement leads to model a larger area, the setback is the increase the Reynolds number mismatch. In this case where geometries are not considered as bluff-bodies (i.e. sharp-edged bodies), the Reynolds number may trigger different flow behaviours, the dependency on the Reynolds number remains an open question.

Lots of questions are similar to numerical modelling: inlet conditions, surface roughness, Reynolds number, area to consider. The quantification of the influence of each modelling parameters is a current area of research. Future field data will contribute as well to the improvement of the physical modelling assumptions.

Acknowledgments

I would like to address a special thanks to S. Buckingham for her support on testing and data processing. This work is realized with the financial support of the European Commission within the WAUDIT Marie Curie Initial Training Network. FP7-PEOPLE-INT-2008-238576.

References

[1] European Wind Energy Platform: http://www.windplatform.eu/.
[2] S. Aubrun, B. Leitl, Development of an improved physical modelling of a forest area in a wind tunnel, Atmospheric Environment 38 (18) (2004) 2797–2801.
[3] "wind tunnel simulation of the wind conditions inside bidimensional forest clear-cuts. application to wind turbine siting.
[4] T. Takahashi, K. e. a. Shinsuke, Wind tunnel tests of effect of atmospheric stability on turbulence flow over a three-dimensional hill, in: 11th Int. Con. On Wind Engineering, Texas, USA.
[5] H. Kim, C. Lee, H. Lim, N. Kyong, An experimental and numerical study on the flow over two-dimensional hills, Journal of Wind Engineering and Industrial Aerodynamics 66 (1) (1997) 17–33.
[6] K. Siddiqui, H. Hangan, A. Rasouli, PIV technique implementation for wind mapping in complex topographies, Measurement Science and Technology 19 (2008) 065403.
[7] J. Cermak, Laboratory simulation of the atmospheric boundary layer, AIAA Journal 9 (9) (1971) 1746–1754.
[8] VDI-Guidelines 3783/12. Physical modelling of flow and dispersion processes in the atmospheric boundary layer - application to wind tunnels., Beuth Verlag, Berlin, 2000.
[9] ESDU Engineering Science Data Unit. Charasteristics of atmospheric turbulence near the ground, 1985.
[10] Eurocode 1: Action on StructuresPart 1-4 Wind Actions (2004).
[11] J. Garratt, The atmospheric boundary layer, Cambridge Univ Pr, 1994.
[12] C. Farell, A. Iyengar, Experiments on the wind tunnel simulation of atmospheric boundary layers, Journal of Wind Engineering and Industrial Aerodynamics 79 (1-2) (1999) 11–35.
[13] A. Iyengar, C. Farell, Experimental issues in atmospheric boundary layer simulations: roughness length and integral length scale determination, Journal of Wind Engineering and Industrial Aerodynamics 89 (11-12) (2001) 1059–1080.
[14] H. Kozmar, Natural wind simulation in the TUM boundary layer wind tunnel, in: Proceedings of the 4th EACWE, Florence, Italy, 2009.
[15] T. Balendra, D. Shah, K. Tey, S. Kong, Evaluation of flow characteristics in the NUS-HDB Wind Tunnel, Journal of Wind Engineering and Industrial Aerodynamics 90 (6) (2002) 675–688.
[16] H. Bruun, Hot-wire anemometry, Oxford University Press Oxford, 2002.
[17] C. Yeung, L. Squire, Numerical calibration and verification tests of an orthogonal triple-hot-wire probe, Measurement Science and Technology 4 (1993) 1446.
[18] D. Cabezón, J. Sanz, J. Van Beeck, Sensitivity analysis on turbulence models for the ABL in complex terrain, in: Proceedings of the European Wind Energy Conference, 2007.
[19] D. Cabezón, A. Iniesta, E. Ferrer, I. Martí, Comparing linear and non linear wind flow models, in: Proceedings of the European Wind Energy Conference EWEC, 2006.
[20] D. Munos Esparza, B. Conan, E. e. a. Croonenborghs, Sensitivity to inlet conditions of wind resource assessment over complex terrain using three CFD slovers and wind tunnel data, in: Proceedings of the European Wind Energy Conference EWEA, 2011.
[21] J. Kaimal, J. Finnigan, Atmospheric boundary layer flows: Their structure and measurement, 289 pp (1994).
[22] M. Raffel, C. Willert, S. Wereley, Particle image velocimetry: a practical guide, Springer Verlag, 2007.
[23] F. Scarano, Iterative image deformation methods in PIV, Measurement Science and Technology 13 (2002) R1.
[24] K. Ayotte, D. Hughes, Observations of boundary-layer wind-tunnel flow over isolated ridges of varying steepness and roughness, Boundary-Layer Meteorology 112 (3) (2004) 525–556.
[25] K. Kondo, M. Tsuchiya, S. Sanada, Evaluation of effect of micro-topography on design wind velocity, Journal of Wind Engineering and Industrial Aerodynamics 90 (12-15) (2002) 1707–1718.

Forecasting of offshore boundary layer conditions using high resolution WRF-PBL schemes for wind energy applications

Domingo Muñoz Esparza

Environmental and Applied Fluid Dynamics Department, domingo.munoz.esparza@vki.ac.be

Supervisor: Jeroen van Beeck

Professor, Environmental and Applied Fluid Dynamics Department, von Karman Institute for Fluid Dynamics, vanbeeck@vki.ac.be.

Promoter: Jean-Marie Buchlin

Professor, Faculté des sciences appliquées , Université Libre de Bruxelles, buchlin@vki.ac.be.

Abstract

Nowadays, wind energy is increasing its contribution into the energy market. Because of that, accurate predictions of the power production are needed and thus, wind speeds need to be properly forecasted. This study shows the ability of the WRF model reproducing Marine Boundary Layer conditions under different stability scenarios. Results are validated against field measurements from FINO1 platform, located in the North Sea.

Keywords: Mesoscale modelling, marine boundary layer, wind energy, weather forecast, stability, FINO1 mast

1. Introduction

Nowadays, numerical weather prediction (NWP) models are commonly used by the wind energy industry for different purposes. They are employed to prognosticate the power out-put of wind farms and to estimate the wind resources of a given area, among others.

One of the advantages of these NWP models is that they are capable to forecast a few days ahead events based on a reduced set of information provided on a very coarse spatial and time resolution, which normally is about 1° and 6 hours, respectively. On the other hand, the standard horizontal discretization of such models is in the order of 10 km, with the corresponding difficulties to handle turbulent processes.

The effect of the vertical mixing due to turbulence in the planetary boundary layer (PBL) is not explicitly resolved by mesoscale models. NWP models parameterize this effect assuming the so-called closure techniques based on gradients of resolved quantities. For some applications, such as wind energy, where the near-surface atmospheric processes are crucial, the choice of PBL modelling becomes an important issue.

The influence of the turbulence closure scheme to predict offshore PBL conditions is analyzed using the Weather Research and Forecasting (WRF-ARW) open-source code. Two periods of stable and convective-neutral boundary layer characteristics are selected based on both sonic anemometer measurements of Obukhov lengths and Brunt-Väisälä frequencies at FINO1 platform, located in the North Sea.

2. FINO1 offshore platform

The FINO1 measurement platform is located 45km north of the island Borkum in the North Sea (lat. $54^o0.86'$ N, lon. $6^o35.26'$ E). The height of the measurement mast is 100m [1]. Seven cup anemometers are installed at heights of 30m to 100m on booms mounted in southeast direction of the mast. One cup anemometer is mounted at the top of the mast at 100m height. Three ultrasonic anemometers are present at heights of 40m, 60m, and 80m on north-westerly oriented booms [2]. Additional meteorological measurements consist of wind direction, air temperature, moisture, air pressure and solar irradiation. Data from January 2005 to December 2005 has been used in this study. The data set contains about 52.560 records of

10-minute averaged values for each one of the variables. A general view of the mast is shown in Fig. 1.



Figure 1: FINO1 measurement mast.

2.1. Data corrections

The FINO1 measurements were obtained from [3], where 10-minute averaged data is available. This row data does not include any kind of correction. First of all, the measurements were controlled by discarding data exceeding set limits (wind speed higher than 35ms^{-1} or lower than 0ms^{-1}, temperature higher than 30°C or lower than -15°C), based on the instrument limitations and the prevalent weather conditions over North Sea. In addition, gradients of temperature higher than -5°C/10min where investigated to find possible spikes even considering 10 min averaged values. Interpolation was applied to reconstruct punctual values considered as spikes or missing data. Furthermore, prolonged anomalous values were discarded and are not considered hereafter.

After filtering the data to remove unphysical values and having defined the periods of quality data, the wind rose and the associated Weibull distribution were computed based on 100m height cup anemometer velocities and direction form 90m height vane. They are shown in Fig. 2. It can be observed that the main winds come from South and South-West directions. The frequency distribution of winds fits quit well to the Weibull distribution with the parameters: $A = 11.36$ms^{-1} and $k = 2.396$, considering that only data from one year was used. As mentioned before, there are both cups and sonic anemometers at FINO1.

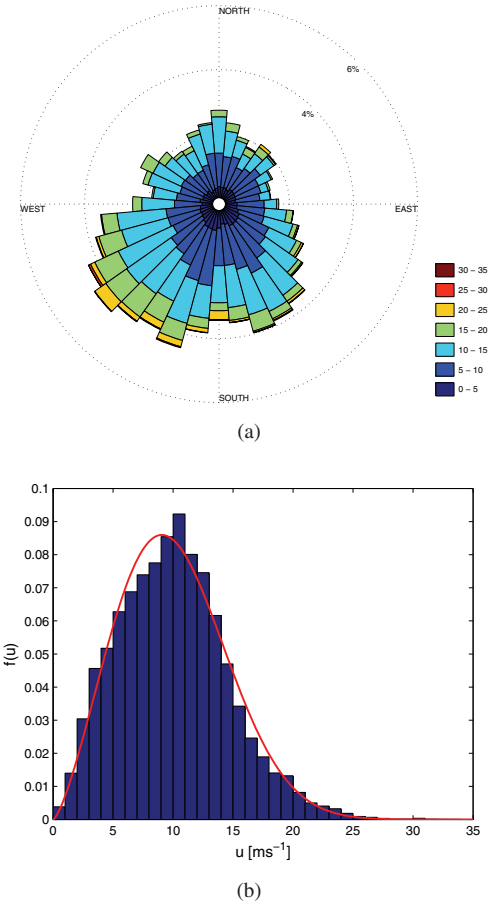

Figure 2: (a) Wind rose at FINO1. Wind direction at 90m and wind speed at 100m from cup anemometer (January - December 2005). (b) Weibull distribution, $A = 11.36$ms^{-1} and $k = 2.396$.

The cup anemometers are located at the upper part booms, North-West direction, whereas the cups are placed on the lower part booms, South-East direction (see Fig. 3). From the arrangement showed in Fig. 3 some effects are expected depending on the wind direction [4]. To quantify these effects the velocity at 100m has been ploted vs. the velocity at 90m (Fig. 4a). There, two different slopes are detected. One of them close to 1 (expected value) and the other one close to 0.7. The last one is explained in Fig. 4b. This behaviour is attributed to the shadow effect of the tower over the cup anemometers when the wind is blowing from 280-360° sector. The tower produces a decreasing of the incoming velocity at 90m that is not present at 100m and because of that the ratio increases dramatically reaching values around 1.8. Small disturbances at about 90°, 180°, 270° and 360° wind direction are found, which probably origin from the bars

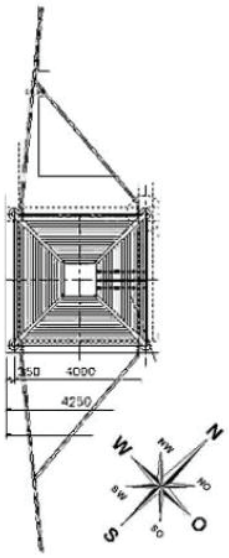

Figure 3: Orientation of sonic (upper booms) and cups anemometers (lower booms) at FINO1. Top view of the platform.

of the lightning protection cage of the cup anemometer. Due to this effect, cup anemometers measurements are discarded if $280^o < wd < 360^o$, where wd is the unperturbed wind direction. Equivalent behaviour is found for all the heights. The sonic anemometers are much more sensitive to the environment, needing corrections against: tilting, humidity and directionality [5]. High frequency row data (0.5Hz) is needed in order to perform all the corrections. Due to the impossibility to have access to that data, only measurements from the cup anemometers are considered hereafter. Notwithstanding, cup anemometers allow one to have a better spatial coverage of the lower part of the boundary layer, from 30m to 100m with a 10m step. Taking into account the different sources of error, the velocity measurements provided by the cup anemometers can be estimated to have an uncertainty of 5% [6].

3. Stabiliity classification

The wind speed profile in the atmospheric surface layer is commonly described by Monin-Obukhov Stability Theory (MOST). In homogenous and stationary flow conditions, it predicts a log-linear profile [7].

$$u(z) = \frac{u_*}{k}\left[\ln\left(\frac{z}{z_0}\right) - \Psi_m\left(\frac{z}{L}\right)\right] \quad (1)$$

where u_* is the friction velocity, k the von Karman constant (~0.4), L is the Obukhov length and Ψ_m is a

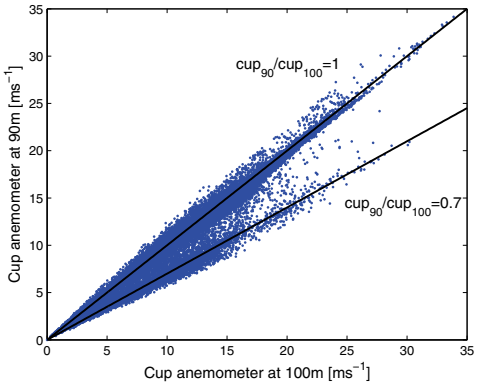

(a)

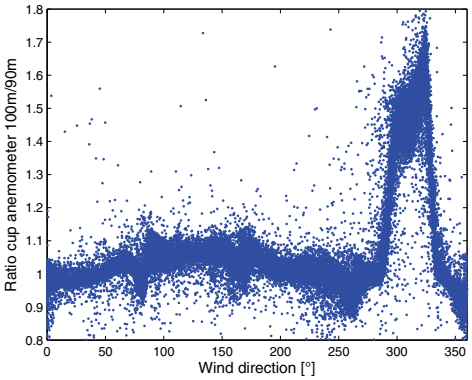

(b)

Figure 4: (a) Cup anemometer measurements at 90m vs. 100m. (b) Ratio cup anemometer 100m/90m as a function of wind direction.

universal stability function. The Businger-Dyer formulation [8], based on the Kansas experiment, is the most widely used and has two expressions, one for unstable (Eq. 2) and another for stable conditions (Eq. 3). For neutral stability $\Psi_m = 0$.

$$\Psi_m = 2\ln\left(\frac{1+x}{2}\right) + \ln\left(\frac{1+x^2}{2}\right) - 2\tan^{-1}(x) + \frac{\pi}{2} \quad (2)$$

$$\Psi_m = -\beta \cdot \zeta \quad (3)$$

where $x = (1 - \gamma \cdot \zeta)^{1/4}$ and $\zeta = z/L$. $\gamma = 19.3$ and $\beta = 4.8$ based on Högström [9].

As can be regarded from Eq. 1, the stability of the atmosphere plays an important role on the wind potential as well as on the wind shear across the rotor area. These two issues motivate the study of the wind conditions under different stability regimes.

There are different ways that are commonly used to estimate the atmospheric stability [10]. The sonic

method determines L directly from sonic anemometer measurements of friction velocity and heat flux:

$$L_{sonic} = -\frac{u_{*s}^3}{k\frac{g}{\overline{T}}\overline{w'T'_s}} \quad (4)$$

where $\overline{w'T'_s}$ is the covariance of temperature and vertical wind speed fluctuations at the surface, u_{*s} the surface friction velocity, $\overline{T}$ the reference temperature and g the gravitational acceleration. Other methods are based on the estimation of L using the gradient Richardson number, the gradient and bulk methods.

Another parameter which can be used to identify the stability class is the Brunt-Väisälä frequency, N. This parameter is also referred as buoyancy frequency and represents the frequency at which a vertically displaced parcel of air will oscillate within a statically stable environment.

$$N^2 = \frac{g}{\theta}\frac{\partial\theta}{\partial z} \quad (5)$$

where θ stands for the potential temperature.

For the FINO1 available data, the sonic method could not be applied due to the fact that only 10 min averaged values of velocity magnitude were available, being impossible to compute turbulent fluxes of momentum and temperature. The same situation happened for the bulk method because of the absence of air and sea temperature measurements and wind speed at 10m height. To apply the gradient method, 30m was the lowest level with simultaneous velocity and temperature measurements. Indeed, the Obukhov length is a characteristic length scale for the surface and considering those levels can produce an underestimation of L [11]. Because of that and taking into account that 10 min averages introduce as well some errors on the calculation of L, the obtained results have not been considered.

Stable and unstable periods based on sonic anemometer values at 40m have been considered by Sušelj et al. [12; 13]. The considered stable period is form 16 March 2005 at 00 UTC to 18 March at 00 UTC, where $0.003 < 1/L < 0.021$. The selected unstable period is shorter, 08 February 2005 at 13 UTC to 09 February 2005 at 06 UTC with $-0.04 < 1/L < -0.005$. The calculated Brunt-Väisälä frequency for the same periods is plotted in Fig. 5.

Based on the results of N^2, the period of 09 February 06 UTC to 10 February 00 UTC can be classified as near-neutral (weak stable) conditions and will be the third selected time interval to cover all the possible stability situations. A good agreement was found among both techniques. These results are further confirmed by plotting the vertical profiles of velocity measured at FINO1 (Fig. 6), for the above presented periods. The neutral velocity profile has been included for clarification (z_0=2mm). This justify the right choice of the simulation time intervals to address all the possible stability scenarios.

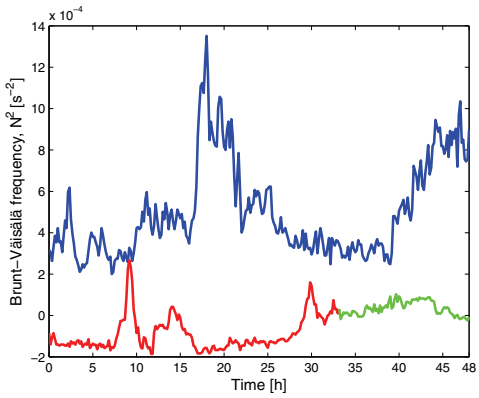

Figure 5: Brunt-Väisälä frequency, N^2, for the stable case (blue line) the starting hour is 16 March 2005 at 00 UTC. The unstable period starts the 08 February 2005 at 00 UTC (red line). Near-neutral period (green line) starts the 09 February 2005 at 09 UTC.

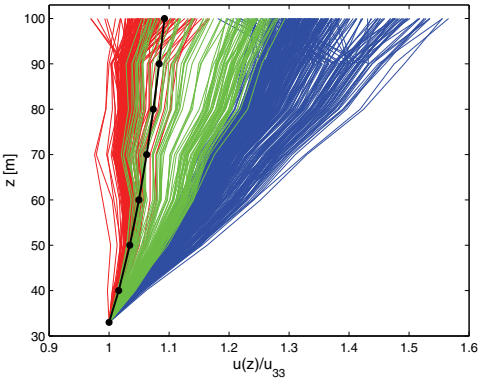

Figure 6: Velocity profiles for the different stability classes. The black line shows the neutral profile (z_0=2mm). The time periods are the same that in Fig. 5.

The synoptic activity was checked by representing the sea level pressure for the selected dates (not shown). For the unstable and near-neutral scenarios, the low pressure system resides over Northern Atlantic (sea level pressure minimum is located above Iceland) and the high pressure system falls around central Europe. For the stable case, the low pressure system resides over the Atlantic and high pres-

sure over the southern Europe. During the simulation time, the high pressure system moves in the northwest direction. The days were selected with no strong synoptic activity which could not be accurately reproduced by limited area models. The absence of incoming wind from $280^o < wd < 360^o$ allows one to use the cup anemometer data for the complete period of study.

4. Weather Research and Forecast, WRF

The NWP model developed by the National Center for Atmospheric Research (NCAR): Advance Research WRF-ARW v3.2 is used in this study. WRF-ARW is a conservative finite differences model that solves the non-hydrostatic compressible Euler equations [14].

The computational domain is composed by 4 domains centered over FINO1 platform. The parent domain has a horizontal grid spacing of 27 km and covers an approximate surface of 3000 km^2. Grid spacing is refined progressively by a factor of 3 through three nested domains until 1 km resolution is achieved for the most inner one, which covers approximately 100 km^2. The vertical grid has a resolution of 10m below 150m. Interactions of the meteorological fields between the domains are accounted for by two-way nesting. The domain configuration is shown in Fig. 7. The time-step is consistently reduced from the parent domain to the most inner domain in order to respect numerical stability constraints (CFL<1). WSM 3-class simple ice scheme microphysics, rapid radiative transfer in the longwave, the Dudhia shortwave scheme, NOAH surface scheme and cumulus Kain-Fritsch scheme (not applied into the two most inner domains) were used.

The parent domain is initialized at 0000 UTC (cold initialization) and 6-hourly forced at the boundaries by meteorological fields derived from NOAA Global Forecast System data with a horizontal resolution of 1° x 1°. The first 24h are discarded as spin-up time of the model in order to generate the appropriate kinetic energy spectrum [15] and 48h ahead forecasts are considered.

As previously mentioned, the turbulent parameterization in the PBL influences the accuracy of the simulated winds. To account for that, six different PBL schemes have been tested. Two first order schemes: the Yonsey University, YSU [16] and Asymmetric Convective Model v2, ACM2 [17; 18], and four one-and-a-half order (or TKE closure) schemes: Mellor-Yamada-Janjć, MYJ [19], Mellor-Yamada-Nakanishi-

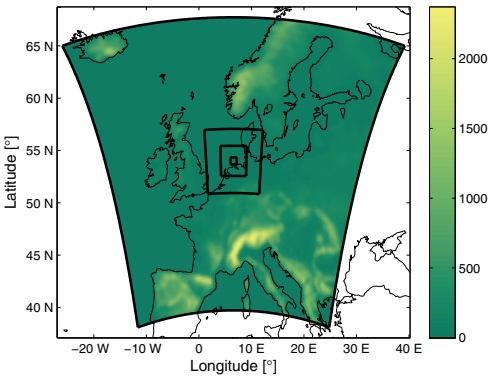

Figure 7: WRF domain configuration. The horizontal resolutions of the four domains are 27 km, 9 km, 3 km and 1 km, from the parent to the most inner domain, respectively. Color bar indicates the altitude of the terrain in meters.

Niino, MYNN [20], Quasi-normal Scale Elimination, QNSE [21] and Bougeault-Lacarrère, BouLac [22]. The differences on the order of closure are briefly described in the following subsection.

4.1. Closure techniques

The turbulent fluxes from momentum, heat and other species in both first and one-and-a-half order closure techniques are formulated similarly [7].

$$< w'\phi' >= -K_z \cdot \left(\frac{\partial \phi}{\partial z} - \gamma \right) \tag{6}$$

where ϕ is a prognostic variable. This kind of modelization is known as gradient transport theory or K-theory. The term γ represents the non-local mixing due to larger convective eddies and it is included or not depending on the scheme. K_z is the eddy diffusivity coefficient, which sometimes has different formulations for momentum and heat. The manner in which K_z is computed introduces the main differences between first and one-and-a-half orders. In first order closure techniques (YSU, ACM2) the eddy diffusivities are calculated in the following way:

$$K_z(z) = \Phi(L) \cdot z \cdot \left(1 - \frac{z}{h}\right)^2 \tag{7}$$

where h is the BL height, L is the Obukhov length and $\Phi(L)$ is a function of stability based on the nondimensional profile functions of heat and momentum [23]. In addition, ACM2 compute K_z as well depending on the gradient of velocity or potential temperature and the local Richardson number and includes some extra terms to explicitly represent the effect of non-local mixing on Eq. 6.

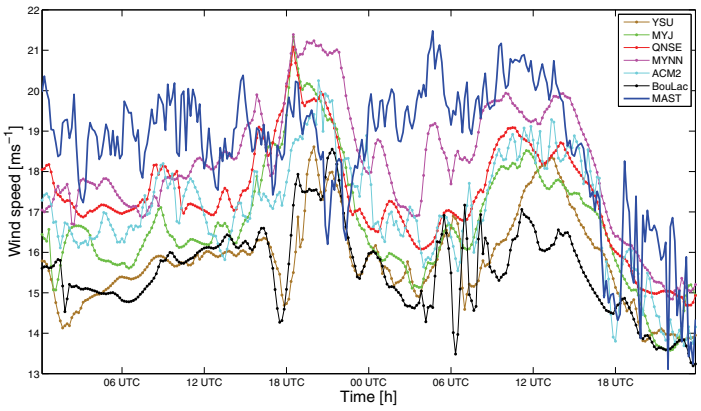

Figure 8: Time evolution of wind speed for the six PBL schemes and FINO1 measurements at z = 100m. Stable period.

Table 1: Statistical metrics to evaluate the accuracy of the six PBL schemes. Thresholds of 1ms $^{-1}$ and 2° are considered for the calculation of the hit rate, HIT, for wind speed, WS, and temperature, T. Stable period at z = 100m.

Scheme	HIT_{WS} [%]	ME_{WS} [ms^{-1}]	$RMSE_{WS}$ [ms^{-1}]	IOA_{WS} [−]	R_{WS} [−]	HIT_T [%]	ME_T [^oC]	$RMSE_T$ [^oC]	IOA_T [−]	R_T [−]
YSU	11.50	-2.83	3.21	0.84	0.46	66.90	-1.74	1.93	0.65	0.14
MYJ	18.47	-1.93	2.60	0.82	0.38	26.83	-2.32	2.40	0.71	0.68
QNSE	24.39	-1.23	1.90	0.82	0.53	2.79	-2.82	2.87	0.74	0.70
MYNN	41.12	-0.44	1.60	0.83	0.55	86.76	-1.18	1.43	0.57	0.22
ACM2	22.65	-1.61	2.13	0.83	0.59	72.13	-1.52	1.80	0.64	0.40
BouLac	9.06	-3.08	3.42	0.84	0.46	73.87	-1.72	1.88	0.65	0.30

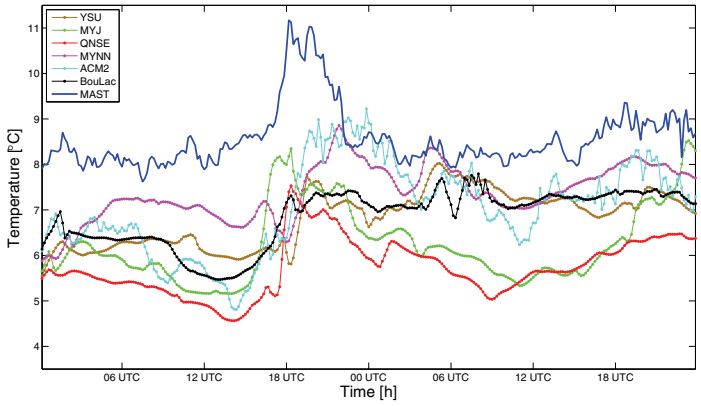

Figure 9: Time evolution of temperature for the six PBL schemes and FINO1 measurements at z = 100m. Stable period.

The one-and-a-half order schemes solve and additional prognostic equation for the turbulent kinetic energy, q, and the parameterization of fluxes depends on q, on the master length scale l, and on the flux Richardson number, Ri.

$$K_z(z) = \chi(Ri) \cdot l \cdot q^{0.5} \tag{8}$$

The diagnostic equations to obtain l and $\chi(Ri)$ differ from MYJ, MYNN and QNSE. In BouLac scheme the stability function is considered constant.

5. Results

In this section, the simulated wind speed and temperature fields are compared with mast observations for the periods described in section 3. In order to check the numerical results against the measurements, five statistical parameters were used: mean error (ME), root mean square error (RMSE), hit rate (HR), index of agreement (IOA) and correlation coefficient (R).

Time series of 10 min averaged wind speed at a height of 100m are shown in Fig. 8. It can be noticed that the tendency of the measured conditions is well reproduced by all the schemes with the presence of some differences. Statistical metrics are presented on Table 1. MYNN scheme shows the highest value of hit rate, 41.12%, whereas for the rest of them, that level is reduced to 20% and even to 10% for YSU and BouLac. The values of ME are slightly lower than the ones of RMSE, in absolut value, which means that wind speed is generally underestimated, due to the minus sign of ME. The best results are found for the MYNN scheme, with a RMSE of 1.60 ms^{-1} and the lower value of ME (-0.44 ms^{-1}). The ability of all the schemes to follow the variations in the observations is good, being IOA of approximately 0.83. By contrary, low values of correlation were found.

An important characteristic to observe is that the forecasted wind speeds present a smoother pattern even considering that the values are averaged over an interval of 10 minutes (see Fig. 8). This is due to the difficulty of the turbulence closure models to reproduce small turbulent scales on a coarse grid of 1km resolution. However, ACM2 scheme presents a more realistic behaviour that is attributed to the explicit treatment of the non-local mixing.

Temperature variations are one of the responsible mechanisms of the generation of turbulence and thus, it is strongly liked to stability. Depending on the distribution of the temperature profiles, it can act like a source/sink of turbulence through a buoyant production/consumption phenomenon.

Forecasted temperatures are reproduced with rather accuracy (Fig. 9). Again, the MYNN scheme shows the best skills with a ME of -1.18ºC and RMSE of 1.43ºC. It has, as well, the highest HR (86.76%). Nevertheless, MYJ and QNSE schemes are better correlated (~0.7) and improve the capability of following the observations, IOA from 0.57 to 0.71-0.74. In general, the values of ME and RMSE are almost equals in module, having the ME a minus sign. This fact evidences that there is an underestimation of the temperature.

The results concerning the statistical analysis were focused on wind speed and temperature at z=100m. Indeed, the behaviour of the whole wind speed profile can be observed in Fig. 10, where the averaged profiles over the stable period are depicted. YSU and BouLac schemes predict a much lower shear, similar to a neutral or convective ABL. The rest of them, present a better agreement with respect to the mast measurements but still some differences can be perceived. None of them matches completely the shape of the profile, being the MYNN scheme the one which yields to the highest degree of correctness (specially above 50m).

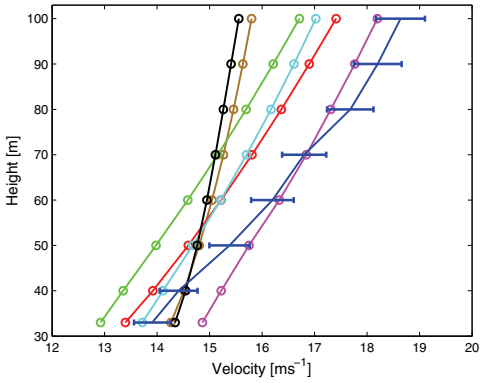

Figure 10: Velocity profiles for the six PBL schemes and FINO1 measurements. Averaged values over the stable period. Legend is the same as in Fig. 8.

An important parameter commonly used to evaluate the shear of the velocity profile is α (Eq. 9), derived from the assumption of a power law distribution [24].

$$\alpha = \frac{\ln\left[u(z_2)/u(z_1)\right]}{\ln(z_2/z_1)} \tag{9}$$

It is employed in the norms to account for the stability effects in wind turbine design and sitting. A

value of 1/7 is considered as a reference for neutral conditions whereas higher and lower values represent stable and convective atmospheric scenarios, respectively. To compute α we considered z_2=100m and z_1=50m. These values are representative of a standard 1MW wind turbine, in which the hub height is about 70m and the rotor diameter ranges from 50 to 60m. The time evolution of α during the stable period is shown in Fig. 11.

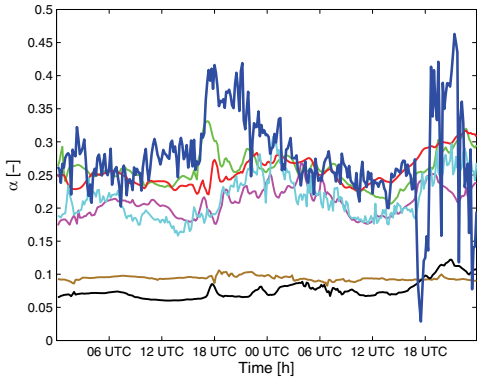

Figure 11: Time evolution of α during the stable period for the six PBL schemes and FINO1 measurements. Legend is the same as in Fig. 8.

MYJ, QNSE, MYNN and ACM2 schemes reproduce quite accurately the observed patter of α. Once more, the numerical results exhibit a smoother trend which is improved by the ACM2 scheme. However, the last shows narrow fluctuations, as happened as well with the wind speed. The previous conclusion on the lower level of shear reproduced by YSU and BouLac schemes is further confirmed by α. These two schemes produce values of α around 0.08, clearly representative of a convective BL and keep it almost constant for the whole analysed period. Similar observations about the YSU scheme have been reported by other authors in onshore terrain [25; 26]. A neutral behaviour was found during nighttime, attributed to an excessive mixing.

6. Conclusions

Field measurements at FINO1 mast for the period January-December 2005 have been analysed. Filtering of the data to remove unphysical values was performed and shadow effects were identified. Two different periods were determined to reproduce stable, unstable and near-neutral conditions by using sonic measurements of Obukhov length, L, available in the literature that where compared against Brunt-Väisälä frequency, N^2. We found a good agreement in between both.

Two PBL schemes of first order of turbulence closure and four one-and-a-half order schemes were compared against mast observations in terms of wind speed and temperature. A parent domain with three nests was used to progressively refine from a resolution of 27km at the parent grid to a resolution of 1km at the most inner one.

For the stable scenario, a RMSE of 1.60 ms^{-1} at 100m was the best agreement, obtained by the MYNN scheme. In general, closer to the surface sea level the bias is reduced whereas the underestimation of the wind speed is increasing with height. All the schemes show good skills following the pattern of the observed wind speeds at FINO1 mast with IOA>0.8 while correlation was lower (R~0.5).

By analysing the vertical structure of the profiles, it was noticed that YSU and BouLac schemes reproduced tendencies characteristic of unstable conditions for the complete stable period. Values of α corroborated such conclusion showing MYJ, QNSE, MYNN and ACM2 similar trends to the measured values whereas YSU and BouLac provided almost constant values which remained below 0.143 (α~0.08).

The temperature was fairly well predicted by all the PBL schemes. Again, the MYNN scheme presented the lowest RMSE, 1.43ºC. In general terms, temperature was systematically underpredicted. Direct correlation between wind speed and temperature skills was not found, even considering that for both magnitudes, the MYNN scheme presented the lowest biases.

During the unstable-neutral scenario, which was not show here, similar results were obtained with a slight improvement. The MYNN scheme provided the lowest RMSE for velocity and temperature at 100m, 1.54 ms^{-1} and 0.81ºC, respectively. For all the schemes bias were reduced and IOA and R improved significantly, being about 0.97 and 0.96 for wind speed and about 0.90 and 0.93 for temperature. In this period, wind speed tends to be overestimated most probably due to unmatching of surface layer variables, L and u_*, and bias were in general decreasing with the distance from the surface sea level. The YSU and BouLac schemes were the ones producing higher overpredictions. Otherwise, the shear was accurately reproduced for all the schemes.

It has been shown that high resolution mesoscale WRF-PBL schemes are able to reproduce 10 min averaged wind speed and temperature fields quite accu-

rately despite of the coarse spatial resolution, from the microscale point of view. The simulated wind speeds and temperatures show a smoother evolution when compared to observed data. This fact comes both from the turbulence modelling, i.e., the averaged form of the equations, and from the coarse resolution with which the local effects cannot be accounted for. In the other hand, WRF-PBL schemes have demonstrated that they are a good approach in order to produce realistic conditions that can be applied to higher resolution turbulence resolving models like Large Eddy Simulation (LES) models.

Acknowledgments

This work has been supported by the European Commission through the Marie Curie FP7 WAUDIT project under grant number # 238576. The author thanks the German Wind Energy Institute (DEWI) for providing the FINO1 data.

References

[1] T. Neumann, K. Nolopp, K. Herklotz, Erste Betriebserfahrungen mit der FINO1- Forschungsplattform in der Nordsee, DEWI Magazi 24 (2004) 27–34.

[2] B. Lange, S. Tautz, Bestimmung von Wärme- und Impulsfluss in der marinen atmosphärischen Grenzschicht für die Offshore-Windenergienutzung (BAGO), ForWind - Zentrum für Windenergieforschung, Universität Oldenburg, Oldemburg, Germany, 2004.

[3] FINO-1 Database, http://www.fino-offshore.com/.

[4] B. Lange, Comparison of wind conditions of offshore wind farm sites in the Baltic and North Sea, Proceedings of the German Wind Energy Conference DEWEK 2004, Wilhelmshaven, Germany, 2004.

[5] B. Cañadillas, A study of the Marine Boundary Layer by LES-modelling and experimental observations with focus on offshore wind energy applications, Ph.D. thesis, University of Hannover (2010).

[6] International Energy Agency: Expert Group Study on Recommended Practices for Wind Turbine Testing and Evaluation, 11, Wind Speed Measurement and Use of Cup Anemometry, 1999.

[7] R. B. Stull, An introduction to boundary layer meteorology, Kluwer Academic Publishers, Dordrecht, 1988.

[8] J. A. Businger, A Note on the Businger-Dyer Profiles, Boundary-Layer Meteorology 42 (1988) 146–151.

[9] U. Högström, Non-Dimensional Wind And Temperature Profiles In The Atmospheric Surface Layer: A Re-Evaluation, Boundary-Layer Meteorology 42 (1988) 55–78.

[10] B. Lange, S. Larsen, J. Højstrup, R. Barthelmie, The influence of thermal effects on the wind speed profile of the coastal marine boundary layer, Boundary-Layer Meteorology 112 (2004) 587–617.

[11] S. E. Gryning, E. Batchvarova, B. Brümmer, H. Jørgensen, S. Larsen, On the extension of the wind profile over homogeneous terrain beyond the surface boundary layer, Boundary-Layer Meteorology 124 (2007) 251–268.

[12] K. Suselj, A. Sood, Improving the Mellor-Yamada-Janic Parametrization for wind conditions in the marine boundary layer, Boundary-Layer Meteorology 136 (2010) 301–324.

[13] K. Suselj, Modelling of the near-surface wind speed: Boundary Layer and Climate aspects, Ph.D. thesis, University of Oldenburg (2009).

[14] W. Skamarock, J. Klemp, J. Dudhia, D. Gill, D. Barker, M. Duda, X. Huang, W. Wang, J. Powers, A description of the advanced research WRF version 3, NCAR Tech. Note NCAR/TN-475+STR, 2008.

[15] W. C. Skamarock, Evaluating mesoscale NWP models using kinetic energy spectra, Monthly Weather Review 132 (2004) 3019–3032.

[16] S. Y. Hong, Y. Noh, J. Dudhia, A new vertical package with an explicit treatment of entrainment processes, Monthly Weather Review 134 (2005) 2318–2341.

[17] J. Pleim, A combined local and nonlocal closure model for the atmospheric boundary layer. Part I: model description and testing, Journal of Applied Meteorology and Climatology 46 (2005) 1383–1395.

[18] J. Pleim, A combined local and nonlocal closure model for the atmospheric boundary layer. Part II: application and evaluation in a mesoscale meteorological model, Journal of Applied Meteorology and Climatology 46 (2005) 1396–1409.

[19] Z. I. Janic, Nonsingular implementation of the Mellor-Yamada level 2.5 scheme in the NCEP meso model, Office Note 437, National Centers for Environmental Prediction: Camp Springs, MD, USA, 2001.

[20] M. Nakanishi, Improvement of the Meyor-Yamada turbulence closure model based on Large-Eddy Simulation data, Boundary-Layer Meteorology 99 (2000) 349–378.

[21] S. Sukoransky, B. Galperin, A. V. Perov, Application of a new spectral theory of stably stratified tur-bulence to the atmospheric boundary layer over sea ice, Boundary-Layer Meteorology 117 (2004) 231–257.

[22] P. Bougeault, P. Lacarrère, Parameterization of orography-induced turbulence in a mesobeta-scale model, Monthly Weather Review 117 (1989) 1872–1890.

[23] A. J. Dyer, A review of flux-profile relationships, Boundary-Layer Meteorology 7 (1974) 363–372.

[24] E. W. Peterson, J. P. Hennessey, On the use of power laws for estimates of wind potential, Journal of Applied Meteorology 17 (2004) 390–394.

[25] B. Storm, S. Basu, The WRF model forecast-derived low-level wind shear climatology over the United States Great Plains, Energies 3 (2010) 258–276.

[26] C. Draxl, A. Hahmann, A. Peña, J. Nissen, G. Giebel, Validation of boundary-layer winds from WRF mesoscale forecasts with application to wind energy forecasting, 19th Symposium on Boundary Layer and Turbulence, Keystone, USA, 2010.

CFD simulations of atmospheric boundary layer flows over complex terrains

Antonino Bonanni

Aeronautics and Aerospace Department, bonanni@vki.ac.be

Supervisor: Herman Deconinck

Aeronautics and Aerospace Department, Dean of the Faculty, von Karman Institute for Fluid Dynamics, Belgium, deconinck@vki.ac.be.

Promotor: Chris Lacor

Chairman Research Group Fluid Mechanics and Thermodynamics, Vrije Universiteit Brussel Pleinlaan 2, B-1050 Brussel, Belgium, chris.lacor@vub.ac.be.

Abstract

The present work is focused on several aspects of the development of a CFD model for Atmospheric Boundary Layer (ABL) simulations over complex terrains. In particular, we describe the development work on the pre-existing solver COOLWinD (based on the framework COOLFluiD), the development of a new C++ code for mesh generation and the application of the package to the Askervein testcase.

Keywords: CFD, Atmospheric Boundary Layer, mesh generation, Askervein, complex terrain

1. Introduction

Recently wind energy has gained an important position among renewable energy technologies. With annual growth rates of 20%, it is one of the fastest growing technologies worldwide and compared to 2007, an increase of more than 700% (718GW) in installed capacity could be reached by 2017[1]. The European Wind Energy Technology Platform identifies *Wind Conditions assessment* as one of the key areas for research activities of the sector [1], aiming at an accuracy better than 3% in predicting the wind resources of wind farms by the year 2030, regardless of the terrain and atmospheric conditions. To reach such ambitious objective, a paradigm shift in the prediction tools at industry's disposal must be achieved. Looking at the tools currently available, they are to a great extent, still dominated by simple solvers based on linear models of the flow (see WAsP [2] [3]). Unfortunately, such tools, do not model accurately the wind flow and therefore do not allow reliable power output prediction, specially in the case of complex terrains. This is because the strong non-linear effects like recirculations behind hills cannot be taken into account. For this reason, this work focuses on the development of a CFD model suitable for complex terrain simulations, including all the stages of the simulation: the physical model, the mesh generation and a proper treatment of non-constant roughness of the terrain itself.

[1]Survey among the main companies on the market, commissioned by Husum Wind Energy Trade Fair (September 2009)

2. COOLWinD

The solver used for this PhD project is called COOLWinD and is based on the Finite Element solver that Tamas Banyai developed at Von Karman Institute [4]. The code is written in the framework COOLFluiD, that is an object-oriented framework for multi-phisics simulations [5] [6] [7] [8] [9]. In the following sections, we briefly review the numerical technique, the specific inlet profiles and wall-functions used in COOLWinD.

2.1. Finite Elements FEM: Basic Principle

The main steps for discretizing partial differential equations by Finite Elements method are shortly recalled.

- Domain tessellation: the computational domain Ω is divided in cells and nodes (In this case we use triangles for bi-dimensional domains and tetrahedrons for three-dimensional ones).
- Approximation of the numerical solution, projecting it into a functional basis. It means that the nodal solution is written as a linear combination of basis functions defined over the whole domain.
- Using the properties of these basis functions, it is possible to write the equations for the nodal solution by minimizing a measure of the global error. All the equations toghether form a system of algebraic equations.
- In the end, the system is solved and the nodal values in the domain are therefore updated. This procedure is repeated iteratively to advance in time.

In this small review of the Finite Elements technique, the 2D Navier Stokes equations for incompressible flows are considered:

$$\begin{aligned} u\frac{\partial u}{\partial x} + v\frac{\partial u}{\partial y} + \frac{1}{\rho}\frac{\partial p}{\partial x} - \nu\left(\frac{\partial^2 u}{\partial x^2} + \frac{\partial^2 u}{\partial y^2}\right) = 0 \\ u\frac{\partial v}{\partial x} + v\frac{\partial v}{\partial y} + \frac{1}{\rho}\frac{\partial p}{\partial y} - \nu\left(\frac{\partial^2 v}{\partial x^2} + \frac{\partial^2 v}{\partial y^2}\right) = 0 \\ \frac{\partial u}{\partial x} + \frac{\partial u}{\partial y} = 0 \end{aligned} \tag{1}$$

As said, each variable solution is written as a combination of basis functions defined over the whole domain.

$$\begin{aligned} \hat{u}(x,y) = \sum_j u_j \cdot N_j(x,y) \\ \hat{v}(x,y) = \sum_j v_j \cdot N_j(x,y) \\ \hat{p}(x,y) = \sum_j p_j \cdot N_j(x,y) \end{aligned} \tag{2}$$

where $\hat{u}(x,y), \hat{v}(x,y), \hat{p}(x,y)$ are the variables over the whole domain, $N_j(x,y)$ the basis functions and u_j, v_j, p_j the nodal values. The shape function of node "i" is different from zero only in the cells containing node "i" (this set of cell is indicated as Ω_e). This property is important because it makes the solution in node "i" depending uniquely on the solution in the nodes of the cells that node "i" belongs to. This property gives the scheme a "compact stencil". If the approximate solution functions (2) are plugged into the original differential equations, the left-hand side does not vanish and a residual error appears:

$$\begin{aligned} R^x_{NS} &= \hat{u}\frac{\partial \hat{u}}{\partial x} + \hat{v}\frac{\partial \hat{u}}{\partial y} + \frac{1}{\rho}\frac{\partial \hat{p}}{\partial x} - \nu\left(\frac{\partial^2 \hat{u}}{\partial x^2} + \frac{\partial^2 \hat{u}}{\partial y^2}\right) \\ R^y_{NS} &= \hat{u}\frac{\partial \hat{v}}{\partial x} + \hat{v}\frac{\partial \hat{v}}{\partial y} + \frac{1}{\rho}\frac{\partial \hat{p}}{\partial y} - \nu\left(\frac{\partial^2 \hat{v}}{\partial x^2} + \frac{\partial^2 \hat{v}}{\partial y^2}\right) \\ R_c &= \frac{\partial \hat{u}}{\partial x} + \frac{\partial \hat{v}}{\partial y} \end{aligned} \tag{3}$$

where $R^x_{NS}(x,y), R^y_{NS}(x,y), R_c(x,y)$ are the residual functions associated to the x-momentum, y-momentum and continuity equation respectively. These residual functions have to be made small in some sense. One way is to use the weighted residual method. A weighted integral of the residual functions over the whole computational domain Ω is set to null:

$$\begin{aligned} \int_\Omega W^x_{NS} R^x_{NS}\, d\Omega = 0 \\ \int_\Omega W^y_{NS} R^y_{NS}\, d\Omega = 0 \\ \int_\Omega W_c R_c\, d\Omega = 0 \end{aligned} \tag{4}$$

where W^x_{NS}, W^y_{NS}, W_c are the weight functions. The choice of the weight functions for the velocity and continuity equations is crucial for the accuracy, stability and consistency of the discretization method.

2.2. SUPG Discretization Method

A popular choice for the weight function is $W_i = N_i(x,y)$. This choice leads to the classic Galerkin method that is somehow similar to the central scheme in finite differences. Neverthless, this approach is not suitable for advection dominated flows and an appropriate correction is needed. It is necessary to introduce a weight function biased on the advection direction, in a way that the contribution of the upwind nodes is weighted more than the one of the downstream nodes. In the SUPG scheme [10] [11] [4], the weight functions in the momentum equations are modified by introducing an artificial diffusion term which acts only in the streamline direction:

$$W_i(x,y) = N_i(x,y) + \tau_{SUPG}\left(\hat{u}\frac{\partial N_i}{\partial x} + \hat{v}\frac{\partial N_i}{\partial y}\right) \tag{5}$$

where τ_{SUPG} is an intrinsic time-scale given by:

$$\tau_{SUPG} = \frac{h}{2\|\hat{u}\|}\zeta(Re^u) \tag{6}$$

$Re^u = h\|\hat{u}\|/2\nu$ is the local Reynolds number (in a specific cell), h a measure of the local cell size and ζ a "dumping" function.A possible choice for ζ is the 'doubly-asymptotic' function:

$$\zeta = max\left[0, min\left(\frac{Re^u}{3}, 1\right)\right] \tag{7}$$

ζ tends to 0 for diffusion dominated elements (some expressions are 0 for $Re^u = 0$, others give a τ value of order h^2/ν) and tends to one for local high Reynolds numbers (giving a τ values of order $h/\|\hat{u}\|$).

2.3. PSPG Discretization Method

Concerning the pressure equation (continuity equation), an appropriate weight function is needed as well. Before describing the PSPG correction, it is worth recalling that in FEM terminology we call equal-order interpolation when the same basis functions $N_j(x, y)$ are used both for the velocity and for the pressure. There exists a condition called "Babuska-Brezzi condition" (BB) stating that equal-order interpolation violates a mathematical compatibility condition of the function space $\hat{p}(x, y)$ and $\hat{u}(x, y)$. A possible solution to overcome the Babuska-Brezzi condition while maintaining the equal-order formulation is the PSPG correction. Stabilization terms are added to the continuity equation as follows:

$$\int_\Omega N_i R_c d\Omega + \sum_e \int_{\Omega_e} \tau_{PSPG} \frac{1}{\rho} \nabla N_i \vec{R}_{NS} d\Omega \tag{8}$$

In this expression, also the residual of the momentum equation R_{NS} is involved. τ_{PSPG} is a coefficient function of a Reynolds number defined as:

$$\tau_{PSPG} = \frac{h}{2U}\zeta(Re^U) \tag{9}$$

where Re^U is based on the element size h and a general velocity measure U:

$$Re^U = \frac{hU}{2\nu} \tag{10}$$

The function ζ is again the 'doubly-asymptotic' function already seen in equation 7.

2.4. K-ϵ Turbulence Model

In COOLWinD we use the standard $k-\epsilon$ turbulence model [12]. For turbulent kinetic energy k and its dissipation ϵ, we have the following equations:

$$\begin{cases} \frac{\partial}{\partial t}(\rho k) + \frac{\partial}{\partial x_i}(\rho k u_i) = \\ \frac{\partial}{\partial x_j}\left[\left(\mu + \frac{\mu_t}{\sigma_k}\right)\frac{\partial k}{\partial x_j}\right] + P_k - \rho\epsilon \\ \frac{\partial}{\partial t}(\rho\epsilon) + \frac{\partial}{\partial x_i}(\rho\epsilon u_i) = \\ \frac{\partial}{\partial x_j}\left[\left(\mu + \frac{\mu_t}{\sigma_\epsilon}\right)\frac{\partial \epsilon}{\partial x_j}\right] + C_{1\epsilon}\frac{\epsilon}{k}(P_k) - C_{2\epsilon}\rho\frac{\epsilon^2}{k} \\ \mu_\tau = \rho C_\mu \frac{k^2}{\epsilon} \end{cases}$$

where $P_K = \mu_T S^2$ and $S \equiv \sqrt{2S_{ij}S_{ij}}$ (where S_{ij} is the rate-of-strain tensor). The classical coefficients are $C_1 = 1.44$ $C_2 = 1.92$ $c_\mu = 0.09$ $\sigma_K = 1$ $\sigma_\epsilon = 1.3$. μ_τ is the turbulent viscosity that acts into the momentum equations as an additional viscosity.

2.5. Boundary Conditions

In COOLWinD, we use both the inlet profile and the wall functions prescribed by Richard-Hoxey [13]. Neverthless, some recast of the terms is needed to use their wall-functions in a Finite Elements framework (sec. 2.5.2). To validate this new formulation, a series of testcases has been set-up (not totally reported here for sake of brevity).

2.5.1. Inlet Profile

Richard and Hoxey [13] started their derivation of the inlet profiles from the system of equations of 2D incompressible k-eps model. The driving idea was to obtain profiles that are kept constant in the streamwise direction, when uniform conditions are applied. This was done by introducing the following assumptions into the system of equations:

- vertical velocity equal to zero
- pressure constant in the domain
- shear stress constant in the domain and equal to $\tau_0 = \rho u_*^2$

after simplifying the system that way, they proposed a possible solution:

$$\begin{cases} U = \frac{u_*}{K}\ln\left(\frac{z+z_0}{z_0}\right) \\ k = \frac{u_*^2}{\sqrt{c_\mu}} \\ \epsilon = \frac{u_*^3}{K(z+z_0)} \end{cases} \tag{11}$$

K is the Von Karman constant and z_0 is the roughness lenght. The friction velocity u_* is a measure of the shear stress in the surface layer of the atmosphere and is calculated starting from the roughness lenght and a reference velocity as:

$$u_* = \frac{KU_h}{ln\left(\frac{h+z_0}{z_0}\right)} \tag{12}$$

2.5.2. *Wall Functions*

As said, in COOLWinD we follow the approach of Richard-Hoxey [13]. The original approach though, needed to be recast to be succesfully used in a finite element framework. Our approach closely resembles the approach of De Mulder [10] and Jeong [14]. The main difference is that both the mentioned authors use a mesh that is lifted off the physical wall. This lifting separates the first layer of points from the wall ($z \neq 0$). By doing this, they can directly use the velocity at the first points to compute u_* and therefore K and ϵ (this also means dropping the K and ϵ equations and replacing their values with the theoretical one). On the contrary, in COOLWinD we do not lift the mesh but we compute u^* directly at the second layer of points far from the wall. To summarize the whole procedure, a pictorial scheme is here proposed:

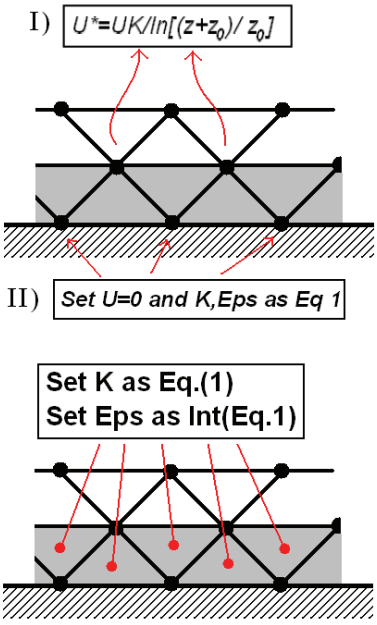

Figure 1: Summary of the procedure to compute the wall-functions.

- The velocity at the second layer of points U_P is used to compute the local friction velocity u_{*P} as $u_{*P} = \frac{KU_P}{ln\left(\frac{z_P+z_0}{z_0}\right)}$
- From the value of u_{*P}, the theoretical value of K and ϵ at the center of the correspondant cells is set as: $k = \frac{u_*^2}{\sqrt{c_\mu}}$ and $\epsilon = \frac{u_{*P}^3}{K(z_P+z_0)}$. (Note that in the case of ϵ, the value is the integral of the profile 11 over the first cell)
- At the wall, all the velocity components are set to zero and the value of K and ϵ are set according to eq. 11.

2.6. *Non-uniform Roughness*

The code COOLWinD has been also provided with the capability of reading a map of terrain roughness to allow simulations over non-constant roughness terrains. To perform this task, an external C++ library called Easy_BMP [15] is employed. This library gives the user some tools to read and write *".bmp"* image files.

3. Mesh Generation

To generate the mesh, a new code has been written. It is entirely written in C language and makes use of the library *Triangle* [16] to perform the initial Delaunay triangulation of cloud of points that describe the terrain surface. The final mesh is composed by Tetrahedron elements. The algorithm proceeds as follow: at first, a triangular mesh is generated from a cloud of points representing the terrain geometry. Subsequently, this 2D mesh is extruded upwards to create Prism elements. Eventually, all the elements are split into tetrahedrons. The code can also count on several other features like mesh refining in the horizontal direction (with the objective of having a finer mesh in the areas of interest) and mesh smoothing to reduce the stretching factor of the elements.

3.1. *Terrain Triangulation*

This first step is done by an open source software called *Triangle* which uses a Delaunay triangulation algorithm [17] [18] to create the triangle mesh from a cloud of points. Based on Delaunay's definition, the circumcircle of a triangle formed by three points from the original point set is *"empty"* if it does not contain vertices other than the three that define it (other points are permitted only on the very perimeter, not inside). The Delaunay condition states that a triangle net is a Delaunay triangulation if all the circumcircles of all the triangles in the net are empty. This algorithm maximizes the smallest angle contained in each triangle. By doing this, this algorithm avoids too stretched triangles and assures a uniform grid. This algorithm is born for 2D sets of points but can be extended to 3D meshes by considering the circumspheres of the

respective tetrahedrons. In this mesh generator, only the 2D Delaunay algorithm is needed since only the terrain surface has to be meshed. At a first stage, in fact, the third dimension is not considered. To smooth the terrain towards the lateral borders, several circular layers of points can be added during this phase to create a smoothing area and set the boundary region farther away.

3.2. Volume Mesh Generation

After creating the surface mesh, this is extruded upwards. Top altitude, number of cells in the vertical direction and height of the first cell are the free parameters to be set by the user. Cells vertical size is expanded towards the top of the domain, in the sense that cell height is incremented by a geometrical progression from the height of the first cell on:

$$h_1 = rh_0 \quad h_2 = rh_1 \quad h_{i+1} = rh_i \quad \dots \tag{13}$$

where h_i is the height of the i-th cell and r is the expansion factor. The process starts by knowing the height of the first cell h_0 and the total height of the desired volume mesh z_{top}. To calculate the height of each cell then, we need to use the analytical solution of the following geometrical progression:

$$\sum_{k=0}^{n} h_0 r^k = h_0 r^0 + h_0 r^1 + h_0 r^2 + \ldots + h_0 r^n = z_{top} \tag{14}$$

The analytical solution of the geometrical progression is:

$$\sum_{k=0}^{n} h_0 r^k = \frac{h_0(1 - r^{n+1})}{1 - r} \tag{15}$$

Since it is an implicit equation in r, it has to be solved iteratively. Bisection method has been preferred for its robustness. Since a flat top of the volume mesh is desirable, each expansion factor has to be rescaled to take into account the initial altitude of the surface points:

$$r_i = \frac{z_{top} - z_i}{z_{top}} r \tag{16}$$

Another option is to specify directly at the beginning the following parameters: height of the first cell, number of elements in the vertical direction and the stretching factor. This way, no additional computation is needed.

3.3. Boundaries Definition

The boundaries are defined according to the wind direction $\vec{n_w}$ specified by the user. each boundary face is set as belonging to a specific boundary according to the orientation of its "external" face normal $\vec{n_f}$. The boundary is set as follows:

$$\begin{cases} \vec{n_f} \cdot \vec{n_w} > 0 & => \ Outlet \\ \vec{n_f} \cdot \vec{n_w} < 0 & => \ Inlet \\ \vec{n_f} \cdot \vec{n_w} = 0 & => \ Side \end{cases} \tag{17}$$

The possibility to use a *Side* boundary is meaningful only for squared plant meshes. In every other case, the faces for which $\vec{n_f} \cdot \vec{n_w} = 0$ can be included either in Inlet or Outlet boundary. Going from bottom to top, the first layer of points (and faces) is included into the *Wall* boundary and the last into the *Top* boundary.

3.4. Surface interpolation

Starting from the consideration that surface interpolation is a subject of research by itself, for the time beeing we limited the code to the two simplest interpolation algorithms known in literature: Closest node approach and Inverse Distant Weighting method (IDW). In particular, IDW is a method for multivariate interpolation, a process of assigning values to unknown points by using values from usually scattered set of known points. Here, the value at the unknown point is a weighted sum of the values of N known points.

$$u(\mathbf{x}) = \sum_{i=0}^{N} \frac{w_i(\mathbf{x}) u_i}{\sum_{j=0}^{N} w_j(\mathbf{x})} \tag{18}$$

where:

$$w_i(\mathbf{x}) = \frac{1}{d(\mathbf{x}, \mathbf{x}_i)^p} \tag{19}$$

is a simple IDW weighting function, as defined by Shepard [19], x denotes an interpolated (arbitrary) point, x_i is an interpolating (known) point, d is a given distance (metric operator) from the known point x_i to the unknown point x, N is the total number of known points used in interpolation and p is a positive real number (called the power parameter) that is a measure of the degree of smoothing desired for the interpolation.

3.5. Surface mesh refinement

As already mentioned, the code has been provided with an "area refinment" option. This means that during the triangulation of the terrain surface, it is possible to specify some areas to refine. This option is directly transferred to the library *Triangle* which set a maximum value for the element size that cannot be exceeded during the triangulation phase in a specified area. To make the transition coarse/fine mesh, a

smooth "maximum cell area" assignement has been set as follows:

$$\begin{cases} A_e = A_{MAX} & d > R_{Ref} \\ A_e = A_e(d) & R_{Ref}/2 < d < R_{Ref} \\ A_e = A_{MIN} & d > R_{Ref} \end{cases} \quad (20)$$

where A_e is the maximum area allowed to the elements of the "new" mesh that will lie into the existing element e, d is the distance of the element e from the center of the refinement area and R_{Ref} is the radius of the refinement area itself. In the end, the function $A_e(d)$ is a smoothing function to be set. The one used as default in this code is a cosinus based function:

$$A_e(d) = A_{MIN} + \Delta A \frac{1 - cos\left(\frac{d}{R_{Ref}}\pi\right)}{2} \quad (21)$$

where, ΔA indicates $(A_{MAX} - A_{MIN})$.

3.6. Surface mesh smoothing

In this code, we use a mesh smoothing algorithm to improve the quality of the mesh. At the moment the smoothing is applied only in the horizontal direction (i.e to the nodes of the terrain surface mesh), to improve the quality of the transition between areas with fine and coarse mesh. The algorithm introduced is the Laplacian algorithm (also described in [20]). In practise it consists of introducing displacements of the nodes by considering each node as subject to forces coming from the connections with its neighbour nodes. Each connection is treated as a spring and therefore each node is subject to a resultant force as:

$$\vec{f_{ij}} = \sum_{j \in K(i)} c_{ij}(\vec{X_j} - \vec{X_i}) \quad (22)$$

where $\vec{f_{ij}}$ is the resultant force acting on the node i, c_{ij} are the stiffness coefficients (generally set to 1), $(\vec{X_j} - \vec{X_i})$ is the distance between node i and its neighbour node j and $K(i)$ is the ensamble of nodes connected to node i. The smoothing algorithm works by imposing a general load balancing of the forces acting on each node of the grid:

$$\sum_{j \in K(i)} \vec{f_{ij}} = 0 \quad (23)$$

This brings to a system of equations that needs to be solved to obtain the displacement of each grid node. In reality, this system of equations is often solved iteratively, by relaxing the system in several iterations:

$$\vec{X}_i^{n+1} = \vec{X}_i^n + \omega \frac{\sum_{j \in K(i)} c_{ij}(\vec{X}_j^n - \vec{X}_i^n)}{\sum_{j \in K(i)} c_{ij}} \quad (24)$$

where n is the iteration number and ω a relaxation factor. In this way it is possible to avoid an expensive matrix inversion and most of all it keeps the code simple. After few iterations, the system reaches its convergence (fully relaxed position of the nodes). As we said, at the moment the code has been provided only with horizontal smoothing algorithm for the surface mesh but it will be next applied to all the nodes too.

4. Askervein Testcase

Askervein hill is located in Scotland and is quite an isolated hill. For this reason it is considered a perfect testcase for ABL simulations. Its highest point is $116m$ above the surroundings, and its plan is almost elliptic with axis of about $1km$ and $2km$ (see Figure 2). Its surface roughness is homogeneous with a roughness height of about $z_0 = 0.03m$ (suggested value by Taylor and Teunissen) [21] [22]. Since Askervein hill project provided both velocity and turbulence intensity measurements, it is a valuable test case for validating the performance of CFD models.

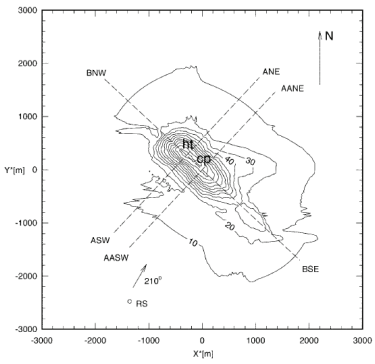

Figure 2: Askervein Hill.

4.1. Mesh Description

For this testcase an unstructured mesh of 389760 cells and 69363 nodes was used. The first cell at the ground is 2 meters high. There are 20 vertical cells and the dimension of the computational domain is $6Km \times 6Km \times 1Km$ (fig. 3). To perform the simulation with COOLWinD, several processors can be used. The parallelization is made by dividing the domain in a number of parts equal to the number of processors and assigning each part to each processor. For the simulation with the mesh shown here, a single processor has actually been used.

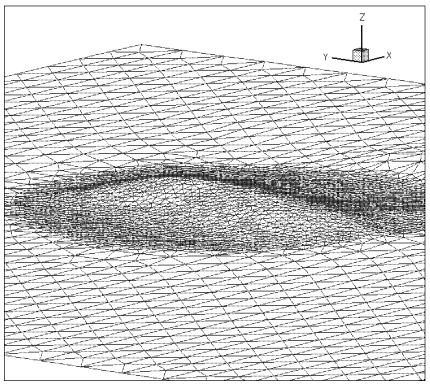

Figure 3: Mesh details: 389760 cells, 69363 points.

4.2. Boundary Conditions

- The inlet profiles used are described in section 2.5.1. They are computed by matching the experimental data at the mast RS (see fig. 2).
- At the ground we used the wall functions as explained in 2.5.2.
- At the top and side boundaries we imposed the velocity to be tangential to the boundaries themselves.
- At the outlet we imposed the pressure (at a value equal to zero)

4.3. Results

Here following the inlet conditions at reference point RS. From these profiles it is possible to verify that the assumption of constant turbulent kinetic energy in the surface layer is indeed realistic and reasonable. Here following the results of the speed-up ratio $\Delta S = (V_h(z) - V_{ref}(z))/V_{ref}(z)$ and the normalized turbulent kinetic energy $K^* = K/V_{ref}^2$ along line A: From these plots it is possible to appreciate a good agreement of the velocity profiles in the upwind side of the hill. In the downstream part there is an over-estimation of the wind speed. This trend is confirmed by former simulations in literature (see [23] and [24]). In particular, this over-estimation seems to decrease by increasing the mesh resolution, but a proper mesh convergence study still has to be performed.

5. Conclusions

In this work, a CFD model for atmospheric flows simulations has been developed. The solver COOLWinD has been set up by using a pre-existing FEM

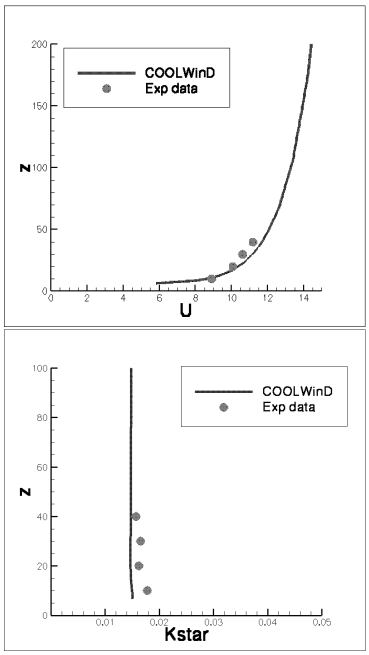

Figure 4: Inlet profiles at point RS

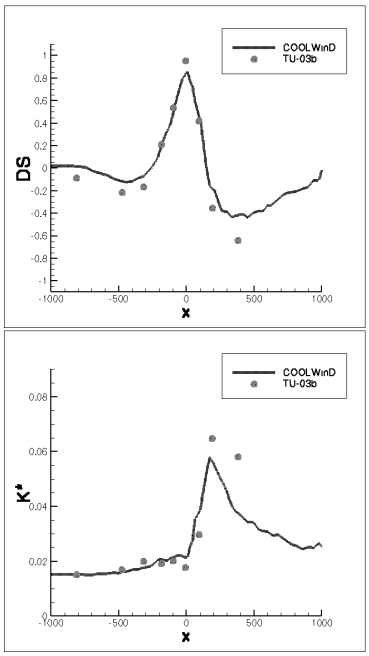

Figure 5: ΔS and k_* along line A.

solver developed by Tamas Banyai at VKI [4]. To validate the model and the implementation itself, we simulated a series of testcases, ranging from simple uniform atmospheric boundary layers (not reported in this abstract for sake of brevity) to the well known Askervein testcase. To make the solver COOLWinD an almost stand-alone tool, we developed also a mesh generator for three dimensional unstructured grids. This mesh generator already features several options to refine areas of interest and smooth the mesh to promote the solver convergence.

Acknowledgments

Many thanks go to my Supervisors Prof Chris Lacor and Prof. Herman Deconinck and to my advisors Tamas Banyai and Tiago Quintino. Special acknowledgment to the company 3E for their support and active collaboration to this project.

References

[1] TPWind, Tpwind strategic research agenda: Market deploiment strategy from 2008 to 2030, synopsis (march 2008), http://www.windplatform.eu/4.0.html.

[2] L. T. K. V. E. Berge, F. Nyhammer, O. Jacobsen, An evaluation of the wasp model at a coastal mountainous site in norway, Wind Energy 9 (2006) 131–140.

[3] J. E.Berge, A.R. Gravdahl, L.Tallhaug, O.Undheim, Wind in complex terrain. a comparison of wasp and two cfd-models., in: proceedings EWEC 2006, Conference EWEC-2006, 2006.

[4] T. Banyai, A stabilized finite element method for a time-dependent incompressible two-phase flow model, Tech. rep., Von KArman Institute, PR-2005-02 (2005).

[5] A.Lani, An object oriented and high performance platform for aerothermodynamics simulation, Ph.D. thesis, Von Karman Institute (2009).

[6] T. Wuillbaut, Algorithmic developments for a multiphysics framework, Ph.D. thesis, Von Karman Institute (2008).

[7] T. Nierhaus, Modeling and simulation of dipsersed two-phase flow transport phenomena in electrochemical processes, Ph.D. thesis, Von Karman Institute (200).

[8] T. Quintino, A component environment for high-performance scientific computing, design and implementation, Ph.D. thesis, Von Karman Institute for Fluid Dynamics (2008).

[9] D. Kimpe, On the scalable parallelisation of unstructured mesh applications, Ph.D. thesis, Katholieke Universiteit Leuven, VKI (2008).

[10] T. D. Mulder, Stabilized finite element methods for turbulent incompressible single-phase and dispersed two-phase flows, Ph.D. thesis, Katholieke Universiteit Leuven, VKI (1998).

[11] T. D. Mulder, Fegas : a finite element solver for 2d viscous incompressible gas flows using supg/pspg stabilized piecewise linear equal-order velocity-presure interpolation on unstructured triangular grids, Tech. rep., Von KArman Institute, TR-184 (1994).

[12] B.E.Launder, D.B.Spalding, Mathematical models of turbulence, Academic Press, London, 1972.

[13] P. Richards, R. Hoxey, Appropriate boundary conditions for computational wind engineering models using k-eps turbulence model, "J. Wind Eng. Ind. Aerodyn." (1993) 145–153.

[14] H. S. L. Un Jong Jeong, Hyun-Moo Koh, Finite element formulation for the analysis of turbulent wind flow passing bluff structures using the rng $k - \epsilon$ model, Journal of Wind Engineering 90, pg 151-169.

[15] easybmp c++ library, paul macklin (2003).
URL `http://easybmp.sourceforge.net/`

[16] J. R. Shewchuk, Triangle: Engineering a 2D Quality Mesh Generator and Delaunay Triangulator, in: M. C. Lin, D. Manocha (Eds.), Applied Computational Geometry: Towards Geometric Engineering, Vol. 1148 of Lecture Notes in Computer Science, Springer-Verlag, 1996, pp. 203–222, from the First ACM Workshop on Applied Computational Geometry.

[17] B. Delaunay, Sur la sphere vide, Estestvennykh Nauk, 7 (1934) 793–800.

[18] D. T. Lee, B. J. Schachter, Two algorithms for constructing a delaunay triangulation., Int. J. Computer Information Sci. 9 (1980) 219–242.

[19] D. Shepard, A two-dimensional interpolation function for irregularly-spaced data, in: Proceedings of the 1968 ACM National Conference, 1968.

[20] J.C.Carette, Adaptive unstructured mesh algorithms and supg finite element method for compressible high reynolds number flows, Ph.D. thesis, Von Karman Institute (1997).

[21] H. T. P.A Taylor, The askervein hill project, report on the september/october 1983, main field experiment, Tech. rep., Meteorological service Research, Canada (1985).

[22] H. T. P.A Taylor, The askervein hill project, report on the september/october 1982, experiment to study the boundary layer flow over askervein, Tech. rep., MSRB83-8, Meteorological service Research, Canada (1983).

[23] J. L. F.A Castro, A. Lopes, Simulation of the askervein flow. part 1: Reynolds averaged navier stokes equations (k - ϵ turbulence model), "Boundary-Layer Meteorology", 107 (2003) 501–530.

[24] A. Bechmann, N. N. Sorensen, Hybrid rans/les method for wind flow over complex terrain., Wind Energ. DOI: 10.1002/we.346 (2009) 3650.

MULTIPHASE FLOW &
HEAT AND MASS TRANSFER
FLOW

Multi-phase fluid hammer: modeling, experiments and simulations

Marcos Lema

Enviromental and Applied Fluid Dynamics Department, lema@vki.ac.be

Supervisor: Patrick Rambaud

Assistant Professor, Enviromental and Applied Fluid Dynamics Department, von Karman Institute for Fluid Dynamics, Belgium, rambaud@vki.ac.be.

Promotors: Jean-Marie Buchlin[♣] and Fernando López Peña[♠]

[♣]*Professor, Enviromental and Applied Fluid Dynamics Department, von Karman Institute for Fluid Dynamics, buchlin@vki.ac.be*
[♠]*Professor, Naval and Oceanic Engineering Department, Mendizábal s/n., University of A Coruña, 15043 Ferrol, Spain, flop@udc.es*

Abstract

The operation of spacecraft propulsion systems is regularly faced with adverse fluid hammering effects during the priming phase. This maneuver is done by fast opening of an isolation valve and the classical water hammer taking place also involves multiphase phenomena, such as cavitation and absorption/desorption of a non-condensable gas. Due to the lack of experimental studies modelling the spacecraft's hardware, the physical models implemented in the numerical codes cannot be validated properly and they fail when computing the corresponding overpressures during priming. This study proposes a new experimental facility to reproduce all the physical phenomena taking place in the propellant lines during the priming process. The parametric study allows characterising the multiphase behaviour of the flow, which has a major influence on the speed of sound and, consequently, on the pressure levels. The comparison of the experimental results and the computations shows an acceptable qualitative agreement, but the numerical models still need to be improved.

Keywords: Multi-phase flow, fluid hammer, water hammer, cavitation, absorption, desorption, priming, spacecraft propulsion.

1. Introduction

When a spacecraft is launched to the space, the propulsion system is inactive and the propellant tanks are isolated from the combustion chamber by three isolation barriers: a single pyrotechnic valve, the latch valves, and the flow control valves, as scketch in figure 1. The propellant lines are vacuum pumped ($P_L < 1kPa$) or filled with a non-condensable gas (NCG) (N2 or He). The same gas is used to pressurize the propellant tank at $20\,bar$, where the driving pressure gas is absorbed into the liquid propellant during storage. Depending on the absorption rate, the speed of sound in the liquid phase can change.

The operation of the spacecraft propulsion systems starts with the filling of the propellant lines with pressurized liquid propellant. This maneuver is called "priming" and is carried out by fast opening of the pyrotechnic isolation valve. This may turn out to be critical if the corresponding overpressures are not correctly taken into consideration in the pipe line and sub-system dimensioning. Furthermore, since the propellant lines are initially vacuum pumped or filled with a non-condensable gas (NCG), the classical water hammer includes various multiphase phenomena, such as cavitation and boiling front. Finally, the driving pressure gas can also desorb during the priming process.

Even if it is possible to find numerous studies dedicated to the priming process [1; 2; 2; 3; 4; 5; 6; 7], due to the complexity of the multiphase phenomena occurring in spacecraft hardware, there are very few literature references describing experiments with all the specifications of the above configuration. Therefore, an extensive experimental database is still miss-

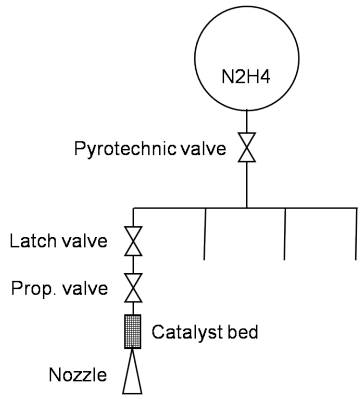

Figure 1: Sketch of a spacecraft propulsion system

ing for a proper validation of the physical models implemented in the CFD codes. Nowadays, various numerical codes are able to accurately predict the effects of liquid compressibility when computing a single-phase fluid hammer, but they still need to be extended and calibrated for cases with cavitation (single component) and two-phase (two-component) flow. Furthermore, the treatment of a dissolved NCG in the liquid phase needs to be improved. In both cases, the existence of a well documented experimental database is mandatory for the improvement and validation of these physical models.

2. Objectives

The aim of this study is to study the fluid hammer phenomenon in a confined environment with experimental and numerical approaches. The experimental results come to complete the data of Lecourt[8] and Gibek[9] already available in the literature, but using an experimental set-up which can reproduce all the physical phenomena taking place in the propellant lines during priming. The numerical investigation is done with 1D and 3D CFD codes and their results are compared against the experimental data. The final objective is to improve and validate the numerical models.

3. Experimental facility

The design of the experimental facility follows the same conception rules than the propulsion systems in satellites and includes all the elements directly involved in the fluid hammer occurrence, i.e. a pressurized vessel, a fast opening valve, and a given length of the propellant line with different configurations, referred to as "test element" hereafter. The facility layout is shown in figure 2.

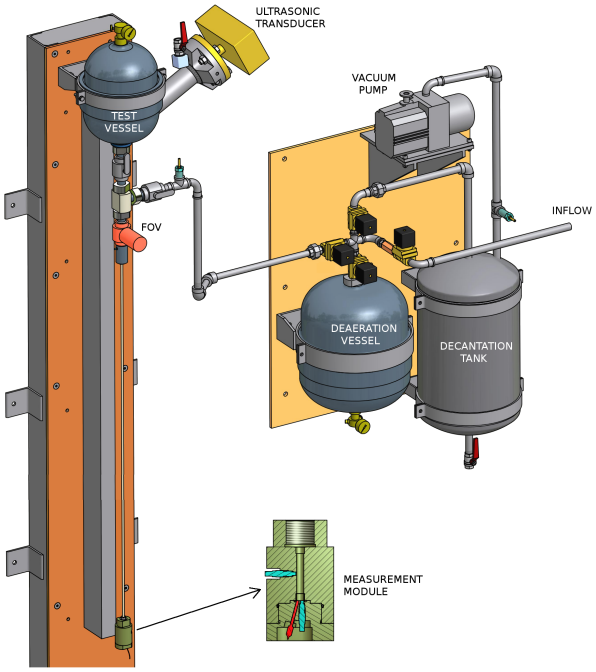

Figure 2: Experimental facility layout

This facility is flexible enough to study different propellant lines configurations. These flexibility in the configuration allows to isolate and study the effect of an elbow and a bifurcation on the pressure wave generated by the fluid hammer. Three interchangeable pipe configurations are proposed as test elements:

- A simple straight pipe of 2 m long.
- Two straight pipes connected by a 90° elbow with an equivalent length equal to 2 m.
- A T-junction with three branches of 1 m long.

The test elements are made with the same titanium tube used for aerospace applications, with 1/4 inches of diameter and 0.4 mm thickness (figure 3). The initial conditions in the test element vacuum pumped or filled with a NCG gas at low-pressure, where both conditions are set with a vacuum system.

The pyrotechnic valve used in spacecrafts should be avoid for parametric studies, since a new valve has to be used for each test. These valves have opening times in the vicinity of 5 ms, and they will be replaced

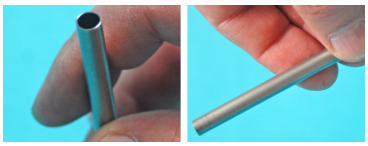

Figure 3: Titanium tube use to build the test elements

in this study for a solenoid valve and a ball valve with a mechanical actuator. Both valves give opening times around 30 ms, which are believed to be fast enough to experience a raise in pressure similar to the one obtained with a pyrotechnic valve.

The pressurized vessel acting as propellant tank is a spherical accumulator of 4 l, equipped with an ultrasonic transducer to measure the speed of sound in the liquid. This vessel includes an elastic membrane to avoid the contact of the test liquid with the driving pressure gas. This solution allows running experiments without absorption of the driving pressure gas in the liquid, and it will provide very useful insights to understand how the dissolved gas affects the fluid hammer mechanism. Furthermore, since the working liquid is already saturated with air in standard conditions, the fluid needs to be deaerated to run experiments without any dissolved gas. The liquid deaeration is done by means of a depressurization process using a second accumulator, called deareation vessel, connected to the vacuum pump, as figure 2 shows. The dissolved gas is removed by keeping the liquid in a low-pressure atmosphere.

The characterization of the wave front induced by the fluid hammer is achieved through interchangeable measurement modules attached to the forward end of the test element. Two types of measurement modules are proposed in this study: an instrumented module with pressure and temperature transducers and a transparent module made out of quartz for flow visualization with high speed imaging. The instrumented module is equipped with dynamic total pressure transducers by PCB Piezotronics and unsteady temperature transducers type E (chromel /constantan) from the University of Aachen (RWTH), both to measure the evolution of the pressure front and the surface temperature change at the forward end wall.

Finally, the facility is designed to allow two configurations: vertical and horizontal, although most of the test are intended to be done with the vertical configuration. The idea behind of going to a horizontal configuration is to check the influence of the gravity on the pressure evolution due to the fluid hammer occurrence. The switch from vertical to horizontal will be done by rotation the platform where the facility is clamped, as figures 4 and 5 show.

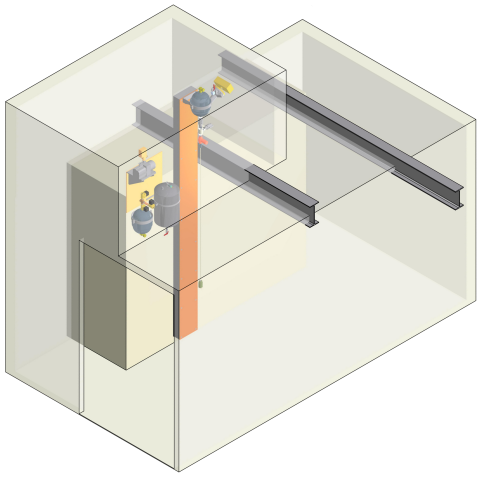

Figure 4: Vertical configuration

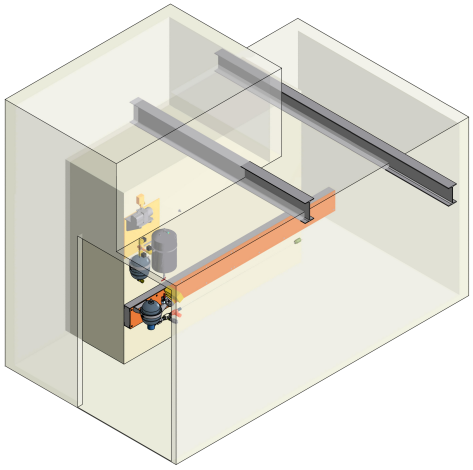

Figure 5: Horizontal configuration

4. Numerical tools

The two numerical tools used in this study are the ones currently used by the European Space Agency to qualify the spacecraft's propulsion systems: EcosimPro and CFD-ACE+. EcosimPro is a 1D simulation tool, object-oriented and capable of computing steady state and transient physical processes that can be expressed in terms of differential-algebraic equations or ordinary differential equations. The code employs the

European Space Propulsion System Simulation (ESPSS) library [10], which is needed to model all aspects of a functional propulsion system. Although the numerical results obtained with this tool have been already compared with ground tests [11], a detailed experimental database is still needed for a fully validation.

On the other hand, CFD-ACE+ is a general 3D computational fluid dynamics and multiphysics solver. It has been updated with a full cavitation module **??**, which allows to work with a homogeneous mixture of liquid, vapor and NCG (with absorption and desorption), to model non-isothermal flows and liquid compressibility for water hammer simulations. This tool, like the previous one, needs to be further validated.

5. Results

5.1. Preliminary results

The construction of the facility is not yet concluded and we can only shown experimental results obtained with a preliminary facility. This facility is a simplified version of the one described previously, and it has been built to support the design process and to validate the experimental procedure.

The simplified set-up is shown in figure 6, which uses a simple tank, a ball valve with pneumatic actuator (opening time 300 ms), and a measurement module with a single unsteady pressure transducer flush mounted at the bottom end. The test element consists of a 2 m straight carbon steel tube, with internal diameter 12, 5 mm, and mounted horizontally. The working liquid is water and the driving pressure gas is air. The graph plotted in figure 7 shows the unsteady pressure evolution recorded at the bottom end of the test element, when the test conditions are $P_t = 0,4\,MPa$ and the test element is vacuum pumped at $P_p = 10\,kPa$. This result is compared in the same graph with numerical data obtained with the numerical code EcosimPro/ESPSS modelling the same set-up. The comparison gives a reasonably good agreement for the first pressure peak. Furthermore, even if the successive pressure spikes are always higher in the experiments, the time delay between peaks is nearly identical and the damping of the successive pressure peaks is also very consistent with the experimental data. Even if these results are promising, this comparison will be improved in the future by using the experimental data obtained with the new facility, where the dissolved gas or the two-phase effects on the speed of sound will be correctly characterized.

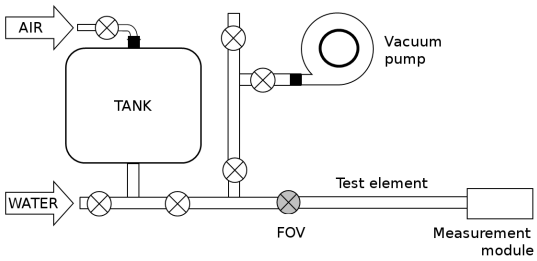

Figure 6: Simplified facility build for experimental procedure validation

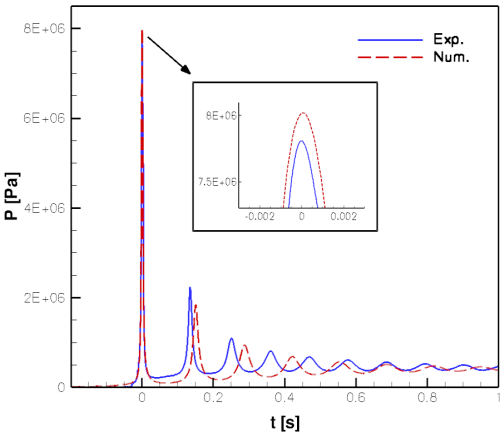

Figure 7: Experimental and numerical results with test conditions $P_t = 0,4\,MPa$ and $P_p = 10\,kPa$

5.2. Pressure front evolution

Although the numerical code EcosimPro/ESPSS is not yet fully validated, it is still a powerful tool to estimate the fluid hammer amplitude. Therefore, we have continued the study modelling the final facility to validate the design

The schematic view of the final experimental set-up is plotted in figure 8 and the numerical results are computed with water and nitrogen as working fluids. The test conditions are $P_t = 2\,MPa$ and $P_p = 1\,kPa$, and the test element configuration is 2 m straight.

Since the pipe flow can be assumed one-dimensional, the numerical results are shown using X-t diagrams. These diagrams allow temporal and spatial representation in the same graph, where the x-axis corresponds to the position along the test element, and the time is plotted in the y-axis. Figure 9 shows a X-t diagram where the colour levels represent the pressure amplitude. The pressure evolution at the bottom end

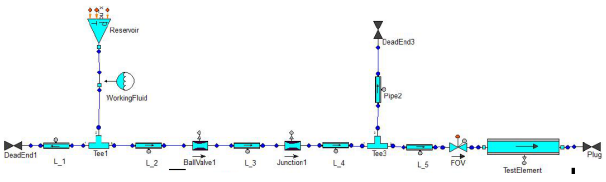

Figure 8: Schematic view of the experimental set-up under Ecosim-Pro

of the test element is plotted at the right side of the figure for a better understanding.

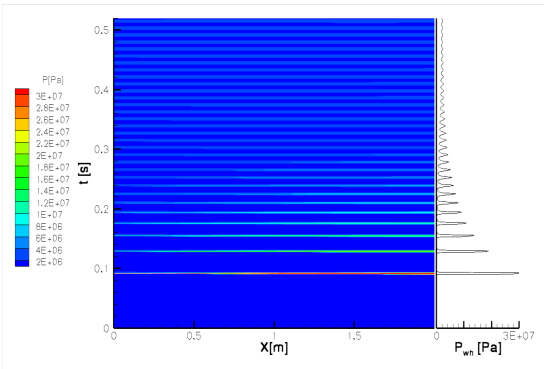

Figure 9: X-t diagram for the pressure variable

At $t = 0$, the FOV opens and the pressurized water stored in the tank propagates downstream as a liquid front, compressing the NCG presented initially in the test element at $P_p = 1\,kPa$. After $0.09\,s$, the liquid front reaches the test element forward end ($X = 2\,m$). According to the Joukowsky equation, $\Delta P = \rho a \Delta U$, all the kinematic energy is converted into pressure, leading to a pressure peak of $30\,MPa$. In the X-t diagram the pressure raise produced by the fluid hammer appears as parallel stripes, whose thickness is equivalent to the pressure spike bandwidth at each location of the test element. The stripes colour intensity decreases as one moves upwards on the diagram (in time), which shows, as in the 1D pressure evolution diagram, that the pressure spikes are damped in time until its complete attenuation. On the other hand, the pressure amplitude also decreases from right to left (in space). Thus, the 2D map is a valuable tool of analysis, providing information that can not be obtained with a 1D history recording.

5.3. Multiphase behaviour of the liquid front

The fluid hammer produced in the present flow configuration involves several multiphase phenomena, including vaporous and gaseous cavitation. Vaporous cavitation occurs when the local pressure drops below the vapour pressure and gaseous cavitation occurs when the pressure drops below the saturation pressure of the NCG dissolved in the liquid, i.e. the tank pressure P_t. That is why the most complex features take place between the opening of the FOV and the arrival of the liquid front at the forward end, when the liquid front faces the vacuum conditions in the test element. In order to identify the physical phenomena involved, two parameters are proposed: the void fraction, α, which expresses the fraction of the gaseous phase (vapour and NCG) in a given volume of fluid, and the NCG mass fraction, x_{nc}.

$$\alpha = \frac{V_{gas}}{V_{total}} \tag{1}$$

$$x_{nc} = \frac{m_{NCG}}{m_{total}} \tag{2}$$

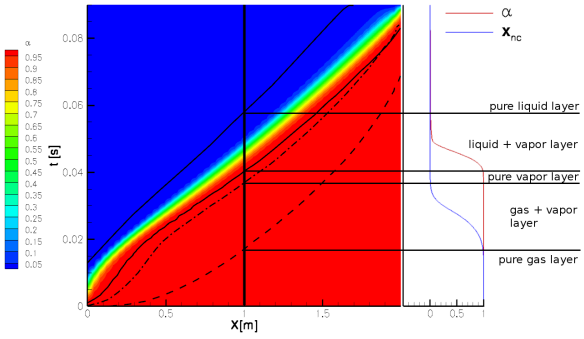

Figure 10: X-t diagram for the void fraction

In equation 2, m_{NCG} refers only to the NCG in evolved state. Therefore, when $\alpha = 1$, the volume is full of gas (vapor or NCG) and when $x_{nc} = 1$ the volume is full of NCG in gaseous state.

Figure 10 shows the X-t diagram coloured with the void fraction, together with a side graph with the void fraction and the NCG mass fraction history obtained at half-length of the test element ($X = 1\,m$). The time interval represented in this diagram goes from the opening of the FOV until the impact of the liquid front at the forward end ($0 < t < 0,09\,s$). According to this graph, five different layers can be distinguished. Initially, the test element is filled with NCG ($x_{nc} = 1$). Later, a thick layer with a mixture of vapour and NCG appears, where the NCG is gradually evacuated and replaced by the vapour phase ($\alpha = 1$ and $x_{nc} < 1$). The

third layer contains only vapour ($\alpha = 1$ and $x_{nc} = 0$). In the fourth layer, droplets of liquid start to appear ($\alpha < 1$), and in the fifth layer there is only liquid phase ($\alpha = 0$). As the liquid layer approaches the forward end, the pressure increases, which makes the vapour condensate and the NCG dissolve into the liquid.

This complex multiphase behaviour has a major influence on all the physical variables that dominate the fluid hammer occurrence.

6. Conclusions

This review describes the design of an experimental facility to study the priming process and shows results obtained with a preliminary set-up. A first comparison of the numerical simulations with preliminary experimental data has validated the prediction of the first pressure peak, but some effort is needed in the prediction of the second and successive peaks. The X-t processing has shown the multiphase nature of the liquid front, where several layers appear. A detailed analysis of the speed of sound is now necessary in each layer, and needs to be taken into account to model correctly the pressure peak level and the time delay between successive peaks.

The work will continue now with measurements undertaken on the final set-up using different test fluids. The experiments will be done for different pressures in the tank and vacuum conditions in the test element, and for three configurations of the test element. The results will be compared to the simulations for a proper validation of the numerical tools. The characterisation of the liquid front mechanism will be also further analysed.

Acknowledgments

This study is supported by the European Space Agency through the GSTP activity AO/1-6210/09/NL/CP.

References

[1] K. L. Yaggy, Analysis of propellant flow into evacuated and pressurized lines, in: 20th AIAA/SAE/ASME Joint Propulsion Conference and Exhibit, 1984.

[2] R. P. Prickett, E. Mayer, J. Hermal, Water hammer in a spacecraft propellant feed system, Journal of Propulsion and Power 8 (3) (1992) 592–597.

[3] T. Y. Lin, D. Baker, Analysis and testing of propellant feed system priming process, Journal of Propulsion and Power 11 (3) (1995) 505–512.

[4] J. Molinsky, Water hammer test of the seastar hydrazine propulsion system, in: 33rd AlAA/ASME/SAE/ASEE Joint Propulsion Conference & Exhibit, 1997.

[5] L. Ounougha, F. Colozzi, Correlation between simulations and experiments on water hammer effect in a propulsion system, in: Proceedings of Second Eurpean Spacecraft Propulsion Conference, 1997.

[6] T. Martin, L. Rockwell, C. Parish, Test and modeling of the mars '98 descent propulsion system waterhammer, in: 34rd AlAA/ASME/SAE/ASEE Joint Propulsion Conference & Exhibit, 1998.

[7] H. C. Hearn, Development and application of a priming surge analysis methodology, in: 41st AIAA/ASME/SAE/ASEE Joint Propulsion Conference & Exhibit, 2005.

[8] R. Lecourt, J. Steelant, Experimental investigation of water hammer in simplified feed lines of satellite propulsion systems, Journal of Propulsion and Power 23(6) (2007) 1214–1224.

[9] I. Gibek, Y. Maisonneuve, Waterhammer tests with real propellants, in: proceedings of 41st AIAA/ASME/SAE/ASEE Joint Propulsion Conference & Exhibit, Tucson (AZ), USA, 10-13 July, no. 2005–4081, 2005.

[10] J. Moral, R. Perez-Vara, J. Steelant, M. de Rosa, Espss simulation platform, in: proceedings of 2010 Space Propulsion conference, San Sebastian, Spain, 2010.

[11] C. Koppel, J. Moral, M. de Rosa, R. P. Vara, J. Steelant, P. Omaly, A satellite platform modelling with ecosimpro: Results of the simulation compared to the ground tests, in: proceedings of SimTecT 2009 Simulation Conference, Adelaide, Australia, 2009.

Experimental investigation of liquid phase detachment and atomization from wall surfaces due to an external air flow field – Application to wiper system[☆]

Evangelos Bacharoudis[*]

TEMPO/DF2T Équipe Dynamique des Fluides et Transferts Thermiques, Université de Valenciennes et du Hainaut Cambrésis, 59313 Valenciennes, France, evangelos.bacharoudis@be.bosch.com

Supervisor: Larbi Labraga

Professor, TEMPO/DF2T Équipe Dynamique des Fluides et Transferts Thermiques, Université de Valenciennes et du Hainaut Cambrésis, 59313 Valenciennes, France, larbi.labraga@univ-valenciennes.fr

Promotor: Jean-Marie Buchlin

Professor, Head of Environmental and Applied Fluid Dynamics Department, von Karman Institute for Fluid Dynamics, Belgium, buchlin@vki.ac.be

Industrial Partner: Hervé Bratec

Dr. Engineer, Robert Bosch Produktie N.V., Hamelendreef 80, B300 Tienen, Belgium, herve.bratec@be.bosch.com

Abstract

Thin liquid film and air flow interactions play an important role in many two phase flows encountered in industry. Overspray is named the result of such interactions in the domain of the wiper systems for the automotive sector. Experiments were conducted in von Karman Institute in a simplified car geometry in order to investigate deeply the mechanisms responsible for liquid phase detachment and atomization from the surfaces of the wiper blades. The focus is on the qualitative description of the parameters that lead a liquid film to be detached and less on the transport of the atomized droplets and their final impact on the windscreen. Further experiments are planned in order to quantify the outcome of this study.

Keywords: two phase flow, liquid film, detachment, atomization, visualization, wiper blades,

1. Introduction

A phenomenon related with thin films has been emerged in the automotive sector in the domain of the wiper systems. Activating the wiping system of a moving car, liquid is ejected from the nozzles and released on the windscreen and the wiper blade surfaces. The liquid remained on the wiper blades is forming a thin film being in motion along the wall surfaces sheared by the external flow. When the car accelerates above 80 km/h the air is strong enough to drive the film in specific locations on the wiper blade where detachment and atomization in fine droplets occurs. The atomized droplets interact with the external air flow field and part of them impact on the windscreen deteriorating the sight of the driver and giving the feeling of a very poor wiping quality. The phenomenon of air-liquid interactions followed by droplet ejections and resulting worsening of the wiping quality is called overspray. Figure 1 shows typical overspray failures on a windscreen.

The physics involved in the overspray phenomenon concern the following research areas in the studies of multiphase flows [1]:

- droplet ejection from wall surfaces
- droplet transport
- droplet impact on a wall surface

[☆] All rights of this paper owned by Robert Bosch Produktie N.V.

[*] Corresponding author

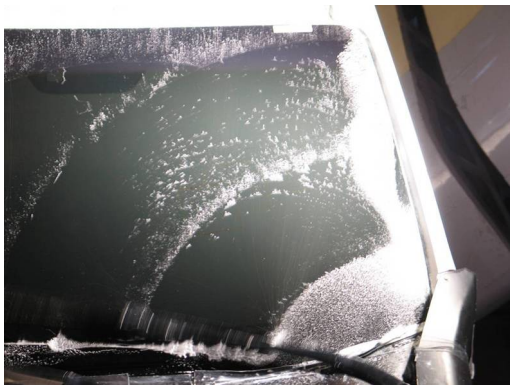

Figure 1: Overspray failures on the windscreen. Only the droplets in the middle of the screen are considered as overspray failure.

The focus in this study is concentrated on the creation of droplets from thin films sheared by a strong air flow. In this point, it should be noticed, that the term 'film' implies always the presence of a wall surface. The behavior of a film immersed in turbulent air flow field is dictated by the action of opposed forces on the film bulk and film surfaces. Generally, aerodynamic forces tend to destabilize the liquid film and atomize it while surface tension forces and viscosity lessen the disturbances and stabilize the film.

Despite the importance of liquid films in different industrial applications, only recently, experimental studies are published in the open literature concerning liquid film detachment and atomization from wall surfaces [2, 3, 4]. The lack of extensive experimental data in the field of film detachment and atomization is related with the significant difficulties encountered to perform measurements in such systems. On the other hand, there is plenty of published work on experiments in liquid jet and liquid sheet atomization processes. The latter constitutes useful database in order to explain many phenomena encountered also in films. Lightfoot [5] gives a good review for the current status of research work on liquid film atomization. Finally, different theoretical models have been developed, based on either simple force balance considerations [2, 4], or on linear stability theory [3] for the prediction of the fastest growing disturbance responsible for film disintegration.

The present study begins with the experimental investigation of atomization phenomena in a simplified car geometry (scale 1:1). Following the identification of the locations of droplet ejections and their result on the windscreen, a qualitative description of the complex interaction between the liquid film and the air flow is given. Different ways of liquid film disintegration on wall surfaces are reported and simplified models are proposed for further investigation. A new experimental facility is presented for the study of the simplified models and future steps concerning the quantification of the above mentioned phenomena are provided.

2. Experiments on car geometry

First, experiments were conducted in a real car geometry in order to explain the behavior of the wiper blades and the presence of the droplet on the windscreen. Different phenomena , mentioned in the introduction, were observed and are described qualitatively.

2.1. Experimental facility and methods

Experiments were performed in the von Karman Institute, in low speed wind tunnel L1-A. Figure 2 shows the open test section of the wind tunnel with the car model in it. The length of the free jet in the open test section is 4.5 m and the platform was located 1.7 m above the ground. The velocity of the jet in the test section was set up at 160 km/h (44.44 m/s), typical for hard overspray conditions on cars.

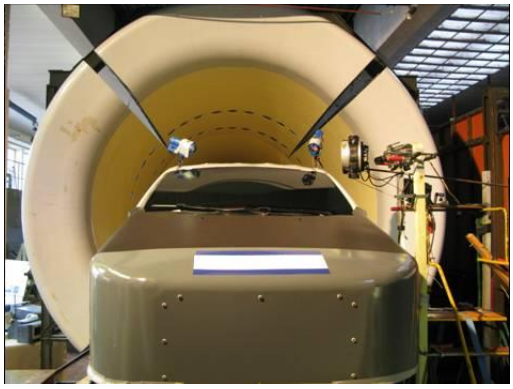

Figure 2: Test section facility.

The car model, of scale 1:1, has been carefully designed and manufactured in Bosch in order to capture the most important features of real cars. The model is consisted mainly of two parts, the hood and the windscreen. All the lateral surfaces were closed with plastic parts. The length of the model was 2.3 m and the maximum vertical dimension was 1.3 m. The car model was positioned on the platform in a way that the center of the windscreen coincides with the center of the free jet.

A system consisting of a micro centrifugal pump and two tanks was built in order to provide the nozzles of the car with the necessary liquid. Motion to the wiper blades is provided by a control unit installed outside the car model with possibility to choose different rotational speeds as well as to change the operational time of the wiper blades. Besides, the centrifugal pump for the liquid supply system was connected also to the same unit. The control unit was programmed and the running of the wiper blades and the pump became an automatic process.

Two types of nozzles were applied on the model in order to spray the liquid to the windscreen, namely the '2-spot' and the 'cloud'nozzles. The former produces a spray of droplets which impacts the windscreen with a shape of a spot and the latter produces a spray like cloud. Different types of wiper blades were tested on the model in order to monitor the behavior of the blades and identify essentials geometrical parameters that influence the overspray phenomenon.

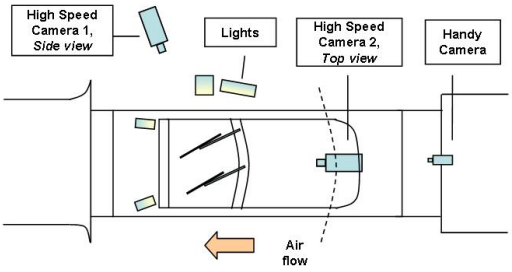

Figure 3: Sketch of experimental equipment used to record the liquid film detachment and atomization.

The general setup of the equipment used to record the droplet generation from the wall surfaces of the wiper blades is shown in Figure 3. A camera was set above and opposite to the windscreen in order to record the droplet failures on it for each tested blade. From the videos a classification of the blades based on their level of overspray was possible.

Two high speed cameras recorded two different views of the blade, the 'top' and the 'side' view at the same time. Setting up the speed of the cameras at 2000 frame/sec, the liquid film flow on the wiper blade and the atomization process were captured. An inductive sensor placed below the hood is used to trigger both cameras when the blades pass from a specified position on the windscreen.

A lot of light sources are necessary in high speed recording for adequate illumination of the object. A great effort made to position the light equipment outside the free jet resulted in very poor videos. Taking that into account and considering the fact that the purpose of the current experiments was to describe qualitatively the phenomena and not to quantify them, the presence of the lights inside the free jet especially those at the driver's side , in Figure 3, was mandatory for high quality videos. Nevertheless, comparing the behavior of the wiper blades for the specific type of car with the behavior of the same blades used in other tests for real cars of similar type, no significant differences were observed and the recorded videos can be considered acceptable to draw conclusions for overspray.

Finally, a mixture of petrol, oil and blande titan, was used to visualize the mean air flow field on the surfaces of the wiper blades and the windscreen. Generally, the oil film technique is combined with topological concepts to predict the 3D flow field above the surface based on the analysis of the film patterns and the critical points formed on them and rely on the fact that a given pattern corresponds to a particular 3D flow topology above the surface. Here, the focus is on capturing the most important characteristics of the local air flow on the blade surfaces and there was no intention to analyze in detail the whole complex flow field developed above these surfaces, which would demand further experimental investigation with different techniques (smoke, PIV).

2.2. Results and discussion

Selective results are presented and discussed in the following sections in order to identify and understand better the physical mechanisms behind overspray.

2.2.1. General characteristics of location of droplet sources

At the speed of 160 km/s, well above the critical speed for onset of overspray (80 km/s), liquid phase detachment with simultaneous droplet generation was observed. The identification of the locations of these droplets sources was achieved with the help of the high speed recording. Figure 4 illustrates the film detachment and droplet generation in the middle of the wiper blade, extracted from the high speed videos.

Seven different locations on the wiper blade were assigned as locations of droplet sources. All of them are located in the region of the adapter (middle of the blade). The activity of each droplet source depends on the amount of liquid in the vicinity of the source. Considerable amount of liquid gives intense activity of the source while insignificant amount can lead even to the

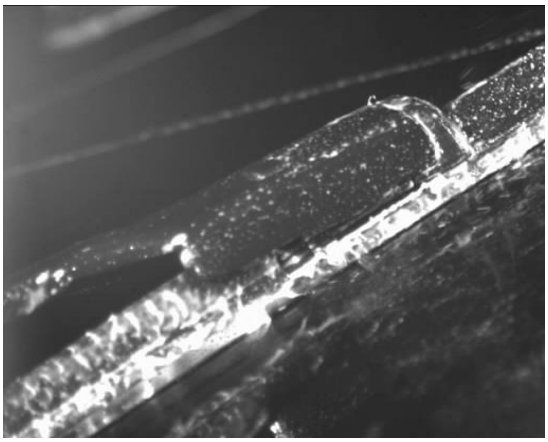

Figure 4: Droplet ejections in the area of the adapter.

deactivation of the source. This fact explains the differences in droplet ejections observed spraying with '2-spot' (less droplet generation) and 'cloud' nozzles (more droplet generation). The former tends to create liquid pools on the wiper blade concentrated in certain points of the blade while the latter form a thick film spread in all over the area of the blade. A common characteristic of all the droplet sources identified before is their geometry. Liquid film sheared by the external air flow field is moving along the blade. Generation of droplets or primary atomization occurs at the locations (droplet sources mentioned before) where the liquid film approaches the proximity of the boundaries of the wall surfaces. In other words, when the liquid film encounters a corner, depending also on the conditions, is detached and atomized. Lightfoot [5] referred to this type of atomization which is unique only to films, giving few reference works. However, as mentioned earlier in the introduction 1, till that time only few experimental works were available in the open literature. Since then, new studies, experimental and numerical, contributed to the understanding of the film detachment and atomization at the proximity of corners. Nevertheless, further investigation has to be done on this field.

There is a significant variety of shapes and sizes of the corners encountered on the wiper blades. Corners varying from some millimeters to few centimeters may act like an obstacle in the liquid film flow. Moreover, there are sharp corners and corners with rounded edges. The variety of angles formed by the two intersecting sides of the corner is also significant. Acute, right and obtuse angles are detected on the corners of the blades. The locations of the corners and consequently of the droplet sources can also form different angles with the gravitational vector. All these information, in one side, are characteristics of the droplet source locations, on the other side, reveal the complexity of the phenomenon. It should be kept in mind that till here, only geometrical parameters of the problem are considered.

The droplet source locations correlated with the droplet failures on the windscreen and interesting results came out. Not all of the locations that generate droplets contribute to failures on the windscreen (overspray). A significant number of them produces droplets which are driven by the air flow field away from the windscreen. Among the sources that contribute to overspray failure, their impact on the windscreen was identified and correlated with their origin. This permitted the detection of the level of contribution of a droplet source in overspray only by scrutinizing the failures on the windscreen for the specific type of wiper blade.

Finally, another important phenomenon observed during the tests is the partial atomization of the liquid film in some locations permitting part of it to flow around the corners. Direct implication was the constant feeding of the droplet sources placed downstream the initial one with the required liquid for atomization.

2.2.2. Local air and liquid flow characteristics

The main cause for droplet generation in wiper blades is the film detachment from corner geometries in fixed positions of the blade due to the shear imposed by the external air flow field.

The study of the air flow around the wiper blade is essential for understanding the liquid film detachment phenomena. The local characteristics of the air flow field close to the wall are of high importance in the current study comparing to the global ones. However, the pictures captured from the oil film visualization on the windscreen permitted to discuss some of the global features of the flow around the wiper blade. These features are presented for the completeness of the work and to assist the rendering of the air flow field around the blade. However, it should be noticed that in no means they comprise any independent and complete study of the general characteristics of the 3D air flow field above the blade.

Figure 5 depicts the flow patterns formed on the windscreen using the oil film visualization technique for a wiper blade fixed on 45 ° to the park position. The analysis of the patterns and their correlation with the flow topologies above the wall surfaces is based

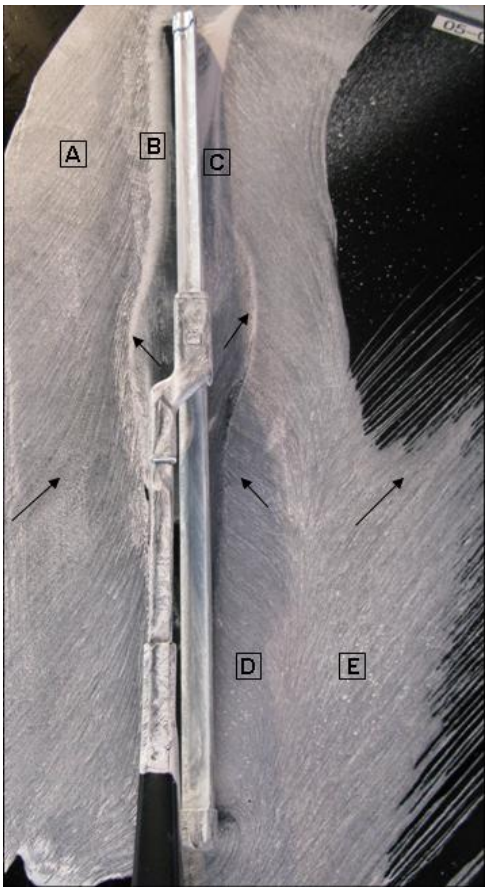

Figure 5: Results from oil film visualization technique (wiper arm in 45 ° from the park position).

on the work of Perry and Chong [6]. Similar analysis has been followed by other researchers for geometries which produce analogous patterns like the wiper blade. Panigrahi et al [7] performed oil film visualization and PIV measurements in surface mounted permeable and non-permeable rib geometries in order to understand the flow structures responsible for enhancing heat transfer/mixing in permeable geometries. The patterns collected in their experiments demonstrate similar characteristics to the ones of the wiper blades. Behind the non-permeable square rib, they detected a main recirculation region, a small counterclockwise vortex in the vicinity of the back of the rib and the region where the main flow reattaches the floor.

In the case of the wiper blades, six different zones and three critical lines were identified. On Figure 5, the main flow is coming from the left and shifts above the windscreen (zone A) to the right. In front of the blade the flow is separated forming a clear separation line. A small counter clockwise vortex (zone B) is generated and the main flow is directed upwards passing over the blade. On the back, the main flow is directed downward, reattaches on the windscreen and one part is moving upstream forming the main recirculation zone (zone D) and another part continues till it leaves the frame of the picture from the right (zone E). The part of the flow which is moving upstream encounters the main body of the blade. The blade causes the separation and the formation of a small counter clockwise vortex (zone C). The adapter and the wiper arm do influence the global characteristics of the flow field. Their sign is apparent observing the variations in the shape and the size of the zones behind and along the wiper blade.

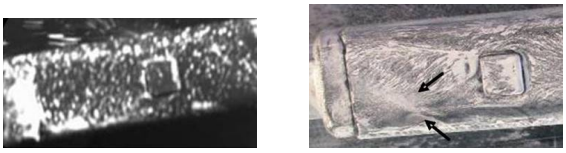

(a) Liquid film flow (b) Local air flow

Figure 6: Top view of the blade. Film and local air flow characteristics extracted from high speed recording and oil film visualization.

As mentioned before, this study was focused on the investigations of the local characteristics of the flow. On the wiper blade surfaces there are two phases moving at the same time, the liquid film and the air flow, interacting each other. Figure 6a shows the liquid film behavior and Figure 6b the local air flow pattern on the adapter. The air flow is oriented from the bottom to the top, on Figure 6. The liquid film behavior extracted from the high speed videos while the local air flow characteristics from the oil film technique. For the case represented in the Figure 6, the local air forms a very complex pattern on the top of the adapter. The pattern reveals two main characteristics, the main flow which attacks the side of the adapter from the bottom of the Figure 6b and the opposing secondary flow which is probably a kind of clockwise vortex formed from the separation of the main flow on the top of the adapter and the complex interaction of local flows coming from the corners and the rest part of the wiper arm (not shown in the picture). On the other hand, liquid is attached on the top of the adapter after the spray and is trapped in the region between the main flow and the opposing one. Depending on the amount of the film, disturbances are created on the interface of the film. The main flow which is stronger in that case comparing to the opposing one results in the detachment and atomization of the film in the downstream

direction. In other words, the liquid is atomized in that position due to the fact that it is captured between the opposed flows and its interface is sheared by the strong component of the complex flow field.

2.2.3. Liquid film atomization models

The method of correlating the local air flow together with the liquid film was followed for every single droplet source for all the types of the wiper blades in order to reveal the underlying mechanisms that cause liquid phase detachment and atomization from the wall surfaces of the blade. The outcome of the analysis is summarized in Figure 7. In this point, it should be mentioned that the results of Figure 7 are indications of the way that a film may be atomized in a corner derived from qualitative observations during the tests. For some of the results, further investigation is needed to confirm their existence.

The liquid film which is thin enough (order of mm) interacts with the local air flow, which is the result of different complex interactions of secondary mainly flows, at the vicinity of the walls. Aerodynamic forces give the necessary inertia to the film in order to overcome the viscosity and surface tension forces which tend to keep the film attached to the wall. Centrifugal forces imposed by the rotation of the blade estimated negligible (linear rotational velocity: 2 m/s approximately) comparing to the aerodynamic forces (40 m/s). Gravitational forces depending on the position of the blade can have dual function, improving or preventing liquid detachment, however is still their influence doubtful because of the thin size of the films and consequently their trivial amount of mass.

Three different air-liquid patterns were identified to comprise the liquid phase detachment and atomization modes observed on the wiper blades, see Figure 7. Based on the type of the geometrical configuration, a first classification distinguishes film atomization in concave corners (Mode A) and convex corners (Mode B, C). A second classification applied only in convex corners has to do with the position of the film relative to strongest current of the air flow. If the film is on the side with the strong stream of air then it is recognized as classic atomization in a corner (Mode B), see Figure 7b. In this mode the film can flow around the corner without any atomization or can be partially atomized or can be atomized completely in the corner depending on the conditions. If the film is located on the side with the weak stream then it is classified as atomization in the weak side of the corner (Mode C), see Figure 7c. The weak flow in that case can be the recirculation zone of the main flow or

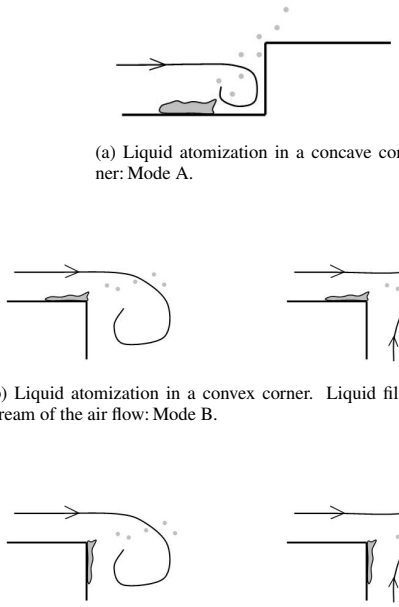

(a) Liquid atomization in a concave corner: Mode A.

(b) Liquid atomization in a convex corner. Liquid film in the strong stream of the air flow: Mode B.

(c) Liquid atomization in a convex corner. Liquid film in the weak stream of the air flow: Mode C.

Figure 7: Models of liquid atomization in a corner

an independent flow less strong than the one on the other side of the corner. For the concave corners the position of the liquid is not important and atomization may happen in front of the stagnation zone (Mode A), see Figure 7a. The dominant mode of atomization in wiper blades is the classic atomization in a corner as described in Figure 7b.

Lightfoot [5] in his review do not refer details for the film separation modes in a corner while experimentalist have identified the two last ones of Figure 7, concentrated more on convex corners studying the classic atomization and less the one at the weak side. As far as concerns our knowledge, there is no report in the open literature for atomization in concave corners and further experiments are needed in order to conclude for its existence.

3. Experiments on simplified models

The experimental analysis of the film behavior on the wiper blades revealed interesting phenomena concerning different film atomization modes acting at the same time on the blade. To gain a deeper understanding on these phenomena, it is necessary to study them separately in simplified geometries and

controlled conditions. For that reason, a new experimental facility, dedicated to the study of liquid films in corners, was designed and built in the TEMPO laboratory. Description of the new facility and first results concerning the quality of the air flow are presented below.

3.1. Experimental facility

3.1.1. Design objectives

For the purpose of the study of the atomization of thin liquid films in corners a small low-speed wind tunnel was designed and manufactured. The wind tunnel needed to be able to operate in different velocities varying between 0-220 km/h [0-60 m/s]. Moreover, the turbulent intensity of the air flow should be low enough (order of 1%) with possibility to increase it.

Different test sections corresponding to the models presented in Figure 7 were meant to be mounted. The flow in the beginning of each test sections needed to be two dimensional on average and uniform, avoiding excessive variations of the mean flow. According to Barlow et al [8] the variations of the time-averaged velocities in the working range of the jet in a cross section should be less than 0.25% of the mean of the section for successful design. Important feature of the wind tunnel is the capability for rotation to form different inclination angles with the ground. This gives the possibility to investigate the influence of the gravity in the atomization of thin liquid films.

3.1.2. General description

The experimental facility is consisted of a wind tunnel and a liquid supply system, see Figure 8. An open circuit, blowing type wind tunnel was constructed with a semi-open test section. The open circuit tunnel has simple construction. The blowing type was dictated by the characteristics of the test section. The total length of the wind tunnel is 3 m with a maximum width of 20 cm. The distance of the test section from the ground is 1.2 m. The whole configuration supported in a metallic frame fixed on the ground. To avoid disturbances of the ambiance flow resulted from the free jet, the whole facility was placed in a big room. Detailed measurements are presented below to assess the quality of the flow and the success of the design.

The wind tunnel has a rectangular cross section and is consisted of six parts, namely, the fan, the flexible pipe, the diffuser, the settling chamber, the contraction and the test section. Crucial part of the design is the test section which determines many of the characteristics of the whole tunnel and is discussed separately

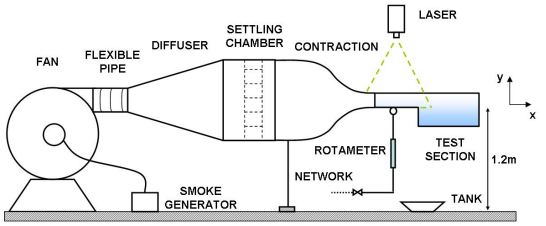

Figure 8: Wind tunnel and liquid system configuration for the study of film atomization in corners.

below. A centrifugal fan with a motor of 11 kW was available to provide the air flow. The connection of the fan with the remaining parts of the facility was made by a flexible pipe in order to achieve the rotation of the tunnel in future experiments.

A long wide angle diffuser was designed and built in order to drive the flow in to the settling chamber in a low velocity. The ratio of outlet to inlet area (diffuser ratio) was 5 and the diffuser angles in the x-y and x-z planes were 6.8 ° and 1.1 ° respectively. According to Mehta and Bradshaw [9] these values give a successful diffuser design avoiding separations due to adverse pressures without being necessary to place screens. The settling chamber is used to reduce the variations of the flow and produce a more uniform flow. A long honeycomb made by plastic straws was placed half hydraulic diameter distance from the inlet of the chamber in order to permit the diminishing of the variations of the flow from the diffuser. The porosity of the honeycomb was 0.87 above the critical value given by Barlow et al [8]. No screens were mounted in the tunnel after the honeycomb, however, enough space was reserved in case of future use.

The most important part for the control and the quality of the flow in the test section is the contraction placed just after the settling chamber. A 2D contraction was designed carefully to provide uniform flow with lowest variations inside the test section. The design method follows the work of Morel [10]. The profile of the contraction was defined by the cubic family curve positioning the inflexion point in the middle of the contraction. The numerical results of Morel [10] show that the previous values suppress the turbulence fluctuations and provide a uniform flow at the end of the contraction. The contraction ends in the dimensions designated from the test section providing it with air of desirable velocity. Before the test section a small distance of half hydraulic diameter is given to the end of the contraction in order for the non-uniformities of the flow to cut down.

The liquid supply system consistes of a small tube of 1 cm diameter and pipes connecting the tube with the network. The small tube is placed at the point of interest for film introduction under the test section. Holes of 1 mm diameter were drilled in one side of the tube and a layer with porous material attached below the holes inside the tube. The water coming from the network enters the tube which is used as a tank to reduce the disturbances. When the tube is filled, the water floods and exits from the small holes continuing to the test section.

3.1.3. Test section

Figure 9 presents the test section used in the current study. The inlet cross section is (20×5 cm) and the whole configuration is made by PMMA. Two thick plates comprise the corner and two lateral walls mounted at the sides in order to confine the liquid film flow in the test section and to avoid disturbances from the environment during liquid atomization. The corner placed 10 cm far from the inlet is sharp with an angle of 90 °. A slit with width of 1 mm and length of 20 cm is drilled on the horizontal plate in a distance of 5 cm from the corner in order to allow the water to come out from the tube and enter the test section to form the film.

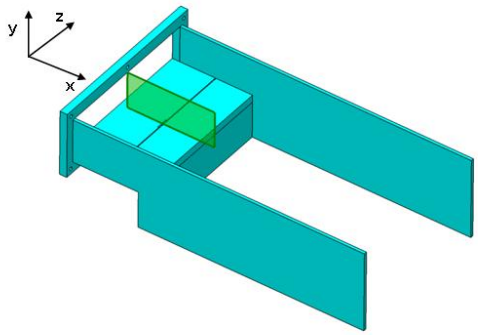

Figure 9: Test section configuration.

The design was meant to provide the test section with a uniform, 2D in average air flow and the lowest possible boundary layer thickness on the wall surfaces. The study of the real car (section 2) revealed that the local air flow field is very complex, there is no developed boundary layer on the surfaces of the wiper blades. Consequently it is not essential and interesting to achieve a developed boundary layer in the new test section. However, it was needed a constant, uniform, 2D in average flow along the horizontal plate capable to realize a wide range of air velocities. According to the boundary layer theory, the thickness of the tourbulent boundary layer at the corner is predicted to be in the order of 4 mm. The test section was designed with the possibility to accommodate also small obstacles of 1 cm of size (typical for wiper blades) retaining the two dimensionality of the flow.

The vertical wall of the corner and the lateral walls of the sides in this study are short extended only 5 cm below the horizontal plate. Numerical simulations were performed for different configurations to conclude that the vertical wall should be long enough in order to avoid the recirculation generated at the bottom tip of the vertical plate due to the entrainment of air from the jet. The reason for keeping the current configuration is the convenience during manufacturing, since the present tests are conducted to control the quality of the flow of the wind tunnel and not to perform detailed experiments on the film atomization phenomena. After the confirmation of the proper operation of the wind tunnel according to the objectives, the walls of the corner and the sides will be replaced by walls almost touching the ground in order to prevent recirculations and disturbances from the entrainment of the air due to the free jet.

Another factor which is considered into account is the reduction of the potential core of the wall jet in the test section. The objective was the following, the corner should always be inside this core. According to literature [11], the core extends 4 to 5 inlet diameters depending the initial conditions. Numerical simulations confirmed the above mentioned statement. For this study the corner located two times the height of the inlet section downstream.

3.2. PIV measurements

PIV measurements were conducted in the test section to assess the quality of the flow provided by the wind tunnel. A double pulsed Nd:YAG laser with a green light of 532 nm wavelength was used in order to illuminate the x-y mid-plane of the test section (see Figure 9). The assessment of the air flow quality was carried out in the maximum frequency of the electrical motor of the fan, at 40 Hz. This frequency corresponds to a maximum air flow velocity inside the test section of 30 m/s. The flow is seeded in the suction side of the centrifugal fan with small oil particles obtained by evaporation. The laser was placed above the test section and the camera perpendicular to the formed laser sheet as presented in Figure 8. The camera is equipped with a 50 mm Canon lens having a res-

olution of 2048 × 2048 and the aperture was adjusted to a value of f-number 8.

Table 1: Settings of laser and camera parameters for PIV measurements

PIV Parameters	
Masked field of view	[120,85] mm
Image size	[2048,2048] pix
Pixel size	64.23 μm
Pulse separation	15 μs
Frequency	7.25 Hz
Number of samples	300
Sub-pixel scheme	Gaussian
Window size	[32,32] pix
Overlap	50%
Number of vectors	[127,127]
Resolution	2 mm

The settings for the laser and the camera are described in Table 1. For the current study the interrogation window was chosen to be 32 × 32 and 300 pairs of images have been acquired. A cross correlation PIV algorithm was used to process the images and PIV measurements were carried out following the criteria for adequate number of particles in the measurement plane and the 1/4 rule for the in-plane motion of particles. No post-process treatment is applied to the images after the calculation of the displacements.

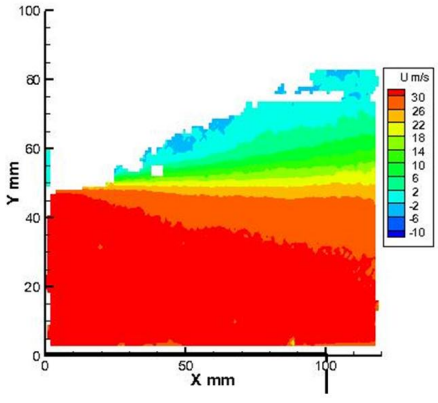

Figure 10: U-velocity contours of average air flow field from PIV measurements.

Figure 10 presents the velocity contours of the U component in the mid-plane obtained from the PIV data after averaging the collected pairs of images. Measurements were achieved till 2.5 mm above the wall. Approaching the wall, reflections of the laser sheet prevent reliable measurements. In the future, it is planned to improve the treatment of the wall surfaces in order to get closer to them. The air flow enters the test section in the mid-plane with a uniform and constant profile. The variations of the U component of the velocity in the mid-plane from the average velocity at the inlet section are estimated less than 1%. The flow is developed on the horizontal plate of the corner like a wall jet. Air from the surroundings entrains the jet resulting in the reduction of the size of the developed potential core. Figure 10 shows that the corner is located inside the potential core of this wall jet.

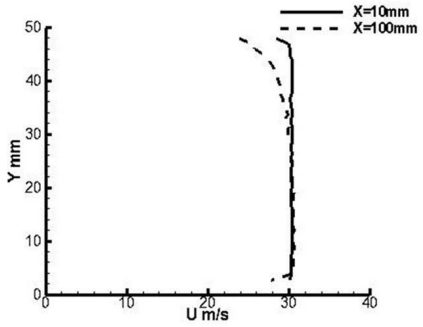

Figure 11: U component of averaged velocity profiles from PIV measurements.

The U component velocity profiles at the inlet of the test section (x=10 mm) and at the corner (x=100 mm) are presented in Figure 11. The results reveal also a constant and uniform flow above the horizontal plate of the corner. The boundary layer at the position of the corner is not more than 4 mm as expected. More PIV experiments are planned to obtain the flow field in other planes for a better understanding of the flow. However, these first results show a wind tunnel design which accomplishes the majority of the objectives defined above. Finally, the current study is interested in the assessment of the flow quality close to the horizontal plate before the corner. The structures emerged from the entrainment of the ambient air on the top of the test section and the ones developed after the corner are not taken into account.

4. Future steps

The current PhD study will focus mainly on the atomization of liquid films placed in the strong air

stream side of a sharp corner, see Figure 7b. Moreover, small obstacles forming a forward step will be mounted on the floor of the test section after appropriate modifications in order to study other types of film atomization (Figure 7a). Furthermore, the implementation of the results from the simplified models (corners) will be investigated to the complex geometries (small obstacles, ribs).

Concerning the atomization (mode B) the following steps are planned:

- to complete the design of the wind tunnel with detailed PIV measurements assessing the air flow quality.

- to record film atomization with high speed camera, measure atomized mass, measure interface film velocity and measure film thickness in order to describe and quantify in detail the film atomization in a corner identifying the critical conditions for the onset of the phenomenon.

- to change different parameters of the model concerning the width of the film, the length of introduction of liquid film, the level of turbulent intensity, the geometrical corner angle and the inclination of the wind tunnel in order to assess their contribution in film atomization in a corner.

5. Conclusions

In this paper, first experimental results are presented considering the complex two phase flow phenomena of liquid film detachment and atomization from the wall surfaces of a wiper blade system sheared by an external air flow.

Experiments were conducted in a simplified car geometry in Von Karman Institute and the qualitative description of the local air and liquid film flow was obtained. Liquid driven by the complex local air flow is moving along the blades of the wiper system. Liquid film detachment and atomization occurs when the liquid film encounters a corner geometry. The analysis of the experimental results reveal the following, three different modes of film atomization take place at the same time on the complex surfaces of the blades:

- Mode A: Atomization in the stagnation zone of a concave corner.

- Mode B: Atomization in the strong air stream side of a convex corner.

- Mode C: Atomization in the weak air stream side of a convex corner.

It should be noticed that the above mentioned atomization modes are indications from observations in a very complex geometry. The study revealed the necessity to investigate deeper the atomization phenomena qualitative and quantitative, separating one another, in simple geometries. For this purpose, a low speed wind tunnel facility with a semi-open test section was designed and presented here. The new experimental facility designed carefully to help the confirmation of the above mentioned modes and the investigation of different parameters that might affect film atomization in sharp corners. Finally, first PIV measurements were demonstrated confirming the successful design of the wind tunnel.

Acknowledgments

For the manufacturing of the car model and the preparations of the tests, the author would like to express his gratitude to the technical team of Bosch (Mr. Vandeput Yves, Mr. Holsbeebs Sven and Mr. Henbens Mathiew) and the technical team of von Karman institute (Mr. Welter Didier, Mr. Bavier Michel, Mr. Gablet Alain) without their help it would be impossible to complete this work. For the manufacturing of the wind tunnel facility, the author feels grateful to Mr. Boussemart David technician in TEMPO. Finally, the author is thankful to Dr. Keirsbulck Laurent , Mr. Planquart Philippe and Mr. Diquas Guillame for their contribution with their comments to the design of the experimental facilities and to Robert Bosch Produktie N.V for supporting financially this study.

References

[1] C. T. Crowe, Multiphase Flow Handbook, CRC Press, Taylor & Francis Group, 2006.

[2] B. J. Azzopardi, K. S. Sanaullah, Re-entrainment in wave-plate mist eliminators, Chemical Engineering Science 57 (2002) 3557–3563.

[3] F. Maroteaux, D. Llory, J.-F. L. Coz, C. Habchi, Liquid film atomization on wall edges–separation criterion and droplets formation model, Journal of Fluids Engineering 124 (2002) 565–575.

[4] M. A. Friedrich, H. Lan, J. L. Wegener, J. A. Drallmeier, B. F. Armaly, A separation criterion with experimental validation for shear-driven films in separated flows, Journal of Fluids Engineering 130 (2008) 1–9.

[5] M. D. A. Lightfoot, Atomization of wall-bounded two-phase flows, in: ILASS Americas, Proceedings of the 19th Annual Conference on Liquid Atomization and Spray Systems, Toronto, Canada, 2006.

[6] A. Perry, M. Chong, A description of eddying motions and flow patterns using critical-point concepts, Annual Review of Fluid Mechanics 19 (1) (1987) 125–155.
[7] P. K. Panigrahi, A. Schröder, J. Kompenhans, PIV investigation of flow behind surface mounted permeable ribs, Experiments in Fluids 40 (2006) 277–300.
[8] J. B. Barlow, W. H. Rae, A. Pope, Low-Speed Wind Tunnel Testing, John Willey & Sons, Inc., 1999.
[9] R. D. Mehta, P. Bradshaw, Design rules for small low speed wind tunnels (Technical note), Aeronaut J (1979) 443–449.
[10] T. Morel, Comprehensive design of axisymmetric wind tunnel contractions, Journal of Fluids Engineering (1975) 225–233.
[11] J. G. Eriksson, R. I. Karlsson, J. Persson, An experimental study of a two-dimensional plane turbulent wall jet, Experiments in Fluids 25 (1998) 50–60.

Shape and temperature field distortions induced by convective effect on hot object in different spectral bands

Anthony Delmas

Environmental and Applied fluid dynamics Department, anthony.delmas@vki.ac.be

Supervisor: Jean-Marie Buchlin

Professor, Environmental and Applied fluid dynamics Department, von Karman Institute for Fluid Dynamics, Belgium, buchlin@vki.ac.be.

Promotor: Yannick Le Maoult

Doctor, Metrology, Identification, Control and Surveillance Department, Institut Clement Ader - Albi, Campus Jarlard 81013 Albi, yannick.lemaoult@mines-albi.fr

Abstract

The goal of this paper is to point out the perturbation induced by convective effect (mirage effect) on shape and temperature measurement and to give an estimation of the error done. This work will explore the sensitivity of several spectral bands: 8-12μm, visible and recently the 0.75-1.7μm band (near IR) with the help of CCD camera (Si) or VisGaAs camera. Several methods will be used in order to highlight the phenomena and to obtain quantitative values of the error done. We will give the displacement and the deformation error for each spectral band.

Keywords: high-temperature, mirage effect, natural convection, infrared, near infrared, visible, hot disk.

1. Introduction

The Institut Clment Ader (ICA) - Mines Albi and the von Karman Institut (VKI) follows since numerous years works about infrared radiometry with the aim to do quantitative thermography (true temperature measurement without contact). The ICA Mines Albi deals also on thermal-dimensional coupling measurements, and so needs to merge usual video data with infrared data. Studies done in this specific domain have underlined some perturbations emphasized at high-temperature (T≥800°C) [1]. This work deals in details with treatment of some perturbations which play a role in the measurement of different parameters in the near IR band. We will focus in this study on perturbations which arises from convective effect present around high-temperature object [2; 3]. Effectively, when a hot object is in a colder surrounding media, a temperature gradient is shaped around the object and so a refractive index gradient too (according to the Gladstone-Dale law). This phenomenon brings inevitably distortion of spatial informations received by the camera. The goal of this work will be in a first time to show clearly this effect and in a second time to estimate errors made on distortion and/or temperature measurement by CCD or VisGaAs camera on hot object. We illustrate the presence of distortion by experimental way (schlieren photography) and numerical way: ray-tracing [6]. Then, we describe different methods used to estimate the convective effect on temperature and distortion measurement and we give our first results. Finally, some possible ways to correct pertubated images are given.

2. Mirage effect

The mirage effect appears as soon as we have a refractive index gradient. What we called mirage effect is when light beams do not arrive at the expected destination (without temperature gradient). Usually this effect does not have a big influence on optic measurement. But, since we are in presence of a strong refractive index gradient, the information measured can be wrong enough to be taken into account. In our case,

the refractive gradient is engendered by a temperature gradient coming from a natural convective plume. Mirage effect induced by natural convection is very frequent and can be observed in numerous cases. The most famous one is the mirage effect which occurs over a road or in the desert when the sun is strongly hitting the ground.

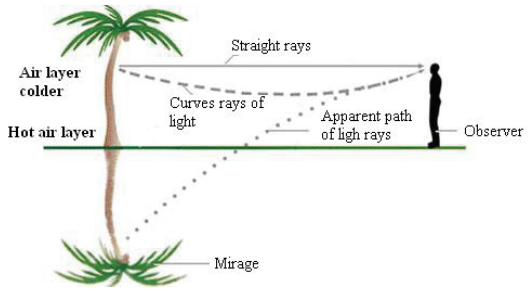

Figure 1: Mirage effect principle.

In our case, we will focus on mirage effect which occurs around hot object. It can be sometimes a real problem when we need to know with accuracy the shape or the temperature of a given point of the object. We give in this work a value of the error made when we are trying to make such measurement. In addition, the deflection induced by the temperature gradient varies with the wavelength. According to the Eq. 1 called Gladstone-Dale law [4], we can obtain for a given temperature field and wavelength, the refractive index distribution.

$$n_\lambda - 1 = K_\lambda \cdot \rho(T) \tag{1}$$

where

$$K_\lambda = (N \cdot \alpha_0)/(2 \cdot \epsilon_0) \tag{2}$$

The Gladstone-Dale constant K is function of the wavelength λ (because α_0: polarizability of one molecule depends on λ) ϵ_0 is the vacuum permittivity and N is the Avogadro number. We choose to work first in the visible band, with the wavelength of the He-Ne laser: λ =652,8nm and K=0,2256.10^{-3} m^3/kg. In our case, air can be taken as an ideal gas, and so:

$$\rho(T) = 352.86/T \tag{3}$$

With combination of Eqs. 1 and 3, we establish for the specific wavelength of an He-Ne laser:

$$n - 1 = 0.079 \cdot T^{-1} \tag{4}$$

We can see in the Fig. 2 how the refractive index depends on the temperature and on the wavelength.

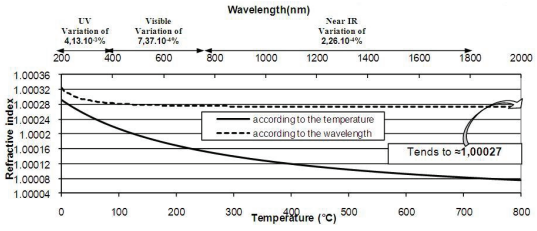

Figure 2: Refractive index evolution according to the wavelength (at 15°C) and to the temperature (at λ=632,8nm) [5].

We are now able to obtain directly from the temperature field, the refractive index distribution for a given wavelength. The next step is then to deduct from this distribution, the displacement induced. A numerical approach based on a ray-tracing code has been used with the purpose to observe the phenomena and to obtain some value of displacement.

3. Numerical approach: ray-tracing tools

This step of our work is divided in three parts. First, we compute the temperature field around the considerate object by means of the software FLUENT. Then, according to the Gladstone-Dale law, we deduce the refractive index field directly linked to the temperature for a given wavelength. Finally, we put this refractive field in our ray-tracing code, working on MATLAB. The study is made in a first step with simple geometry, as reference test case before to go on with more complex geometry. With this aim, we deal first with axisymmetric geometry (as cylinder or horizontal disk). Here, we show only result for the disk.

3.1. Fluent

To obtain the refractive index distribution necessary for the ray-tracing code, we need to know the temperature field around the studied object. We choose here to study the convective plume which appears above a horizontal heated disk of 9,2cm diameter. A cylindrical perturbation permits to create easily a good mirage effect, not only along x but also along y. We obtain with this device a laminar perturbation around 4,5cm width, 10cm above the disk. The temperature field is computed by numerical simulation with the software FLUENT. The simulation is made in axisymmetric; a rotation around the centre of the disk will give the entire temperature field. The figure 3 shows the 2D temperature map above a disk at 1000K (temperature of studied materials in the laboratory ICA range from ≈

400K to 1700K, corresponding from polymers forming and thermal barriers processing and testing temperatures).

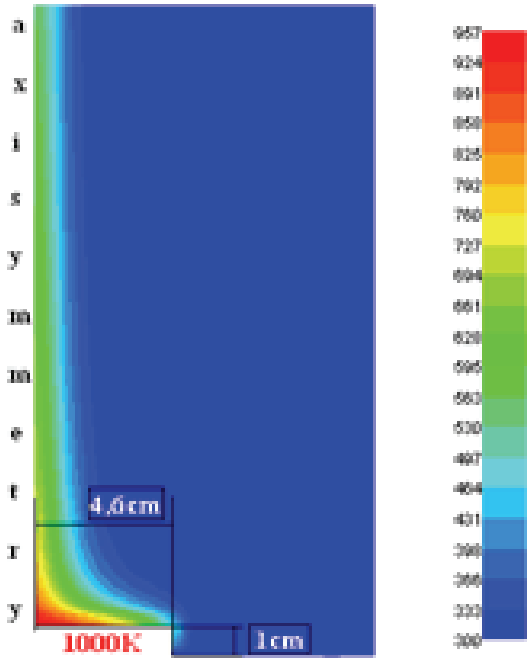

Figure 3: Temperature contours obtained with FLUENT.

3.2. *Ray-tracing software*

After to have converted the temperature field in refractive field thanks to the Eq. 4, we incorporate this data in our ray-tracing code [cosson] as the Fig. 4 illustrates it. The original plan is composed of radiating elements located with their y and z coordinates. Each element launches one ray perpendicularly to the original plan. The refractive index field is around and above the disk is discretized according to the radial and axial coordinates, r and z in order to create a large number of cells with constant refractive index. Transition from one cell to another is governed by the Snell-Descartes law Eq. 5 (transition between a cell i to a cell j with n and θ respectively the refractive index of the cell and the angle between the ray and the normal to the surface of the cell surface):

$$n_i \cdot sin(\theta_i) = n_j \cdot sin(\theta_j) \quad (5)$$

Then, when the ray goes out of the last cell, so from the thermal perturbation, it continues his path until the arrival plan, which the position according to x can be adjusted to accentuate the distortion effect.

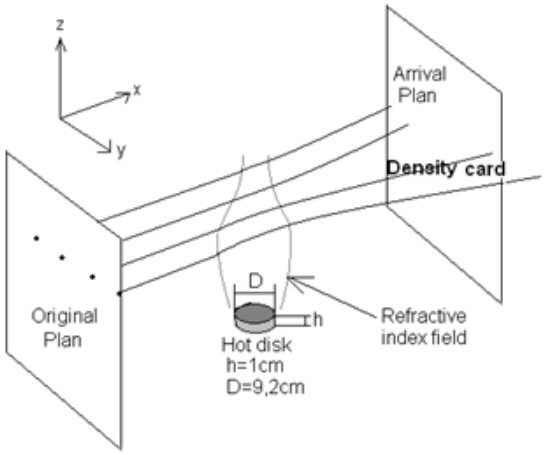

Figure 4: Diagram showing the functioning of the code and its geometry.

Indeed, the further the screen is, the more the deviation is. If we discretize sufficiently the original plan and enough rays are launched, here 340000 to obtain the Fig. 5, we obtain on the arrival plan a density map which show convergence zones of rays or at the opposite, dark zones, corresponding to regions where few or none rays arrive. The Fig. 5 provides an example of result get for the case of the disk heated at 1000K, with the arrival plan located at 5m behind the center of the disk and for the specific wavelength of the He-Ne laser (λ=652,8nm). It shows the distortion effect, every ray passing near the edge of the disk goes towards colder temperature (higher refractive index) creating the dark zone. Consequently, we obtain a convergence zone (more clear) corresponding to rays missing in the dark zone. Above the disk we can also notice that rays passing close to the center are not deviated, which is in agreement with Snell-Descartes law.

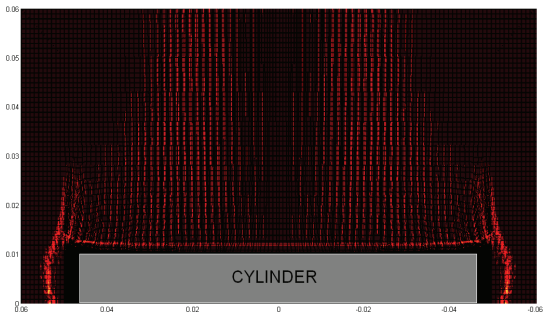

Figure 5: Density map after the passage of rays around and above the disk (1000K).

The ray-tracing code permits also to obtain the displacement field along x, y and the result of this two displacements w. In this way, we can have a good idea of the error made by the camera for each point while watching an object throw a hot plume. As the Fig. 5 shows it, we find again in the Fig. 6 a strong displacement (corresponding to the divergence zones) close to the disk, where the highest temperature gradients are. We notice also that in the center of the plume, the deviation almost doesn't exist.

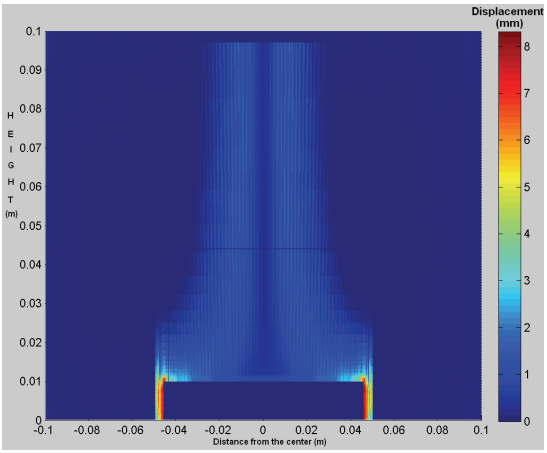

Figure 6: Displacement map (w) after the passage of rays around and above the disk (1000K).

4. Comparison of the convective plume geometry between numerical approach and schlieren photography

Schlieren photography is a visual process that is used to photograph the fluids flow of varying density. The basic optical schlieren system uses light from a single collimated source shining on a target object. Variations in refractive index causes by density gradients in the fluid distort the collimated light beam. This distortion creates a spatial variation in the intensity of the light, which can be visualised directly with a shadowgraph system (Fig. 7).

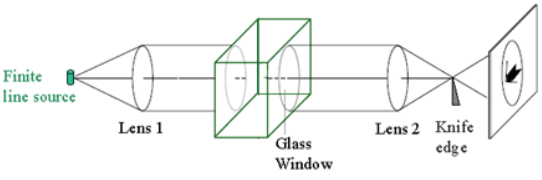

Figure 7: Diagram of the Schlieren photography technique.

In schlieren photography, the collimated light is focused with a lens, and a knife-edge is placed at the focal point, positioned to block about half the light. In flow of uniform density this will simply make the photograph half as bright. However in flow with density variations the distorted beam focuses imperfectly and parts which have been focused in an area covered by the knife-edge are blocked. The result is a set of lighter and darker patches corresponding to positive and negative fluid density gradients in the direction normal to the knife-edge. The sensitivity of the schlieren device is adjusted moving the knife-edge more or less in the focal point. In the case of our heated disk, we obtain the following pictures.

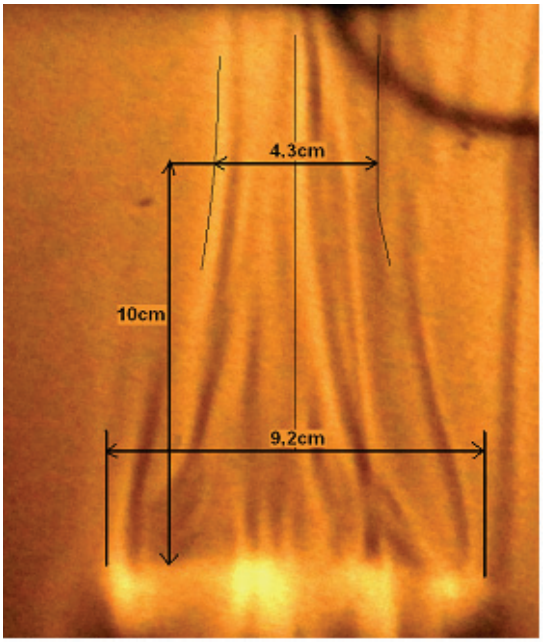

Figure 8: Plume width measured with schlieren photography.

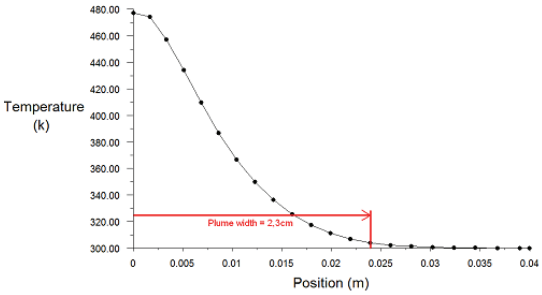

Figure 9: Plume radius measured with FLUENT at 10cm high.

Thanks to this technique, we notice first the devel-

opment of the boundary layer from the edge of the disk toward the center. Then, near the center the flow must separate to form a plume. If undisturbed, the plume will be a steady flow whose energy transport rate is equal to the heat transfer rate from the disk surface. Theoretically, the plume width (at a given elevation) should decrease with increased source strength [7]. But the main problem which occurs here is the heating of the disk support with time. Thats why the picture is more pertubated for high temperature. Moreover, natural convection coming from under the disk can be seen, going up straight from the edge of the disk. A comparison with results obtain with FLUENT has been made in order to validate its. We have compared, for a given temperature surface (650K), the plume width at a given elevation (see Fig. 8 and 9). The width measured with FLUENT and with the schlieren photography are respectively of 4,6cm and 4,3cm. The difference between the two techniques is about 6%. We can assume that the result obtain with FLUENT correspond to the real case and so that we put real refractive index field in the ray-tracing code. We notice finally that, whatever the disk temperature, the flow stay laminar ($Gr<10^8$). Obstacles should be added in order to agitate the plume, and simulate a turbulent flow.

5. Experimental approach

5.1. Displacement measurement method

5.1.1. Principle of the Background Oriented Schlieren method

Background Oriented Schlieren (BOS) [8] is a novel technique for flow visualization of density gradients in fluids using the Gladstone-Dale relation between density and refractive index of the fluid. BOS simplifies the visualization process by eliminating the need for the use of expensive mirrors, lasers and knife-edges. In its simplest form, BOS makes use of simple background patterns of the form of a randomly generated dot-pattern. In its initial stages of implementation, it is mostly being used as a qualitative visualization method. But in our case, thanks to a PIV software, we are able to obtain a quantitative displacement. The Fig. 10 gives the working of the BOS method:

The density variation comes from the disk and is created in a plexiglas enclosure (40cm*30cm in surface and 1m high) in order to avoid external perturbations (see picture in Fig. 14). The disk is heated by a wire resistance bamboozled under a steel disk

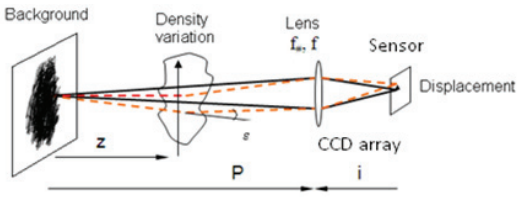

Figure 10: Diagram explaining the BOS technique.

and needs a supply of 13A and 40V. To obtain result of displacement, two images of the background are recorded, one with perturbation and one without. Then, an analysis of these images is made in order to deduct the displacement of each element from the dot-pattern. This analyze is realized with the help of the software WIDIM (Window Displacement Iterative Multigrid) [9], software developed by the Von Karman Institute and usually utilized in PIV. WIDIM makes a cross-correlation between the two pictures and gives as result the displacement of each element in pixel along the x direction and y direction.

5.1.2. Results

Results can be represented as a displacement map of each element of the background in order to see where the displacement occurs. The picture of the background has been taken passing through the perturbation right above the disk.

- *Visible spectral band*

  In this case the distance Z is 1m and P 1,6m. The lens used has a focal distance of 50mm. The camera is a Pixelfly QE model with a CCD sensor resolution of 1392x1036. As we can see in the figure 11, we obtain a displacement maximum around 10 pixels close to the disk and around 5 pixels in the plume, which are respectively a displacement of 2,4mm and 1,2mm on the board. We can notice that in the center of the plume (the center of the plume is also in the center of the sensor so around the pixel number 680) we do not have a displacement. Its in agreement with what we have seen with the numerical approach of ray-tracing.

- *Near Infrared spectral band (preliminary results)*

  In this case the distance Z is 1m and P 1,25m. The lens used has a focal distance of 75mm.

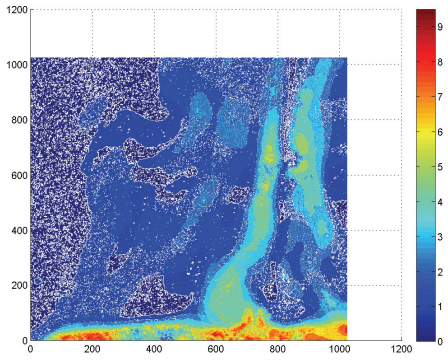

Figure 11: Displacement map above the disk in the visible band.

And the resolution of the sensor is 320x256. The camera used is a Xenics camera with VisGaAs CCD sensor working from 0,75μm to 1,7μm. The light used to illuminate the pattern comes from an incandescent lamp with filter window centered around 830nm. As for results shown for the visible band., we obtain the maximum displacement right above the disk with a displacement of 7 pixels, or 3,5mm on the pattern. However, to be able to measure a displacement big enough (because of the poor resolution of IR camera) we had no choice to use a lens with bigger focal distance.

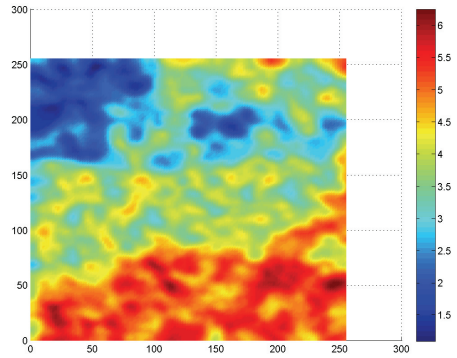

Figure 12: Displacement map above the disk in the near infrared band.

- *Far Infrared spectral band (preliminary results)*

For the infrared camera the BOS method is revealed impossible to apply. The resolution of the camera is too big to allowing the detection of small random point. The numerical resolution is 280x280 and the angle of view is 20. The distance Z is 25cm and P 50cm. The camera is an AGEMA 880 LW with scanning device and cold by stirling cycle. We use in this case big black circle on a white paper. We warm the paper with incandescent lamp. Black circles absorb more than white circle and become hotter, the difference of temperature permits to detect enough circles edge. Then, with a code written in MATLAB we can determine the center of the circle and so obtain the displacement between two pictures. The displacement measured is around 0,4 pixel, corresponding to 0,18mm on the pattern.

5.2. Contour following method

5.2.1. Principle of the contour following method

The distortion field measurement is often used when we want to control the material forming, that is to say when we want to confer to a piece (generally metallic) a specific shape in a given range of tolerance. It needs so to find a distortion measurement system which allows to compare the success of the forming. For this purpose, its common to use forms predefined, drawn on the piece before the constraint application. We chose in our study to use circles, which will become ellipses during the distortion [10]. As the BOS method, the technique is to observe the background with and without perturbation and then to analyze the recorded picture. Once that we have the two recorded pictures, we realize an image processing in order to obtain ellipses parameters needed to compute the distortion. Distortions along x and y (ϵ_x and ϵ_y) are respectively calculated by these following equations:

$$\epsilon_x = ln(a/r) \text{ and } \epsilon_y = ln(b/r) \quad (6)$$

With r the initial radius of the circle and a and b the radius of the ellipse respectively along x and y.

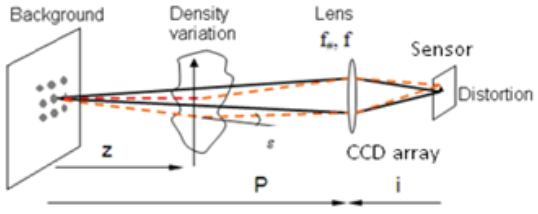

Figure 13: Diagram explaining the contour following method.

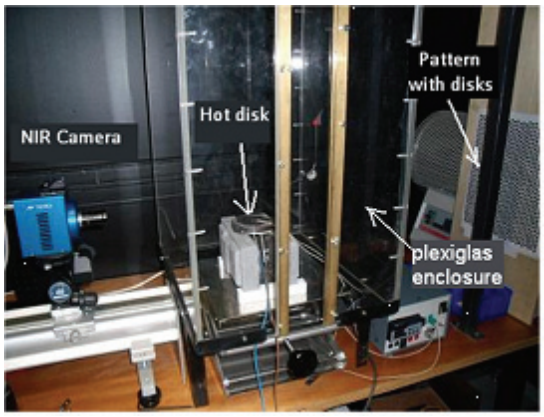

Figure 14: Pictures of the set up.

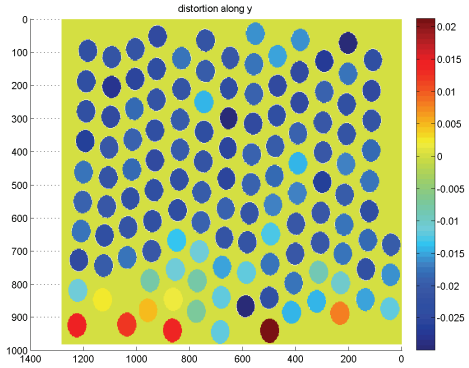

Figure 16: Distortion along y.

5.2.2. Results

Results can be represented as a distortion map of each element of the background in order to see where the distortion occurs. The picture of the background has been taken passing through the perturbation right above the disk.

- *Visible spectral band*

  Like for the displacement measurement, the distance z is 1m and P 1,25m. The lens used has a focal distance of 50mm. And the resolution of the sensor is 1392x1036.

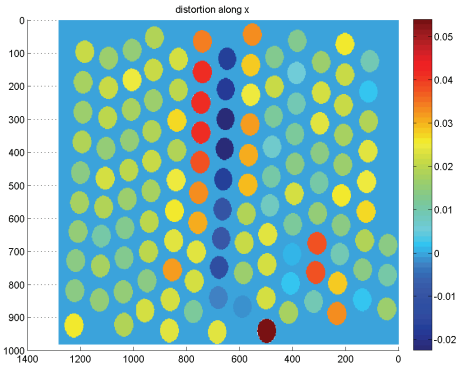

Figure 15: Distortion along x.

As we can see, this technique permits to locate where the distortions occur and in which direction circles are enlarged or narrowed. For exemple, in the Fig. 15, representing distortion along *x*, we can see that the main distortions are situated on the edge of the plume, and on the contrary, are small in the middle. About the distortion along *y* (Fig. 16), since the biggest vertical gradient is right above the hot disk, we observe only distortions in the bottom of the picture (above the disk).

- *Near infrared spectral band*

  Like for the displacement measurement, the distance z is 1m and P 1,25m. The lens used has a focal distance of 75mm. And the resolution of the sensor is 320x256.

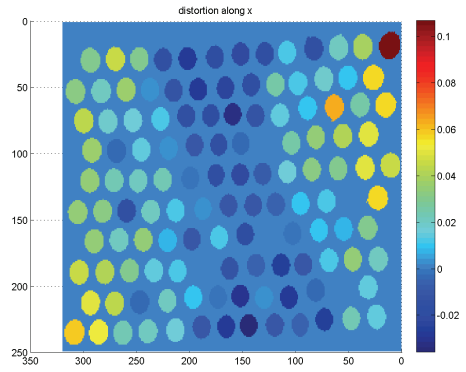

Figure 17: Distortion along x.

As shown in the visible band, Figs. 17 and 18 point out that the distortion along x is not very important in the center but on the edge of it. Moreover, since the resolution resolution of the near infrared camera is low, we need to use

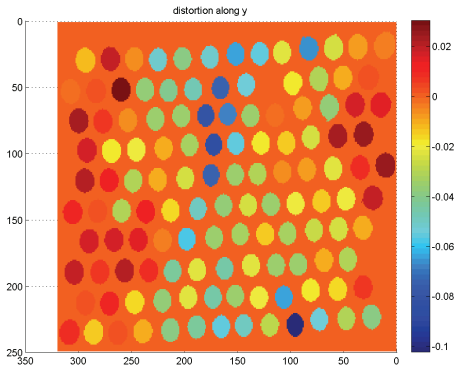

Figure 18: Distortion along y.

bigger circle in the background. That's why, we are not able to see in this case the dirsortion occuring above the disk like we can see in Fig. 16. Indeed, circles are bigger than the size of the thermic boundary layer.

- *Infrared band (priliminary results)*

In the far infrared band, disks edges on the background picture were not sharp enough to give acceptable result. So, we dont have yet suitable values to show in this part. However we can see how look like our "infrared background disks" used to find the displacement in the chapter 5.1.2 (Fig. 19).

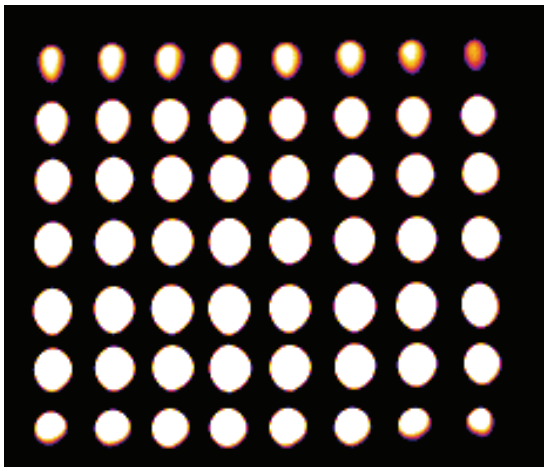

Figure 19: Infrared background seen through the plume.

5.3. Error on the temperature (preliminary results)

In this part, we give an estimation of the error made when we want to make a temperature measurement through a perturbation made of hot air. To do this, we simply observe a stabilized black body. We write down the value and then we put the perturbation between the black body and the camera. We observe in both cases (near infrared and far infrared) an increase of the temperature measured. The temperature of the black body in near infrared was 473K and 323K in far infrared. The error estimated is about the same in near and far infrared and is around 0,9K (big enough to be detected). This result is a preliminary result and more experiments have to be made to validate this value. Indeed, we have to validate if this temperature increase doesn't come from various reflections inside the enclosure of the radiation emits by the hot disk.

6. Conclusion and perspectives

The study done here has pointed out the mirage effect phenomena in several spectral bands and has started to give some quantitative information about the displacement and the distortion induced by the perturbation. We showed that the displacement is about 3mm for the visible and near infrared bands, and much more little for the far infrared band with around 0,2mm. These results are in agreement with the chart shown in the Fig. 2. The distortion measurement shows that the mirage effect can induce more than a displacement and can enlarge or narrow a motif. However, improves has to be made on our experiment to allow a good measurement in all the spectral bands (particularly in the infrared band). One of the futur work will be to buil a new set-up, avoiding reflection inside the enclosure and permitting good infrared measurement. Moreover, the error made in temperature measurement has to be validated and we have to know precisely the role of CO2/H20 absorption and reflection in each spectral band. We will also improve the BOS method in order to deduce the axisymmetric temperature field above the disk thanks to the displacement map. Then, the finally step is to correct pertubated images and to obtain images without perturbation coming from refractive index gradient. In the case of a laminar convection, the ray-tracing code can be used to predict the deviation of each point. But for a turbulent flow, a statistic analysis should be realized in an attempt to correct images [11].

References

[1] Claudinon S. - *Contribution l'tude des distorsions au traitement thermique*, Thse Ecolde des Mines de Paris, 2000

[2] Badoz J., Fournier D., Boccara A. C. - *Photoacoustics : a hundred years old technique revised*, Journal Optics 11, pp 399-408, 1980

[3] El Motassadeq A., Chechouani H., Waqif M., Benet S. - *Simulation des effets de la rfraction dans la couche limite thermique au-dessus d'un disque horizontal*, Congrs franais de thermique, 2000

[4] Mayinger F., Feldmann O. - *Optical measurements* 2nd *Edition*, Springer, 2001

[5] Lide D. R. - *Handbook of Chemistry and Physics* 88th, 10-253, 2007-2008

[6] Cosson B., Schmidt F., Le Maoult Y., Bordival M. - *Infrared heating stage simulation of semi-transparent media (PET) using ray-tracing method*, International Journal of Material Forming, 2010

[7] Robinson S. B., Liburdy J. A. - *Prediction of the natural convective heat transfer from a horizontal heated disk*, Journal of Heat Transfer, vol. 109, November 1987

[8] Klinge F. - *Investigation of background oriented schlieren towards a quantitative density measurement system*, Project report, von Karman Institute, 2001

[9] Scarano F., Riethmuller M. L. - *Iterative Multigrid approach in PIV image processing with discrete windonw offset*, Experiment in Fluids 26, von Karman Institute, 2001

[10] Morestin F., Bogaert P., Boivin M. - *Mesure de dformation par imagerie*, Colloque Photomcanique 95, ENS Cachan (France). pp 195-202 Ed. Eyrolles, 1995

[11] Rondeau X. - *Imagerie travers la turbulence: mesure inverse du front d'onde et centrage*, Thse de l'Universit de Lyon1 - Claude bernard, 2008

Numerical simulation of turbulent incompressible Eulerian-Eulerian two-phase flows

Tamás Bányai

Aeronautics and Aerospace Department, tamas.banyai@vki.ac.be

Supervisor: Herman Deconinck

Professor, Aeronautics and Aerospace Department, von Karman Institute for Fluid Dynamics, Belgium, herman.deconinck@vki.ac.be.

Promotor: Herman Deconinck

Professor, Aeronautics and Aerospace Department, von Karman Institute for Fluid Dynamics, Belgium, herman.deconinck@vki.ac.be.

Abstract

Within the IWT/SBO project MuTEch (www.vki.ac.be/mutech), the VKI collaborates with Flemish academic institutions (VUB, KUL, UGent) and large industrial partners (Agfa-Gevaert, Bekaert) on the development of experimental and numerical tools to study turbulent heat, mass and charge transfer in electro-chemical reactors. This PhD project aims at fulfilling part of the MuTEch objectives, by constructing an LES solver for turbulent flows in complex 3D geometries. Emphasis is put on the development of very fast solution techniques for the unsteady incompressible single and two-phase Navier-Stokes equations, on 3D unstructured meshes.

Keywords: Large Eddy Siumulation, LES, Two-Phase Flow, Two-Fluid Model, Finite Element, FEM, PSPG, SUPG, Cylinder, Muffler, Faucet, T-Junction

1. Introduction

As started within the propject MuTEch, this PhD project's goal was stated to arrive to a turbulent, incompressible two-phase flow solver for electrochemical applications. In order to achieve that, four milestones can be defined. At first a robust unsteady, laminar, incompressible Navier-Stokes solver needs to be developed which as a second step can then be applied to large eddy (LES) simulations. The third milestone is to implement the two-phase model. Finally, merging the LES and two-phase solvers, the forth milestone can also be achieved. At current, the first three milestones have been achieved through development of the software called Morpheus. Most of the ongoing work focuses on the fourth milestone.

2. Single Phase Navier-Stokes Solver

The model for simulating fluid flow is described by the so-called Navier-Stokes equations. It joins the conservation laws of mass, momentum and energy transfer. In the present case the unsteady incompressible Navier-Stokes equations are considered.

$$\frac{\partial \vec{u}}{\partial t} + (\vec{u} \cdot \nabla)\vec{u} + \frac{1}{\rho}\nabla p - \nu \nabla^2 \vec{u} = 0 \tag{1}$$

$$\nabla \vec{u} = 0 \tag{2}$$

2.1. Finite Element Method

To solve the equations above both in time and space the finite element method was employed at each time step.

$$\vec{R}(\vec{\phi}(t, \vec{x})) = 0 \tag{3}$$

where R is the left hand side of the governing equations 11 and 12, $\vec{\phi}[u, p]^T$ is the vector of unknowns. The discrete solution is represented by means of piecewise linear (P1) elements. These are defined on 2D triangular or 3D tetrahedral meshes as:

$$\phi(t, \vec{x}) = \sum_j \phi_j(t) N_j(\vec{x}) \tag{4}$$

Here N_j is the P1 basis function, which is equal to one in node i and decreases to zero on the neighbouring nodes in a linear manner:

$$N_j(\vec{x_i}) = \delta_{ij} \tag{5}$$

In order to obtain a dicrete solution, the equations are multiplied by a set of test functions (ω_i) and integrated over the whole computational domain. The result is set equal to zero in order to minimize the residual. This is called the weighted residual finite element (FE) formulation:

$$\int_\Omega \omega_i(\vec{x})\vec{R}(t,\vec{x})d\Omega = 0. \tag{6}$$

The most common approach is to set the test functions equal to the basis functions, in this case the so-called Galerkin FE formulation (GFEM) is being applied.

$$\omega_i(\vec{x}) = N_i(\vec{x}) \tag{7}$$

For linear elements, the GFEM method is known to be of second order accurate in space. In steady one-dimensional cases, the GFE method can easily be seem to be be equivalent to the central finite differencing scheme; it suffers from the same oscillations as central finite difference methods, unless appropriate stabilization terms are added. Pressure wiggles are eliminated by using the well-known Pressure Stabilized Petrov-Galerkin method (PSPG). The idea is to add an extra term based upon the divergence of the momentum equation to the mass conservation law. The pressure laplacian in this term keeps the pressure field smooth. This approach is known to remain second order accurate [1].

$$\int_\Omega \tau_{PS} \bigtriangledown N_i \cdot \vec{R}_m d\Omega \tag{8}$$

For convection dominated flows, moreover, the momentum residual needs to be formulated in an upwind manner. This is done by adding the Streamline Upwind Petrov Galerkin stabilization (SUPG) to the Galerkin discretization of the momentum equation. It can be interpreted as a modification of the test functions to increase the influence of the upstream values to mimic the behaviour of the convection-diffusion equation. Analogous to the PSPG method, this term is also designed in such a manner that second order accuracy is kept [2]. The same approach is implemented for the scalar transport equation.

$$\int_\Omega \tau_{SU}\vec{u} \cdot \bigtriangledown N_i \vec{R}_m d\Omega \tag{9}$$

And finally at high Reynolds numbers the PSPG term induces oscillations in the velocity field, which can be shown by use of stability analysis, therefore application of the so-called bulk viscosity becomes necessary.

$$\int_\Omega \tau_{BK} \bigtriangledown N_i \vec{R}_c d\Omega \tag{10}$$

2.2. Time Integration

The unsteady incompressible Navier-Stokes equations can be expressed in terms of the velocity components $u = [u, v]^T$ and pressure p. The most straightforward way of reaching second order accuracy in time, is to use the Crank-Nicholson method. The resulting system of equations can then be written in semi-discrete form:

$$\frac{\vec{u}^{n+1} - \vec{u}^n}{\Delta t} \tag{11}$$
$$+\frac{1}{2}\left[(\vec{u}\cdot\bigtriangledown)\vec{u} + \frac{\vec{u}\bigtriangledown\cdot\vec{u}}{2} + \frac{\bigtriangledown p}{\rho} - \nu\bigtriangledown^2\vec{u}\right]^{n+1}$$
$$+\frac{1}{2}\left[(\vec{u}\cdot\bigtriangledown)\vec{u} + \frac{\vec{u}\bigtriangledown\cdot\vec{u}}{2} + \frac{\bigtriangledown p}{\rho} - \nu\bigtriangledown^2\vec{u}\right]^{n} = 0$$
$$\bigtriangledown\vec{u}^{n+1}. \tag{12}$$

In this section the derivation of the numerical method is presented. The main idea is to transform the Navier-Stokes equation into a series of Oseen problems, by replacing and extrapolating in time the convective velocity in the advective term, thereby transforming each timestep into a single linear problem. The resulting scheme is of second order accuracy in both space and time. To linearize the governing equations, it is necessary to extrapolate the velocity fields in time. This can be done by an appropriate extrapolation, in the current implementation up to 4th order extrapolation is accessible, assuming constant time steps.

$$\phi^{n+1/2} = c_0\phi^n + c_1\phi^{n-1} + c_2\phi^{n-2} + c_3\phi^{n-3} \tag{13}$$

Where the coefficients can be obtained by Taylor series expansion and their values are given in Table 1:

The equations that need to be solved and discretized, where according to the practice of finite element methods the viscous terms are treated in the so-called weak formulation. The method outlined above has the following properties:

Table 1: Extrapolation factors.

	c_0	c_1	c_2	c_3
$O(h)$	1	0	0	0
$O(h^2)$	1.5	-0.5	0	0
$O(h^3)$	1.875	-1.25	0.375	0
$O(h^4)$	2.1875	-2.1875	1.3125	-0.3125

- Since all approximations made involve errors of second order only, the method remains second order accurate.
- Since the Crank-Nicholson time integration is used, the method has absolute stability from a linear stability point of view. In other words a von Neumann stability analysis indicates, that there is no time step restriction.
- The method may still be sensitive to nonlinear instabilities and, obviously, the made extrapolations (eq. 13) is only valid for sufficiently small time steps. However, this was already the case for the original Crank-Nicholson scheme (eq. 11 and 12); therefore the approximation caused no further inaccuracy.
- Because eq. 11 and 12 became linear in the unknowns $\phi^{n+1} = [u^{n+1}, p^{n+1}]^T$, only a single linear system needs to be solved per time step. This is to be compared with several inner iterations (Newton, SIMPLE, PISO, or other steps) per time step for the pure Crank-Nicholson scheme. It is therefore expected that the present linearized scheme will be much faster than the original nonlinear Crank-Nicholson method.

3. Extension to LES

The key idea is that the mesh is fine enough to resolve turbulent structures such that the mesh size is still magnitudes larger than the Kolmogorov scale. This is possible by spatial averaging with a low pass filter:

$$\Phi = \int \phi(x) G(x, x') dx' \qquad (14)$$

After applying the filtering process [11] to the Navier-Stokes equations (1) and (2), the so-called subgrid-scale stresses (SGS) appear in the filtered equations, which need to be modelled. Several models were developed over the years for modelling the SGS, the most popular ones are as following:

- (Static) Smagorinsky [13]
- Dynamic Smagorinsky [14]
- Wall-Adapting Local Eddy-viscosity (WALE) [15]

3.1. Cylinder

The abundance of interesting flow features attracts a lot of researchers concerning the flow past a circular cylinder. The Reynolds number was chosen to be Re_D=3900, for which choice the reason is twofold. The flow is already in the unstable region (1), so 3D structures are definitely present, but the Reynolds number is low enough to have a reasonable size of the computation. There also exists numerous experimental and numerical data to compare against [16] [17] [18] [19] [20]. In this paper the computation with WALE model is shown, showing good agreement with [20].

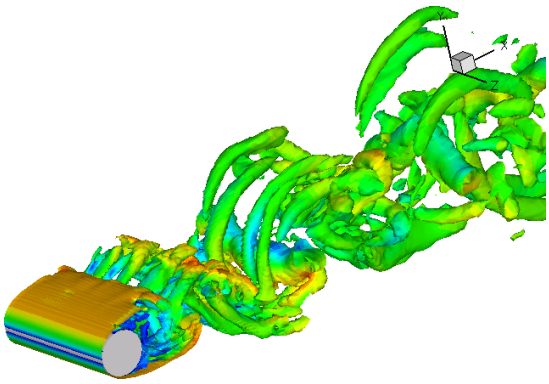

Figure 1: Visualization of the structures in the flow past a circular cylinder, Q iso-contours coloured with velocity magnitude.

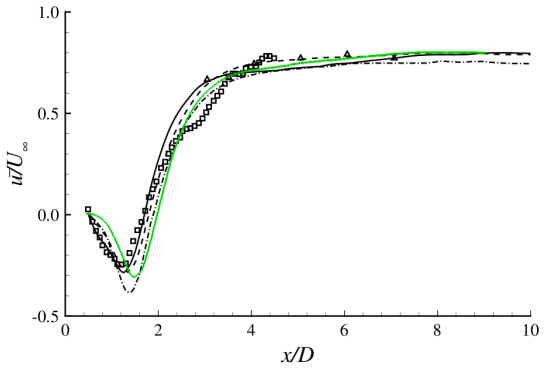

Figure 2: Cylinder: evolution of axial average velocity on the centerline (black: measurement of [20], green LES with Morpheus

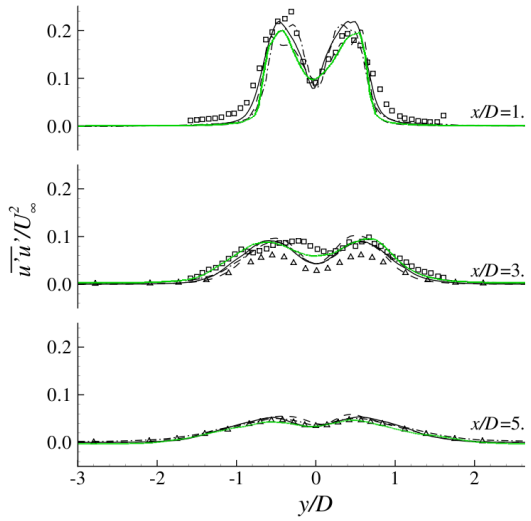

Figure 3: Cylinder: evolution of axial velocity fluctuation at 1,3 and 5D distance from the center of the cylinder (black: measurement of [20], green LES with Morpheus

3.2. *Muffler*

Within the project CAPRICORN, need for an LES calculation of the so-called muffler configuration (figure 4) arised. The geometry of the muffler consists of an excentric sudden expansion, which is followed by a sudden contraction. The reference diameter of 0.04m and reference velocity of 17.4m/s results in a reynolds number of 50000. In this case the standard Smagorinsky model was used and in-house comparison with experiments were available [12], showing good agreement (figure 5, 6)

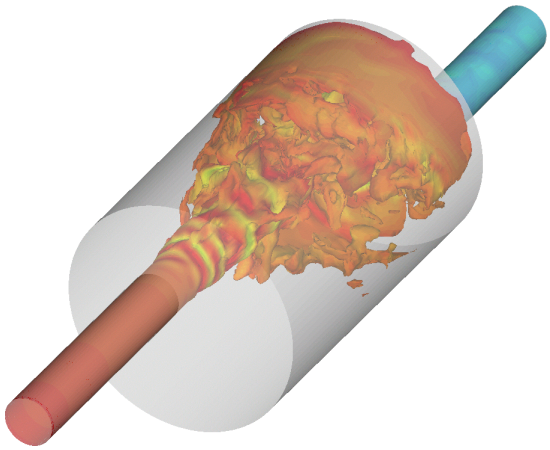

Figure 4: Muffler testcase.

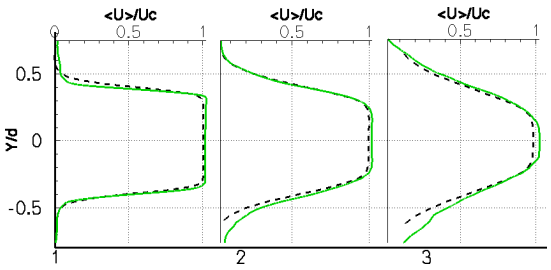

Figure 5: Muffler: evolution of axial average velocity after 1,2 and 3D after the expansion to the inner chamber (black: measurement of [12], green LES with Morpheus).

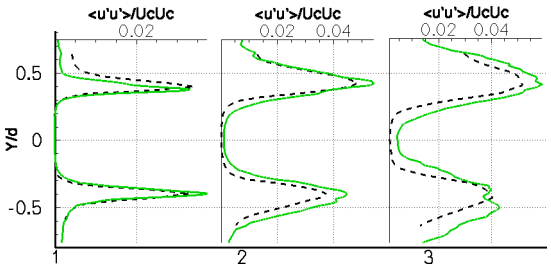

Figure 6: Muffler: evolution of axial velocity fluctuation after 1,2 and 3D after the expansion to the inner chamber (black: measurement of [12], green LES with Morpheus).

4. Two-Phase Flow Solver

For modelling bubbly two-phase flows there are several possibilities, where one of them is the *Eulerian-Eulerian* model. Both the primary and the secondary phases are modelled as a continua. The two phases are treated as interpenetrating, non-mixing continua. The aim of this section is to give an overview about the phenomena by explaining the governing equations of this Eulerian-Eulerian model and demonstrate the capabilities of the solver through simulating well-known testcases. Since the two phases are non-mixing, each of them occupies a certain space volume

$$V_Q = \int_\Omega \alpha_Q d\Omega \tag{15}$$

where Q indicates the appropriate phase and the term α_Q represents a quantity called the *volume fraction* for this phase. The summation of both volumes, denoted in terms of liquid and gas, equals the whole domain:

$$V_L + V_G = \Omega \tag{16}$$

The volume fractions α_L and α_G for the liquid and the gas phase are thus dependent on each other by a

constitutive law, which states that their sum is one in any chosen control volume.

$$\alpha_L + \alpha_G = 1 \tag{17}$$

As a further assumption, a local pressure equilibrium between the two phases is defined:

$$p = p_L = p_G \quad . \tag{18}$$

The models obtained in this way go under the name of *One Pressure Models*. In many practical cases, the pressure differences between the two phases are indeed expected to be very small and surface tension effects to be negligible.

4.1. Governing Equations

The flow represented by the Eulerian-Eulerian two-fluid and single-pressure model has to fulfill the conservation laws for mass and momentum, according to the incompressible Navier-Stokes equations. For this reason, the continuity equation and the momentum equation are considered as governing equations for the two phases of the flow. The equations are obtained through a kind of averaging process, which can be found in [3] and [4]. For reasons of clarity, the two phases are assumed to be of liquid and gas. The notation system used is the following:

- **Q** : General notation for a generic phase
- $\hat{\mathbf{Q}}$: Opposite phase
- **L** : Primary (Liquid) phase
- **G** : Secondary (Gas) phase

4.2. Conservation of Momentum

The momentum conservation has to be taken into account for both phases, liquid and gas. The momentum balance for a generic phase, written in non-conservative form, reads

$$\rho_Q \alpha_Q \frac{\partial \vec{u}_Q}{\partial t} + \rho_Q \alpha_Q (\vec{u}_Q \cdot \nabla)\vec{u}_Q + \nabla(\alpha_Q p_Q) - \nabla \cdot (\alpha_Q \bar{\bar{\tau}}_Q) = \alpha_Q \rho_Q \vec{g} + \Gamma_Q \vec{u}^i_Q + p^i_Q \nabla \alpha_Q - \bar{\bar{\tau}}^i_Q \nabla \alpha_Q + \vec{F}^D_Q + \vec{F}^L_Q + \vec{F}^V_Q \tag{19}$$

Here, $\bar{\bar{\tau}}_Q$ indicates the stress tensor

$$\bar{\bar{\tau}}_Q = \mu_Q (\nabla \cdot \vec{u}_Q + \nabla \cdot \vec{u}^T_Q) - \frac{2}{3}\mu_Q \, \bar{\bar{I}} \, \nabla \cdot \vec{u}_Q \tag{20}$$

Here, p^i_Q is the interface pressure, $\bar{\bar{\tau}}^i_Q$ is the interface stress, $\vec{F}^D_Q$ the drag force, $\vec{F}^L_Q$ the lift force and $\vec{F}^V_Q$ the virtual mass force.

One can expand the pressure and stress gradient formulations as follows

$$\nabla(\alpha_Q p) = \alpha_Q \nabla p + p \nabla \alpha_Q \tag{21}$$

$$\nabla \cdot (\alpha_Q \bar{\bar{\tau}}_Q) = \alpha_Q \nabla \cdot \bar{\bar{\tau}}_Q + \bar{\bar{\tau}}_Q \nabla \alpha_Q \tag{22}$$

when using the single-pressure assumption, the original momentum equation (19) turns to:

$$\rho_Q \alpha_Q \frac{\partial \vec{u}_Q}{\partial t} + \rho_Q \alpha_Q (\vec{u}_Q \cdot \nabla)\vec{u}_Q + \alpha_Q \nabla p - \alpha_Q \nabla \cdot \bar{\bar{\tau}}_Q = \alpha_Q \rho_Q \vec{g} + \Gamma_Q \vec{u}^i_Q + (p^i_Q - p)\nabla \alpha_Q + (\bar{\bar{\tau}}_Q - \bar{\bar{\tau}}^i_Q)\nabla \alpha_Q + \vec{F}^D_Q + \vec{F}^L_Q + \vec{F}^V_Q \tag{23}$$

It is a reasonable approximation to neglect the interface mass transfer Γ_Q and the interfacial stress correction term $(\bar{\bar{\tau}}_Q - \bar{\bar{\tau}}^i_Q)$. As the flow is regarded to be incompressible, we can divide the above equation by ρ_Q. It is well-known in the literature [5] that the numerical solution process behaves more stable if the momentum equations are divided by the volume fraction. This is due to the fact that the system's nonlinearity decreases from the point of view of the solver (the volume fraction disappears from the advection and viscous terms and appears only in terms which are handled as sources).

$$\frac{\partial \vec{u}_Q}{\partial t} + (\vec{u}_Q \cdot \nabla)\vec{u}_Q + \frac{1}{\rho_Q}\nabla p - \frac{1}{\rho_Q}\nabla \cdot \bar{\bar{\tau}}_Q = \vec{g} + \frac{1}{\rho_Q \alpha_Q}(p^i_Q - p)\nabla \alpha_Q + \frac{1}{\rho_Q \alpha_Q}\left(\vec{F}^D_Q + \vec{F}^L_Q + \vec{F}^V_Q\right) \tag{24}$$

The source terms on the right hand side of the momentum equations constitutes the extra forces which have to be modeled to couple the two phases. The physical meaning of these forces and their analytical expressions will be discussed in the following. Since the momentum equations for the two phases have to follow the 3rd principle of dynamics concerning action and reaction, the forces of one phase have to be of equal amount and opposite sign as the according forces of the opposite phase, which in terms of liquid and gas reads

$$\vec{F}^i_Q = -\vec{F}^i_{\hat{Q}} \tag{25}$$

When regarding the global macroscopic system of conservation laws for the mixture, the coupling forces

of the two phases vanish. The single extra force terms appearing in the model are drag force, lift force, virtual mass force and interfacial pressure force.

4.2.1. Drag Force

The drag force represents an interphase momentum transfer. It acts because the secondary phase gas bubbles travel with a different velocity in the primary phase, and like a sphere in flow, drag induces. It is acting to reduce this velocity difference and can be stated as:

$$\vec{F}_L^D = -\vec{F}_G^D = \frac{3}{4}\frac{C_D}{d_B}\rho^*\alpha_L\alpha_G|\vec{u}_G - \vec{u}_L|(\vec{u}_G - \vec{u}_L) \quad (26)$$

where C_D is the drag coefficient and can be defined by different models:

- Constant
- Schiller and Naumann
- Morsi and Alexander

These are the most common models, but there exists of a significant amount of modifications, usually for given material combination (for example in [6]).

4.2.2. Lift Force

The lift force represents the lift induced on the secondary phase and acts mainly for the presence of velocity gradients in the primary phase flow field. It can be written in the following form:

$$\vec{F}_L^L = -\vec{F}_G^L = C_L\rho^*\alpha_L\alpha_G(\vec{u}_G - \vec{u}_L) \times (\nabla \times \vec{u}_L) \quad (27)$$

Where C_L is the lift coefficient. The usual value is between 0.4 and 0.6 (taken from [7] and [8]). The lift phenomena becomes dominant where the velocity gradient for the liquid phase becomes large, for example in boundary layers or shear layers.

4.2.3. Virtual Mass Force

The drag force expression discussed above is valid for the case of a constant velocity difference between the two phases. If one of the phases accelerates relative to the other phase, it will immediately experience a deceleration due to its inertia to the other phase. This effect is known as the virtual mass effect and represents the amount of volume of one phase displaced by the other in its relative motion. It can be expressed in terms of a virtual mass force:

$$\vec{F}_L^V = -\vec{F}_G^V = C_V\rho^*\alpha_L\alpha_G\left(\frac{\partial\vec{u}_G}{\partial t} - \frac{\partial\vec{u}_L}{\partial t} + (\vec{u}_G\cdot\nabla)\vec{u}_G - (\vec{u}_L\cdot\nabla)\vec{u}_L\right) \quad (28)$$

4.2.4. Interfacial Pressure Correction

This force models a pressure discontinuity at the phase interface. As mentioned above, it is a differential term of the form

$$\vec{F}_Q^P = (p_Q^i - p)\nabla\alpha_Q \quad (29)$$

where the following model was chosen:

$$(p - p_G^i) = (p - p_L^i) = C_P\rho^*\alpha_L\alpha_G(\vec{u}_G - \vec{u}_L)^2 \quad (30)$$

4.3. Conservation of Mass

The conservation of mass is described by the continuity equation. For a generic phase Q, representing either the liquid or the gas phase, the continuity equation can be written in general form as

$$\frac{\partial(\rho_Q\alpha_Q)}{\partial t} + \nabla\cdot(\rho_Q\alpha_Q\vec{u}_Q) = \Gamma_Q \quad (31)$$

where Γ_Q represents the interface mass transfer and is neglected in the following, as was done in the momentum equations. As the flow is assumed to be incompressible, the density can be regarded as constant and the mass conservation reduces to a volume conservation:

$$\frac{\partial\alpha_Q}{\partial t} + \nabla\cdot(\alpha_Q\vec{u}_Q) = 0 \quad (32)$$

It can be written in expanded form, leading to

$$\frac{\partial(\alpha_Q)}{\partial t} + \alpha_Q\nabla\cdot\vec{u}_Q + \vec{u}_Q\cdot\nabla\alpha_Q = 0 \quad (33)$$

4.4. Pressure equation

To gain an equation for the coupling of pressure, velocity and volume fraction, various approaches can be applied. From the previously stated continuity equations for the liquid and the gas phase, one can obtain an expression referred to as *pressure equation* by summing these two equations of mass conservation:

$$\frac{\partial\alpha_L}{\partial t} + \nabla\cdot(\alpha_L\vec{u}_L)\frac{\partial\alpha_G}{\partial t} + \nabla\cdot(\alpha_G\vec{u}_G) = 0 \quad (34)$$

The time derivatives of the volume fractions vanish because if the linking law stated in (17) is imposed, we implicitly get

$$\frac{\partial}{\partial t}(\alpha_L + \alpha_G) = 0 \quad \forall t \tag{35}$$

Equation (34) written in expanded form thus turns out to be

$$\alpha_L \nabla \cdot \vec{u}_L + \vec{u}_L \cdot \nabla \alpha_L + \alpha_G \nabla \cdot \vec{u}_G + \vec{u}_G \cdot \nabla \alpha_G = 0 \tag{36}$$

4.5. Resulting System of equations

We can assemble a system of seven equations. The continuity and momentum equations are stated for both phases while the pressure equation closes the system of equations for the vector of seven unknown variables

$$\vec{U} = \begin{pmatrix} p & \alpha_L & u_L & v_L & \alpha_G & u_G & v_G \end{pmatrix}^T \tag{37}$$

This *seven-equation-model* features a symmetrical appearance, since exactly the same types of equations are used for both phases and the phase coupling in terms of the linking law for the volume fractions is only accomplished in the pressure equation. The resulting system of seven equations is thus formed by assembling the conservation equations for mass and momentum for both phases. The pressure equation closes the system of equations.

4.6. Laminar Two-Phase Flow Testcases

In order to show the capabilities of the code Morpheus, two of the most commonly used testcases are showed. First the water faucet, which has a known closed-form solution and finally the flow inside a T-Junction with all the interaction mechanisms acting between the phases.

4.6.1. Water Faucet

This testcase was first proposed by *Ransom* [9]. The test consists of a 12m tall vertical tube with a water jet inside, which accelerates under the effect of gravity. This causes narrowing of the jet and a volume fraction wave propagating downward. The system will reach steady state when the volume fraction discontinuity leaves the tube. Due to the existence of an analytical solution, this problem has been used by different authors, for example [10].

Figure 7 shows the geometry of the water faucet testcase. The boundary conditions at the inlet are specified velocities ($u_{L0} = 10m/s$ and $u_{G0} = 0m/s$) and volume fraction ($\alpha_{G0} = 0.2$), the two sides are symmetric BC's and the pressure at the outlet is fixed to a constant value. The same values are used for the initial conditions, too. The time step is set to $\Delta t = 10^{-3}s$. Gravitational acceleration is set to $g = -10m/s^2$. Under these circumstances a one-dimensional analytical solution is possible to derive for the horizontally averaged values if Euler equations are used. All the extra forces are neglected and the pressure gradient is supressed. Then the solution has the form:

$$\alpha_G(y,t) = \begin{cases} 1 - \frac{(1-\alpha_{G0})u_{L0}}{\sqrt{u_{L0}^2+2gy}} & if y < \frac{gt^2}{2} + u_{L0}t \\ 0.2 & otherwise \end{cases} \tag{38}$$

$$\alpha_L(y,t) = 1 - \alpha_G$$

$$u_G(y,t) = 0.0 \quad \forall x,t$$

$$u_L(y,t) = \begin{cases} \sqrt{u_{L0}^2 + 2gy} & if y < \frac{gt^2}{2} + u_{L0}t \\ u_{L0} + gt & otherwise \end{cases}$$

For simplicity the testcase is turned upside down, meaning that the inlet is at the bottom and the gravitational acceleration vector points upward. The material properties used in this case are listed in the Table 2. To reach conditions close to the Euler equations, relatively low viscosities have been applied:

Table 2: Material properties for the water faucet testcase.

ρ_L	$1000kg/m^3$
ρ_G	$1kg/m^3$
ν_L	$10^{-5}m^2/s$
ν_G	$10^{-5}m^2/s$

As results, the liquid velocity and the gas volume fraction are plotted and compared to the analytical solution. It is clear to see that the numerical solution nicely follows the analytical one. There is a damping near the volume fraction discontinuity, due to the numerical artificial dissipation (see Figure 8). The difference between the calculated and the analytical velocity on the constant segment stays within one percent, this can be seen in Figure 9.

4.7. T-Junction

The fourth testcase to be considered is the two-phase flow through a combining T-junction with two inlets, one of them orientated horizontally and the other one orientated vertically. The two branches (already transporting a mixture) mix in the junction

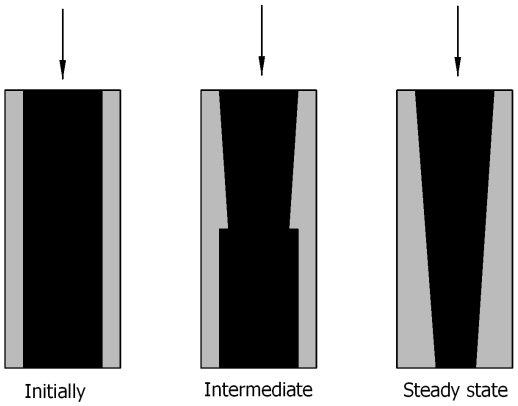

Figure 7: Water Faucet case.

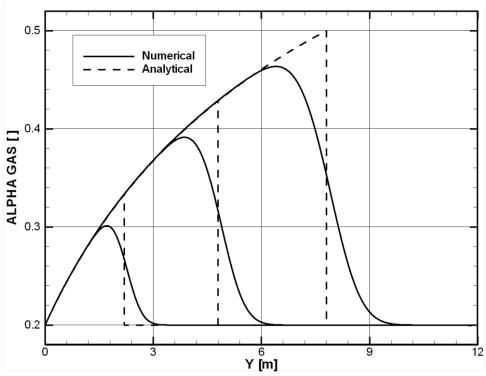

Figure 8: Water Faucet: Evolution of the volume fraction of the gas phase at time instances 0.2, 0.4 and 0.6s.

under an angle of 90°. The code has already been validated for this testcase with model properties (reduced density ratio and increased viscosity), and successful steps have been made with using real material propeties, including only the drag force. The aim of this testcase is to test the complete model, where all the extra forces are included.

In Figure 10 the basic geometric data D (the width of the channel) equals to $0.01m$. The simulation in this testcase was obtained by imposing constant velocity profiles with $u = 0.01m/s$ for both phases at the two inlets, and fixing a uniform pressure at the outlet. The remaining parts of the boundaries are treated as no-slip walls.

By plotting the results (Figure 11 - 12), one can obtain that by turning on the lift force, the gas volume fraction increases at the walls, which is realistic for low-reynolds number flows. It has also be stressed that near to the top boundary, wiggles appear. The origin of these wiggles is under investigation. The velocity and pressure field seem to be realistic.

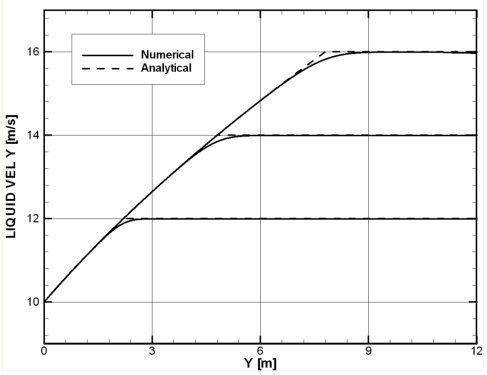

Figure 9: Water Faucet: Evolution of the velocity of the liquid phase at time instances 0.2, 0.4 and 0.6s.

Table 3: Material properties for T-Junction problem.

ρ_L	$1000kg/m^3$
ρ_G	$1.28kg/m^3$
ν_L	$1.025 \cdot 10^{-6}m^2/s$
ν_G	$1.359 \cdot 10^{-5}m^2/s$
C_D	0.44
d_B	$10^{-4}m$
C_L	0.5
C_V	0.5

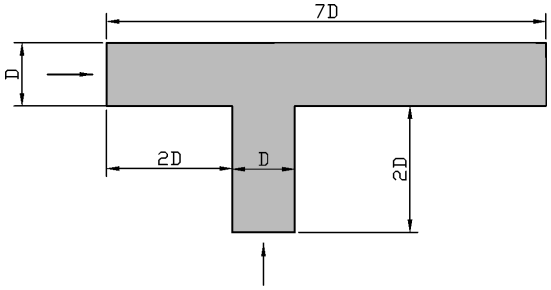

Figure 10: Geometric layout of the T-Junction problem.

5. Conclusion

As an alternative to unsteady solvers based upon an explicit or a fully implicit nonlinear treatment of the convective terms, a fully implicit scheme has been proposed. The resulting method is of second order accurate in both space and time, has absolute linear stability and requires only a single or two linear system solution per time step. The scheme proved to

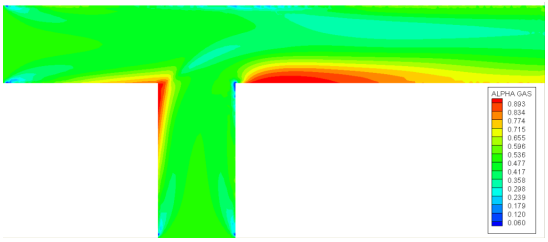

Figure 11: T-Junction: Volume fraction contour plot of the gas phase.

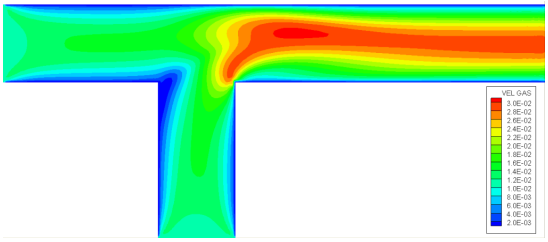

Figure 12: T-Junction: Velocity magnitude contour plot of the liquid phase.

be applicable, numerical results on both 2D and 3D test cases indicate that substantial savings in computational times can be realized for certain test cases.

Further improvements have been achieved with the unsteady, incompressible, laminar Eulerian-Eulerian two- phase flow solver. Focus has been put on the proper stabilization mechanism, which now allows computations with real material properties (like combination of water and air as primary and secondary phase). This achievements allow now to focus on the final stage, namely to couple turbulence modelling (LES) with two-phase flow models.

The technology of the single-phase Navier-Stokes/LES solver of Morpheus has also been implemented in COOLFluiD environment and currently used in several industry-related projects. In the past year it has also been extended and partially validated for solving RANS (Spalart-Allmaras and k-epsilon models) and/or variable density flows.

References

[1] Hughes, J. R., Franca, L. P., Balestra, M., A New Finite Element Formulation for Computational Fluid Dynamics: V. Circumventing the Babuska-Brezzi Condition: A Stable Petrov-Galerkin Formulation of the Stokes Problem Accommodating Equal-order Interpolations, Comp. Meth. App. Mech. and Eng., 59 (1986) 8599

[2] T.J.R. Hughes, L.P. Franca, M.Mallet, A new finite element formulation for computational fluid dynamics: VI. Convergence analysis of the generalized SUPG formulation for linear time-dependent multi-dimensional advective-diffusive systems, Comput. Meths. Appl. Mech. Engrg. 63 (1987) 97–112.

[3] M. Ishii : Thermo-Fluid Dynamic Theory of the Two-Phase Flow, Eyrolles (1975)

[4] D. A. Drew : Mathematical Modelling of Two-Phase Flow, Annual Review in Fluid Mechanics, Vol. 15, p.261-291 (1983)

[5] C. Thompson, P. Lezeau : Application of the Full Approximation Storage Method to the Numerical Simulation of Two-Dimensional Steady Incompressible Viscous Multi-Phase Flows, International Journal for Numerical Methods in Fluids, Vol. 28, p.1217ff (1998).

[6] M. Schuh, C. Schuler, J. Humphrey : Numerical Calculation of Particle-Laden Gas Flows Past Tubes, AIChE Journal, Vol. 35, p.466ff (1989).

[7] T. Uchiyama : Numerical Analysis an Incompressible Two-Fluid Model by Finite Element Method Based on a Fractional Step Method, Computer Modeling and Simulation in Engineering, Vol. 2, p363-385 (1997)

[8] M. Giordano : Finite Element Based Solver for Two-Phase Flow, Project Report 2003-14, von Karman Institute for Fluid Dynamics (2003).

[9] V.H. Ransom : Numerical Benchmark Tests, Multiphase Science and Technology, Hemisphere, volume 6 (1992)

[10] E. Valero : Advanced 2D two-phase flow simulation tool for application to reactor safety, Technical Note 198, von Karman Institute for Fluid Dynamics (2001).

[11] S. B. Pope : Turbulent Flows, Cambridge University Press, 2000

[12] M. Bilka, J. Anthoine Experimental investigation of flow noise in a circular expansion using PIV and acoustic measurements. 14th AIAA/CEAS Aeroacoustics Conference (29th AIAA Aeroacoustics Conference) 5-7 May 2008, Vancouver, British Columbia Canada

[13] J. Smagorinsky General Circulation Experiments With the Primitive Equations Monthly Weather Review, Volume 91, Number 3, March 1961

[14] Germano, M., Piomelli, U., Moin, P. and Cabot, W. H. (1991), A Dynamic Subgrid-Scale Eddy Viscosity Model Physics of Fluids A, Vol. 3, No. 7, pp. 1760-1765

[15] F. Nicoud, F. Ducros Subgrid-scale stress modelling based on the square of the velocity gradient tensor Flow, Turb. Combust. 62, 183200, 1999

[16] L. M. Laurenco and C. Shih : *Characteristics of the plane turbulent near wake of a circular cylinder. A particle image velocimetry study.* (1993) Not published. Results obtained from [20]

[17] L. Ong, J. Wallace : *The velocity field of the turbulent very near wake of a circular cylinder.* Experiments in Fluids **20**, 441 (1996)

[18] R. Mittal and P. Moin : *Suitability of upwind-biased finite-difference schemes for large-eddy simulation of turbulent flows.* AIAA Journal **35**, 1415 (1997)

[19] P. Beudan and P. Moin : *Numerical experiments on the flow past a circular cylinder at sub-critical Reynolds number.* Technical report TF-62, Department of Mechanical Engineering, Stanford University (1994)

[20] A. G. Kravchenko and P. Moin : *Numerical studies of flow over a circular cylinder at Re_D=3900.* Physics of Fluids **12**, 403 (2000)

Experimental study and modeling of single- and two-phase air water flow in singular geometries and safety relief valves

Vasilios Kourakos

Environmental and Applied Fluid Dynamics Department, kourakos@vki.ac.be

Supervisor: Jean-Marie Buchlin

Professor, Environmental and Applied Fluid Dynamics Department, von Karman Institute for Fluid Dynamics, Belgium, buchlin@vki.ac.be

Co-supervisors: Patrick Rambaud and Saïd Chabane

Professor, Environmental and Applied Fluid Dynamics Department, von Karman Institute for Fluid Dynamics, Belgium, buchlin@vki.ac.be
Dr. Engineer, Centre Technique des Industries Mécaniques, TFE department Said.Chabane@cetim.fr

Promotor: Jean-Marie Buchlin

Professor, Environmental and Applied Fluid Dynamics Department, von Karman Institute for Fluid Dynamics, Belgium, buchlin@vki.ac.be

Abstract

The use of relief valves is crucial for the safety of power plants. Indeed, these simple and robust in their design valves are the ultimate protection when all other systems are insufficient. This study is focused on flowforces applied at the valve disk since the knowledge of these forces for the smallest openings is of significant importance for adjustment of the valve ring and for its optimal use. A spring loaded safety relief valve (1 ½" G 3") and transparent model of this valve are tested. The spring is removed and the forces exerted at the valve disk for different inlet pressures and lift positions are measured. Compressible, incompressible and two-phase flow behaviors are investigated. Inversed force of air and water is noticed above a certain value of valve lift. Numerical simulations are performed to verify experimental findings.

Keywords: safety, relief, valve, two-phase, flow, flowforce, discharge, hazard

1. Introduction

The international standard concerning safety devices for protection against excessive pressure in incompressible and compressible fluid has been well established in ISO 4126-1 [1], however for two-phase flow the latest project of standard ISO 4126-10 [2] is to be updated and implemented. The proper design and sizing of these devices is a critical issue which would prevent its malfunction or accidental operation failure that could cause a hazardous situation. So far the reliability of existing models predicting the pressure drop and flow discharge in two-phase flow through the valve, under various flow conditions, is questionable.

A safety relief valve (SRV) is mainly composed of a disc constantly pressed against a nozzle by a spring (Fig. 1). When the pressure forces on the upstream facade of the disc are inferior to the force applied by the spring, the valve remains closed. If an accidental overpressure appears in the process under protection, the pressure forces become high compared to the elastic forces of the spring and the safety valve opens. Thus, the pressure of the system to be protected is reduced to an acceptable value. The stresses exerted by the pressure on a disc of a safety valve are essential for the proper dimensioning of the spring and the inner ring.

2. Experiments

Inversed flow behavior between air and water is noticed at 3 mm valve lift. For the lowest openings, force for air flow is superior than for water while for highest

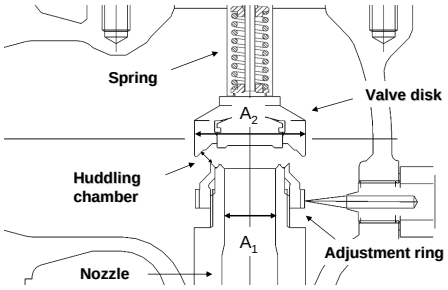

Figure 1: Detailed view of nozzle-valve disk components of SRV

openings vice versa (Fig. 2). Two-phase flow tends to compressible behavior for the highest lifts with equal forces of air and 20% air mixture. Below the flow-force inversion position, although two-phase mixtures are slightly biased toward air forces, they still remain closest to incompressible behavior.

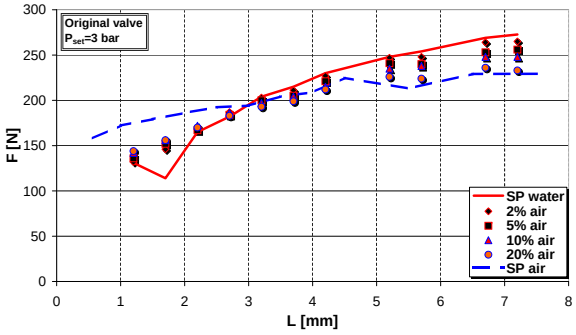

Figure 2: Comparison of flowforce for air, water and two-phase flow at P_{set}=3 bars.

3. CFD

Contours of total pressure close to the valve disk at 3 mm valve opening and streamlines of water flow for P_{set}=6 bars are shown in Fig. 3(a). Flow contracts upstream the valve, resulting in flow acceleration, then passes through the very narrow section between the disk and valve seat and then, due to change in flow direction, recirculation regions are created with fluid impacting on valve body. Small vortices are entrained in the area defined by adjustment ring and valve disk. Therefore, fluid is reflected with a 90° angle approximately. In compressible flow, contours of density close to the valve disk and flow streamlines are shown in Fig. 3(b) for P_{set}=6 bars and same lift. Solid thick white line denotes sonic iso-contours (Ma=1). Contrary to water flow, the discharged fluid jet seems to be only slightly influenced by valve lift with an approximate 45° angle. The previously analyzed different flow behaviors of air and water provide an explanation of inversed flowforce noticed in Fig. 2.

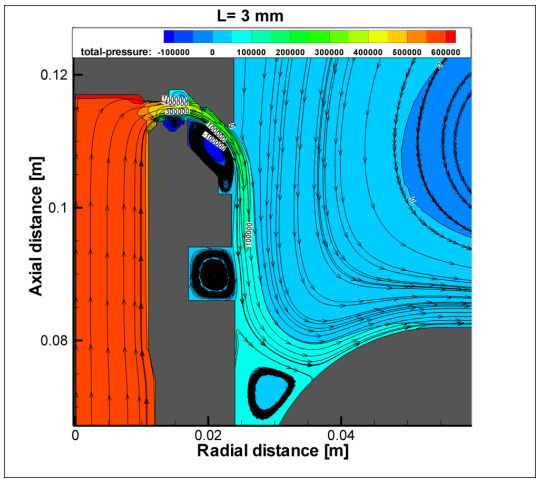

(a) Total pressure contours and streamlines for water flow.

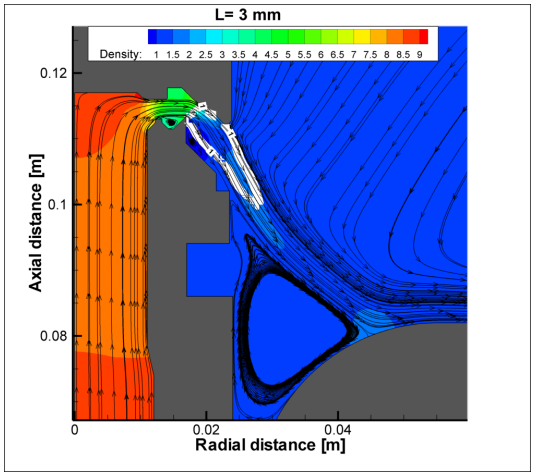

(b) Density contours and streamlines for air flow. Solid white thick line indicates sonic position.

Figure 3: Incompressible and compressible flow behaviors of SRV for P_{set}=6 bars and 3 mm valve lift

4. Conclusions

Experimental results indicate that compressible and incompressible flowforces in SRV are inversed above a certain value of valve lift. This value varies with critical pressure ratio, therefore is linked to the position at which chocked flow occurs during air valve operation. In two-phase flow, for volumetric quality of air

β=20%, pure compressible flow behavior, in terms of flowforce, is remarked at full lift.

Acknowledgments

The financial support of the French company CETIM (Centre Technique des Industries Mécaniques) situated in Nantes, France is gratefully acknowledged.

References

[1] ISO 4126-1, Safety devices for protection against excessive pressure, International Organization for Standardization, 2004.

[2] ISO 4126-10, Safety devices for protection against excessive pressure-Part 10: Sizing of safety valves and connected inlet and outlet lines for gas/liquid two-phase flow, avant-projet de Norme Française homologuée (Nov. 2006).

AEROACOUSTICS

Broadband scattering of the incoming turbulence noise of a stationary airfoil

Korcan Kucukcoskun

PhD Candidate, Environmental and Applied Fluid Dynamics Department, von Karman Institute for Fluid Dynamics and LMS International, Simulation Division, korcan.kucukcoskun@vki.ac.be

Supervisor: Christophe Schram

Assistant Professor, Environmental and Applied Fluid Dynamics Department, von Karman Institute for Fluid Dynamics, Belgium, christophe.schram@vki.ac.be

Promotor: Michel Roger

Professor, Laboratoire de Mecanique des Fluides et d'Acoustique, Ecole Centrale de Lyon, michel.roger@ec-lyon.fr.

Abstract

This paper deals with simulations and measurements of the scattered acoustic field of a stationary airfoil in turbulent stream. A semi-analytical model based on Amiet's theory for incoming turbulence noise is derived including a geometrical near-field correction. An innovative BEM approach is proposed in order to compute the broadband scattering. A good agreement is obtained in comparison with the measurements.

Keywords: Aeroacoustics, Broadband Scattering, Amiet, ATV

1. Introduction

The broadband noise generated by the interaction between turbulent flow and an airfoil is a concern in many industrial contexts. In the aeronautical industry, slat and flap noise are important components of the airframe noise. In the energy sector, the broadband noise emitted by the rotating blades of wind turbines is one of the factors hindering their landside development.

Several approaches, ranging from semi-empirical methods[1] to highly accurate and CPU intensive transient CFD calculations [2], have been proposed to address this problem. Amiet and co-workers[3; 4] proposed a theory assuming statistical turbulence models combined with the application of Curle's analogy for a distribution of point dipoles[5] and derived semi-analytical Green's functions to link the pressure jump of the airfoil to the subjected incoming turbulence or to its own turbulent boundary layer. The present work is focused on the incoming turbulence noise problem.

One of the assumptions in the derivation is that the airfoil located in a turbulent flow which is homogeneous in the spanwise direction. When the blade is subjected to spanwise varying turbulent flow conditions (such as convection speed, intensity or spanwise coherence), averaged conditions can be assumed. However, averaging can be delicate since various parameters of the flow field appear with different powers in the model. In a more accurate procedure called the strip method[6; 7], the blade is divided into short segments in the spanwise direction and local turbulence properties are used for each segment.

Another important point is related to the scattering of the broadband noise emitted by the airfoil. While uniform free-field propagation can be assumed for wind turbines (neglecting wind and temperature gradients), the installation effects are nowadays regarded as significant for other applications such as aircraft flap or slat noise or the noise emitted by cooling fans in ground transportation or domestic appliances. Therefore the acoustic scattering effects have to be taken into account.

A variety of theories have been proposed to calculate the sound propagation and scattering at solid surfaces. Helmholtz solvers, based on the Finite Element Method (FEM) or Boundary Element Method (BEM), are already in use in industry[8]. Other more sophis-

ticated methods based on the resolution of Linearized Euler Equations[9] can account for refraction effects in the propagation region. A common denominator of those techniques is the requirement of a deterministic description of the acoustic field. However, due to the statistical characterization of the turbulence, the noise prediction lacks the phase information. We propose in this work a formalism based on the auto- and cross-power spectra of the noise, calculated through an extension of Amiet's theory[10] combined with BEM[11]. This new approach is applied to the scattering of the broadband noise, emitted by an airfoil placed in the developing region of a turbulent jet, by a finite screen.

2. Prediction of the Acoustic Field

Two hybrid approaches, where the flow and acoustic fields are solved separately, are applied in order to compute the acoustic field of an airfoil subjected to incoming turbulence. The first one is a direct numerical method based on the pressure distribution on the airfoil surface obtained from the unsteady CFD computation [5]. The second one is a semi-analytical method [3; 10] employing an analytical turbulence model using the flow profile impinging to the airfoil obtained from the same CFD computation.

2.1. Curle's Analogy

Since the hydrodynamic pressure fluctuations over the airfoil surface is the dominant source mechanism compared to the other ones, such as viscous stresses, only the dipolar radiation is taken into account. The acoustic pressure generated by a point dipole in its near-field is defined as [5]

$$p(x,y,z,\omega) = \frac{\mathrm{i}\omega z F\,\mathrm{e}^{\mathrm{i}\omega t}}{4\pi c_0 R^2}\,\mathrm{e}^{-\mathrm{i}\omega R/c_0}\left(1+\frac{1}{i\,k\,R}\right). \quad (1)$$

ω and c_0 are the angular frequency and the speed of sound, respectively. R is the linear dipole-observer distance and k is the acoustic wave number for the frequency of interest. The parenthesis on the right hand side of the equation contains the acoustical near-field effects. $F\mathrm{e}^{\mathrm{i}\omega t}$ is the source strength of the dipole obtained through the surface integration of the unsteady pressure field on the airfoil. The airfoil is then reduced to a point dipole. This assumption is only valid if the airfoil is acoustically compact for the frequencies of interest.

An advantage of this numerical method is that the acoustic pressure field can be computed in a deterministic manner since the source field is already defined deterministically. The amplitude and phase information of the acoustic pressure are then known. This will be related to the acoustic scattering computations detailed in Section 3.

On the other hand, this methodology is limited with the resolution of the numerical mesh of the flow field computation since very fine numerical mesh is required in order to predict the acoustic source field for the higher frequencies[7]. A semi-analytical method is therefore proposed in order to predict the acoustic field of the airfoil for the high frequency range.

2.2. Generalization of the Semi-Analytical Model

The acoustic response of an airfoil subjected to incoming turbulence involves the radiation of spanwise and chordwise distributed dipoles on the airfoil surface. The acoustical far-field pressure generated by each point dipole is defined as [5]

$$p(x,y,z,\omega;x_0,y_0) = \frac{\mathrm{i}\omega z F(x_0,y_0)\,\mathrm{e}^{\mathrm{i}\omega t}}{4\pi c_0 \sigma_t^2}\,\mathrm{e}^{-\mathrm{i}\omega\sigma_t/c_0} \quad (2)$$

in which acoustic near-field terms have been neglected. The strength of the wall-normal dipole $F\,\mathrm{e}^{\mathrm{i}\omega t}$ is obtained from the distribution of the pressure jump across the airfoil encountering a sinusoidal gust [12] according to linearised airfoil theory. The observer-dipole distance, including the convective effects, is:

$$\sigma_t = \left(\sqrt{(x-x_0)^2+\beta^2\,(y-y_0)^2+\beta^2 z^2} - M(x-x_0)\right)/\beta^2 \quad (3)$$

(x_0, y_0) are the chordwise and spanwise positions of the point dipoles on the airfoil surface linearized as a flat plate with zero thickness and camber, and at zero angle of attack. (x, y, z) are the coordinates of the observer with respect to an origin located at the center of the airfoil surface. M is the convection Mach number and $\beta = \sqrt{1-M^2}$ is the compressibility factor.

Integrating explicitly the distribution of dipoles over the airfoil surface of chord c and span $2d$ yields the following expression for the sound power spectral density (PSD) (See reference [3] for further details on the derivation):

$$S_{pp}(x,y,z,\omega) = \int_{-d}^{d}\int_{-c/2}^{c/2}\left(\frac{\omega\rho_0 z}{2c_0\sigma_t^2}\right)\left(\frac{\omega\rho_0 z}{2c_0\sigma_t'^2}\right)\ldots$$

$$U\mathrm{e}^{-\mathrm{i}\omega(\sigma_t-\sigma_t')/c_0}\int_{-\infty}^{\infty} g(x_0,K_x,k_y)\,g^*(x_0',K_x,k_y)\Phi_{ww}(K_x,k_y)\ldots$$

$$\mathrm{e}^{-\mathrm{i}k_y(y_0-y_0')}\mathrm{d}k_y\mathrm{d}x_0\mathrm{d}x_0'\mathrm{d}y_0\mathrm{d}y_0' \quad (4)$$

where $K_x = \omega/U$. The superscripts $'$ and * stand for the second integration variable and the complex conjugate operator, respectively. Φ_{ww} is the power spectrum of the incident upwash velocity component, which can be represented by a von Karman model for example, tuned by the turbulence intensity and the spatial correlation length. $g(x_0, K_x, k_y)$ is the transfer function linking the incoming gust upwash velocity to the pressure jump on the airfoil.

In the geometrical far-field of the airfoil, the propagation distance can be simplified with a first order approximation in the phase variation and the following expression can be used for the term in the denominator

$$\sigma_t \approx \sigma = \sqrt{x^2 + \beta^2 y^2 + \beta^2 z^2} \tag{5}$$

which allows carrying out a straightforward analytical integration over the airfoil planform in Equation 4, to obtain Amiet's classical result

$$S_{pp}(x, y, z, \omega) = \left(\frac{\omega \rho_0 z c}{2 c_0 \sigma^2}\right)^2 U... \int_{-\infty}^{\infty} \frac{\sin^2\left[d\,(k_y + K_y)\right]}{(k_y + K_y)^2} \left|\boldsymbol{L}(x, K_x, k_y)\right|^2 \Phi_{ww}(K_x, k_y)\, \mathrm{d}k_y \tag{6}$$

where $K_y = \omega y/(c_0 \sigma)$. $\boldsymbol{L}$ is the aeroacoustic response function [6].

One of the main hypotheses in the final formulation of Amiet's theory [3] for incoming turbulence noise is the consideration of an observer placed in the far-field such that a simplified formulation can be obtained (Equation (6) above). In many industrial applications such as the scattering of fan blades sound in a duct, the acoustic pressure (or velocity) used for the scattering computation has to be obtained at a short distance from the considered airfoil. The first key aspect of this paper is the generalization of Amiet's developments to place the listener at a distance which can become comparable to the span of the airfoil – referred as *spanwise geometrical near-field*.

2.2.1. Spanwise geometrical near-field correction

In the case of large-span airfoils and for observer distances similar to the spanwise extent, supposing that $(x - x_0)^2 \simeq x^2$ can be still quite reasonable while $(y - y_0)^2 \simeq y^2$ may become questionable. We introduce therefore an intermediate level of approximation to Equation (5) with

$$\sigma \simeq \sqrt{x^2 + \beta^2 (y - y_0)^2 + \beta^2 z^2}\,. \tag{7}$$

Using this spanwise near-field approximation and the same first-order approximation of the phase variation [3] as above, the power spectral density becomes[10]

$$S_{pp}(x, y, z, \omega) = \left(\frac{\omega \rho_0 z c}{4 c_0}\right)^2 U... \int_{-\infty}^{\infty} \left|\boldsymbol{S}(x, y, z, K_y, k_y)\right|^2 \left|\boldsymbol{L}(x, K_x, k_y)\right|^2 \Phi_{ww}(K_x, k_y)\, \mathrm{d}k_y \tag{8}$$

which differs from Amiet's classical solution by the modified function $\boldsymbol{S}$, expressed as a combination of exponential integrals E_1[13]:

$$\begin{aligned}\boldsymbol{S}(x, y, z, K_y, k_y) = {} & \frac{\mathrm{i}\, \mathrm{e}^{\mathrm{i}\widetilde{K_y} y}}{2\sqrt{x^2 + z^2}} \\ & \Big\{ \mathrm{e}^{-\widetilde{K_y}\sqrt{x^2+z^2}} E_1\left[-\widetilde{K_y}\sqrt{x^2 + z^2} - \mathrm{i}\,\widetilde{K_y}(d - y)\right] \\ & - \mathrm{e}^{-\widetilde{K_y}\sqrt{x^2+z^2}} E_1\left[-\widetilde{K_y}\sqrt{x^2 + z^2} - \mathrm{i}\,\widetilde{K_y}(-d - y)\right] \\ & - \mathrm{e}^{\widetilde{K_y}\sqrt{x^2+z^2}} E_1\left[\widetilde{K_y}\sqrt{x^2 + z^2} - \mathrm{i}\,\widetilde{K_y}(d - y)\right] \\ & + \mathrm{e}^{\widetilde{K_y}\sqrt{x^2+z^2}} E_1\left[\widetilde{K_y}\sqrt{x^2 + z^2} - \mathrm{i}\,\widetilde{K_y}(-d - y)\right] \Big\},\end{aligned} \tag{9}$$

where $\widetilde{K_y} = K_y + k_y$.

A test is first performed in order to compare the results provided by the far-field expression (6), the spanwise near-field expression (8) and the direct numerical integration of formulation (4) valid in both spanwise and chordwise geometrical near-field. The numerical integration of the 5-dimensional integral (4) was carried out employing a specific Monte Carlo integration technique [10], which won't be detailed in the present paper for the sake of conciseness. We remind that Equation 4 accounts for both amplitude and phase modulation effects. Figure 1 shows the variation of the sound power level emitted by a stationary airfoil subjected to homogeneous turbulence properties, with the distance z along the line $(x, y) = (0, 0)$ for a fixed frequency $f = 2000$ Hz. A von Karman spectrum model is selected for the turbulent energy spectrum with an incoming velocity $U = 13.2$ m/s, a turbulence intensity $TI = 0.2$, and a turbulent length scale $\Lambda = 0.005$ m. The airfoil chord is fixed to $c = 0.041$ m, and a large aspect ratio airfoil is assumed by using a span $2d = 40\,c$ [7].

The results show that all formulations converge asymptotically for $z > 2d$, pointing out the limit of application of the far-field formulation without taking the geometrical near-field effects into account. The

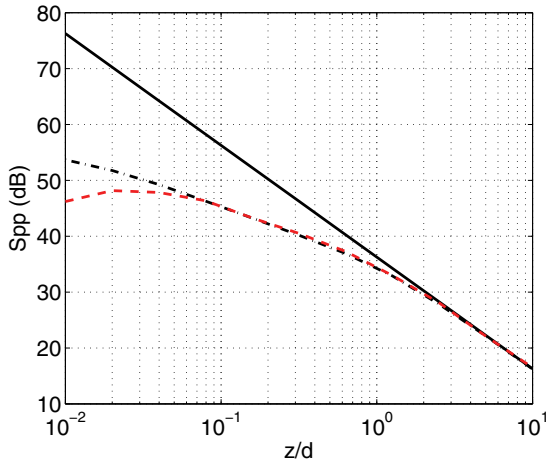

Figure 1: The predicted sound power level above the airfoil using Amiet's far-field solution (6) (solid line), the geometrical spanwise near-field formulation (8) (dash dot line), the direct numerical integration of formulation (4) without any geometrical assumption (dash line)

use of the general formulation, Equation (4) exhibits a deviation from the far-field approximation at $z = 2d$ corresponding to the size of the spanwise extent of airfoil. On the other hand, the new spanwise near-field expression (8) follows the reference solution, Equation (4), up to $z/d < 0.04$, addressing the geometrical chordwise near-field effects. The chordwise near-field terms become significant and cause discrepancies up to 5 dB between the geometrical near-field solution (8) and the reference solution (4). Figure also points that the first-order approximation of the phase variation results negligible errors for the values of z/d between 0.04 and 2.

It is seen that the new formulation highly improves the solution compared to Amiet's far-field solution and shows agreement with the general solution up to the chordwise geometrical near-field. Since Equation (8) is attractive for geometrical near-field computations due to its accuracy and robustness, it will then be used in the following sections involving spanwise segmentation and scattered-field computations.

2.2.2. *Spanwise segmentation*

In most industrial applications including the one presented in Section 4, the incident flow is strongly non-uniform along the spanwise direction. This must be accounted to ensure an accurate prediction of the sound power emitted by the airfoil. In order to take the spanwise varying incoming flow conditions into account, the airfoil is split into small segments assuming that the impinging flow for each segment is uniform and homogenous. Then the total PSD of the airfoil is obtained via the summation of the PSD of all segments, assuming that each segment has a span greater than the turbulence spanwise correlation length. This method is referred as *direct segmentation*. Since large spanwise hydrodynamic wavelengths can't be represented over short strips, the direct segmentation underpredicts the acoustic field in lower frequencies. In order to predict the acoustic field accurately over the entire frequency spectrum, an extended segmentation method is proposed by Christophe[14] where the PSD of the segments are calculated through the subtraction of the ones of two large-span airfoils. This approach is called *inverse segmentation* method.

In a first stage, both segmentation methods are applied to an airfoil for which the impinging flow features are uniform along the span and compared to the prediction obtained using the entire airfoil as a whole. Differences between two approaches are then meant to highlight the numerical deficiencies in the segmentation method.

The results are shown in Figure 2 with the geometry and flow conditions given in Section 2.2.1. The airfoil is split into 64 segments and the listener is placed at $(x, y, z) = (0, 0, 5\,c)$. The geometrical near-field formulation, Equation (8), is then used for each segment. The inverse segmentation method is found to minimize the error. Although it doubles the computation time, due to its reliability, it will be used later on in this paper.

3. Acoustic Scattering

The experiment described in Section 4.2 involves an airfoil placed in the developing region of a turbulent jet in the presence of a scattering screen. The free-field response of the airfoil can be addressed by the approaches described above, and the scattering problem can be solved by means of a Boundary Element Method[15] (BEM).

3.1. *Boundary Element Method*

In the BEM approach, the acoustic pressure field is first decomposed into incident and scattered components:

$$p = p_i + p_s. \tag{10}$$

The incident field pressure, p_i, is obtained from Equation (1) using the deterministic source field described in Section 2.1. The scattered pressure, p_s, is then computed using the Indirect Boundary Elements Method,

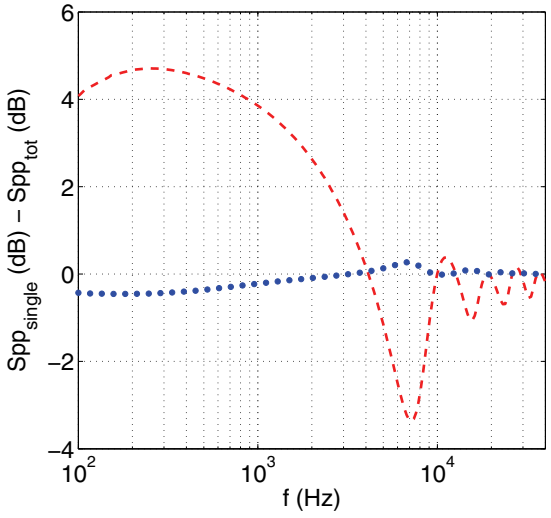

Figure 2: Error defined by the differences between the complete airfoil formulation and the summation of the PSD of segments, 64 segments with direct segmentation (dashed) and inverse segmentation (symbols) methods, using spanwise-homogeneous turbulence properties.

where the rigid Neumann boundary conditions are satisfied on the scattering surface. (See Reference [8] for the derivations of Indirect Boundary Element Method.)

However, since the broadband noise model described in Section 2.2 is based on a statistical description of the source field, the BEM formulation employed is not capable to handle this problem. Therefore, we have to reformulate the deterministic BEM problem.

3.2. Acoustic Transfer Vectors

In the present scattered field approach, using the same decomposition in Equation (10), the total power spectrum is represented as

$$S_{pp} = S_{p_i p_i} + S_{p_i p_s} + S_{p_s p_i} + S_{p_s p_s} \tag{11}$$

where the first term on the right hand side of the equation is the free-field response of the airfoil which can be solved with the Equation (4). The remaining terms are solved by the BEM methodology. In this BEM framework, an Acoustic Transfer Vector (ATV) formulation is employed to relate the acoustic pressure at a listener point to the wall-normal velocity of the elements that discretize the surface of the scattering body;

$$p_s(\omega) = \{\mathbf{ATV}(\omega)\} \cdot \{v_{n_s}(\omega)\} \tag{12}$$

where $\{\mathbf{ATV}(\omega)\}$ is the Acoustic Transfer Vector obtained by solving the BEM problem with unit normal velocities on the acoustic mesh. In order to satisfy the the rigid Neumann boundary condition on the acoustic mesh, the velocities $\{v_{n_s}(\omega)\}$ in Equation (12) correspond to minus the projection of the incident velocity, $v_{n_s} = -v_{n_i}$. The incident velocity term, v_{n_i}, is computed from the gradient of the incident pressure obtained by using the acoustic far-field approximation:

$$v_{n_i}(\mathbf{x}, \omega) = \frac{\mathrm{i}}{\rho_0 \omega} \frac{\partial p(\mathbf{x}, \omega)}{\partial n}. \tag{13}$$

Therefore the same acoustic far-field assumption applies to the position of the scattering surface next to the source, as for the listener position. Combining Equations (11) to (13), the total spectrum yields

$$S_{pp} = S_{pp,i} - S_{pv} \cdot \mathbf{ATV}^T - \mathbf{ATV}^* \cdot S_{vp} + \mathbf{ATV}^* \cdot S_{vv} \cdot \mathbf{ATV}^T \tag{14}$$

where S_{pv} and S_{vp} are the cross-power spectra of the incident velocity evaluated over the acoustic mesh and the incident acoustic pressure at the listener point. The S_{vv} is the auto and cross-power spectra of the incident velocities over the acoustic mesh. The $\{\mathbf{ATV}(\omega)\}$ is now a matrix composed of the Acoustic Transfer Vectors for each listener point. The superscripts ^{T} and * stand for the matrix transpose and the complex conjugate operator, respectively.

4. Experimental Validation

Experiments have been conducted for comparison of the measured sound power levels with the broadband noise predictions in free-field and including scattering effects. The jet-airfoil mock-up mentioned above consists in a NACA 0012 airfoil with $c = 0.041$ m chord and $8.78c$ span, placed in the transitional region of a turbulent jet. The jet nozzle is circular with an outlet diameter $D = c$. The airfoil is placed at zero angle of attack with its leading edge located at $6c$ from the nozzle outlet plane as seen in Figure 3. The jet outlet Mach number $M \cong 0.04$ results in a Reynolds number based on the chord $Re_c = 36,000$. The jet and the airfoil are placed in the anechoic room of the von Karman Institute for Fluid Dynamics. The dimensions of the room are $4 \times 3 \times 4$ m^3, and walls, floor and ceiling are covered with acoustic absorbing material. The cut-off frequency of the room is 350 Hz. Sound measurements are taken with Bruel & Kjaer microphones using a high-pass filter of 100 Hz and a low-pass filter of 12 kHz. The sampling frequency is 2^{19} Hz and measurements are acquired in series of 0.1 s duration.

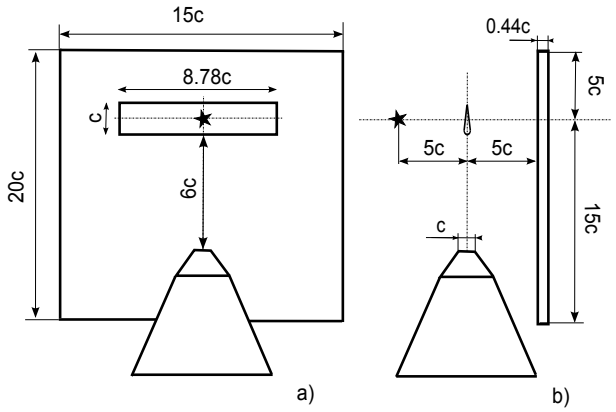

Figure 3: The experimental jet-airfoil mock-up, a) Front view, b) Side view

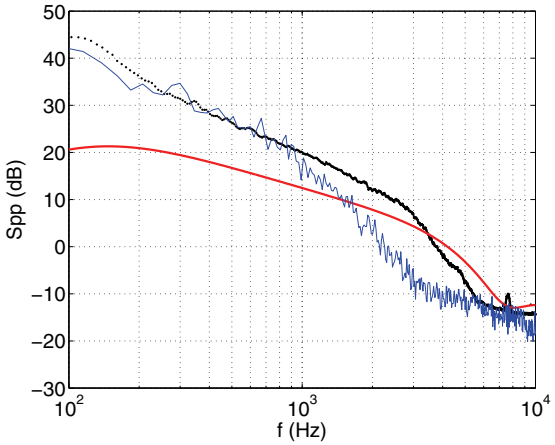

Figure 4: Sound power spectra measured (black dots), calculated by Amiet's theory with 8 spanwise segmentats (red solid line) and Curle's deterministic analogy (thin blue line).

4.1. Acoustic free-field

The comparison of the acoustic field emitted by the airfoil for an observer located at $5c$ above the airfoil, as obtained from the measurements, a deterministic solution based on Curle's analogy and the solution (8) using 8 spanwise segments is seen in Figure 4. It is seen that there is a fair agrement between the measurements and the solution (8) in the frequency range of $500 - 10000$ Hz where the differences between two spectrum is not larger than 5 dB. The discrepancies between the solution (8) and the measurements at low frequencies can be mainly related to the strongly anisotropic character of the corresponding energetic turbulent scales, which are missing in von Karman model employed. Additionally, the formulation (2) neglects the acoustic near-field effects, which may contribute to the sound field at this listener position for the lowest frequencies. However, as seen in the figure, the low frequency range can be predicted using the deterministic hybrid method based on Curle's analogy in which the acoustic near-field terms are already taken into account. The deterministic method provides a reasonable sound prediction up to 1000 Hz which is the cut-off frequency of the CFD. Therefore, in order to complete the spectrum for the full frequency range, it is required to combine the deterministic solution and the solution (8).

4.2. Scattered acoustic field

As mentioned in the Section 3.2, a flat scattering screen is introduced to the jet-airfoil mock-up, keeping the microphone at the same location (see Figure 3). The screen is $15c$ in the width and the airfoil is located in the middle of it on the horizontal axis. However, due to the supports of the screen, it covers $5c$ in downstream and $15c$ in the upstream directions on the vertical axis, with a total height of $20c$. In order to respect the assumptions of the model, the scattering plane should be placed in the geometrical near-field and acoustical far-field for a large part of the frequencies considered in this study. Therefore a distance of $5c$ has been selected. Additionally, the screen is located outside of the turbulent region of the jet in order not to disturb the incoming turbulent flow.

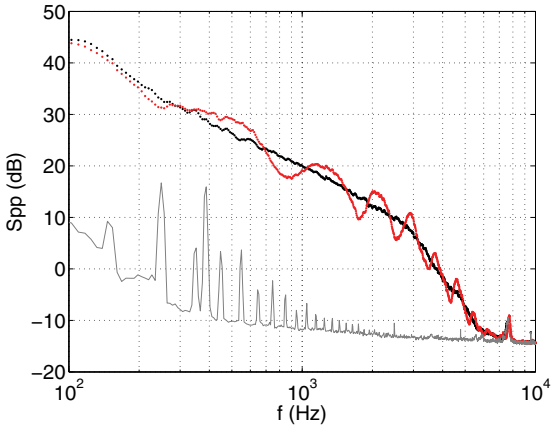

Figure 5: Sound power spectra measured in free-field (black dots), with the plane (red dots) and the background noise (thin line).

The measurements with and without the screen are shown in the Figure 5. The black and red dots represent the free-field and scattered-field measurements, respectively. It is seen that the presence of the flat screen results in deviations of the measured spectrum

around the free-field spectrum. The thin line is the measurements of the background noise. According to the measurements, for the frequencies more than 7500 Hz, the sound measured by the microphone is already disturbed by the background noise.

The contribution of the flat scattering screen can be calculated with three different numerical models; first with the infinite plane assumption, secondly using the classical BEM methodology with the deterministic source definition and finally with the ATV method described above. The former assumes that the flat screen is infinite and it is replaced with a phase shifted airfoil symmetrical to it. However, this case is ideal and neglects the effects of the waves scattered by the free edges of the flat plate. On the other hand, the other two methods take the effects of the free edges into account.

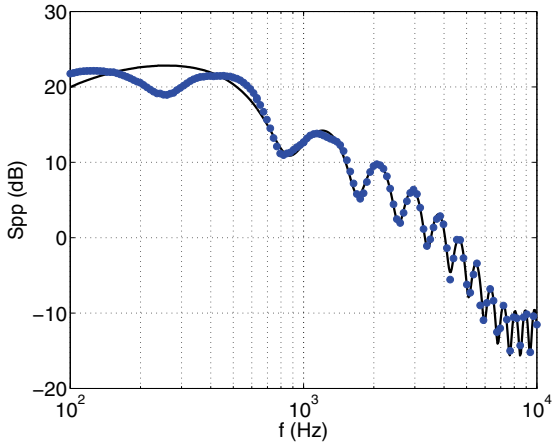

Figure 6: Sound power spectrum computed with the infinite plane model (solid), ATV model (circles) using 8 segments.

Figure 6 shows the comparison of the infinite plane (plain) and ATV (circles) methods with the same configuration using the segmentation method defined in Section 2.2.2. Both methods follow the same wavy patterns for the frequencies higher than 700 Hz. However, the ATV model captures one additional deep in the low frequency zone, which can be addressed as the scattering of the large waves from the free edges.

Comparison of the ATV model (circles), the BEM model (thin line) and the measurements (dots) is also seen in the Figure 7. The positions of the lobes due to the scattering from the screen are captured accurately in both mathematical models. Since the scattered-field computations of the ATV model are based on the ones in free-field, the reason of the discrepancies at low frequencies is the same as addressed for Figure 4. However, the lower frequencies can be captured accurately using Curle's deterministic analogy combined with the deterministic BEM methodology[8]. Therefore, the complete spectrum can be predicted with the combination of the deterministic methodology and the solution (14).

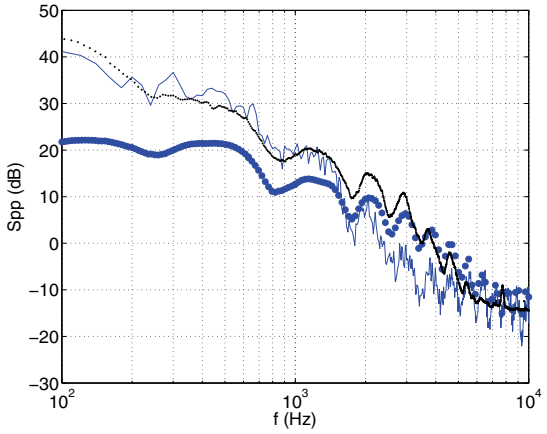

Figure 7: Sound power spectrum computed with the ATV model (circles) using 8 segments, Curle's deterministic analogy combined with BEM (blue thin line) compared with the measurements (dots).

In order to check the consistency of the numerical model, another set of experiments is performed with a plate rotated 45° with respect to the xy plane. Due to the supports of the plate in the anechoic chamber, the rotation center is shifted $0.07c$ in the y direction, as seen in the Figure 8.

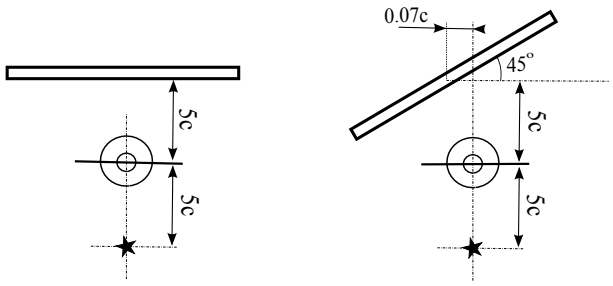

Figure 8: Sketches of the experimental set-ups: parallel plate (left) and 45° rotated plate (right).

Figures 9 and 10 show the ratio of the scattered-field PSD to the free-field PSD in logarithmic scale for parallel and 45° rotated screen, respectively. Plain, circles and dots represent the infinite plane model, ATV model and the experimental results, respectively. The figures prove that the effect of the scattered screen is captured accurately by the ATV model for both con-

figurations. It can be seen that the infinite plane model shows good agreement with the ATV model starting from 800 Hz, the difference below is due to the free edge effects as pointed above. Figures also indicate that the ATV model is consistent with the arbitrary positions of the scattered plate.

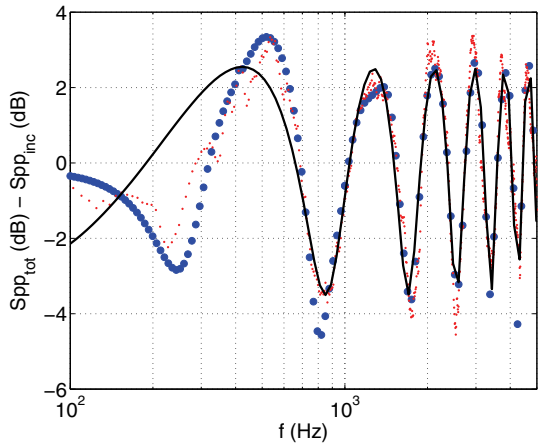

Figure 9: Ratio of the scattered sound power spectrum to the free field spectrum, infinite plane model (solid), ATV model (circles) and experiments (dots) with the parallel plate.

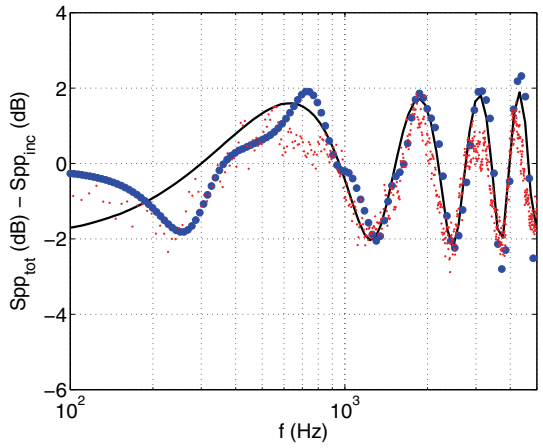

Figure 10: Ratio of the scattered sound power spectrum to the free field spectrum, infinite plane model (solid), ATV model (circles) and experiments (dots) with the 45° rotated plate..

5. Conclusions

Predicting the broadband noise emitted by large aspect ratio airfoils is a relevant issue for applications such as high-lift devices or wind turbines. Amiet's theory provides an interesting approach to tackle this problem, and has been used by a number of authors with success, especially for configurations where the statistical properties of turbulence and airfoil geometry are fairly constant in the spanwise direction. The present work considers the cases where those parameters can vary significantly along this direction.

The results shown above demonstrate that in order to obtain numerically consistent results where the far-field assumption is not valid, spanwise near-field effects must be included in a generalized derivation of Amiet's theory for incoming turbulence noise. The solution is compared with a direct numerical integration and an important improvement is observed.

Finally, the presence of solid surfaces in the neighborhood of the radiating airfoil, as for airframe flap or slat noise for example, imposes to compute the scattering of the incident sound field obtained by the generalized Amiet model presented herein. A method based on Acoustic Transfer Vectors, obtained by means of a commercial Boundary Element solver, is proposed and validated against experiments for two different configurations. The results showed that the analytical model combined with Acoustic Transfer Vector approach is a useful tool to predict the scattered acoustic field of a stationary airfoil due to its installation effects.

Acknowledgements

This work is supported by the European Commission in the framework of the Marie Curie project AETHER (contract no MRTN-CT-2006-035713) and the FP7 Collaboration Project ECOQUEST (grant agreement no 233541).

References

[1] Brooks, T.F. , Marcolini, M.A. , Pope, D.S., "Airfoil trailing edge flow measurements", AIAA Journal 24 (8):12451251, 1986.

[2] Choudhari, M., Khorrami, M., Lockard, D., Atkins, H., Lilley, G., "Slat Cove Noise Modeling: A Posteriori Analysis of Unsteady RANS Simulations", AIAA Paper, 2002-2468, 2002.

[3] Amiet, R.K., "Acoustic radiation from an airfoil in a turbulent stream", Journal of Sound and Vibration, 41 (4):407-420, 1975.

[4] Paterson, R.W., Amiet, R.K., "Acoustic radiation and surface pressure characteristics of an airfoil due to incident turbulence", NASA CR-2733, 1976.

[5] Curle, N., "The influence of solid boundaries upon aerodynamic sound", Proc. R. Soc. London Ser. A, Vol. 231 (1187): 505514, 1955.

[6] Rozenberg, Y., "Modelisation analytique du bruit aerodynamique a large bande des machines tournantes: utilisation de calculs moyennes de mecanique des fluides", (Ecole Centrale Lyon, 2007-44.)
[7] Christophe, J., Anthoine, J., Rambaud, P., Schram, C., Mathey, F., Moreau, S., "Prediction of incoming turbulent noise using a combined numerical / semi-empirical method and experimental validation", AIAA Paper, 2007-3468, 2007.
[8] Virtual Lab Rev 9: User manual, LMS International, 2009.
[9] Bailly, C., Juve, D., "Numerical Solution of Acoustic Propagation Problems Using Linearized Euler Equations" AIAA Journal 38 (1):22-29, 2002.
[10] Kucukcoskun, K., Christophe, J., Schram, C., Anthoine, J., Tournour, M., "An Extension of Amiet's Theory for Spanwise Varying Incoming Turbulence Noise and Broadband Noise Scattering Using BEM", AIAA Paper 2010-3987, 2010.
[11] Gerard, F., Tournour, M., Masri, N.E., Cremers, L., Felice, M., Selmane, A., "Numerical modeling of engine noise radiation through the use of Acoustic Transfer Vectors: A case study", SAE Paper, 2001-01-1514, 2001.
[12] Amiet, R.K., "High frequency thin-airfoil theory for subsonic flow", AIAA Journal 14 (8):1076-1082,1976.
[13] Abramowitz, M., Stegun, I. A., "Handbook of mathematical functions", Dover Publications, 1972.
[14] Christophe, J., Anthoine, J., Moreau, S., "Amiet's Theory in Spanwise Varying Flow Conditions", AIAA Journal Technical Notes 47 (3), 2009.
[15] von Estorff, O., "Boundary Elements in Acoustics", WIT Press, 2000.

Beamforming in non-ideal acoustic environments

Péter Tóth

Environmental and Applied Fluid Mechanics Department, tothp@vki.ac.be

Supervisor: Christophe Schram

Assistant Professor, Environmental and Applied Fluid Dynamics Department, von Karman Institute for Fluid Dynamics, Belgium, schram@vki.ac.be

Promotor: Máté Márton Lohász

Assistant Professor, Department of Fluid Mechanics, Budapest University of Technology and Economics, H-1111 Budapest Bertalan Lajos utca 4-6, lohasz@ara.bme.hu

Abstract

This paper presents the current achievements of the acoustics beam-forming technique developed in the VKI. The microphone array beamforming is under innovation in order to be able to perform aerodynamic source localization in a high background noise open jet wind tunnel developed for low speed aerodynamic tests (VKI L1A tunnel). Preliminary tests of source localization on an airfoil geometry has been made in a semi anechoic room with an array of 32 low cost elctret microphones. The array geometry is obtained from an optimization procedure of the microphone position in order to improve the beamformer point spread function characteristics. The conventional (or Least Squares) beamforming and two different implementation of the Generalized Inverse Beamforming algorithm have been used to retrieve aerodynamic sources at the airfoil plane. Results are promising with both implementation however the robustness of the iterative algorithms has to be increased before it can be applied in high background noise environments. The convergence properties of the algorithms are investigated, results showed that the algorithm with cost function minimization by optimization method gives preferable results, however the physical correctness of the applied method has to be validated.

Keywords: acustics, generalized inverse, bemforming, microphone array, airfoil noise

Nomenclature

α_{op}	Complex optimization parameter
β	Reference solution reduction factor
ϵ	Regularization factor
$\epsilon user$	User defined regularization parameter
λ_m	The mth eigenvalue of the of the cross spectral matrix
$\lambda_{\mathbf{lag}}$	Lagrangian multiplier
$\mathbf{A}$	Acoustics transfer matrix between source candidates and microphones
$\mathbf{a}_i$	Vector of source amplitudes for mode i
$\mathbf{G}$	Vector of the Green's functions for the lth microphone $G(\mathbf{x}_m^{cand}, \mathbf{x}_l, \omega)$
$\mathbf{I}$	Identity matrix
$\mathbf{q}$	Vector of the measured pressure signals $q_l(\omega)$
$\mathbf{u}_m$	The mth eigenvector of the of the cross spectral matrix
$\mathbf{w}_i$	Mode i
$\mathbf{x}$	Observer position
$\mathbf{x}_l$	Position of the lth microphone
$\mathbf{x}_m^{cand}$	Is the position vector for the mth source candidate on the scanning grid
$\mathbf{x}_s$	Source position

ω Angular frequency

ω Circular frequency

a_s Complex source amplitude

c Speed of sound

D Diameter of the nozzle

f Frequency

$G(\mathbf{x}_s, \mathbf{x}, \omega)$ Is the Green's function

j Square root of -1

k Wave number

L Airfoil microphone array distance

M Mach number

N_{final} Final number of source candidates

N_{grid} Number of scanning grid points

N_{mic} Number of microphones

N_{types} Number of scanning source types

$p(\mathbf{x}_s, \mathbf{x}, \omega)$ Acoustics pressure at position $\mathbf{x}$, from the source located at $\mathbf{x}_s$

$P_{conv}(\omega, \mathbf{x}_m^{cand})$ Position of the source candidate m

$q_l(\omega)$ Measured pressure signal at microphone l

Re Reynolds number

v jet exit velocity

1. Introduction

The aim of this PhD project is to develop acoustics beamforming measurement configuration for aeroacoustic source localization in an non ideal noisy acoustics environment of an open jet wind tunnel. Since there is an increasing desire for aeroacoustic noise reduction, the need for experimental testing is also increased. The conversion costs of a non-anechoic wind tunnel or the construction of new anechoic wind tunnel can be prohibitive. Since aerodynamic wind tunnels are more common, a technique for implementing noise-source identification in a non-anechoic environment would further extend the use of these tunnels in a cost efficient way. The beamforming techniques was first used in radio astronomy and radar technology to obtain a directionally sensitive antenna for the detection of the incoming signal direction [1]. The principle of this technique is to use several, fixed position microphones, to obtain a highly directional sensitive measurement device those characteristics can be easily changed with the signal processing technique used on the simultaneously acquired dataset. In this way the acoustics field can be scanned by 'steering' the array into different directions and registering the output level of the system. The result is called the beamforming map that, shows the source amplitude distribution in the scanning zone. Today's this technique is widely used in different configuration for acoustics source identification. Many application dependent microphone arrangement exist using advanced data processing algorithms in order to obtain high resolution and clean source maps. The advent of digital data acquisition and processing systems at reasonable costs have accelerated the development, since relatively cheap data acquisition chains can be built up for high number of microphones [2]. The technique is actively developed to reach higher spatial resolution and accurate source strength identification of different kind of aeroacoustic source types. However the application of these techniques in strong background noise environment is still challenging. In the present study, investigation with algorithms based on the generalized inverse formulation of the beamforming problem will presented in an airfoil geometry and compared to the conventional Least Squares (LS) beamforming technique.

2. Theory

Many different beam-forming methods have been developed in the past few years for aeroacoustic applications [2]. In this section two of them is presented shorty the conventional Least Squares algorithm and the Generalized inverse beamformer [3].

2.1. The Least Squares Method

The principles of the beamforming can be easily understood on the Least Squares method. The idea of this processing technique is to formulate a phase matching problem between the measured signals and a predefined reference solution. The unknown parameter is the location of the source (i.e. the direction of the radiation, or the source amplitude distribution in a specified scanning zone). In case of good matching with the reference solution the output of the beamformer is at high level and this indicates the direction or the location and amplitude of the reference

sources that are best matching with the measured data. This can be considered as a least squares minimization of the difference between the measured signal and reference solution [4]. If a monopole source is assumed with source amplitude a_s, the sound pressure $p(\mathbf{x}_s, \mathbf{x}, \omega)$ can be expressed at point $\mathbf{x}$ as follows:

$$p(\mathbf{x}_s, \mathbf{x}, \omega) = G(\mathbf{x}_s, \mathbf{x}, \omega) a_s(\omega) \equiv \frac{1}{2} \frac{a_s(\omega)}{4\pi |\mathbf{x} - \mathbf{x}_s|} e^{jk|\mathbf{x}-\mathbf{x}_s|} \tag{1}$$

where $G(\mathbf{x}_s, \mathbf{x}, \omega)$ is the free field Green's function for a monopole, $\mathbf{x}_s$ is the position of the source, a_s is the complex source amplitude, $k = \omega/c$ is the wave number, c is the speed of sound and ω is the angular frequency. If the pressure data $q_l(\omega)$ is available at the lth microphone that position is $\mathbf{x}_l$ the following cost function can be defined.

$$J(\mathbf{x}_l, \mathbf{x}_s, a_s, \omega) = \sum_{l=1}^{N_{mic}} |p(\mathbf{x}_s, \mathbf{x}_l, a_s) - q_l(\omega)|^2 \tag{2}$$

This cost function representing the error between the monopole source model and the measured acoustics filed in a least squares sense. Therefore the minimum of this cost function indicates good representation of the true acoustics sources by the model sources. By differentiating $J(a_s, \omega, \mathbf{x}_s)$ according to a_s we can found that minimizing $J(a_s, \omega, \mathbf{x}_s)$ is equivalent to maximizing the following output of the beamformer [5]

$$P_{conv}(\omega, \mathbf{x}_m^{cand}) = \frac{\mathbf{G}^\dagger}{|\mathbf{G}|} \mathbf{q}\mathbf{q}^\dagger \frac{\mathbf{G}}{|\mathbf{G}|} \tag{3}$$

where $\mathbf{q}$ is the vector of the measured pressure signals $q_l(\omega)$, $\mathbf{x}_m^{cand}$ is the position vector for the mth source candidate point on the scanning grid, $\mathbf{G}$ is the vector of the Green's functions for the lth microphone and m^{th} source candidate $G(\mathbf{x}_m^{cand}, \mathbf{x}_l, \omega)$, and $\dagger$ denotes complex conjugate transpose. Thus the maximization of P_{conv} leads to the a phase matching problem between the cross spectral matrix $\mathbf{q}\mathbf{q}^\dagger$ and the steering vector $\mathbf{G}/|\mathbf{G}|$. When the candidate source position $\mathbf{x}_m^{cand}$ corresponds to the source position $\mathbf{x}_s$ the output P_{conv} is maximum (J is minimum) and it is indicates the source position. The main drawback of the conventional bemforming method is its moderate resolution especially at low frequencies. This issue is addressed by advanced beamforming algorithms. In the present work different implementations of the Generalized Inverse beamformer (GIBF) have been used.

2.2. The Generalised Inverse Beamformer

This generalised inverse beamformig method is published in [3]. The idea of the GIBF is to assume several source candidates in the predefined scanning plane and retrieve their amplitudes by solving the inverse propagation equation with the array measurement data. In mathematical form the inverse sound propagation problem can be written as:

$$\mathbf{a}_i = \mathbf{A}^{-1} \mathbf{w}_i \tag{4}$$

where A is the matrix contains the transfer function from each of the source candidates to each of the microphones. The size of this matrix is $(N_{grid} N_{types}) \times N_{mic}$, the vector of source amplitudes for mode i is $\mathbf{a}_i$ of length $N_{grid} N_{types}$ and eigenmode i is $\mathbf{w}_i$ of length N_{mic}. The eigenmodes, $\mathbf{w}_i$, are calculated from the eigenvalues λ_i, and the eigenvectors $\mathbf{u}_i$, of the time averaged cross spectral matrix that can be diagonalised since it is Hermitian. So the following relation can be written:

$$\overline{\mathbf{q}\mathbf{q}^\dagger} = \sum_{m=1}^{N_{mic}} \lambda_m \mathbf{u}_m \mathbf{u}_m^\dagger \tag{5}$$

where λ_m is the mth eigenvalue of the of the cross spectral matrix, and the corresponding eigenvector is $\mathbf{u}_m$. So the eigenmodes can be computed:

$$\mathbf{w}_i = \sqrt{\lambda_i} \mathbf{u}_i \tag{6}$$

The source amplitude can be found by the inversion of $\mathbf{A}$ which is a non-square matrix. The shape of the matrix and therefore the behaviour of Equation 4 varies with the ratio of the number of source candidates and the number of microphones. Generally the beamforming problem is underdetermined since the number of source candidates is higher than the number of microphones ($(N_{grid} N_{types}) > N_{mic}$). In this situation Equation 4 is ill posed and does not have a unique solution. However this problem can be handled by a minimization of the following cost function:

$$J_2^u = \frac{1}{2} \sum^{N_{type} N_{grid}} |a_i|^2 + \lambda_{\mathbf{lag}} (\mathbf{w}_i - \mathbf{A}\mathbf{a}_i) \tag{7}$$

where $\lambda_{\mathbf{lag}}$ denotes the Lagrangian multiplier, used to formulate an unconstrained minimization problem with the constraint of Eqn. 4. The approximate direct

solution for this equation is given by Tikhonov regularization.

$$a_i \approx \mathbf{A}^\dagger(\mathbf{A}\mathbf{A}^\dagger + \epsilon\mathbf{I})^{-1}\mathbf{w}_i \tag{8}$$

The reason for application of a regularization method is that usually the inversion of $\mathbf{A}\mathbf{A}^\dagger$ leads to a non-physical source amplitudes, therefore additional constrain is formed by the regularization method to ensure the smoothness of the solution. The value of ϵ is in the order of 0.1% to 5% (denote by ϵ_{user} defined as $\epsilon = \epsilon_{user} max(eig(\mathbf{A}\mathbf{A}^\dagger))$) of the greatest eigenvalue of $\mathbf{A}\mathbf{A}^\dagger$ [6]. It is believed that only a small error is introduced in the solution by addition of a diagonal term to the $\mathbf{A}\mathbf{A}^\dagger$ matrix.

In the other case when the system is overdetermined (i.e. the number of source candidates are smaller than the number of microphones ($N_{grid}N_{types}$) < N_{mic}) the inverse problem can be solved by the minimization of the following least squares cost function:

$$J_2^o = |\mathbf{w}_i - \mathbf{A}\mathbf{a}_i|^2 \tag{9}$$

The solution of this minimization in an approximate sense is given in the following form again with the help of Tikhonov regularization.

$$a_i \approx (\mathbf{A}\mathbf{A}^\dagger + \epsilon\mathbf{I})^{-1}\mathbf{A}^\dagger\mathbf{w}_i \tag{10}$$

In this way the source (mode) amplitudes can be calculated. (Source amplitudes for each modes can be summed up as $\sum_{I=1}^{N_{mic}} |\mathbf{a}_i|^2$).

In the usual case when J_2^u should be minimized the blurring of the source map can be occur, which is a disadvantage of this cost function. For demonstration, consider a monopole source with amplitude one so $J_2^u = 1/2 \sum |\mathbf{a}|^2 = 1/2 \cdot 1 = 1/2$. By solving the under determined inverse problem (as long as the constraint (Eqn. 4) is approximately satisfied) two closely placed sources with amplitude for example 1/2, 1/2 gives smaller cost function value ($J_2^u = 1/2 \sum |\mathbf{a}|^2 = 1/2\left((1/2)^2 + 1/2)^2\right) = 1/4$). In order to avoid this behaviour and increase the resolution of the GIBF algorithm a modified cost function is introduced.

$$J_1 = \sum^{N_{type}N_{grid}} |\mathbf{a}_i| + \lambda_{\mathbf{lag}}(\mathbf{w}_i - \mathbf{A}\mathbf{a}_i) \tag{11}$$

This function however does not have a direct solution like in case of J_2^u and J_2^o. The minimization of J_1 directly by an optimization method is hard and computational demanding. A solution of this cost function can be obtained by iteratively reducing the components of $\mathbf{a}_i$ and minimizing the norm of the following linear combination of the subsequent results of the iteration steps, as it was proposed by [3]:

$$\mathbf{a}_i^{n+1} = \left(1 - \alpha_{op}\right)\mathbf{a}_i^n + \alpha_{op}\mathbf{a}_i' \tag{12}$$

where $\alpha_{op} \in \mathbb{C} : |\alpha_{op}| = 1$ is the optimization parameter, n denotes the iteration step, and $\mathbf{a}_i'$ denotes the initial solution for $\mathbf{a}_i$ from Eqn. 8 or Eqn. 10. By minimizing $|\mathbf{a}_i^{i+1}|$ the cost function J_1 is also minimized with $\lambda_{lagj} = 1/(2\epsilon)$. This was estimated by plotting the cost function J_1 and $|\mathbf{a}_i^{i+1}|$ in function of $\Re(\alpha_{op})$, $\Im(\alpha_{op})$. The linear combination of the two particular solutions of the system is also a solution if $\mathbf{A}$ is a linear operator as it is the case of simple sound propagation. This solution procedure can create spurious spikes on the source map and Gaussian spatial filter may be necessary to apply [3].

The complete solution procedure for producing the source maps using the measurement data from a microphone array can be summarized in the following list:

1. Create the cross spectral matrix $\overline{\mathbf{q}\mathbf{q}^\dagger}$
2. Calculate the eigenmodes defined by Eqn.: 6 from the eigenvalue eigenvector decomposition of $\overline{\mathbf{q}\mathbf{q}^\dagger}$
3. Define the scanning grid and the reference solutions types and create the transfer matrix $\mathbf{A}$
4. Depending on the problem size calculate the initial solution from Equation 8 (if the problem is underdetermined) or Equation 10 (if the problem is overdetermined)
5. Reduce the number of source candidates with a factor of β (e.g. remove $\beta N_{grid}N_{types}$ sources from the system) by removing the smallest amplitude sources. Obtain the solution $\mathbf{a}_i'$ for the reduced system from Equation 8 or Equation 10 depending on the problem size.
6. Pad the reduced system solution ($\mathbf{a}_i'$) with zeros to have the same size as $\mathbf{a}_i^n$
7. Minimize $|\mathbf{a}_i^{i+1}|$ (by for e.g. a quasi Newton method) and compute $\mathbf{a}_i^{i+1}$ with the minimized α_{op}
8. Update the results matrix with $\mathbf{a}_i^{i+1}$
9. Reduce the number of points in $\mathbf{a}_i^{i+1}$ by factor of β and repeat the procedure from 4 to 9 till the desired number of points minimum grid points are reached.

2.3. Algorithm Implementation

All algorithms have been coded in Octave. There are two different implementation of the GIBF algorithm. One is without using the optimized linear combination of previous step results and the current Tikhonov regularization result (Eqn. 12). Therefore this algorithm uses only the Tikhonov regularized solution and successive smallest amplitude source candidate removal to obtain the solution without explicitly minimizing the J_1 cost function [7]. The algorithm is noted in the figures as "GIBF No Optim." and the solution procedure for this algorithm is the following:

1. Create the cross spectral matrix $\overline{\mathbf{qq}^\dagger}$
2. Calculate the eigenmodes defined by Eqn.: 6 from the eigenvalue eigenvector decomposition of $\overline{\mathbf{qq}^\dagger}$
3. Define the scanning grid and the reference solutions types and create the transfer matrix $\mathbf{A}$
4. Depending on the problem size calculate the solution from Equation 8 (if the problem is underdetermined) or Equation 10 (if the problem is overdetermined)
5. Reduce the number of source candidates with a factor of β (e.g. remove $\beta N_{grid} N_{types}$ sources from the system) by removing the smallest amplitude sources. Put the removed sources to the solution vector. Continue form 4 with the reduced number of source candidates till desired number of points minimum grid points are reached.
6. Put all the remaining sources to the solution vector.

The other solution is the full GIBF algorithm with presented in Section 2.2. The optimization procedure is done by using optimization and signal processing packages from the Octave-Forge open source community. For the minimization of Equation 12 the quasi Newton algorithm called 'bfgsmin' is used with two parameters (the real and imaginary part of α_{op}). This algorithm is noted by "GIBF" in the figures and the text. The built in solver of Octave is used for the cross spectral matrix decomposition and for the solution of the matrix inversion problem. Gaussian source map filtering is not applied in the present investigation.

3. Application jet airfoil interaction

The Least Squares and the Generalized Inverse Beamformer have been applied to a jet airfoil noise source placed in the semi anechoic room of the VKI. This is the first test of the implemented algorithms (in Octave software package) in a relatively low background noise environment. The chord of the airfoil is $1D$, where D is the nozzle diameter of the jet. It is placed $6D$ downstream of the nozzle exit plane. The jet exit Mach number is approximately $M = v/c \approx 0.11$, and the Reynolds number computed by the airfoil chord and jet velocity is $Re \approx 140000$. The measurement is completed by the use of a multi-arm spiral depicted in Figure 1. The microphone array is placed at $L = 1$ m distance away from the airfoil. The alignment of the array plane with the airfoil span is not perfect causing that source map should be a bit shifted (about -4cm) in the x direction. The centre of the array is approximately at the same height as the leading edge of the airfoil. The setup photographed from behind the array is shown in Figure 5 . Knowles low cost electret microphones are used in the array with VKI amplifiers and signal conditioners. The 32 microphone data is collected simultaneity by a National Instruments data acquisition system. Phase and amplitude correction factors obtained previously from the calibration are used for correcting the measured cross spectral matrix [8]. The sampling frequency was 80kHz and 600000 samples are collected on each microphone channel. The size of the averaged blocks in the preparation of the cross spectral matrix is 2^{13} with block overlapping of 50%.

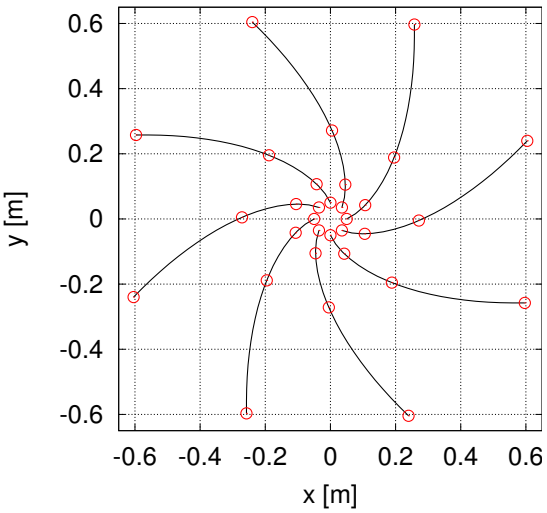

Figure 1: Optimized multi-arm spiral array geometry

The results of the LS algorithm and the results of the two different implementation of the GIBF beamformer compared in Figures 2, 3, 4 at 2, 6, 16 kHz

respectively. The scanning grid size was 0.5 by 0.5 m and 101 by 101 reference monopole source candidates are paced in the region uniformly. For the GIBF algorithm only the highest mode ($i = 1$ see Eqn.6 since modes are descending ordered) of the decomposed cross spectral matrix is used for the reconstruction.

At 2kHz the source region corresponding to the airfoil geometry can be seen at the jet impingement. The centre of this region is more or less located at the leading edge of the airfoil. This is expected from theoretical consideration of acoustics analogies like Ffowcs Williams Hawkings since the high turbulence level of the jet causing significant surface pressure fluctuations that is a source of sound. At higher frequencies the detected sources are more localised to the leading edge part of the airfoil geometry and at 16kHz some tails can be also observed over the trailing edge elongated from the main source zone. The size of the jet impingement region is approximately 4D in the span wise direction of the airfoil. This is approximately corresponding to the source region detected by the GIBF algorithm at 2kHz.

Concerning the different algorithms it can be clearly seen that the increase of the frequency comes with the increase of the resolution on all types of algorithms. The resolution of the GIBF algorithms are better than the LS algorithm. However there is no big difference between them on the highest frequency 16kHz. The resolution benefit of the advanced processing algorithms is shown at low frequencies like 2kHz, although one can complain that the calibration accuracy of the measuring microphones should be considered as an issue at high frequency and therefore the resolution is limited by the inaccurate calibration also, that can especially affect the GIBF algorithms since the more sensitive processing techniques. Not only the resolution of the source maps are affected by the processing algorithms but also the dynamic range. Clearly the best dynamic range is obtained in case of the GIBF algorithm with the J_1 optimization. Here the removal of the smallest amplitude source and the weights from the optimization procedure resulting to set the background source contribution to almost zero. On the other hand the implementation GIBF algorithms has some user defined parameters greatly influence the outcome of the source identification. These parameters basically the regularization parameter ϵ_{user} and the final number of source candidates N_{final} related to the iteration number. (The β parameter is also user dependent but it has not dramatic effect if it is in the range of 0.1). The determination of these user defined parameters in the present case is somewhat arbitrary, only the evolution of the J_1 cost function and the norm of the normalised solution residue $|\mathbf{w}_i - \mathbf{A}\mathbf{a}_i|/|w_i|$ (where $|\cdot|$ denotes L_1 norm) is used to verify the choice. The parameters used in the preparation of the presented source terms listed in Table 1. The stoping criteria of the algorithms for the presented cases were the minimum of the norm of the residual. The higher ϵ_{user} and the higher number of final grid points are drawbacks of the GIBF algorithm without the additional optimization procedure.

Table 1: Parameters for the GIBF source maps

Algo.	f kHz	ϵ_{user} -	N_{final} -	β -
GIBF No Optim.	2	0.05	3800	0.1
	6	0.08	3500	0.1
	16	0.08	6000	0.1
GIBF	2	0.01	1100	0.1
	6	0.06	1700	0.1
	16	0.06	3800	0.1

The convergence of the GIBF algorithms can be followed in Figure 6. The J_1 cost function is plotted for processing at 2kHz. The evolution of of the curve is very similar for both algorithms with and without optimization. The arrow on the figures shows where the iteration is stopped. It is stopped before the J_1 curve reaches its minimum due to the fact that the normalized constrain norm $|\mathbf{w}_i - \mathbf{A}\mathbf{a}_i|/|w_i|$ already started to increase. (The L-curve can be used also to follow this evolution and use as an assessment of different regularization parameters and stopping criteria.) Continuing further the iteration cycle the constrain norm starts to increase meanwhile J_1 is still decreasing. This behaviour can be changed by changing the regularization parameter and different evolution of the constrain norm and cost function have been observed. Some cases regularization parameter can be chosen in such a way that the minimum of the cost function corresponds to the minimum of the constrain norm, however this is not always the case. In the present implementation of the algorithm the regularization parameter is directly affected by the user defined ϵ_{user} parameter that introduce significant arbitrariness in the algorithm and the results. The user can preform a parameter study by different object functions e.g. maximize the iteration number to reduce the size of the source zone or decrease the regularization parameter value to increase the resolution of the inversion process or try

to align the minimum of J_1 with the minimum of the constrain norm etc.. Creating an objective procedure to asses the regularization parameter of the GIBF algorithm is one of the most important research topic concerning the algorithm.

Practically the requirement of the higher regularization parameter is arising when the measurement is performed in a noisy environment, or the reference solution that is defined by transfer matrix $\mathbf{A}$ is not appropriate for the measured case, but at the same time the inaccurate calibration of the microphones can be also the reason. The higher regularization means that there is more smoothing introduced to the solution procedure that is suppressing the differences between our reference solution and the obtained cross spectrum matrix. The accuracy of the calibration procedure that was applied on the microphones is decreasing with increasing the frequency (free field calibration was applied on a bunch of microphones in the VKI semi anechoic room see [8]) that is a possible reason of the requirement of higher regularization value at higher frequencies.

Concerning the GIBF algorithm results the reason of the strong removal of the background sources can be looked with the help of Eqn. 12. The linear combination of the current and the previous iteration step solution is done by padding with zeros the current iteration step source candidate vector $\mathbf{a}_i'$ in order to have the same length as the previous iteration step source candidate vector $\mathbf{a}_i^n$. This means that during the optimization procedure the if the non-zero values of $\mathbf{a}_i'$ and $\mathbf{a}_i^n$ is similar then giving more weight on $\mathbf{a}_i'$ can leads to smaller $|\mathbf{a}_i^{n+1}|$ therefore the padded zeros can dominate the next iteration step source vector leading to strong removal of the smallest source amplitudes in the scanning zone. This is imposing that the source candidate reduction parameter β should not be increased much, and it's effect should be assessed. This behaviour is identified but not investigated in the present study but it should be addressed in the further development process of the algorithm and verification of this effect on the convergence of the cost function J_1 should be done.

4. Conclusion

Aeroacoustic noise sources on an airfoil geometry paced in a jet stream have been localised with different beamforming techniques. The conventional Least Squares bemaforming technique was used as a reference and two different implementation of the Generalized Inverse Beamformer are applied that are the part of the current development of beamforming in the VKI. The comparison of the methods showed that both implementation of the Generalised Inverse beamformer show significantly better resolution at low frequencies than the Least Squares technique. At high frequency the differences are smaller. The evolution of the cost function and constrain residue norm of the Generalised Inverse algorithms are investigated and the simplified implementation of the Generalised Inverse beamformer (without an optimization procedure) found to have higher cost function value and it is able to reach lower number of grid reduction steps. The user dependent choice of the regularization parameter and iteration stopping criteria found to be one of the most acute problem of the Generalized Inverse algorithms. The Generalised Inverse algorithm with the optimization method to reduce the defined cost function shows strong background source removal capabilities, however it is found that the zero padding of the source vector used in the optimization procedure cause this effect and therefore artificially introduce the decrease of the cost function. This question should be addressed also in the further studies. The founding of the paper helps to understand the principles of the Generalised Inverse beamforming and emphasize the problem of the rather heuristic and user dependent approaches in the implementation of the cost function minimization procedure. These can be used as basis of further studies and improvements in the algorithm. These questions should be clarified before the technique will be able to used in a non anechoic high background noise environments such as open jet aerodynamic wind tunnels

Acknowledgments

This project is the part of ongoing research project called VALIANT coordinated by the VKI.

References

[1] R. P. Dougherty, Noise source imaging by beamforming, in: Society of Automotive Engineers Brazil Noise and Vibration. Conference, Florianopolis SC, 2008.

[2] L. Koop, Beamforming methods in microphone array measurements theory, practice and limitations, in: M. L. Riethmuller, M. R. Lema (Eds.), Experimental Aeroacoustics, von Karman Institute, 2007.

[3] T. Suzuki, Generalized inverse beam-forming algorithm resolving coherent/incoherent, distributed and multipole sources, in: 14th AIAA/CEAS Aeroacoustics Conference (29th AIAA Aeroacoustics Conference), Vancouver, British Columbia Canada, 2008.

[4] T. Suzuki, Identification of multipole noise sources in low mach number jets near the peak frequency, Journal of Acoustical Society of America 119 (6) (2006) 3649–3659.
[5] T. Suzuki, T. Colonius, Instability waves in a subsonic round jet detected using a near-field phased microphone array, Journal of Fluid Mechanics 565 (2006) 197–226.
[6] H. Cox, R. M. Zeskind, M. M. Owen, Robust adaptive beamforming, IEEE Transactions on Acoustics, Speech and Signal Processing ASSP-35, (10) (1987) 1365–1376.
[7] P. A. G. Zavala, W. D. Roeck, K. Janssens, J. R. F. Arruda, P. Sas, W. Desmet, Generalized inverse beamforming with optimized regularization strategy, Mechanical Systems and Signal Processing 25 (Issue) (2011) 928–939. doi:10.1016.
[8] P. Tóth, Beamforming development for open-jet wind tunnel configuration, Pr, Von Karman Institute (2010).

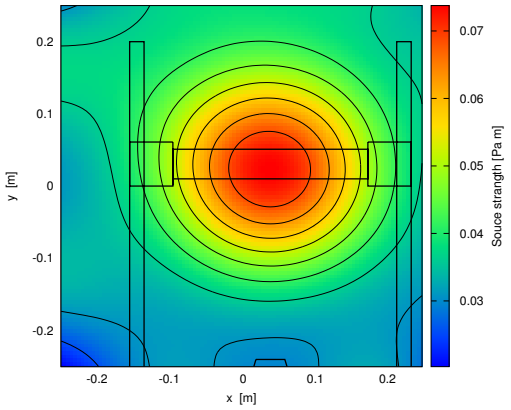

(a) LS

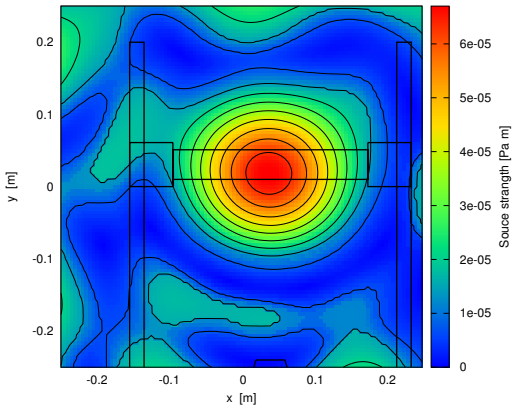

(b) GIBF No Optim.

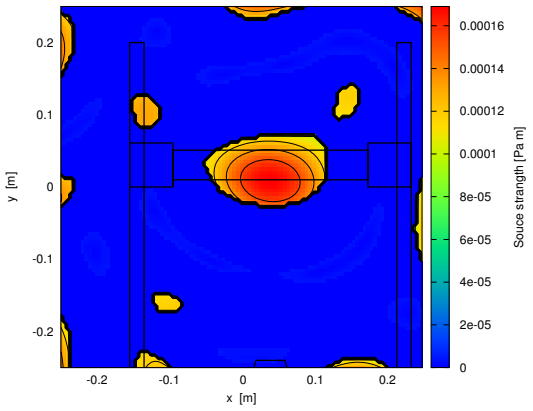

(c) GIBF

Figure 2: Sourcemaps with different algorithms at 2kHz

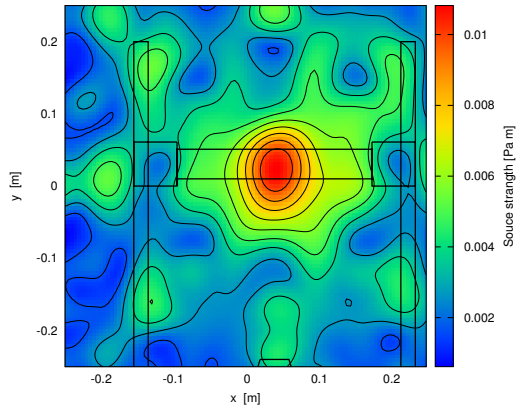

(a) LS

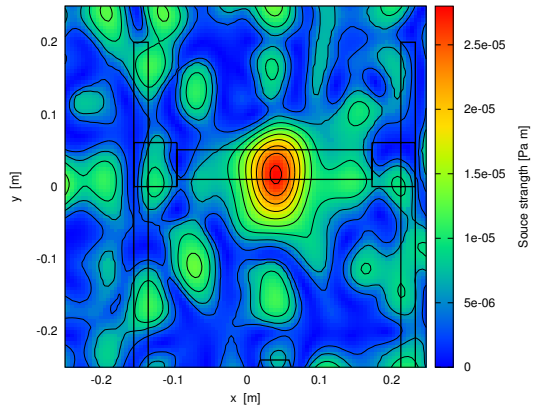

(b) GIBF No Optim.

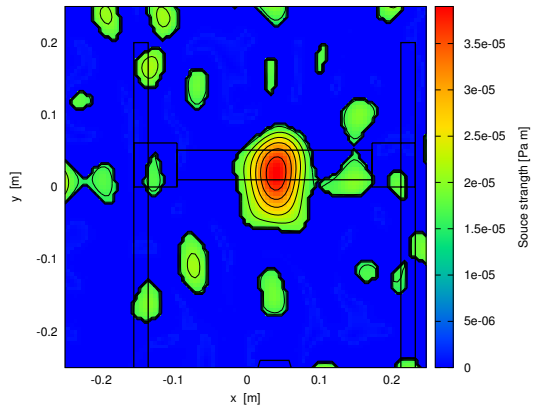

(c) GIBF

Figure 3: Sourcemaps with different algorithms at 6kHz

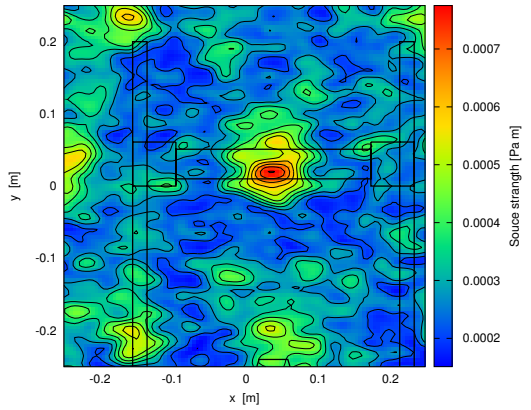

(a) LS

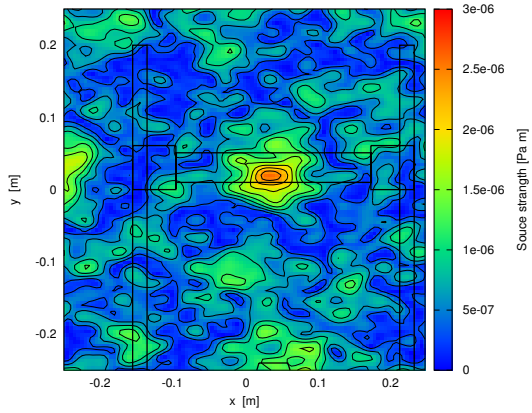

(b) GIBF No Optim.

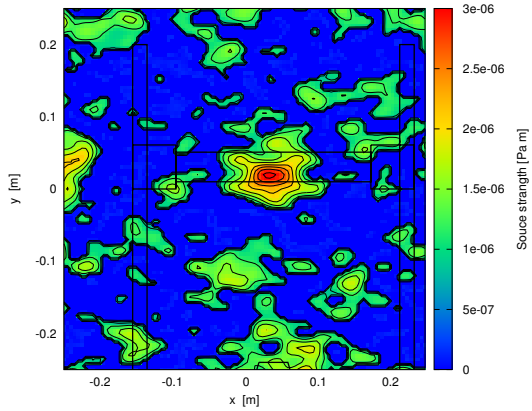

(c) GIBF

Figure 4: Sourcemaps with different algorithms at 16kHz

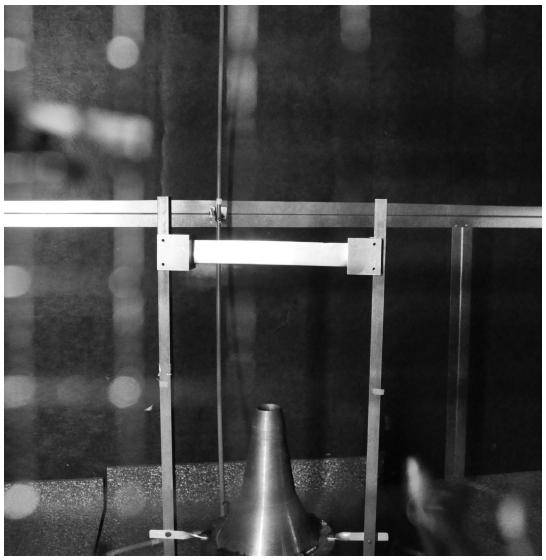

Figure 5: The jet airfoil setup in front of the microphone array

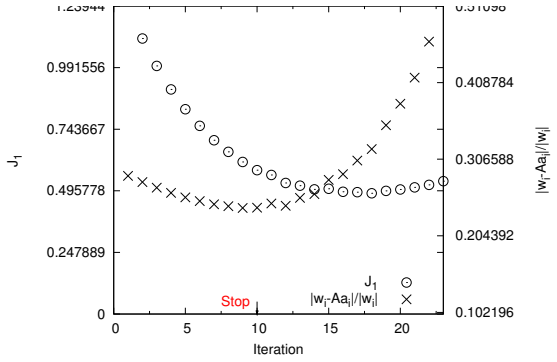

(a) GIBF No Optim.

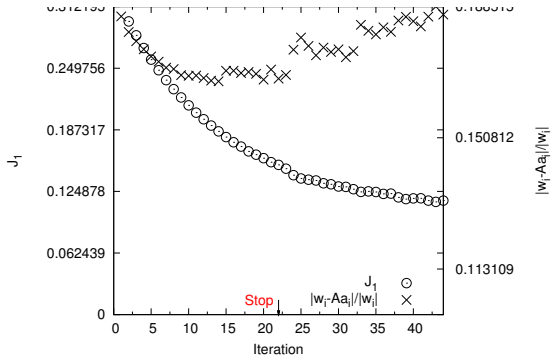

(b) GIBF

Figure 6: J_1 cost function evolution at 2kHz

Numerical prediction of noise production and propagation

Lilla Koloszár

Environmental and Applied Fluid Dynamics Department, koloszar@vki.ac.be

Supervisors: Patrick Rambaud and Jérôme Anthoine

Assistant Professor, Environmental and Applied Fluid Dynamics Department, von Karman Institute for Fluid Dynamics, Belgium, rambaud@vki.ac.be,

Visiting Professor, Environmental and Applied Fluid Dynamics Department, von Karman Institute for Fluid Dynamics, Belgium, anthoine@onera.fr.

Promotor: Herman Deconinck

Professor, Faculté des sciences appliquées, ULB, deconinck@vki.ac.be

Keywords: aeroacoustics, numerical simulation, airfoil, RDS

1. Introduction

The thesis deals with numerical simulation of sound generation and propagation by turbulent flows. Numerical simulation of noise production and propagation is a very complex problem. A methodology fitting for one particular problem can fail for an other one. So there are no general guideline how to deal with such phenomena. In the present work, a Controlled Diffusion (CD-) airfoil placed in the potential core of a jet is considered. Noise is generated mainly by the fluctuating body forces on the profile and it is scattered by the solid walls, as well as, by the shear layers of the jet. The flow velocity is low and it can be assumed that there are no coupling between acoustic and hydrodynamic. Therefore, in the source region an incompressible LES simulation is adequate. Moreover, due to the low Mach-number, the acoustic propagation can be considered as linear, so a hybrid approach can be an efficient way of dealing with this problem. In the propagation field there is a rather significant region, where the mean flow is not uniform, but the sound production is neglegible compared to the noise emitted by the airfoil. In this nearfield a linear set of propagation equation may be considered (LEE). Finally, the noise in the uniform flow can be propagated further by an integral method (if required).

For the noise simulation produced by a CD airfoil in a jet flow the following 3-step approach seems to be the most adequate:

1. Incompressible LES simulation in the source region.
2. Linearized Euler Equations to propagate the noise through the shear-flow.
3. Acoustic analogy in the farfield, if necessary.

This thesis deals with the second item of this system (LEE), including interfacing with the other two steps. The discretization of the LEE is done through Residual Distribution Method (RDM). Since this method was not applied before for acoustic problem, an extensive theoretical study was performed to discover its properties if wave propagation phenomenon is considered. The implementation is than verified with different analytical testcases both in 2D and 3D. Through the verification an important issue was discovered. The basic non-reflecting boundary conditions in the literature was giving rather significant reflections if vortical structures were passing the boundaries. A special focus was given to these problem and new boundary formulation was proposed. In the verification process the source of waves were was always analytical expressions. In order to be able to handle aerodynamically generated noise problems a reconstruction method was implemented. Such way LES/DNS simulations resolving noise production can be directly used as sources for the propagation simulation. The developed hybrid method was finally applied to compute the wave propagation pattern of the noise emitted by a Controlled-Diffusion CD-airfoil through shear

flow due to the windtunnel.

2. Residual Distribution Method

The Residual Distribution or Fluctuation Splitting Method is may be classified between the Finite Element and Finite Volume approach. The idea was introduced in 1982 by P.L. Roe [1] and extended in 1986 [2] for the solution of conservation laws on unstructured meshes. In the last decades several multidimensional upwind schemes have been developed [3; 4] and proved to be accurate and robust. A new strategy in the computation of the residuals have been designed involving contour integrations and leading to conservative discretization even for problems where it is not possible to linearize the system of equations [5]. Higher order discretization techniques has been worked out as well over non-linear elements and their superior behaviour is accessed by Villedieu [6].

Several methods has been developed to solve unsteady problems [7; 8; 9; 10] . This work focuses on two of them, representing the two major types of time discretization in RDS. The first one was developed by Mezine *et al.* [7] and uses a finite element-like approach with a mass matrix. The second method considers the time as an additional space-like dimension yielding space-time elements and was first presented by Ricchiuto *et al.*[11] .

As already mentioned in the Introduction, there are special requirements against the numerical discretization technique if acoustic wave propagation is considered. Residual Distribution Method can fulfill several of these requirements. The finite element character of the method gives the possibility to use it on unstructured grids allowing computation around complex geometries. Its high accuracy helps to resolve the problem coming from the scale separation between the mean flow quantities and the acoustic perturbations. Since multidimensional upwinding introduces less dissipation the computation over long distances are possible without loosing the sound signal due to numerical dissipation. Moreover, because it is based on the compact stencil of the nearest neighbours, it is relatively easy to implement in a parallel environment. The aim of the present work is to show that, thanks to the properties mentioned above, RDS can be an alternative to Discontinuous Galerkin and Finite Difference Method for wave propagation problems.

3. Wave propagation analysis

Aerodynamically generated noise, and noise in general, is a decomposition of different sound wave modes. Thus, any numerical method used to compute noise generation and/or propagation must be able to represent these modes and their behaviour properly. An important constrain for the numerics is that the numerical dissipation and dispersion error must be as small as possible for all the relevant frequencies. Therefore, it is necessary to perform a wavelength based numerical analysis in order to identify the limits of the chosen discretization. Since Residual Distribution Method has been never used before for acoustic problems, it is neccessary to explore its abilities if such phenomena are considered. Propagating waves with broadband frequency range is very difficult computationally. The performed Fourier-analysis gives insight to the behaviour of the RD discretization technique solving wave propagation.

Residual Distribution Method is a bit different from Finite Difference or Finite Element Methods where this type of wavenumber analysis already ellaborated. Therefore, first the RD discretization on one spatial dimension was considered to validate the derivation procedure. It was shown that the LDA scheme is reducing to first order upwind scheme (as expected). The methodology established through the analysis of the space operator was applied for 1D full discretizations, as well as, for 2D problems.

The one dimensional full (space+time) analysis showed that there is a general difference between the mass-matrix type time discretization and the space-time method. The mass-matrix discretization more follows the trends observed in other methods, like Finite Difference or Discontinuous Galerkin Method. As the Courant number is decreasing, its perfomance increasing gradually, resulting in less and less dissipation and dispersion error. On the other hand, reducing the Courant number (i.e. decreasing the time step Δt) without limit is practicly not applicable due to the increasing computational cost.

In case of space-time discretization there is a optimum Courant number ($\nu \approx 0.6$) where the least number of points are needed to resolve a given wavelength. The space-time LDA scheme is very close to the optimized 4th order Dispersion-Relation-Preserving (DRP) Finite Difference Scheme [12]. In general, the analysis gave that the system discretized by space-time method requires less nodes per wavelength than the one connected to mass-matrix time integration. This observation was numerically confirmed by sim-

ulating a sinusoidal acoustic wave propagating in a straight channel. The theoretical values obtained through the 1D analysis were recovered.

The optimal Courant number is found empirically between $5.5 \div 6$. It is the same for 1D and 2D problems and seems not depend on the grid topology. By now, the author has no explanation why ν_{opt} takes this value.

A 2D space, and after a 2D space-time analysis was performed as well. The separate 2D space analysis showed that the dissipation is indeed reducing due to the upwinding along the streamlines. Numerical test was performed to test the isotropy of the different time discretization methods. The propagation of entropy pulse (scalar transport in practice) reveals that the mass-matrix method is less capable to preserve the original shape of the pulse (independently from the mesh topology) while the space-time method introduces more dispersion in the propagation direction.

4. The Linearized Euler Solver

The implementation of the Linearized Euler Equations via Residual Distribution Method has some adventages. First of all, the solver is unstructured. With multidimensional upwinding the code is stabilized by the inbuilt numerical dissipation, but the accuracy of the solution can be kept high due to the low dispersion error of the space-time method. In practice this means, that no additional filtering is neccesary, unlike for high order schemes, and despite the low order of the applied scheme $8 \div 10$ nodes are enough to resolve a given wavelength. However, selective artificial damping is developed for unstructured grids based on the work of Tam and Shu [12] in order to be able to handle numerically noisy source-terms.

5. Boundary Conditions

One of the major difficulty of simulation noise is the imposition of stable and accurate boundary conditions. The characteristic type BCs of Thompson [13] found to work well if acoustic perturbations are considered. However, if vortical structures try to leave the domain strong artificial acoustic reflection was observed. In the literature it is suggested to treat this problem with adding extra layers of cells (buffer zone) between the boundary and the domain where the variables forced to gradually converge to an average state. Indeed, this way is very effective, but depending on the problem in hand it requires a lot of additional cells, i.e. computational resources.

The objective of the work on the boundary conditions was to develop a method which reduces the neccesary size of the buffer zone with a better fitting BC. In order to achive this the characteristic equations was reorganized. With a proper choice of variables it was possible to identify the source terms generating the acoustic disturbances while vorticity waves are leaving the domain. The new boundary condition reduces the overall reflection to less than 1%, so no buffer zone is neccesary.

The verification of the LEE solver was done with several initial condition problems (2D and 3D), as well as, by acoustic source problems. The three main acoustic sources were simulated in order to see if the present implementation can deal with the multipolar nature of general acoustic problems. Acoustic reflection and scattering problems was considered as well. The implementation served with accurate and stable solutions for all simulated cases.

6. Source reconstruction

In practical aeroacoustical problems the unsteady flow is generating the sources. So the information obtained by DNS/LES has to be provided for the LEE solver in order to be able to propagate it. Different approaches exist to pass these physical sources to the LEE solver. One approach follows the principle of injection, meaning that the instantaneous solution at a certain time periode and location is provided to the LEE by means of boundary conditions and transported through the acoustic domain. Usually, the location where this time-varying boundary condition is defined is the boundary between the source region and the propagation region. However, this method can be used only in case of compressible source simulations where the acoustic waves are directly resolved. Another approach is the reconstruction of the acoustic source terms on the right-hand side of the LEE system of equations from the DNS/LES simulation. This approach can be used both for incompressible and compressible simulations. The drawback of the source reconstruction, however, is that the reconstructed source terms have to be stored for every time-step in all gridpoints of the source region.

As an appropriate test case, a system of two corotating vortices was selected. The source simulations were performed by Finite Volume Method on collocated grid. The usage of central schemes resulted in a solution contaminated by high frequency numerical oscillations due to odd-even coupling. A cure of this problem can be the use of more resolved grid ([14]),

but in a certain moment it was not any more feasible to improve further the results with this technique. The authors decided to rather change the spatial discretization method from 2nd order central to 2nd order upwind scheme. Such way the odd-even oscillation phenomenon is avoided, however more numerical dissipation introduced. In order to keep the accuracy of the source simulation the grid was refined compared to the original central simulation.

Even in this way, in the regions where the cells have high aspect ratio, numerical noise can be observed. The reconstructed sources are computed from the derivative of the variables, therefore they are very sensitive to such numerical waves. To be able to stabilize the LEE simulation artifical selective damping was used.

7. Propagation simulation of noise emitted by a CD airfoil

A two-step noise simulation was performed in the Controlled Diffusion Airfoil of Valeo. The LES simulation was provided by J. Christophe, and the propagation simulation was the interest of the current work. Since the geometry is quasi-2D, it was possible to perform just a 2D propagation simulation based on the 3D source data. The pressure data was corrected as suggested by Ewert[15]. For the Linearized Euler simulation an acoustic grid was design based on two consideration. The minimum cell size on the boundary layer was chosen to resolve the boundary layer and the source region adequately. The maximum cell size was considered to have around $3kHz$ maximum resolution. Two different propagation simulations were performed. One without taking into account the mean shear flow coused by the wind tunnel and an other one with it. The pressure contour plots of the two simulations showed that the presence of the shear flow clusters the sound waves inside the wind tunnel and much weaker waves can propagate through them (around 10% weaker).

Acknowledgments

This research is supported through the Marie Curie Research Training Network Project AETHER (contract no MRTN-CT-2006-035713) and the European FP7 Project VALIANT (contract no AGCP8-GA-2009-233680).

References

[1] P. L. Roe, Fluctuations and signals - a framework for numerical evolution problems, Numerical Methods for Fluid Dynamics.

[2] Lecture Notes in Physics, Springer-Verlag, 1986, Ch. Upwind Methods and Multidimensional Splittings for the Euler Equations.

[3] P. Roe, D. Sidilkover, Optimum positive linear schemes for advection in two and three dimensions, SIAM J. Numer. Anal. 29 (1992) 1542–1568.

[4] D. Sidilkover, P. Roe, Unification of some advection schemes in two dimensions, Technical Report 95-10, ICASE.

[5] M. Ricchiuto, R. Abgrall, H. Deconinck, Application of conservative residual distributive scheme to the solution of the shallow water equations on unstructured meshes., J. Comput. Phys. 222 (2007) 287–331.

[6] E. Villedieu, High order discretization by residual distribution schemes, Ph.D. thesis, Université Libre de Bruxelles (2009).

[7] R. Abgrall, M. Mezine, Construction of second-order accurate monotone and stable residual distribution schemes for unsteady flow problems, J. Of Comp. Physics 188 (2003) 16–55.

[8] A. G. Csík, M.Ricchiuto, H. Deconinck, S. Poedts, Space-time residual distribution schemes for hyperbolic conservation laws, in: 15th AIAA Computational Fluid Dynamics Conference, Anaheim, CA, USA, 2001.

[9] J.Dobeš, M.Ricchiuto, H. Deconinck, Implicit space-time residual distribution method for unsteady laminar viscous flow, Comput. Fluids 34 (2005) 617–640.

[10] P. De Palma, G.Pascazio, G. Rossiello, M. Napolitano, A second-order accurate monotone implicit fluctuation splitting scheme for unsteady problems, J. Comput. Phys. 208(1) (2005) 1–33.

[11] M. Ricchiuto, Construction and analysis of compact residual discretizations for conservation laws on unstructured meshes, Ph.D. thesis, Université Libre de Bruxelles (2005).

[12] C. K. W. Tam, C. W. Shu, Dispersion-relation-preserving finite difference schemes for computational acoustics, J. of Comp. Physics 107.

[13] K. Thompson, Time dependent boundary conditions for hyperbolic systems, J. of Computational Physics 68.

[14] E. de Villiers, The potential of large eddy simulation for the modeling of wall bounded flows, Ph.D. thesis, Imperial Collage of Science, Technology and Medicine (2006).

[15] R. Ewert, Q. Zhang, W. Schröder, J. Delfs, Computation of trailing edge noise of a 3d lifting airfoil in turbulent subsonic flow, AIAA 2003-3114.

Experimental investigation of rotor broadband self noise by means of rotating controlled diffusion blades

Michael Bilka

Environmental and Applied Fluid Dynamics Department, bilka@vki.ac.be

Supervisor: Jérôme Anthoine

Associate Professor, adjunct, Aeronautics and Aerospace Department, von Karman Institute for Fluid Dynamics, Belgium, jerome.anthoine@onera.fr

Promotor: Patrick Guillaume

Professor, Mechanical Engineering, Vrije Universiteit Brussel, patrick.guillaume@vub.ac.be

Abstract

Broadband self noise for low speed axial fans has been shown to be a significant noise source for automotive cooling fans. The has led to many studies mostly using 2D airfoils or complete fan mock-ups. This thesis proposes to bridge the two extremes by utilizing rotating controlled diffusion blades to study broadband trailing edge noise. This work has resulted in the development of a novel acoustic wind tunnel for low speed fan acoustics. Measurements of the fan noise show that there is a dominant range of trailing edge noise, which compares well with theoretical predictions. Near wake measurements are made with an x-wire probe to glean some flow physics as well as to provide validation data to future numerical predications.

Keywords: Fan aeroacoustics, anechoic wind tunnel, broadband noise

Thesis Summary

Axial flow fans are important in many engineering applications from small ventilation fans to large jet engines. With the reduction of jet noise in aero engines, continued proliferation of wind turbines and the reduction of mechanical component noise surrounding cooling and ventilation fans, the noise produced by axial turbomachines is increasingly important. Sources of noise for axial flow machines can include the interaction of the rotor with upstream or downstream stators, guide vanes or struts, interaction with casing boundary layer or flow inhomogeneities as well as the blades themselves, such as the turbulent boundary layer convected past the trailing edge. Several reviews on the subject can be found in, for example, [1; 2; 3; 4].

Low-speed fan systems, such as those found in automotive cooling systems - the subject of the present work, face increasingly stringent design requirements in order to increase passenger comfort through the reduction of cabin noise. The aerodynamic noise produced by such systems must be considered in any design in order to meet the requirements. An example of an automotive cooling system is given in Figure 1, showing an exploded view of the full cooling system. Potential sources of sound can be introduced from the flow passing through the heat exchanger introducing some velocity distortion and shed vorticity, inflow distortion due to the shroud, rotor-turbulence interaction and interaction of the rotor wake with the fan support struts. These multiple source types can also have varying acoustic signatures. Potential interaction due to inflow velocity defect or rotor-strut interaction can display a significant tonal component at the blade passing frequency (BPF) and its harmonics. Additionally, there can be sources of noise that are more broadband in nature which are due to the random interaction of turbulence with the rotor blades as in it is ingested by the rotor or boundary layer turbulence convected past the trailing edge of the the blades.

As stated above, broadband sound produced by rotors can be described as the rotor response to turbu-

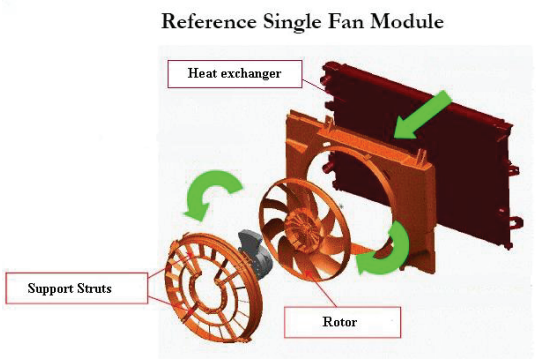

Figure 1: Exploded schematic of full cooling fan and components

lent flow. For ingested turbulence, the random inflow fluctuations create an unsteady lift on the airfoils which can propagate to an observer as sound. This mechanism has been studied previously and models have been proposed to estimate the sound produced by airfoils subjected to a turbulent inflow, for example [5]and [6], as well as for rotors, as in [7] and [8].

The focus of the present work is the rotor self noise, which is the noise that can be produced by a rotor, or airfoil, in the absence of inflow inhomogeneities. These type of noise can include, for example, turbulent boundary layer (TBL) noise, vortex noise due to trailing edge bluntness, separation/stall noise, tip-vortex noise or laminar boundary layer-vortex noise, [9; 10]. TBL noise can be considered the minimum noise that an airfoil can produce (assuming clean inflow) as other self noise mechanisms can be reduced or eliminated by having a sufficiently thin trailing edge (removing noise from trailing edge bluntness), proper incident angle (removing separation/stall noise), shrouded tip (remove tip-vortex) and tripping the boundary layer to turbulent (removing laminar boundary layer). It is this mechanism that has provided the inspiration for the present work. As TBL noise provides, essentially, the noise floor for any airfoil or rotor configuration, it has been the subject of extensive study and modeling effort.

In general, these efforts can be categorized in two ways: stripping away as many of the geometrical complexities as possible in order to study the specific mechanism or using an existing geometry and attempting to estimate the contribution of the specific source or model the complete spectra. The first method has mostly resulted in isolated airfoil studies, especially if the interest is the behavior of a true lifting geometry, for example [11; 12; 13; 14; 15]. The second method attempts to address the true fan

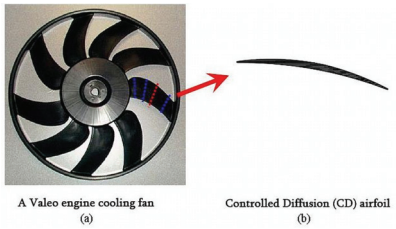

Figure 2: (a) Full Valeo automotive cooling fan (b) Mid-span profile of CD airfoil

geometry and express the contribution of the multiple sources or the complete spectra, for example [16; 17; 18; 19; 20; 21; 22; 23; 24; 25; 26; 27; 28]. However, little has been done to try and bridge these two extremes, at least for lifting airfoils ([29] had made an extensive experimental study of fan trailing edge noise, however the fan consisted of two thin-flat-elliptical-plates rotating in an anechoic room). It is within the context of bridging this gap that Valeo thermal systems, [30], had designed a geometrically simplified fan based on their controlled diffusion airfoil used within their automotive cooling module. It is this geometry that will be employed in the context of this thesis and its use as a fan self noise test case will be assessed.

1. The Rotating Controlled Diffusion Blade (RCDB)

The fan utilized in the present work was first proposed by [30]. The design objective was to create a new geometry that is simplified, i.e. no sweep, change in blade thickness or tip ring, but still maintaining some generality to be a relevant case study in low speed axial fans. The base of the design is a stationary controlled diffusion (CD) airfoil, as previously studied in [31; 32; 14; 15]. The stationary airfoil itself was a midspan cut of a full automotive cooling fan employed by Valeo, [33; 34; 35], shown in Figure 2. Full details of the design process can be found in [30]. A summary of the design criteria is given herein. Since the RCDB was designed to create a rotating analog of the stationary CD airfoil the following criteria were applied:

- Identical chord length and blade shape across the entire radial span
- No sweep or lean
- Matching Reynolds number for relative velocity at midspan

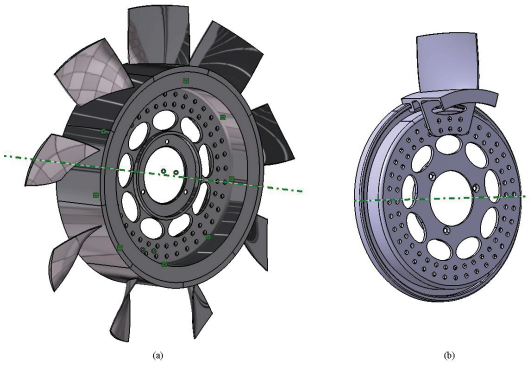

Figure 3: (a) 9 blade RCDB fan, front view (b) RCDB single blade, rear view

- Matching incidence angle at midspan
- Equivalent loading at midspan

The idea was to attempt to make a rotating geometry devoid of many of the complexities that make up a low speed fan and try to make a working geometry that is more representative of the simplifications that are assumed by modeling efforts, i.e. to have a rotating geometry where the broadband self noise contributions would not have to be assumed but would dominate, as in the 2D CD airfoil experiments. Figure 3 illustrates the final design of the RCDB. It was manufactured to be modular, such that the number of blades could be altered in order to match the loading of a the single airfoil experiments, [30]. Additionally, the variation of the solidity allows to avoid sound scattering from adjacent blades which has been a common modeling assumption, [18; 16], although more recently attempts have been made to address this, [36]. [37] argues the consequence of the complexities of investigating real turbomachinery geometries is it does not allow for a systematic approach in isolating individual phenomena and, as a result, such research has of necessity been carried out on significantly simplified configurations. The RCDB represents an attempt to bridge the gap between the relatively simple 2D airfoil aeroacoustic studies, where source mechanisms can be isolated through careful control of boundary conditions, and the full axial cooling fan, binding the studies through the use of the common denominator of the CD airfoil profile. It should be noted, however, that this design had imposed that operating point, at midspan, should be consistent with the conditions of the 2D airfoil. Initial measurements of the midspan wake have been presented in [30] and a large eddy simulation has been conducted by [35].

This lead to the development of a reduced scale version of the RCDB, to fit experimental constraints at the time, at the VKI which had been used in a previous investigation of ducted stator-rotor interaction, [38; 39]. The uniqueness of this geometry and its availability lead to its selection as the test case for the present work, which marks the first experimental aeroacoustic characterization of this simplified, modular fan geometry.

However, the fan size reduction requires a change in the absolute operating parameters that should some of the design constraints listed previously, specifically, the angle of incidence should be respected for any operating point regardless of Reynolds number or loading. A table of the fan blade parameters is given in Table 1. It can be seen that designed fan blade keeps a constant profile shape (also constant chord length) as evidenced by the constant leading and trailing edge metal angles,m_{le} and m_{te} respectively. It also has blade twist, such that it can preform as an axial flow machine, and the stagger angle λ at the hub, mid-span and tip is given. The metal angles are defined by the blade arc as it intersects with the chord line at the leading and trailing edges. The angle of attack, α, defined in the design from the stationary experiments, is given from the metal angle plus the incidence angle, which for this design is -4°. The stagger angle is angle given by the chord line and the axis of rotation and varies along the span. With this information, velocity diagrams can be constructed such that the design point can be respected for the experiments. This is determined by the axial velocity, V_{axial}, the linear blade velocity at mid span, $U_b(r, \omega)$ and the relative inflow velocity, W, which determines the Reynolds number based on the chord, Re_c. The inflow angle, β, can be determined such that the design incidence angle is respected. The operating point considered and the implications of its selcction will be considered in a later section.

2. Low speed fan aeroacoustic wind tunnel

No suitable facility had previously existed at the von Karman Institute for the measurement of fan aeroacoustics. As such, the design of a new facility was undertaken that would be suitable for the measurement of low speed fan acoustics. In addition to being designed around the needs of axial fans, constraints were placed on space and maximum modularity, such that it has utility beyond fan acoustics. This facility was created after reviewing current methods of fan acoustic measurement facilities,

r(mm)	$\lambda(^o)$	$m_{le}(^o)$	$m_{te}(^o)$
0.097	35.1	12	10
0.120	51.4	12	10
0.144	61.5	12	10

Table 1: Stagger and metal angles for RCDB

[28; 26; 27; 23; 24; 40; 41], and it was decided to model the facility after the axial fan research and development facility at MSU, [42]. The novelty of this design lies in the two chamber approach while using an external blower to adjust the mass flow rate allowing for finer control of the operating point, necessary for self noise studies, than standard arrangements that control the operating point through throttling. This is also necessary condition when working with the RCDB since meeting the design point at midspan requires the operation to be a negative pressure rise, which is not a normal condition for fan operation. Additionally, it follows the constraint of maintaining a modular wind tunnel, since the flow is imposed by an external blower non-fan geometries can be investigated as well. This method of operation also assists in reducing contribution from other noise sources or scattering surfaces as it can allow for the design of a setup that can remove the need of a duct and reduce the effect of supports. An overview can be seen in Figure 4.

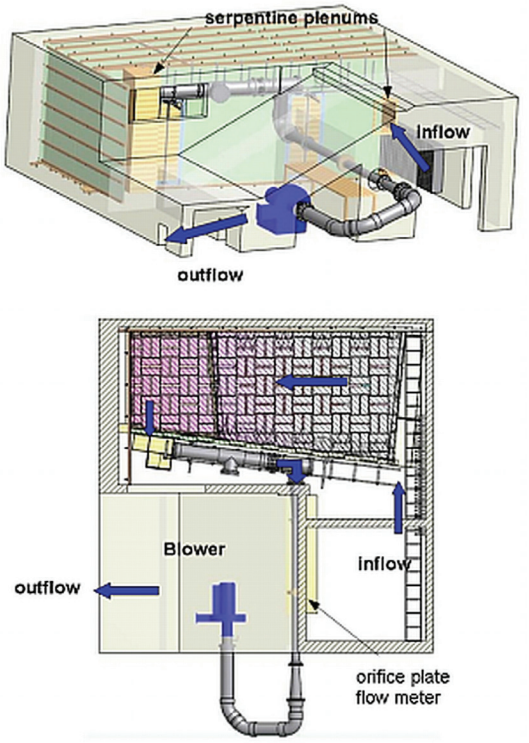

Figure 4: Top: Isometric view of Anechoic Wind Tunnel; Bottom: Top view

3. Measurement and Analysis

Figure 5 illustrates the measurement locations for the microphone measurements. located in the acoustic measurement chamber and the near wake measurements made with an x-wire probe, in the secondary chamber. The sound pressure level power spectral density of an observer upstream of the RCDB is measured and shown in Figure 6. The far field spectra is compared to a trailing edge noise model of Amiet [16] using an empirical model for the trailing edge surface spectra based on boundary layer integral parameters for low Reynolds number flat plates [43]. It can be seen that the model matches well with experiments within the frequency range where the trailing edge noise would be expected to dominate, considering the 2D CD airfoil data found in the literature. The small peaks in the low frequency range are likely due to the interaction of the blades with the tip vortex of the adjacent blade. The additional high frequency information, above that of the trailing edge noise, is considered to be due to high frequency broadband noise

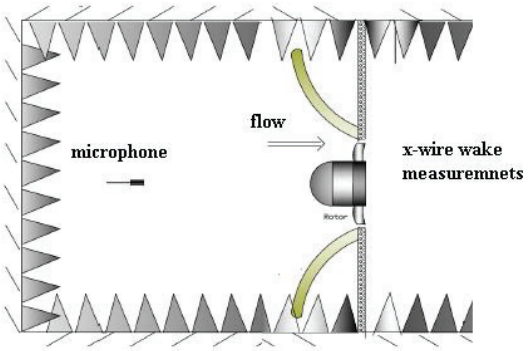

Figure 5: Fan measurement schematic

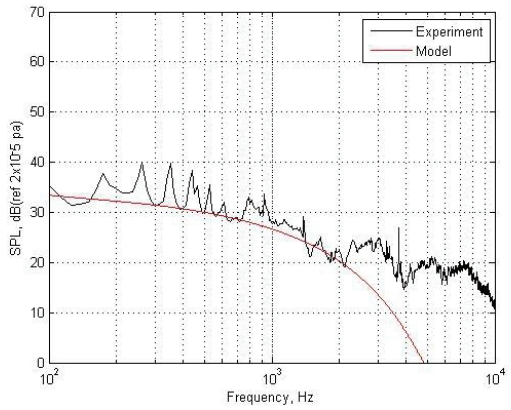

Figure 6: Comparison of 3 blade RCDB measurement with theoretical model

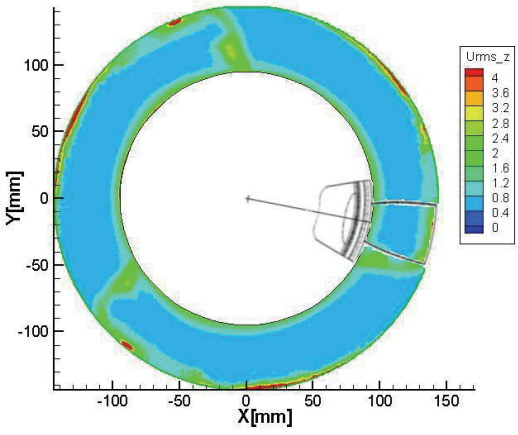

Figure 7: Axial velocity rms for near wake of 3 blade RCDB

produced by tip leakage flow or through interaction with the convergent boundary layer. Comparison has been made for the various operating conditions and final work is under way to verify the source mechanisms of the additional noise sources present in the spectrum Utilizing x-probe hot-wires, measurements are made downstream of the RCDB near the trailing edge to gain some information on the flow development and its potential impact on the acoustic field. Figure 7 shows the axial rms velocity for three rotating controlled diffusion blades. By imposing the flow rate to match the velocity triangle at the mid span, it can be seen that there is a narrow wake at that location, however, due to high large inflow angles and secondary flow effects the wake is much thicker hubwards and near the tip the tip-leakage flow (tip-vortex) creates another separated region, as evidenced by the wake thickness. The effect of the rotor pitch (solidity) can be assessed in this way and has been undertaken for the same operating point, according to the mid span flow angles.

4. Conclusions

A novel set of experiments has been undertaken with the view of analyzing a set of Rotating Controlled Diffusion Blades as a possible benchmark for rotating self-noise. This has resulted in the design and construction of a unique facility for the measurement of low-speed fan noise which is shown to perform well for the ISO standards for acoustic measurements as well as maintaining a low turbulent inflow to allow for self noise sources to be dominant. Acoustic measurements are made upstream of the rotor and compared with theoretical models. It can be seen that the trailing edge noise is a dominant noise source of a frequency range that is comparable to the two-dimensional stationary airfoil cases found in the literature. Near wake measurements are made of the RCDB to gain information on the flow properties as well as facilitate comparisons to numerical simulations.

References

[1] M. Roger, 5 lectures on the noise from rotating machines, in: F. Bruegelmans, J. Anthoine (Eds.), Noise in Turbomachines, von Karman Institute, 2000.

[2] C. Morfey, Rotating blades and aerodynamic sound, Journal of Sound and Vibration 28(3) (1973) 587–617.

[3] B. Mugridge, C. Morfey, Sources of noise in axial flow machines, Journal of the Acoustical Society of America 51(5) (1972) 1411–1426.

[4] S. Wright, The acoustic spectrum of axial flow machines, Journal of Sound and Vibration 45(2) (1976) 165–223.

[5] R. Amiet, Acoustic radiation from an airfoil in a turbulent stream, Journal of Sound and Vibration 41(4) (1975) 407–420.

[6] R. Patterson, R. Amiet, Noise and surface pressure response of an airfoil to incident turbulnece, Journal of Aircraft 14(8) (1977) 729–736.

[7] A. George, Y. Kim, High frequency broadband rotor noise, AIAA journal 15 (1977) 538–545.

[8] R. Patterson, R. Amiet, Noise of a model helicopter rotor due to ingestion of turbulence, Tech. rep., NASA CR 3213 (1979).

[9] T. Brooks, D. Pope, M. Marcolini, Airfoil selfnoise and prediction, Tech. rep., NASA RP 1218 (1989).

[10] W. Blake, Mechanics of flow induced sound and vibration, Academic Press, 1986.

[11] T. Brooks, T. Hodgson, Trailing edge noise prediction from measured surface pressures, Journal of Sound and Vibration 78(1) (1981) 69–117.

[12] S. Moreau, M. Roger, Effect of aerodynamic loading in trailing edge noise sources, AIAA journal 43(1) (2005) 41–52.

[13] M. Roger, S. Moreau, Broadband self noise from loaded fan blades, AIAA journal 42(3) (2004) 536–544.

[14] J. Christophe, J. Anthoine, S. Moreau, Trailing edge noise of a controlled diffusion airfoil at moderate and high engle of attack, in: 15th AIAA/CAES aeroacoustics conference, no. AIAA-2009-3196, 2009.

[15] J. Christophe, S. Moreau, C. W. Hamman, J. Witteveen, G. Iaccarino, Uncertainty quantification for the trailing edge noise of a controlled diffusion airfoil, in: Proceedings of the Center for Turbulence Research summer program, 2010.

[16] R. Schlinker, R. Amiet, Helicopter rotor trailing edge noise, Tech. rep., NASA CR3470 (1981).

[17] Y. Kim, A. George, Trailing edge noise from hovering rotors, AIAA journal 20(9) (1982) 1167–1174.

[18] A. George, S.-T. Chou, Broadband rotor noise analyses, Tech. rep., NASA CR 3797 (1984).

[19] S. Moreau, M. Roger, Competing broadband noise meachanisms in low speed fans, AIAA journal 45(1) (2007) 48–57.

[20] S. Wu, S. Su, H. Shah, Modeling of spectra of axial flow fans in the free field, Journal of Sound and Vibration 200 (4) (1997) 379–399.

[21] S. Wu, S. Su, H. Shah, Noise radiation from engine cooling fans, Journal of Sound and Vibration 216 (1998) 107–132.

[22] T. Fukano, Y. Kodama, Y. Senoo, Noise generated by low pressure axial flow fans i: modeling if the turbulent noise, Journal of Sound and Vibration 50(1) (1977) 63–74.

[23] T. Fukano, Y. Kodama, Y. Takamatsu, Noise generated by low pressure axial flow fans ii: effect of number of blades, chord length and camber of blade, Journal of Sound and Vibration 50(1) (1977) 75–88.

[24] T. Fukano, Y. Kodam, Y. Takamatsu, Noise generated by low pressure axial fans iii: effects of rotational frequency, blade thickness and outer blade profile, Journal of Sound and Vibration 56(2) (1978) 261–277.

[25] N. Chandrashekhara, Experimental studies of discrete tone noise from an axial flow fans, Journal of Sound and Vibration 13 (1970) 43–49.

[26] N. Chandrashekhara, Tone radiation from axial flow fans running in turbulent flow, Journal of Sound and Vibration 18 (1971) 533–543.

[27] N. Chandrashekhara, Sound radiation from inflow turbulence in axial flow fans, Journal of Sound and Vibration 19 (1971) 133–146.

[28] A. Cattanei, E. Canepa, G. Milanese, D. Parodi, Further study of the test configuration for axial flow fans noise measurements, in: 16th AIAA/CEAS aeroacoustics conference, no. AIAA-2010-3810, 2010.

[29] Y. Rozenberg, M. Roger, S. Moreau, Rotating blade trailing edge noise: experimental validation of analytical model, AIAA journal 48(5) (2010) 951–962.

[30] D. Neal, Effect of rotation on the wake of a lift generating body, in: M. Bilka, P. Rambaud (Eds.), Effect of Rotation on Turbulence with Applications to Turbomachinery, von Karman Institute, 2010.

[31] S. Moreau, D. Neal, J. Foss, Hot-wire measurements around a cd airfoil in open-jet anechoic wind tunnel, Journal of Fluids Engineering 128 (4) (2006) 699–706, open rotor.

[32] S. Moreau, D. Neal, Y. Khalighi, M. Wang, G. Iaccarino, Validation of unstructured mesh of the trailing edge flow and noise of a controlled diffusion airfoil, in: Studying turbulence using numerical simulation databases -XI: proceedings of the summer program 2006, Center for Turbulence Research, Staford University, 2006.

[33] S. Moreau, M. Henner, J. Brouckaert, D. Neal, Numerical and experimental investigation of rotor-stator interaction in automotive cooling fan systems, in: Proceedings of 2006 ASME International Mechanical Engineering Congress, ASME, 2006.

[34] S. Moreau, D. Neal, M. Henner, 3d rotor stator interaction in an automotive engine cooling fan, in: 6th European Conference on Turbomachinery - Fluid Mechanics and Thermodynamics, Lille, France, 2005.

[35] F. Perot, M. Kim, S. Moreau, M. Henner, D. Neal, Direct aeroacoustics prediction of a low speed fan, in: 16th AIAA/CAES aeroacoustics conference, 2010.

[36] S. Glegg, Airfoil selfnoise generated in a cascade, AIAA journal 36(9) (1998) 1575–1582.

[37] J. P. Johnston, Effect of system rotation on turbulent structure: A review relevent to turbomachinery flow, International Journal of Rotating Machinery 4(2) (1998) 97–112.

[38] M. Bilka, F. Presezniak, J. Sousa, J. Anthoine, Experimental investigation of acoustic and flow phenomena of a simplified subsonic ducted rotor, in: 16th AIAA/CAES aeroacoustics conference, 2010.

[39] M. Bilka, J. Sousa, J. Anthoine, Experimental investigation of stator wake behavior with a variable solidity ducted rotor, project Report, CAPRICORN.

[40] A. Maaloum, S. Kouidri, R.Rey, Aeroacoustic performance evaluation of axial flow fans based on the unsteady pressure field on the blade surface, Applied Acoustics 65 (2004) 367–384.

[41] S. Moreau, D. Neal, J. Foss, M. Henner, Evaluating cfd models of axial fans by comparison with phase averaged experimental data, in: Vehicle Thermal Management Systems Conference, 2001.

[42] S. Morris, J. Foss, J. Pakkala, The automotive cooling fan research and development facility, in: 3rd Vehicle Thermal Management Systems Conference, no. paper 971784, 1997.

[43] D. Moreau, L. Brooks, C. Doolan, Broadband trailing edge noise from a sharp-edged strut, Journal of the acoustical society of america 129(5) (2011) 2820–2829.

FLOW IN TURBINES

Tubine base pressure active control through trailing edge blowing

Bayindir H. Saracoğlu

Turbomachinery and Propulsion Department, saracog@vki.ac.be

Supervisor: Guillermo Paniagua

Associate Professor, Turbomachinery and Propulsion Department, von Karman Institute for Fluid Dynamics, Belgium, gpaniagua@me.com

Promoter: P. George Huang

Professor, Wright State University Mechanical and Materials Engineering, 3640 Colonel Glenn Highway - Dayton, Ohio - 45435, george.huang@wright.edu

Abstract

This paper presents the use of pulsating trailing edge coolant flow to modulate the trailing edge shocks and possible improvements in the profile losses by increasing the base pressure. A scaled model derived from a real cooled high-pressure inlet guide vane has been experimentally investigated at the VKI. Test campaigns have been carried out in the short duration isentropic compression tube facility at engine representative conditions.

Keywords: High pressure turbine, pulsating cooling, trailing edge shocks, base pressure

1. Introduction

Developments of efficient aeronautical propulsion systems with higher thrust, reduced noise and pollutants emissions request a thorough knowledge of complex aerodynamics phenomena. Performance advances in turbine based propulsion systems, largely depend on the ability to control unsteady flows in a passive or active manner. Highly loaded single stage gas turbines, developed to minimize the turbine size, are characterized by transonic or supersonic vane outlet conditions. Yasa et al.[1] quote a drop in 4% efficiency when the vane outlet Mach number is increased from 0.9 to 1.2. Additionally, the large vane exit pressure gradients associated to the vane shocks sweep the rotor front suction side, originating large rotor force fluctuations and highly unsteady heat fluxes. In the fully rotating transonic turbine stage investigated at the VKI, the amplitude of the fluctuations in the blade tangential force is about 70% of the mean level [2]. Additionally, the vane shock impact on the rotor blade boundary layer, results in the intermittent generation of separation bubbles. In supersonic turbines an active control of the vane shocks can be utilized to minimize the unsteady force and boundary layer separation in the rotor, resulting in an amelioration of the mechanical and aero-thermodynamical turbine performance. The shock control system should be able to effectively modify the vane trailing edge shock at the rotor passing frequency (few kHz). Furthermore, the shock intensity is naturally modified by the instantaneous blockage of the rotor. Therefore, the optimal system to adjust the shock requires a deep physical insight into the vane-rotor interaction. Practical solutions could involve the use of MEMS or pulsating jets. In high-pressures compressed cold air is used to internally cool down both vanes and blades. Part of this coolant air is ejected at the trailing edge into the airfoil wake. This continuous coolant blowing cools down the trailing edge region and additionally it is an efficient way of mixing the coolant and main flows. Prust at NASA, carried out an important research program concerning the aerodynamic effects of trailing edge cooling on the overall performance of the airfoil [3]. On transonic airfoils various research groups have performed substantial research [4–6]. However the published work is constrained to a continuous blowing. The current research program would investigate the effect of an unsteady blowing (at several kHz) at the trailing edge of a transonic airfoil. The experimental research is supported a numerical investiga-

tion. Pulsating flows have already been investigated by the authors in low pressure turbines to control separation using synthetic jets. The unsteady investigation of HP turbine stages already allowed recognizing the effect of non uniform boundary conditions and shock reflection in transonic turbine stages ([7; 8]), while the numerical analysis of pulsating cooling at various frequencies and mass-flows still represents an open issue. The beneficial effect of pulsating cooling has already been addressed on a simplified environment, with emphasis on the flow physics[9]. In this paper HybFlow code is used to model the real cascade, supporting the experimental analysis.

2. Experimental apparatus

2.1. Turbine test rig

Fig. 1-a shows the light-piston compression tube facility, which allows the independent control of the Reynolds and Mach number. The air in the cylinder is isentropically pressurized by a light piston, driven by the high-pressure line. When the right level of pressure and temperature (controlled by the initial pressure and temperature prior to compression) is attained, a shutter releases the warm flow into the test section (Fig. 1-b). Afterwards, the flow is vented through a silencer into the atmosphere. The test section consists of two turbine vane passages. The vane airfoils were carefully designed to provide a pressure distribution representative of a conventional transonic high-pressure vane. The central vane is internally cooled, being the coolant fed by a perforated rotating disk [10]. The system allows to switch easily from no-cooling conditions, to continuous blowing, or pulsating cooling at 200 Hz.

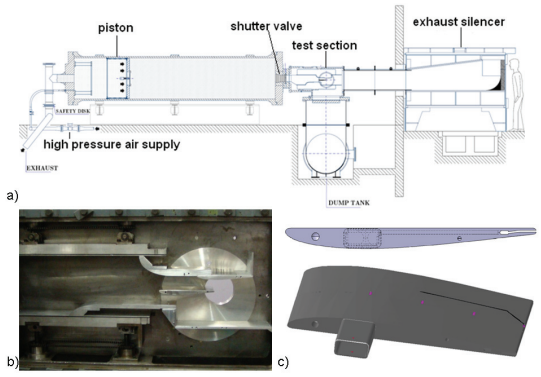

Figure 1: a) Layout of the turbine cascade test rig; b) Photograph of the section layout; c) Cooled central vane airfoil

2.2. Measurement planes and instrumentation

The lateral walls of the test section allow optical access for high-speed Schlieren. The airfoils were designed to allow a visualization of the cooling duct into the base region as displayed in Fig. 2-a. There are three measurement planes. In plane 1, the total pressure and temperature are measured at the cascade inlet. Planes 2 and 3, located downstream of the cascade, at 25% and 50% of the axial chord of the cascade are instrumented exclusively with low-frequency pressure gauges (Scanivalve). The central airfoil is instrumented with pneumatic pressure tappings, monitored by low-frequency sensors (Sensym 140PC) and high-frequency sensors (Kulite XCQ-062). The pressure side of the lower passage and the suction side of the upper passage are instrumented with 13 pressure taps and 14 taps at mid-span respectively, sampled by the Scanivalve. Additionally, the upper suction side is instrumented with thin film sensors (Tao Systems), to monitor the steady and unsteady surface temperature fluctuations generated by the central airfoil trailing edge shocks.

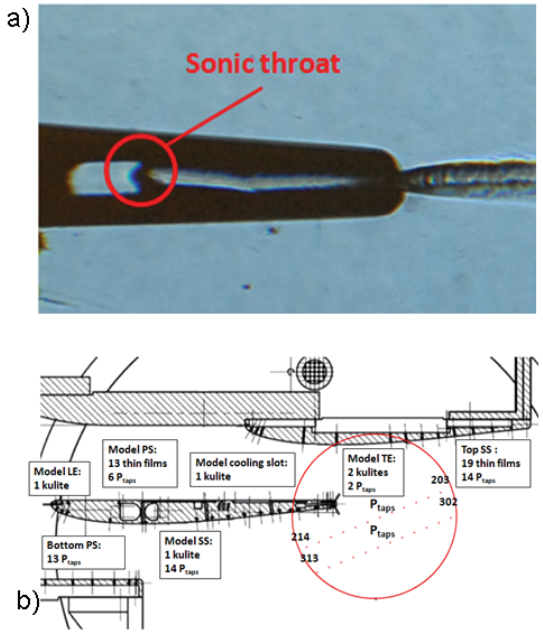

Figure 2: a) Schlieren image of the cooling slot; b) Layout of the measurement planes

3. Numerical resources

The HybFlow CFD code is based on a numerical scheme developed by Adami et al. and Adami et

al. for the compressible Navier-Stokes equations in strong conservative form [11; 12]. The treatment of the turbulent variables refers to the classical eddy-viscosity approach using the two-equation model k-ω proposed by Wilcox [13]. Adopting the perfect gas model and a Favre averaging, the set of governing equations characterizes the flow field through the solution vector Q for the density, the momentum vector, the total energy ρE and the turbulent variables ρk and $\rho\omega$. Concerning the turbulence evaluation, the correction of the production term suggested by Kato and Launder [14] and the physical realizability constraint of Durbin [15] are considered for the turbulence production terms. Furthermore, the low Reynolds variant proposed by Wilcox [13] for computing turbulent transition has been implemented. A residual smoothing routine is also present to improve the stability of the computation. The solver has been developed and validated in the frame of internal compressible/incompressible flow regimes. A brief description of the basic numerical scheme follows while a more detailed discussion can be found in the suggested references. Simulations were performed following two levels of sophistication. In a first attempt the actual cascade geometry was considered. Fig. 3-a displays the cascade grid (around 537,000 elements) and a detail of the blade zone. This grid allows capturing the main flow patterns related to the airfoil shock-end-wall interactions, and recirculating zones. In a second attempt the central airfoil is modeled assuming periodicity, as shown in Fig. 3-b. The latter mesh has around 566,000 elements, with special attention to the base and wake region. The periodic test case has been also studied without the coolant channel using a structured non-conformal mesh of 170,000 elements. The y^+ value is around 1 over all the surfaces of interest.

The inlet boundary conditions comprise the total pressure, total temperature and absolute flow angle at the inlet plane (P_{01} and T_{01} upstream of the valve). At the outlet the static pressure P_{s2} was imposed. All the walls are assumed to be isothermal with imposed wall temperature and no-slip boundary condition. The computational time required to achieve full convergence was around 120 hours. All the calculations are second order accurate in space and time with a second order gradient reconstruction.

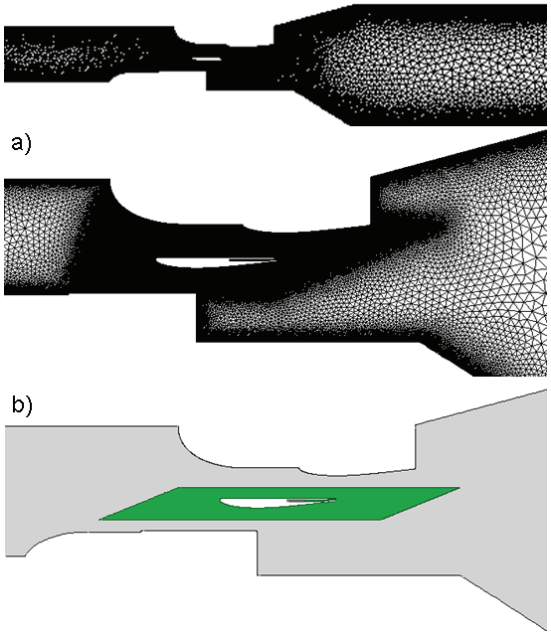

Figure 3: a) Cascade mesh, differences between a coarse and the final used grid; b) Single airfoil grid

4. Results and discussion

4.1. Airfoil Isentropic Mach number distribution

Isentropic Mach number is alternative representation of static pressure distribution around an airfoil. The characteristics of this distribution exhibits important flow patterns in the test section. For instance, the peak on the suction side corresponds to the impingement location of the left running shock of the bottom wall that interacts with the model SS boundary layer. That interaction causes the transition from laminar to turbulent status of the boundary layer indicated by the big drop in the Mach number distribution. The same kind of impinging shock-SS boundary layer interaction is present for a downstream Mach number equal to 1.1, for the two researched Reynolds. The steep inclination of the M_{is} distribution indicates the transition to a turbulent boundary layer. As expected, the location of the shock impingement is shifted upstream with respect to the previous case. This is due to the fact that increasing the Mach number, the trailing edge shocks are characterized by a higher inclination. In fact at "limit load condition" the left running trailing edge shock would be just behind the base region of the next vane.

Numerical results obtained by a steady and unsteady analysis of the periodic blade reproduce the experimental data up to the shock region and on the

pressure side, while the behaviour of the flow is much different. It can be explained by considering the topological differences between the geometries. Looking at the results, it can be underlined that the presence of a continuous blowing changes the flow acceleration on the rear suction side reducing the peak velocity (Fig. 4). The flow behavior before the shock impingement remains completely unchanged. Coming to the pulsating coolant case (Fig. 5) a slight increase in the time averaged peak velocity is visible as well as a stable flow Mach number (1.2) up to the blade trailing edge. The blade model also reproduces well the mean exit Mach number. An open issue on the flow incidence on the blade remains and is under consideration of the authors.

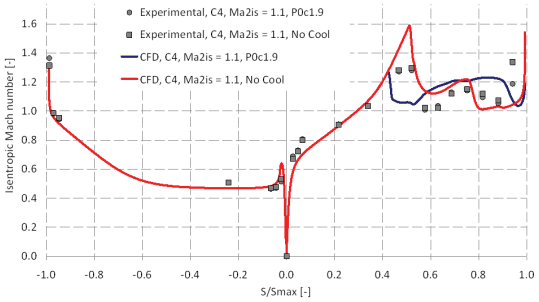

Figure 4: Comparison between experimental and numerical data for $M_{2,is}$=1.1, no cool and P_{0c}=1.9

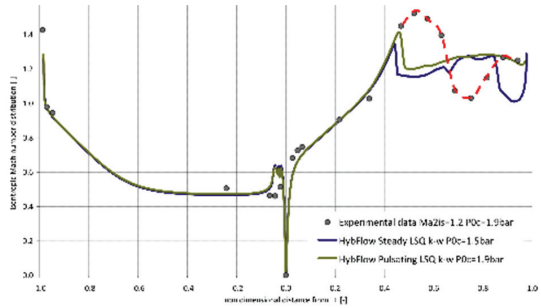

Figure 5: Comparison between experimental and numerical data for $M_{2,is}$=1.2

In conclusion, the comparisons between experimental and numerical data for the exit Mach number 1.1 and the P_{0c} =1.5bar is shown in Fig. 6. Except for the peak value of Mach number, the flow behaviour is well reproduced also in the region behind the shock impingement. The exit Mach number value is also matched, and the 20% error near 0.9 S/S_{max} is under investigation. For the present case, the analysis of the effect of a pulsating coolant is running.

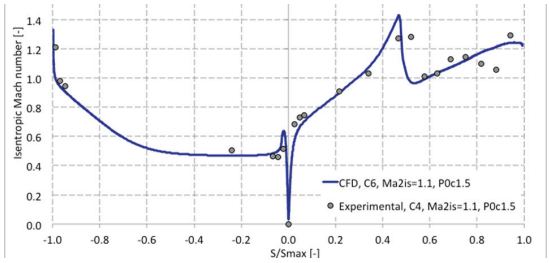

Figure 6: Comparison between experimental and numerical data for $M_{2,is}$=1.2, P_{0c}=1.5

4.2. Time-resolved pressure measurements

Time-resolved analysis of the kulites signals beigins with designating the resonans frequencies of the sensors. The two kulites on both sides of the TE, plus the kulite on the SS, are characterized by a natural resonant frequency of the chip equal to 240 kHz. In order to check such a frequency value directly from the measured signals, some acquisitions have been done at a sampling frequency of 500 kHz with an anti-aliasing filter at 250 kHz. In the FFTs reported in Fig. 7, it is possible to notice resonant frequencies very close to the natural frequency around 240 kHz. The kulite located at the leading edge of the model and the kulite inside the cooling channel have higher pressure range as well as higher natural frequency of their chip (300 kHz). Therefore their resonant frequencies are not observed in these FFTs.

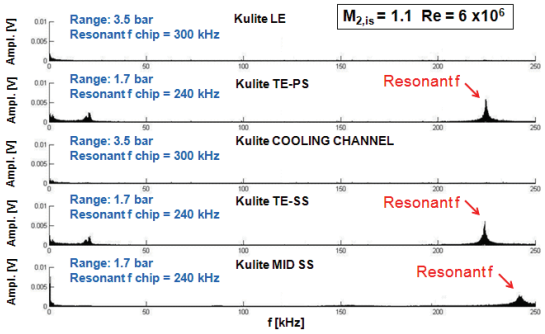

Figure 7: FFT kulite signals without filter & f_{samp}=500 kHz

By restricting the analysis to the bandwidth in which we are expecting the amplitude peaks related with the trailing edge vortex shedding, the obtained results are illustrated in Fig. 8. As an example, only one kulite at the trailing edge has been considered, for no coolant case and for all the five downstream Mach number conditions. As expected, the vortex shedding frequency increases together with the total

inlet temperature. For the test condition $M_{2,is}$=1.1 and Re=6x10^6 the vortex shedding frequency decreases slightly because of the lower total inlet temperature imposed to get a higher Reynolds. For the continuous and pulsating coolant tests, no peaks are visible. This is probably due to the fact that the coolant causes a higher momentum of the flow in the base region, pushing its end downstream together with the origin of the vortex shedding. In such a way the vortex shedding is not detectable any more by the trailing edge kulites. That observation is in agreement with the experimental results obtained by Motabelli and Norbury[16]. They observed the vortex shedding from the blunt trailing edge of a blade model over a range of mainstream Mach numbers from 0.7 to 1.3, with and without bleed air discharged from a slot in the trailing edge.

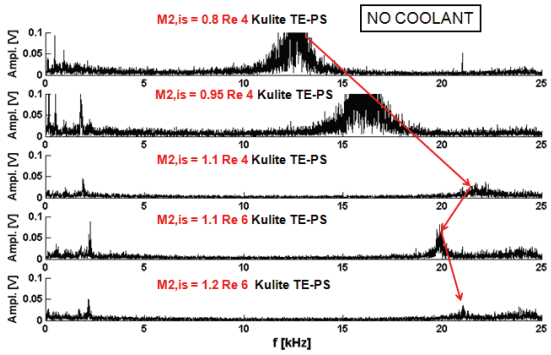

Figure 8: FFT kulite signals with high pass filter (100 Hz) & f_{samp}=300 kHz

Strouhal number values Motallebi and Norbury also computed for the different test conditions are very similar to those resulting from the measurements. The Strouhal numbers computed for the five test conditions in absence of coolant bleed are plotted in Fig. 9 and their values lie in a range between 0.23 and 0.28. In the same plot, it is also shown the base pressure non-dimensionalized by the static pressure downstream of the vane model. It is interesting to notice that the two plots in Fig. 9 are characterized by an almost symmetric shape mainly for transonic and supersonic flow conditions. In particular it has to be noticed that the maximum values of the Strouhal numbers almost correspond to the minimum base pressure values and the opposite behaviour is present for supersonic conditions. Motallebi and Norbury tried to explain such a relation between base pressure and Strouhal number by relating it to the mechanics of the vortex formation and the distance of the region of vortex formation from the trailing edge, both of which depending on the test conditions.

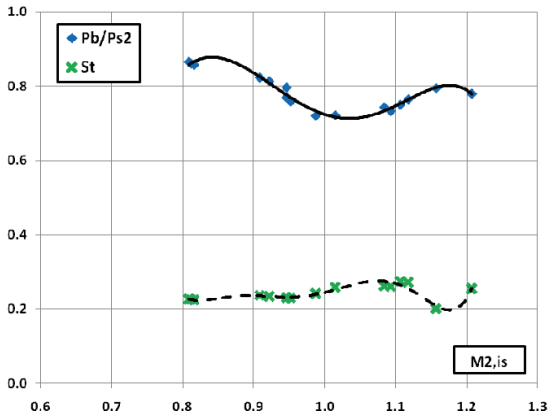

Figure 9: Strouhal numbers and base pressure vs. $M_{2,is}$: NO COOLANT

4.3. Schlieren images

For the purpose of the present analysis the shock intensity and position are key parameters to be checked. Then, the flow behavior in the wake region is evaluated by comparing the density gradient magnitude with the Schlieren visualization. A selected number of results are reported in Fig. 10 and Fig. 11. Numerical results obtained for the test case (in Fig. 10-a, subsonic exit Mach, no cool) and the blade profile (Fig. 11-b-c, exit M = 1.1, two Reynolds numbers, no cool) are compared with the experimental data obtained for the corresponding cases. Flow structures are well reproduced by the CFD analysis. In Fig. 10-a the shock chopped by the shear layer detached from the lower plate is individuated as in the experiments. It must be also pointed out that the shock reflections and the lips shock individuated in the blade simulation (Fig. 11-b-c) reproduce the flow field depicted by the experiments. This result is very important since the use a simplified model for the evaluation of the pulsating flow effects is allowed only when the flow fields correspond.

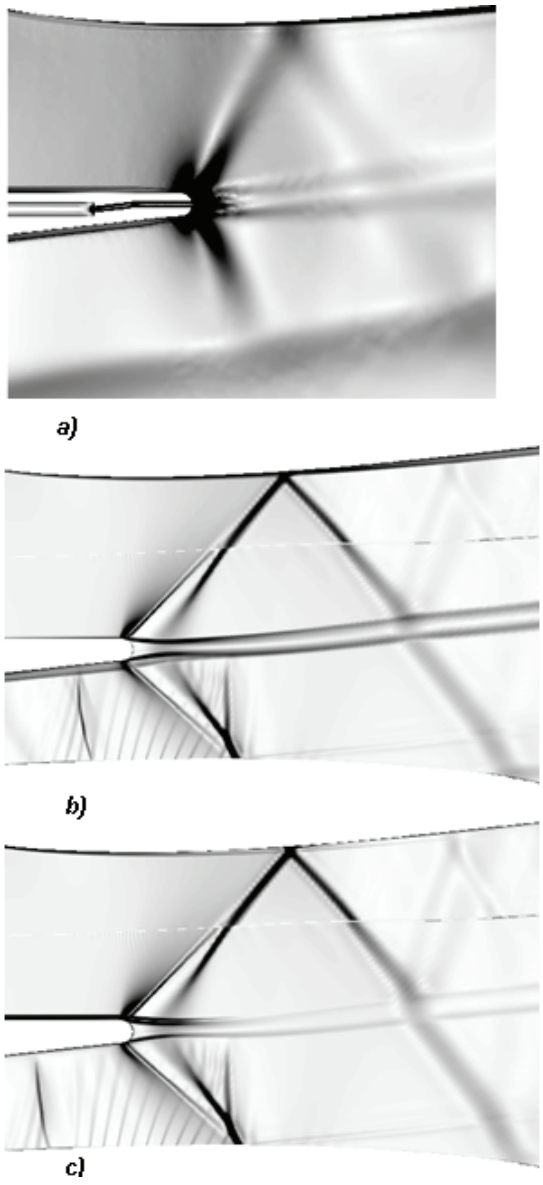

Figure 10: CFD: a) $M_{2,is}$=0.95, P_{0c}=1.5 ; b) $M_{2,is}$ = 1.1 Re=6M no cool; c) $M_{2,is}$ = 1.1 Re=4M no cool

4.4. *Unsteady suction side wall temperature*

The wall temperature on the suction side of the upper passage is monitored by using 11 high frequency response thin film gauges located at the mid-span. The Nusselt number distribution along the wall gives information about the state of the boundary layer, in particular the location of the laminar to turbulent boundary layer transition. The magnitude root mean square (RMS) of the unsteady temperature signal, on the other hand, is an indicator of the shock intensity level

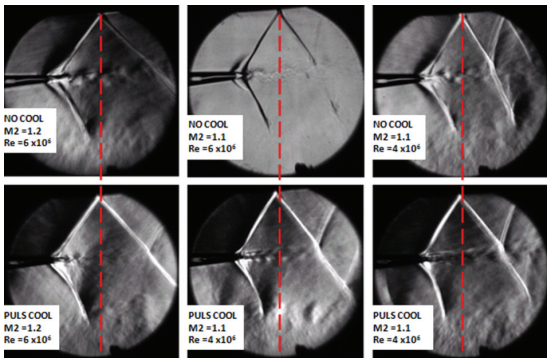

Figure 11: Instantaneous Schilieren pictures for supersonic conditions at two different Reynolds numbers

at the impingement region. Fig. 12 shows the RMS of the unsteady temperature values related to the experiments at 1.1 Mach number and Reynolds number of $4x10^6$. The high RMS values at the rear suction side gauge experienced by using the continuous coolant has decreased for the pulsation coolant ejection. This indicates that utilizing unsteady cooling decreases the intensity of the left running trailing edge shock.

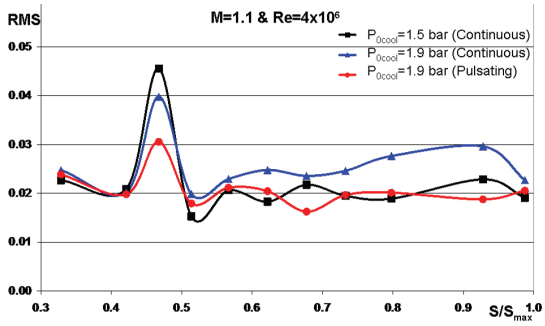

Figure 12: The RMS of unsteady temperature on the suction side of the upper passage for various cooling cases

4.5. *Base pressure*

The analysis of base pressure is restricted on the model trailing edge and in particular on the comparison between the data obtained during from the experiments and the base pressure correlation after Sieverding [17]. For that purpose it has needed to use the static pressure signals delivered by the pneumatic taps located on both sides of the trailing edge with respect to the coolant slot. The plot in Fig. 13 shows the comparison of base pressures among all the coolant cases with the Sieverding's base pressure correlation. The continuous black line represents the absence of coolant while the dashed lines the presence of coolant

at the trailing edge. It is clearly visible how, in agreement with Sieverding and other authors, it is verified that it is possible to obtain a higher base pressure by introducing a continuous coolant flow at the trailing edge. Another important result is that with a pulsating trailing edge coolant (purple dashed line with little segments) it is still feasible to increase the base pressure, with respect to the no bleed case, and even of the same amount it is done with continuous trailing edge coolant jet.

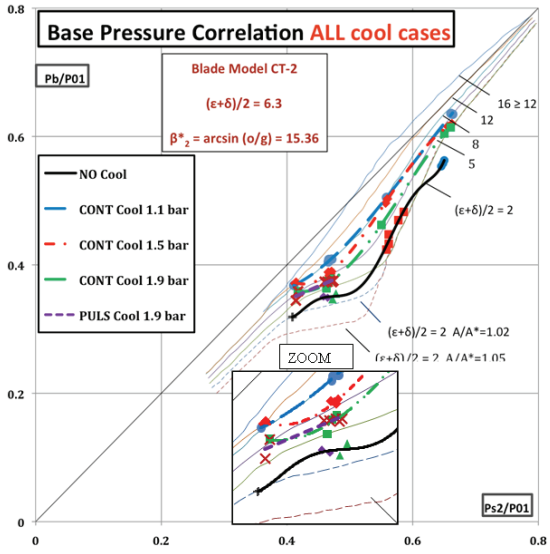

Figure 13: Comparison with Base Pressure Correlation after Sieverding in the case of pulsating coolant

5. Conclusion

The effects of pulsating trailing edge cooling on trailing edge shocks and base pressure is being investigated experimentally and numerically. For this purpose an extensive experimental campaign on a linear cascade test section is realized on a short - duration facility. The test are performed at engine representative Mach (0.8-1.2) and Reynolds (4-6×10^6) numbers. Simultaneously, a series of numerical simulations have been performed by using HybFlow finite volume solver. The results have been compared in order to understand the flow physics behind the phenomena.

Time-averaged and time-resolved pressure measurements are performed on the model, flow passages and the lateral windows of the test section. The isentropic Mach number distributions around the model are calculated for different downstream Mach numbers and cooling conditions. The regions of sudden drop in Mach number help to demonstrate the shock impingement locations. The results are compared with the numerical simulations. A good agreement is attained. Time-averaged base pressure data obtained from the pneumatic pressure taps located on each side of the trailing edge is plotted over the Sieverding's base pressure correlation. The experimental data showed good agreement with the corresponding data of Sieverding. A slight increase in the base pressure observed for the pulsation coolant blowing as compared to the continuous blowing at the same cooling pressures. This indicates that lower base pressure losses can be reached by using pulsating blowing at the trailing edge. Time-resolved pressure measurements is performed by high response pressure sensors located around the airfoil and the trailing edge. The data coming from the trailing edge sensors are further post processed the calculate the vortex shedding frequencies and eventually Strouhal numbers for different downstream Mach numbers.

The Schlieren flow visualizations of the downstream flow field have been performed both numerically and experimentally. The experimental data is being post processed in order to measure the unsteady changes in trailing edge shock properties, shock impingement locations on the suction side of the upper flow passage and possibly identify the vortex shedding frequencies from the Schlieren images.

The unsteady heat transfer measurements have been performed on the suction side of the upper flow passage. The data is post processed to understand the effect of the cooling on shock strength by looking at the RMS values of the signal. The results showed that the pulsating cooling reduces the shock strength on the impingement location as compared to the continuous coolant blowing cases.

Acknowledgments

The author would like to acknowledge the financial support of U.S. Air Force under the frame of the Project AFOSR FA 8655-08-1-3033.

References

[1] T. Yasa, G. Paniagua, A. Bussolin, Performance analysis of a transonic high pressure turbine, Journal of Power and Energy. Part A. 221 (6) (2007) 769–778.

[2] G. Paniagua, R. Denos, and S. Almeida, Effect of the Hub Endwall Cavity Flow on the Flow-Field of a Transonic High-Pressure Turbine, Journal of Turbomachinery 126 (4) (October 2004) 578–586.
[3] H. W. Prust, Cold flow study of the effect of turbine stator blade aerodynamic performance of coolant ejection from various trailing edge slot geometries, Technical report TM-X-3190, NASA (1975).
[4] C. H. Sieverding, The Influence of Trailing Edge Ejection on the Base Pressure in Transonic Turbine Cascades, Journal of Engineering Power 105 (July 1983) 215–222.
[5] C. Kapteijn, J. Amecke, V. Michelassi, Aerodynamic Performance of a Transonic Turbine Guide Vane with Trailing Edge Coolant Ejection: Part I Experimental Approach, Journal of Turbomachinery 118 (April 1996) 519–528.
[6] C.H. Sieverding, T. Arts, R. Denos, F. Martelli, Investigation of the flowfield downstream of a turbine trailing edge cooled nozzle guide vane, Journal of Turbomachinery 118 (April 1996) 291–300.
[7] S. Salvadori, F. Montomoli, F. Martelli, K.S. Chana, I. Qureshi, T. Povey, Analysis on the Effect of a Non-uniform Inlet Profile on Heat Transfer and Fluid Flow in Turbine Stages, no. GT2010-23526, Proc. of the ASME Turbo Expo, Glasgow, UK, 2010.
[8] A. de la Loma, G. Paniagua, D. Verrastro, Transonic turbine stage heat transfer investigation in presence of strong shocks, no. GT2007-27101, Proceedings of the ASME-IGTI Conference, Montreal, Canada, 2007.
[9] C. Bernardini, S. Salvadori, F. Martelli, G. Paniagua, B. Saracoglu, Time-Resolved Analysis of the Base Region in Cooled Transonic Turbine Airfoils, no. V European Conference on Computational Fluid Dynamics ECCOMAS CFD, Lizbon, Portugal, 2010.
[10] M. Gonzalez, G. Paniagua, B. H. Saracoglu, A. O. Tiseira, Pulsating Cooling System for High Pressure Turbine Blades, no. AIAA-2010-4587, 5th Flow Control Conference, Chicago, IL, 2010.
[11] P. Adami, V. Michelassi, F. Martelli, Performances of a NewtonKrylov scheme against implicit and multi-grid solvers for inviscid flows, no. AIAA 98-2429, 29th AIAA Fluid Dynamics Conference, Albuquerque, NM, 1998.
[12] P. Adami, F. Martelli, V. Michelassi, Three-dimensional investigations for axial turbines by an implicit unstructured multi-block flow solver, no. 2000-GT-636, Proceedings of the ASME-IGTI Turbo Expo, Munich, Germany, 2000.
[13] D. Wilcox, Turbulence modeling for CFD, Technical Report 2006-18, DCW Industries Inc (1993).
[14] M. Kato and B. E. Launder, The Modeling of Turbulent Flow Around Stationary and Vibrating Square Cylinders, no. Proc. 9th Symposium on Turbulent Shear Flows, Kyoto, Japan, 1993.
[15] P. A. Durbin, On the k-epsilon Stagnation Point Anomaly, International Journal of Heat and Fluid Flow 17 (1996) 89–90.
[16] F. Motallebi, J.F. Norbury, The Effect of Base Bleed on Vortex Shedding and Base Pressure in Compressible Flow, Journal of Fluid Mechanics 110 (1981) 273–292.
[17] C.H. Sieverding, The influence of trailing edge ejection on the base pressure in transonic turbine cascade, Journal of Engineering for Power 105 (2) (April 1983) 215–222.

Conjugate heat transfer characterization in a ribbed cooling channel

Beni Cukurel

Turbomachinery and Propulsion Department, cukurel@vki.ac.be

Supervisor: Tony Arts

Head of Turbomachinery and Propulsion Department, von Karman Institute for Fluid Dynamics, Belgium, arts@vki.ac.be.

Promotor: Anil Bajaj

Professor, Purdue University, Mechanical Engineering, 585 Purdue Mall West Lafayette, IN 47907-2088, bajaj@purdue.edu

Abstract

The implicit assumption of most studies in literature of internal cooling channels is that the influence of the thermal boundary condition is negligible, however, in case of large spatial thermal gradients the impact of the wall temperature distribution are much greater.

Keywords: conjugate heat transfer, turbine, cooling channel, convection

1. Introduction

The cooling technology of gas turbine components, primarily ensured via internal forced convection, is aimed towards withdrawing thermal energy from the airfoil. Therefore the goal is to obtain the highest possible cooling effectiveness at the lowest possible pressure drop penalty. Under the majority of practical system constraints, this means the highest achievable internal convective heat transfer coefficient with the lowest achievable friction coefficient and pressure loss respectively. This involves convective heat transfer in the fluid domain and conduction in the solid domain. Considerable effort has been invested to develop methodologies to account for the coupled character of the problem.

1.1. Turbine Cooling

The trend towards higher efficiency and improved cycle performance of modern gas turbines gave rise to the considerable effort invested in this field. Increasing the turbine inlet temperatures is clearly one of the key parameters in raising gas turbine performance significantly. Surface temperatures beyond 1300 C, far exceeding the melting temperature of the materials, are commonly encountered in todays applications. Being exposed to such a harsh environment, engine components are subjected to many forms of degradation including oxidation, creep deformation and promoted thermal cycle fatigue. They arise from the combination of high temperatures and mechanical stresses which are caused by the non-uniform temperature distributions, significant aerodynamic loads and centrifugal forces, as well as the unsteady flow and thermal fields created by stator-rotor interactions. When the blade temperature exceeds detrimental limits, thermal stresses become excessive and affect the structural integrity; blade life decreases, possibly resulting in thermal failure. Changes in metal temperatures as little as 30K are reported to reduce the life cycle of blades by half. [1] [2] From this perspective, operating temperatures can be raised by either increasing the amount of thermal stress the blade material can withstand, or by decreasing the thermal stress on the blade through directed cooling strategies. Considerable effort has been invested in both research fields.

In cooling, the compressor air is introduced from the hub channeled via intricate serpentine passages inside the airfoil, extracting heat by means of forced convection from the rectilinear channel walls and is eventually discharged into the main gas stream from both the trailing edge and the tip of the blade, as well as the film cooling holes. By cooling the internal blade surface, the heat conduction through the solid results

in decreased metal temperatures at the outer blade surface, where it encounters the hot gas environment. In anticipation of promoted heat exchange, the passage walls are lined with repeated geometrical disturbance elements and surface non-uniformities which are referred to as turbulence promoters, thus introducing the expression of roughened cooling channels. The effect of these artificial roughness elements is twofold: not only they increase the total surface area involved in the heat transfer process, but also they induce high levels of turbulence in the core flow, which is even of greater significance for improved heat transfer. [3] Among the common types of disturbance elements, are rib turbulators. In general, the application of these turbulence promoting geometrical elements in cooling passages are effective in raising the heat transfer to considerably higher levels at the expense of increased pressure loss.

1.2. Conjugate Heat Transfer Theory

When investigating a model of a real internal cooling channel (numerically or experimentally) the reproduced thermal boundary conditions should resemble the engine environment. If this is not the case, the modeling of the heat transfer process can be inaccurate. The implicit assumption of most studies in the literature of internal cooling channels is that the influence of the thermal boundary condition is negligible. This is sometimes a fair assumption. However, in case of large spatial thermal gradients and/or geometrical asperities, the impact of the wall temperature distribution can be much greater. In purely convective studies, where uniform temperature or uniform heat flux are usually imposed along the wetted surface, the thermal boundary conditions are clearly not realistic; the effect of the thermal history of the flow field is neglected. On the contrary, in conjugate heat transfer theory, where the effects of solid domain conduction are coupled with the convection over the surface (i.e. the thermal history of the boundary layer is accurately modeled), no constraint is enforced at the solid-fluid interface, except thermal equilibrium and heat flux continuity. The methodology of conjugate heat transfer analysis presents the opportunity to accurately model real engine conditions.

In essence, the conjugate heat transfer problem considers the thermal interaction between a body and a fluid flowing over or inside it. As a result of such interaction, a particular temperature distribution establishes on the bodyfluid interface. This temperature field determines the heat flux distribution on the interface and the intensity of heat transfer. Hence, the properties of heat transfer of any conjugate problem are actually the same as those of some nonisothermal surface with the same temperature field, no matter how this field is established, as a result of conjugate heat transfer or given a priori. Thus, in general, a theory of conjugate heat transfer is in fact a theory of an arbitrary nonisothermal surface, but the temperature distribution on the interface in a conjugate problem is unknown a priori. In short, the properties of a conjugate problem are the same as those of a purely convective problem where an identical temperature field is imposed along the wall surface.

The problem of generally unknown temperature and heat flux distributions at the solid-fluid interface, determined by the coupled solving of the thermo-fluid dynamic equations in the fluid and the energy equation in the solid, is defined as conjugated heat transfer problem by Perelman. [4] Analytical solutions of conjugated problems rely on methods that determine the heat transfer from arbitrary non-isothermal surfaces. [5] Fundamental analytical studies have been presented by Luikov and Aleksashenko [6], who solved the heat transfer problem for the case of an incompressible laminar fluid flow along a flat plate with applying a uniform temperature distribution at the bottom surface of the solid. The local Brun number, giving the thermal resistance ratio of the plate to that of the laminar boundary layer, has been introduced by Luikov [7] as a measure of conjugation criterion. Dorfman [5] introduced a new kind of boundary condition to the coupled heat transfer problem, which allowed a conjugate problem to be reduced and further expressed by an equivalent problem subject to heat conduction only.

In this regard, the present study is focusing to a deeper understanding of the conjugate heat transfer phenomenon by conducting experiments for fundamental understanding, as well as creating a baseline database for numerical investigations. Uniform heat flux is applied at the bottom side of a geometrically scaled test section to model the underlying physics of the conjugate heat transfer phenomena across a turbine blade. The investigation focuses on surface heat flux calculations over a ribbed slab configuration through local temperature measurements made by Infrared Thermography. The heat flux distribution along the upper side of the slab, computed from an energy balance within the metal domain, ultimately yields to a Nusselt number distribution over the wetted surface. The investigation compares the convective (isoheatflux boundary condition on the wetted surface) liquid crystal thermometry results with the conjugate

heat transfer investigations.

1.3. Ribbed Cooling Channel Mean Flow Field

The relatively simple geometry of rib roughened internal cooling passages is misleading in a sense that the employed upward and backward facing step disturbance elements inside the channel introduce a number of complex secondary flow features into the mean stream.

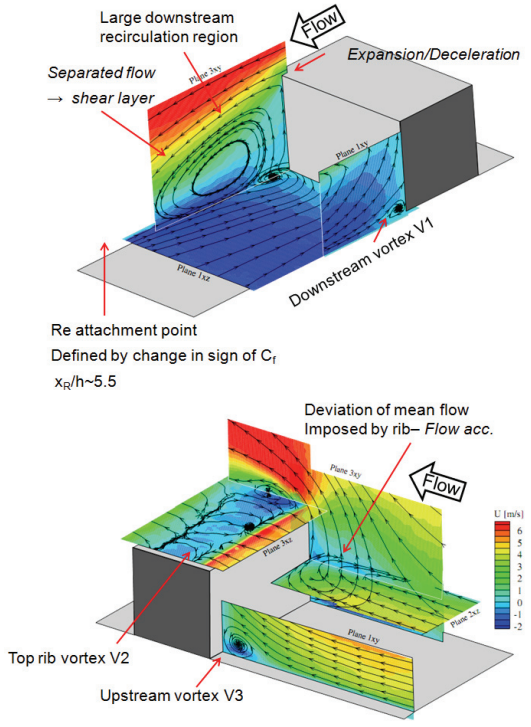

Figure 1: Visualization of the ribbed flow field

As an overview, the mean flow field inside the rib-roughened cooling passage is presented by the distinct structures observed in Fig. 1. From the stream traces, representing the mean velocity field, one can clearly locate the main and secondary flow features mentioned a priori. The general acceleration of the flow while passing over the rib is indicated by the higher magnitude of the streamwise velocity, Fig. 1. The vortex structures V_3 upstream and V_1 downstream of the rib are clearly identified by their vortical rotational behavior. The stream traces highlights the presence of the small recirculation bubble V_2 on top of the rib and the large recirculation region in its wake. [8]

Approaching from the right hand side of the figure the fluid enters the test section and encounters the rib. The stream experiences a strong deviation imposed by the obstacle, forcing it to adapt to the decreased channel cross section. It is accelerated in order to pass the rib and subsequently experiences an expansion further downstream, as the cross sectional area abruptly increases due to the backward-facing step. This is also supported by the large pressure drop located in the proximity of the rib. [9] The periodic behavior of consecutive acceleration in the vicinity of the obstacle and deceleration of the fluid in the inter-rib spacing is one most dominant aspects of the flow field in rib-roughened channels.

Since the fluid flow is not able to follow the abrupt changes of the surface, it is the sudden enlargement of the channel after passing the perturbator which causes the flow to separate from the surface. A free shear layer is formed upon the interaction between the separated flow and the reverse flow in the recirculation region downstream of the rib, Fig. 1. Apart from this recirculation region, the flow field exhibits a separated flow region V_2 on top of the perturbator as well as a small vortex V_1 in the downstream corner between the rib and the channel bottom, as indicated by Rau et al. [9]. While V_2 rotates in the clockwise direction, V_1 exhibits a counter-clockwise rotation. Unlike the large recirculation region in the wake of the obstacle, these two vortex cells not only statistically represent the mean flow behavior, but also exist in the instantaneous velocity field.

Within the wake of the rib, the small vortex cell V_1 exhibits a counter-clockwise rotary motion, this recirculation region in the downstream corner of the rib and the large global separated flow region exhibit opposite mean angular velocities. Towards the obstacle, their stream traces coincide, such that the flow impinges onto the downstream surface of the rib, opposing the mainstream flow direction. Similar to V_2, this recirculation region develops over the entire spanwise channel direction.

Further downstream, the mean flow passes the rib and the sequent recirculation zone, and at the reattachment region, there exists an impingement towards the channel bottom wall. Once the flow reattaches and aligns with the channel wall, the boundary layer redevelops and grows within the inter-rib spacing, until it approaches the next turbulator. The stream strongly impinges on the front surface of the rib so that its vorticity and the repeatedly induced separation of the boundary layer give rise to the vortex structure V_3. [8]

1.4. Flow over Backwards Facing Step

The flow over abrupt contraction/expansion regions is not capable of following the sharp turns induced by

the surface geometry; when the channel cross section is abruptly enlarged, the turbulent flow downstream of the rib exhibits complex flow features, including: reversal and recovery in the presence of a strong adverse pressure gradient, turbulent mixing, regions of reattachment and redeveloping boundary layers. The region of separated flow in the wake of the rib, between its back face and the reattachment line, is occupied by the recirculation region. With its length confined by the point of reattachment, its size is substantially dependent on the state of separation. This exact location of reattachment, where the wall near flow initially begins to realign with the surface again, is regarded as a key parameter for the separated flow. Experiments reported the near wall flow region to be substantially different from an ordinary boundary layer. When the flow passes the rib obstacle, a free shear layer is formed upon the separation of the upstream boundary layer at the sharp corner due to the interaction between the separated mainstream flow and the reverse flow in the recirculation region downstream of the rib.

Regarding heat transfer in a backward-facing step geometry, the Nusselt number within the reattachment zone is controlled by the turbulence level near the wall. The fluctuating skin friction is substantially increased compared to an ordinary boundary layer. The larger skin-friction fluctuations in turn result in a proportionally larger Nusselt number. Further downstream, the steady decrease in the Nusselt number coincides with the growth of the thermal boundary layer following reattachment.

The direct relation of flow reattachment region with local heat transfer distribution has been extensively studied in the literature. The maximum in the streamwise local Nusselt number profile has been considered a significant indication for the location of reattachment point. The local Nusselt number distribution is typically characterized by an initial increase within the separation bubble, followed by a peak in the vicinity of the reattachment region.

1.5. Ribbed Channel Geometric Similarity

The geometric scales which are of fundamental importance for the development of the flow inside the rib roughened rectilinear or squared channel can be represented as, aspect ratio, blockage factor, rib pitch to height ratio, rib angle of attack, rib shape and profile and number of ribbed channel walls.

The blockage ratio is of major importance for the flow behavior in a rib-roughened channel. The majority of studies on heat transfer enhancement in literature involve configurations characterized by noteworthy small blockage or rib height to hydraulic diameter ratios with h/Dh = [0.02-0.08]. The rib pitch-to-height ratio represents another significant aerothermal influence; it parametrizes the channels wall roughness effects on the flow field and thus on heat transfer and pressure drop.

In the present work, the test section geometrical dimensions are similar to the former studies carried out in this field. The squared channel geometry parameters are chosen to have a blockage ratio of 0.3, rib pitch to height ratio of 10, and angle of attack of 90.

The chosen configuration combines the setting of a standard reference case, squared cross section, with a high blockage ratio of the channel. The pitch to height ratio of 10 lies within the optimal range which has been experimentally determined to yield the highest enhancement of heat transfer rate in the respective geometrical arrangement. It results in a particularly complex flow behavior with high levels of turbulence and a substantially three-dimensional flow character [8]. Therefore it is suitable for a fundamental analysis of the rib-roughened channel flow. From the perspective of aerodynamic similarity to engine conditions, experiments are conducted at Re= 40,000. For conjugate heat transfer considerations, engine representative Biot number, Bi, and solid to fluid thermal conductivity ratio, K, are used, 1 and 600 respectively. At such a high thermal conductivity ratio and Biot number being in the order of unity, considering both thermal and convective resistances are of the same order, the effects of nonisothermicity are augmented.

In this regard, the presented work is devoted to a deeper understanding of the conjugate heat transfer phenomenon by conducting experiments geared towards ribbed internal cooling channels. A test section, based on the serpentine channels of a turbine blade and satisfying the true similarity conditions, is built to model the underlying physics of the conjugate heat transfer. In addition, considering the scarcity of experimental data geared towards conjugate heat transfer, the present work can be considered a benchmark case for CFD validation. Most of the investigations in literature present solely either the thermal or the aerodynamic field in the region of interest. This study is one of the rare opportunities to analyze the different effects of various flow structures (through Particle Image Velocimetry experiments conducted a priori) on local heat transfer coefficient. In addition, the presented work is among the few comparative heat transfer studies (purely convective iso-heatflux and/or isothermal boundary condition versus the fully cou-

pled conjugate one), and exemplifies the pioneering experimental efforts to include the effects of conduction coupling in forced convection applications.

2. Experimental Facility

The channel built is the simplified model of an internal cooling blade channel that is scaled up by a factor of 15. It consists of three pieces such as the inlet, test and exit sections and each section has a cross-sectional dimension of 75x75mm, with longitudinal dimension of 1400mm, 1260mm, 800mm respectively. The basic schematic of the test section can be found in Fig. 2.

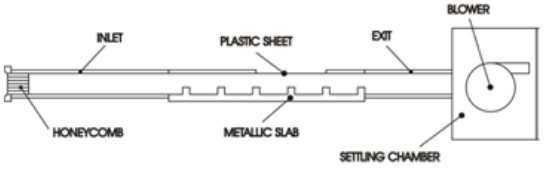

Figure 2: Schematic of the Experimental Setup

The flow in the channel is expected to be in the fully turbulent regime, considering the fact that experiments are conducted at Reynolds number based on hydraulic diameter, Dh, equal to 40,000 which is much larger than the laminar threshold imposed by the Moody chart (Re > 3000) . The test section consists of several components, where at the base of the channel a flat slab made of Steel AISI304 rests. The thickness of the slab, 25mm, has been chosen such that it respects the similarity with the serpentine channels of a turbine blade where the Biot number, which is the ratio between the conductive resistance to the advective term, is approximately equal to 1. At such a high thermal conductivity ratio and Biot number being in the order of unity, considering both thermal and convective resistances are of the same order, the dependence on thermal boundary condition (conjugate case) is amplified.

The steel slab is painted black with uniform highly emissive layers of Nextel Primer 5523 and Nextel Suede Coating 428-26, by means of an airbrush. The black coating is mat, soft and due to diffuse reflection the surface is non-dazzling. The end finish is found to be suitable for infrared measurements due to its black-body like behavior, albeit the camera is calibrated for the specific setup and the performance of the black paint is merely a matter of measurement quality. The slab is heated by means of a 25m thick Inconel sheet which is powered by a 16V-150A DC power supply. The current is dissipated as thermal energy by the Joule effect and is conducted away by the parts in contact. Inconel is known to provide uniform heat flux across the applied area and retains strength over a wide range of temperatures.

The slab is instrumented with 14 T-type thermocouples, held in place by Omega OB-101 thermally conductive, electrically insulating paste, applied to 3mm holes drilled in the metallic slab at several locations along the slab. The thermocouples are located 0.5 mm away from the surface of the slab, and considering the Biot number, approximately 10^{-3}, for this characteristic length, it is observed that the temperatures measured at the thermocouple bead locations are equivalent to surface measurements.

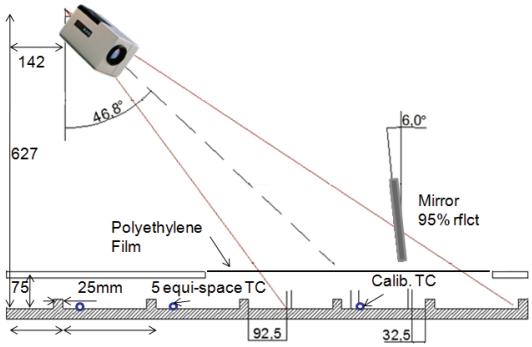

Figure 3: Ribbed Slab Test Section Camera

The camera is located at 46.8 degrees from the vertical, Fig. 3; since the radiation exchange of surfaces are linearly proportional with the view factor, this configuration is selected to provide a good compromise for pixels on both the vertical and horizontal surfaces. The downstream face of the rib, along with the rib-shadowed portion of the inter-rib space is observed via Newport 75K00ER.3 mirror, featuring a reflectance in the order of 95 percent in the 8-9 micron range of the camera.

In this experimental campaign, a FLIR SC3000 infrared camera with long-wave Quantum Well Infrared Photo-detector has been used. The nominal response of the photo-detector peeks in the 8-9 micron wavelength range, and since each pixel relates to a single IR detector, the spatial image deformation due to the optical system aberration is negligible. The total resolution of the camera is 240x320 pixels, and thermal sensitivity is 0.02K. A Labview code is generated to interface the data acquisition cards with the computer as well as for online monitoring of the measurement samples. This program manages the data acquisition

and synchronization of various components during the initial experimental setup, calibration procedure of the infrared camera and the measurements campaigns.

3. Experimental Methodology

Single point calibration methodology is based on the assumption that the slope of the calibration curve is constant for all the pixels of the image, which enables the use of a single curve found for a reference point, the temperature of which is well known, to retrieve the complete temperature map.

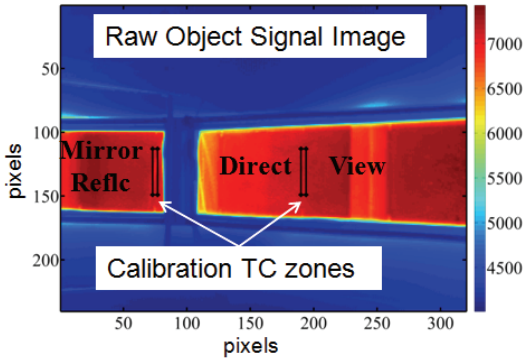

Figure 4: Raw IR Image with Thermocouples

Fig. 3 presents the raw object signal image acquired by the camera. The superimposed rectangular regions (calibration reference zones) indicate the location of the thermocouples embedded into the slab, as observed directly and reflected from the mirror, from the view point of the infrared camera.

Since this calibration methodology is based on the assumption that the slope of the calibration curve is constant for all the pixels of the image, considering the large difference in view factors of the direct and reflected portions of the image, independent calibration curves are established for the directly observed and mirror reflected portions of the image.

Fig. 5, presents an exemplary temperature distribution along the measurement section, while the test section is at steady state. This distribution is achieved by utilizing the two calibration curves with local out of focus compensation. The black lines superimposed on the image indicate the regions which consist of the different geometric features such as the upstream, top, downstream portions of the rib, along with the direct and reflected views of the inter-rib space.

All portions of the image are transformed independently by a perspective transformation, which uses

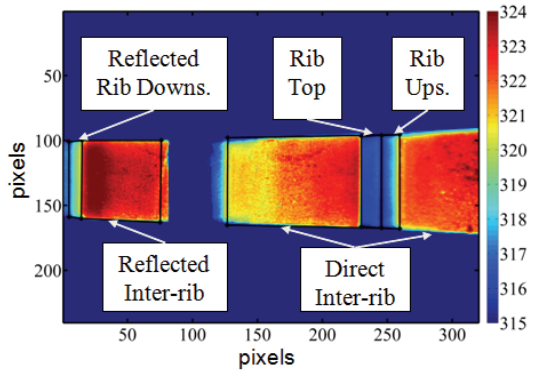

Figure 5: Temperature Distribution [K]

bicubic interpolation, and are projected onto a plane. The resolution of the transformed image is superficially augmented in each dimension through sub-pixel interpolation. Since this procedure is conducted independently on different regions of the geometry and the perspective of the camera which varies significantly along the image, it is not possible to define a true uniform scale factor.

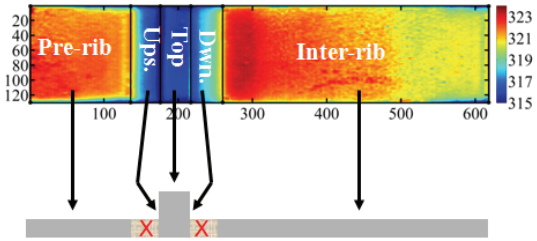

Figure 6: Temperature Distribution - Perspective Corrected [K]

The temperature data presented in Fig. 6 has several limitations, one being the fact that the data, as is, clearly is not periodic in the rib domain indicated by the fact that the temperatures at the end of the pre-rib region do not coincide with the temperatures towards the end of the following domain, inter-rib space. The aperiodicity is evoked by several factors, such as the edge effects, heating of the bulk flow, and the aerodynamically non fully- developed flow field. This aperiodicity would have been unproblematic if there existed surface temperature data for the entire test section. In this case the entire section could have been modeled by a FEM solver to retrieve the local surface heat flux distributions. The issue arises when there exists surface temperature data for only a portion of the test section, hence only a limited region of the slab is modeled for computation of surface heat flux, but the

necessary boundary conditions to impose on the transverse faces of the cut geometry are ambiguous. Imposing adiabatic boundary condition would be highly unrealistic considering the fact that there are large local thermal gradients present within a rib passage. Furthermore, imposing periodicity boundary condition on an aperiodic temperature domain, results in superficial heat sources and sinks. Thus, one of the reasonable approximations, which also makes this data set more generic and applicable in a broader sense, is to perform a linearly weighted averaging in the overlap region (pre-rib and the overlapped inter-rib space), based on axial direction, such that the original pre-rib temperature data is more dominant in the vicinity of the rib. This doesnt only result in a smoother transition, but also creates a realistic temperature distribution for a generic ribbed channel where periodicity holds. This is as well the general philosophy of the image post-processing methodology, which is to generalize the currently studied case as much as possible. Nonetheless, the results acquired by periodicity corrected and raw temperature boundary conditions are compared within the results. In order to reduce these effects a median filtering methodology is used; this is typical for applications where the goal is to simultaneously reduce peek noise and preserve edges. The temperature distribution across the channel is averaged with respect to the symmetry plane followed by a Gaussian low pass filter to smooth out the local gradients of temperature induced by the averaging process, Fig. 7.

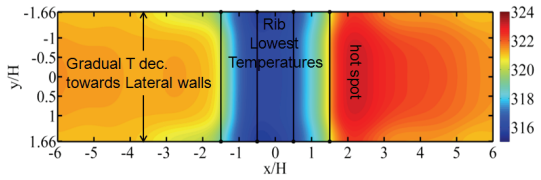

Figure 7: Temperature Distribution Gaussian Low Pass Filter [K]

To acquire the surface heat flux distribution, the wetted surface of the ribbed channel is modeled by a commercial FEM solver, COMSOL. The boundary conditions for the numerical problem are uniform heat flux, in this case 1733 W/m^2 along the bottom surface of the slab, measured temperature distribution on the wetted surface, adiabatic side walls and periodic boundary condition on the transverse direction where the solid, in reality, is interrupted. In the numerical model, the only modeled portion of the slab volume is a single complete passage where the surface Infrared Thermography temperature measurements exist. The passage is modeled in a way such that the rib is preceded by 45mm of inter-rib space and after the downstream face of the rib, the remaining 15.75mm of the inter rib space is modeled.

Over the surface of the ribbed passage, the 160 micron paint layer is modeled, measured a priori by the Fischer Mp20 sensor. The thermal conductivity of the paint layer is imposed as k=0.3 W/m-K and shows consistency with the heat flux distributions in the passage. There exist 85787 and 132538 mesh elements in the paint layer, and ribbed metal slab domain respectively. The convergence criterion is set to 10^{-10} for the relative pre-conditioned residuals. It has been shown that further grid refinement does not significantly affect the solution computed in the model.

4. Results

4.1. Heat Flux and Nusselt Number Distribution

Fig. 7 presents the measurement imposed projected surface boundary temperature within the passage. By applying this temperature distribution to Comsol as boundary condition, it is possible to acquire the heat flux normal to the boundary, as presented in Fig. 8; where the values are normalized by the heat flux imposed on the bottom surface of the ribbed channel. It is important to point out that there is a large effect of heat flux redistribution within the solid. Having the temperature and the heat flux distributions, it is possible to calculate enhancement factor distributions over the wetted surface presented in Fig. 9.

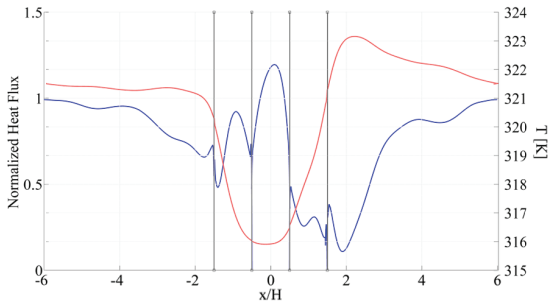

Figure 8: Symmetry line Temperature and Normalized Heat Flux Distribution

Considering the insight about the flow structures which Particle Image Velocimetry experiments of Casarsa [8] provide, it is possible to identify some unique distributions of enhancement factor associated with the nearby flow feature, on half of Fig. 9 are

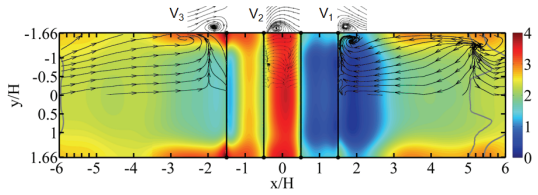

Figure 9: Comsol Enhancement Factor Distribution at the Projected Boundary

the surface streamlines superimposed from [8]. The schematics denoted on the side of the figure are the V_3, V_2 and V_1 vortex structures, located in front of, over, and behind the rib respectively, observed around the channel centerline.

The -6<x/H<-3.8 region, is the part of the ribbed channel where the flow is attached immediate downstream of a large separation region. Slight overall decrease in enhancement factor is associated with the boundary layer growth of an attached flow; this is the portion of the ribbed channel which resembles the behavior of a developing flat plate boundary layer. Due to the increase in boundary layer thickness the heat transfer decreases in the stream-wise direction. Most of the benefit associated with the high overall level of heat transfer, EF=2.4, is caused by the increased turbulence levels and the complex flow structures associated with the flow field. The enhancement factor is observed to be higher towards the edges caused by the increased level of fresh cold fluid entrainment due to the secondary flow features.

Downstream, for the region bounded by-3.8<x/H<-1.5 |y/H| <1.3, the initial decrease in the enhancement factor, from to x/H=-3.8 up to x/H=-2.5 is due to the potential effect of the rib reducing the axial component of the velocity, causing an adverse effect on the boundary layer (an increase in boundary layer thickness). Further downstream, in the region -2.5<x/H<-1.5, the flow is dominated by the existence of the clockwise rotating corner vortex V_3. In the vicinity of the rib, -1.8<x/H<-1.5, this vortex creates a local downwash zone where the flow impinges on the bottom surface, indicated by the local peak in EF.

The upstream facing of the rib is denoted in Fig. 9 in the -1.5<x/H<-0.5 domain. Initially, concentrating on the core flow region, |y/H| <1.3, at first in the -1.5<x/H<-0.8 domain, due to blockage created by the V_3 flow structure, the mainstream flow cant come in contact with this portion of the upstream surface of the rib, indicated by a low enhancement factor region. Around x/H=-0.8, a peak in EF can be observed; this peak is the combined effect of the downwash of the V_3 vortex along with the impingement of the mainstream flow to the upstream surface of the rib, the location of this peak is consistent with the PIV data. In the upstream bubble V_3 cold flow impinges on the rib side wall and then moves towards the floor of the channel. Even though this fluid is heated before it reaches the floor, the flow impingement cools the lower wall at the base of the rib.

The top face of the rib, -0.5<x/H<0.5, is where the overall highest EFs are observed. This is caused by the reduction in effective area of the mainstream flow (due to the existence of the rib), in turn resulting in much higher momentum flow, generating a region of high heat transfer rate. Locally, the location of the peak, at x/H=0.15, is consistent with the downwash caused by the V_2 vortex, which is the dominant flow feature in this portion of the passage. Towards the lateral wall, at the edge, the EF peak is observed to be slightly wider, in agreement with the larger, more diffuse, V_2 vortex formation.

The downstream surface of the rib, 0.5<x/H<1.5, along with the immediate downstream in the axial direction, 1.5<x/H<2, are the regions where the lowest EF values are observed. This is caused by the large separation region behind the rib, generating a local low momentum region with reversed flow, where the heat transfer is considerably less than the rest of the passage. This is clearly observed by the sudden drop in EF for 0.5<x/H<0.9. In addition to the global separation, there is the existence of a counter clockwise rotating vortex V_1, further isolating the region from the mainstream flow, 0.9<x/H<1.5. The local peak at x/H=1.2 is caused by the downwash of the vortex impinging on the downstream surface of the surface, locally increasing EF.

4.2. Reattachment and Peak Enhancement Factor

The reattachment region is estimated in Fig. 9 by the gray lines drawn in between 5<x/H<6.1. The earlier line presents the local maximum in axial derivative of enhancement factor. This line indicates a strong increase in EF in a region bordering the large separation bubble, the sudden increase in EF can only be indicative of the beginning of the reattachment zone. If a reattachment point is to be selected, this would be the lower limit on the reattachment region. The gray line further downstream indicates the location of the axial maxima in EF, considering that, for this geometry, the maxima in heat transfer is expected to occur downstream of the reattachment, the second line is an upper limit for the reattachment point.

In reality, the reattachment point, selected aerodynamically by the change of sign in the skin friction coefficient, is suggested to lie in between. In this case, the aerodynamic investigations of Casarsa [8] suggested that the aerodynamic reattachment occurs at around 5.3<x/H<5.7. This is consistent with the observation of the suggested upper and lower limits of reattachment region. When compared with convective measurements conducted in literature [10], it has been observed that the peak heat transfer occurred at 4.5<x/H<6; the results seem to be in good agreement with the current study.

4.3. Comparison with Literature

Comparing some of the averaged EF quantities with the liquid crystal measurements conducted by Cakan [10], purely convective case study at a lower Reynolds number of 30,000, the data seems to be in agreement. The average EF on the upstream face is relatively high, 2.35, due the impingement of the mainstream flow on the surface. On the top face, the EF is even further augmented, 3.02, due to the local increase of momentum by the decrease in effective area. On the downstream side of the rib, the lowest average EF is observed, 0.86, due to the large separated region behind the step. The rib, inter-rib and domain averaged EFs are 2.08, 2.01 and 2.03 respectively. When the findings are compared with the results by Cakan [10], there seems to be a trend of redistribution of heat flux such that the enhancement factor is more distributed across the domain, maintaining a more uniform enhancement factor under conjugate conditions.

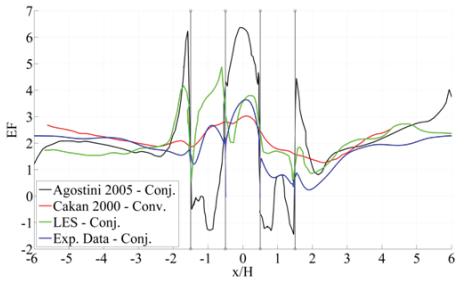

Figure 10: Symmetry Line Enhancement Factor Comparison

Fig. 10 presents the comparison of the findings in the current study with respect to similar studies conducted in prior literature, investigated for the channel symmetry line. The convective liquid crystal data are the results gathered by Cakan [10] in his experiments conducted with the iso-heatflux boundary condition. The LES data is from an internal study at VKI, based on the current test case for the conjugate problem. [11] The Conjugate IR data are the result of the conjugate heat transfer infrared thermography experiments conducted by Agostini [12]. All test cases show remarkable resemblance to the current experimental data set.

Comparing the convective case study [10] with the conjugate one, it is apparent that the level of enhancement factor in the vicinity of the rib, |x/H| <3, is greatly influenced by the conjugate boundary condition imposed on the solid domain. In the upstream inter-rib space close to the rib, -3<x/H<-1.5, the effect of conjugate boundary condition can be as large as 35 percent in EF. On the upstream facing region of the rib, -1.5<x/H<-0.5, especially towards the bottom wall where the V_3 vortex is located, the maximum difference in EF is 55 percent. This vortex creates an isolated region where the flow impinges on the side of the rib x/H=-0.8, being heated up, moves towards the bottom wall with reversed flow. Due to the increase in bulk flow temperature, the temperature head decreases in the flow direction. In consistency with the fundamental conjugate heat transfer theory, a decrease in temperature head in the flow direction results in lower than isothermal EF levels, which is by definition lower than the compared iso-heatflux case.

On the top face of the rib, the effect of thermal boundary condition seems to have reduced to 20 percent. At this region, due to the existence of the V_2 flow structure, mainly located in the upstream portion of the top rib surface, in the axial direction, more and more entrainment of cold fluid on the surface is possible, which results in a stream-wise decrease in wall bulk flow temperature. In combination with the greatly increased axial momentum at this region, these result in the highest heat transfer coefficients observed for both the conjugate and the convective cases. Additionally, in the presence of conduction within the rib, the top surface acts as a heat sink as it is surrounded by much lower EF regions. This additional heat sink effect may explain the slightly higher conjugate EF values observed at the top rib surface. Downstream of the rib, over the vertical rib surface and in the rib vicinity bottom wall, 0.5<x/H<3, the convective case over estimates EF in the order of 150 percent and 450 percent at the vertical and bottom walls respectively. This is believed to be attributed to the dominant conduction coupling, particularly observed in proximity of the rib as a result of closely distributed local heat sinks and sources. Such large values are consistent with the conjugate heat transfer theory, which suggests that in regions of lower velocity and lower tur-

bulence levels, the thermal boundary condition has a much more dominant effect on heat transfer.

5. Conclusions

The conjugate heat transfer investigation is conducted for the ribbed roughened internal cooling channel geometry. The enhancement factor trends are compared with the basic flow features observed in prior literature and reflected excellent agreement. Basic errors in conjugate modeling, used in the evaluation of surface heat flux from experimental temperature data are identified and the effects are demonstrated.

For the attached flow immediate downstream of the large separation region, a slight overall decrease in enhancement factor is observed, associated with the boundary layer growth; this is the portion of the ribbed channel which resembles the behavior of a developing flat plate boundary layer. Approaching the rib, there is an initial decrease in the enhancement factor, from due to the potential effect of the rib reducing the axial component of the velocity, causing an adverse effect on the boundary layer (an increase in boundary layer thickness). In the direct vicinity of the rib upstream face, the flow is dominated by the existence of the clockwise rotating corner vortex V_3, which not only prevents the cold fluid from coming in contact with the heated surface, due to blockage created by this flow structure, but also creates a local low momentum zone, yielding to a region of low EF. The top face of the rib is where the overall highest EFs are observed. This is caused by the reduction in effective area of the mainstream flow (due to the existence of the rib), in turn resulting in much higher momentum flow, generating a region of high heat transfer rate. The downstream surface of the rib, until reattachment, is the region where the lowest EF values are observed; this is caused by the large separation region behind the rib, generating a local low momentum region with reversed flow, where the heat transfer is considerably less than the rest of the passage. A double peak in enhancement factor is observed, the initial weaker peak is located prior to the reattachment point, where the local minima in skin friction, local maxima in fluctuating component of the shear stress, and local sharp maxima in reverse flow velocity are observed. The second global maximum in enhancement factor is observed after the reattachment point, typical considering the relatively narrower separation region.

Acknowledgments

I would like to thank my advisor and my promoter Prof. Tony Arts and Prof. Anil Bajaj for their support. This research was funded in part by the US Air force Office of Scientific Research. This support is most gratefully acknowledged. Finally, I would like to express my gratitude to Red Bull GmbH, and Sara Lee Coffee/Tea.

References

[1] Han, J.C., Turbine Blade Cooling Studies at Texas AM University 1980-2004, Journal of Thermophysics and Heat Transfer 20 (2) (2006) 161–187.

[2] Bogard, D.G. and Thole, K.A., Gas Turbine Film Cooling, Journal of Propulsion and Power 22 (2) (2006) 249–270.

[3] Schiele, R. and Wittig, S., Gas Turbine Heat Transfer: Past and Future Challenges, Journal of Propulsion and Power 16 (4) (2000) 583–589.

[4] Perelman, L.T., On Conjugated Problems of Heat Transfer, Int. J. Heat Mass Transfer 3 (4) (1961) 293–303.

[5] Dorfman, A. and Renner, Z., Conjugate problems in Convective Heat Transfer: Review, Mathematical Problems in Engineering 3 (4) (2009) 293–303.

[6] Luikov, A.V. and Aleksachenko, A.A., Analytical Methods of Solution of Conjugate Problems in Convective Heat Transfer, Int. J. Heat Mass Transfer 14 (8) (1971) 1047–1056.

[7] Luikov, A.V., Conjugate Convective Heat Transfer Problems, Int. J. Heat Mass Transfer 17 (2) (1974) 257–265.

[8] Casarsa, L., Aerodynamic Performance Investigation of a Fix Rib-Roughened Internal Cooling Passage, Ph.D. thesis, Universit degli Studi di Udine (2003).

[9] Rau G., akan M., Moeller D., Arts T., The Effect of Periodic Ribs on the Local Aerodynamic and Heat Transfer Performance of a Straight Cooling Channel, J. Turbomach. 120 (2) (1998) 368–376.

[10] Cakan, M., Aero-Thermal Investigation of Fixed Rib-Roughened Internal Cooling Passages, Ph.D. thesis, Universit Cathilique de Louvain (2000).

[11] D. Nakhle, LES in ribbed cooling channel, PR 2008-18, von Karman Institute for Fluid Dynamics (2008).

[12] Agostini, F., Arts, T., Conjugate Heat Transfer Investigation of Rib-Roughened Cooling Channels, no. ASME TURBO EXPO 2005, Reno, Nevada, 2005.

Accurate turbine blade tip clearance measurements in a short-duration wind tunnel

Sergio Lavagnoli

Turbomachinery and Propulsion Department, lavagnoli@vki.ac.be

Supervisor: Guillermo Paniagua

Professor, Turbomachinery and Propulsion Department, von Karman Institute for Fluid Dynamics, Belgium, paniagua@vki.ac.be.

Promotor: José Maria Desantes

Universidad Politécnica de Valencia, Camino de Vera, s/n 46022 Valencia

Abstract

A capacitance-based measurement system has been used to successfully measure the running tip clearance over the rotor of a transonic turbine stage. Sensor performances and a detailed procedure to calibrate the system in-situ are described. Results point out that tip clearance is a crucial parameter to be constantly monitored in short duration turbine test rig

Keywords: Tip clearance; capacitance probe; transonic turbine; short-duration rig; in-situ calibration

1. Introduction

The development of gas turbine engines with increased efficiency and reliability demand for accurate monitoring of running clearances of the compact rotating machinery. The tip blade clearance plays a major role in the characterization of the whole machine performance. In a modern turbine stage, the hot leakage flow that past above the airfoil tips can account up to 30% of the total stage losses [1]. Therefore, the gap between the rotor blade tip and the stationary shroud must be minimized. However, turbine designers commonly set a safe minimum gap to prevent mechanical rubbing between the blade tips and the casing that may result in rotor damage or catastrophic failure. Thus, the selection of an optimum tip clearance results from a trade-off between aerodynamic performance and mechanical integrity. Unfortunately, as a consequence of manufacturing and installation tolerances, vibrations, different expansion rates of blades, rotor disk and casing induced by thermal and speed transients, blade erosion, the rotor tip clearance undergoes large variations during engine service operations [2]. Hence, advanced tip clearance active control concepts must rely on accurate real-time clearance measurement systems to achieve highest engine efficiency with increased safety margins. Additionally, blade tip clearance measurements are routinely used in engine development programs and flight tests to verify the mechanical design and tune numerical code predictions. Tip clearance measurements in current gas turbine applications are mostly based on capacitance systems. These sensors have demonstrated the best potential to adapt to the harshest working conditions thanks to their robustness, simple design and reliability. Intense research has targeted the development of capacitive probes for testing in gas turbine engines. Sheard et al. [3] performed accurate blade-to-blade tip clearance measurements on the casing on an HP compressor using a hybrid self-calibrating electromechanical-FM capacitance sensor. Developments of high temperature capacitance probes for tip clearance measurements in engine validation tests were proposed by [4], [5] and [6]. However, no sensors for engine flight have yet been realized [7]. Gas turbine industry therefore has a strong interest for improved tip clearance instrumentation for routine use on in-service engines. Further technology development is needed to provide measurement systems with enhanced accuracy, increased working

range, extended lifetime and reliability at high temperatures. This paper reports the implementation and testing of a novel capacitance-based system to measure single-blade tip clearance over the rotor of a modern gas turbine stage. The sensing apparatus is composed of a robust capacitive probe connected to the signal conditioning unit via a co-axial cable. The tip clearance instrumentation presented here allows high bandwidth measurements and large distances to be set between the sensor and the electronics without any performance reduction. The tip clearance probe is calibrated on a simplified test bench to assess the factors influencing the sensor output and determine the measurement uncertainty. In a second phase the probe is mounted on the shroud of a large transonic turbine rotor. The turbine stage is tested in a short-duration facility that allows reproducing real aero-engine operating conditions characterized by speed and thermal transients. A procedure to calibrate the tip clearance probe in-situ by means of wearing gauges is described and a sophisticated technique that ameliorates the calibration data reduction is presented and validated. Blade-to-blade and average rotor tip clearance is measured through an extensive experimental campaign. Results are used to assess the measurement system performance and characterize the rotor tip clearance variations in a typical run of a short duration turbine rig.

2. Experimental Apparatus

2.1. System concept

Tip clearance measurements in civil and military aero-engines demand the usage of advanced instrumentation. The most challenging application is the high pressure turbine where temperature, pressure and rotor speed are the highest. Sensors should then be capable of withstanding temperatures above 1500 K, should have reduced size and improved working range (0-5 mm), high bandwidth to resolve blade passing frequencies in the order of tens of kilohertz. In the current research work a capacitive probe system, developed by Hytron GmbH, is used to perform tip clearance measurements over the rotor of a transonic turbine stage. The proximity measurement system is based on the detection of the capacitance between a probe and a moving conductive blade. Figure 1-left displays a schematic representation of a rotor blade and the tip of a typical capacitance-based probe installed in the turbine engine casing. The sensor head is composed of two coaxial conductors, the round-rod electrode and the guard electrode, separated by

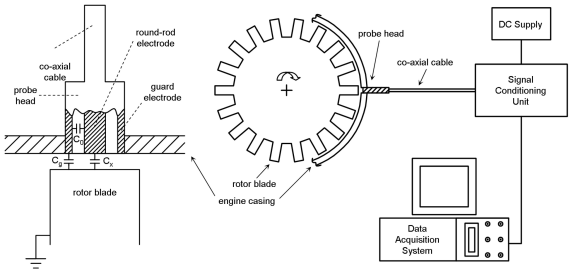

Figure 1: Cut view of the sensor head (left). Tip clearance measurement system block schematic (right).

an insulator. The guard electrode ensures that the central electrode is electrically insulated from the metallic shroud in which is mounted. As a rotor blade sweeps under the probe head, the sensor electrode and the blade tip form the plates of a variable capacitor. The resulting capacitance is a function of the plates geometry, the properties of the medium in between and the gap between the plates. If fringe effects are neglected, the probe-to-target capacitance can be expressed by the relationship:

$$C_x = \frac{\varepsilon_r \, \varepsilon_0 \, A}{d} \tag{1}$$

where ε_r and ε_0 are the permittivity of the medium and the vacuum, A represents the common area between the two plates and d is the probe-to-target distance. Therefore, the capacitance C_x represents a direct measure of the required tip clearance. The capacitance C_g that forms between the guard electrode and the blade tips can be neglected since the rotor blades are electrically grounded to the engine casing via roller bearings and seals. Thus, the total capacitance sensed by the proximity measurement system is the sum of the shunt capacitance of the probe alone (C_0) and the probe-to-target capacitance (C_x).

2.2. System description

The configuration of the tip clearance capacitive measurement system is represented in Figure 1-right as a simplified block diagram. The system is composed of three main elements: a sensing probe, a cable and a signal conditioning unit. The sensing probe surface is mounted in the turbine shroud, located immediately above the rotor blades whose clearances are to be measured. The probe head is connected via coaxial cable to the signal conditioning electronics fed by a DC power supply. The conditioning unit controls the probe head, perform the signal pre-processing and

provide an analog voltage that represents the measurement of the running rotor blade tip-to-casing gap. The output signal is then recorded by a data acquisition system and stored for further data processing. The probe head is composed of two co-axial cylinders made of steel and separated by an electrical insulator of PTFE (Poly-Tetra Fluoro Ethylene). This ensures that the probe can withstand a maximum temperature of 530 K, below the operative temperature levels encountered in the turbine test rig used for the experiments. The probe has an external diameter of 10 mm and the outer screen surface has a screw-shape in order to facilitate the mounting in the rotor casing (Figure 2-top). The diameter of the inner sensing electrode, 5 mm, has been selected as an optimum value that offers a small probe size and a wide measurement range, typically estimated as half of the central electrode diameter.

The connection between the sensor head and the conditioning unit is provided by a co-axial cable made out of copper with PTFE as insulator, covered by an outer screen of FEP (Fluorinated Ethylene Propylene) that guarantees flexibility and mechanical protection. The cable has a total length of 8 m and allows transmitting high frequency signals for long distances with no loss in performances. The overall system shunt capacitance (probe head + cable) amounts to approx. 900 pF while the capacitance change induced by a blade passage is less than 100 fF. The processing of such small capacitance variations and the extraction of the tip clearance information are performed by the conditioning unit, the core component of the measurement system. The signal conditioning unit is composed of several sub-units that serve specific functions and are strictly interconnected, Figure 2-bottom. The *Clock-Generator* module generates a low distorted and phase-stable sine wave at high frequency (60 MHz) hat is fed to the sensor head. The frequency has been selected according to the probe characteristics and the total cable length. The oscillator signal is also used to synchronize all the other circuitry. In the *Input Stage* unit the probe-modulated reflected HF signal and the original input from the oscillator are overlapped to generate a heterodyne signal that carries the tip-to-sensor distance information. The raw signal is then amplified by multi-stage operational amplifiers (*HF Process* sub-unit), digitalized in the Flash *Analogue-Digital-Converter* (12 bit resolution, 10 MHz sample rate), and sent to the *Digital Control* unit. At this step the amplified digital signal undergoes further processing to compensate for all the spurious alterations of the original blade-to-sensor capacitance. This function is carried out by a sophisticated Field Programmable Gate Array (FPGA) circuit that executes a combination of operations in the time and frequency domain to generate a compensation signal. The auxiliary signal is fed back via a fast *Digital-Analogue-Converter* to the *HF Process* unit to compensate the HF signal from the input stage. In the current set-up, the output signal is sampled by a Data Acquisition System from a bypass analog output located after the *HF Process* stage.

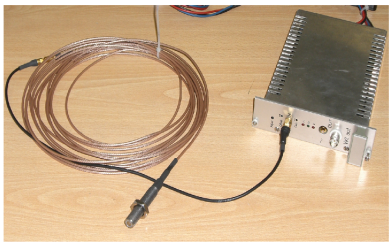

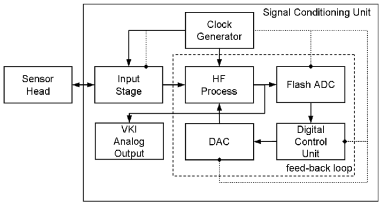

Figure 2: Capacitive probe head, cable and electronics (top). Conditioning unit scheme (bottom).

The feedback loop is an essential feature of the current system working principle. It is based on the tracking of the signal "idle" working point, when no target faces the sensor, to calculate an auto-compensation function. Therefore, the system is able to correctly measure only time-varying clearances and for the current application the limit is approx. 160 Hz. However, this approach allows canceling out measurement capacity errors caused by a number of spurious factors such as probe shunt capacitance drifts due to temperature changes or vibrations, mechanical stress on the cabling, or crosstalk interference with other electronics. The use of modern FPGA technology and a high frequency clock-oscillator module extend the sensor frequency bandwidth up to 60 kHz.

2.3. Calibration procedure and signal processing

The characteristics and the performance of the proximity measurement system were first evaluated in a simplified calibration bench that allows running a full probe calibration under controlled operative conditions. This also served to develop a robust methodology for the processing of the capacitance probe raw

signal and optimize the system set-up for measurements in the turbine test rig. It was considered unnecessary and prohibitive to exactly replicate the actual rotor geometry and the turbine operative conditions as the turbine facility allows in-situ calibration to be carried out. Therefore, preliminary calibration tests were run on a lathe that drives a small cogwheel (Figure 3-left). A brass wheel with twelve teeth was manufactured with an external diameter of 70 mm and a tooth height of 10 mm. An inter-tooth spacing of 10 mm was considered in order to test the ability of the capacitance probe to correctly detect the idle position between two passing targets. The cogwheel was mounted on a 15 mm-shaft and clamped into the chuck of the lathe on one side and on the tailstock on the other side. The probe head was fitted on a support mounted on the lathes cross slide to permit its independent displacement. An absolute reference gap between the capacitance probe and the bladed wheel is determined using a thin metallic wire of known length mounted in the proximity of the probe sliding support. The wire is moved towards the rotating blading till contact occurs, thus datuming the sensor tip on the longest tooth. The calibration data set was obtained traversing the measurement head at 0.10 mm intervals over the sensor operating scale (0.2-3 mm). Tests were performed at shaft speeds ranging between 1000 and 3000 RPM to guarantee a minimum tooth passage frequency of 200 Hz and a safe operation of the sensor. During the calibration, the voltage output

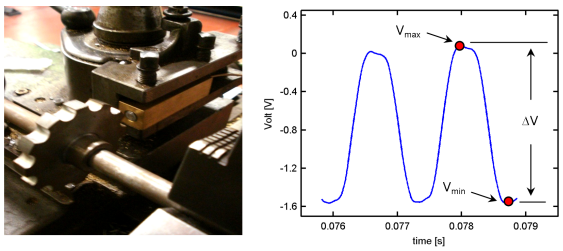

Figure 3: Calibration rig set-up (left). Example of typical sensor output (right).

for a set of known distances between the probe tip and the cogwheel is recorded. The capacitance sensor signal is sampled for 2 s at 250 kHz. This ensures that the unsteady signal features are well captured and a sufficient number of wheel turns is available for statistical analysis. Figure 3-right shows a typical trace of the raw voltage output acquired during a calibration step. As a tooth sweeps under the probe sensing area, the voltage increases proportionally to the actual target distance. The signal does not show any abrupt discontinuity but a gradual variation as the sensor-to-target area variation is non-linear [8], and not because of a narrow system bandwidth. The raw signal was digitally low-pass filtered before performing any further treatment. The filter cut-off frequency was selected to be approximately 15 times the target passing frequency to remove the high-frequency noise while preserving unaltered the blade-by-blade signal variations. The measurement system calibration is generated by performing a curve fit through the data set associated to the longest wheel tooth using a least-square optimization routine. The equation that describes the relationship between the sensor output (V) and the gap between the probe tip and the target (D) is assumed to be:

$$D = A_1 + \frac{1}{A_2 + A_3 V} \tag{2}$$

where A_1, A_2 and A_3 are the coefficients of the curve fit. The form of eq. 2 was selected among others for providing the best fit of the available calibration data sets. The physics of a capacitor suggests that as the distance between two plates approaches zero the capacitance must tend towards infinity. Likewise, a thorough analysis of the data exposed that the voltage variation across a tooth passage was a more robust parameter than the maximum peak-to-peak voltage to represent the sensor response. Indeed, the voltage amplitude is a direct function of the capacitance change induced by the actual target proximity [9]. Once a calibration test is completed, a routine was programmed to perform the required data reduction procedure. The software sorts through the data sets to identify the longest blade corresponding to the largest signal amplitude. Usually 10 to 20 data sets are used to obtain a

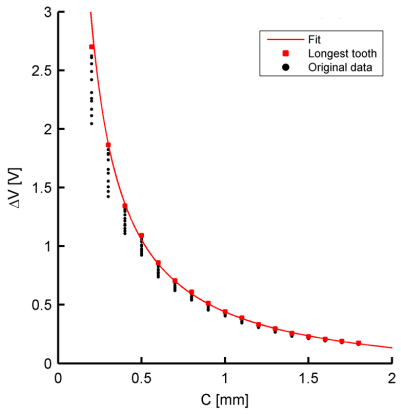

Figure 4: Classical probe calibration.

reliable probe calibration. At this point the actual dis-

tance of the probe head to the other tooths tips is unknown therefore a conventional calibration curve fit is based only on the longest tooth data points, Figure 4. In the present work an advanced calibration refinement method is implemented in the data reduction routine that allows including into the calibration fit the voltage values of each wheel tooth. This procedure was firstly introduced and validated by Sheard et al. [10] and here it will be only briefly described. The entire data set of a calibration run can be organized in a matrix $[V]$ that contains in each row the voltage values associated to a single tooth, and in each column the voltage value obtained at each traverse position. Once a preliminary calibration becomes available from the longest tooth curve fitting, a matrix of distances $[C1]$ can be defined. A second distance matrix $[C2]$ can be generated that has the same first column of $[C1]$ and the remaining columns computed by adding to the value of the first column the known offset distance traversed during the calibration. The distance matrices would be ideally identical but small differences exist due to calibration inaccuracies. An error matrix $[E]$ is calculated as the difference between $[C2]$ and $[C1]$. The rows of $[E]$ represent the distance error over a single tooth at each probe step while the columns account for the error in distance of the entire blading at a certain calibration point. Each row was averaged to provide a resulting row $[F1]$ that represents the error due to the proximity sensor readings. Likewise, each column of the error matrix was averaged to generate a column vector which values provide an estimate of the error due to the probe traversing position.

The initial matrix $[C1]$ was modified by subtracting from each column the vector $[F1]$ and from each row the vector $[F2]$ to generate a third distance matrix

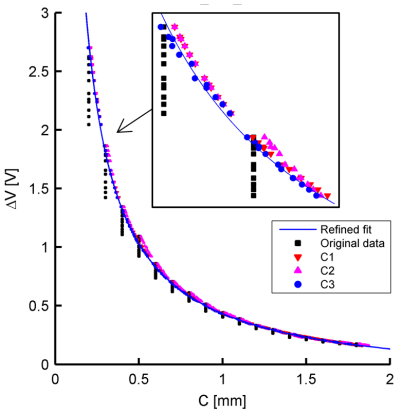

Figure 5: Calibration refinement procedure.

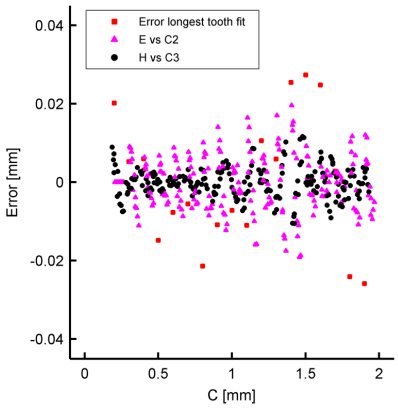

Figure 6: Error in clearance.

$[C3]$. Finally, a new set of refined calibration coefficients is calculated by performing a second curve fit, using $[V]$ and the matrix of corrected clearance $[C3]$. As previously done for $[E]$, a second error matrix $[H]$ is calculated by subtracting $[C3]$ from the matrix $[C4]$, a matrix of clearances obtained with the refined calibration coefficients. Figure 5 displays all the steps of the reduction procedure for the sensor calibration refinement. The capacitance probe output $[V]$ is plotted against the corrected distance matrices $[C2]$ and $[C3]$ together with the original and refined calibration laws. It is apparent that the proposed procedure has significantly enhanced the quality of the calibration result. The improved methodology enables to generate the probe calibration based on the entire data set available, thus providing a more robust estimation of the calibration coefficients. The calibration error distribution can be appreciated by plotting $[C2]$ against $[E]$ and $[C3]$ against $[H]$ together with the clearance error associated with the calibration based only on the longest tooth, Figure 6. After the last calibration refinement, the data scatter has visibly reduced from ±0.025 mm (longest tooth calibration) to ±0.01 mm. The ±0.01 mm error band can be reasonably assumed as an indication of the measurement system accuracy over the calibration range.

2.4. System performance and uncertainty analysis

The system performances can be described considering the results of the capacitance sensor calibration in the small spinning rig. Calibration tests were run to verify the performance of the measurement system at increased working temperatures. The probe head and the blading disk were directly exposed to a hot air jet blown by a heat gun for the time the calibration

was completed. Thermocouples were used to monitor the air temperature and the probe head temperature. Calibrations were performed at two air temperatures, 500 and 600 K, while the probe head temperature was measured to reach the same level in both cases, approx. 360 K. The resulting calibrations superimpose with calibrations performed at room temperature as shown in Figure 7. This clearly indicates that the measurement system is virtually not affected by relatively high working temperature. The sensor electronics is actually able to compensate for capacitance drifts due to variations with temperature of the electrical properties of the probe head components. Results also suggested that changes in the probe-to-target capacitance due to variation of the air dielectric characteristics with temperature are negligible over the tested temperature range. Figure 7 also shows calibration curves

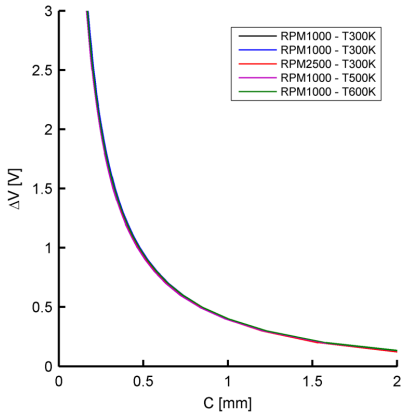

Figure 7: Capacitance probe calibrations performed at different working conditions.

for tests performed at different disk speeds. Comparison of calibrations run at 1000 and 2500 RPM expose that the sensor response remains unaltered when the system is operated at low rotor speed that corresponds to target passing frequency (200 Hz) close to the lower bandwidth limit of the probe. The amount of voltage change with clearance size provides the probe sensitivity. At a working clearance of 0.5 mm, the signal voltage amplitude is approximately 0.8 V and probe sensitivity is typically 1.5 V/1 mm (Figure 7). At extended range, capacitance sensor signal approaches the system noise floor, estimated to be around 10 mV. Thus, the signal-to-noise ratio is normally 80. The 5 mm diameter capacitance probe is able to operate over a range of 2.5 mm. As the distance between the sensor tip and the rotor increases the probe sensitivity degrades, and becomes more and more difficult to distinguish a voltage pulse induced by a passing target from a random noise peak. The smallest clearance detectable with the current system settings is 0.2 mm, below which the amplifiers in the signal conditioning unit saturate. The accuracy of the clearance measurement sensor is limited by a number of errors that arose during probe calibration, system installation and data reduction. The error generated in the calibration process can be thought as the uncertainty of the standard used to datum the probe to a known reference distance. This error is estimated to be 0.005 mm, i.e., half of the dial gauge resolution used to monitor the probe displacement. Uncertainties due to the deviation between the real blade and disk geometry and the calibration rig are not accounted in this analysis since in-situ probe calibrations are possible in the turbine test rig where tip clearance is measured. During the operation of the system, uncertainties are introduced by changes in the gas dielectric properties that affect the sensed capacitance as described by (1). Errors of the order of 0.5% of the full scale can be engendered by variations of the air humidity [11]. Likewise, large air temperature and pressure changes result in slight variations of the measured capacitance, less than 0.1% in standard turbine applications [12]. System noise introduces a random error in the voltage amplitude readings of a measurement. This error can be statistically determined to cause a ±0.012 mm (95%) variation at a nominal clearance of 1 mm. Lastly, during the data reduction process, the conversion of the measured voltage amplitude into clearance generates an error, estimated with the precision interval associated to the calibration curve fit. Based on the calibration results, this uncertainty is approx. ±0.01 mm (95%). An RSS (Root of Sum of Squares) method is used to combine all the error contributions and Table 1 provides a summary of the bias and random uncertainty of the measurement system.

2.5. System installation on a turbine test rig

The proximity measurement system was installed on the casing of a large transonic turbine stage to provide detailed measurements of the rotor tip clearance. The high-pressure turbine is tested in von Karman Institute compression tube facility. This short duration facility is able to simulate the aero-thermal performance of highly loaded high pressure turbines in a larger scale. It reproduces independently temperature ratios, Reynolds and Mach numbers of the actual engine conditions. The facility consists of two volumes separated by a fast opening valve (Figure 8-top). The

Error Source	Type	Uncertainty
Calibration standard	Bias	±0.005 mm
Calibration curve fit	Random	±0.010 mm
Probe head installation	Bias	±0.005 mm
System Noise / Data reduction	Random	±0.012 mm
Quantization error	Bias	±0.0001mm
Gas effect		
Air humidity	Bias	±0.005 mm
Air temperature & pressure	Bias	±0.0005mm
Random uncertainty		±0.016 mm
Bias uncertainty		±0.009 mm
Total system uncertainty		±0.018 mm

Table 1: Proximity system uncertainty analysis.

air is compressed quasi-isentropically by a free piston in the large cylinder. The pressurized air is then discharged into the test section and dump tank. In a typical test cycle, the test section is initially under vacuum. The turbine rotor is spun up to nearly its design speed by an auxiliary power turbine that is stopped right before the hot gas blow-down takes place. As a consequence of the work exchange with high enthalpy flow, the rotor accelerates during the test reaching a maximum speed of 7600 RPM. When all the mass-flow from the upstream piston has been discharged, air brakes are activated that quickly slow down the rotor disk. Figure 8-bottom displays an example of the rotor speed and acceleration history over 1 s after the blow-down start. With a diameter of nearly 700 mm, the

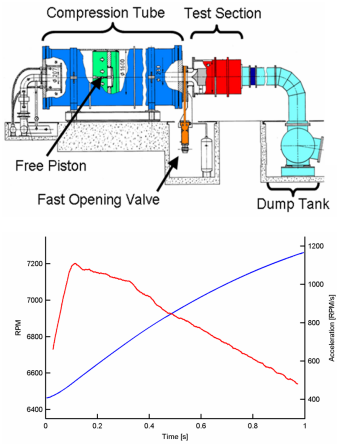

Figure 8: Turbine test rig (top). Typical rotor speed and acceleration levels during a test (bottom).

high-pressure rotor disk mounts 64 blades. The airfoils height is, on average, 50 mm and the inter-blade spacing is 34 mm at the blade tip. The airfoil thickness varies along the chord and in correspondence of the proximity probe location is 3 mm. For aerodynamic testing purposes, the turbine was rotated at two design speeds of 4500 and 6790 RPM. For high speed

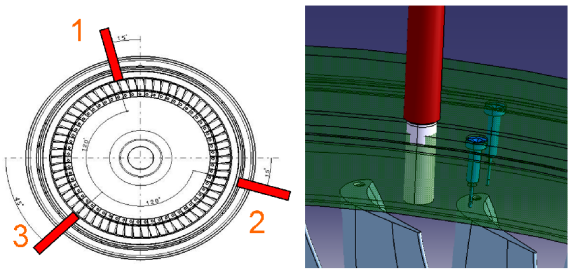

Figure 9: Installation of the clearance system on the turbine casing (left). Capacitance probe head and wear gauges (right).

testing this corresponds to a blade passing frequency of approx. 7400 Hz. In order to properly detect the passage of a single blade and correctly resolve the running tip clearance fluctuations, the sensor signal is sampled with 16 bit acquisition card at 1 MHz, i.e., a minimum of 135 samples per blade passage event. The experimental set-up and the tip clearance system installation in the turbine test section were designed to enable the calibration of the capacitance probe in-situ. This entails the advantage of calibrating the sensor against the actual blading geometry and minimizes the system installation uncertainties. The tip clearance measurement installation on the turbine stage was performed by fitting the probe head into an extension support. The probe-support assembly is guided trough the turbine casing to the rotor shroud. The sensor external surface is equipped with a screw that allows the correct positioning and displacement of the probe head inside the turbine casing. The capacitance probe can be mounted on three different slots located in the casing at equally spaced circumferential positions, Figure 9-left. The in-situ calibration is performed thanks to two wear gauges fitted in the rotor shroud in proximity of the sensor head, one of the two positioned at the same axial probe location, Figure 9-right.

As the rotor speed increases, the wear tip is gradually machined by rubbing with the longest blade. The calibration is performed by rotating the rotor disk at increasing speeds that result in increasing wearing of the reference gauges. At the end of each run-up, the actual distance between the wear gauge tip and the sensor head is measured, thus providing a zero reference to datum the capacitance probe position. The rotor shroud endwall is covered with a thin layer of abradable liner. This allows performing a planned blade-tip

procedure at the beginning of the experimental campaign once the clearance system calibration is completed. When the rotor disk spins up to its maximum speed, the blade tips rub the abradable liner resulting in a defined running clearance. To avoid damage to the probe in the event of a tip rub, the sensor head was positioned recessed 0.7 mm within the casing during the experimental test campaign.

3. Turbine tip clearance measurements

An extensive measurement campaign was carried out in a short duration test rig to measure the tip clearance over the rotor of a transonic high-pressure turbine stage. The experimental program served to verify the performance of the proximity measurement system in a real engine environment and to provide a detailed investigation of the tip clearance levels that characterize the operation of a short duration wind tunnel. Once the procedure to calibrate the capacitance sensor in-situ was completed, the calibration curve was generated using the refinement approach described in section 2.3. During the test campaign, the rotor tip clearance was monitored at each facility run. The capacitance sensor signal was acquired for 500 ms after the starting of the blow-down in order to provide tip clearance information at the same time aerodynamic measurements were performed. The raw output voltage amplitude is reduced to a data set of clearance and each single clearance value is associated with the corresponding blade passage event. The time-varying tip clearance signal is also utilized to estimate the rotor speed and acceleration. The single clearance data is averaged over one rotor revolution to provide a mean value representative of the turbine tip clearance variation during a test run. As the rotor disk speed constantly increases during a test, it is convenient to select as a reference, hereby referred to revolution ”0”, the rotor revolution in which the turbine speed reaches the target design value, 4500 and 6790 RPM. Figure 10-left shows typical trends of the average blade tip clearance for the two design operative speeds. As the turbine speed increases, the tip clearance reduces due to larger centrifugal loads and consequent growth of the rotor blades and disk. A constant clearance shift of approx. 0.2 mm is observed between high and low speed regimes, while the variation during a test run is similar for the two speed levels, around 0.045-0.050 mm over a rotational speed change of about 400 RPM. In order to investigate the test-to-test repeatability, the mean tip clearance traces was further averaged on a window of 8 rotor revolutions around the revolution zero, Figure 10-right. Surprisingly, the data exhibit a scatter of 0.1 mm over a large number of tests, for both low and high rotor speed regimes. This test-to-test variation was judged too large and at least twice the capacitance sensor uncertainty at a working distance of 1-1.2 mm. A further examination of the test running conditions revealed that part of the data scatter was due to the warming up of the wind tunnel when repeated tests were performed in a single day. In fact, the short duration facility allows running up to 6-7 tests a day. At every test, a hot gas blow-down releases a considerable amount of heat towards test section surface. Thus, the whole wind tunnel increasingly warms up during the day and this cause a thermal growth of both the turbine casing and the rotor disk. Figure 11 shows again the test-to-test tip clearance variations but this time the data are grouped according to the time a test was run during a day. The fifth, sixth and seventh test of the day were grouped together due to their small number. Data are reported only for high speed regime, since tests at low speed expose a similar behavior. After ranking the

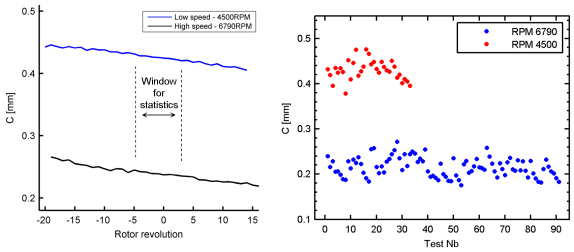

Figure 10: Typical tip clearance variation during a wind tunnel test (left). Tip clearance test-to-test repeatability (right).

tests, results clearly display a significant reduction of the data scatter. The tip clearance measurements now show a test-to-test repeatability of 0.045 mm that is consistent with the capacitance probe error of ±0.025 mm predicted by the uncertainty analysis. On a daily basis, the mean tip clearance level is measured to vary by as much as 0.05 mm because of the thermal transient in the wind tunnel. Table 2 summarizes the repeatability results for both rotor speed conditions. Unexpectedly, the tip clearance exhibit a reduction as the wind tunnel heats up during the day. This phenomenon can be explained if the thermal dilatation of the rotor and the turbine casing is somehow different. Over small temperature linear thermal expansion for a metal is function of three variables, the initial length, the coefficient of thermal expansion and the temperature change. In the present

High Speed 6790 RPM	1st Test	2nd Test	3rd Test	4th Test	5-6-7th Test
Mean Tip Clearance [mm]	0.234	0.216	0.207	0.195	0.184
Test count	30	25	16	9	7
Repeatability (95%)	±0.028	±0.028	±0.029	±0.023	±0.013
Low Speed 4500 RPM	**1st Test**	**2nd Test**	**3rd Test**	**4th Test**	**5-6-7th Test**
Mean Tip Clearance [mm]	0.456	0.449	0.422	0.416	0.411
Test count	4	8	11	4	6
Repeatability (95%)	±0.043	±0.036	±0.028	±0.047	±0.052

Table 2: Mean tip clearance statistics.

case, the casing has a larger diameter than the rotor as well as a higher thermal coefficient. Therefore, the only reason for a tip clearance reduction is that the rotor assembly (blades + disk) heats more than the turbine shroud as the hot gas is repeatedly blown into the test section. This hypothesis is consistent with the fact the rotor surface, directly exposed to the incoming hot flow, absorbs more heat than the shroud. Additionally, the thick turbine casing has a much larger thermal capacity than the rotor disk.

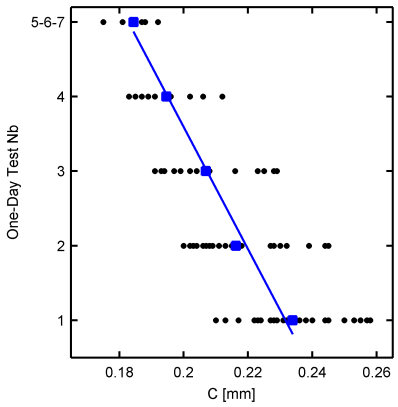

Figure 11: Corrected tip clearance test-to-test repeatability.

The capacitance proximity system was used to measure the tip clearance over each blade. As previously done for the mean rotor clearance, the individual tip clearance values for each blade are averaged over 8 revolutions around the design rotor speed and ranked according to the test run number in which they were measured. The individual clearance is plotted against the blade number in Figure 12 for the high speed regime only. The clearance drift due to the facility warming is clearly visible on each rotor blade and its amplitude appears to be independent of the blade number. The rotor exposes a maximum tip clearance variation of approx. 0.35 mm around the 64 blades. On the other hand, except for few blades, the blade-to-blade variation is within 0.1 mm. The overall blade-to-blade tip clearance variation, measured in rotation, is plotted together with the static blade height deviation measured using a dial gauge against the blade number, Figure 13, as offset with respect to the longest blade. The two data sets show a high degree of overlap, the largest deviation being within the ±0.025 mm error of the probe, giving confidence on the accuracy of the capacitance sensor to measure running single-blade tip clearance. Additionally, based on the smallest blade height variation detected by both methods, the measurement system resolution can be estimated to be approx. 0.01 mm.

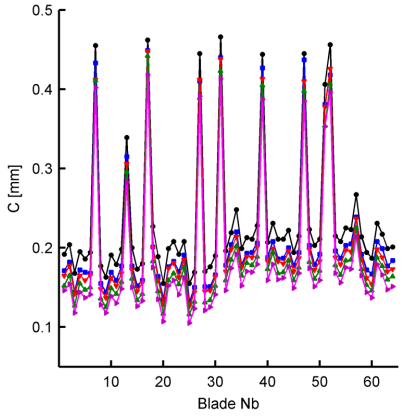

Figure 12: Blade-by-blade tip clearance at high speed testing, daily variation.

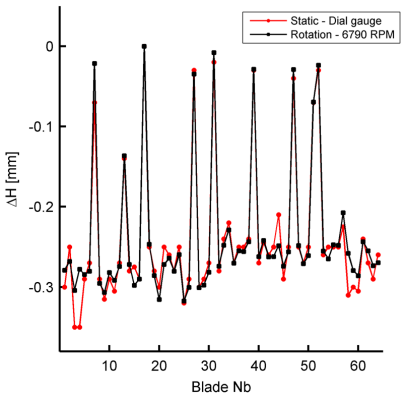

Figure 13: Offset of the rotor blades from the longest blade for static (dial gauge) and running (capacitance probe) measurements.

4. Conclusions

The main purpose of the present research is to experimentally determine the tip clearance variations that characterize a typical test run in a short duration turbine facility. A capacitance-based proximity measurement sensor has been successfully used to detect tip clearance over individual blades around a rotor. The measurement system components have been described and its performances evaluated by means of repeated calibrations in a simplified test rig. An advanced procedure to calibrate the capacitance probe is implemented that allows producing a set of refined calibration coefficients based on the data sets available from all the blades. Calibrations at different working conditions have proven that the system electronics fully compensate for temperature drifts of the gas temperature and of the probe head. An uncertainty analysis is proposed that identify the bias and random error sources that affect the measurement system and explain the rise of the measurement error as the probe working distance increases. The analysis predicted that clearance can be measured within 0.025 mm at a working distance of 1 mm. Experience on a real running turbomachine gives confidence that this uncertainty was actually achieved in practice. The tip clearance sensor was mounted on the shroud of a large transonic turbine stage and calibrated in-situ using wear gauges fitted into the casing endwall. Blade tip clearance measurements were carried out in a short duration turbine test rig where the rotor speed constantly increases during test. Results show the working tip clearance to reduce of approx. 0.05 mm from the test start till the rotor reaches the design speed. The clearance was observed to vary 0.2 mm for tests run at 4500 and 6790 RPM, with typical mean levels of 0.45 mm and 0.20 mm respectively. Analysis of the test-to-test repeatability revealed that the tip clearance level is sensitive to the thermal conditions of the wind tunnel as the test section warms up due to repeated hot gas blow-down. At the end of a the day, tip clearance was found to decrease up to 0.05 mm, as the rotor heats up more than the casing. The blade-by-blade tip clearance measurements showed a maximum variation of 0.35 mm over the 64 rotor blades. Comparison of the blade height measured in static condition and in rotation exposes an excellent match, therefore allowing the estimate of the probe resolution to be 0.01 mm. Overall, the experimental investigation pointed out that tip clearance significantly change during the operation of a short duration wind tunnel and accurate measurement are required to support and validate detailed aerothermal measurements in such turbine test rig. Lastly, the tip clearance measurement system can be considered an effective tool to improve the safe operation of the turbine wind tunnel.

5. Acknowledgements

The author would like to thank Tolga Yasa for his assistance during the experimental campaign. Likewise, the author is grateful to Gerard Goosens and Julien Desset who helped in the design of several pieces. The authors would also like to acknowledge the financial support of the European Commission and Industrial Partners involved in the European Project TATEF2 "Turbine Aero-Thermal External Flows 2".

References

[1] J. Denton, Loss mechanisms in turbomachines, ASME J. Turbomach. 115 (1993) 621–658.

[2] D. K. Hennecke, Active and passive tip clearance control, in: VKI LS *Tip Clearance Effects in Axial Turbomachines*, 1985.

[3] A. G. Sheard, B. Killeen, A blade-by-blade tip clearance measurement system for gas turbine applications, ASME J. Turbomach. 117 (1993) 326–331.

[4] G. D. Bailleul, S. Albijat, Review of progress in the development of capacitive sensors for blade tip clearance measurement, ASME Turbo Asia Conference, Jakarta, Indonesia.

[5] S. M. D. Muller, A. G. Sheard, E. Johann, Capacitive measurement of compressor and turbine blade tip to casing running clearance, J. Engineering for Gas Turbines and Power 119 (1997) 877–885.

[6] S. G. O. A. G. Sheard, J. F. Stringfellow, High temperature proximity measurement in aero and industrial turbomachinery, J. Engineering for Gas Turbines and Power 121 (1999) 167–173.

[7] J. Roberts, The potential of tip timing and tip clearance measurements: The aero-engine perspective, in: VKI LS *Tip Timing and Tip Clearance Problems in Turbomachines*, 2007.

[8] C. Lawson, P. Ivey, The use of commercially available capacitance tip-clearance probes for tip-timing of aero-engine compressor blades, Proceedings of 38th AIAA/ASME/SAE/ASEE Joint Propulsion Conference & Exhibit, July 2002, Indianapolis, Indiana.

[9] J. Barranger, Low-cost fm oscillator for capacitance type of blade clearance measurement system, Tech. rep., NASA TP (1987).

[10] G. C. W. A. G. Sheard, B. Killeen, An on-line calibration technique for improved blade by blade tip clearance measurement, Proceedings of the 38th ISA International Instrumentation Symposium (1992) 31–51.

[11] K. Chana, Fundamentals of tip timing and tip clearance sensors, in: VKI LS *Tip Timing and Tip Clearance Problems in Turbomachines*, 2007.

[12] J. W. H. Chivers, A technique for the measurement of blade tip clearance in a gas turbine, AIAA paper No. 89-GT-24.

A high temperature cooled fast response total pressure probe for measurements in gas turbine combustor and hot gas paths

Mehmet Mersinligil

Turbomachinery and Propulsion Department, mersinli@vki.ac.be

Supervisor: Jean-François Brouckaert

Associate Professor, Turbomachinery and Propulsion Department, von Karman Institute for Fluid Dynamics, Belgium, brouckaert@vki.ac.be

Promotor: Tony Arts

Professor and Chairman, Turbomachinery and Propulsion Department, von Karman Institute for Fluid Dynamics, Belgium, arts@vki.ac.be

Abstract

This paper presents the first experimental engine and test rig results obtained from a fast response cooled total pressure probe. The first objective of the probe design was to favor continuous immersion of the probe into the engine to obtain time series of pressure with a high bandwidth and therefore statistically representative average fluctuations at the blade passing frequency. The probe is water cooled by a high pressure cooling system and uses a conventional piezo-resistive pressure sensor which yields therefore both time-averaged and time-resolved pressures. The initial design target was to gain the capability of performing measurements at the temperature conditions typically found at high pressure turbine exit (1100-1400K) with a bandwidth of at least 40kHz and in the long term at combustor exit (2000K or higher). The probe was first traversed at the turbine exit of a Rolls-Royce Viper turbojet engine, at exhaust temperatures around 750 °C and absolute pressure of 2.1bars. The probe was able to resolve the high blade passing frequency (≈23kHz) and several harmonics up to 100kHz. Besides the average total pressure distributions from the radial traverses, phase-locked averages and random unsteadiness are presented. The probe was also used in a virtual three-hole mode yielding unsteady yaw angle, static pressure and Mach number. The same probe was used for measurements in a Rolls-Royce intermediate pressure burner rig. Traverses were performed inside the flame tube of a kerosene burner at temperatures above 1600 °C. The probe successfully measured the total pressure distribution in the flame tube and typical frequencies of combustion instabilities were identified during rumble conditions. The cooling performance of the probe is compared to estimations at the design stage and found to be in good agreement. The frequency response of the probe is compared to cold shock tube results and a significant increase in the natural frequency of the line-cavity system formed by the conduction cooled screen in front of the miniature pressure sensor were observed.

Keywords: Instrumentation, Unsteady Pressure Measurement, High Temperature, Time-Resolved Measurements

Nomenclature

Roman Symbols

a	[m/s]	Speed of sound
d	[m]	Cavity diameter
D	[m]	Probe diameter
f	[Hz]	Frequency
L	[L]	Line length
M	[-]	Mach number
P	[bar]	Pressure
q	[bar]	Dynamic pressure
RMS	[-]	Root mean square
SN	[-]	Singal-to-noise ratio
T	[K]	Temperature
V	[m^3]	Volume
W	[m]	Width

Greek Symbols

φ	[°]	Yaw angle

Subscripts

bp	Blade pitch

c	Cavity
gas	Gas property
L	Left
n	natural
o	total
probe	Measured by probe
R	Right
s	Static
sensor	of the Sensor

1. Introduction

Accurate hot gas path measurements (including combustion diagnostics) are recognized as a major need for the assessment of engine component health and performance. This fact has been highlighted in a recent study, "The Lab Gap Matrix" carried out by EVI-GTI (the European Virtual Institute for Gas Turbine Instrumentation) [1], following the inputs of engine OEM's, instrumentation vendors and research groups to identify the gaps in the instrumentation capability for measuring in gas turbines and aero-engines. In the United States, a similar organization, PIWG (Propulsion Instrumentation Working Group [2]) has performed a similar survey and issued specifications for the missing instrumentation capabilities required "to fill the gaps". Regarding sensor needs and measurement requirements at high temperatures in gas turbine applications, the reader is also referred to the recent contributions of Roberts [3], 2004 and Niska [4], 2009, which provide an excellent summary of the state-of-the art in gas turbine instrumentation needs.

Besides the interest to validate numerical predictions of engine performance, efficiency, and component life, the availability of high temperature steady and unsteady pressure and temperature data would also enable much progress in the field of condition monitoring and active control technologies, as outlined by Simon et al. [5], 2004, in their review of sensor needs for control and health management of future intelligent aircraft engines.

Due to the limitations of current experimental techniques and of the severe flow conditions, the measurement of pressure and temperature in the hot sections of modern gas turbines still remains a true challenge for test engineers.

Regarding unsteady pressure measurements above temperatures of 1300K; few, if any, accurate and reliable technique exists to measure the time-resolved gas path total pressure. The long term goal of the probe development presented this paper is the measurement of combustion instabilities inside the combustion chamber at temperatures up to 2000K and above, and in the short term, proof of the concept through measurements at the temperature conditions typically found at high pressure turbine exit (1100-1400K) with a high bandwidth. To resolve the highly three-dimensional and unsteady flow field within turbine stages, it is required to record continuous time series of pressure. At those elevated temperatures, it is therefore mandatory to design a highly efficient cooling system for a probe continuously immersed into the gas path.

The design concept is based on the use of a conventional piezo-resistive pressure sensor, located at the probe tip, to achieve the highest possible bandwidth and provide both the average and fluctuating pressure components. The objective of the design study was first to investigate different probe arrangements and cooling solutions aiming at gas temperatures of 1400K. Both gas and liquid coolants may be considered but emphasis was given on water cooling because of its higher heat capacity. A thermal barrier coating (TBC) is envisaged to reduce the probe metal temperature. Besides the cooling of the probe stem, which requires creating a uniform cooling stream, avoiding stagnating fluid regions inside the probe channels, the most challenging part of the cooling design is the reduction of the gas temperature in the cavity ahead of the sensor diaphragm.

A high temperature total pressure probe would yield the unsteady pressure field between turbine blade rows, including turbulence level, shock position and wake passing events. The single sensor probe can also be used in a virtual 3-hole mode, yielding the periodic flow angle fluctuations as already demonstrated by Kupferschmied et al. [6].

2. State-of-the-Art

Various review papers were authored regarding unsteady pressure measurements. A short summary will be provided in this paper, recommending thorough review by the authors in reference [7] as further reading.

Among other interesting review papers, Sieverding et al. [8], 2000, have reviewed the progress in a wide variety of measurement techniques for unsteady flows in turbo machines with emphasis on fast response pressure and temperature probes and blade surface sensors including pressure, heat transfer and shear stress determination. A similar review rather focused on unsteady pressure measurements can be

found in the recent contribution of Ainsworth et al. [9], 2000 as well as in the excellent review of Kupferschmied et al. [10], 2000, on fast response aerodynamic probes. Most of the information contained in these contributions is however limited to low temperature applications, i.e. below 400K.

In gas turbine burners or in hot turbine sections, attempts to measure unsteady pressures have traditionally been accomplished using two different types of devices: flush mounted wall pressure sensors or immersion type instruments.

Wall Pressure Measurements. Existing literature for wall pressure measurements may be categorized into high temperature sensors and cooled sensors. For an excellent review of high temperature sensors the reader is referred to the lecture note by Chivers [11], 2009.

In recent years, some air or water-cooled sensors became commercially available with quoted temperature capabilities up to 1370K in the water-cooled configuration and up to 1070K in the air-cooled configuration. Ferguson and Ivey have conducted numerous studies regarding cooling of these transducers [12; 13], and have presented an air-cooled jacket design, to protect an unsteady pressure transducer and demonstrated survival up to 1170K [14], 2002. However, the overall dimensions of those cooled sensors remain inappropriate for implementation in a probe assembly.

Immersion Type Instruments / Probes. Immersion type instruments or probes can be divided into two groups as fast immersion probes and cooled probes.

A new approach, pioneered by the University of Oxford is the fast immersion technique where an uncooled probe is fitted onto a rapid injection mechanism and external air cooling system. Pressure and temperature probes have been built, incorporating a commercially available piezo-resistive sensor, a pneumatic pressure port, a thermocouple and a dual thin film sensor on an 6 mm outer diameter probe head, yielding the steady and unsteady total pressure and temperature. Measurements have been performed in an industrial gas turbine combustor by Passaro et al. [15], 2006.

However, the drawback of this ingenious method is the short injection time, of the order of 100ms, which is mandatory for the survival of the probe. The transient, which both fast response sensor and pneumatic pressure port undergo during the injection make it difficult to obtain statistically representative pressure data at a given position of the traverse. The response of the pneumatic line must be sufficiently high to be able to use this value as a reference for the pressure given by the fast response sensor which is submitted to a very strong thermal transient during the injection and retrieval. For a complete description of the fast immersion technique and pressure and temperature probe details, the reader is also referred to the lecture note by Oldfield and Lubbock [16], 2009.

Cooled Probes. Historical development of probe techniques in high temperature gases is to be found in early plasma research. This development began with Langmuir's studies [17], 1923, in ionized gases of very low density and therefore low heat flux to the probes. The first example of a relatively sophisticated diagnostic probe utilizing forced cooling methods was the double-sonic-orifice probe developed in the late 1940's, and described in detail by Grey [18].

Most of this early work was performed at relatively low pressures. Subsequent developments to study higher pressures, i.e. dense plasmas, have led to the evolution of sophisticated cooled probe techniques mainly for calorimetric, electrostatic, heat flux, or gas sampling probes. A detailed review of these probe techniques was given by Grey [19] in 1970.

Regarding probe assemblies continuously immersed into the flow path, Ashby [20], 1988 and Lagen et al. [21], 1991, were amongst the first researchers to patent pneumatic pressure probes employing water cooling for thermal protection. The work of Warnack [22], 2002, who presented a pneumatic 4-hole probe designed to be operated up to 1070K, including a thermocouple, where the probe shaft is water cooled and the 6 mm diameter probe tip is uncooled is also worth to mention while summarizing average pressure measurements in gas turbines.

One of the latest developments in terms of high temperature probes specifically designed for aero-engine tests has been presented by Anderson et al. [23], 2008. The main elements of their work was to design a pneumatic 3-hole probe and an in-engine radial traversing system downstream of the HP and IP turbines for a RR Trent engine performance test. The probe was capable of measuring total pressure, yaw angle, total temperature and Mach number across the entire operating range of the engine and was designed for pressure and temperature conditions up to 1600K and 30bar. The design of the traverse system was to be as compact as possible to fit under the engine covers and withstand the hostile environment at the traverse system location (550K).

Currently some attempt is being made to develop a high temperature intermittent aspirated probe to measure simultaneously pressure and temperature. This method is based on a similar principle as the tare measurement probe of Grey [19]. A laboratory capability has been demonstrated by Yang et al. [24], 2002, in a furnace up to 1800K but the maximum service temperature of the probe designed for engine environments is currently limited to 1300K [25]. A cooled probe design is being developed to increase the probe operational temperature. For an extensive description of this technique, the reader is referred to the lecture note by Massini et al. [26], 2009.

Unsteady Pressure Probes. Regarding higher response designs, an original design of a transient pressure probe for the measurement of detonation wave characteristics inside rocket thrust chambers experiencing high-frequency combustion instabilities was also presented by Grey in 1970 [19]. A 5.6mm O.D. piezo-electric crystal transducer was mounted in the probe tip and the transducer diaphragm was splash-cooled by a ring of tiny re-entrant jets directed at different angles so as to completely cover the transducer face.

Nieberding and Englund [27] presented a Pitot-type combined steady-state and dynamic pressure probe with a far recessed water cooled transducer in 1972. This probe design incorporates an steady state flow passage bleed-by around the high frequency sensor for the average pressure measurement. However, due to the recess of the sensor, the bandwidth should be limited to a few kHz only.

In 1977, Moore [28] successfully demonstrated the capability to acquire high response (100Hz-10kHz) fluctuating pressure data for acoustic measurements in a high temperature flowing gas stream such as an aircraft engine exhaust. Miniature pressure transducers are mounted in a 12.7mm diameter water-cooled probe with their sensing surfaces parallel to the flow and flush with the probe outer wall, while the probe is immersed in a high temperature gas stream (1250K, 2atm). The transducers are cooled below 400K by using ordinary tap water (31N/cm^2, 143cm^3/sec).

Larguier [29] also presented in 1985 a fast response cooled probe designed for the study of the cooling systems of high temperature turbines. The measuring part of the probe has the shape of a cylindrical rod: 4mm in diameter with a pressure hole 0.8mm in diameter, normal to the sidewall. The position of the pressure hole is the result of an adjustment between the end effects, the effects of variation in diameter and the stiffness of the measuring part of the probe. The sensitive face constituted by a piezoelectric ceramic is located as close as possible to the pressure hole. The connection between the hole and the sensitive face is made by means of an elastomer. This one, very good transmitter for high frequency pressure, has the function of a thermal screen. In order to keep the piezoelectric sensing element temperature below the Curie point, a cooling water system runs across the measuring head of the probe. This temperature can be controlled at every time during the tests by means of a thermocouple. The broadband of the probe is quoted to be around 500kHz but there is no indication in the paper of Larguier about operating conditions at which the probe was tested.

3. Probe Design and Manufacturing

3.1. Probe Concept

In order to obtain both periodic and random fluctuations, and appropriate data for phase-locked-averaging and determination of turbulence levels, a cooled probe design is favored enabling continuous immersion in the hot flow. The probe concept is illustrated in Figure 1a.

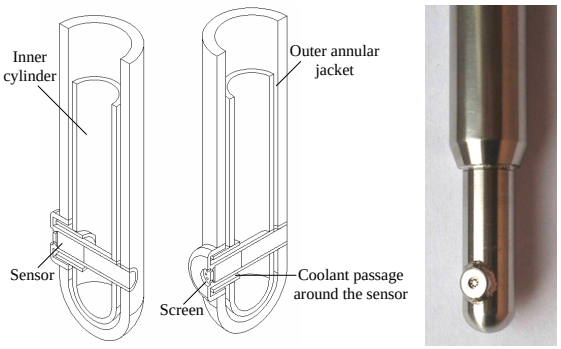

Figure 1: Fast response cooled total pressure probe concept (left) and tip region of the finished probe (right).

The probe is essentially based on a concentric tube assembly to bring and return the coolant fluid from the sensor region. The sensor itself is located transversally to the probe axis inside a tube which also incorporates the protective screen ahead of the sensor diaphragm. The sensor and screen cooling are performed by creating a narrow return channel around the

sensor by another transversal concentric tube assembly. The full details of the probe design can be found in Brouckaert et al. [30].

3D Navier-Stokes computations were carried out to determine the optimum cooling configuration, in particular to detect flow separation or stagnation regions possibly causing a local heating of the probe or sensor. The mechanical design was validated by comparison to FEM calculations.

4. Prototype Manufacturing and System Integration

4.1. Probe Material

The probe material is selected using the heat transfer predictions described previously and other properties such as corrosion resistance, welding considerations, structural and fatigue strength, resistance to creep and thermal stresses, as well as the amount of data available particularly at high temperatures, prior experience with the specific alloy under consideration, etc. In the present case, Inconel 600 was selected as it has the ability to retain a protective oxide coating under conditions of cyclic exposure to the temperature, while having a good resistance to carburization.

4.2. Manufacturing and Assembly

In order to manufacture the probe, a complex process including very small scale conventional CNC machining and electric discharge machining and laser welding is employed. Weld design is verified with the help of a dummy probe manufactured for the purpose, allowing hydraulic verifications for proper sealing and weld strength verifications.

Following the final assembly, the probe final welding was accomplished and the four cables connected to the sensor were soldered to the socket placed at the top of the probe (see Figure 1b). In order to seal the wires hermetically, the soldered regions were covered with resin. The threaded connector at the very left of Figure 6 is the socket for the sensor wires, where the two high-pressure hoses are the coolant feed and return lines. At the bottom-left are the temperature sensors to monitor the coolant feed and return temperatures.

4.3. Cooling System

The objectives of the design of the cooling system itself are twofold. Firstly, the system is conceived to provide the necessary cooling mass flow rate to the probe at high pressure. The objective of a highly pressurized water supply is to increase the boiling temperature of the cooling water. From the water phase diagram, at 50 bar, the water boiling temperature is near 560K ($\approx$287 °C). Pressurizing the probe internally also has the advantage to possibly equalize internal and external probe pressures to minimize mechanical stresses at high temperature. Finally, the system is conceived to reach the highest possible reliability and safety level in order to avoid any damage to an engine in case of failure of the system itself or leakage of the probe. The system is therefore designed with all necessary controls and alarms, bypass valves or switches in case of filter clogging, piston pump failure, loss of connection to the control room, etc.



(a) (b) (c)

Figure 2: Left, front and right views of the cooling system

A semi-closed loop system was favored in the present case, which is essentially a closed loop but with a non-pressurized reservoir. The main components of the system are a low pressure feed pump and a high pressure feed pump (up to 150 bar) with a 32 kW heat exchanger and a double set of filters placed on the low pressure line. The complete system is made of stainless steel to avoid corrosion problems and distilled water is used to avoid deposit of stains in the probe. The system also includes a high precision Coriolis mass flow meter and both coolant pressure and temperature are monitored to and from the probe. Finally, the system is equipped with a data acquisition board and a remote control for operation from a test cell control room. While the system is equipped with a programmable logic controller with full authority, all system parameters (mainly pressures, temperatures and cooling massflow) are monitored via a LabView program. Figure 2 shows a photograph of the system.

5. Calibration and Uncertainty

Static Calibration. The probe has been calibrated for both temperature and pressure. The pressure uncertainty and the zero offset were found to be decreasing with increasing temperature. Bearing in mind that the probe is calibrated for a pressure range of 2 bar, using a 14-bit acquisition system with a span of ±10 VDC and a calibrator that has an uncertainty of 0.05 mbar, the static calibration uncertainty on pressure was found to be 1.54 mbar which corresponds to 0.077% of the full-scale.

Aerodynamic Calibration. Following the static calibration, the cooled probe was placed in the VKI-C4 calibration facility in order to determine the pressure recovery ratio distribution with respect to yaw angle. The probe was yawed within ±90° range as shown in Figure 3. The pressure recovery ratio, C_p is defined as: $C_p = (P_{o,probe} - P_s)/(P_o - P_s)$. This allows to correct for the total pressure values measured when the relative flow angle is known; and furthermore, allows to operate the probe in the virtual 3-hole mode, yielding a number of additional flow parameters including yaw angle, static pressure and Mach number. The probe is found to be insensitive to incidence within 1% in the ±20° range. The yaw angle uncertainty in the virtual 3-hole mode is calculated as 0.59°, whereas the aerodynamic calibration uncertainty on the total pressure corrected for incidence is found to be 3.37 mbar. The uncertainties for static pressure and Mach number are calculated as 7.00 mbar and 0.004848 rescpectively.

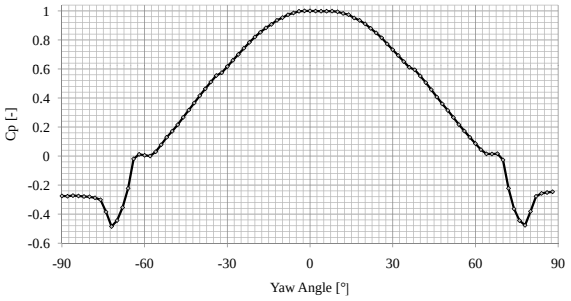

Figure 3: Yaw calibration in VKI-C4 Calibration Facility, Pressure recovery ratio plot, M=0.3

Dynamic Calibration. Finally, the probe has been tested in the VKI shock-tube facility in order to determine the transfer function and the natural frequencies of the screen-cavity system and the diaphragm. The result obtained from the shock-tube test on the probe is shown in Figure 4. The frequency spectrum obtained reveals the screen-cavity resonance around 60 kHz as expected from the predictions previously obtained by using the in-house code PreMeSys based on the line-cavity theory of Bergh & Tijdeman [31], 1965.

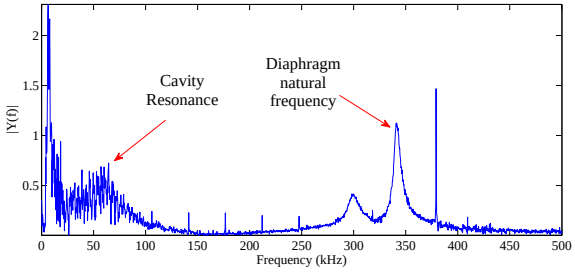

Figure 4: Experimental frequency spectrum from the shock tube test for the frequency response of the probe tested

6. Testing

6.1. Gas Turbine Exhaust Measurements

6.1.1. Experimental Set-Up

The very first testing of the cooled probe system in industrial environment was accomplished on the Rolls-Royce Viper test engine provided by Rolls-Royce within the HEATTOP project. The probe and the traverse system installed approximately three chords downstream of the turbine rotator is shown in Figure 6. The probe is traversed radially over approximately 75mm (Figures 7a and 7b).

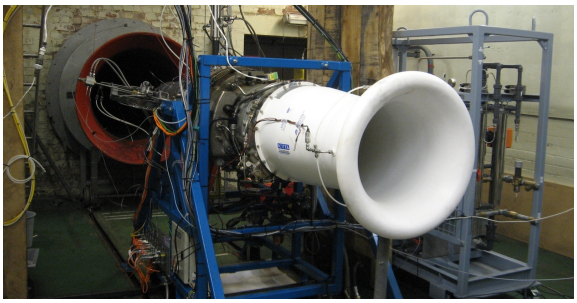

Figure 5: Photograph of the Rolls-Royce Viper test engine at Ansty, UK.

Although the probe was calibrated in pressure and temperature in the laboratory before the test campaign, an additional pressure calibration was per-

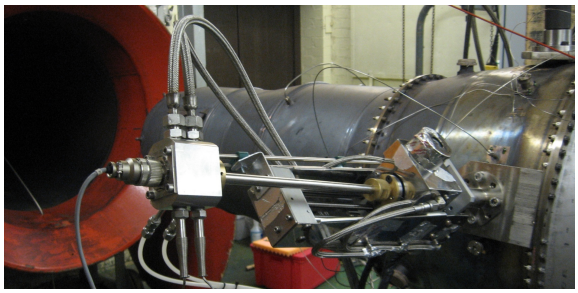

Figure 6: Photograph of the probe installed on the traverse gear mounted on the Viper turbine casing.

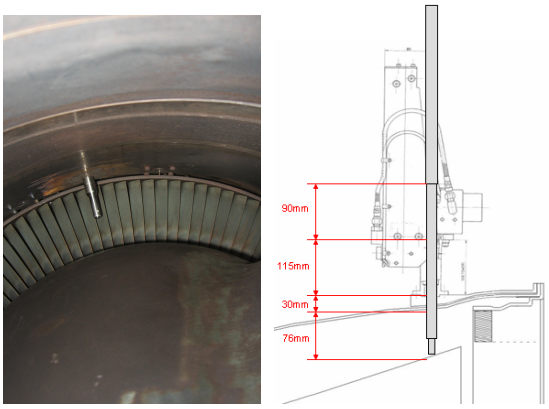

(a) (b)

Figure 7: Photograph of the probe inside the Viper engine jet pipe (left) and Sketch of the probe installed on the traverse gear mounted on the Viper turbine casing (right).

formed on site before the tests to avoid any drift errors.

A summary of the testing conditions is provided in Table 1. Test were performed at idle (≈4000 RPM), 8000, 10000 and 12800 RPM, which is the full thrust setting limited by the EGT (≈750 °C). The probe survived all tests including the full throttle conditions. However due to severe noise interferences on the electronics, no pressure data could be retrieved at these conditions. This motivated the use of a Faraday cage in further test campaigns to host amplifiers and data acquisition system as well as a UPS power supply including an isolation transformer to avoid interferences from the net.

6.1.2. Time-Averaged Measurement Results

The probe was traversed at zero degree setting angle with respect to the machine axis, the flow direction at part speed being unknown. An example of

Engine RPM	8000	10000	12800
Exhaust Gas Temp	440 °C	503 °C	750 °C
Comp. Delivery Press.	1.67bar	2.26bar	3.6bar
Cooling Mass Flow Rate	1.02 *l*/min	1.13 *l*/min	1.62 *l*/min
Cooling Pressure	50 bar	60 bar	72 bar
Water In Temp.	19.25 °C	20 °C	22.2 °C
Water Out Temp.	25.5 °C	28.25 °C	36.35 °C
Heat Extracted	0.5 kW	0.7 kW	1.75 kW
Sensor Membrane Temp.	73.5 °C	94.9 °C	99.3 °C

Table 1: Summary of test conditions and probe data for the Viper engine runs.

probe traverse is shown in Figure 8a in terms of time-averaged total pressure at 8000 and 10000 RPM. At these conditions, the exhaust gas temperature was respectively 440 °C and 503 °C. With the cooling pressure and flow rates indicated in Table 1, the sensor temperature was found to remain below 100 °C obtained by monitoring the sensor bridge voltage and is presented in Figure 8b. At full throttle conditions, the cooling water temperature increase did not exceed 15 °C, indicating a maximum cooling rate of 1.75kW at almost full immersion.

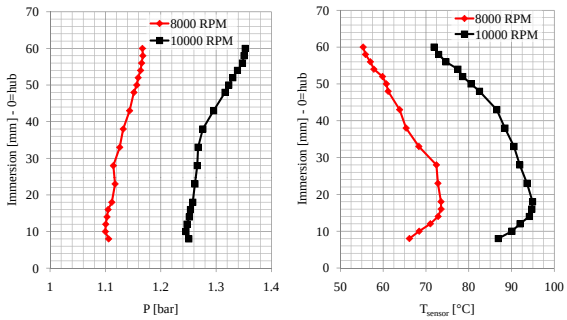

(a) (b)

Figure 8: Average total pressure (left) and sensor temperature (right) distributions behind the rotor at 8000 RPM and 10000 RPM

Yawing the probe at a fixed immersion depth yields the typical bell curves expected from angular calibrations. As it can be seen from the corresponding curves of Figure 9 at 8000 and 10000 RPM, the turbine exit absolute flow angle at this radial position can be assumed to be around -15 degrees from this data.

6.1.3. Unsteady Measurement Results

The sensor signal was acquired on a high speed 14-bit data acquisition system at a sampling rate of 1 MHz. At full throttle conditions (12800 RPM), with 113 rotor blades, this yields a blade passing frequency

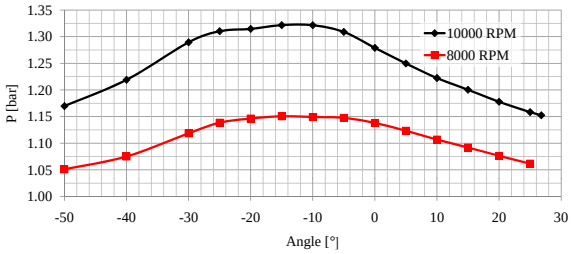

Figure 9: Probe angular response in engine at 8000 and 10000 RPM.

of 23.9 kHz, i.e. a resolution of 42 points per blade passage. The maximum storage capacity of the system being 262144 points, more than 6241 blade passages were recorded, or 55 full rotor revolutions.

Frequency Analysis. The recorded signals are first analyzed in the frequency domain. Figure 10 shows the power spectrum of a recording during a traverse at 10000 RPM. The fundamental frequency of blade passing (18.84 kHz) can be clearly seen as well as 3 harmonics up to 75.36 kHz. Another very clear frequency peak can be seen around 340 kHz which is the diaphragm natural resonance frequency for the 25 psi sensor.

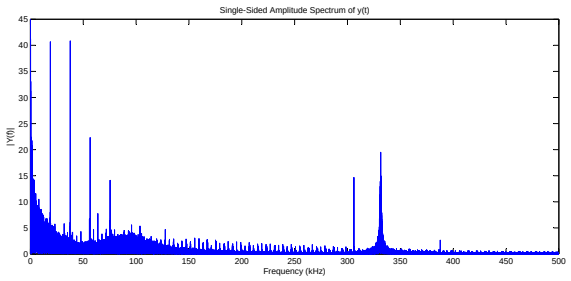

Figure 10: Power spectrum at 10000 RPM, immersion depth=43mm, T_{gas}=503 °C.

The resonance in the 90 kHz range is attributed to the sensor screen cavity resonance. As Ferguson explained in reference [14], the temperature of the gas in the recess cavity of the sensor-screen configuration affects the frequency response in such a way to increase the resonance frequency which is explained using the Helmholtz frequency (Eq. (1)) for a short line such as a hole in a thin plate. The Helmholtz frequency is directly proportional to speed of sound for a given geometry, hence a function of temperature. In Figure 11, the increase in Helmholtz frequency is plotted versus temperature and compared to the screen-cavity resonance frequency calculated using PreMeSys. An average temperature inside the cavity in front of the sensor can then be determined on the basis of the frequency found in the probe spectrum under hot conditions. The three points on Figure 11 show the cavity temperature estimated from the natural frequency of the screen-cavity resonance obtained by frequency spectra using this principle. According to this plot, the cavity temperature is estimated as approximately 350 °C, 470 °C and 730 °C at 8000, 10000 and 12800 RPM respectively whereas the gas turbine exhaust temperatures were 440 °C, 505 °C and 750 °C.

$$f_n = \frac{a}{2\pi}\sqrt{\frac{\pi d^2}{4LV_c}} \tag{1}$$

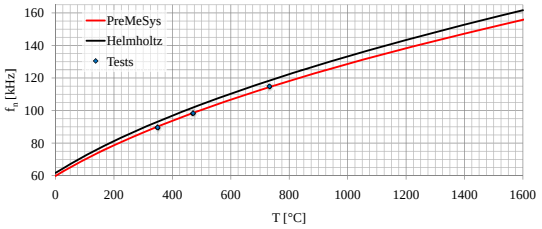

Figure 11: Comparison of screen-cavity resonance frequencies calculated using PreMeSys and Helmholtz formulation in eq. (1)

Raw Signal and Signal-to-Noise Ratio. Returning to the time domain, an example of raw signal is shown in Figure 12 over 10 blade passages. The simplest information to be extracted from the signal is the time averaged pressure level presented in Figure 8a as well as the corresponding pressure fluctuations. These are presented in terms of RMS in Figure 13 along the radial traverses at 8000 and 10000 RPM. An increase in the overall pressure fluctuations are seen proportional to the engine RPM and show a region of higher fluctuations in the hub region with peak values of 40mbar at 10000 RPM.

The signal-to-noise ratio is defined according to the following ratio:

$$SN = 20\ log\left(\frac{RMS_{signal}}{RMS_{noise}}\right) \tag{2}$$

The RMS value of the noise is taken from recordings with no flow prior to the engine runs. After amplification, the background electronic noise on the sensor was found to remain below ±3.52mbar RMS without the engine running. This value was found to

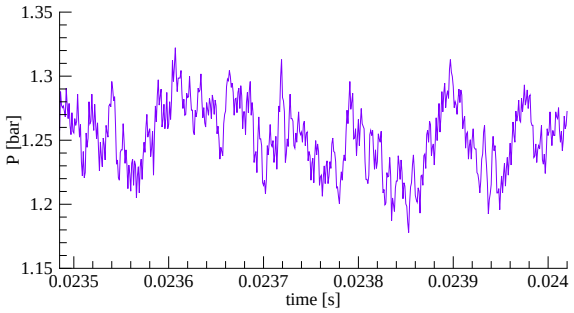

Figure 12: Example of raw pressure signal at 10000 RPM, immersion depth=5mm, T_{gas}=503^oC.

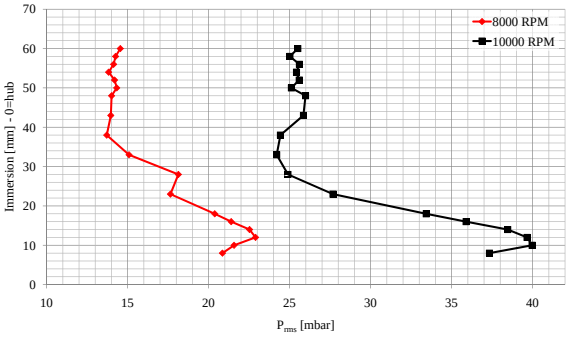

Figure 13: Pressure fluctuations at 8000 and 10000 RPM, T_{gas}=503^oC.

increase to ±7.18mbar when the engine was running but with the probe retracted. The hypothesis of no flow conditions on the sensor is of course questionable in this case. Nevertheless, as already mentioned earlier, it was found that the 3-phase generator on the engine, also used to generate a once-per-rev signal, was introducing electric interferences on the sensor signal increasing with engine RPM. The calculation of the signal-to-noise ratio according to Equation 2 yield 14.32 when the engine was running for midspan conditions (i.e. ≈25mbar RMS) at 10000 RPM, which is believed to be satisfactory.

Phase Locked Averaging and Filtering. In order to retrieve the average pressure fluctuation over a blade passing period, phase-locked averaging (PLA) is applied. The phase-locked averaging procedure applied to the raw data is based on the determination of the highest peak (corresponding to the blade passing frequency) in the Fourier spectrum of the signal.

A great advantage of the probe designed is having the probe continuously immersed in the hot gas path. This allows to study the effects such as length of the signal used at processing, effects of RPM variations, blade-to-blade non-uniformities or random unsteadiness of the flow. An important factor is the determination of the length of the signal used for phase-locked averaging. Normally, a once-per-revolution signal is used to correct for RPM changes during the recordings by re-sampling the recorded pressure signal while performing phase-locked-average computations. However, the Viper test rig was equipped with a once-per-revolution signal that comes from a triple-phase generator on the engine and was reconstructed from one of the sine waves, which is not stable with respect to RPM. In this test, due to the lack of a reliable once-per-rev trigger signal, the variations in the engine speed could not be taken into account. In addition, the phase information is lost. In the absence of the trigger, PLAs are performed for different lengths of the signal as shown in figure 14, and it is decided to use 2 revolutions corresponding to 226 blade passages.

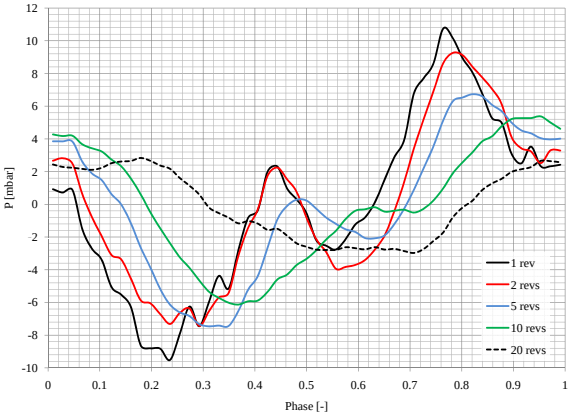

Figure 14: Phase-locked average of the pressure signal at 10000 RPM for different number of blade passages, immersion=23 mm from hub, T_{gas}=503^oC.

Effects of filtering on the signal are also evaluated. Statistics, such as minimum, maximum and RMS of the PLAs of raw, high-pass and low-pass filtered signals are shown in Figure 15. RMS of the PLAs are expressed using error bars. Applying a 10th order low-pass Butterworth filter with a cut-off frequency of 250 kHz slightly reduces the RMS of the phase-locked average whereas a 4th order Butterworth filter with a cut-off frequency of 10 kHz greatly reduces the RMS values as the low frequency content of the signal is also filtered out narrowing the min/max band. The low-pass filter applied only has a small effect on min/max values linked to the sensor natural frequency.

In the figure, the DC level is matched by adding the average pressure to the PLA of the high-pass filtered signal. It is worth to mention that PLA of the three signals fit perfectly on top of each other.

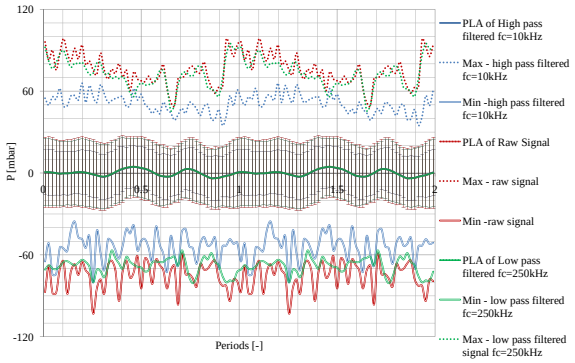

Figure 15: Phase-locked average of the pressure signal at 10000 RPM, immersion=23 mm from hub, T_{gas}=503^oC.

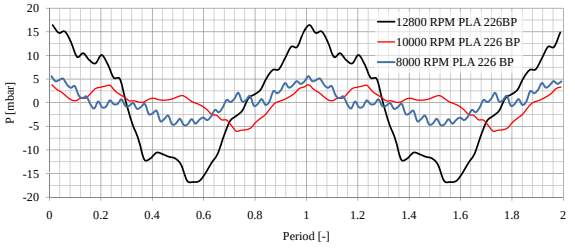

Figure 16: Phase-locked averages of the pressure signal at 8000 RPM, 10000 RPM and 12800 RPM. immersion=33 mm from hub.

Examples of PLAs obtained from recordings at mid-span at 8000, 10000 and 12800 RPM are shown in Figure 16 using 2 revolutions, where each period denotes a blade passage. The peak-to-peak value of the PLA now only amounts ≈8mbar (i.e. ±4mbar), far less than the RMS value of ≈25mbar at the same location. This corresponds to the periodic content of the signal and may be influenced by parameters like the total number of passages taken for statistics, blade-to-blade non uniform flow conditions or geometry, the stability of the turbine rotational speed, or a low frequency component in the signal. The phase-locked averaging should therefore be applied on the high-pass filtered signal.

The final result is obtained by plotting all phase locked averages over the full radial traverse. This may be done in a phase-span contour plot showing the unsteady pressure contours (see Figure 17) over several blade passages or even over a full rotor revolution.

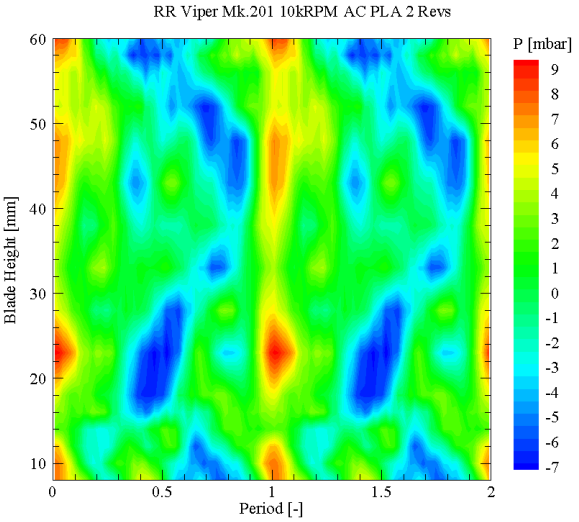

Figure 17: Phase-locked average map of the turbine exit total pressure at 10000 RPM, T_{gas}=503 °C.

6.2. *Virtual 3 hole mode*

Although the probe developed is a single-sensor probe, its angular characteristics can be further exploited as explained before. By yawing the probe at two different symmetric angular positions, the recordings will be equivalent to those obtained from the left, right and center pressures of a conventional 3-hole directional probe. The corresponding calibration curve is obtained by shifting the angular calibration curve for the single hole (see Figure 3). For the present study, this displacement between the three holes is chosen as 35 °. The yaw angle calibration coefficient as given in eq. (3) is then calculated and plotted with respect to yaw angle in Figure 18, allowing one to determine the yaw angle using left, right and center pressure values from subsequent recordings at those angular settings. It is important to note that the limitations of this procedure are inherent to the fact that the recordings are not simultaneous, and therefore only a periodic content of the fluctuations can be retrieved, provided that the flow conditions remain constant.

$$K_{yaw}(\varphi) = \frac{P_L(\varphi) - P_R(\varphi)}{P_{o,probe}(\varphi) - \frac{P_L(\varphi)+P_R(\varphi)}{2}} \qquad (3)$$

Mean flow angle was determined by yawing the probe within the hot gas path (see Figure 9). Flow angle being known to be around -15 °, the signals

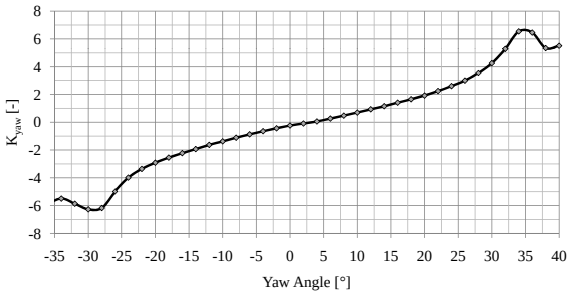

Figure 18: Yaw coefficient with respect to yaw angle

recorded at -50 °, -15 °and +20 °were used the virtual left, center and right holes respectively. Using the yaw angle calibration coefficient, the unsteady yaw angle can be calculated as shown in Figure 19. Using the calculated unsteady yaw angle, a new value of the unsteady total pressure, corrected for non-zero incidence according to the total pressure calibration coefficient is calculated as given in eq. (4). Corrected unsteady total pressure distribution is given in figure 20.

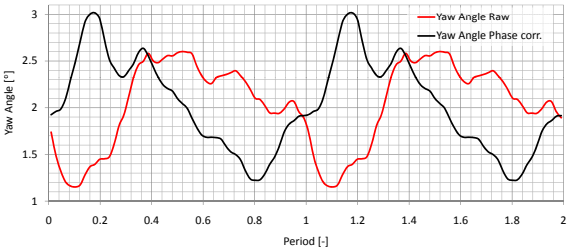

Figure 19: Unsteady yaw angle calculated - raw and phase shifted

$$K_o(\varphi) = \frac{P_o - P_{o,probe}(\varphi)}{P_{o,probe}(\varphi) - \frac{P_L(\varphi)+P_R(\varphi)}{2}} \tag{4}$$

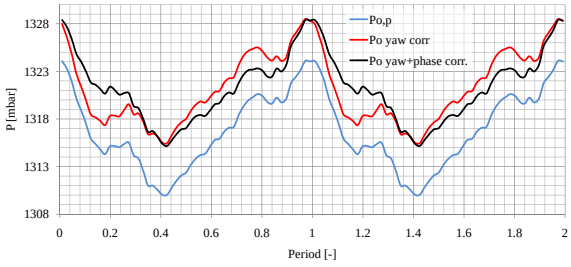

Figure 20: Total pressure distribution - Raw, Corrected for yaw angle, Corrected for phase shift and yaw angle

Mach number can also be exploited from the given set of data by defining a dynamic pressure calibration coefficient and a static pressure calibration coefficient, eq (5) and eq (6). The unsteady static pressure calculated (Figure 21) is then used to calculate the unsteady Mach number by the help of the isentropic relations.

Aerodynamic corrections. It is important to bear in mind that the virtual holes are not at the same position with the center hole. Hence, the left and right virtual holes are sensing the arrival of a blade at different phases with respect to the central hole requiring a corresponding shift to the left and right recordings (≈19.270% of a blade pitch) to be applied yielding the new unsteady yaw angle curve in Figure19. New curves for the corrected unsteady total pressure, static pressure and Mach number as well, as shown in Figures 20, 21 and 22.

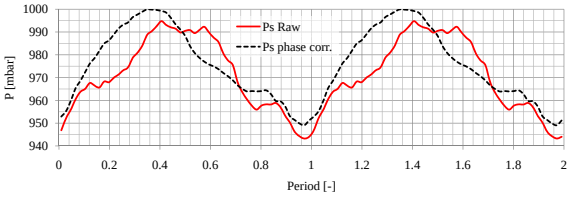

Figure 21: Pseudo-static pressure distribution at 10000 RPM, immersion=23 mm from hub, T_{gas}=503^oC.

Many of the unsteady aerodynamic errors affecting fast response pressure probes (added mass effects, unsteady lift, dynamic stall, von Karman vortex interactions, etc.) are directly proportional to probe size for a given probe geometry. Cylindrical probes have been shown to be the least sensitive to those errors [6]. However, blockage effects and phase corrections become mandatory here, even if the probe diameter (8 mm) can be considered as relatively small for a cooled probe arrangement.

The Viper turbine has a very high solidity design (113 blades) with a pitch of 12.54 mm. Although the probe was placed approximately 3 axial chords downstream of the rotor trailing edge, those blockage effects must be taken into account. This is done using the relation by Wyler [32], for cylindrical probes inserted sidewards halfway into an axisymmetric jet, eq. (7). The resulting corrected unsteady Mach number distribution is given in Figure 22. The average corrected Mach number is now around 0.61, rather than 0.68, which matches with the expected value but underlines once more the difficulty of obtaining available

comparison data for validation at those temperature levels.

$$q_{probe}(\varphi) = P_{o,probe}(\varphi) - \frac{P_L(\varphi) + P_R(\varphi)}{2} \quad (5)$$

$$K_{stat}(\varphi) = \frac{P_o - P_s}{q_{probe}(\varphi)} \quad (6)$$

$$\frac{\delta M}{M} = \frac{1}{\pi}\left[\frac{1 + \frac{\gamma-1}{2}M^2}{1 - M}\right][1.15 + 0.75(M - 0.2)]\left(\frac{D}{W_{bp}}\right) \quad (7)$$

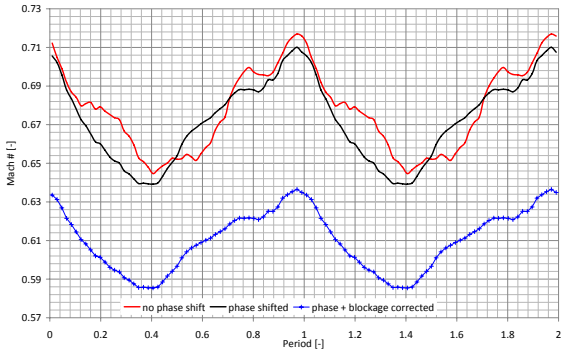

Figure 22: Mach number distribution at 10000 RPM, immersion=23 mm from hub, T_{gas}=503^oC.

6.3. Combustion Rig Measurements

The second testing opportunity for the probe and cooling system in industrial environment was again provided by Rolls-Royce within the HEATTOP project. A two-days testing slot was made available on the intermediate pressure combustion rig at Rolls-Royce Derby, UK.

6.3.1. Experimental Set-Up

The IP combustion rig allows testing of single or twin burners at pressures up to 7bar. The rig is composed of a central flame tube either metallic or quartz and has optical access through a side quartz window (Figure 23). This concentric arrangement allows the passage of a secondary air flow around the central flame tube for cooling purposes. The temperature of the cooling air is of the order of 20 °C. The flame tube was instrumented with thermocouples and with a wall-mounted high temperature piezo-resistive static pressure transducer and a pneumatic pressure tap to monitor the can pressure and temperature.

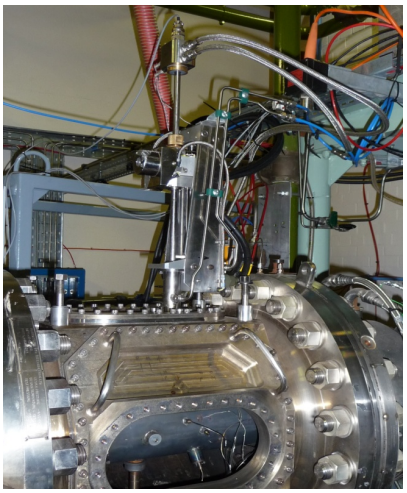

Figure 23: Rolls-Royce IP Combustion Rig, optical access window, probe and traverse gear mounted.

Tests were conducted on a twin burner with kerosene at various air-fuel ratios, up to the maximum allowable can wall temperature of approximately 1000 °C (see Table 2). The rig was operated at pressures remaining below 4 bar so as not to exceed twice the rated pressure range of the probe sensor (25psiA≈1.72 bar absolute). The flame temperature can not be accurately measured and is therefore calculated for centered or mixed out conditions. The highest and most severe conditions obtained were exceeding 1650 °C bulk temperature. At these temperatures, the flame tube is glowing red as seen in Figure 24.

Point	T_{can} [°C]	P_{scan} [bar rel]	T_{bulk} [°C]	$T_{exhaust}$ [°C]
1	337	1.42	648	544
2	472	1.66	868	637
3	550	1.68	953	658
4	583	1.69	1018	689
5	640	1.66	1176	751
6	580	1.69	916	645
7	882	1.82	1521	840
8	922	1.8	1585	862
9	951	1.84	1658	886
10	984	2.28	1556	912

Table 2: Rolls-Royce IP Combustion Rig, summary of test conditions.

6.3.2. Results

The traverse gear is mounted on the external mount plate, allowing the probe to be traversed through the secondary air flow down inside the central flame tube

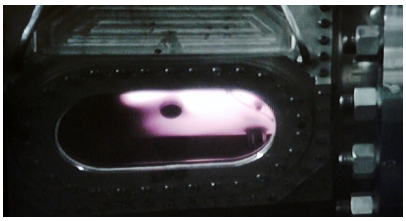

Figure 24: Rolls-Royce IP Combustion Rig, flame tube at maximum operating temperature (T_{wall}=984 °C, T_{bulk}=1556 °C)

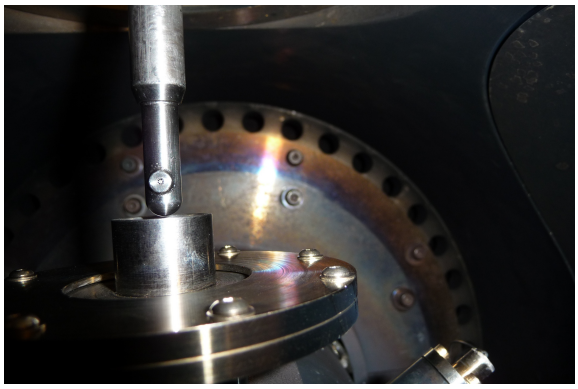

Figure 25: Rolls-Royce IP Combustion Rig, probe retracted in secondary air flow channel, before tests.

(Figure 25). The probe was retracted from the flame tube, remaining in a cylindrical jacket into the secondary air flow (Figure 25) during the burner startup.

Data was sampled at 1 MHz on a high speed data acquisition system for measurements at a fixed location in the flame tube or at 2 kHz during continuous traverses into the flame tube over slightly more than 2 minutes. The acquisition system and signal conditioning amplifiers were placed in the test cell protected by a Faraday cage and an electrical isolation system comprising of an isolation transformer and an on-line UPS filtering any spikes or noises transmitted through the electrical network and providing a regulated voltage to the systems.

An example of signal recorded during a continuous traverse down to the center of the flame tube is shown in Figure 26. The can pressure as measured by the pneumatic pressure transducer is indicated by the continuous line . Under these conditions (T_{bulk}=1521 °C, P_{can}=1.82bar relative), and with a cooling rate of approximately 10 *l*/min at 32bar water pressure, the sensor diaphragm temperature was found to have reached 210 °C. The probe survived all tests, up to these extremely harsh conditions (Figure 24). The probe after the IP rig test campaign is shown in Figure 27.

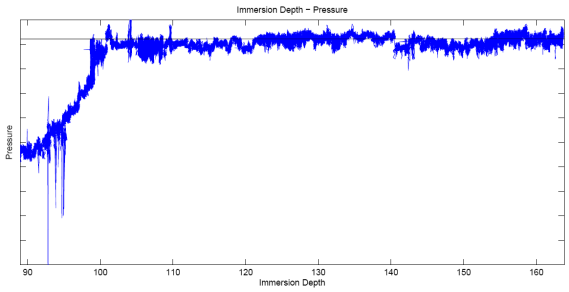

Figure 26: Rolls-Royce IP combustion rig, total pressure along a continuous probe traverse down to the center of the flame tube. T_{bulk}=1521 °C, P_{can}=1.82bar relative

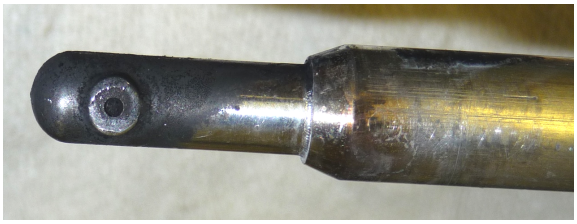

Figure 27: First prototype of the VKI fast response cooled total pressure probe after testing in the RR IP combustion rig.

An example of raw pressure signal showing fluctuations under rumble conditions is shown in Figure 28. Again, the continuous line indicates the can pressure as measured by the pneumatic pressure transducer. Under the same probe cooling settings, the measured sensor diaphragm temperature was 178 °C, for a flame temperature of T_{bulk}=1556 °C for a different air-to-fuel ratio and hence a different temperature distribution.

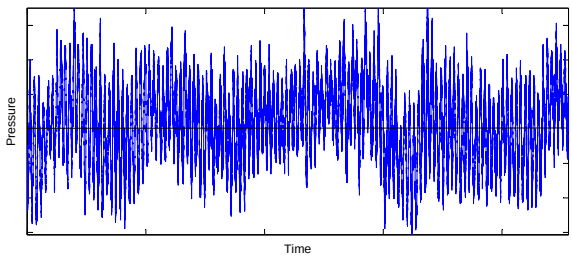

Figure 28: Rolls-Royce IP combustion rig, time series of fluctuating pressure at rumble conditions. T_{bulk}=1556 °C, P_{can}=2.28bar relative

The power spectrum of a recording at the center of the flame tube is shown in Figure 29 during rumble conditions. Unlike the measurements behind the turbine rotor of the Viper engine, the sensor natural resonance frequency is barely visible, practically not excited due to the low frequency instabilities. The screen cavity resonance is also barely visible for the same reasons. No significant frequency content can be found beyond 40 kHz and most of the frequencies of interest are to be found in the range of a few kHz (Figure 29) as expected.

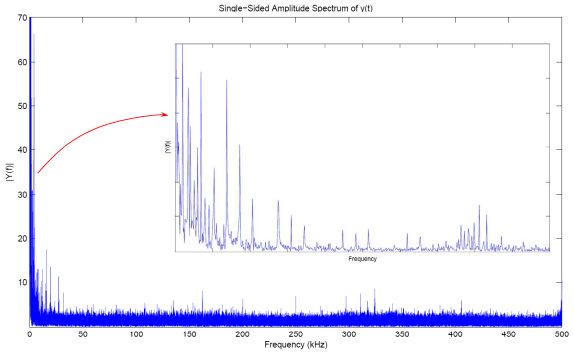

Figure 29: Rolls-Royce IP combustion rig, full power spectrum and low frequency content at rumble conditions. T_{bulk}=1556 °C, P_{can}=2.28bar relative

7. References

8. Conclusion

First experimental results obtained with the fast response cooled total pressure probe developed during a three year research and development program witin the EU FP6 program HEATTOP are presented. The design process is explained in detail by Brouckaert et al. [30] and [7]. Summarizing, a commercial off-the-shelf piezo-resistive miniature pressure transducer is employed within an 8 mm diameter probe, with heat transfer to the probe, internal cooling and structural engineering of the probe being the most challenging issues. Following the probe design an appropriate cooling system is designed and built allowing safe operation of the probe in extremely harsh conditions. The probe has been first fully characterized in terms of static, aerodynamic, and dynamic calibrations.

First testing in real turbo-machinery environments is reported. Full radial traverses were performed in the exhaust gas stream of a Rolls-Royce Viper engine to measure the high frequency pressure fluctuations downstream of the turbine. At full throttle conditions, 12800 RPM, the probe was able to pick up the blade passing frequency (23.9kHz) as well as several harmonics up to 95.6kHz, at a pressure of 3.2bar and a temperature of 750 °C. Not only the steady and unsteady total pressure at the scale of a blade passage, but also the unsteady yaw angle are presented using the probe in a virtual 3-hole mode. The unsteady static pressure and Mach number are also derived by means of this technique. Suitable corrections are applied for blockage and for phase shift of the recordings. First measurements in an intermediate pressure combustion rig are reported as well. The probe survived extreme temperature conditions in the flame tube up to 2000K.

Acknowledgments

This work is supported by the EU Framework Program 6 project HEATTOP (Accurate High Temperature Engine Aero-Thermal Measurements for Gas Turbine Life Optimization Performance and Condition Monitoring) under Contract No. AST5-CT-2006-030696. HEATTOP is a new collaborative research project, which aims to develop new, more durable, more accurate instrumentation for high temperature gas turbine applications. It has a total budget of 9 million Euros, including 5 million Euros in funding from the European Commission. Siemens PG leads a consortium of 17 partners gathering major European engine manufacturers, supply chain companies, universities and research centers. The work in this paper has been performed under WP4 “Advanced Gas Path Measurements”.

References

[1] EVI-GTI, The lab gap matrix, On the WWW, at `http://www.evi-gti.com`, excel file.

[2] PIWG, Sensor specifications, On the WWW, at `http://www.piwg.org`.

[3] J. Roberts, Requirements for instrumentation technology for gas turbine propulsion systems, in: Advanced Measurement Techniques for Aero Engines and Stationary Gas Turbines, VKI LS 2004-04, 2004.

[4] H. Niska, Requirements for advanced high temperature instrumentation and measurements in gas turbine engines, in: Advanced High Temperature Instrumentation for Gas Turbine Applications, VKI LS 2009-06, 2009.

[5] D. L. Simon, S. Garg, G. W. Hunter, T.-H. Guo, K. J. Semega, Sensor needs for control and health management of intelligent aircraft engines, in: Proceedings of the ASME Turbo Expo, ASME GT2004-54324, 2004.

[6] P. Kupferschmied, P. Koppel, W. Gizzi, G. Roduner, C. andGyamarthy, Time-resolved flow measurements with fast-response aerodynamic probes in turbomachines, Measurement Science and Technology 11 (7) (2000) 1036–1054.

[7] J. Brouckaert, M. Mersinligil, J. Desset, M. Pau, Development of a high temperature fast response cooled total pressure probe, in: Advanced High Temperature Instrumentation for Gas Turbine Applications, VKI LS 2009-06, 2008.
[8] C. Sieverding, T. Arts, R. Dénos, J. Brouckaert, Measurement Techniques for Unsteady Flows in Turbomachines., Experiments in Fluids, Springer Verlag Vol. 28 (Nr. 5), presented at IGTI Conference Stockholm 1998.
[9] R. W. Ainsworth, R. J. Miller, R. W. Moss, S. Thorpe, Unsteady Pressure Measurement, Meas. Sci. Technol. Vol. 11.
[10] Kupferschmied, P.; Köppel, P.; Gizzi, W.; Roduner, C.; Gyamarthy, G., Time-Resolved Flow Measurements With Fast Response Aerodynamic Probes In Turbomachines., Meas. Sci. Technol. Vol. 11.
[11] J. Chivers, High temperature pressure sensors for gas turbine applications, in: Advanced High Temperature Instrumentation for Gas Turbine Applications, VKI LS 2009-06, 2009.
[12] D. G. Ferguson, P. C. Ivey, Unsteady pressure measurement in a high temperature environment using water cooled fast response pressure transducers, in: IGTI TURBO/EXPO paper no 95-GT-345, Houston, Texas, The U.S., 1995.
[13] D. G. Ferguson, P. C. Ivey, A high-temperature assessment of air-cooled unsteady pressure transducers, Transactions of the ASME 120 (1998) 608–612.
[14] P. C. Ivey, D. G. Ferguson, An air cooled jacket designed to protect unsteady pressure transducers at elevated temperatures in gas turbine engines, in: Proceedings of ASME Turbo Expo 2002, Amsterdam, The Netherlands, 2002.
[15] A. Passaro, J. E. LaGraff, M. L. G. Oldfield, L. Biagioni, Fast acting probe for measurement of turbulent pressure and temperature fluctuations in a gas turbine combustor, in: 44th AIAA Aerospace Sciences Meeting and Exhibit, AIAA 2006-550, Reno, Nevada, 2006.
[16] M. L. G. Oldfield, R. Lubbock, Fast insertion pressure and temperature probes, in: Advanced High Temperature Instrumentation for Gas Turbine Applications, VKI LS 2009-06, 2009.
[17] I. Langmuir, The pressure effect and other phenomena in gaseous discharges, in: J. of the Franklin Institute, Vol. 196, 1923, pp. 751–762.
[18] J. Grey, Thermodynamic methods of high temperature measurement, in: ISA Transactions, Vol. 4, 1965, pp. 102–115.
[19] J. Grey, Probe measurements in high-temperature gases and dense plasmas, in: E. R. G. Eckert, R. J. Goldstein (Eds.), AGARDograph on 'Measurement Techniques in Heat Transfer', Vol. 130, NATO AGARD, 1970, pp. 269–307.
[20] G. C. Ashby, Jr., Pressure measuring probe, United states patent 4783994 (1988).
[21] N. T. Lagen, G. D. Reece, J. W. Eves, S. L. Geissinger, Water cooled static pressure probe, United states patent 5076103 (1991).
[22] D. Warnack, An optimized pneumatic probe for investigation of gas turbine aerodynamics in full scale gas turbines, in: Proceedings of ASME Turbo Expo 2002, Amsterdam, The Netherlands, 2002.
[23] S. J. Anderson, K. S. Chana, A. J. W. Wilson, Design, development and testing of an in-engine radial traverse system for the trent engine, in: Proceedings of ASME Turbo Expo 2008, Berlin, Germany, 2008.
[24] X. L. Yang, R. Miller, H. P. Hodson, A new probe for the measurement of high-temperature gases, in: 16th Symposium on Measuring Techniques in Transonic and Supersonic Flow in Cascades and Turbomachines, Cambridge, UK.
[25] M. Massini, R. Miller, H. Hodson, A new intermittent aspirated probe for the measurement of high temperature gases, in: Proceedings of the ASME Turbo Expo, ASME GT2008-50581, 2008.
[26] M. Massini, R. Miller, H. Hodson, Intermittent aspirated probe for measurements of stagnation pressure and temperature, in: Advanced High Temperature Instrumentation for Gas Turbine Applications, VKI LS 2009-06, 2009.
[27] W. C. Nieberding, J. Englund, D. R., Modularized instrument system for turbojet engine test facilities, in: A. Fuhs, M. Kingery (Eds.), Symposium on Instrumentation for Air-breathing Propulsion, Progress in Astronautics and Aeronautics, Vol. 34 of NASA-TM-X-68123, MIT Press, 1972, pp. 206–215.
[28] M. T. Moore, High temperature-high response fluctuating pressure measurements, in: G. G. Fazio (Ed.), ASSL Vol. 63: Infrared and submillimeter astronomy, 1977, pp. 469–473.
[29] R. Larguier, Experimental analysis methods for unsteady flows in turbomachines, in: International Symposium on Air Breathing Engines, 7th, Beijing, People's Republic of China, September 2-6, 1985, Proceedings (A86-11601 02-07). New York, AIAA, 1985, p. 279-289., 1985, pp. 279–289.
[30] J. Brouckaert, M. Mersinligil, M. Pau, A conceptual design study for a new high temperature fast response cooled total pressure probe, Transactions of the ASME, Journal of Engineering for Gas Turbines and Power 131 (2).
[31] H. Bergh, H. Tijdeman, Theoretical and experimental results for the dynamic response of pressure measuring systems, NLR-TR-F.238, 1965.
[32] Wyler, J.S., Probe blockage effects in free jets and closed tunnels, Journal of Engineering for Power Vol. 97 (No 4).

FLOW IN COMPRESSORS

Numerical investigation of secondary flows in low pressure axial compressor stage for contra-rotating turbofan architectures

Balazs Farkas

Turbomachinery and propulsion Department, farkas@vki.ac.be

Supervisor: Jean-François Brouckaert

Assistant Professor, Turbomachinery and propulsion Department, von Karman Institute for Fluid Dynamics, Belgium, brouckaert@vki.ac.be.

Abstract

The following paper presents the extended numerical studies of a one and a half stage axial compressor designed for the LP compressor of a contra-rotating fan engine architecture. The particularity of this design is given by the fact that the LP compressor rotor is mounted on the same shaft as the second fan stage which results in a lower rotational speed and therefore a much higher loading as encountered in conventional high bypass-ratio aero-engines. The compressor itself was designed and manufactured at VKI and subsequently tested in the closed loop test facility (VKI-R4) which allowed to compare numerical predictions with experimental data. In this study, particular interest was given to investigate the effect of the seal-leakage flow around the stator hub platform on the performance. To study the effect the seal-leakage flow, three different seal cavity configurations with different seal-tooth gap sizes were simulated in comparison with eliminated cavity effect and furthermore with a case where the effect of the cavity flow was simulated by injection and suction implemented at the position of the seal cavity trenches. This set of investigations allowed to assess the different models by comparison with the results obtained experimentally. This comparison was made on the global performance of the stage, including the impact on the stability range, as well as on the flow field itself in particular in the rotor and stator exit planes. The computations were performed by using Numeca developed code Fine-Turbo with steady RANS solver.

Keywords: axial compressor, secondary flow, numerical stability, labyrinth sealing

1. Introduction

Because of mechanical considerations booster stages in in aero engines are mostly hub shrouded therefore the investigation of the effect of the seal cavity flows when it turns to low pressure compressor stages seems to be inescapable. Wellborn *et al.* [1] & [2] performed a detailed study on a multi row low speed axial-flow compressor to investigate the effect of the seal cavity flows of shrouded stators. They found that increased seal-tooth leakage degraded the performance and radially redistributed the loading. Similar tendencies were shown by Lange *et al.* [3] where a 4-stage low speed axial compressor representative for rear stages of a large multistage machine was investigated. It is important to mention that apparently none of the above mentioned studies found any change in the stall margin as different leakage mas flow rate was imposed. Demargne *et al.* [4] investigated the stator shroud leakage flow effect on a straight cascade which allowed to change the tangential velocity component of the leakage flow independently which they showed has also effect the performance until high cavity tangential velocities where the stagnation pressure loss generated in the hub region becomes insensitive to the leakage. Demargne also showed that imposing extraction at the downstream cavity affects the loss at the passage exit, but has a negligible effect on the mechanisms generating loss at the upstream slot. Similar experiment was performed by Shon *et al.* [5]. Here they found that increased leakage tangential velocity reduces the mixing loss between leakage and passage flow and also reduces the overall loss. Investigating the governing mechanisms of the three-dimensional flow separation in axial compressors Lei [6] found that cross stream mo-

mentum introduced to the flow in the direction opposite to the blade passage secondary vorticity can mitigate the hub corner stall. In accordance with this Heidegger *et al.* [7] found that in their particular case there was an optimal leakage flow rate with respect to the leading edge incidence of the given high-speed compressor stator which was not at zero leakage flow.

2. Numerical setup

2.1. Geometry

The geometry used for the numerical simulation is representative for the first stage of the booster of a high by pass ratio counter-rotating turbofan (CRTF) engine. The design was made in the framework of the European FP7 project VITAL (EnVIronmenTALy Friendly Aero Engine) work package 3.2 by the Von Karman Institute (VKI) and was manufactured and tested in VKI-R4 closed loop test facility. Compared with conventional Direct Drive Turbofan (DDTF) engine boosters this compressor has higher loading coefficient as well as higher flow coefficient and as a result of further design considerations also relatively low aspect ratio. To simulate the effect of the upstream fans there was an Inlet Guide Vane (IGV) was installed to match the rotor relative inlet angle distribution, and hence the correct loading distribution when the work distribution is imposed. Important to note that the work distribution of the rotor which is typical of a booster stage, i.e. mainly hub loaded to straighten the highly non-uniform radial flow profile leaving the fan hub region before entering the HP compressor. The peak diffusion factor and peak rotor work coefficient are therefore located at the hub. The cross section of the machine is presented in Fig. 1 and further details about the design can be found in Brouckaert *et al.* [8][9] . As one can see in Fig. 1 the geometry of the seal cavity is quite different from the geometries of the seal cavities used at the stators of shrouded multistage axial compressors. One of the important differences is that the downstream wall of the downstream trench (the intake of the seal cavity) is not rotated and it is not connected with labyrinth sealing although according to Heidegger *et al.* [7] most of the energy in case of conventional built up is added to the leakage flow by the rotating wall of the downstream trench and the rotating wall of the cavity ahead of the seal tooth connected to it. Also the volume of this part of the cavity is significantly higher than as it is in conventional sealing channels allowing to form larger vortex structures. As one can also notice, in this design the seal cavity is also connected to the bearing house across an other labyrinth sealing. However it was assumed that there is no difference in pressure between this cavities at steady operational circumstances which means that the mass-flow across this sealing can be neglected.

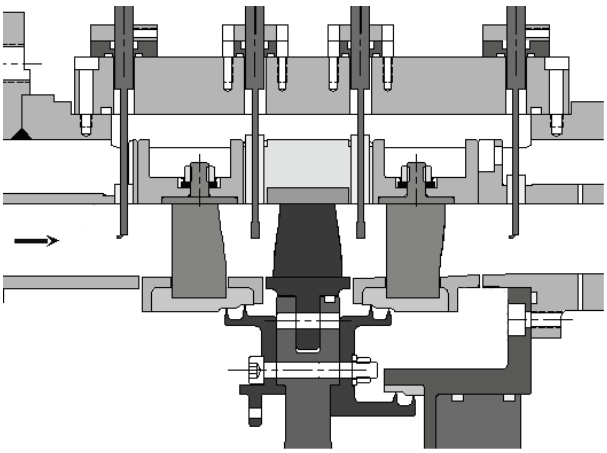

Figure 1: Cross sectional view of the compressor stage

2.2. Numerical domain

The 3D blocks representing the numerical domain are presented in Fig. 2.The mesh was generated with Numeca‘s AutoGrid5 mesh generator. In the blade passage the mesh is based on its general O4H topology combined with a butterfly OH grid in the tip-gap. To achieve grid independent solutions several grids were tested and as a result the mesh holds in total 12 Millions grid points (0.8 Millions for IGV, 3.1 millions for the rotor, 1.9 millions for the stator and 6.1 millions for the seal cavity). The first cell height at the solid boundaries allows to run low-Re models, i. e. the y+ values at the first cell are around one and nowhere exceeding two. The seal cavity was slightly simplified and the connection with the bearing house was neglected. Between the cavity and main channel full-matching connection was applied. The cavity is also divided to two parts using a rotor-stator (R/S) interface as it shows in Fig. 2. This is due to the fact that the upstream trench (the axial gap between the hub of the rotor and the stator) of the seal cavity is connected to the main channel upstream of the R/S interface between the rotor and stator blocks. Such a set-up allows to study the effect of the non-axisymmetric flow field on the seal leakage flow injection which dissipates downstream of the R/S interface because of the circumferential averaging process applied to connect the

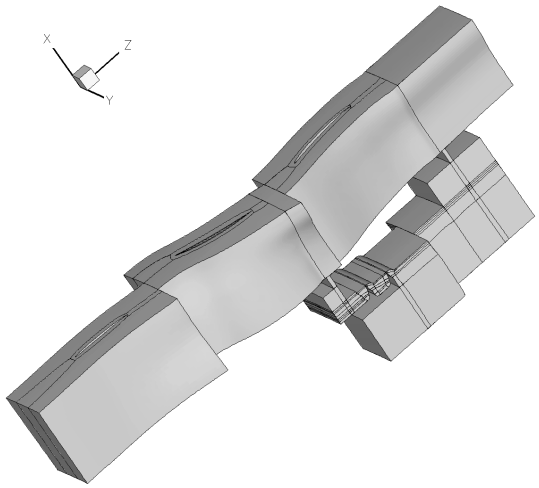

Figure 2: 3D blocks of the numerical domain

rotating and non rotating blocks. Meanwhile the non-axisymmetric effects inside a seal cavity are less determinate therefore applying the same averaging method here has less significant effect on the final result.

For the numerical simulations, Numeca's Fine/Turbo Software package was used. This code solves the steady compressible Reynolds Averaged Navier-Stokes equations with using a second order cell centered finite volume method and employing a 4-step Runge-Kutta method with an implicit (Zhu) residual smoothing phase for the (pseudo-) time and central scheme with Jameson type dissipation for the space discretization. The closure problem was faced with using the in-build low-Reynolds Yang-Shih k-ε turbulence model which showed the best performance from the other available models in case of loss prediction and stability.

As boundary condition (BC), axial injection was applied at the inlet with the measured total pressure, total temperature and turbulence profiles where the turbulence profiles were corrected at the solid boundaries by using the results of the computations on the inlet bulb. At the outlet, radial equilibrium throttle condition was applied, fixing the static pressure at the shroud.

This study involved the simulation of 4 different cavity configurations. In the first case, referred as Base-line configuration, the cavity itself was eliminated. The second case was performed with nominal gap size between the stator shroud and the tip of the seal-tooth (Fig.3), for the third case gap size was reduced to its half and the fourth case was performed with removing the seal tooth. An additional case were also studied where the effect of the seal cavity flow was simulated by applying forced injection at the upstream trench location and suction at the downstream trench location.

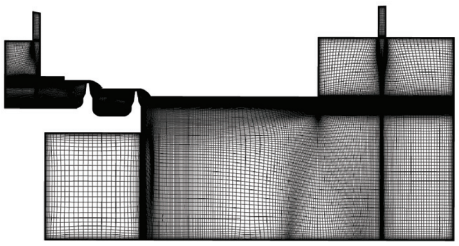

Figure 3: Cross sectional view of the cavity mesh

3. Discussion

3.1. Overal Performance

The overall performance curves of the compressor stage are presented in Fig. 4 where the total-to-total and total-to-static pressure ratio and total isentropic efficiency is plotted in the function of the reduced mass-flow. Numerically the last converged point was found by increasing the imposed static back-pressure until the solution did not converge anymore. Experimentally the performance was measured at four throttling points from choke to stall. At intermediate points it was found that at no knife case where the highest mass flow is passing through the seal cavity the performance is unambiguously dropped compared with the base-line case and this difference is increased with increased loading. On Fig. 5 where the change in pressure ratio and efficiency is plotted in the function of the gap height it can be seen that in case of other clearances this tendency is not that straightforward anymore. At nominal gap size case the performance is dropping as the loading increases although at design it shows small improvement compared to the base line case, meanwhile at half gap size there is an unexpected peak in efficiency with increased throttling. The leakage mass-flow rate relative to the main mass flow rate increases with increased loading in every cavity configurations (Fig. 6) and this increasement has a sudden drop as the throttling reaches the stall condition meanwhile the absolute value of the leakage mas flow rate just slightly increases and in case of forced injection this flow rate is hold constant. It also has to be mentioned here that the difference

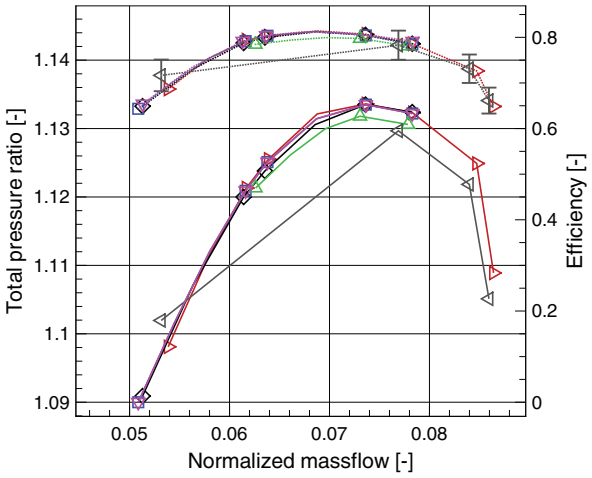

(a)

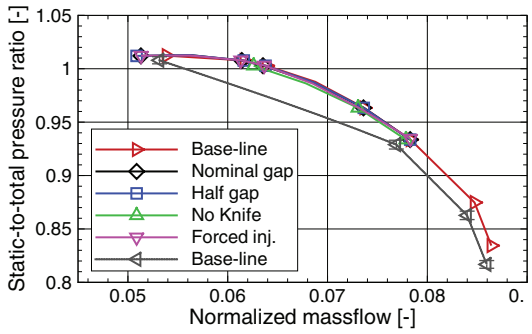

(b)

Figure 4: Total pressure-ratio, efficiency and static pressure-ratio in function of normalized mass-flow at different seal cavity configurations

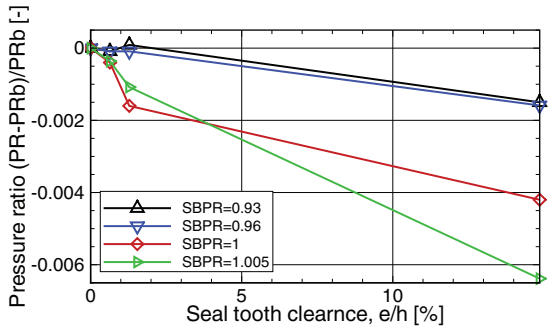

(a)

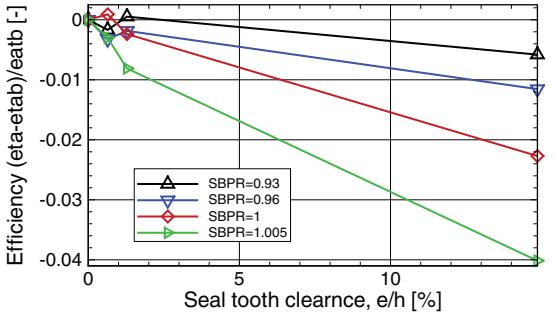

(b)

Figure 5: The variation of pressure ratio (a) and efficiency (b) in function of seal tooth clearance at different throttling conditions (SBPR static-back-pressure-ratio)

of the flow rate between the inlet and the outlet of the cavity reaches 5% respect to the cavity inlet mass-flow rate due to computational errors.

3.2. Blade element performance

Figure 7 shows the pitch wise average radial distribution of the absolute total pressure at the outlet of the rotor. The data were extracted in a plane downstream from the seal cavity trench at the location of the probe inserts. It shows that at design Fig. 7(a) the predictions are roughly consistent with the measurements however there is a noticeable difference appearing at the hub region. Touyeras *et al.* [10] faced with similar discrepancy and found that simulating leakage flows in their computations significantly reduced the difference between numerical and experimental results but nevertheless the expectations in our case the difference were barley changed. Due to the blockage imposed by the leakage flow there is just a moderate drop in Stagnation pressure which increases proportionally with the injected mass flow. Due to the interaction between the main and leakage flow the axial velocity and tangential velocity (Fig. 8(a)) decrease at the hub which can be interpreted as an increasement in axial momentum thickness as also pointed out by Demargne *et al.* [4]. As it can be seen on the tangential velocity distribution the injected flow effects the main flow distribution within the lower 15 % of the blade height by increasing the boundary layer thickness but also pushing fluid with higher tangential velocities toward the mean radius. Noticeable change in the incidence distribution just appears in case of high injected mass flow rate when the seal knifes were removed and also when forced injection was applied since the injection in this case is almost purely radial without significant circumferential velocity component which further increases the tangential momentum thickness.

Figure 9 shows the distribution of pressure loss co-

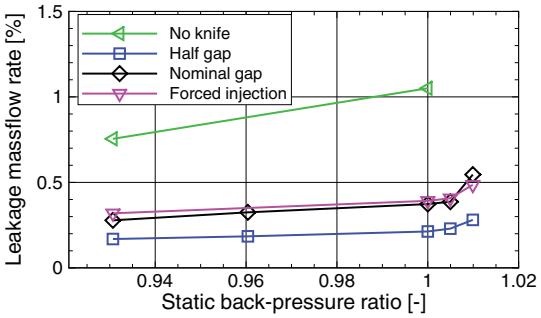

Figure 6: Leakage mass-flow rate in function of static back-pressure ratio

efficient along the blade height. As it is expected the most severe changes occur in no-knife case where high amount of the low energy fluid coming from the seal cavity piles up at the stator blade suction side and also displaced radially toward the mid-span as a result of the increased momentum thickness which enhanced the end-wall secondary flows. The secondary flows also effects the deviation which appears in slightly decreased turning (Fig. 10) within the first 40 % of the span. Contrary to previous observations by other authors the appearance of the leakage flow does not modify the main flow above mid-span.

Comparing with the experimental results all cases predict less losses and higher gradients in total pressure distributions (Fig.11 & 12). There is also a significant difference in the extension of low stagnation pressure area at the hub corner where the measured distribution of the stagnation pressure might also indicate hub corner stall. However using the D parameter criteria from Eqn. 1 derived by Lei [6] it was found that at 10% of the stator span the D parameter is 10.8 at design (calculated form the measured absolute flow angles) which is well below 20 which was set as critical value. Therefore the appearance of hub corner stall is unlikely.

$$D = \frac{(1 - (\frac{\cos \alpha_{in}}{\cos \alpha_{out}})^2)(\alpha_{in} - \alpha_{out})}{\sigma} \qquad (1)$$

At this point it also has to be mentioned that significant difference in turning occurs at the shroud area where apparently the effect of the tip leakage is not caught by the numerical solution. According to the fact that the extension and strength of the vortex is well predicted behind the rotor the differences must be caused by the averaging process across the R/S interface between the rotor and stator blade rows.

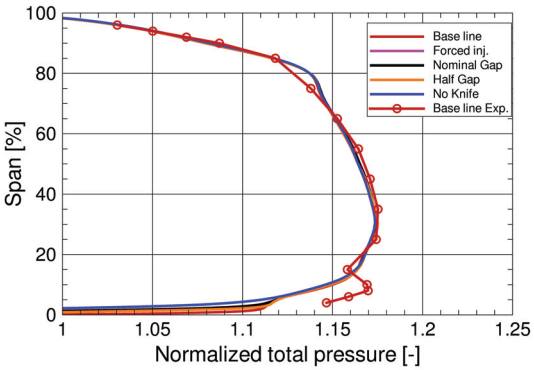

(a)

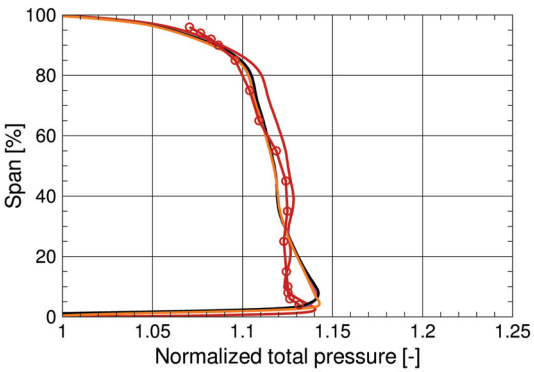

(b)

Figure 7: Radial distribution of pitch wise averaged total pressure behind the rotor at SBPR=0.93 (a) and at SBPR=1.01 (b)

3.3. Blade performance at critical throttling

The stream traces of viscous stress at Base-line case are presented in Fig. 13 (a) (b) at different throttling cases. The stream traces show a growing separation area on the stator surface originating from the hub which at stall covers almost the whole blade span and is attached also to the hub end-wall. The reason of the extensive separation already at design is due to the low solidity and high loading imposed at the rotor. Figure 13(d) shows the distribution of the stream traces of viscous stress at nominal-gap condition at critical throttling condition which shows a slight increasement in the area effected by the separation compared with the base-line case close to stall. As it can seen in Fig. 6 the leakage mass flow rate relative to the main mas flow rate at this point has a sudden jump which means similar significant growth at the momentum thickness upstream the seal cavity outlet trench

according again to Demargne *et al.* [4] Eqn. 23.

$$\Delta\Theta = \frac{\dot{m}_j}{\rho u_{in}} \tag{2}$$

$$\Delta\Theta = \frac{\dot{m}_j}{\rho u_{in}}(1 - \frac{v_j}{v_i n}) \tag{3}$$

Figure 14 (a) & (b) represent the distribution of viscous stress stream traces on the stator blade at the last stable operating point in case of base-line and nominal-gap configuration. In the nominal-gap cases, the forming separation at critical throttling is significantly bigger as it also appears on the radial distribution of the pressure loss coefficient (Fig. 9(b)).

The measured data have good agreement with the Base-line computations especially at hub (Fig. 7; 9; 10) but the discrepancies are higher when the leakage flow was taken into account as well. It has to be recalled again that in all cases at the last operating point, the same static pressure was imposed at the shroud with radial equilibrium outlet boundary condition. Therefore the difference shown on the global performance map does not mean that in case of base-line configuration the the stall margin is smaller but at the same boundary conditions the equilibrium in compressor operation is evolved at higher mass flow rate on its speed-line.

In case when the seal tooth were removed from the cavity channel the computations have not converged anymore when the same fixed static back-pressure was imposed at the outlet boundaries. These results suggest that the imposed back-pressure and the blockage generated by the leakage flows push the rotor beyond its stability limit.

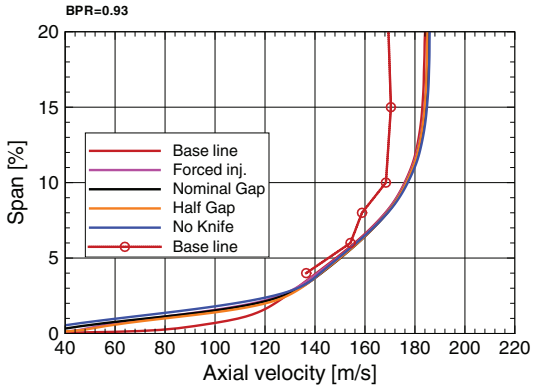

(a)

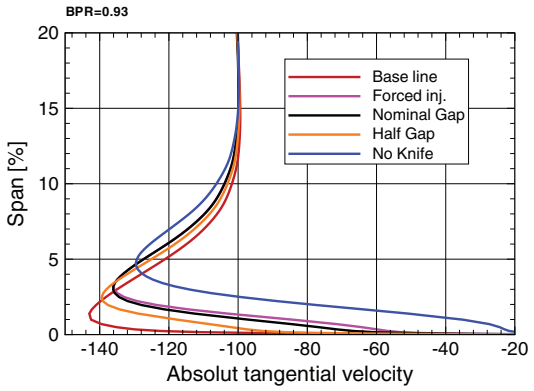

(b)

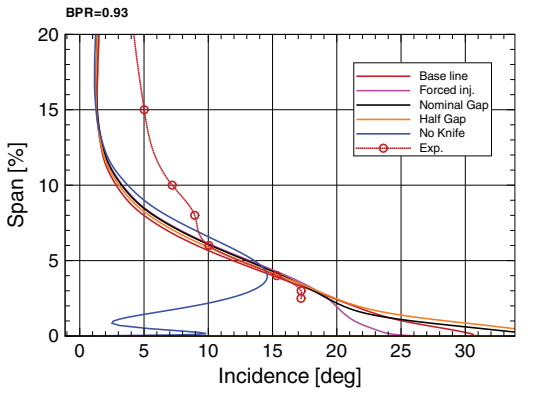

(c)

Figure 8: Span wise distribution of Axial velocity (a) Absolute tangential velocity (b) and Incidence (d) behind the rotor at SBPR=0.93

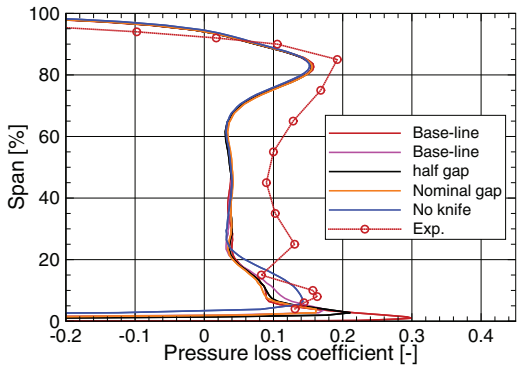

(a)

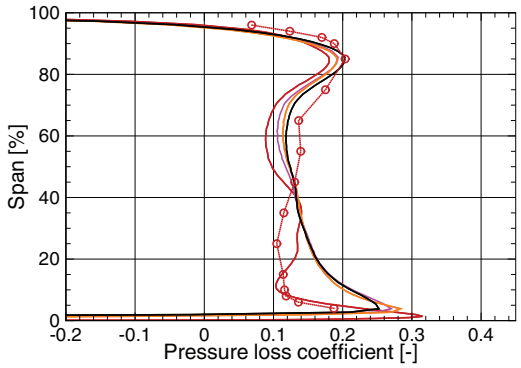

(b)

Figure 9: Pressure loss coefficient of the stator blade row at SBPR=0.93 (a) and at SBPR=101 (b)

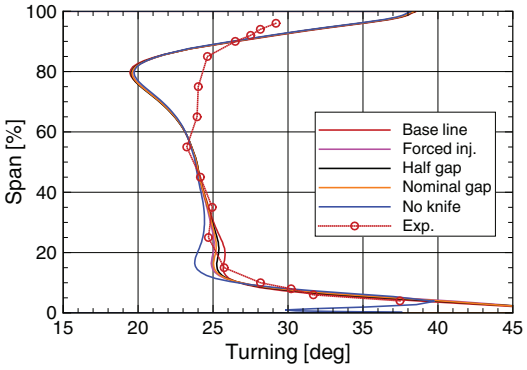

(a)

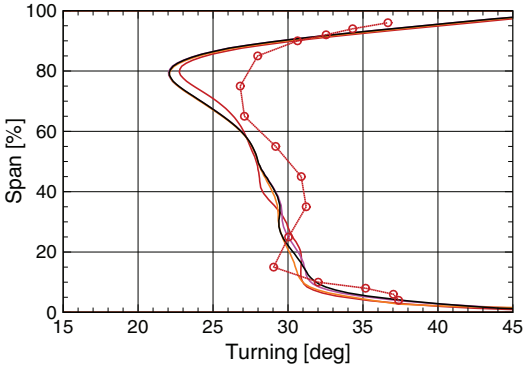

(b)

Figure 10: Turning across the stator blade row at SBPR=0.93 (a) and at SBPR=101 (b)

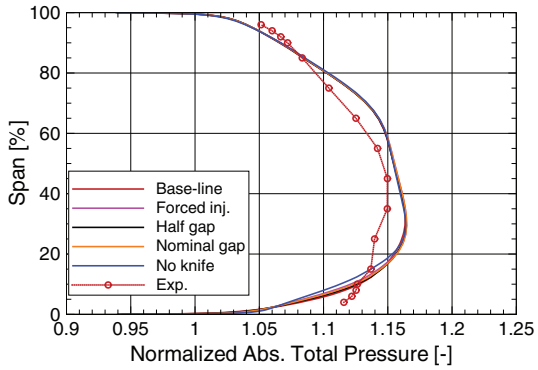

(a)

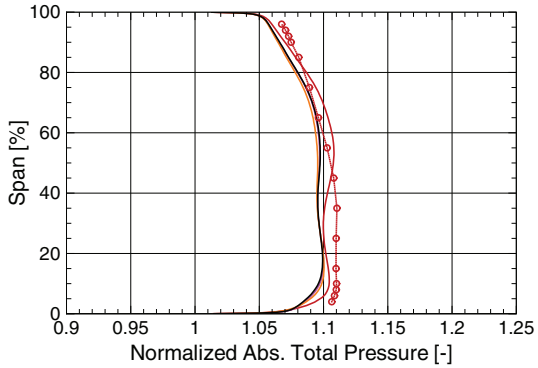

(b)

Figure 11: Radial distribution of total pressure at the outlet of the stage at SBPR=0.93 (a) and at SBPR=1.01 (b)

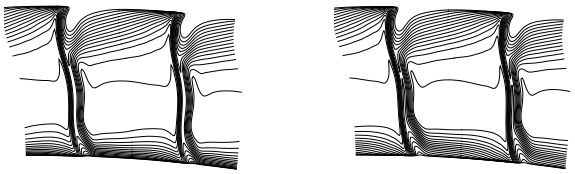

(a) (b)

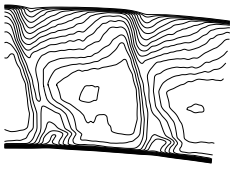

(c)

Figure 12: Total pressure distribution behind the stage at half-gap (a) and no-knife (b) configurations compared to the measurements at Base line config. (c) at SBPR=0.93

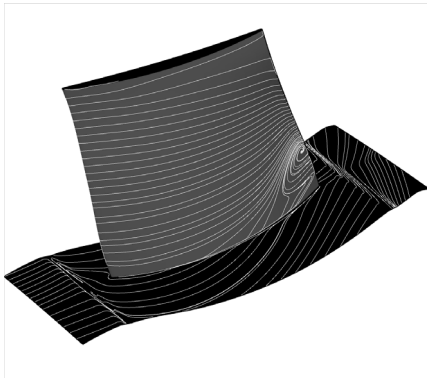

(a)

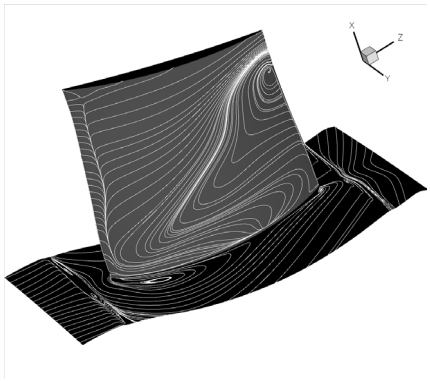

(b)

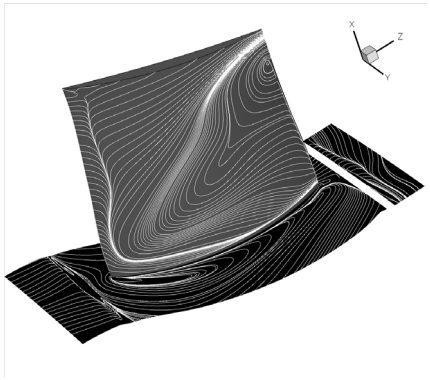

(c)

Figure 13: Stream-traces of viscous stress on the surface of the rotor blade at Base-line configuration at SBPR=0.93 (a) and SBPR=1.01 (b) compared to the Nominal-gap configuration at SBPR=1.01 (c)

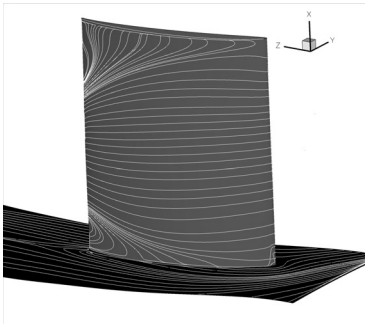

(a)

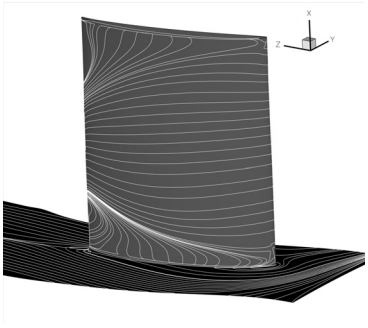

(b)

Figure 14: Stream-traces of viscous stress on the stator-blade surface at SBPR=1.01 at Base-line (a) and Nominal-gap (b) configuration

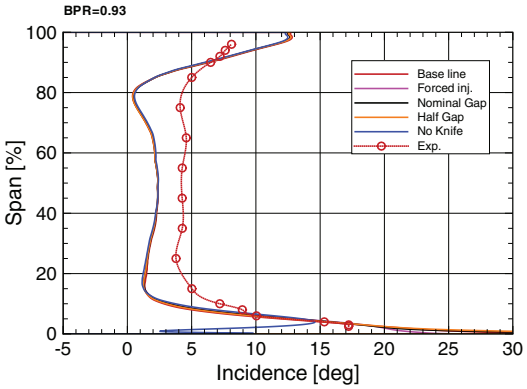

(a)

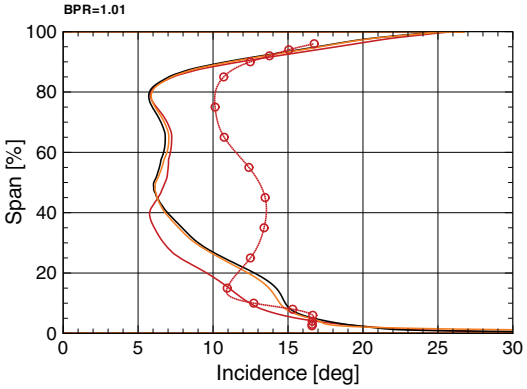

(b)

Figure 15: Incidence angle radial distribution at the stator inlet at SBPR=0.93 (a) and at SBPR=1.01 (b)

References

[1] S. R. Wellborn, T. H. Okiishi, The influence of shrouded stator cavity flows on multistage compressor performance, ASME Journal of Turbomachinery 121.

[2] S. R. Wellborn, I. Tolchinsky, T. H. Okiishi, Modeling shrouded stator cavity flows in axial-flow compressors, ASME Journal of Turbomachinery 122.

[3] M. Lange, R. Mailach, K. Vogeler, An experimental investigation of shrouded and cantilevered compressor stators at varying clearance sizes, ASME Paper No. GT2010-22106.

[4] A. A. J. Demargne, J. Longley, The aerodynamic interaction of stator shroud leakge and mainstream flows in compressor, ASME Paper No. GT2000-GT-570.

[5] D. W. Sohn, T. Kim, S. Song, Influence of the leakage flow tangential velocity on the loss generation and leakage flow kinematics in shrouded axial compressor cascades, ASME Paper No. GT2006-90979.

[6] V.-M. Lei, A simple criterion for three-dimensional flow separation in axial compressors, PhD Thesis, Massachusetts Institute of Technology (February 2006).

[7] N. J. Heidegger, E. J. Hall, R. Delaney, Parametrized study of high-speed compressor seal cavity flow, 32nd AIAA/ ASME/ SAE/ ASEE Joint Propulsion Conference And Exchibit Paper No. AIAA96-2807.

[8] J.-F. Brouckaert, N. V. de Wyer, J. Desset, B. Farkas, J. G. Perez, Experimental and numerical investigation of a single stage low pressure compressor for counter-rotating turbofan engine architectures, ETC.

[9] J.-F. Brouckaert, N. V. de Wyer, J. Desset, B. Farkas, F. Ullman, J. de laborderie, M. Chome, Unsteady pressure measurements in a single stage low pressure axial compressor : Tip vortex flow and stall inception, ASME Paper No. GT2009-59771.

[10] A. Touyeras, M. Villian, Aerodynamic design and test result analysis of a three stage research compressor, ASME Paper No. GT2004-5394.

Experimental investigation of the unsteady flow field in the tip region of a single stage axial compressor with a circumferential groove casing treatment

Nicolas Van de Wyer

Turbomachinery and Propulsion Department, vandewye@vki.ac.be

Supervisor: Jean-François Brouckaert

Assistant Professor, Turbomachinery and Propulsion Department, von Karman Institute for Fluid Dynamics, Belgium, brouckaert@vki.ac.be

Promotor: Tony Arts

Professor, Turbomachinery and Propulsion Department, von Karman Institute for Fluid Dynamics, Belgium, arts@vki.ac.be

Abstract

This paper deals with the experimental investigation of the influence of a circumferential groove casing treatment on the global performance, stability margin and unsteady secondary tip flow of a single stage low pressure axial compressor. The design of the compressor stage is representative of a booster stage for the new counter-rotating turbofan engine architecture and is characterized by unusually high loading and flow coefficients.

Keywords:
Axial compressor, casing treatment, tip leakage vortex

1. Introduction

The work presented here is part of the large European research project VITAL (EnVIronmenTALly Friendly Aero Engine) (Korsia [1]). The global objective of this project is the study of the capability to reduce the perceived noise and emissions of civil engines by the use of the Counter-Rotating Turbofan (CRTF) architecture. In this scope, a single stage low pressure compressor representative of such a CRTF booster was designed, manufactured, tested and numerically simulated. The aerodynamic design and the steady state performance of the LP compressor stage at two different Reynolds numbers as well as the detailed time-resolved flow field analysis, including the tip leakage vortex topology and stall inception process have been presented by Brouckaert et al. [2] [3]. In the counter-rotating turbofan engine architecture, two fans instead of one are rotating in opposite direction at lower speed. The booster being mechanically linked to the second fan, a higher loading is required to compensate for the lower rotational speed in order to keep the same pressure ratio without increasing the number of stages. This will also imply a reduced stability margin (Hiernaux et al. [4]). The present work focuses on the possibility to increase the stability margin by using casing treatment without loss of efficiency or pressure ratio with respect to the baseline configuration (smooth casing). The objective of this work is therefore to characterize the compressor overall performance and stability at design and off-design in the presence of a casing treatment. The detailed near casing flow field topology is studied, with a focus on the tip leakage vortex behavior and the impact on blade loading. An extensive review of passive endwall treatments has been provided by Hathaway [5]. Several numerical (Wilke and Kau [6], Shabbir and Adamczyk [7], Lu et al. [8]) and experimental (Bailey and Voit [9], Prince and al. [10]) studies have shown the possibility of stall margin increase using passive casing treatments. Typical arrangements are axial slots or circumferential grooves. Slots (Osborn [11], Gelmedov [12], Seitz [13]) have been shown to generate the largest improvements in stall margin but with a large efficiency loss (Prince and al. [10] and Wilke and Kau [6]). Groove based treatments (Osborn [11]) generate smaller improvements in stall margin but cause a smaller efficiency drop (Fujita and Takata [14]). To

quantify the casing treatment effectiveness, three criteria have therefore to be taken into account: ” the percentage of decrease of flow rate at stall, ” the gain in pressure ratio, ” the gain in efficiency. Furthermore, considering the efficiency of a real turbo compressor, the working line does not always correspond to the maximum efficiency due to the stall margin requirements. An extension of the stall margin with casing treatment may allow a shift of the working line to the maximum efficiency. The extension of the working range of a compressor by using casing treatment results from the impact on the tip leakage flow and its resulting vortex. Beheshti et al. [15], explained the effect of a circumferential groove by a migration of the fluid from severe blade loading and high pressure region to a location where the pressure is more moderate. This flow relocation allows relieving the locally severe blade loading thus inducing a stability improvement. Shabbir et al. [7] performed the budget analysis of the axial momentum equations for a control volume adjacent to the casing from numerical results. They found that, in the case of grooved casing, the net axial pressure force at the casing in the tip gap is compensated by the net axial shear viscous force (as in the smooth casing case) and by the net axial force due to the radial transport of axial momentum across the groove. They concluded that this radial transport is the flow stabilizing mechanism. The possibility of stabilization by the use of casing treatment was demonstrated by an amount of experimental and numerical investigations in the last 40 years. But the complex physical phenomena that induce the positive impact on the tip clearance flow are not yet fully understood and the literature sometimes shows contradictory results. Designing a grooved casing treatment remains therefore difficult.

2. Casing Treatment Configuration

The circumferential groove casing treatment investigated in this study was chosen primarily on the basis of industrial considerations. Circumferential grooves are probably the simplest and most cost effective geometry to apply on a real engine as far as machining is concerned. Furthermore this kind of casing treatment allows an improvement of the stall margin with the smallest efficiency or pressure ratio loss, which is an essential requirement for engine applications. The stall margin improvement with a circumferential groove is usually lower than with other casing treatments but is generally sufficient for aircraft engine application. The greater mechanical integrity of grooved casing treatment is also an important aspect. The geometry of the groove was also dictated by real engine considerations like forward axial displacement of the rotor, rub-in when hard landing, erosion or fouling. The basic geometry selected by the industrial partner (Techspace Aero) is therefore somewhat remote from the usual design recommendations which may be found in literature so far. The groove depth necessary to achieve a substantial effect only needs to be of the order of the clearance gap (Rabe et al. [16]) and an optimum depth may be found for best peak efficiency. Houghton and Day, 2009 [17] performed a detailed parametric study on the optimum axial location of grooves both for shallow and deep grooves. They concluded that several axial locations may be chosen to maximize the stall margin improvement and that shallow grooves give a negligible efficiency loss over a wider range than deep grooves. In their study, the aspect ratio of the shallow groove was unity whereas the deep groove had an aspect ratio of 2, both with an axial width of 14% Cax,r. The depth of the shallow and deep grooves was respectively 5 and 10 times larger than the tip gap. In the present study, the actual tip clearance under running conditions at nominal speed (100% NN) was found to be between 0.12 and 0.25 mm, i.e. between 0.5% and 1.08% of the blade height (Brouckaert et al. [3]). A groove depth of 1 mm was chosen, which corresponds to 4.5% of the blade height or 4 to 8 times the tip gap. The length or axial extent of the groove was chosen to be 3 mm (12.7% of rotor axial chord), i.e. with an aspect ratio of 1/3. This configuration is presented in Fig. 1 (a groove of 1mm depth by 3mm wide centered at 15% c_ax from the blade leading edge.

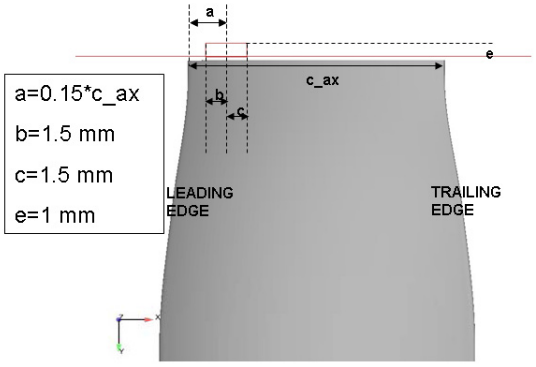

Figure 1: Circumferential groove casing treatment geometry.

3. Numerical Simulation

In order to compare the experimental data against computations, two commercial software were used for simulations of this compressor stage. The commercial software package Fine/Turbo (Flow Integrated Environment from Numeca) was used at VKI by the PhD candidate Balazs Farkas and in parallel computations were carried out by CENAERO with the elsA software (Ensemble Logiciel de Simulation en Arodynamique) developed at ONERA . The numerical simulations with both codes were performed on the full stage for the configuration with the smooth casing and with the casing treatment. The meshes of each blade row have been generated with the AutoGrid5 software. In the passage, they are based on its general O4H default topology combined with a butterfly OH gridding in the tip gap. The mesh used for FINE/elsA counts 0.85/1.1 million grid points for the IGV, 1.6/1.8 million for the rotor and 0.9/1.1 million for the stator. The structured groove mesh is connected to the main channel with the chimera technique. The measured total pressure and temperature distributions as well as the turbulence level were imposed as inlet conditions. A radial equilibrium throttle condition was applied downstream, fixing the static pressure at the shroud. The Yang-Shih k-ϵ [18] was used as turbulence model for FINE simulations and the the Launder-Sharma k-ϵ [19] for elsA. Numerical simulations did not model the seal leakage flow at the stator hub and were performed with the nominal tip clearance gap of 0.3 mm.

4. Experimental Set-up

4.1. Test Rig

The experimental study of the compressor stage was performed in the VKI high speed compressor test rig R4. This closed loop facility allows testing of axial or radial compressors. It can be pressurized from vacuum to 3 bars. The rotor is driven by a 450 kW DC motor with a maximum shaft speed of 9000 RPM. A detailed description of the facility, as well as the main aerodynamic and geometric characteristics of the stage may be taken from Brouckaert et al. [3].

4.2. Test Conditions

All tests were performed at a Reynolds number corresponding to cruise conditions. During the tests, the rotational speed was adjusted to compensate the temperature variation in the loop to keep the nominal non-dimensional rotational speed constant. Detailed measurements were performed at four throttling conditions corresponding to choke (point A), point B, design point (point C) and near stall (point D) as presented in Fig. 4.

4.3. Stage Performance Instrumentation

The mass-flow was determined from the inlet radial distributions of total pressure P01, static pressure Ps1 and temperature T01. The total pressure ratio was obtained from the detailed exit total pressure maps over 2 pitches (P04) divided by the inlet total pressure P01 at mid-span. The efficiency was calculated as a total-to-total efficiency, based on the exit total pressure P04 and temperature T04 maps, and inlet radial distribution of pressure P01 and temperature T01. It is important to note that the temperatures T01 and T04 were recorded simultaneously to reduce the uncertainty. Taking into account the uncertainty of the calibration as well as of the acquisition chain, the uncertainty on the pressures are 0.05% and 0.1% on the temperatures, including the recovery factor uncertainty. From these values, the mass-flow uncertainty is between 1.5% (choke) and 3.2% (near stall). Regarding efficiency, the uncertainty was calculated to be between 2.8% (design) and 3.8% (near stall), also partly due to the small pressure ratio of the compressor.

4.4. Casing Instrumentation

The rotor casing was instrumented with 11 small inserts (Fig. 2 (left)), each of them containing a fast response piezoresistive pressure transducer and a pneumatic pressure tap to measure the steady and unsteady static wall pressure distribution over the rotor. The fast response sensor having a diameter of 1.7 mm, it was decided to use a slight recess (0.2 mm) rather than to have them flush-mounted in order to reduce the pressure sensing area with respect to the blade thickness at the tip (max 1.42 mm). However, in order to keep a sufficient bandwidth, the diameter of the sensing hole was kept to 0.8 mm. The corresponding arrangement is shown in Fig. 2 (right) and the resulting cavity in front of the sensor yields resonance frequencies between 85 and 115 kHz for all sensors.

For the smooth casing configuration, 9 inserts were distributed over the rotor tip along the axial direction from -45% (K8) of the axial chord with respect to the leading edge to 45% (K9) downstream the trailing edge as shown in Fig. 3. They were circumferentially displaced by one rotor pitch in order to avoid a downstream insert being influenced by the wake of

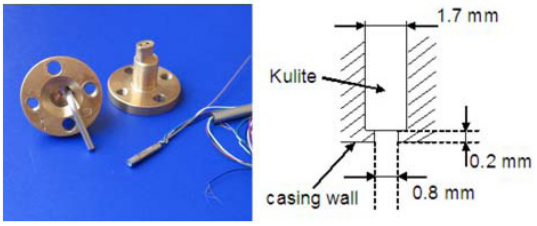

Figure 2: Photograph of casing inserts and schematic view of cavity in front of the sensor.

an upstream insert. For the grooved casing configuration, the inserts were placed at the same position except the one at 25% Cax downstream of the leading edge (K4) which was shifted to 30% due to the presence of the groove. Two additional inserts were placed in the groove (K1C at 9% Cax,r and K1D at 21% Cax,r). The groove then contains 3 static pressure measurement points, 2 in each corner (K1C and K1D) and one at the center (K5). Fig. 3 presents the fast pressure sensors arrangements for both cases. The uncertainties corresponding to the static pressure measurement were found to be +/- 0.5% for the fast sensor and 0.17¡% for the pneumatic transducer. Finally, upstream of the blade row, at -15% of the axial chord with respect to the leading edge, 3 inserts are placed respectively at 0 (K7), 120 (K10) and 220 (K11) for the detection of the number of stall cells.

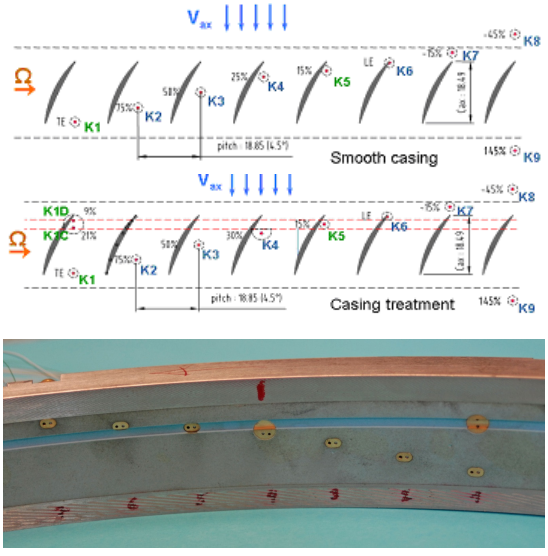

Figure 3: Schematic view and photograph of casing static pressure measurement locations.

4.5. *Flow Path Instrumentation*

Simultaneous measurements of the unsteady total pressure at the rotor exit were performed with a miniature single sensor fast response probe of 2.5 mm. Full details about the probe design and calibration can be found in Brouckaert [20]. The probe has a bandwidth of over 100 kHz and the sub-surface mounted chip is located behind a 0.5 mm sensing hole. At Mach = 0.6, the probe is insensitive to incidence (within 1%) in an angular range of +/- 11.8. During the radial traverses, the probe was set at the average rotor absolute exit angle for every operating point. Total pressure was corrected for incidence by using the average exit angle measured by prior pneumatic 3-hole probe traverses. All rotor exit radial traverses were performed in the same measurement plane as the last casing insert (K9), i.e. 45% Cax downstream of the rotor trailing edge, from 16.3% to 98% of blade height. The small dimensions of the compressor considered in this work (blade height 23 mm) cause additional uncertainty sources. Indeed, despite the very small size of the unsteady pressure probe, the dimension of the fast pressure-sensing hole (0.5mm) represents 2.7% of the blade pitch at rotor tip. The probe itself introduces a flow blockage (in terms of frontal area) of 13.3% of the blade pitch. In radial direction, due to the distance between the fast response sensing hole and the probe tip, measurements could only be performed between 16.3% and 98% of the blade height.

5. Experimental Results

5.1. *Overall Stage Performance*

The overall stage performance is presented in Fig. 4 in terms of total pressure ratio, relative efficiency change and static-to-total pressure ratio versus reduced mass flow. The experimental data for the configuration with smooth casing (Smooth) and with casing treatment (CT) are presented with the corresponding error bars and are compared to the results from the numerical simulations performed with both codes (FINE and elsA). Experimentally, except at choke conditions (point A), the groove slightly improves the PR. Slight changes on efficiency are noticeable but remain within the uncertainty range of the measurements, Near stall (at point D), for the same static-to-total pressure ratio, i. e. the same throttling, the configuration with casing treatment shows an increase of 3% of the mass flow, 1% of total-to-total pressure ration and 2% of efficiency. This increase of mass flow however does not correspond to a reduction of stall

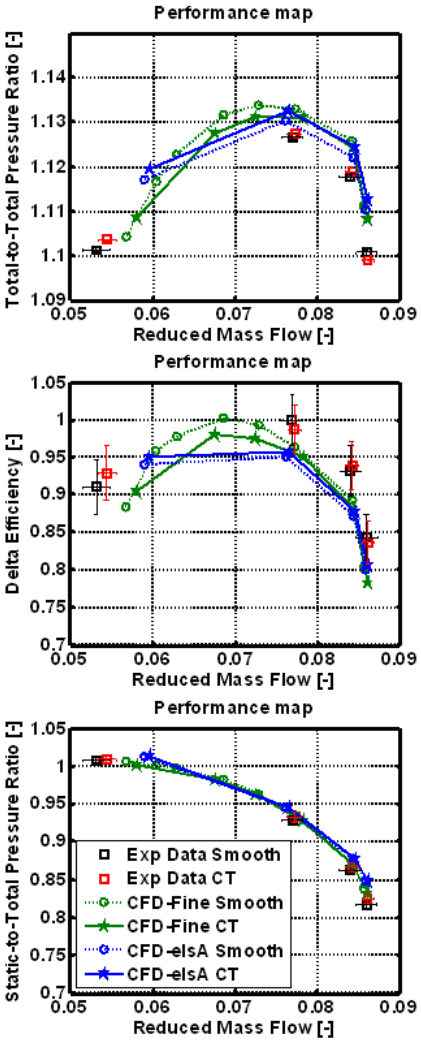

Figure 4: Total pressure ratio, relative efficiency and static-to-total pressure ratio versus reduced mass flow at nominal speed for smooth casing and casing treatment configurations.

margin for the grooved compressor. It rather hints to a reduction of blockage due to the groove. The stall margin of the compressor is unaffected as will be seen from Fig. 5. Numerically, for the smooth casing, from choke (point A) until maximum PR (point C), the CFD results are consistent between both codes but overestimate the pressure ratio and underestimate the efficiency when compared to the experimental data. Growing discrepancies appear as throttling is further increased towards point D (near stall) which is due to the relative ability of the turbulence models to predict separation correctly. For the grooved casing, the conclusions of both codes are opposite, Indeed in the simulations with FINE, the presence of the casing groove induces a decrease of both pressure ratio and efficiency. On the contrary, elsA predicts an increase of these parameters with the casing treatment. This difference of behavior evidences the influence of the CFD code (mainly through the turbulence model, but also mesh density or topology) on the numerical results. It underlines once more the fact that great care is required when making engineering decisions based on CFD. For point D (near stall), the CFD does not allow reaching the last stable experimental point in terms of mass flow and the difference between the two codes is difficult to interpret since at this condition the flow is mainly driven by unsteady effects which are hard to capture by steady RANS computations. The static-to-total pressure ratio evolution in function of reduced mass flow presents a nearly zero slope near stall. This behavior is typical of a modal stall inception process (Tan [21]). Brouckaert et al [3] have already confirmed that the stall inception mode of the compressor was of modal type and was linked to blade stall at the rotor hub in this particular machine. They concluded also that no flow alteration methodology acting at the tip would be effective in the present case. Although not covered in detail in this paper, it is important to note that stall occurs through the same modal type inception mechanism with and without casing treatment.

5.2. *Off-Design Performance*

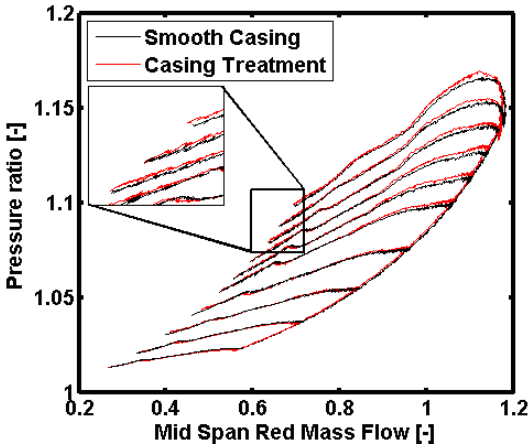

Figure 5: Total-to-total pressure ratio iso-speed versus reduced mass flow at mid-span for the two casing configurations.

In order to investigate the influence of the treatment on the stability limit at off-design, the stage inlet

and outlet midspan total pressure were acquired during throttle valve closing until stall at different rotational speeds. This experiment was performed for the two casing configurations. The mid-span total-to-total pressure ratio iso-speed lines are presented in Fig. 5. The iso-speed lines correspond to a rotational speed of 105%, 100%, 95%, 90%, 85%, 80%, 70%, 60%, 50% and 40% of the nominal rotational speed. At design and off-design, a slight improvement in pressure ratio is observed but the stall margin of the compressor remains unchanged.

6. Casing Wall Pressure Measurement

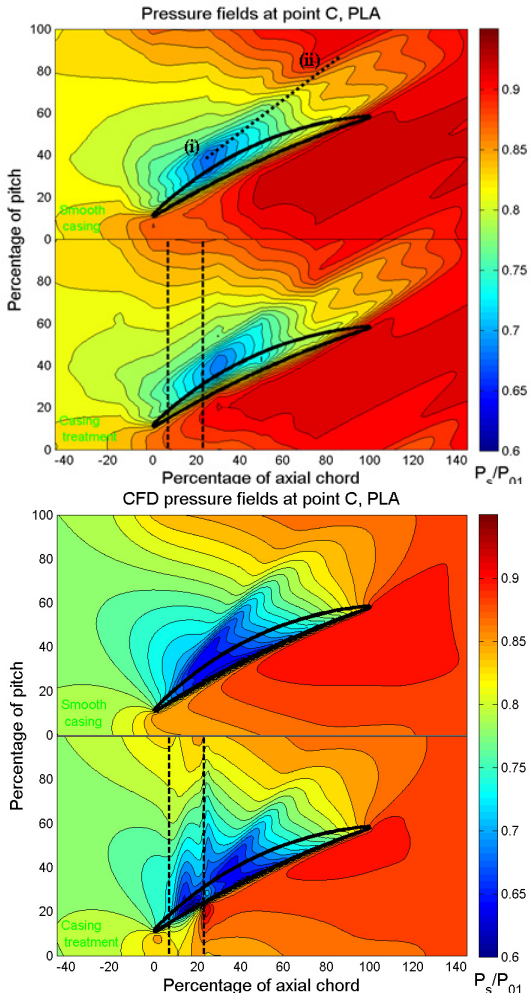

Figure 6: Experimental (up) and numerical (down) casing pressure maps for smooth casing (top of the figures) and casing treatment (bottom of the figures) at point C.

In order to obtain the full static pressure map on the casing wall, the following post processing procedure was applied to the signals from the fast sensors K1 to K9. A phase-locked average (PLA) was applied on the signals at the blade passing frequency. This frequency was determined from a one-per-revolution trigger. Then an appropriate interpolation is applied to the different signals to establish the static pressure map from the measurements at discrete locations. In the case of casing treatment, the sensor K5 was not considered for the pressure maps establishment due to its location at the bottom of the groove. The experimental pressure map for point C is compared to the CFD results in Fig. 6 for both casing configurations. The minimum pressure area (i), origin of the tip leakage vortex, as well as the vortex trajectory (ii) is clearly visible on experimental and numerical results. This figure shows that the CFD predicts well the location of the origin of the tip vortex. However, the numerical vortex trajectory shows a higher inclination with respect to the axial direction, which may be attributed to differences in the actual tip gap size under running conditions. The experimentally measured vortex angle was shown to be always smaller than the numerical one, for all operating points from choke to stall, but with a constant offset. The numerical static pressure contour plot also shows an important variation at the groove inlet due to the flow circulation in it. This variation of the static pressure is obviously not visible in the experimental results which is due to impossibility to place pressure sensors in this region.

The impact of the casing treatment on the tip vortex path is negligible. The observations made for point C are as well valid for point A and B. This shows that the casing treatment does not have any influence on the tip flow when it is placed upstream of the origin of the tip leakage vortex. On the contrary, the tip leakage vortex path is strongly influenced by the casing treatment at point D (Fig. 7). In the experimental results, the vortex angle presents a lower inclination with respect to the axial direction in the casing treatment case. This change of vortex trajectory is also visible in the CFD results. The elongation of the experimental vortex trajectory is due to the shift of pressure sensor K4 to a further downstream position because of the groove. Outside the sphere of influence of the tip leakage vortex, the flow field is similar for the two configurations. The unsteadiness produced by the tip leakage vortex was investigated by computing the RMS pressure field at the casing. The conclusions from the RMS fields for point A to C are similar to those of the pressure fields of Fig. 7. The RMS fields at point D are presented in Fig. 8 for both casing configurations on two blade

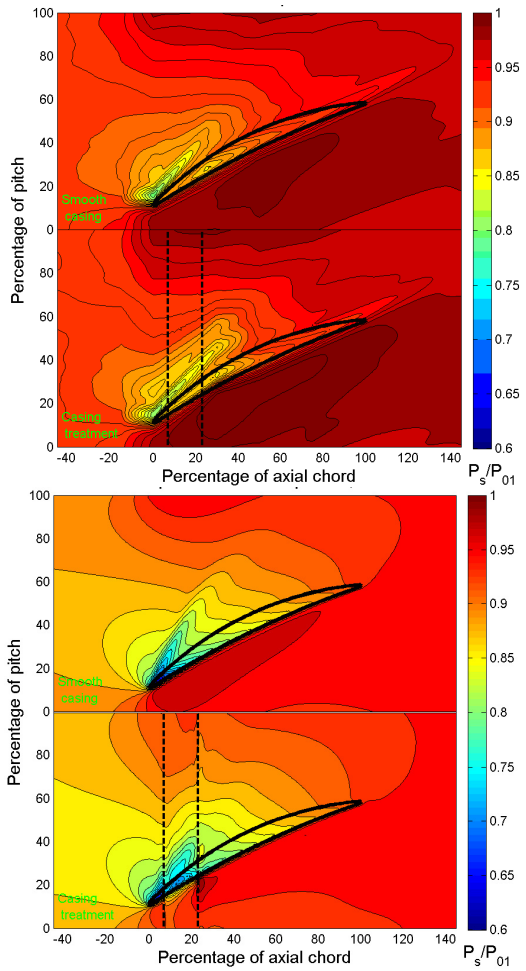

Figure 7: Experimental (up) and numerical (down) casing pressure maps for smooth casing (top of the figures) and casing treatment (bottom of the figures) at point D.

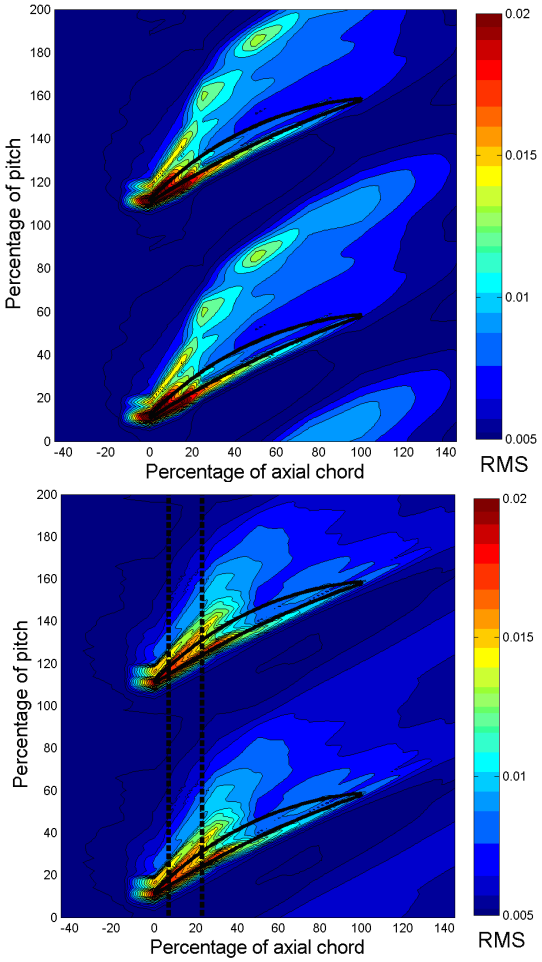

Figure 8: RMS files for smooth casing (up) and casing treatment (down) at point D.

passages in order to visualize the complete extension of the tip leakage vortex. In the case of smooth casing, the interaction zone of the vortex with the core flow, represented by the high unsteadiness area, covers 75% of the blade passage at 50% Cax. In the casing treatment case, the unsteadiness produced by the tip leakage vortex is strongly reduced, which may be explained by the reduction of the rotational intensity of the vortex due to the fact that the velocity components of the tip leakage flow exiting the groove are negligible perpendicular to the blade [6].

7. Tip Leakage Vortex Downstream Loss Core

In order to investigate the influence of the casing treatment on the blockage in the passage induced by the tip leakage vortex, radial traverses downstream the rotor with fast response pressure probe were performed. The experimental and numerical fluctuations around the mean axial value of casing pressure fields and total pressure downstream the rotor, non-dimensionalized by the inlet total pressure at midspan, are presented together in Fig. 9 and Fig. 10 for point D. The data from casing pressure sensors and fast response total probe were acquired simultaneously. The results for points A to C are similar for the two casing configurations. At point D, the first observation is related to the large separation region at the hub on the suction side. This separation is considered as the cause of stall onset and this also explains the absence of effect of the casing treatment on the stability margin since this rotor is not tip-critical (Greitzer et al. [22]). Then, regarding the tip leakage vortex, the low total

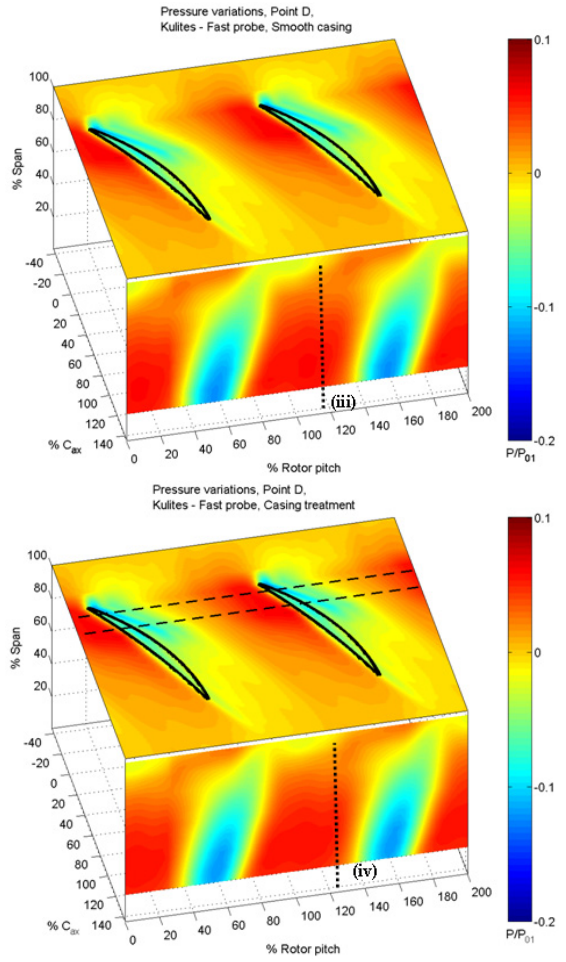

Figure 9: Experimental casing pressure and downstream rotor total pressure fluctuation for smooth casing (up) and casing treatment (down) at point D.

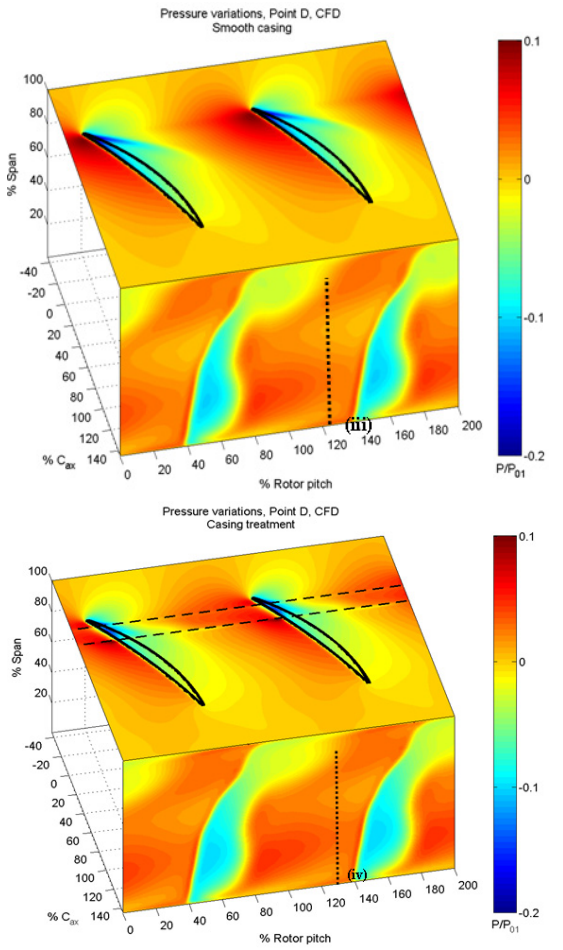

Figure 10: Numerical casing pressure and downstream rotor total pressure fluctuation for smooth casing (up) and casing treatment (down) at point D.

pressure zone spreads more into the passage in pitch direction for the casing treatment application (iii and iv). The radial extension does not seem to be affected by the casing groove but is overestimated numerically. In order to get a more explicit view of the extension of tip vortex in the core flow, the RMS fields of the casing pressure and rotor downstream total pressure at point D are plotted in Fig. 11 for both casing configurations. In this figure, the circumferential extension of the tip leakage vortex in the case of casing treatment is clearly visible. The tip vortex at 98% radial position extends from 100% to 130% pitch for the smooth casing and 140% for the casing treatment case. The RMS in the tip vortex shows lower values in the case of casing treatment. This signals to a lower unsteadiness in this region and thus a smaller interaction with the core flow. It must be mentioned that the high unsteadiness zone produced by the hub separation covers about 35% of the passage at this operating point.

8. Conclusion

A one and a half highly loaded stage low speed compressor was modeled and tested to investigate the capability of a circumferential groove to improve the stability range but in particular, its effect on the steady and unsteady flow field near the casing. Two different commercial CFD codes were used to allow detailed flow-field investigations and were compared with the experimental data sets. The results suggest that using casing treatment or any passive control on the tip leakage flow in booster stages has only a slight effect on the performance and no effect on the stability. This is

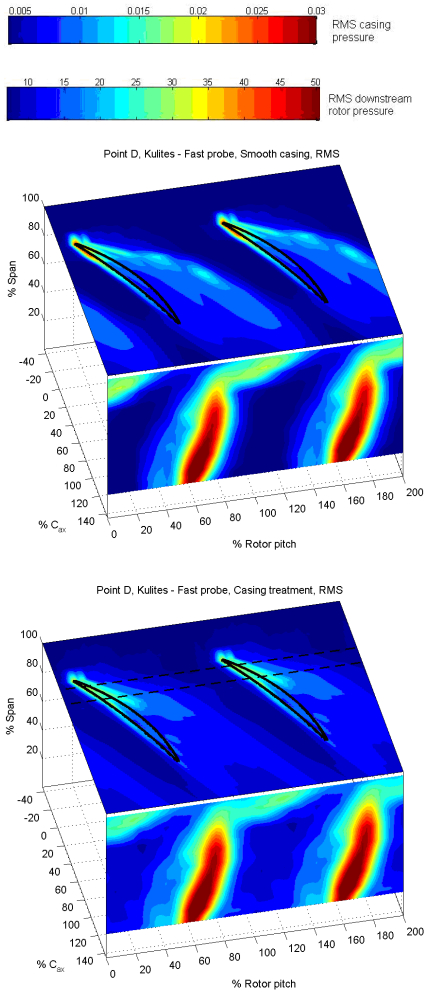

Figure 11: RMS fields for smooth casing (up) and casing treatment (down) configuration at point D.

due to the fact that in high by-pass ratio aero-engines the booster stages are strongly hub loaded to redistribute the highly skewed flow coming from the fan stage, before it enters the high pressure compressor. This result was indeed anticipated but the experiment was intended to study the effect of a circumferential groove on the near casing flow field from a steady and unsteady point of view. The simultaneous measurements of the unsteady casing pressure and unsteady rotor downstream total pressure are presented. This unique combination of measurements allows isolating the secondary flows topology. Phase locked averaging these pressure recordings at the scale of the blade passing frequency provides an average trajectory of the tip leakage vortex along the casing and in the blade to blade plane. The measurements at different operating conditions allow monitoring the change in the vortex trajectory inside the passage and the forward displacement of the origin of the tip leakage vortex along with the maximum blade loading. This technique also highlighted the high unsteadiness related to this particular flow phenomenon. The effect of the circumferential groove could be isolated in this particular way and is supported by the CFD simulations. Close to stall the casing treatment causes a reduction of the rotational intensity of the tip leakage vortex as well as its circumferential displacement. The two CFD simulations show contradictory results. the effect of the casing treatment on the global stage performances is positive for the elsA simulations and negative for the FINE ones. This points once again to the important influence of turbulence models on the numerical results and shows that great care is required when making engineering decisions based on CFD.

Acknowledgments

The author acknowledge gratefully Balazs Karkas from the von Karman Instituite and Jean-Francois Thomas from the Cenaero for providing the numerical results. VITAL is a new collaborative research project, running for four years, which aims to significantly reduce aircraft engine noise and CO2 emissions. It has a total budget of 90 million euros, including 50 million euros in funding from the European Commission. Snecma leads a consortium of 53 partners gathering all major European engine manufacturers: Rolls-Royce, MTU Aero Engines, Avio, Volvo Aero, Techspace Aero Rolls-Royce Deutschland and ITP, and the airframer Airbus. This work was carried out under SP3 ”Booster”, Work Package 3.4. ”Advanced Aerodynamic Technologies”. The author gratefully acknowledge the financial support of the European Commission and the support of Stephane Hiernaux from Techspace Aero as work package leader.

References

[1] Korsia, J.-J., VITAL Integrated Project, in: Proceedings of the XVIII ISABE Symposium, Beijing, China, 2007.

[2] Brouckaert, J.-F., Van de Wyer N., Desset J., Farkas B., Capart R., Thomas J-F., Isaac N., Hiernaux S., Gonzalez Perez J., Experimental and numerical investigation of a single stage Low Pressure compressor for counter-rotating turbofan Engine architectures, in: Proceedings of the 8th European Turbomachinery Conference, Graz, Austria, 2009.

[3] Brouckaert, J.F., Van de Wyer, N., Farkas, B., Ullmann, F,,Desset, J., de Laborderie, J., Chom, M. Hiernaux, S. , Unsteady pressure measurements in a single stage low pressure

axial compressor : tip vortex flow and stall inception, in: Proceedings of of ASME Turbo Expo 2009, no. GT2009-59771, Orlando, USA, 2009.

[4] Hiernaux S.,Lebas C.,Brouckaert J-F., Lepot I. , Next generation booster, in: Proceedings of the XVIII ISABE Symposium, Beijing, China, 2007.

[5] H. M.D., Passive endwall treatments for enhancing stability, in: VKI LS 2006-06 on Advances in Axial Compressor Aerodynamics, 2006.

[6] K. H.-P. Wilke, I., A numerical investigation of the influence of casing treatments on the tip leakage flow in a hp front stage, in: Proceedings of ASME Turbo Expo 2002, no. GT2002-30642, 2002.

[7] A. J. Shabbir, A., Flow mechanism for stall margin improvement due to circumferential casing grooves on axial compressors, in: Proceedings of ASME Turbo Expo 2004, no. GT2004-53903, 2004.

[8] Z. J. W. Y. Lu X., Chu W., Mechanism of the interaction between casing treatment and tip leakage flow in a subsonic axial compressor, in: Proceedings of ASME Turbo Expo 2006, no. GT2006-90077, 2006.

[9] V. C. H. Bailey E. E., Some observations of effects of porous casings on operating range of a single axial-flow compressor rotor, NASA technical memorandum NASA TM X-2120, NASA (1970).

[10] H. D. E. Prince D. C., Wisler D. C., Study of casing treatment stall margin improvement phenomena, NASA report NASA CR-134552, NASA (1974).

[11] H. L. Osborn W., Lewis G., Effect of several porous casing treatments on stall limit and overall performance of an axial compressor rotor, Tech. Rep. NASA report TN 6537, NASA (1971).

[12] O. L. S. M. Gelmedov F., Lokshtanov E., Anti-stall tip treatment means (1998).

[13] S. P., Casing treatment for axial flow compressors, Ph.D. thesis, Cambridge University (1999).

[14] T. H. Fujita H., A study on configurationsof casing treatment for axial flow compressors, JSME Bulletin 27 (1984) 230.

[15] I. P. G. K. F. B. Beheshti B., Teixeira J., Parametric study of tip clearance-casing treatment on performance and stability of a transonic axial compressor, in: Proceedings of ASME Turbo Expo 2004, no. GT2004-53390, 2004.

[16] H. C. Rabe D., Application of casing circumferential grooves for improved stall margin in a transonic axial compressor, in: Proceedings of ASME Turbo Expo 2002, no. GT2002-30641, 2002.

[17] D. I. Houghton T., Enhancing the stability of subsonic compressors using casing grooves, in: Proceedings of ASME Turbo Expo 2009, no. GT2009-59210, 2009.

[18] S. T. H. Yang Z., New time scale based k-eps model for near-wall turbulence, AIAA Journal 31 (1993) 1191–1198.

[19] S. B. Launder, B.E., Application of the energy dissipation model of turbulence to the calculation of flow near a spinning disc, Letter Heat Mass Transfer 1 (1974) 131138.

[20] J. Brouckaert, Fast response aerodynamic probes for measurements in turbomachines, in: Proceeding of IMechE, Part A: J. Power and Energy, Vol. 221, 2007.

[21] T. C. S., Three-dimensional and tip clearance flows in compressor, in: VKI LS 2006-06 on Advances in Axial Compressor Aerodynamics, 2006.

[22] H. D. M. R. J. H. Greitzer E., Nikkanen J., A fundamental criterion for the application of rotor casing treatment, Journal of Fluid Engineering 101 (1979) 273.

Design of a Compressor Cascade for Flow Control Tests

Fatma Ceyhun Şahin

Turbomachinery and Propulsion Department, sahinc@vki.ac.be

Supervisor: Jean-Franois Brouckaert

Assistant Professor, Turbomachinery and Propulsion Department, von Karman Institute for Fluid Dynamics, Belgium, brouckaert@vki.ac.be

Promotor: Tony Arts

Professor, Département de Mécanique, UCL, B-1348 Louvain-la-Neuve, Belgium, arts@vki.ac.be

Abstract

For low aspect ratio blades, core flow suppression by secondary flow is significant. Passive vortex generators(VGs), requiring precise design, are to be utilized on endwalls of a compressor stage which was scaled from compressible to incompressible regime. In order to observe effects of VGs, cascade test is designed including endwall geometry, pressure taps, measurement chain and a variety of VGs.

Keywords: vortex generator, 5-hole probe

1. Introduction

Variety of numerical simulations around VGs are to be helpful in order to obtain a comparable data base of VG characteristics. Scale up of compressor blade to incompressible regime has been derived according to a chosen cascade facility, C1. Boundary layer development in C1 has been considered in numerical simulations regarding VGs.
Design of the experimental cascade includes choosing appropriate VGs as well as locations of pressure taps and a method to implement instrumented blades with VGs into the facility.
Besides an unavoidable pressure loss behind VGs, they should be sufficient in decreasing the boundary layer thickness. Previously calculated numerical simulations around the blade provide a reference point for the locations of pressure taps on the blade and also on the endwalls. Size and location of VG is also to be considered. One passage is to be instrumented and neighbouring passages will also be controlled.
Before any unsteady measurement regarding vortices, flow velocity and time averaged pressure is to be measured behind the blades and also behind VGs. A 5-hole probe has been calibrated for that purpose.

2. Numerical Simulations on Vortex Generators

With the aid of literature, an appropriate geometry for VGs in a compressor passage, where the flow experiences adverse pressure gradient, should be chosen. CFD calculations are conducted prior to any measurement on VGs. Since the simulations are only on VGs but not on cascade, they provide qualitative information more than a quantitative one.

2.1. Type of Vortex Generator

As the literature suggests vortex strength downstream of joined VGs is reduced more rapid than that for the spaced or co-rotating VGs in an adverse pressure gradient flow and adverse pressure gradient tends to promote interaction between the vortices of the counter-rotating spaced vanes [1] a couple of co-rotating VGs are simulated in the flow condition of C1. Triangular VGs instead of rectangular ones will introduce less drag loss.
Two normal triangular VGs which receive the flow at apex are spaced twice of their height. Single VG is depicted in Fig. 1. Thickness of the VGs might be 1/10h. However, numerical simulations showed that pressure loss behind VGs is not significantly depended on that thickness. In order to avoid any manufacturing adversity for small h values, also assuming that in real case

VGs will be scaled down as well as blades, thickness of VG is fixed to 1 mm. Base length, L, is either twice of the VG height or equal to h.

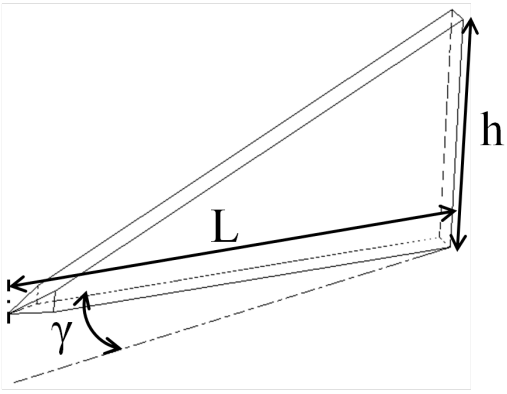

Figure 1: Single vortex generator; h is the height of the VG, L is the base length of the VG (h or 2h), γ angle of incidence between the flow and the VG.

2.2. Mesh Around the Vortex Generators

In the literature, it is recommended to simulate VGs separately because of possible gridding problems [1]. Two triangular VGs are placed in a box which has half height of one chord length in C1, as depicted in Fig. 2 with notations of cascade. Predefined boundary layer in C1 is the inlet boundary condition, compressor exit static pressure is the outlet boundary condition. Side walls have periodic boundary condition and the top wall is symmetric.
Boundaries for the angle between VGs and flow direction has already been chosen as 20° and 70°.

The height of the domain is fixed to half of chord

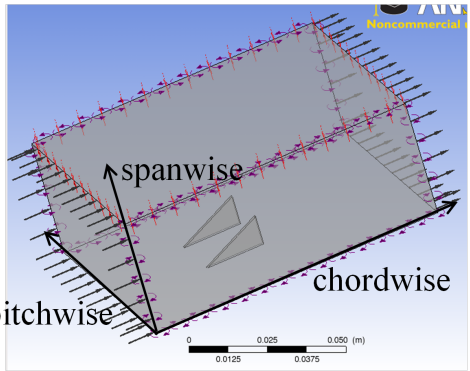

Figure 2: Numerical simulation domain for the flow around VGs.

length but the width changes according to the height of VGs because the distance between VGs depends on h. Number of structured mesh elements vary between 800K and 1200K.

2.3. Optimization of Vortex Generators

A VG, promising in terms of postponing boundary layer separation, should be capable of reducing the shape factor. Optimization will also consider pressure loss in the presence of VG. Several cases of two VG geometry have been simulated. Both geometries are normal triangles, one with a base length of VG height where the second has the base length twice of VG height. VG height, h, varied between 2 mm and 10 mm. Flow angle varied between 20o and 70o. A list for all simulated cases are in Table 2.3.

Height/ base length	h (mm)	Flow angle	Name	Height/ base length	h (mm)	Flow angle	Name
1/2	10	20	c10a20	1	10	20	i10a20
1/2	10	30	c10a30	1	10	45	i10a45
1/2	10	48	c10a48	1	10	70	i10a70
1/2	10	60	c10a60	1	7	30	i7a30
1/2	10	66	c10a66	1	7	60	i7a60
1/2	10	70	c10a70	1	5	30	i5a30
1/2	5	30	c5a30	1	5	60	i5a60
1/2	5	60	c5a60	1	3	30	i3a30
1/2	5	70	c5a70	1	3	60	i3a60
				1	2	60	i2a60
				1	2	66	i2a66
				1	2	70	i2a70

Table 1: Numerically simulated cases for VGs in flow

2.4. Results of numerical simulations

Pressure loss behind VGs are calculated on certain planes from area averaged total pressure on each plane.

$$(P_{o_1} - P_{o_2})/P_{o_1} \quad (1)$$

In Eq. 1, P_{o_1} is area averaged total pressure before VGs and P_{o_2} is area averaged total pressure for individual planes behind VGs.
Instead of shape factor, boundary layer thickness (δ) is more basically extracted from CFD results. It is defined according to the total pressure gradient in the spanwise direction of blades;

$$(\Delta P_o)/\Delta y \quad (2)$$

Behind the VGS, d would vary in pitchwise. However, a pitch length averaged information is more robust in comparison base. Hence, instead of local vorticity values, Eq. 2 where P_o is length averaged total pressure gives a simpler gradient value. Viscous flow is considered up to a point where the value of Eq. 2 drops 1% of its maximum value.

2.4.1. *Pressure Loss Behind VGs*

Area averaged total pressure loss behind VGs are plotted for each case in the following figures. Pressure loss because of c-type VGs which have a base length twice the height are in Fig. 3 and loss because of i-type VGs which are isosceles triangles are in Fig. 4. In Fig. 5, VGs having the same height are compared. Flow angle is as effective as the size of VGs if causing loss is considered.

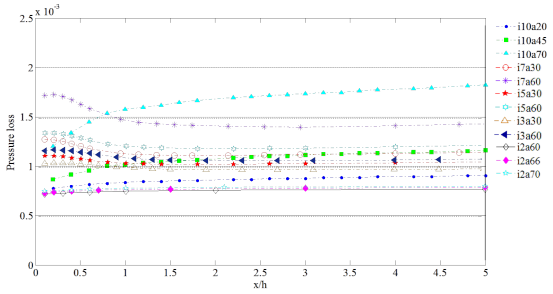

Figure 3: Pressure loss behind VGs with h/L=1/2

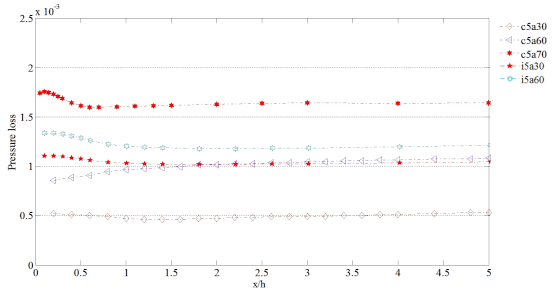

Figure 4: Pressure loss behind VGs with h/L=1

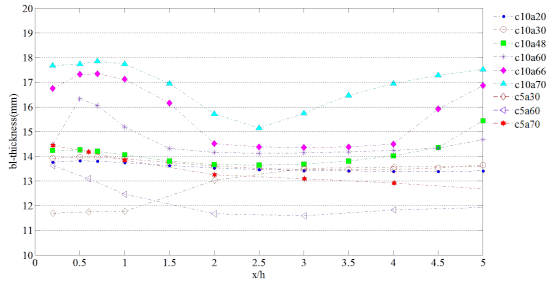

Figure 5: Pressure loss behind VGs with h=5 mm

2.4.2. *Boundary Layer Thickness Behind VGs*

Boundary layer thickness behind VGs is plotted with respect to the distance from trailing edge of VG, nondimensionalized by the height of VG, h. The following plots Fig. 6, Fig. 7, Fig. 8 depict d for the same conditions with the previous three plots. Among several size and flow angle conditions, 60o of angle between flow and VG provide severe drop in d for all types of VGs simulated.

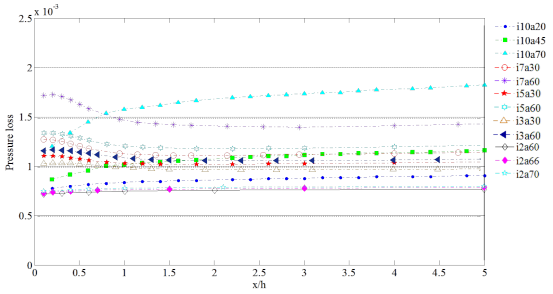

Figure 6: Pressure loss behind VGs with h/L=1/2

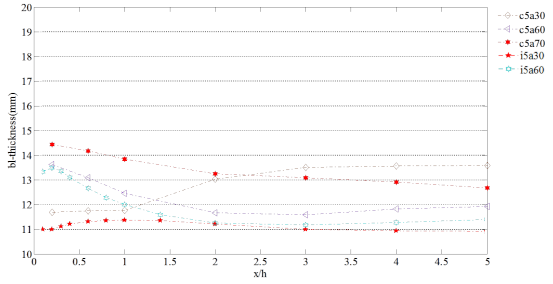

Figure 7: Pressure loss behind VGs with h/L=1

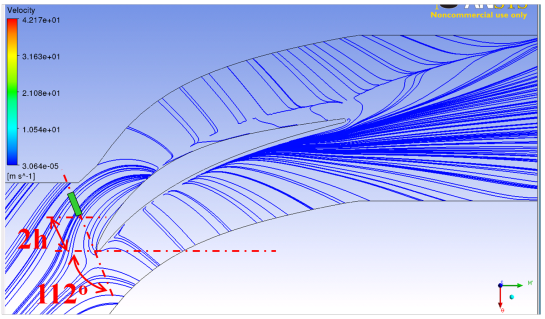

Figure 8: Pressure loss behind VGs with h=5 mm

2.5. *VGs to be Tested in Cascade*

It will not be possible to test all VGs numerically simulated in cascade. Five different geometries are selected among several numerical simulations. Those

are: c10, c5, c2, i7, i5. 60o is selected as flow angle because of providing maximum drop in boundary layer thickness. A possible orientation of VG in the cascade is depicted in Fig. 9.

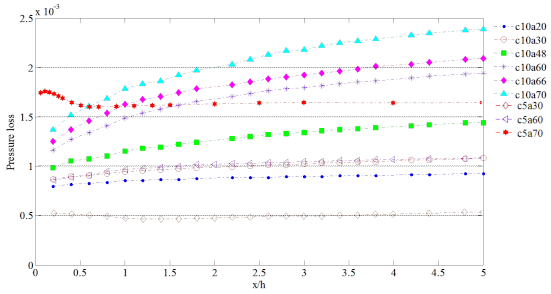

Figure 9: Single VG at the compressor passage inlet.

3. Instrumentation of the Cascade

Inlet stagnation condition of the compressor blades will be available in terms of reservoir temperature and pressure of facility the C1. Numerical simulations provide surface streamline information on the blades and also on the endwalls for uncontrolled case. A flow visualization technique will be utilized in order to assure that information and also provide same type of information for controlled cases. Correct rate for pressure taps will be determined after such experimental information. In order to increase flexibility of static pressure measurement, finely instrumented blades and endwalls are designed. Centre passage will be controlled and pressure distribution for this passage with two neighbouring ones will be measured. Blades in those passages will be fixed via shells representing endwall. Among the pressure taps on those shells, in Fig. 10, ones in the vicinity of VG will be connected to a scany valve. The instrumented blades will be available for shifting in chordwise direction. Thus, a constant precision in boundary layer measurements for different VG heights will be possible. Pressure taps on suction and pressure side of a blade is depicted on a single blade, in Fig. 11 Deviation angle at the trailing edge is a parameter for the effectiveness of VG. Flow angle at the exit plane will be measured via 5-hole probe. A hot-wire is to be utilized for unsteady measurements

4. 5-Hole Probe

Considering that the height of VG will be one order of magnitude lower than chord length of the blade, a

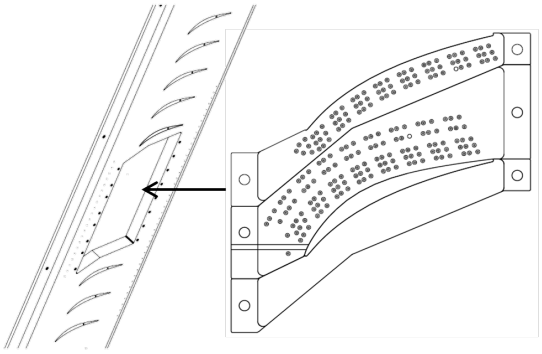

Figure 10: Pressure taps on the endwall of the cascade

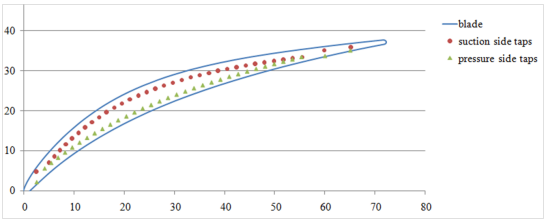

Figure 11: Static pressure taps on a blade

5-hole probe as small as possible should be utilized. A hemispherical probe would be a good choice in terms of confident calibration coefficients [1]. On the other hand, 5-hole probe requires a significant volume even it is only open-ended. For the current study, a probe with a separate kiel probe is chosen. Flow direction is measured via 4-hole probe and the total pressure is averaged by kiel probe. The probe is depicted in Fig. 12.

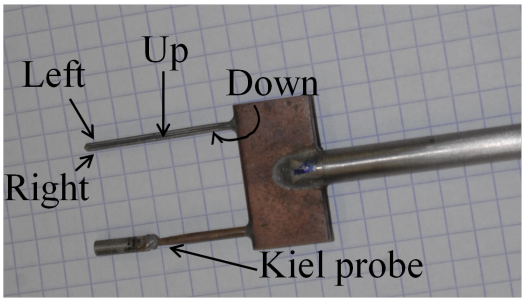

Figure 12: 5-hole probe

4.1. Calibration of the 5-Hole Probe

The probe is calibrated according to non-nulling technique [1]. Response of each probe is recorded for angles -25° 25° with increment of 5°, at three different free stream velocities. Pressure difference from

the probes right and left are assumed to give an angle information of theta, θ, and the difference between up and down are assumed for an angle of phi, ϕ. Data reduction is held according to that notification.

$$p_{ave.} = (p_R + p_L + p_U + p_D)/4 \quad (3)$$

$$Cp_\theta = (p_R - p_L)/(P_K - p_{ave.}) \quad (4)$$

$$Cp_\phi = (p_U - p_D)/(P_K - p_{ave.}) \quad (5)$$

$$Cp_K = (P_K - p_{atm.})/(P_o - p_{atm.}) \quad (6)$$

$$Cp_{ave.} = (p_{ave.} - p_{atm.})/(P_o - p_{atm.}) \quad (7)$$

p_R, p_L, p_U, p_D are pressure values measured from the holes right, left, up and down, respectively. pave. is the mean of those values. PK is the value measured by kiel probe. P_o and p_atm are the total and static pressure values of the free stream where the probe is calibrated. The probe had been calibrated in atmospheric conditions and gauge pressures are measured, hence denominators of Cp_K and Cp_{ave}. values are basically the total pressure in calibration tube.

5. Calibration Map

Four calibration maps are obtained. Two of them are for two different angles. The other two are in order to determine static and stagnation pressure for the angles read in two previous maps. Former maps represent angle theta and phi, respectively, with respect to Cptheta versus Cpphi in Fig. 13 and Fig. 14. Latter maps represent pave. and PK, respectively, with respect to angle information from the previous maps. Those maps are in Fig. 15 and Fig. 16. A Mat-

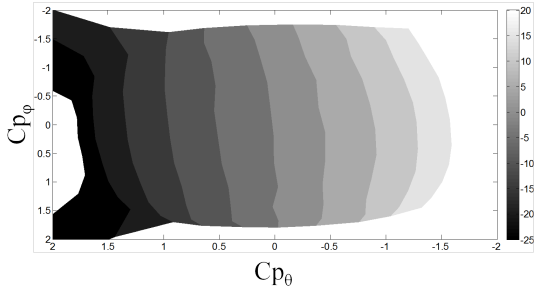

Figure 13: Calibration map; variable theta

lab code helps to interpolate measured Cp values on present maps and find the angles of an unknown flow. In the next step, angle values are interpolated on pressure maps and correct speed and static pressure of the flow is obtained.

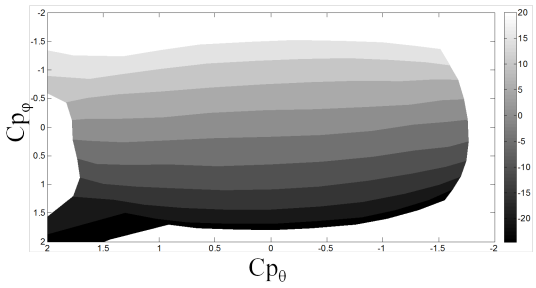

Figure 14: Calibration map; variable phi

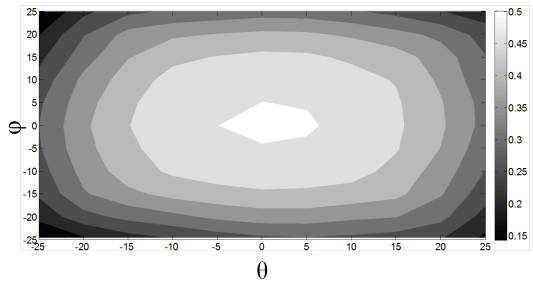

Figure 15: Calibration map; variable p_ave.

6. Future Plans

The blades and endwalls are expected in order to construct the cascade. Base line of the cascade will be covered with special oil paints in order to view surface streamlines. The same procedure will be applied when the stages are controlled. Solution for the paint is already determined and at least three different colours will be used on different surfaces such as the blade surface, endwall and VG surface. The quantitative measurements will start with exit flow conditions using the 5-hole probe and selected pressure taps on the surfaces. The aim is proving that the selected VGs give out expected gain in boundary layer thickness decrease without pressure losses exceeding estimated levels

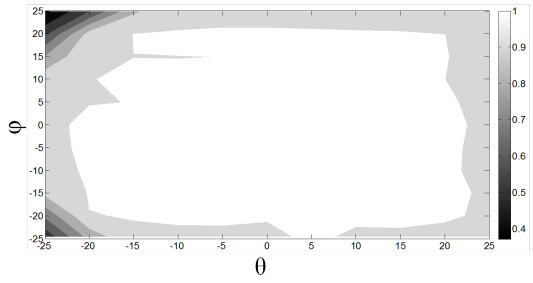

Figure 16: Calibration map; variable p_K

References

[1] P.R. Ashill and J.L. Fulker and Hackett, K.C., Studies of flows induced by Sub Boundary layer Vortex Generators (SBVGs), Reno, Nevada, 2002.

[2] Morrison, G.L.and Schobeiri, M.T. and Pappu, K.R., Five-Hole Pressure Probe Analysis Technique, Flow Measurement and Instrumentation (9) (1998) 153–158.

[3] Mukhopadhya, S. and Dutta, A. and Mullick, A.N. and Majumdar, B., Studies of flows induced by Sub Boundary layer Vortex Generators (SBVGs), Journal of Aero Soc. Of India 3 (14) (2001) 271–279.

[4] R.V. Chima, Computational Modeling of Vortex Generators for Turbomachinery, NASA/TM GT-2002-30677.

ENGINE ANALYSIS AND IMPROVEMENTS

Numerical modeling of a combined cycle for high speed propulsion

Víctor Fernández Villacé

Turbomachinery and Propulsion Department, villace@vki.ac.be

Supervisor: Guillermo Paniagua

Associate Professor, Turbomachinery and Propulsion Department, von Karman Institute for Fluid Dynamics, Belgium, paniagua@vki.ac.be.

Promotor: José L. Montañés

Professor, Aerothermodynamics and Propulsion Department, Universidad Politécnica de Madrid, joseluis.montanes@upm.es

Abstract

The high temperature regenerator of Scimitar is modeled with Ecosimpro together with the libraries of the European Space Propulsion Simulation System. New turbomachinery models have been developed with enhanced robustness. An optimum design that maximizes the regenerator efficiency has been identified. The present research demonstrates that there is not a design that fulfills the engine specifications. Consequently a new engine architecture is proposed.

Keywords: Numerical Modeling, Combined Cycle, Variable Cycle, High Speed Propulsion, Air-Breathing Engines.

1. Introduction

The Scimitar engine is the hydrogen-fueled propulsive plant of the airplane A2, developed by Reaction Engines Ltd. for antipodal hypersonic cruise. The Scimitar features a variable cycle engine that combines a turbofan based cycle with an air-turbo-rocket cycle, Fig. 1. The turbofan based cycle operates from take-off to Mach 2.5. Between Mach 2.5 and Mach 5 the engine have the dual operation of an air-turbo-rocket with a ramjet burner in the bypass. At Mach 5 the vehicle cruises and the cycle is that of a pure air-turbo-rocket engine [1]. In the propulsive cycle, the helium flows through the precooler (PC) during the supersonic cruise (above Mach 3.1) in order to recuperate the thermal energy of the incoming air. Cryogenic hydrogen acts as heat sink of the system and allows the conversion of the recuperated thermal energy into useful work to drive the turbine. The energy interchange between helium and hydrogen is done through a complex recuperator (R), which contains two modules: the high temperature and the low temperature regenerators.

The high temperature regenerator (R4H) compresses and cools the helium coming directly from the counter-rotating turbine (T1), as Figure 2 shows. The efficiency of the system is enhanced by using a set of inter-coolers ($HX4*$) in cascade, as displayed in Fig. 3, among the compressor stages ($C*$). In order to compute its exergetic efficiency, an availability balance is applied to the control volume (CV) containing the regenerator. In steady state with only mass exchange through the rigid boundaries of the control volume, the expression [2]:

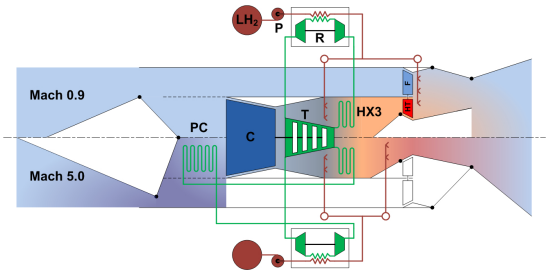

Figure 1: Turbofan (upper half) and air-turbo-rocket (lower half) configurations of Scimitar.

$$\dot{\Phi}_{CV} = (1 - T_0/T)\dot{Q}_T + \dot{W} + p_0\dot{V} +$$

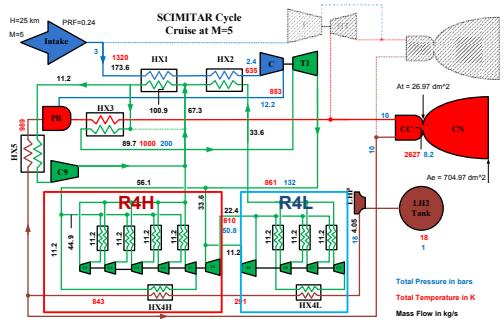

Figure 2: The thermodynamic cycle of Scimitar.

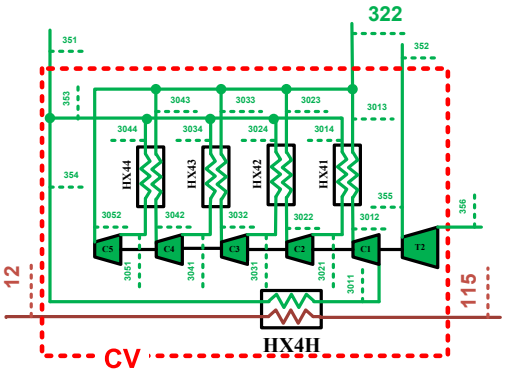

Figure 3: Detail of the regenerator R4H.

$$+\sum_i (\dot{m}\phi)_i - \sum_o (\dot{m}\phi)_o - T_0\dot{\sigma}_p \tag{1}$$

reduces to:

$$\underbrace{\dot{m}_{355}(\phi_{355}-\phi_{356})+\dot{m}_{115}(\phi_{115}-\phi_{12})}_{\dot{Q}_a}+$$

$$+\underbrace{\dot{m}_{351}(\phi_{351}-\phi_{322})}_{-\dot{Q}_u} - T_0\dot{\sigma}_p = 0, \tag{2}$$

with $\dot{Q}_u$ being the useful power rejected from the hot stream and $\dot{Q}_a$ the available power from the turbine and the hydrogen flows. In the calculation of the exergy, the temperature of the hydrogen source is taken as reference, $T_0 = T_{115}$. The exergetic efficiency holds:

$$\eta_\phi = \frac{\dot{Q}_u}{\dot{Q}_u + T_0\dot{\sigma}_p} \tag{3}$$

The entropy balance applied to the same control volume stands the expression of the entropy production term:

$$\dot{\sigma}_p = \sum_o (\dot{m}s)_o - \sum_i (\dot{m}s)_i \tag{4}$$

The second law analysis provides an expression for the efficiency that weights the performance against that of the ideal machine working under the same constraints. An analysis based on the first principle would provide an absolute efficiency value regardless of the feasibility of the design.

2. Numerical Model

Ecosimpro is an object oriented programming platform for the simulation of complex physical systems, which can be build assembling its constituent components. Each component incorporates the proper mathematical formulation, built upon a number of hypothesis, to reproduce a physical phenomenon: the component heat exchanger reproduces the heat transfer along two parallel fluid streams; the turbomachinery components reproduces the interchange of power between the fluid stream and the rotating parts. The different components communicate with each other through entities called ports. In order to arrange the set of differential algebraic equations (DAE) that describe the complete system, the port contains the variables (pressure, enthalpy, composition, mass flow rate, ...) that are transfered between linked components and the directionality of the interchange (output or input). A more thorough description of Ecosimpro algorithms can be found in [3].

The integration algorithm employed in this analysis is the Differential Algebraic Equation Solver (DASSL) [3] and [4]. DASSL approximates the time derivative in the differential algebraic equation system by finite differences of order and time step that depends on the evolution of the solution in time.

The symbolic model relies on the European Space Propulsion Simulation System (ESPSS), which comprises a set of libraries with thermodynamic data on the working fluid as well as the heat exchanger and the linking elements (volumes and valves). A description of the heat exchanger follows below. For a more exhaustive insight into the heat exchanger component or the linking elements the reader is entitled to read [5]. The compressor and turbine elements are part of the contribution to the ESPSS by the von Karman Institute.

2.1. Heat Exchanger

This is a 1-Dimensional model of a type shell and tube heat exchanger with counter flow disposition and no fins, Fig. 4. The shell fluid (external to the pipes) and the fluid into the pipes (internal fluid) are discretized in finite volumes in which the conservation equations of mass, momentum and energy apply. The heat transfer and flow rate of the internal fluid equals the contribution from a single pipe times the number of pipes of the heat exchanger, hence only one pipe is calculated.

Neighboring nodes interchange heat flux as shown by equation (5) where: N is the number of nodes, inlet is at node 1 and outlet at node N. The flux $\dot{q}_{shell}$ accounts for the heat transfered from one pipe to the shell, being the total heat flux to the shell the result of multiplying this quantity times the number of tubes in the heat exchanger.

$$\{\dot{q}_{wall\ i} = -\dot{q}_{pipe\ i} - \dot{q}_{shell\ N-i+1}\}_{i=1,N} \tag{5}$$

$$\{S_i \cdot \dot{q}_{wall\ i} = (m \cdot C)_{wall\ i} \cdot \dot{T}_{wall\ i}\}_{i=1,N} \tag{6}$$

$$\{\dot{q}_{pipe/shell\ i} = h_{c\ i} \cdot (T_{wall\ i} - T_{pipe/shell\ i})\}_{i=1,N} \tag{7}$$

$$h_c = Nu \cdot k/D_h \tag{8}$$

The transient wall heating (or cooling) is described by equation (6) where: S_i is the surface of the wall-shell interface (or wall-tube, which has the same extension) and $m \cdot C$ is the product of the tube wall heat capacity and mass. The heat flux entering the fluid volume $\dot{q}_{pipe}$ or $\dot{q}_{shell}$ is computed from equation (7), where the convective heat transfer coefficient $h_{c\ i}$ is calculated at each node from the Nusselt number given by the semi-empirical correlation (11), as explained in [5]. No heat loss is considered through the casing.

$$Nu_{lam} = 4 \tag{9}$$

$$Nu_{tur} = 0.023 \cdot Re^{0.8} \cdot Pr^{0.4} \tag{10}$$

$$Nu = (Nu_{lam}{}^{16} + Nu_{tur}{}^{16})^{1/16} \tag{11}$$

The friction factor f is calculated from a correlation valid for laminar, turbulent and transient flow:

$$f = 8 \cdot \left(\left(\frac{8}{Re} \right)^{12} + (A+B)^{-3/2} \right)^{1/12} \tag{12}$$

$$A = \left(2.457 \cdot ln \frac{1}{(7/Re)^{0.9} + 0.27 \cdot \epsilon/D_h} \right)^{16} \tag{13}$$

$$B = (37530/Re)^{16} \tag{14}$$

and is then introduced in the 1-D momentum equation as:

$$\frac{\partial(\rho v)}{\partial t} + \frac{\partial(\rho v^2 + p)}{\partial x} = \frac{-k_f}{2} \cdot f \cdot \frac{\rho \cdot v^2}{D_h}, \tag{15}$$

where k_f is a correction to the friction factor. The momentum equation (15) is discretized in finite volumes using a centered scheme. Further details are given in [5].

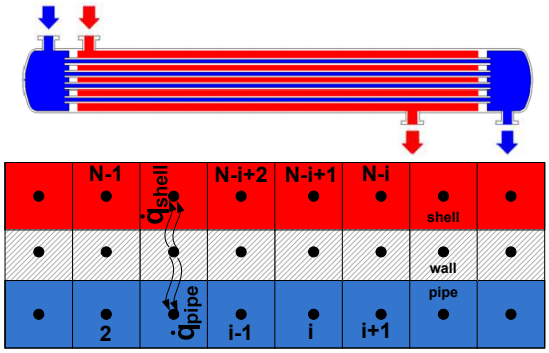

Figure 4: Sketch of the heat exchanger model and discretization in finite volumes.

2.2. Turbomachinery elements

They make use of steady experimental characteristics to predict the machine off-design performance in terms of its pressure ratio π, mass flow rate $\dot{m}$ and adiabatic efficiency η. The characteristic maps are given as functions of the corrected speed $\tilde{N}$ and the β-parameter:

$$\pi(\tilde{N},\beta)\,; \qquad \tilde{m}(\tilde{N},\beta)\,; \qquad \eta(\tilde{N},\beta) \tag{16}$$

$$\tilde{N} = \frac{\Omega/N_d}{\sqrt{\theta}} \cdot \frac{30}{\pi_n} \tag{17}$$

$$\tilde{m} = \dot{m} \cdot \sqrt{\theta_{in}}/\delta_{in} \tag{18}$$

In order to fulfill the performance at the design point, the turbomachine is resized applying constant factors to the characteristic map $(\Pi, \tilde{M}, H)$ of a known machine:

$$\pi = 1 + K_\pi \cdot (\Pi(\tilde{N},\beta) - 1) \tag{19}$$

$$\tilde{m} = K_{\dot{m}} \cdot \tilde{M}(\tilde{N},\beta) \tag{20}$$

$$\eta = K_\eta \cdot H(\tilde{N},\beta) \tag{21}$$

The energy balance yields that the mechanical power in the shaft equals the power to the fluid side:

$$P = \dot{m} \cdot \Delta h_t \tag{22}$$

$$P = T \cdot \Omega \tag{23}$$

$$\frac{\Delta h_{t,s}(p_{t_{in}}, T_{t_{in}}, p_{t_{out}})}{\Delta h_t} = \begin{cases} \eta; & (turb.) \\ 1/\eta; & (comp.) \end{cases} \tag{24}$$

In Eq. 24, $\Delta h_{t,s}$ is the total enthalpy change of an isentropic evolution from inlet to outlet status.

The excess of torque $T_{sh} - T$ accelerates the rotor, with inertia I:

$$T_s(\Omega; t) - T = I \cdot \dot{\Omega}, \tag{25}$$

This equation relaxes the mechanical constraint by allowing a difference between the torque applied on the shaft T_{sh} and the torque that the rotor transfers to the fluid T. In a similar way the constraint on the machine discharge duct is relaxed:

$$\dot{m} - \dot{m}' = \tau \cdot \ddot{m}', \tag{26}$$

being $\dot{m}$ the flow rate read from the map and $\dot{m}'$ the actual flow rate passing through the machine. The time τ is a measure of the convective characteristic time in the duct of the turbomachine:

$$\tau \approx \frac{l_{c_{in}} + l_{c_{out}}}{2 \cdot a_{in}}, \tag{27}$$

where $l_{c_{in/out}}$ is the characteristic length of the inlet/outlet ducts and a_{in} the speed of sound computed at the inlet of the machine. The solution of this differential equation must satisfy the constraint imposed by the discharge duct:

$$\dot{m}'(\dot{m}, \tau, t) = f(\pi; t), \tag{28}$$

where f is the characteristic of the discharge duct.

The combination of Eq. 16-25 establishes the form of the mechanical constraint on the operating point, $I_\Omega \equiv 0$; whereas Eq. 16, 18-20, 26 and 28 determine the constrain imposed by the discharge duct, $I_{\dot{m}} \equiv 0$. The solution of the system of equations:

$$\begin{cases} I_\Omega(\tilde{N}, \beta; K_\pi, K_{\dot{m}}, K_\eta, N_d, T_s, \vec{B}, \vec{P}; t) = 0 \\ I_{\dot{m}}(\tilde{N}, \beta; K_\pi, K_{\dot{m}}, f, \vec{B}, \tau; t) = 0 \end{cases} \tag{29}$$

$$\vec{B} = (\delta_{in}, \theta_{in}); \ \vec{P} = (\Omega_0, I) \tag{30}$$

is the transient operating line of the turbomachine $\tilde{N}(t), \beta(t)$ which, for a given machine size $\{K\}_{\pi,\dot{m},\eta}, N_d$, is determined by the inlet conditions $\vec{B}$, the discharge characteristic f and the mechanical constraint T_s. The integration constant Ω_0 is the initial shaft speed.If $\dot{\Omega} = \ddot{m}_{out} = 0$, the previous system for the steady operating line is:

$$\begin{cases} I_{\Omega_0}(\tilde{N}_0, \beta_0; K_\pi, K_{\dot{m}}, \vec{B}, T_s \cdot N_d, \eta_0 \quad) = 0 \\ I_{\dot{m}_0}(\tilde{N}_0, \beta_0; K_\pi, K_{\dot{m}}, \vec{B}, f \quad) = 0 \end{cases} \tag{31}$$

Normally the turbomachine is linked to other fluid components like pipes, manifolds or heat exchangers and mounted on the same spool than other $m - 1$ machines. The steady state of this assembly cannot be known a priori. However the stagnation pressures and temperatures in the fluid components can be approximated by those of the design cycle. These provide the inlet conditions $\vec{B}$ and the value f. The speed N_d, operating point $(\tilde{N}_0, \beta_0)$ and efficiency η_0 are design values. The size of the machines is then determined by m equations like Eq. 31 and the closure equation introduced by the common spool: $\sum_{i=1}^{m} T_{s_i} = 0$. Fig. 5 shows the input data and design values required for the matching of a compressor with a turbine on the same shaft.

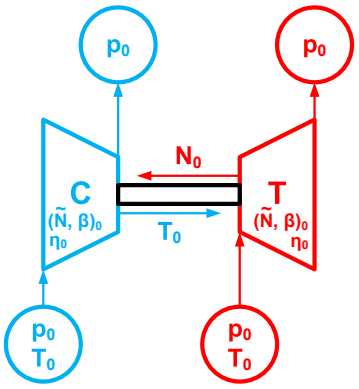

Figure 5: Input data for sizing the compressor-turbine matching.

With the above procedure the machines are sized using the equations of the steady operating line, but the simulation is not necessarily in equilibrium. When the integration converges to the steady solution, the operating point moves away from its design value and the machine needs to be rescaled using now the steady solution as first guess, Fig. 6. After few iterations the steady state with all the turbomachines working on-design is achieved.

However the numerical integration will not converge if the supposed stagnation magnitudes are far from the stationary solution, unknown a priori, because the transient growing can lead the solution inside instable regions. This occurs for instance when the operating point of the turbomachine moves out of its characteristic map. In other occasions there exists a domain of instability inside machine characteristic map, like in the compressors when $\partial\pi/\partial\dot{m}|_{\tilde{N}} > 0$.

3. Simulation

The inter-cooling stages are modeled as heat exchangers whose shell and the tubes are discretized in finite volumes. Because the efficiency of the heat exchange depends on the temperature jump between both fluid veins, it is influenced by the number of finite volumes. The discretization in 5 finite volumes is a trade-off between an accurate prediction of the heat exchanger efficiency and the too expensive computation with a fine mesh.

At the beginning of the computation, each node in the same fluid vein is initialized with the same temperature and pressure, provided by the design cycle of Scimitar. During the initial steps of the numerical integration, pressure waves originate inside the elements while the initial pressure distribution accommodates to the boundary conditions at the inlet and outlet. These oscillations move the operational point of the turbomachinery components outside its characteristic map and may cause the calculation to diverge. In order to draw the operational points back inside the maps to their design values, the components are resized following the sizing procedure explained previously. The Fig. 6 plots the β-parameter for the compression stages and the turbine $T2$ during the initial transient. Extrapolation of the turbomachine map values occurs for $\beta > 1$. The targeted value of β_o is 0.5.

The thermodynamical steady state is achieved when the temporal variation of the total energy of the system is less than 0.01% of the power supplied by the hydrogen:

$$\frac{|\sum_i (\dot{m}h_t)_i - \sum_o (\dot{m}h_t)_o|}{(\dot{m}h_t)_{115}} = \frac{|\dot{E}_{CV}|}{(\dot{m}h_t)_{115}} < 10^{-4} \quad (32)$$

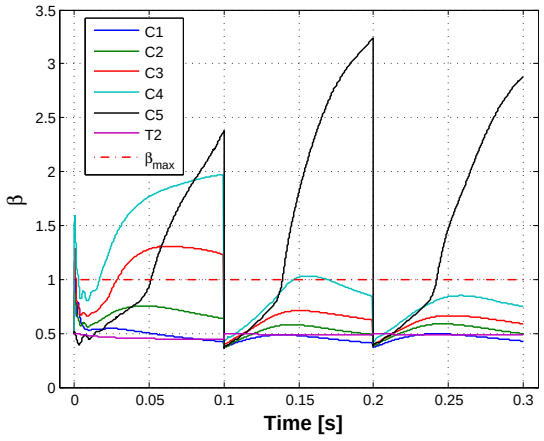

Figure 6: Evolution of the β-parameter during the initial transient.

4. Design Point Optimization

A first attempt to improve the efficiency of the regenerator design consist in redesigning the turbomachinery in order to have the optimum power distribution along the compressor stages. This is done by resizing the stages for the prescribed helium and hydrogen supply conditions and discharge pressures.

According to Eq. 3, diminishing the global entropy generation in the system $\dot{\sigma}_p$ is equivalent to increasing its efficiency. The search of the optimum design must follow the direction of decreasing $\dot{\sigma}_p$. A differential evolution algorithm is used to search for the optimum size of the compressor stages that minimizes the irreversibility, $T_0\dot{\sigma}_p$.

The regenerator compresses and refrigerates the hot stream of helium (351 – 322) by using a cold stream of hydrogen (115 – 12) and an additional hot source of helium (355 – 356), Fig. 7. The overall design cycle provides the boundary conditions (in red). Varying freely the size of the tubomachinery stages, i. e. their power consumption, will change the efficiency of the system but also its performance, i. e. the helium delivery mass flow of both hot and cold streams $(\dot{m}_{356}, \dot{m}_{322})$. It is obvious that the helium delivery temperature is prescribed by the system efficiency. The performance of the system is then assessed by constraining the helium discharge mass flows.

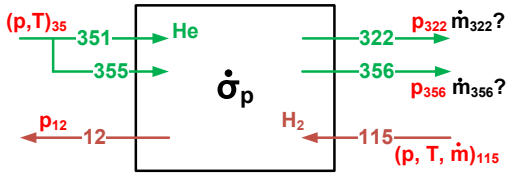

Figure 7: The system as a black box.

Table 1 shows the inputs of the 5 optimization runs and Table 2 shows the performance of the best design found for each one of the cases. The baseline (BL) individual is used for comparison with the performance of the optimized designs. The optimization is run synchronously in 4 processors: the individuals of each generation are dispatched for its evaluation whenever there is a processor available. Each generation contains 20 individuals. The computational time is in the order of $10h$ per CPU.

The optimization run a is subject to the constrain $\dot{m}_{322} \geq 56.1\ kg\ s^{-}$ in the helium delivery mass flow. This is: any design found during the search for which the delivery mass flow is lower than that of the design cycle is not considered as a candidate for opti-

mum. Both inlet and outlet pressures of the compression stages are boundary conditions of the calculation, therefore the figures of power distribution along the stages are proportional to their mass flow rates. Fig. 8 shows that the mass flow through stage $C4$ is null, hence the heat exchangers $HX43-44$ are removed from this optimum solution. The reason is that the regimen in these two heat exchangers is inverse: the helium delivered by the compression stage $C3$ is heating up the inlet stream of the following stage instead of cooling it down, and the same occurs in the stage $C4$. The temperature distribution along the heat exchangers is similar to that of the baseline shown in Fig. 9. A more efficient design is found pumping through $C5$ all the remaining flow rate without pre-cooling.

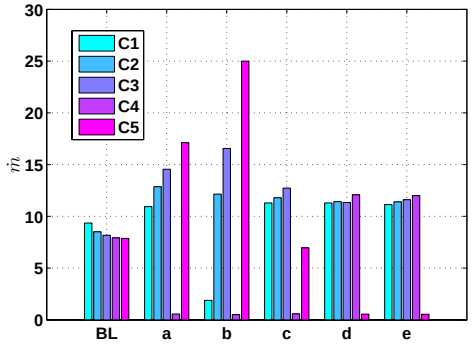

Figure 8: Flow rates through the compression stages.

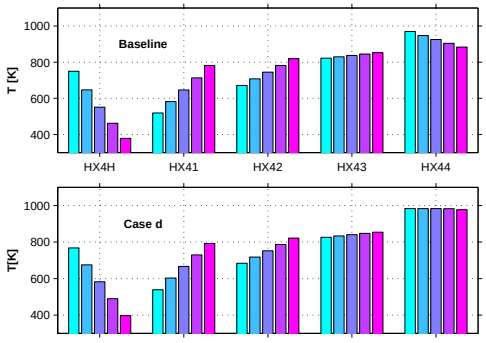

Figure 9: Nodal temperatures of the helium along the cascade of inter-coolers (the inlet nodes are shown in light blue, the outlet nodes in pink).

The optimization case b is run supposing isentropic evolutions ($\eta = 1$) in the compression stages and the turbine. The delivered flow rate of helium is constrained as in case a. The purpose is checking if the inverse behavior can be originated by the heating of the helium stream due to the losses incurred in the turbomachinery. However the last cooling stages are still inverted. With no loss incurred in the turbomachinery, the amount of entropy production is due to heat transfer only. A large contribution comes from the heat exchange with the hydrogen stream, which explains the significant reduction of mass flow through $HX4H$. The 46% of the compressed helium delivery flows uncooled trhough the stage $C5$. This and the reduced heat exchange with the hydrogen stream increase the overall helium temperature, hence the compression work and mass flow through the turbine increase as well. The helium delivery temperature of $1000\,K$ is $140\,K$ higher than at the inlet (station 351).

This design is more efficient than the baseline. However it requires a higher rate through the turbine than the value $\dot{m}_{T2} = 22.4\ kg\,s^{-}$ specified by the design conditions. The losses incurred in the heat exchangers and the turbomachinery prevent a design with a so low turbine mass flow rate.

In the cases a and b the power of the turbine $T2$ exceeds the design requirements, which specify a mass flow rate of $22.4\ kg\,s^{-}$ through it. The optimization case c is run with the turbine mass flow constrained to that value. As a result the delivered helium flow rate decreases and the efficiency is penalized respect to the design a. The entropy production slightly decreases and the cause of the lower efficiency is the decrease of useful power $\dot{Q}_u$ due to the lower helium flow rate and despite of the decrease of the flow exergy ϕ_{322} at the delivery temperature of $867K$. The minimum helium flow rate cannot be satisfied with the constraint on the turbine power.

Case d shows that an increase in the turbomachinery efficiency of 1% raises the system efficiency almost in the same amount and the helium delivered in 2% respect to the design c. The turbine power is constrained with a higher ceiling of $28.6\ MW$ and this is limiting the helium delivery at a value 17% below the design performance. Notice that the turbine flow rate is lower than before because of its efficiency increase.

The increase of the turbomachinery efficiency in d respect to the case c causes a drastic change in the configuration of the cycle. Only the last heat exchanger $HX44$ is removed, whereas the design c cancels both two last heat exchangers. The flow rates are kept close to their design values of $11.2\ kg\,s^{-}$ through the compression stages $C1-4$.

The case e is run with helium delivery temperature T_{322} as objective value to be minimized instead of the entropy production term $\dot{\sigma}_p$. The purpose is checking the independence of the results using either objective

values. The optimum design coincides with the of d, hence minimizing the delivery temperature or the entropy production term are both equivalent strategies.

It can be observed that, in the most optimistic case with an efficiency of 98% for the turbomachinery, the helium delivery temperature equals its suply temperature of $T_{351} = 861\ K$. For none of the optimum designs this temperature is below the supply value. The design is a trade-off between the reduction of energy consumption by lowering the stages inlet temperature and the energy degradation incurred by heat transfer.

Table 1: Optimization cases

Run	Constr.	OF	η
BL	-	-	0.9
a	$\dot{m}_{322}$	$\dot{\sigma}_p$	0.9
b	$\dot{m}_{322}$	$\dot{\sigma}_p$	1.0
c	$\dot{m}_{322}$ & $\dot{m}_{T2}$	$\dot{\sigma}_p$	0.9
d	$\dot{m}_{322}$ & $\dot{m}_{T2}$	$\dot{\sigma}_p$	0.98
e	$\dot{m}_{322}$ & $\dot{m}_{T2}$	T_{322}	0.98

Table 2: Optimization results

Run	$\dot{m}_{322}$ $kg\ s^-$	T_{322} K	$\dot{m}_{T2}$ $kg\ s^-$	$\dot{\sigma}_p$ $kW\ K^-$	η_ϕ %
BL	50.9	900	28.6	28.6	71
a	56.1	907	31.6	29.3	73
b	56.1	1000	32.4	11.2	93
c	43.4	867	22.4	24.9	62
d	46.8	866	20.6	17.7	72
e	46.8	867	20.6	17.7	72

5. Conclusion

The developed optimization procedure provides the most efficient cycle attainable. In addition, the optimizer proofs to be able of designing for the best cycle topology in function of the imposed constraints. Starting from the given baseline design the optimizer decides whether each compressor and cooling stage have to be removed from the thermodynamical cycle. On this respect, the optimum design found eliminates the last cooling stage.

The optimized design does not require the last cooling stage of the regenerator. This is probably due to an inappropriate modeling of the heat exchanger using the component from the ESPSS libraries. In fact, it was later confirmed by the engine designer that the geometry of the cooling stages does not correspond to the proprietary design. Neither is appropriate the correlation for the heat transfer, Eq. 11. On this respect some investigations have been done on previous works involving the heat transfer in a bank of tubes in cross flow. Authors like [6; 7; 8] propose correlations for the Nusselt number in function of the bank geometry and the Reynolds and Prandtl numbers. The reformulation of the components using this correlations will enhance the heat transfer predictions by the numerical model.

The stability issues of the computations have been identified. The new turbomachinery model allows dynamical rescaling of the machine during the simulation and with it a robust numerical model can be achieved.

With the achievement of a numerical model of the high temperature regenerator, the modeling of Scimitar in the Mach 5 configuration will continue with the inclusion of the low temperature regenerator, of similar characteristics, and the engine core, which comprises the precooler, the turbo-compressor, the preburner and the core chamber and nozzle. In fact, the core of Scimitar shows the same architecture than in the engine Sabre, which has been already modeled [9]. The final goal is to dispose of a numerical tool able to predict the performance of the engine in its early design status.

Nomenclature

I	mechanical inertia $[kg \cdot m^2]$
N_d	design speed $[rpm]$
P	power $[W]$
$\dot{Q}$	thermal power $[W]$
R	gas constant $[J \cdot kg^- \cdot K^-]$
S	entropy $[J \cdot K^-]$
T	temperature or torque $[K]$,$[N \cdot m]$
U	internal energy $[J]$
V	volume $[m^3]$
$\dot{W}$	mechanic power $[W]$
h	enthalpy $[J \cdot kg^-]$
h_t	total enthalpy, $h + v^2/2$ $[J \cdot kg^-]$
$\dot{m}$	mass flow rate $[kg \cdot s^-]$
p	pressure $[bar]$
s	entropy $[J \cdot kg^- \cdot K^-]$
v	flow velocity on the engine frame $[m \cdot s^-]$
δ	dimensionless pressure, p/p_{ref}
θ	dimensionless temperature, $R \cdot T/(R \cdot T)_{ref}$
π_n	pi number
ρ	density $[kg \cdot m^{-3}]$

$\dot{\sigma}_p$	entropy production $[W \cdot K^-]$
τ	characteristic time $[s]$
ϕ	exergy, $h - h_0 + v^2/2 - T_0(s - s_0)$ $[J \cdot kg^-]$
Φ	availability, $(U - U_0) + p_0(V - V_0) + v^2/2 - T_0(S - S_0)$ $[J]$
Ω	rotational speed $[s^-]$

subscripts

$_i$	inlet
$_o$	outlet
$_t$	stagnation value

Acknowledgments

The author thanks the European Space Research and Technology Center (ESTEC) for the founding of this doctoral research, and the contract 20366/07/NL/EM. In particular, thanks to J. Steelant, technical supervisor at ESTEC.

This work is a part of the contribution of the von Karman Institute to the project LAPCAT II, co-funded by the the European Commission Framework 7th Programme.

References

[1] F. Jivraj, R. Varvill, A. Bond, G. Paniagua, The scimitar precooled mach 5 engine, in: 2nd European Conference for Aerospace Sciences, EUCASS, Brussels, Belgium, 2007.

[2] M. J. Moran, H. N. Shapiro, Fundamentals of engineering thermodynamics, 5th Edition, 2004.

[3] Empresarios Agrupados International, EcosimPro: Mathematical Algorithms and Simulation Guide, version 4.4.

[4] L. R. Petzold, DASSL: Differential Algebraic System Solver, Tech. rep., Sandia National Laboratories, Livermore, California (1983.).

[5] Astrium-Bremen, Cenaero, Empresarios Agrupados Int. and Kopoos, ESPSS EcosimPro Libraries User Manual, Tech. Rep. TN-2240, European Space Agency, version 1.4.1 (May 2009).

[6] H. Hausen, Heat Transfer in Counterflow, Parallel Flow and Cross Flow, McGrawHill, New York, 1983.

[7] W. A. Khan, J. R. Culham, M. M. Yovanovich, Convection heat transfer from tube banks in crossflow: Analytical approach, International Journal of Heat and Mass Transfer 49 (2006) 4831–4838.

[8] A. Nakayama, F. Kuwahara, T. Hayashi, Numerical modelling for three-dimensional heat and fluid flow through a bank of cylinders in yaw, Journal of Fluid Mechanics 498 (2004) 139–159.

[9] V. Fernández Villacé, G. Paniagua, Simulation of a Combined Cycle for High Speed Propulsion, in: 48th AIAA Aerospace Sciences Meeting, AIAA-2010-1125, Orlando, Florida, 2010.

Aerodynamic characterization of helicoidal fin arrays in transonic flow conditions

Laura Villafañe

Turbomachinery and Propulsion Department, laura.villafane@vki.ac.be

Supervisor: Guillermo Paniagua

Assistant Professor, Turbomachinery and Propulsion Department, von Karman Institute for Fluid Dynamics, Belgium, paniagua@vki.ac.be.

Promotor: Francisco Payri

Ordinary Professor, Máquinas y Motores Térmicos, Camino de Vera 14, Valencia, fpayri@mot.upv.es.

Abstract

The current research focuses on the aerodynamic investigation of the three dimensional turbofan bypass-flow and its interaction with a finned an air/oil surface heat exchanger integrated at the inner wall of the secondary duct. This work is driven by the interest to improve the thermal management of the lubrication system of future high bypass ratio turbofans.

Keywords: gas turbine engine, turbofan bypass flow, wind tunnel modeling, transonic flows, annular sector test section, heat exchanger, instrumentation, oil dot technique, particle image velocimetry.

1. Introduction

The evolution towards more efficient engine architectures capable of higher performance with lower specific fuel consumption, demands the development of advanced cooling and lubricating systems. Thermal management technologies must address, among others, the continuous increase of the maximum temperatures in the combustor, the lubrication and refrigeration of new complex engine architectures and the increase of heat sinks caused by the automated controls. Innovative materials and high-performance heat management solutions are required to this goal.

Oil systems hold a double function as lubricant and coolant fluid, demanding efficient heat removal solutions for a continued operation of the aero-engine. Streifinger [1] introduced fuel as the preferred oil heat sink for the lubricating systems. However its capacity is limited by several factors, namely fuel degradation and vapor locking at high temperatures within the fuel pump and combustion instabilities in the burners. Additionally, the fuel capacity as a heat sink is also limited by the development of aircraft wings in composite materials. Air is extensively used to refrigerate engine components as combustor liners, turbine vane and rotor airfoils and platforms, cavities and shrouds. For the purpose of cooling the lubrication oil, air is mainly used in combination with fuel coolers [2]. Limitations presented by air cooled heat exchangers within the aero-engine are the increased drag, the increase in mixing losses and the decrease of the main mass flow if the air is bled from the compressor.

In the frame of improved refrigerative systems for ultra-high bypass ratio turbofans, an innovative solution is proposed to help the heat removal of the lubrication oil circuit. Research is focused on an efficient air cooled oil cooler integrated at the inner wall of the secondary duct of a turbofan, Fig 1. The global objective is the analysis and understanding of the flow structure resulting from the interaction between the bypass flow and the heat exchanger. This knowledge will lead to the design of an efficient air cooled oil cooler located downstream of the air separator nose to help the cooling of the oil circuit while introducing minimum aerodynamic losses.

Little public research has been performed on turbo-

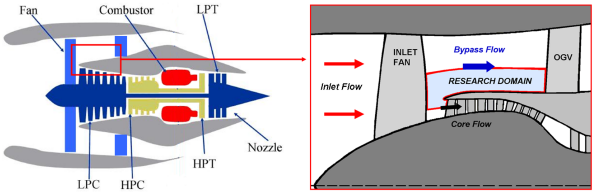

Figure 1: Heat exchanger location and research domain

fans bypass flow and the aerodynamic effects caused by the inclusion of an object within the transonic flow have not been addressed. Authors referring to bypass flow analysis have focused mainly on the impact of the outlet guide vanes on the fan performances and on the acoustic effects [3,4], or on inlet sonic boom attenuation in supersonic flight [5].

The literature is also scarce on heat transfer and friction effects on heat exchangers at high Reynolds and high Mach number flows. By contrast, multiple studies have been focused on the performance and optimization of heat exchangers at low Reynolds and Mach numbers with applications on industrial, electronic or internal cooling systems. Most of the work deals with fully shrouded heat sinks, optimizing the geometry of the fins and the arrays. Sparrow and Grannis [3; 4], investigated diamond-shaped pin fin arrays, Metzger et al. [5] oblong fins at various angles of attack, Ota and Nishiyama[6] , and Li et al. [7] studied elliptical fins, and Chen et al.[8] drop-shaped pin fins. Heat sinks in ducted flow with tip and/or lateral clearance have been thoroughly researched for electronic applications. The effect of tip and lateral bypass on the pressure drop characteristics and thermal performance of plate fin and pin heat sinks has been addressed by Sparrow and Beckey [9], and Lee et al. [10]. Numerically, the ability of methods to predict the bypass performance has also been examined. Many authors have worked on the development of correlations [11; 12] and analytical models[13; 14; 15] . However, an analytical model is not yet available to be used in an optimization procedure for heat sink design, and each different situation requires experimental and numerical studies.

Although the utilization of heat exchangers in high Reynolds number flows or in the turbofan bypass has not been subjected to public investigation, it has been proposed in several patents. References [16] to [23], propose the implementation of heat transfer systems in the same context of this investigation. This unexplored field could lead to improvements in the thermal management of future gas turbine engines.

In order to combine experimental, theoretical and numerical studies for a proper evaluation of the flow/finned heat exchanger interaction and its optimization, a new wind tunnel test facility has been specifically designed. The new blowdown wind tunnel allows the duplication of the flow in the region where the finned array will be located. The annular type test section is characterized by a complex three-dimensional geometry to simulate the bypass-flow. Numerical tools have been used to optimize the design and mathematical models computed to analyze the global wind tunnel behavior.

Aerodynamic characterization of the three-dimensional bypass-flow, with and without the presence of different finned array geometries, will be performed by means of different experimental measurement techniques. Conventional intrusive aerodynamic instrumentation is used to perform map measurements at different locations along the 3D channel. Probe rakes have been specifically optimized for this application. Two different optical measurement techniques are used to provide more extensive information of the flow interaction with the optimal fin array. Surface flow visualization techniques applied on the splitter surface allow studying wall-streamlines behavior. A new procedure based on the surface oil dot technique is under development to obtain quantitative information of the wall shear stress by analyzing the dot deformation. Information on the flow field development will be provided by Particle Image Velocimetry measurements. The application of this technique to the present investigation is an ongoing challenge due to the complex 3D test section geometry. Experimental results will be supported by computational flow analysis within the test section domain. Numerical studies are carried out in the absence of the heat exchanger both on the clean channel flow and including the insertion of instrumentation. They allow studying the modification of the flow and the blockage effects caused by the presence of instrumentation, as well as understanding the 3D flow-field to be measured.

From the evaluation of the experimental and numerical data, the flow structure resulting from the interaction of the bypass flow with different fin array models will be analyzed and the perturbations introduced by each model comparatively quantified. This investigation allows to evaluate the aerodynamic effectiveness of a new refrigerative solution on turbofans. Additionally it proportionates valuable source of experimental data for the validation of engine models.

2. Bypass-Flow and Test Rig

The region of the turbofan under investigation is the portion of the engine comprised between the fan trailing edge and the leading edge of the Outlet Guide Vanes. The air flow conditions to be reproduced correspond to the aerodesign point characterized by cruise flow velocities and standard pressure and temperature conditions at the turbofan inlet. The flow characteristics along the region of interest are known from a calibrated non viscous through-flow computation on the real engine. In this domain flow magnitudes present variations of the same order of magnitude in radial and axial directions and also the same order of magnitude show the azimuthal and axial velocity components.

The new test facility aims to replicate the 3D turbofan bypass-flow environment, which requires simulating the flow gradients. To this goal a complex annular sector type test section, sketched in Fig 2, has been designed. The flow evolves over the splitter, duplicated at real scale, as it does in the engine downstream of the engine fan. The flow bifurcation into the bypass and the core flow is also reproduced allowing to simulate the real boundary layer developing over the separator nose. Along the test section the flow is guided by lateral walls defined by flow stream-surfaces obtained from axilsymmetric computations. For an easier understanding of the 3D channel flow the end-walls can be considered in a simplificative approximation, as two concentric cylinders which axis is the turbofan axis. The intersection lateral walls/cylinders can be thought as four cylindrical helices of different pitches in the hub and casing walls, but constant angle helix/generatrix. In the real geometry the radius of the end-walls change slightly along the axis position, and the tangent to the lateral surface in the direction of the axis is different at each radial and axial position. As a result distorted annular sectors define the transversal sections along an axial length six times the characteristic transversal dimension. Numerical tools have been used to perform two and three dimensional flow computations for the optimization of the design focusing in the test section, the inlet blades optimized to duplicate the flow downstream of the engine fan, and the test section outlet. Detailed information regarding the wind tunnel design is described in Ref. [24]

The new transonic blowdown facility is driven by a pressurized storage of 72 m^3 at 40 bar. The pressurized air flows along a duct circuit to a settling chamber, passing through a pressure control valve. The valve is operated to keep the total to static pressure ratio defining the operational Mach number in the test section constant. The turbulence intensity of the flow in the settling chamber is controlled by the use of screens and honeycombs. From the settling chamber the air is first accelerated in a contraction. A set of Inlet Guide Vanes turn and accelerate the flow to reproduce the radial distributions of Mach number and flow angle downstream of the engine fan. The flow then evolves along the three-dimensional test section. The air under the splitter is evacuated through a variable area restriction, allowing the control of the mass flow and hence the pressure distribution around the stagnation nose. The core flow is expanded in a diffuser and later exhausted to the atmosphere.

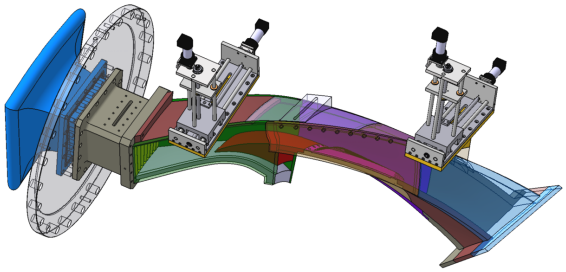

Figure 2: Test Section Sketch with instrumentation carriage

At the design conditions, the Mach number within the test section varies between 0.6 and 0.9 and the Reynolds number based on a standard fin height of 15mm is of the order of $2.7 \cdot 10^5$. The characteristic area perpendicular to the flow at the location of the heat exchanger is about 0.013 mm^2 and the mass flow rate through the test section main channel is about 4.5 kg/s.

3. Research Methodology

Steady state flow computations that helped the aerodynamic design of the test section do not give however any information regarding the wind tunnel behavior or the evolution of the flow properties with time. An estimation of the wind tunnel performances is required for the test design. To this goal mathematical and zero-dimensional models have been analyzed.

The methodology to be followed for the experimental flow investigation includes the performance of aerodynamic flow measurements, by means of intrusive and non intrusive measurement techniques, surface flow characterization and numerical flow results. Different fin array configurations will be first investigated using probe rakes at different locations. The

flow interaction with the resultant optimal array will be further investigated making use of non intrusive optical techniques.

From the combination of the measurements performed through the different techniques, the flow structure developing in the presence of the fin array will be characterized. Creation of vortical structures, flow recirculation and separation will be identified and the flow disturbances created by the fins quantified in terms of pressure losses and entropy generation.

3.1. Numerical Wind Tunnel Performance Analysis

Simplified governing equations of each component were used during the wind tunnel conception to ensure a correct design. Zero-dimensional schematic models have been programmed to analyze the temporal evolution of the flow variables along the complete wind tunnel and to study their sensibility to estimated losses. The mathematical tool used is Ecosimpro simulation tool in combination with the ESPSS libraries. [25].

Two schematic models have been analyzed depending on the control strategy and the variables of interest. However the flow results are independent of the control strategy under the same loss coefficients and geometrical characteristics. In both of them a proportional-integral-derivative (PID) control system has been included to act on the regulation valve located at the entrance of the settling chamber. The mission of the PID control is to keep constant and equal to a target value, the ratio total to static pressure either in the test section or upstream the IGVs. The model shown in Fig. 3 is based on the control of the isentropic Mach number in the Test Section.

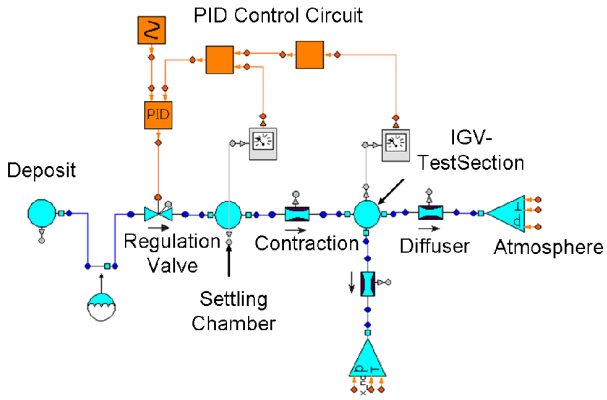

Figure 3: Schematic model for the control of M_{is} in the test section

In Fig. 4 the static pressure and Mach number are shown to remain constant in time while the aperture of the valve is able to keep the pressure ratio imposed. The Reynolds number increases with the continuous decay of temperature due to the discharge of the air storage tank, proportionally to $(\mu\sqrt{T_s})^{-1}$. The evolution of the test section Reynolds number based on a standard heat exchanger fin height of 15mm is plotted during the first six minutes, in which it changes approximately by 24%. The mass flow in the test section increases with time proportionally to $(\sqrt{T_s})^{-1}$. Variations of the pressure levels, and hence the test duration, when considering valve and duct losses have been analyzed. In agreement with Fung and Ray[26] the optimum PID constants for each condition were found to vary slightly. Constant values can be taken without penalizing significantly the control process. This schematic modeling will allow a finer wind tunnel performance prediction after calibrated with experimental results.

3.2. Intrusive Flow Aerodynamic Measurements

In the first measurement campaign several fin arrays with different geometrical configurations will be tested under the same flow conditions to obtain a better understanding of the flow fins interaction, and to identify the optimal array configuration. To this goal aerodynamic map measurements are performed at the five transversal planes shown in Fig 5, to measure the three-dimensional flow with and without the presence of the investigated finned array. Traverse measurements of total temperature, total and static pressure, flow angle and turbulence intensity will be carried out in those five planes and also upstream of the array of blades that reproduces the flow distributions characteristics of the engine inlet fan. Static pressure is also measured at the walls along the wind tunnel and circumferentially at the location of the measurement planes.

From the comparison of flow results at the different measurement planes with and without the influence of the fin arrays, the flow effects caused by the latter ones will be studied. Downstream of the finned arrays analysis will be done of the vortical structures created, their intensity and development between the measurement planes MP4 and MP5. Blockage effects and upstream flow modifications will be analyzed by comparison of flow results at the two measurement planes upstream the fin array leading edge. The aerodynamic effectiveness of the heat exchanger will be evaluated in terms of the ratio of the total pressure loss between two measurement planes upstream and downstream, in the presence of the array with respect to the clean

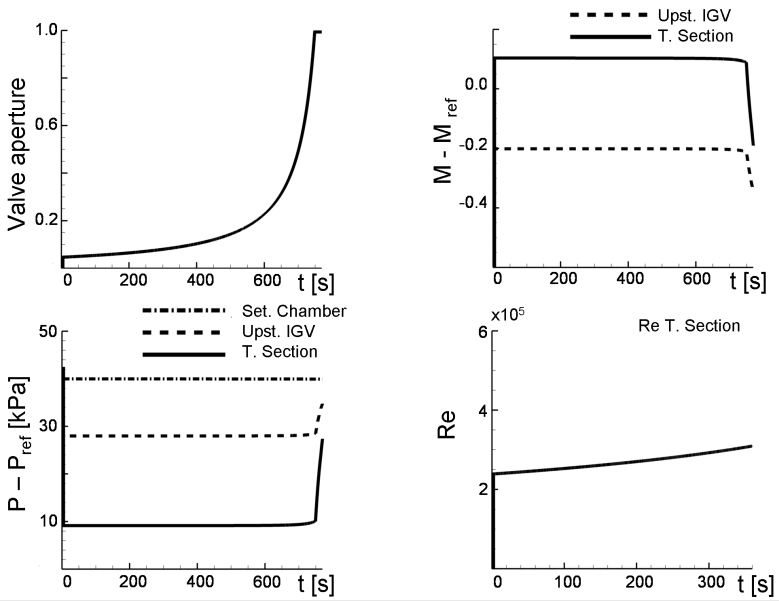

Figure 4: Computed temporal evolution in the wind tunnel of static pressure, Mach number, valve position and Reynolds number.

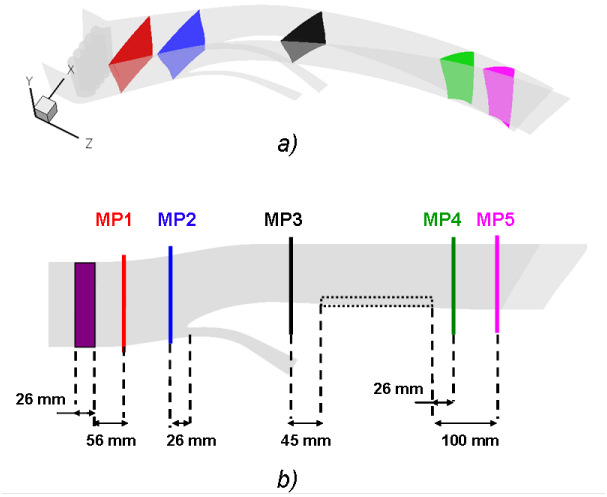

Figure 5: Measurement planes, a) 3D view, b) meridional view.

configuration. Balances of entropy generation will be also analyzed to quantify the flow disturbances.

3.3. End-Wall Flow Analysis

To this date, measurement based on skin-friction lines constitute the main source of information to determine the boundary layer status and drag, and in general, for the understanding of the 3D separation. Surface flow visualization techniques are widely used to visualize wall streamlines, or skin-friction lines, due to the simplicity and low cost of their application. However the quantitative determination of the shear stress is a complex task in most of the experimental applications. Some precise techniques capable to measure the wall shear stress are based on the diverging fringe shear stress sensor (OFI) [27] and on the micro-pillar shear stress sensor (MEMS) [27]. The complexity of those techniques prevents their routinely application in complex geometries. Tian et al. [28] succeed in measuring the wall shear stress in a low speed linear cascade by means of LDA measurements. Naughton [29] demonstrated that, at least in two-dimensional flows Oil Flow Interferometry may be effectively used for skin friction measurements.

In the present investigation oil dots will be used for conventional wall-streamlines visualization, but also for the development of an innovative technique to attempt the determination of wall shear stress. The technique will be applied over the splitter surface downstream of the location of the final configuration of the array of fins.

Since the movement of the oil depends on the flow velocity and other parameters (i.e. oil viscosity, surface tension, pressure gradient, gravity, etc.) it is possible to get some quantitative information by monitoring the oil displacement during a test. The procedure investigated is based on the thin film theory, and in the work of Hubner and Carroll [30], who derived the wall shear stress as a function of the oil viscosity

and the pattern of the oil displacement. This technique is been first tested by performing tests on a flat plate. The surface evolution of the oil dots is recorded and the oil dots velocity profiles computed. Knowing the volume of the oil dots and assuming the pattern of the oil dot evolution, it is possible to estimate the wall shear stress.

3.4. Flow-field Particle Image Velocimetry Measurements

The bypass flow interaction with the final configuration of the finned array chosen after the first test campaign with intrusive probes, will be also characterized by means of two-dimensional Particle Image Velocimetry (PIV). PIV will be applied downstream of the heat exchanger. The aim is to get information about the flow evolving downstream of the fins that can not be obtained with punctual intrusive instrumentation. The use of optical flow measurements eliminates the local probe effect on the modification of the quantity measured, and also the global flow modification due to the blockage introduced by the instrumentation. Intrusive measurements been performed in planes perpendicular to the axis proportionate punctual information at different time instants. PIV will be performed in vertical planes orientated in order to contain as much as in plane flow vectors as possible, and also in blade to blade planes. This technique will provide information on the instantaneous flow development, the generation of turbulence, and will allow identifying the coherent vortical structures generated by the fins, without been affected by the presence of an object within the flow.

The three-dimensional characteristics of the flow, and the curved test section walls, complicates the application of PIV to this particular case. Different possibilities are been considered for the final set-up configuration.

3.5. Computational bypass flow characterization

Numerical computations of the flow in the test section without the presence of the finned array, are performed to analyze the bypass-flow structure under investigation. The numerical flow prediction will support the experimental results and will help in their understanding.

Additionally, numerical computations are used to study the flow modifications and blockage effects caused by the presence of instrumentation in the test section. With this aim, computations are performed both on the clean channel and also including the presence of an intrusive probe. The analysis has been done for the most critical probe location.

The numerical flow simulations are performed using FINE/turbo (Numeca Int.©) solver. The Navier-Stokes equations are solved using the Spallart-Almarras turbulence model. The grid domain, including the array of blades responsible of the reproduction of the engine gradients and the test section, consist of approximately 30 million points.

4. Measurement Techniques

Numerical flow and wind tunnel performance analyses proportionate information regarding the magnitudes to be measured, their order of magnitude and variation. At the design conditions and in the absence of the fins, the test section Mach number is expected to vary between 0.6 and 0.9, the maximum variation of total pressure in the order of 600 mbar, and the angle is expected to show a maximum variation around 15 degrees. Variations of temperature are expected downstream of the finned array due to the flow disturbances introduced. The characteristic area perpendicular to the flow at the location of the heat exchanger is about 0.013 mm^2.

4.1. Intrusive instrumentation

4.1.1. Aerodynamic Probes

Aerodynamic probes have been specifically designed for this application. Rakes were chosen to allow performing map measurements in shorter test duration. The main design objectives been: robustness, minimum blockage, high spatial resolution and flow angle sensitivity. Blockage is one of the main constraints for probe design and it is specially critical in the present case combining transonic flow regime and limited test section area. Interest was focused on the miniaturization of the probes in order to reduce the blockage effect and increase the spatial resolution. All probes are designed to introduce similar frontal blockage and thus similarly affecting the flow.

The aerodynamic map measurements in the five transversal planes are performed by means of a six shrouded pitot heads rake , two five hole probe heads rake, five shielded T-thermocouple rake and a six hot wires rake, as sketched in Fig. 6. In the same figure are shown the combined temperature and pressure probe for reference measurements. A single head five hole probe for measurements in the proximity of the surfaces is also considered.

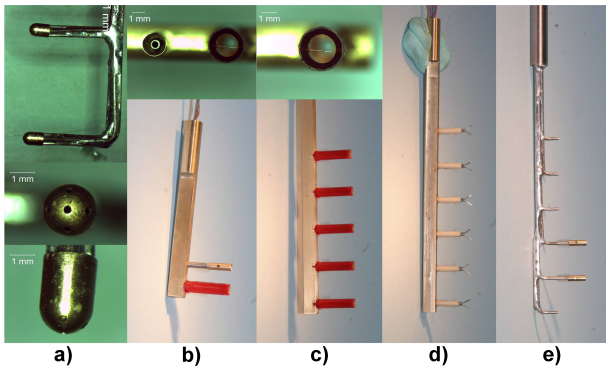

Figure 6: a) hemispherical five hole probe rake, b) reference probe, c) shielded thermocouple rake, d) hot-wire rake, e) shielded pitot probe rake.

Shielded pitot probe heads are used for total pressure determination since they are more insensitive to angle effects. For the same reason hemispherical five hole probe heads have been selected for flow angle and pressure measurements. For the temperature measurements plastic shielded head probes with the wires perpendicular to the flow and suspended within the plastic shields are been manufactured. The use of shields increase the recovery factor although it also causes a loss of frequency response [31]. This configuration is convenient in the present case since allows a proper l/d_w value, a high recovery factor, the wire is more protected than with a bare thermocouple, and the frequency response is not a critical factor on the present temperature measurements.

Considerable attention is given in the literature to the calibration of aerodynamic probes in the transonic range, acknowledged to be the most challenging regime [32]. Fransson et al. [33] describe the main uncertainties. The calibration of the probes will be done in the subsonic free jet facility (VKI-C4).

The instrumentation is inserted in the test section by the external radius surface and it is held in a carriage system at a different angular position with respect to the radial direction in each measurement plane. The direction of insertion of the instrumentation is optimized at each plane in order to maximize the accessibility due to the different geometry of the measurement planes. The movement of the instrumentation in the carriage will be automatized by means of two programable engines.

4.1.2. Flow instrumentation effects

Numerical flow analyses were performed to study the blockage, the local effects of the instrumentation on the flow-field and the modification of the flow magnitudes on the measurement area for different flow conditions. Comparisons between flow magnitudes with and without the presence of the probe in the test section were performed for three different sets of pressure boundary conditions, i.e. three different flow velocities. The mesh is identical in both cases to avoid mesh dependency except for the area occupied by the probe (grid filled in the free flow case). The flow is computed using the same solver as for the aerodynamic evaluation of the flow in the test section for design purposes, FINE/turbo ((Numeca International ©). The grid size is increased to 33 million points to model the effect of the instrumentation.

The study was based on the most adverse case in terms of area blockage. It corresponds to the five hole probe rake as displayed by Fig. 7, mounted in plane P3. The geometry is simplified, by replacing the real hemispherical head, and using a rectangular stem instead of the U shaped one. Several authors have treated the experimental evaluation of the blockage by means of static pressure measurements with different acceptance criterion [34; 35; 36]. From the numerical computations the change on the test section mass flow due to the blockage can be directly computed. The modeled probe introducing 1.2% area blockage, reduces the mass flow through the test section by 1.1 % for the same pressure boundary conditions.

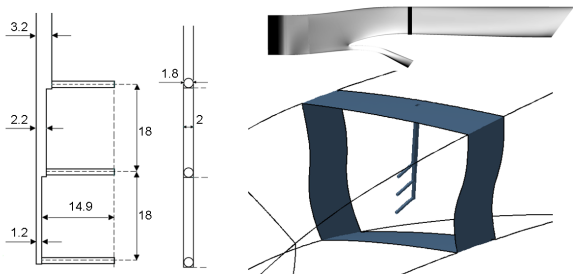

Figure 7: Simplified five hole probe rake. Probe mounted in measurement plane 3

Figure 8 shows the deviation between the total pressure in the measurement plane without and with the presence of the probe, relative to the total to static pressure difference without instrumentation. Results are presented for each probe head and local reference Mach number at each flow regime. The pressure deviation has been computed in a plane right upstream the probe head through two approaches: considering the central point of the probe head and the average on

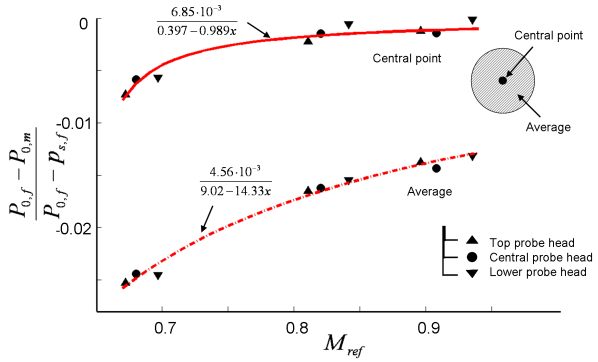

Figure 8: Total pressure deviation caused by the presence of an aerodynamic probe

the probe frontal area. The averaged total pressure deviation in the frontal area is about 2 % at M ~ 0.75. It corresponds in terms of pressure to a difference of 2-3 mbar between the total pressure with and without the instrumentation. The deviation between total pressure with and without instrumentation is reduced as the flow velocity increases. No difference is found between each probe head measurement for the same flow condition. The total pressure in the lower head probe is not more affected by the proximity of the wall than the one of the middle head probe as it may be expected. However, a small single head probe is considered for measurements close to the inner wall and the heat exchanger, to limit as much as possible the flow interaction.

4.2. Oil Dot Measurement Technique Development

The new methodology based on the oil dot technique for the determination of the shear stress is been first investigated over a flat plate. A flat plate test bench is set up at the VKI free jet facility (C4) shown in Fig.9 a). The plate is vertically located in the jet and test are performed at different velocities ranging from Mach 0.18 to 0.55.

For the selection of the oil mixture to be used, different mixtures are examined. The paint selected for the flate plate test case is composed by a base of silicon oil mixed with titan-bioxide pigment. The viscosity plays a fundamental role in the calculation of the wall shear stress. Therefore it is important to have a precise characterization of the dynamic viscosity of the oil mixture used. It has been characterized in function of the temperature and the velocity gradient.

The velocity distribution on the plate is measured by means of pneumatic taps in the center line of the plate. A shutter plate is placed at the exit of the jet to prevent the exposure of the oil dots to the air flow while the velocity is being adjusted. The plate is monitored by means of a CCD camera. The images are recorded with a rate of 200 fps with a resolution of 800x600 pix. An image processing software has been developed for their analysis. A light source heading to the flat plate is used to to increase the contrast between dots and background.

Tests are performed at different velocities ranging from Mach 0.18 to 0.55. Several tests are done at each velocity to ensure measurement repeatability. Fig. 9b) shows an image of the oil dot displacement and the computed values of the wall shear stress for a test performed at M=0.35, at two distances along the flat plate. The wall shear stress is obtained under the hypothesis of two-dimensional flow, small oil-film-height to oil-film-length ratio, no flow disruption caused by the oil, negligible surface pressure gradients and gravity effects, and with the condition of a spatially-constant shear stress along the path of integration. It is also assumed a certain pattern for the oil displacement. In the same plot the computed results are compared with three analytical expressions for the wall shear stress over a flat plate for the tested flow conditions. A good agreement is found for this model test case.

This methodology will be applied to the present investigation at the inner wall of the bypass duct, downstream of the array of fins.

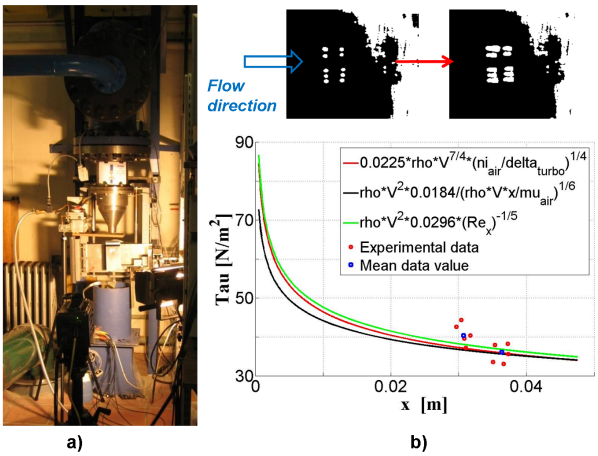

Figure 9: a)Flat plate test set up. b) Analytical and computed wall shear stress as function of position along flat plate LE for M=0.35

4.3. Particle Image Velocimetry

PIV provides the simultaneous measurement of the velocity distribution over a planar domain. Small

tracer particles are added to the flow and illuminated twice by a laser light-sheet. The orientation of the light-sheet plane is such that it contains the dominant flow direction. The light scattered from the particles is collected at 90 deg and recorded by a camera in two exposures. From the time interval between the two exposures the magnitude of the velocity vector can be computed. PIV is extensively used nowadays for multiple applications. Its application to the present study faces some difficulties due to the geometrical complexity of the test section. Previous PIV applications to turbomachinery environments constitute a good reference for a successful set-up design. The final set-up configuration is on development.

A uniform seeding of a sufficiently high concentration, but without affecting the flow or introducing strong light absorption is essential for PIV. In order for the tracers to follow the flow, extremely small particles must be used when transonic flows or high frequency flow phenomena are to be observed. But it is also important to keep in mind that small particles scatter less light. The tracers will be introduced in this case from the settling chamber, in such a way that the seeded flow goes into the test section passing through the inlet blades and following the flow streamlines.

The light sheet will be introduced using a periscope probe. The use of this kind of light-sheet probe is common in turbomachinery applications where the optical access is limited. Balzani et. al [37] used it at the von Karman Institute for the application of PIV to the investigation of the blade-to-blade flow in a compressor. This periscope allows to change and control the height of the light-sheet plane independently of the laser optics placement. A most sophisticated periscope allowing also angular alignment has been developed at DLR [38]. The periscope solves the difficulty of setting the laser sheet both in terms of the necessity of a window and on the distortion of the laser sheet when crossing the window. Bricaud et al. treat in Ref. [39] the distortion of the laser due to cylindrical and prismatic windows.

The optical access for the camera presents a challenge in annular turbomachinery applications. The utilization of a periscope for the acquisition of images is not suitable for PIV due to the low optical resolving power. So in practice at least one viewing window is required to properly resolve particles suspended in the flow. The most common solution is the utilization of a planar window, although it introduces modifications on the flow. Another possibility is the installation of a window reproducing the internal wall geometry. In this case image compensation may be required depending on the distance between the window and the laser sheet, and the distortion introduced. An example of utilization of curved window and required image correction can be found in the work of Lang et al. [40]. In the present case, and due to the 3D configuration of the test section lateral wall, the utilization of small planar windows is under consideration.

5. Conclusion

An innovative high speed subsonic wind tunnel has been designed to reproduce the real bypass flow conditions downstream of the fan of a gas turbine engine. This facility will support the research on a finned Air Cooled Oil Cooler integrated surface heat exchanger placed at the inner wall of the bypass duct.

The performances of the new facility have been estimated by means of Zero-dimensional schematic models. They allow computing the temporal evolution of the flow variables along the complete wind tunnel and to study their sensibility to estimated losses. From those analysis it is seen that the required test section Mach number will remain constant while the aperture of the pressure valve communicating the air storage tank and the settling chamber, is able to keep the correspondent pressure total to static pressure ratio. For the ideal conditions studied, the target Mach number could be kept for about 11 minutes. However, the increase of the Reynolds number due to the temperature decrease as the air in the deposit is expanded during the discharge, will limit the testing time. The schematic models will allow predicting the real wind tunnel performances after their experimental calibration.

Different measurement techniques will be applied for the aerodynamic characterization of the bypass flow interaction with the helicoidal fins conforming the heat exchanger. The first measurements will be performed by means of conventional aerodynamic instrumentation. During the fist test campaign different configurations of the finned arrays will be tested. It will allow selecting the geometrical configuration that introduces less distortion on the bypass flow. The chosen configuration will be tested by means of optical techniques to fully characterize the flow structure resulting form the interaction bypass flow/heat exchanger. Experimental results will be supported by computational flow analysis performed within the test section domain.

To accomplish this aerodynamic investigation both intrusive and non intrusive measurement techniques are adapted to the test scenario. Probe rakes have

been specifically designed for with the objectives of minimizing the flow effects due to area blockage, and reducing the time required to complete map measurements. Numerical simulations have been performed to study the interaction test section-instrumentation. Comparison of test section flow-fields with and without the presence of instrumentation allows analyzing the modifications caused by the use of an aerodynamic probe, and the blockage effects. Errors of almost 2% in the total pressure difference with and without instrumentation relative to the total to static pressure difference have been obtained at M $\sim$ 0.75.

A new procedure based on the surface oil dot technique is under development to obtain quantitative information of the wall shear stress by recording the dot deformation. It is been first applied to the flat plate test case for validation purposes. Initial results show good agreement with the existent analytical expressions for this simple case.

The application of Particle Image Velocimetry to characterize the flow evolution downstream of the finned array is under development. The selection of the best set-up regarding geometrical complexity, optical access and image quality will allow measuring the instantaneous flow field and identifying the vortical structures created by the presence of the fins.

Acknowledgments

Thanks to Julien Desset for his contribution to the design process and to Johan Prinsier for his valuable help on the CFD simulations. Likewise thanks to Terence Boeyen for his painstaking work in the instrumentation manufacturing.

This work is carried out in the frame of the INTELLIGENT COOLING SYSTEM project. The authors would like to acknowledge the financial support of the Region Wallone, the pole of competitiveness Skywin, and the industrial support of TechSpace Aero.

References

[1] H. Streifinger, Fuel/Oil System Thermal Management in Aircraft Turbine Engines, in: RTO-Applied Vehicle Technology Panel, Symposium on Design Principles and Methods for Aircraft Gas Turbine Engines, Toulouse, 1998.

[2] A. Linke-Diesinger, Systems of Commercial Turbofan Engines: An Introduction to Systems Functions, Springer, 2008.

[3] E. M. Sparrow, V. B. Grannis, Pressure Drop Characteristics of Heat Exchangers consisting of Arrays of Diamond-Shaped Pin Fins, International Journal of Heat and Mass Transfer 34 (1991) 589–600.

[4] V. B. Grannis, E. M. Sparrow, Numerical Simulation of Fluid Flow Through an Array of Diamond-Shaped Pin Fins, Numerical Heat Transfer, Part A: Applications 19 (1991) 381–403.

[5] D. E. Metzger, C. S. Fan, S. W. Haley, Effects of Pin Shape and Array Orientation on Heat Transfer and Pressure Loss in Pin Fin Arrays, Journal of Engineering for Gas Turbines and Power 106 (1984) 252–257.

[6] T. Ota, H. Nishiyama , Heat Transfer and Flow Around an Elliptic Cylinder, International Journal of Heat and Mass Transfer 27 (1984) 1771–1779.

[7] Q. Li, Z. Chen, U. Flechtner, H. J. Warnecke, Heat Transfer and Pressure Drop Characteristics in Rectangular Channels with Elliptic Pin Fins, International Journal of Heat and Fluid Flow 19 (1998) 245–250.

[8] Z. Chen, Q. Li, D. Meier, H. J. Warnecke, Convective Heat Transfer and Pressure Loss in Rectangular Ducts with Drop-shaped Pin Fins, Heat and Mass Transfer 33 (1997) 219–224.

[9] E. M. Sparrow, T. J. Beckey, Pressure Drop Characteristics for a Shrouded Longitudinal-Fin Array with Tip Clearance, ASME Journal of Heat Transfer 103 (1981) 393–395.

[10] R. S. Lee, H. C. Huang, W. Y. Chen, A Thermal Study of Extruded Type Heat Sinks in Considering Air Flow Bypass Phenomenon, in: Proc. Sixth IEEE Semi-Therm Symposium, 1990, pp. 95–102.

[11] R. A. Wirtz, W. Chen, R. Zhou, Effect of Flow Bypass on the Performance of Longitudinal Fin Heat Sinks, ASME Journal of Electronic Packaging 116 (1994) 206–211.

[12] H. Jonsson, B. Moshfegh, Modeling of the Thermal and Hydraulic Performance of Plate Fin, Strip Fin, and Pin Fin Heat Sinks - Influence of Flow Bypass, in: Proc. 2000 Intersociety Conf. on Thermal Phenomena (ITherm 2000), Las Vegas, 2000, pp. 185–192.

[13] S. Lee, Optimun Design and Selection of Heat Sinks, in: IEEE Transactions on Components, Packaging and Manufacturing Technologies, Vol. 18, 1995, pp. 812–817.

[14] R. Simons, R. Schmidt, A simple Method to Estimate Heat Sink Air Flow Bypass, Electronics Cooling 3 (2) (1997) 36–37.

[15] M. A. Butterbaugh, S. S. Kang, Effect of Airflow Bypass on the Performance of Heat Sinks in Electronic Cooling, Advances in Electronic Packaging 10 (1995) 843–848.

[16] D. Bajusz, A. Cornet, J. Friedel, N. Raimarckers, Air-Oil Heat Exchanger placed at the Location of the Air Separator Nose of a Turbojet, and a Turbojet Including such an Air-Oil Heat Exchanger, TechSpace Aero S.A., Milmort (BE) (US2009/0165995A1, Jul. 2, 2009).

[17] A. Cornet, N. Raimarckers, D. Bajusz, Heat Exchange System in a Turbomachine, TechSpace Aero S.A., Milmort (BE) (Pub. No.: US 2009/0159246 A1, Jun. 25, 2009).

[18] B. Olver, A. Ciampa, R. Marrano, R. Trepanier, S. Lamarre, M. Bernard, P. Germain, Turbofan Bypass Duct Air Cooled Fluid Cooler Installation, Pratt & Whitney Canada Corp. (CA) (Pub. No.: US 2008/0053059 A1, Mar. 6, 2008).

[19] M. G. Anderson, W. E. Alford, M. L. Trego, R. Haugland, A. K. Winstanley, Cooling Systems for Use on Aircraft, HoneyWell International, INC. Morristown, NJ (US) (Pub. No.: US 2008/0314047 A1, Dec. 25, 2008).

[20] T. Wakeman, Compact Air-to-Air Heat Exchanger for Jet Engine Application, The United State of America as represented by the Secretary of the Air Force, Washington, D.C. (US) (Pub. No.: US 004187675, Feb. 12, 1980).

[21] E. Elovic, Cooling Air Cooler for a Gas Turbofan Engine, General Electric Company, Cincinnati, Ohio (US) (Pub. No.: US 004254618, Mar. 10, 1981).

[22] A. Vermejan, P. Daiber, S. Mortosa, M. Taylor, Gas Turbine

Engine Fan Cooled Heat Exchanger, General Electric Company, Cincinnati, Ohio (US) (Pub. No.: US005269135A).
[23] V. Bruno, B. Olver, A. Logan, Bypass Duct Fluid Cooler, Pratt & Withney Canada Corp., Longueuil (CA) (Pub. No.: US 007377100 B2, May 27, 2008).
[24] L. Villafañe, G. Paniagua, M. Kaya, D. Bajusz, S. Hiernaux, Development of a Transonic Wind Tunnel to investigate Engine Bypass Flow Heat Exchangers, Proc. IMechE, Part G: J. Aerospace Engineering (Status: accepted. Waiting for publication).
[25] ESA, ESPSS EcosimPro Libraries User Manual.
[26] Y. T. Fung, G. S. Settles, A. Ray, Microprocessor Control of High Speed Wind Tunnel Stagnation Pressure, AIAA 2 (1988) 429–435.
[27] J. W. Naughton, M. Sheplak, Modern Developments in Shear Stress Measurement, Progress in Aerospace Sciences 38 (2002) 515–570.
[28] Q. Tian, R. L. Simpson, G. Tang, Flow Visualization on the Linear Compressor Cascade Endwall using Oil Flows and Laser Doppler Anemometry, Measurement science and technology 15 (2004) 1910–1916.
[29] J. W. Naughton, High-Quality Skin Friction Measurements in 2-D Flows Using Oil Film Interferometry, in: 21st International Congress on Instrumentation in Aerospace Simulation Facilities, ., 2005.
[30] J. P. Hubner, B. F. Carroll, Thin-oil-film Interferometric Skin-friction Measurements in Short-duration Supersonic Flow, Experiments in Fluids 15 (1993) 315–322.
[31] G. Paniagua, R. Denos, M. Oropesa, Thermocouple Probes for Accurate Temperature Measurements in Short Duration Facilities, in: Proceedings of ASME TURBO EXPO 2002, Amsterdam, The Netherlands,, June 3-6, 2002.
[32] P. E. Hancock, A Theoretical Constraint at M=1 for Intrusive Probes and Some Transonic Calibrations of Simple Static-Pressure and Flow-Direction Probes, in: Proceedings of the 9th Symposium on Measuring Techniques in Transonic and Supersonic Flow in Cascades and Turbomachines, Oxford, UK, 1988.
[33] T. H. Fransson, F. Schaller, K. Schulz, Change of Flow Conditions due to the Introduction of an Aerodynamic Probe during Calibration, in: Proceedings of the 9th Symposium on Measuring Techniques in Transonic and Supersonic Flow in Cascades and Turbomachines, Oxford, UK, 1988.
[34] U. W. Schaub, R. G. Williamson, J. P. Huot, S. H. Moustapha, An Experimental Assesment of the Influence of Downstream Conditions on the Performance of a Transonic Turbine Nozzle of High Turning, Journal of Turbomachinery 112.
[35] T. Depolt, F. Vinnemaier, W. Koschel, Investigation of Minimazing Blockage Effects of Multi-hole Pressure Probes in Transonic Flow, in: Measuring Techniques for Transonic and Supersonic Flows in Cascades and Turbomachines, 1990.
[36] S. P. Harasgama, K. S. Chana, Turbine Nozzle Guide Vane Exit Area Traversing in a Short Duration Light Piston Test Facility, in: Measuring Techniques for Transonic and Supersonic Flows in Cascades and Turbomachines, 1990.
[37] N. Balzani, F. Scarano, M. L. Riethmuller, F. A. E. Breugelmans, Experimental Investigation of the Blade-to-Blade Flow in a Compressor Rotor by Digital Particle Image Velocimetry, Journal of Turbomachinery 122 (2000) 743–750.
[38] M. Voges, M. Beversdorff, C. Willert, H. Krain, Application of particle image velocimetry to a transonic centrifugal compressor , Experiments in Fluids 43 (2007) 371–384.
[39] C. Bricaul, B. Richter, K. Dullenkopf, J. Bauer, H., Stereo PIV measurements in an enclosed rotor-stator system with pre-swirl cooling air, Experiments in Fluids 39 (2005) 202–212.
[40] H. Lang, T. Morck, J. Woisetschlger, Stereoscopic particle image velocimetry in a transonic turbine stage, Experiments in Fluids 32 (2002) 700–709.

MULTIDISCIPLINARY OPTIMIZATION IN TURBOMACHINERY

Toward multidisciplinary optimization of propeller blades

Marinus Benoît

Turbomachinery and Propulsion Department, benoit.marinus@vki.ac.be

Benoît Marinus has been awarded the best presentation during the PhD Symposium 2011

Supervisor: René Van den Braembussche

Honorary Professor, Turbomachinery and Propulsion Department, von Karman Institute for Fluid Dynamics, Belgium, vdb@vki.ac.be

Promotor: Walter Bosschaerts

Professor, Department of Mechanical Engineering, Royal Military Academy, av. de la Renaissance 30, Brussels-Belgium, 1000, walter.bosschaerts@rma.ac.be

Promotor: Michel Roger

Professor, Laboratory for Fluid Mechanics and Acoustics, Ecole Centrale de Lyon, av. Guy de Collongue 36, Ecully-France, 69134, walter.bosschaerts@rma.ac.be

Abstract

Aeroacoustic and aerodynamic, multi-objective and multi-point optimization of propeller blades using Differential Evolution has been performed. The main results are discussed together with a stress analysis that was conducted a posteriori. This analysis opens the path to multidisciplinary and multi-objective optimization with several disciplines considered concurrently. Both optimization processes rely on the combined use of a metamodel to allow spreading the process over large numbers of generations, with high-fidelity aerodynamic, aeroacoustic and, for the last optimization, aeroelastic analysis in order to safeguard the accuracy. The optimization parameters comprise the control points of b-spline parameterizations of the radial distributions of sweep, twist, chord and thickness as well as the points controlling the shape of the two airfoils used to manufacture the blades.

Keywords: propeller, aerodynamics, aeroacoustics, aeroelastics, optimization

1. Introduction

Recent studies highlighted the potential benefits of short- and medium-haul aircraft flying at Mach 0.72 especially if they are equipped with propellers. In the search for better performance of propellers, Evolutionary Algorithms (EA) offer the possibility for improvement thanks to the large amount of design parameters that can be dealt with. If the design parameters are chosen adequately, innovative blade shapes resulting from an automated multidisciplinary optimization procedure might have interesting performances.

In (1), optimization results are discussed extensively but in the optimization and the subsequent discussion, no account was given for the feasibility of the optimized design in terms of structure and stresses. In preparation for the insertion of structural considerations in the optimization procedure, a stress analysis has been conducted a posteriori on some illustrative individuals that resulted from the aerodynamic and aeroacoustic optimization.

2. Optimization set-up

2.1. Optimizer architecture

T. Verstraete (2) developed the optimizer presented in Fig. 1. A particular EA, Differential Evolution (DE) developed by Price and Storn (3), is used. It uses real-coding of the design parameters. Each new generation of N individuals is formed by mutation

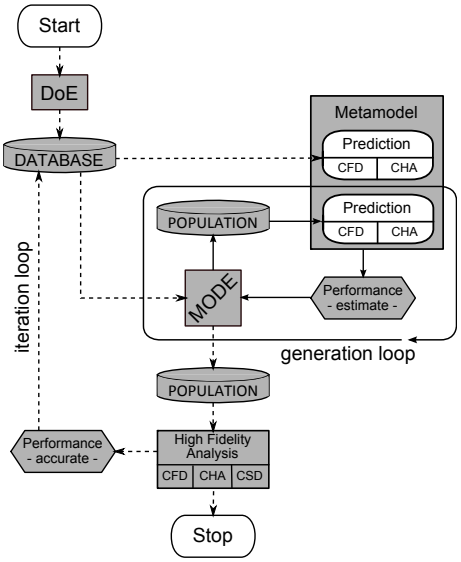

Figure 1: Layout of the MODE-optimizer with the two-level approach.

and recombination among the parent population. The vector of design parameters of an offspring is a recombination of parameters that are randomly chosen either from the parent or from a linear combination of parameters from three other individuals chosen randomly in the Pareto front obtained by multi-objective selection (4). The population size for the next evolutionary step is restored to its original size by selecting only the N best ranked individuals. Diversity and feasibility of the population are preserved by special rules.

As shown on Fig. 1, a two-level approach is used with performance estimates computed by metamodels in the generation loop and performance values obtained by CFD and CHA analysis in the iteration loop. The estimates provided by the Artificial Neural Network (ANN) metamodels, allow a reduction of the computational cost so that the evolutionary process can be continued over a very large number of generations. The recursive call to high-fidelity analysis ensures proper training of the metamodels in new regions of the search space and safeguards their accuracy. Typically, off-line training is performed every 1000 generations on the 10 best out of 50 individuals.

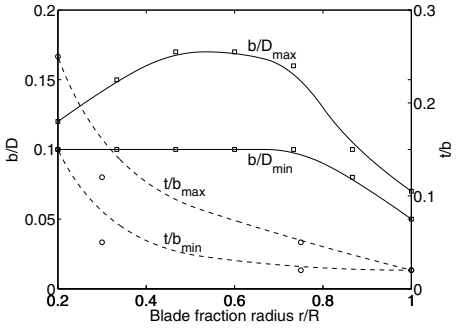

(a) Chord ($b(r)/D$ - □) and thickness ($t(r)/b(r)$ - ○).

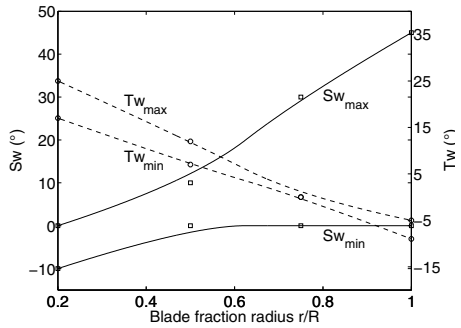

(b) Sweep ($Sw(r)$ - □) and twist ($Tw(r)$ - ○).

Figure 2: Minimum and maximum ordinates of the control points for the blade distributions together with the corresponding distributions.

2.2. Design variables

The value of a design variable $x(r)$ at a given radius r is determined through 3rd order b-spline interpolation using a given set of control points. The ordinates x_i of those points determine the shape of the variable distribution $x(r)$ and are allowed to fluctuate over specific intervals as shown in Fig. 2. The width of the allowable intervals is chosen such that the optimization process bears a lot of freedom. The choice of b-spline parameterization results from the more local influence of control points which ensures a direct relationship between the design parameters (i.e. the ordinates of the control points) and the shape of the curve (i.e. the radial distribution) so that mutual interferences between parameters are reduced and metamodeling is eased.

Two airfoils are described by b-spline parameterized thickness- and camber-distributions (5). One is used from the blade root to 35% radius and the other

	Take-off/Landing	Cruise
ISA altitude (m)	0	10665
ρ_∞ (kg/m^3)	1.225	0.380
T_∞ (K)	288.15	218.81
M_∞	0.2	0.75

Table 1: Operating conditions.

from 45% radius to the tip. Between the two intermediate radii, both airfoils are blended into one by interpolation so that no abrupt geometry variation is encountered. The design parameters consist of the ordinates of the control points but for some of them, the abscissa is also used.

2.3. Operating conditions, objectives and constraints

The multi-objective and multi-point optimization is based on operating conditions representative of cruise at transonic speed and take-off/landing at low Mach number, each comprising 3 advance ratios. The central take-off/landing advance ratio $J_{TO,2}$ is adapted to match the constraint on minimum take-off thrust $T_{TO,2}$ while $J_{TO,1}$ and $J_{TO,3}$ are at a fixed distance from $J_{TO,2}$. At cruise, $J_{CR,2}$ is adapted to match the constraint on minimum cruise thrust $T_{CR,2}$ while $J_{CR,1}$ and $J_{CR,3}$ are also at a fixed distance. The external operating conditions are summarized in table 1.

In a multidisciplinary optimization, the drive comes from the objectives and constraints. The obvious advantage of a multi-objective approach is that each discipline can be treated on its own, without the difficult necessity to assign weights between performance values stemming from different disciplines. In the current approach, both disciplines have their own objectives but instead of having one objective for each operating point, some performance factors are aggregated in one single objective consisting of elements from either aeroacoustics or aerodynamics solely. The aggregated objectives consist of:

1. an aggregate of the propeller power at the three advance ratios both in the cruise and take-off/landing conditions (Ω_1),
2. an aggregate of the Sound Pressure Level (SPL) in the propeller plane (at receiver 3) both in the cruise and take-off/landing conditions (Ω_2),
3. and an aggregate of the SPL at three receiver locations (receivers 2, 3 and 4) both in the cruise and take-off/landing conditions (Ω_3).

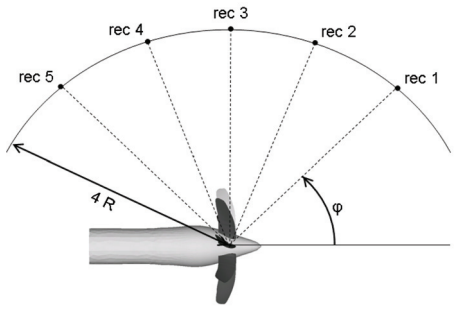

Figure 3: Location and nomenclature of acoustic receivers.

Constraints are formulated in terms of propeller net thrust and advance ratio at cruise condition. The advance ratio $J_{CR,2}$ is constrained to less than 3.57 in order to limit the associated tip helical Mach number $M^{tip}_{CR,2}$ below 1.0. On top of this, a thrust constraint is associated with each operating condition $J_{.,i}$ both for the cruise and take-off/landing sets so that the thrust of a benchmark propeller is at least matched. This benchmark propeller has no sweep, a semi-constant chord ($b/D = 0.15$ up to 75% radius) and is build with thin NACA 16 and 65 airfoil sections. It delivers $11kN$ thrust in cruise condition at $J = 3.37$ ($M_{tip} = 1.03$) with an efficiency η of 0.68 and $35kN$ in take-off/landing condition at $J = 0.95$ with an efficiency of 0.54.

2.4. CFD and CHA solvers

Aerodynamic computations rely on Fluent (6) to perform periodic steady RANS simulations of a single blade passage in free air under zero angle of attack. The full propeller is modeled using cyclic boundary conditions with continuity of pressure and temperature between two adjacent blade passages. The $k-\epsilon$ turbulence model is used in combination with wall treatment. Adiabatic no-slip wall conditions are used for the spinner and blade surfaces whereas the test-section radial boundary is reproducing the effects of a pressure far-field. The surface mesh of the blade is made of quadrilateral elements that are extruded into an O-type boundary layer mesh such that the average $y+$-value on the blade surface amounts 35. The spinner surface mesh consists of triangles which are the basis for the tetrahedric blade passage mesh.

In the post-processing of the aerodynamic results, the Sound Pressure Level (SPL) is computed at various receiver locations by the aeroacoustic solver. Receivers are located at different angles (φ = 45°, 67.5°, 90°, 112.5°, and 135°) at a distance of 4 tip radii from the axis as shown in Fig. 3. To compute the SPL, the inhomogeneous wave equation derived from Lighthill's acoustic analogy by Ffowcs Williams - Hawkings (FW-H) is chosen as the theoretical background because it benefits from the partial decoupling of the acoustic and aerodynamic aspects. Solving the FW-H equation with the use of free-space Green's function and standard derivation, one obtains formulation 1A from Farassat (7) expressed in a medium-fixed coordinate system (8; 9) (i.e. the observer is assumed to translate forward at the same speed as the propeller). Equations are obtained for the thickness noise and loading noise respectively whereas the quadrupole source term has been dropped from the FW-H equation (10). The blade surface is chosen as integration surface. More details about this model and the aeroacoustic results are presented in Marinus et al (11).

3. Optimization results

Among the optimized blade shapes, 4 are pinpointed because of their respective performance (see Fig. 4). Individuals *A* and *B* have extremely low sweep combined with humps made of wide chord portions. Individuals *C* and *D* have high sweep combined with a distinct chord-width hump that is enclosed by regions of more narrow chord. Noticeably, all four have thin airfoils and the highest twist distribution. These 4 are discussed in detail in (1) though the main aerodynamic and aeroelastic results are repeated here for completeness.

3.1. Aerodynamic performance

Figure 5 shows the thrust and power coefficients (C_T and C_P respectively) as well as the efficiency η at all operating conditions. The benchmark and the central individual (i.e. the individual with all parameter values set to their respective mid-range position) are also shown. As expected, the efficiency is raised (at constant thrust) in the cruise condition and the advance ratio is increased, hence the rotational velocity is decreased. Because of their sweep, individuals *C* and *D* have more flat efficiency curves. Unexpectedly, no significant increase in efficiency is obtained for the take-off/landing condition. In this case, the advance ratio is also increased whereas the higher power coefficients of all blades, at take-off/landing but also at cruise, indicate higher loading of the propeller.

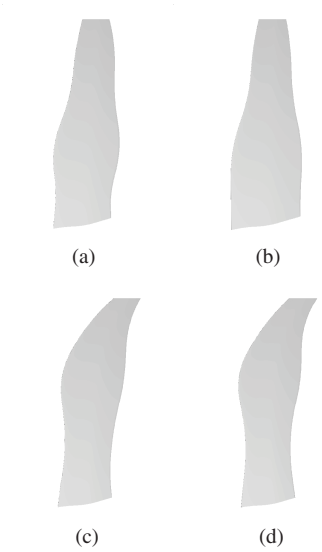

Figure 4: Blade geometry of the individuals *A*, *B*, *C* and *D*.

3.2. Aeroacoustic performance

In terms of aeroacoustics, significant gains have been achieved, especially in the rotational plane were the benefits of sweep are clearly visible. Unfortunately, swept individuals radiate the corresponding acoustic energy more in the up- and down-stream directions. The unswept individuals gain their advantage from very low noise emissions in any direction at TO/landing and in the streamwise directions in cruise.

3.3. A posteriori stress analysis

3.3.1. CSM solver

The FEA-solver Samcef (12) is used to compute the total mass of the blade as well the stresses resulting from the centrifugal and aerodynamic forces. Because of the possibility to tailor the blade structure to properly take on the stresses, only a simplified blade model is implemented. The aeroelastic problem is decoupled from the aerodynamic one as the analysis is performed solely on the 'cold' blade shape with the pressure distribution interpolated form the corresponding aerodynamic solution by a Radial Basis Functions-based interpolator. Hence

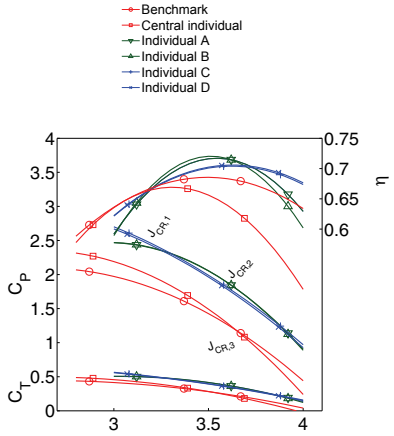

(a) Cruise condition.

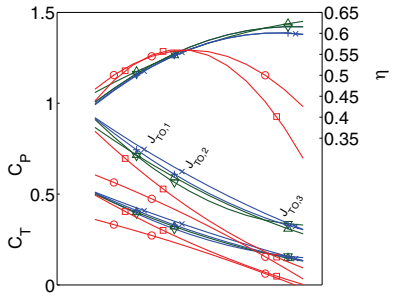

(b) TO/Landing condition.

Figure 5: Aerodynamic performance curves.

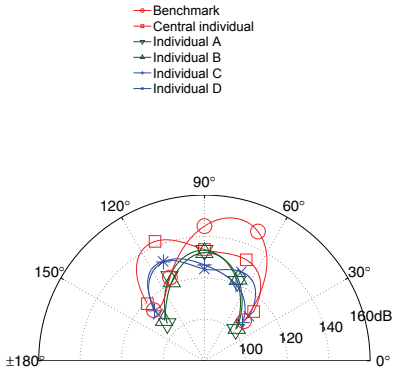

(a) Cruise condition.

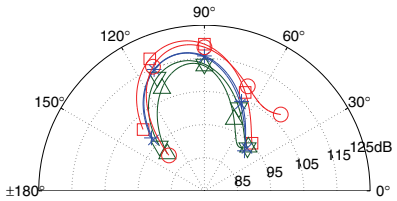

(b) TO/landing condition.

Figure 6: Sound directivity at the central operating point $J_{.,2}$.

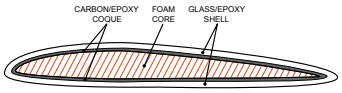

(a) Monocoque blade structure.

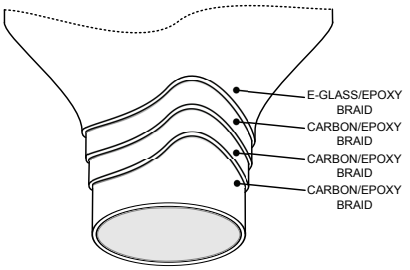

(b) Blade structure close to the root.

Figure 7: Blade structure.

the CSM computations provide a convenient yet rudimentary sanity check from a structural point of view. The simplified blade is a monocoque design as shown in Fig. 7(a). The shell is composed of stepped layers of braided composite (carbon/epoxy (13; 14) or E-glass/epoxy (14; 15)). The number, thickness and order of the braided layers vary with the radial position, as suggested on Fig. 7(b), though at least one carbon/epoxy and one E-glass/epoxy layer run along the whole blade. The core consist of a polyurethane foam-fill of aeronautical quality. The modeling of the bounding of the composite material with the metal sleeves composing the shank assembly (16) is achieved by a clamp condition applied to the composite part of the shank.

For each operating point, the stress criteria rely on the maximum value of the Tsai-Wu criterion $\zeta_{.,j}$ (for the shell) and the maximum value of the von Mises equivalent stress normalized by the tensile yield strength $\sigma^v_{.,j}/\sigma_{yield}$ (for the foam core).

3.3.2. Stress levels

Figures 8-11 show the maximum value of $\zeta_{TO,2}$ and $\sigma^v_{TO,2}/\sigma_{yield}$ in the middle advance ratio in take-off/landing condition for some specific blades. This condition has been chosen because of the high RPM and high pressure loading associated with it. Discontinuities on the lower part of the blade are related to the staggering of braid layers that form discontinuities in the skin material. For individual *A*, stress concentrations in the skin exist close to the shank but are still within reasonable limits (< 0.35). These result mainly from the additional mass due to the large chord at low radius and are thus absent in the case of the central individual. At higher radius, stress levels in the skin and in the core are low. For the part of the core within the shank, stress levels reach critical values close to the skin (≈ 0.5). Individual *D* has a completely different stress pattern. In this case, stresses in the skin are high just below the hump (see Fig. 9(a)) though still within acceptable limits. No high stresses are encountered in the core. This is a much better situation than for the central individual (Fig. 10) where high stress concentrations exist just up of the shank both in the skin and in the core (≈ 0.35 in both cases).

4. Conclusion

A multi-point and multidisciplinary optimization procedure of transonic propeller blades based on MODE has been developed and includes aerodynamics coupled with aeroacoustics. The procedure relies on a scope of design variables that covers the radial distributions of standard blade-shape determining quantities (sweep, twist, chord and thickness) as well as the shape of the airfoils used to manufacture the blade. It resulted in interesting geometries that feature higher efficiency for constant thrust but also considerably less tonal sound emissions. Some of these blades have been analyzed for the integrity of their hybrid structure made of a composite skin and a foam core. This cursory analysis revealed that, provided adequate tailoring of the material is applied, the stress levels might fall within safe limits. This a posteriori analysis, opens the path to a more integrated optimization procedure where structural considerations are included within the optimization. This last optimization is ongoing.

Acknowledgments

The author wishes to acknowledge the Belgian Defence Scientific and Technologic Research initiative for its funding of the present study, as well as the von Karman Institute, in particular R. Van den Braembussche and T. Verstraete, for the resources and expertise made available for the present work.

References

[1] B. Marinus, M. Roger, R. Van den Braembussche, Aeroacoustic and aerodynamic optimization of aircraft propeller blades,

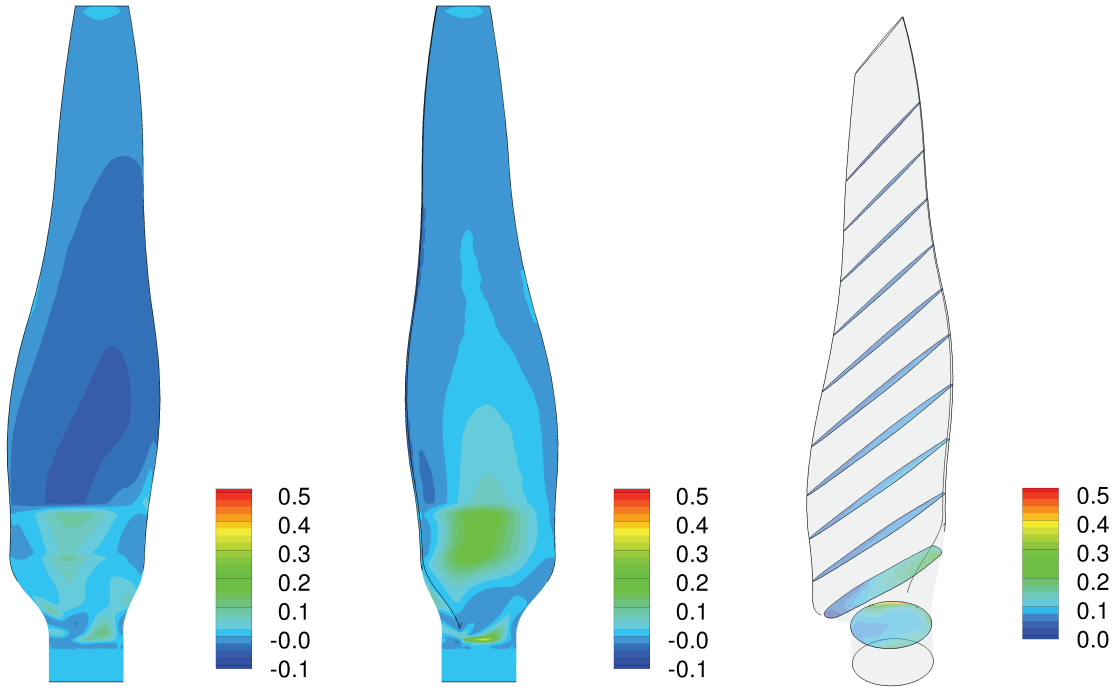

(a) $\zeta_{TO,2}$ on the pressure side. (b) $\zeta_{TO,2}$ on the suction side. (c) $\sigma^v_{TO,2}/\sigma_{yield}$ in the foam core.

Figure 8: Stress criteria for individual *A*.

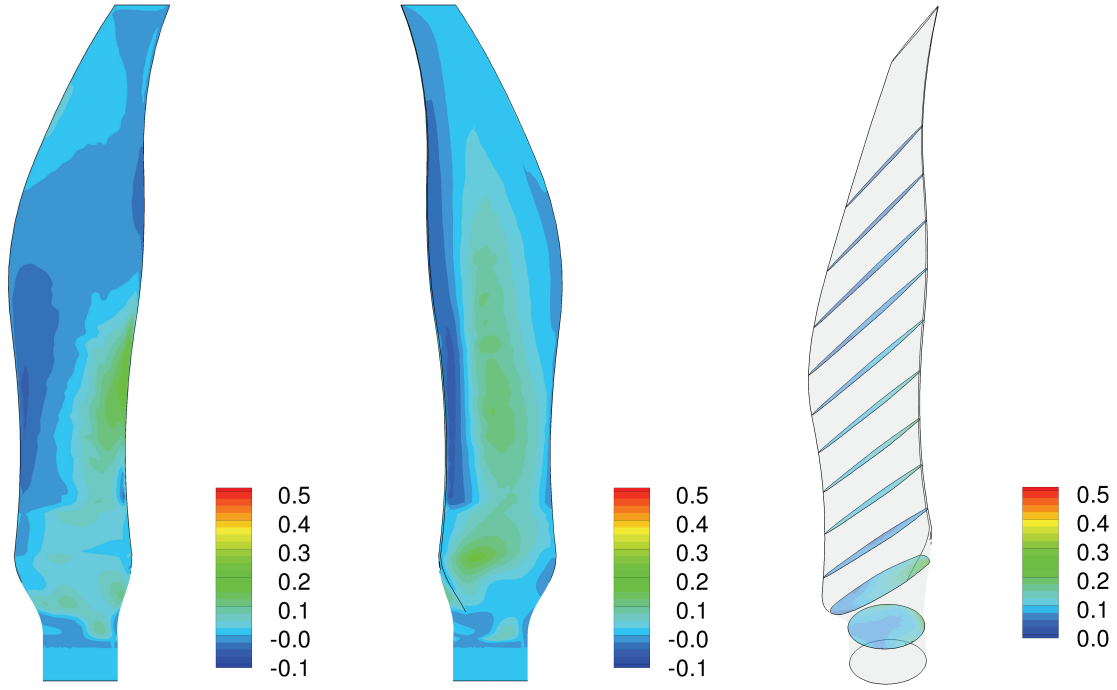

(a) $\zeta_{TO,2}$ on the pressure side. (b) $\zeta_{TO,2}$ on the suction side. (c) $\sigma^v_{TO,2}/\sigma_{yield}$ in the foam core.

Figure 9: Stress criteria for individual *D*.

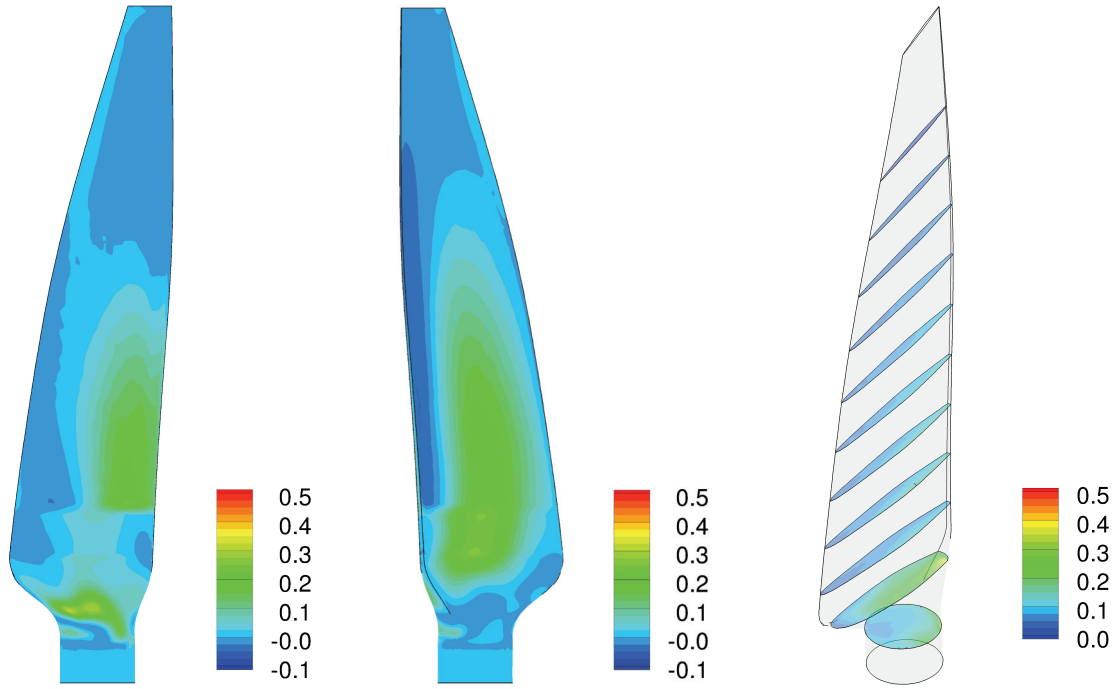

(a) $\zeta_{TO,2}$ on the pressure side. (b) $\zeta_{TO,2}$ on the suction side. (c) $\sigma^v_{TO,2}/\sigma_{yield}$ in the foam core.

Figure 10: Stress criteria for the central individual.

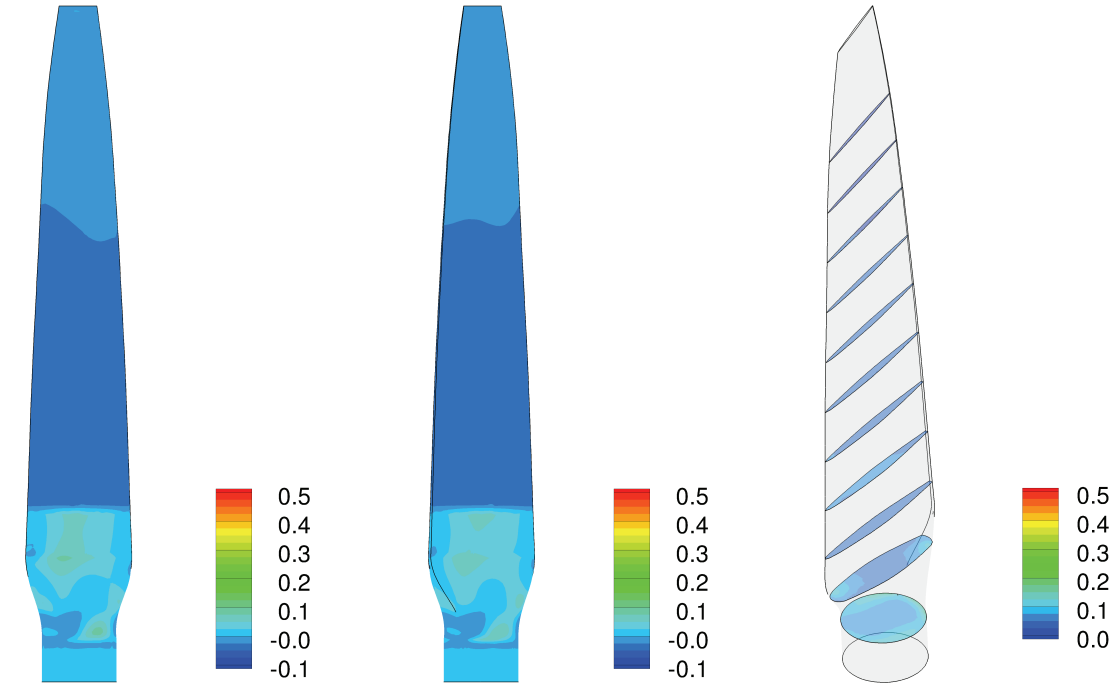

(a) $\zeta_{TO,2}$ on the pressure side. (b) $\zeta_{TO,2}$ on the suction side. (c) $\sigma^v_{TO,2}/\sigma_{yield}$ in the foam core.

Figure 11: Stress criteria for the benchmark.

in: 16th AIAA/CEAS Aeroacoustics Conference, no. AIAA 2010-3850, AIAA, Stockholm (SWEDEN), 2010.
[2] T. Verstraete, Multidisciplinary turbomachinery component optimization considering performance, stress and internal heat transfer, Phd thesis, von Karman Institute for Fluid Dynamics - Universiteit Gent, Rhode-Saint-Genèse - Gent (Belgium) (June 2008).
[3] K. Price, R. Storn, Differential evolution, Dr Dobb's Journal (1997) 18–24.
[4] N. Madavan, Multiobjective optimization using a Pareto Differential Evolution Approach, in: Proceedings of the Congress on Evolutionary Computation, Vol. 2, Honolulu (USA), 2002, pp. 1145–1150.
[5] B. G. Marinus, Current status of propeller blade multidisciplinary optimization, in: T. Magin (Ed.), 2010 Symposium on VKI's Doctoral Candidate Research, von Karman Institute for Fluid Dynamics, Brussels (Belgium), 2010.
[6] Fluent, Fluent 12.0.16 (January 2009).
URL www.ansys.com
[7] F. Farassat, G. Succi, The prediction of helicopter rotor discrete frequency noise, Vertica 7 (4) (1983) 309–320.
[8] F. Farassat, Derivation of formulations 1 and 1a of Farassat, Technical Memorandum TM-2007-214853, NASA, NASA Langley Research Center (USA) (March 2007).
[9] J. Frota, P. Lempereur, M. Roger, Computation of the noise of a subsonic propeller at an angle of attack, in: 4th AIAA/CEAS Aeroacoustics conference, AIAA, Toulouse (France), 1998.
[10] B. Marinus, M. Roger, R. Van den Braembussche, W. Bosschaerts, Truncated method for propeller noise prediction up to low supersonic helical tip Mach numbers, in: 15th AIAA/CEAS Aeroacoustics Conference, no. AIAA 2009-3330, AIAA, Miami (USA), 2009.
[11] B. Marinus, M. Roger, R. Van den Braembussche, W. Bosschaerts, Multidisciplinary optimization of propeller blades: focus on the aeroacoustic results (to be published), in: 17th AIAA/CEAS Aeroacoustics Conference, AIAA, Portland (USA), 2011.
[12] Samcef 13.1-02 (June 2010).
URL www.samtech.com
[13] L. Gause, J. Alper, Structural properties of braided graphite/epoxy composites, Journal of Composites technology and Research 9 (4) (1987) 141–150.
[14] L. Tong, A. Mouritz, M. Bannister, 3D fibre reinforced polymer composites, Elsevier Science, Oxford (United Kingdom), 2002.
[15] J.-H. Byun, T.-W. Chou, Stress-strain behavior of 3-D braided composites, Vol. MD-Vol 29, ASME, New York (USA), 1991.
[16] R. McCarthy, G. Haines, R. Newley, Polymer composite applications to aerospace equipment, Composites Manufacturing 5 (2) (1994) 83–93.

Accelerated optimization for multi-disciplinary design of contra-rotating and transonic turbomachinery components

Michael Joly

Turbomachinery and Propulsion Department, joly@vki.ac.be

Supervisor: Tom Verstraete

Assistant Professor, Turbomachinery and Propulsion Department, von Karman Institute for Fluid Dynamics, Belgium, verstraete@vki.ac.be

Supervisor: Guillermo Paniagua

Associate Professor, Turbomachinery and Propulsion Department, von Karman Institute for Fluid Dynamics, Belgium, paniagua@vki.ac.be

Abstract

The present work investigates optimization strategies to design complex turbomachinery components. A first application on high-pressure turbine demonstrates the capacity of optimization techniques to reduce unsteady flow phenomena by considering robust and low cost steady-state evaluations. A methodology is then proposed to design highly-loaded fans based on multi-fidelity evaluations integrated in two successive optimization loops of through-flow and Navier-Stokes evaluations. The implementation of Computational Fluid Dynamics algorithms on Graphic Processing Unit is also investigated to enable fast multi-disciplinary design-optimization of contra-rotating turbomachinery components.

Keywords: Multi-disciplinary optimization, GPU accelerated CFD, High-pressure turbine, Highly-loaded fan, Contra-rotating fan

1. STRATEGIC CONCERNS

Engineering systems require nowadays to have cost-effective development and eco-efficient operation. In propulsion system design, optimization strategies provide solutions to the attempt of reduced time-to-market costs and improved fuel consumption.

Able to address multidisciplinary problems, optimization techniques offer the designer the opportunity to handle several constraints and objectives in a single design process. An immediate application is the reshape of existing designs for enhanced performances. Compared to conventional industrial design methodologies that require several exchanges between different specialized departments, optimization strategies are able to merge these interactions into a single activity, leading to reduced time-to-market costs.

The simultaneous multidisciplinary evaluations have moreover the potential to increase efficiency and effectiveness in finding innovative solutions. Applied to original design challenges, Evolutionary Optimization techniques are able to evaluate a large set of candidates, to select promising individuals and eventually to provide the designer a collection of optima that represents the possible solutions answering all the conflicting requirements. New opportunities in design are therefore extended, potentially leading to innovative configurations.

The design of innovative turbomachinery components for reduced fuel consumption is currently tackled by reducing the number of stages to save weight, while increasing the efficiency of every single component. The related challenges are inherently multidisciplinary and optimization strategies provide promising perspectives.

2. INTRODUCTION TO THE PROJECT

The design of turbomachinery components involves demanding compromises between aerodynamics and structural requirements. In particular, transonic turbine vanes should be designed for reduced unsteady

forcing on the downstream rotors and contra-rotating fans design require multi-level approaches with fluid and solid evaluations.

Optimization techniques, such as Evolutionary Algorithms, enables to address multidisciplinary problems and offer to designers the opportunity to handle several constraints and objectives in a single process. The simultaneous evaluation of performances leads to increased efficiency and effectiveness in finding innovative solutions. The main drawback of evolutionary algorithms is however the computational time required to evaluate the performances of a very large set of candidates. In an aero-structural design problem, each design individual must be assessed by a Computational Fluid Dynamics (CFD) solver and Finite Element Method (FEM) structural analysis. CFD computations being much more time consuming than FEM, it is a logical path to try to improve the speed of aerodynamics analysis.

Parallel computations enables to perform one computation on several computing units. Central Processing Units (CPUs) are the typical architecture to process computations, with a computational power increasing proportionally to the number of CPUs used. The efficiency of a parallel computation decreases however with this number, due to communication between the different units. Graphics Processing Units (GPUs) are processors specialized in graphics rendering and much work has recently been focused on them as devices for general-prupose computing. Applications of GPU in aerospace (1; 2; 3) and turbomachinery (4) CFD cases highlight the potential acceleration of computing time with convergence obtained from 15 to 40 times faster.

The present project proposes to investigate acceleration techniques in Computational Fluid Dynamics by means of Commodity Graphics Hardware. The accelerated solver will be integrated into an aero-structural optimization strategy to address two distinct original turbomachinery design cases: reduced shock interaction in a turbine stage and coupled design of contra-rotating fans. On the one hand, high-pressure turbines operating in the transonic regime experience strong shock interaction between the vane and the rotor (5). An attempt to redesign a transonic turbine vane will be made to reduce the unsteady forcing on the downstream rotor. On the other hand, the benefit of contra-rotation in highly loaded axial flow compressors have been known at least since the 50's (6), but to date attempts have remained unsuccessful. Intent is to apply an aero-structural optimization strategy for the simultaneous design of both rotors, enabling an optimized coupling of the contra-rotating components.

3. RESEARCH CONTENT

3.1. Reduced Unsteady Shock Interaction in Transonic Turbine Stage

Single-stage high-pressure turbines often operate in the transonic regime, resulting in strong shock interaction between the vanes and the rotor blades. In particular, the vane trailing edge shock system (7; 8) propagates downstream and impinges periodically on the rotor suction side (9).

In order to limit the forcing on the rotor, the stage should be designed to limit the inter-stage shock interaction. An optimization strategy is applied to control the steady-state vane distortion, aiming at a reduction of the unsteady shock interaction. It is proposed to design transonic vanes with downstream steady-state static pressure fields as uniform as possible, controlling the pitch-wise standard deviation (eq. 1), to attenuate the strength of the shock waves emanated from the vane trailing edge (See Fig. 1). The optimal vane is then analyzed by an unsteady computation to assess the actual benefit on the rotor unsteady forcing.

$$\sigma = \sqrt{\int_{y_0}^{y_0+pitch} \frac{(p(1.35 * \lambda, y) - \bar{p})^2}{pitch} .dy} \qquad (1)$$

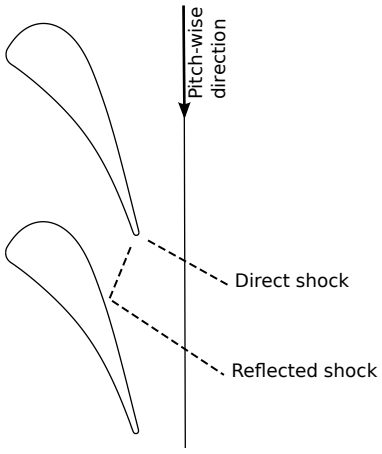

Figure 1: Vane trailing edge shock system

3.1.1. Geometry generation and Steady Evaluation

Turbine vane geometries are generated using parametric two-dimensional blade profiles and a three-dimensional stacking law. Within the Evolutionaty Algorithm, each candidate is processed by an automatic mesh generator and evaluated with a steady-state Navier-Stokes solver.

Two-dimensional airfoil sections are defined for a specific radius, starting from the definition of the camberline by the following set of parameters: axial chord, stagger angle, inlet metal angle and outlet metal angle. The suction and pressure side curve are defined by Bézier curves, for which the control points are specified relative to the camber line. Control points at the edge leading are computed by specified radii of curvature, allowing geometric continuity in the second derivative between the suction side and pressure side curve. The distance to the last point is equal to the trailing edge radius, which is also specified. Finally, the second last control point is computed by a specified wedge angle.

High-pressure turbines are characterized by the passage ducted by two adjacent airfoils. The parametrization enables a detailed control of the throat region (See Fig. 2), with control points uniformly distributed all along both the suction and pressure sides. To be integrated in the optimization process, the mesh generation is parametrized and can therefore be executed in an automated manner independently of the blade shape. A H-type periodic non-matching mesh is used and particular care is addressed to the meshing of the throat area and the non-matching boundaries.

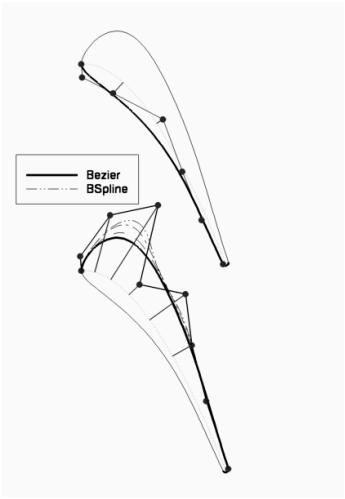

Figure 2: Parametrization of 2D section profile

Three-dimensional annular vane geometries are generated from the stacking of several sections at different radii. A stacking law defines the relative circumferential position of the leading edge for each section, introducing lean to the 3D blade. This law is defined by a Bézier curve with 3 degrees of freedom depicted in Fig. 3, left: tangent angle at the hub (alpha1), tangent angle at the tip (aplha2), circumferential position of the tip leading-edge relative to the hub one (xtip). From this law, the positions of 5 radially equally spaced sections are extracted. The individual 2D sections are connected by a smooth surface and finally a 3D mesh is generated based on this blade definition (Fig. 3, right).

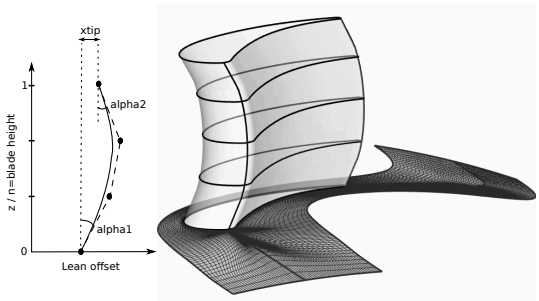

Figure 3: Stacking line parametrization (left), Typical 3D geometry and mesh (right)

The code TRAF 3D (10) is used to evaluate the aerodynamics performances for the geometry candidates. The Reynolds-averaged Navier-Stokes equations are solved using a Runge-Kutta scheme. A low level of artificial dissipation is guaranteed by eigenvalue scaling. The two-layer eddy-viscosity model of Baldwin and Lomax is used for the turbulence closure. The acceleration strategies of variable-coefficient implicit residual smoothing and Full-Approximation-Storage multigrid scheme of Brandt and Jameson are implemented. The solver has been validated on a baseline geometry (see Fig. 4).

3.1.2. Optimization strategy

The optimization strategy used the differential evolution method developed by Price and Storn (11). The algorithm, implemented in CADO code (12), has been tested on a typical two-dimensional mathematical optimization problem with the two following objectives. It is formulated as:

$$\begin{aligned} \text{Minimize} \quad & f_1(\vec{x}) = 5sin(\pi x_1) + cos(\pi x_2) \\ & f_2(\vec{x}) = sin(\pi x_1)cos(\pi x_2) + x_1 x_2 \\ \text{Subject to} \quad & -1 \leqslant x_1 \leqslant 1 \\ & -1 \leqslant x_2 \leqslant 1 \end{aligned}$$

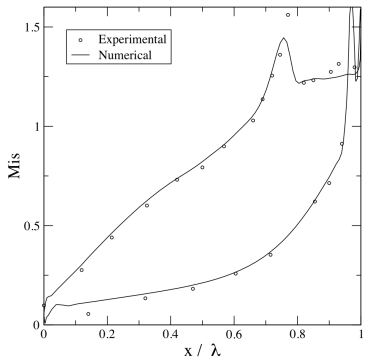

Figure 4: Mach number distribution, mid-span

The population size is set to 30 and the number of generations equals 20. The constants used by the DE algorithm are $F = 0.3$ and $C = 0.8$. The optimization problem results into a discontinous Pareto front with following mathematical expressions:

$$f_2 = -\frac{f_1 + 1}{2} + \frac{1}{\pi} asin\left(\frac{f_1 + 1}{5}\right) \tag{2}$$

$$f_2 = -f_1 - 5 - \frac{1}{2\pi} acos\,(f_1 + 5) \tag{3}$$

In Fig. 5 the final population after 20 generations is plotted. All individuals are laying on the Pareto front and are equally spread over the Pareto front. This later feature is very important and is caused by the constraint on the diversity of the population implemented by the NSGAII algorithm.

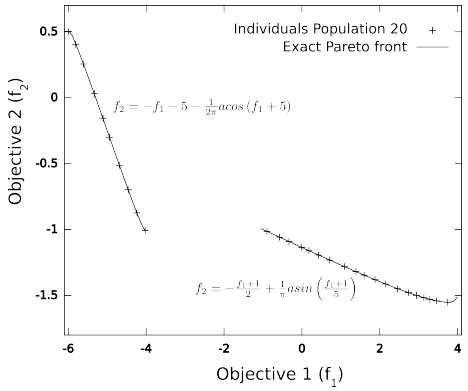

Figure 5: Comparison of the exact Pareto front and the population after 20 generations

3.1.3. Optimization process and optimal geometry

The objective of minimal downstream distortion is considered. The loss coefficient and mass flow are constrained to be lower and higher than the baseline values, respectively. Acceptable values of the outlet flow angle are considered within the range of±0.5 deg.

An optimization run with 200 generations of 60 individuals is performed and the evolution of the process is illustrated in Fig. 6. Through the optimization process, the individuals of each population are progressively satisfying the constraints. Hereafter the objective value is minimized, leading finally to a 43.2% attenuation of the downstream distortion. The loss coefficient is 1.4% lower than the baseline, the outlet flow angle 0.02 degree larger and the mass flow increased by 0.3%.

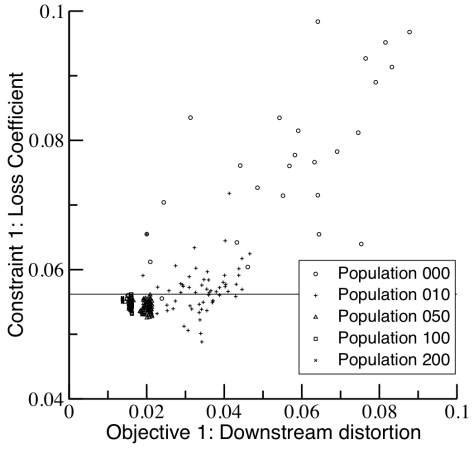

Figure 6: Optimization iterations for single-point strategy

The optimal geometry provides a larger thickness on the pressure side with a similar suction side compared to the baseline. The downstream pitchwise static pressure distribution shows a clear reduction of the direct shock strength. The reflected shock is however slightly stronger. Density gradient fields confirm this observation (See Fig. 7). The left running shock, i.e. direct shock, clearly appears with lower intensity for the optimized airfoil. By contrast, the right running shock has a stronger intensity than the baseline, also revealed by the higher inclination of the oblique shock. Its reflection on the adjacent blade suction side, i.e. reflected shock, appears with higher intensity. A strong impingement on the suction side of the adjacent vane is also observed on the Mach number distribution.

With a similar suction side and increased thickness on the pressure side, the contraction channel of the

optimized airfoil is narrower than the baseline's. The channels are choked and therefore sonic sections impose the mass flows. For the baseline, the sonic section is located at the end of the convergent channel and coincides with the geometric throat. On the other hand, the channel resulting from the optimized airfoil is convergent-divergent. The sonic section moved upstream and appears inclined. This explains how similar mass flows could be reached with different geometric throats. The convergent-divergent shape of the optimized contraction channel over-accelerates the flow downstream of the sonic line, increasing the Mach number levels on the rear pressure side and mid suction side. With a faster flow within the contraction channel, the trailing edge shock system is modified and the propagation of shock waves downstream is remarkably attenuated.

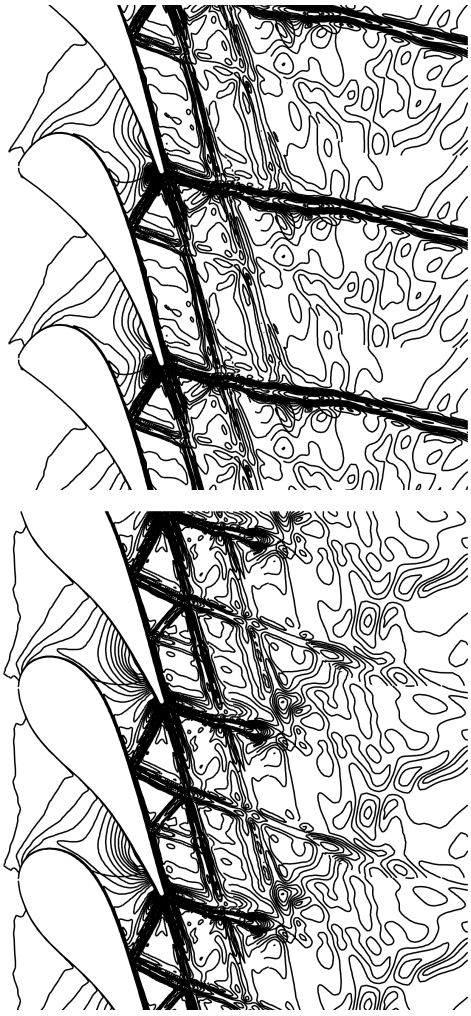

Figure 7: Density gradients fields for baseline (up) and optimized (down) geometries

Sieverding et al. (13) proposed a loss correlation for transonic airfoils. Trailing edge loss is reduced as the addition of the trailing edge wedge angle and the suction side curvature increases. Correlations also indicates that convergent-divergent configurations result in higher loss levels than convergent ones. The obtained optimal geometry presents larger thickness on the pressure side compared to the baseline, resulting in a greater trailing edge wedge angle. With similar suction side curvature, a positive effect on the losses could be expected from the correlation. A contradiction still remains about the configuration of the contraction channel. The authors believe that the present optimization techniques revealed an unprecedented geometry that correlations from the published literature did not allow to investigate. The obtained combination of a convergent-divergent contraction channel with large trailing edge wedge angle and straight rear suction side enables to reduce the downstream propagation of shock waves emanating from the trailing edge shock system, while preserving low losses.

In the attempt to further improve the downstream distortion with no drop of efficiency, a three-dimensional optimization is performed. The 45-parameters optimization includes 3 parameters for the lean and 14 parameters for each of the three adaptable sections at hub, mid-span and tip. An optimization run is performed with the objective of minimal downstream distortion and several constraints. The loss coefficient and mass flow are constrained to be lower and higher than the baseline values, respectively. Acceptable levels of outlet flow angle are considered within the range of ±0.5 deg. The optimization consists in 40 iterations of 60 individuals, leading to a 56.1% attenuation of downstream distortion with all constraints fully respected. The outlet flow angle is similar to the baseline (-0.38 deg.) and the mass flow slightly larger (+3.5%). The kinematic loss is reduced (-0.4%), leading to a very similar stage efficiency of 91.37% (-0.07%). Therefore the 3D optimization with lean and section adaptation enables a further improvement in downstream distortion, while offering similar efficiency compared to the baseline.

The comparison of density gradients fields downstream of the vane between the baseline, the 2D optimum and the 3D optimum (Fig. 8) shows a further reduction of the direct shock and a close to complete attenuation of the reflected shock for the 3D optimal geometry. The remaining gradients, appearing as a diagonal along the span, are the trace of the adjacent vane's wake.

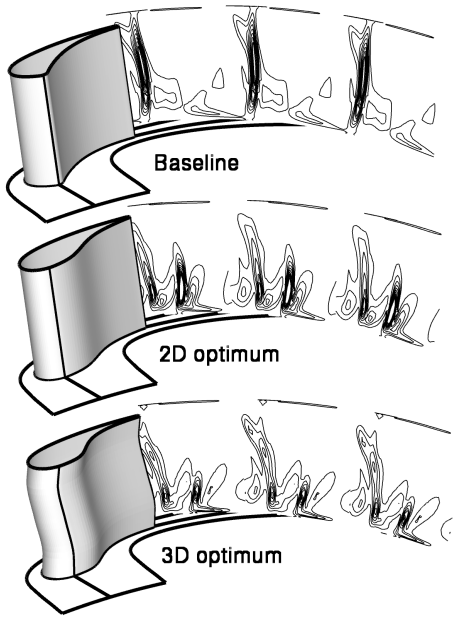

Figure 8: Geometry and density gradient fields downstream at x=1.35*Cax, baseline (up), radial stacking of 2D optimum (mid), 3D optimum (down)

3.1.4. Unsteady validation

To verify the interaction of the optimal vane with the downstream rotor, the unsteady flow is simulated by Fine of Numeca International (14). The grid has an O-H topology and the Spalart Allmaras turbulence model is used. With a nonlinear harmonic method, the flow is decomposed into a time averaged field and an unsteady perturbation around the mean flow field. The unsteady component are decomposed in Fourier modes in time and conservation laws for each harmonic are solved in the frequency domain.

In the time domain, the unsteady force is extracted at 3 radial positions (10%, 50% and 90% of the blade height). The axial and tangential forces are computed for 60 time steps along a rotor pitch. Comparison with experiments (See Fig. 9) shows a relatively good agreement on the axial forcing. On the other hand, the prediction of the tangential forcing highlights some offset with the experimental data.

Computations of unsteady forcing on the rotor downstream of the different design is presented in Figure 10. Attenuation in terms of amplitude and standard deviation are summarized in Table 1. Reductions up to 61% of the unsteady force response on the rotor are observed and validate the reduction in high-cycle fatigue risks.

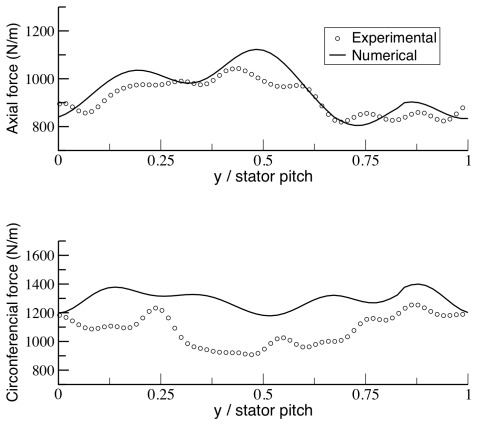

Figure 9: Validation of non-linear method, unsteady forcing at 85% of the span

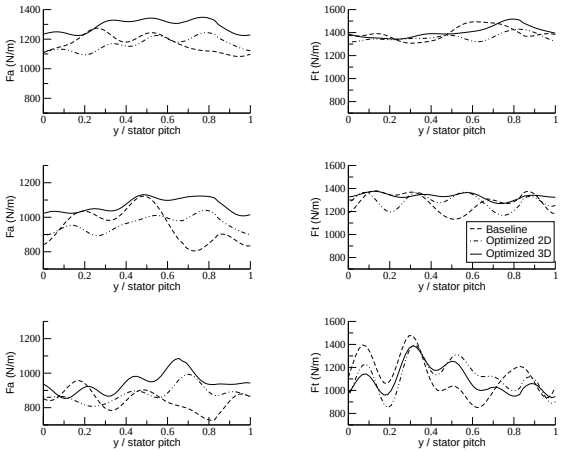

Figure 10: Unsteady forcing on the rotor downstream of the 3D optimized vane, axial force (left) and tangential force (right), at 90% (top), 50% (mid), 10% (bottom) of the span

	Amplitude	Standard deviation
$F_{ax}at90\%$	-35%	-33%
$F_{tan}at90\%$	-19%	-18%
$F_{ax}at50\%$	-61%	-57%
$F_{tan}at50\%$	-52%	-58%
$F_{ax}at10\%$	+0.9%	-4.8%
$F_{tan}at10\%$	-28%	-24%

Table 1: Unsteady forcing on the rotor at 10%, 50% and 90% of the blade height downstream of the 3D optimal vane compared to the baseline

3.2. Design of Highly-Loaded Transonic Fan with Compactness and Robustness

The aim the present design is to produce a fan that provides a pressure ratio as high as does the Rotor 37, but with enhanced efficiency, compactness and robustness. Rotor 37 is a supersonic compressor (inlet relative Mach number is above 1.0 along the whole span) and delivers a pressure ratio of 2.1. With the same limitation of wheel tip speed of 450m/s, a transonic configuration (section profiles ranging from subsonic to supercritical) is targeted and expected to provide higher efficiency, lower machine diameter and larger operating range.

The proposed method is based on multi-fidelity evaluations integrated in two successive optimization loops. A first cycle is performed with a through-flow solver that provides the required end-walls, wheel speed and radial distribution of flow turning. From these, a range of possible blade camber and thickness is defined for the optimization of the three-dimensional fan geometry, whose candidates are assessed by a Navier-Stokes solver. The intent of the authors is to not present in details the not-yet-published methodology in the present paper.

The obtained geometry (See Fig. 11) provides a pressure ratio of 2.1 for an efficiency of 90% (See Fig. 12). The tip diameter is reduced by 19% compared to the Rotor 37 for an increased choke mass flow (22.2kg/s, against 20.2kg/s for the rotor 37). The operating range is about 25% of the choke mass flow rate, compared to the 8% of the Rotor 37.

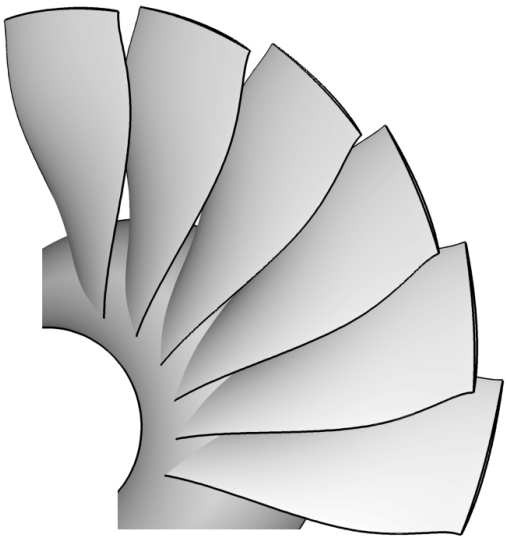

Figure 11: Optimal fan geometry generated by CADO

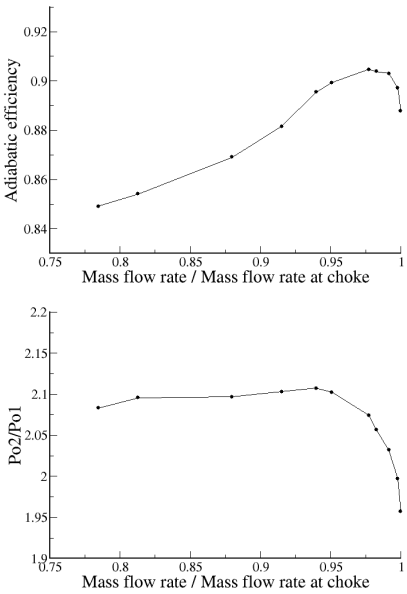

Figure 12: Optimal fan geometry performances

The design exhibits a radial distribution of total pressure rise increasing along the span (See Fig. 13). Absolute flow turning is performed with the combination of shock compression and relative flow turning. Density field on the suction side shows the bow shock impingement on the surface (See Fig. 14). Density field at 90% of the span illustrates the bow shock structure in more details at the design point (See Fig. 15). Close to the shall point, the bow shock appears as expelled (See Fig. 16); on the opposite, it merges with a passage shock at the choke mass flow rate (See Fig. 17).

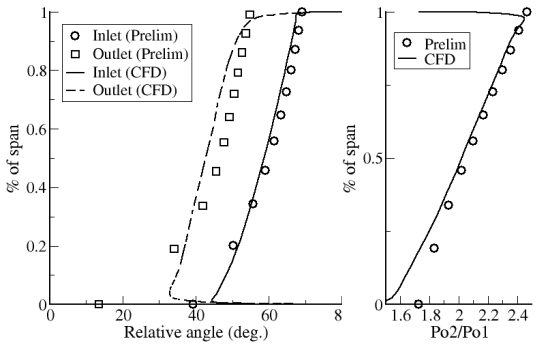

Figure 13: Comparison of relative flow angles (left) and total pressure rise (right) between preliminary design prediction and actual values after three-dimensional optimization

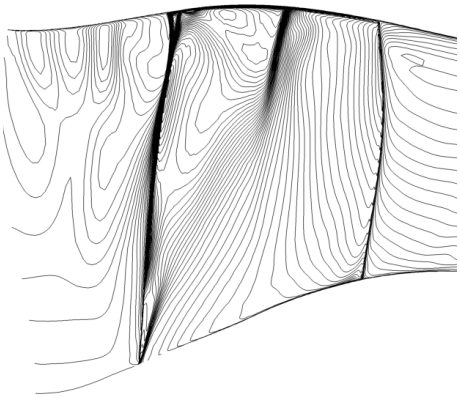

Figure 14: Density field at design point, suction side surface

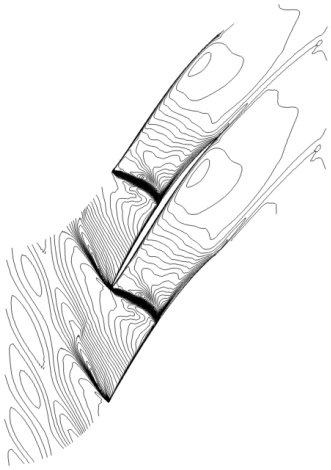

Figure 15: Density field at design point, 90% of span

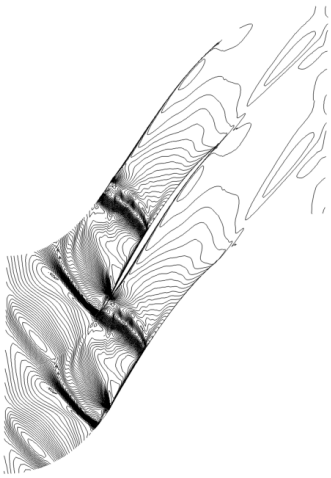

Figure 16: Density field near the stall point, 90% of span

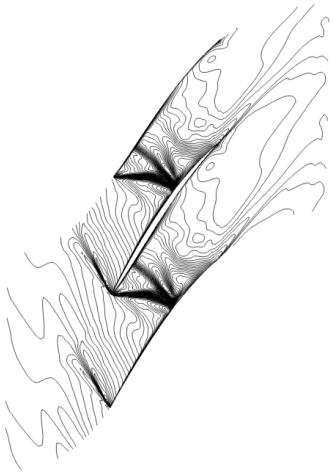

Figure 17: Density field at choke point, 90% of span

3.3. Investigation of GPU Accelerated CFD for Mutli-Disciplinary Optimization

Computational Fluid Dynamics (CFD) has a history of seeking and requiring ever higher computational performance. This quest has in the past been satisfied by faster clock speeds, which has reached a plateau mainly due to heat dissipation constraints. Currently, a boost in computational performance is being supplied by parallelism. Within the last five years, while companies such as Intel and AMD have taken a multi-core approach with an expected increasing number of core chips in conventional Central Computing Units (CPUs), companies such as NVIDIA and ATI are leveraging the inherent parallelism of their powerful graphics rending processors to provide solutions to general computing applications. A Graphics Processing Units (GPUs) is a processor that exhibits higher level of parallelism than conventional CPUs (higher rate of floating-point operations per second) and has the strong potential to accelerate scientific computing. Extensive parallelism within GPU accelerated CFD requires however significant changes to the implementation of the underlying code. NVIDIA provides in this concern an extension to the C programming language called CUDA (15), in which the developer can set up a large number of threads that are grouped into thread blocks. Each block is then associated with one of the multi-processors of the GPU, where the threads could be scheduled and synchronized to handle memory concerns.

The present project targets the development of a CFD viscous solver with GPU capacities, aiming at the integration of fast and robust Navier-Stokes

evaluations inside aero-structural design-optimization loops. The Reynolds-Averaged Navier-Stokes equations will be discretized in space using a cell-centered finite volume scheme. The temporal discretization of the time-dependent equations will be achieved using an explicit four stage Runge Kutta scheme. The two-layer eddy-viscosity model of Baldwin and Lomax will be used for the turbulence closure. The GPU-implemented code will be first assessed on a two-dimensional transonic turbine case. Based on the lessons learned from this initial work, more advanced techniques will be progressively implemented.

3.4. Investigation of Multi-Discplinary Design-Optimization of Contra-Rotating Turbomachinery Components

Conventional turbomachinery configurations consist of several stages spinning on a same shaft. Research trends (6; 16) includes contra-rotating components turning around a same axis but in opposed directions. It is proposed within the present project to investigate the application of optimization strategies to the design of contra-rotating turbomachines.

The coupled design of the two stages of a contra-rotating fan is initiated using the radial equilibrium concept, prescribing flow conditions in-between blade rows. With defined total pressure distributions downstream of each rotor, streamline curvatures and radial gradients are solved considering the parametrized end walls, axial lengths, solidity distributions and wheel tip speeds (See Fig. 18). The objective is to find the best compromise in loading balance between the two stages for maximum efficiencies and minimum machine size. Detailed design of two-dimensional profiles is then performed at different radii for both rotors. Optimization of supersonic profiles requires specific considerations in the Navier-Stokes solver inlet boundary condition type to handle the unique incidence phenomena. The performance maps of the three-dimensional contra-rotating fans is eventually computed and compared to a single-stage configuration that satisfies the same specifications.

Based on the preliminary aerodynamic design, the contra-rotating fans will be optimized with three-dimensional aero-structural evaluations. For each individual, the computation of performance maps will require the evaluations of about 14 operating points, which is currently very expensive. The GPU accelerated CFD code is expected to ease such CFD-FEM optimization cases and could enable the simultaneous optimization of the two contra-rotating rotors.

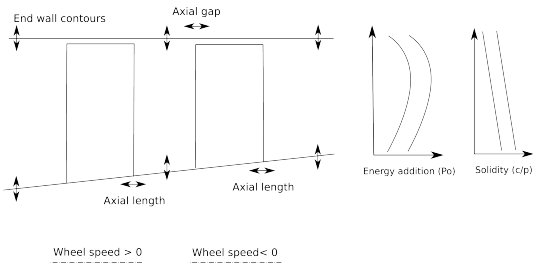

Figure 18: Parametrization of contra-rotating configuration in meridian plane

References

[1] E. Elsen, P. LeGrelsey, E. Darve, "Large calculation of the flow over a hypersonic vehicle using a GPU", Journal of Computational Physics, 227(24), pp. 10148-10161, 2008

[2] D. Jespersen, "Acceleration of a CFD Code with a GPU", NASA Technical Report, NAS-09-003, 2009

[3] J. Dongarra, S. Moore, J. Allred, V. Natoli, "Exploring New Architectures in Accelerating CFD for Air Force Applications, "DoD HPCMP Users Group Conference", 2008

[4] T. Brandvik, G. Pullan, "An Accelerated 3D Navier-Stokes Solver for Flows in Turbomachines", ASME GT2009-60052, 2009

[5] M.B. Giles, "Stator/Rotor Interaction in a Transonic Turbine", Journal of Propulsion, Oct. 1990, Vol.6, No.5, pp.621-627.

[6] A. J. Wennestorm, "Highly Loaded Axial Flow Compressors: History and Current Developments", Journal of Turbomachinery, 112, pp. 567-578, 1990

[7] C.H. Sieverding, M. Stanislas M, J. Snoeck, "The Base Pressure Problem in Transonic Turbine Cascades", Journal of Engineering for Power, 102, pp. 711-718, 1980

[8] J.D. Denton, L. Xu, "The Trailing Edge Loss of Transonic Turbine Blades", Journal of Turbomachinery, 112, pp. 277-285, 1990

[9] G. Paniagua, T. Yasa, A. de la Loma, L. Castillon, T. Coton, "Unsteady Strong Shock Interactions in a Transonic Turbine: Experimental and Numerical Analysis", Journal of Propulsion and Power, 24(4), pp. 722-731, 2008

[10] A. Arnone. 1994. "Viscous Analysis of Three-Dimensional Rotor Flow Using a Multigrid Method" Journal of Turbomachinery, Vol. 116, pp. 435-445

[11] K. Price, N. Storn, "Differential Evolution", Dr. Dobbs Journal, pp. 18-24, 1997

[12] T. Verstraete, "CADO, a Computer Aided Design and Optimization Tool for Turbomachinery Applications", 2nd International Conference of Engineering Optimization, 2010

[13] C. Sieverding, M. Stanislas, J. Snoeck, "The base pressure problem in transonic turbine cascades", Journal of Engineering for Power, Vol. 102, pp. 711718, 1980

[14] Numeca International, "Fine turbo users manual", 2010

[15] NVIDIA, "NVIDIA CUDA Programming Guide", Version 3.1.1, 2010

[16] J. Kerrebrock, A. Epstein, A. Merchant, G. Guenette, D. Parker, J. F. Onnee, F. Neumayer, J. Adamczyk, A. Shabbir, "Design and Test of an Aspirated Counter-Rotating Fan", Journal of Turbomachinery, 130, pp. 021004-1, 2008

STATIC AND DYNAMIC STABILITY OF RE-ENTRY VEHICLE

Experimental determination of the dynamic derivatives of a reentry capsule in transonic supersonic regime

Sébastien Paris

Aeronautics and Aerospace Department, paris@vki.ac.be

Supervisor: Patrick Rambaud

Assistant Professor, Aeronautics and Aerospace Department, von Karman Institute for Fluid Dynamics, Belgium, rambaud@vki.ac.be

Promoter: Gérard Degrez

Professor, Universite libre de Bruxelles, Belgium, degrez@ulb.ac.be

Abstract

Aerodynamic damping is investigated in the subsonic and transonic regimes for re-entry vehicles. Static moment, free oscillations and forced oscillations experiments are carried out on replica models in the von Karman Institute (VKI) S-1 supersonic-subsonic wind tunnel. The frequency of oscillations induced in wind tunnel is made to match the reduced frequencies of flight vehicles based on their natural frequencies. In free oscillation mode, the inertia of the vehicle is adjusted for the same reason. Recent results on this vehicle with a sting as support are compared with existing data in literature and with a previous campaign carried out in the VKI-S1 with a transversal support on a different experimental set-up. It shows significant effects of the support on the static and dynamic measurement. Proper validation of the methods should give better confidence into the results for the dynamic characterization of the vehicles.

1. Introduction

Entry capsules provide an attractive option for planetary exploration missions. Designed to survive during early phases of atmospheric entry, these vehicles often become dynamically unstable at low altitudes. Proper characterization of aerodynamic damping can allow drogue chute deployment at lower Mach number. Such findings may permit smaller drogue chute designs, thus enabling a payload volume and weight increase as well as a vast decrease in drag penalties.

The aerospace vehicle is exposed to unsteady flow fields that may have significant effects on its characteristics of motion. As a result, the dynamic stability information, considered of rather lesser importance for a number of years, has became an object of relatively high interest. The reason is obvious: in the past, for aircrafts at low angles of attack, most of the dynamic stability parameters were relatively easy to predict analytically, exhibited as a rule only smaller variations with varying flight conditions and therefore, had only a relatively insignificant or at least, a relatively constant effect on the resulting flight characteristics of the vehicle. With the advent of flight at high angles of attack at high speeds, all that has drastically changed. The dynamic stability parameters are now found to depend strongly on the non-linear effects and can no longer be calculated using relatively simple linear analytical methods as in the past and new methods are needed. As the nonlinear instability phenomena are not well known for the moment, it is in general difficult to simulate them using CFD. Thus, the experimental techniques in wind tunnels are certainly the best way to obtain dynamic stability information at realistic Reynolds and Mach numbers.

2. Objective

The objective of this project is to develop the experimental tools for the study of the dynamic stability in the subsonic and supersonic range. The wind tunnel S1 was selected for this purpose. Different experimental technique need to be implemented in it. The free

oscillation technique consists in releasing the model in a given position and observing the model oscillating around its axis. It gives directly the behavior of the model. The forced oscillation technique does not give directly the characteristic of the model. Oscillations are forced by a crankshaft mechanism and the pitching moment is measured during the oscillations thanks to a balance. These techniques have been developed and used with various reentry vehicle and need to be properly validated in order to assess the uncertainty of the methods.

3. Theory

3.1. Motion equations

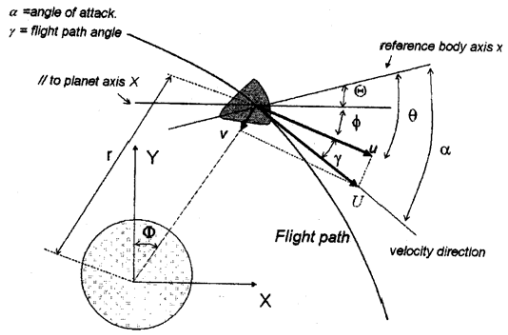

Figure 1: Space vehicle entering the atmosphere

The motion of a space capsule during planetary reentry can be seen, by classical mechanics, as a combination of translation and rotation around its center of gravity. The classical equations of motion of the vehicle are obtained using a fixed system of coordinates, and assuming the vehicle to be rigid. Then one can deduce the six equations governing the movement of the object in the three dimensions. However since the system obtained is quite complex to solve (impossible analytically), one usually makes some assumptions: the displacement is made in two dimensions, the rotation of the earth is neglected and the gravity force is constant.

In the wind tunnel, the angle of attack and the pitch angle are equals:

$$\theta = \alpha \Leftrightarrow \gamma = 0 \tag{1}$$

A set of three equations governing the movement of the vehicle in two dimensions can be obtained:

$$m\frac{dU_x}{dt} = q_\infty S C_D \tag{2}$$

$$m\frac{dU_z}{dt} = q_\infty S C_L - mg + m\frac{U^2}{r} \tag{3}$$

$$I\ddot{\theta} = q_\infty S C_m D \tag{4}$$

This third equation represents the rotation of the capsule around his pitch axis. And the pitching moment coefficient can be written depending on the other parameters:

$$C_m = \frac{\partial C_m}{\partial \alpha}(\alpha - \alpha_0) + C_{m_q}\frac{D}{2U}\dot{\theta} + C_{m_{\dot{\alpha}}}\frac{D}{2U}\dot{\alpha} \tag{5}$$

C_m may be separated into two parts (reminding that α and θ equivalent here):

- a static one: $\frac{\partial C_m}{\partial \alpha}(\theta - \theta_0)$
- and a dynamic one: $\left(C_{m_q} + C_{m_{\dot{\alpha}}}\right)\frac{D}{2U}\dot{\theta}$

Hence the equation 4 can be written:

$$I\ddot{\theta} = q_\infty S C_{m_\alpha} D(\theta - \theta_0) + q_\infty S \frac{D^2}{2U}\left(C_{m_q} + C_{m_{\dot{\alpha}}}\right)\dot{\theta} \tag{6}$$

This equation describes the motion of the model around his pitching axis. The C_{m_α} coefficient is the static coefficient which can be known thanks to the static measurement of the pitching moment.

The aim of the present activities is to determinate the dynamic coefficient: $C_{m_q} + C_{m_{\dot{\alpha}}}$.

3.2. Similarity parameters

The experiment conditions are based on the similarity with flight data. The similarity can be made on several parameters, but it is usually impossible to make all of them respected in the same time. As a consequence, one has to choose which ones are of primary importance. Geometry of the model is of course one of them and means that the model should be a scaled representation of the vehicle outer shape. In order to reproduce correctly the movement, the CG location of the flight vehicle should correspond to the center of rotation of the wind tunnel model. Another important parameter to match while performing experiments in transonic and supersonic regime is the Mach number. Here, the experiments deal only with Mach numbers high enough not to neglect the compressible effects, and hence the Mach number similarity has to be applied. Finally, the third parameter to match for

the similarity concern is the oscillations reduced frequency. This non-dimensional number is very similar to a Strouhal number, but is based on the frequency of the model oscillations and not on a frequency relating to the flow. It is assumed that this parameter should be matched in order to obtain the same aerodynamic behavior as in flight. The reduced frequency matching depends on the test technique that is used and its computation is presented below. It is worth to mention that the Reynolds number similarity, which is very often a major concern in fluid dynamics experiments, cannot be fulfilled in the classical facilities: it is in fact much lower for the experiments than for the flight due to the large scaling factor, while the other parameters do not changed a lot. However, it is usually admitted that the stability phenomena are affected by the flow regime (meaning laminar or turbulent), and not much by the exact matching of the Reynolds number. For the similarity of this study, the flow in flight is certainly fully laminar and as the Reynolds number reached during experiments is much lower than the one of flight, one can assume that the flow is completely laminar for experiments as well as for the flight.

3.3. Reduced Frequency (Strouhal Number)

The reduced frequencies of both the model and the flight vehicle for the forced oscillation tests should be maintained to equate the dissipation or input of energy from the surrounding flow field (aerodynamic influences) on the model during testing with the flight vehicle. It is defined by the Strouhal number (St). Oscillations occur at the natural frequencies of the actual flight vehicle upon atmospheric re-entry condition. Thus, during free and forced oscillations tests on the models, the Strouhal number based on the natural frequency and characteristic length of the flight vehicle is used. The general formulation is given by:

$$St = \frac{fD}{U_\infty} \tag{7}$$

Extraction of the natural frequency f of the flight vehicle is obtained from the 'spring' and 'damping' constant in equation 6.

$$f_{flight} = \frac{1}{2\pi}\left(\sqrt{\frac{q_\infty S\, D\, |(\partial C_m/\partial\theta)|}{I} - \left(\frac{q_\infty S\, D\left(C_{m_q} + C_{m_{\dot\alpha}}\right)}{2I}\right)^2}\right)_{flight} \tag{8}$$

The aerodynamic damping (right hand term) can be neglected due to its magnitude relative to the static restoring moment contribution (left hand term). Thus, the Strouhal number of the flight vehicle becomes:

$$\begin{aligned}(St)_{flight} &= \left(\frac{fD}{U_\infty}\right)_{flight} \\ &= \left(\sqrt{\frac{\rho_\infty S\, D^3\, |(\partial C_m/\partial\theta)|}{8\pi^2 I}}\right)_{flight}\end{aligned} \tag{9}$$

ρ_∞ is the free stream density. The respect of the similarity provides the value of the inertia and of the driving frequency respectively for the free and forced oscillations:

$$I_{experiment} = \left(\frac{I}{\rho_\infty D^5}\right)_{flight} \times \left(\rho_\infty D^5\right)_{experiment} \tag{10}$$

$$f_{experiment} = \frac{1}{2\pi}\left(\sqrt{\frac{\rho_\infty S\, D^3\left(-\frac{\partial C_m}{\partial\alpha}\right)}{2I}}\right)_{flight} \times \left(\frac{U_\infty}{D}\right)_{experiment} \tag{11}$$

4. The free oscillations technique

For this technique, the model is free to rotate around an axis passing by the CG location. It is release in a position different of the trim angle. The model is then free to oscillate around the trim angle. The incidence angle is recorded over time. In order to simplify the writing of the equation of motion, it is replaced by a more general form:

$$\ddot\theta(t) + a\dot\theta(t) + b\theta(t) = 0 \tag{12}$$

a and b are two coefficients One can obtain the damping in pitch parameter from the resolution of this equation with:

$$C_{mq} + C_{m\dot\alpha} = -\frac{I\alpha}{q_\infty S\, D\frac{D}{2U_\infty}} \tag{13}$$

4.1. Envelope Method

The method used for the resolution of the differential equation and the extraction of the damping in pitch parameter is the envelope method. It consists in using only the maximum or the minimum value of the signal for each oscillation, and in computing the logarithmic decrement between two extrema. For a theoretical second order signal, the oscillations damping is computed by:

$$a = \frac{2}{nT}\ln\left(\frac{x_2}{x_1}\right) \tag{14}$$

T is the period of the signal x_1 and x_2 are two extreme values separated by n periods.

In computing the damping over the whole signal (either by using the first and the last extremum or by making an envelope fitting of the whole signal), a single value is found for the damping in pitch parameter. However, due to the large variation of the oscillations amplitude during the tests, it appeared that this method is too global and does not take into account the possible changes in the damping term: it is not satisfactory.

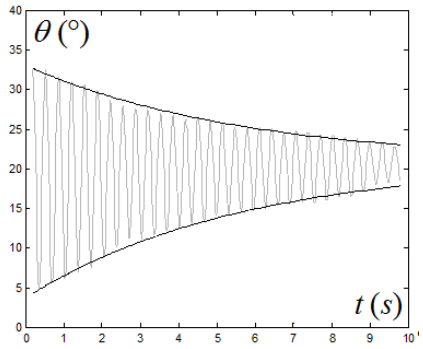

Figure 2: Envelope curves

On the opposite, by calculating the damping value between each two consecutive maxima or minima, the experimental uncertainty has a large influence on the results, which are therefore very scattered and not usable properly. As a consequence, what it seems to be the best technique is a compromise between the two: the use of about seven oscillations of the signal to perform the average damping over them gives results of a quite accuracy and without a large scattering.

4.2. The forced oscillations technique

Models oscillate about an axis of rotation over a fixed range of oscillation angles in a periodic pattern. The forced oscillations induce moments on the model in addition to the aerodynamic loads. Moments and incidence angles are recorded over time. Contrary to the free oscillations equation of motion, the equation for forced oscillations cannot be solved directly for the damping in pitch parameter because of the mechanical moments, which cannot be evaluated independently from the actual experiments. However, in performing the so-called no flow measurements (which consist in forcing the oscillations of the model, with the wind tunnel not working), one gets the following equation of motion (like the equation 5 without the aerodynamic terms):

$$I\ddot{\theta}(t) - c\dot{\theta}(t) - k\theta(t) = M_{nf}(t) \tag{15}$$

$M_{nf}(t)$ is the external forcing moment as a function of time in no flow conditions. Then, in computing the difference between the equation 15 with flow and without flow, one finds:

$$q_\infty S\, D \frac{D}{2U_\infty}\left(C_{mq} + C_{m\dot{\alpha}}\right)\dot{\theta}(t) + q_\infty S\, D C_{m\alpha}\theta(t) = M_{nf}(t) - M_f(t) \tag{16}$$

$M_f(t)$ is the external forcing moment as a function of time in flow conditions In a more general form, it gives:

$$A\dot{\theta}(t) + B\theta(t) = \frac{\Delta M(t)}{qS\, D} \tag{17}$$

The mechanical moments as well as the inertial part of the original equation of motion do not appear anymore for the resolution of the problem. However, the use of the two sets (with and without flow) of experiments requires absolutely the equality in the evolution of the angle of attack ($\theta_f(t) = \theta_{nf}(t)$ at every instant). One can obtain the damping in pitch parameter from the resolution of this equation with:

$$C_{mq} + C_{m\dot{\alpha}} = A\frac{2U}{D} \tag{18}$$

The principle of the energy resolution consists in integrating the work absorbed by the system (corresponding to amplification) or dissipated (corresponding to damping) during one oscillation cycle. In fact, since the mechanical friction is not null in the driving system, some energy injection is always necessary to compensate the losses. The energy is injected by the power supply. Depending on the loop direction, one can deduce if the system oscillations would be amplified or damped while subjected to free oscillations. The first case is represented by a counter clockwise loop associated to a dissipation of energy, whereas the second situation is associated to a clockwise loop associated to an input of energy.

The general expression of the damping in pitch parameter is the following [2]:

$$C_{m\dot{\alpha}} + C_{mq} = \frac{\oint C_m d\theta}{\int_T \dot{\theta}^2 dt}\frac{2U}{D} \tag{19}$$

One can notice that, as the graphical representation has shown it, the damping in pitch parameter (about

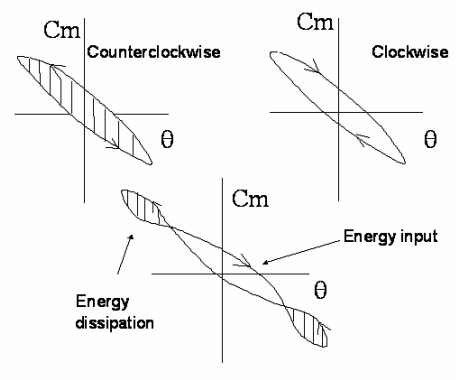

Figure 3: Energy method representation

which it has been said that a negative value means dynamic stability) and the pitching coefficient integral are of the same sign.

5. Equipment

5.1. Supersonic / Transonic S-1 Wind Tunnel

The VKI supersonic/transonic wind tunnel S-1 is a continuous closed circuit facility of the Ackeret type, driven by a 615 kW axial flow compressor. Two 40 cm x 36 cm test sections are used: a contoured nozzle with M = 2.0 and a slotted transonic section with variable Mach number, from 0.4 to 1.05. The tunnel is equipped with scani-valves for pressure distribution measurements, multi-component strain gage balances, and a free-to-tumble mounting system for investigations of dynamic stability of aerospace vehicles.

Mach	P_0	p_∞	$Re_{L_{ref}}$	T	ρ_∞	U_∞
-	Pa	Pa	-	$°C$	$kg.m^{-3}$	$m.s^{-1}$
0.5	26685	22514	169306	26	0.2755	168.72
0.6	26681	20891	198116	32	0.2558	203.42
0.69	26772	19421	223702	40	0.2374	234.54
0.8	26695	17565	247673	48	0.2151	269.50
0.89	27710	16248	262591	56	0.2000	299.32
2.0	9430	1193	875900	25	0.0249	519.25

Table 1: Typical Flow conditions

5.2. Experimental set-up

Several experimental set-ups have been designed and build over the years for the static and for the dynamic measurement.

5.2.1. Static experiments

First configuration

The first experimental set-up was built during the CTV phase A and one of the purposes was to cover the full domain of interest for the AEDB (360°). The figure 4 shows the new set-up where a stepping motor was added in order to rotate the model during the test. The reference length is 50mm. Static force and moment measurements are now possible in a range of [-225;+225°]. Axial and normal forces are measured by two strain gage balances implemented in the arms. The stepping motor and the angle measurement digital device are mounted on this balance so that all aerodynamic efforts are applied on the balances.

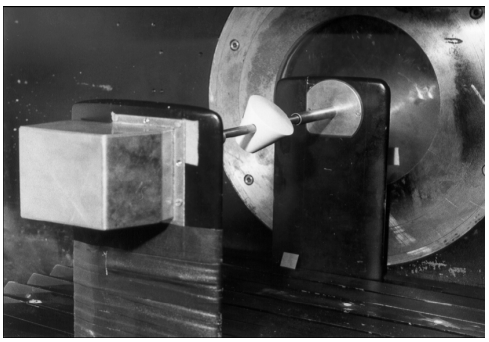

Figure 4: Experimental set-up for the static test(old)

The main interest of this set-up was the possibility to measure the aerodynamic effort for any angle of attack but the presence of the transversal support interfere with the flow and can introduce significant error.

Second configuration

The second configuration is similar to the first one but the balance and the driving mechanism are not in the wind tunnel but outside. The set-up designed for the dynamic testing (see figure 8) was used for this purpose.

Last configuration

For the recent testing, the support is now a sting. The model for the static measurement is made in Ureol; a light material easy to machine. The reference length is 77mm. The balance was designed to fit into the model along the symmetry axis. The center of reduction of the balance is close to the center of mass for a better sensitivity (figure 5 and figure 6).

5.2.2. Dynamic experiments

Old configuration

The free to tumble set up used for the first campaign was developed during a previous study and modification was done in order to improve the quality of the

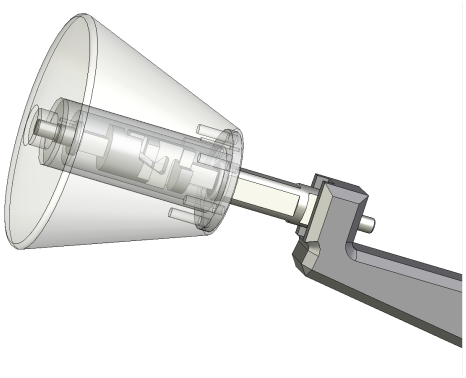

Figure 5: Model for the static tests with the balance

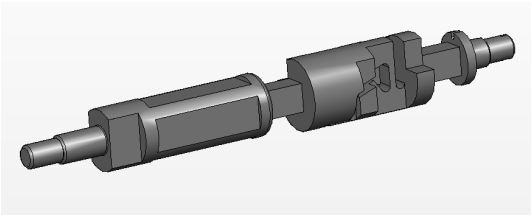

Figure 6: Balance for the static measurement

angular measurement. The encoder is now able to give the angular position with 0.18° of accuracy. The picture (Figure 7) gives a general view of the set-up in the wind tunnel. The rod is mounted on two ball bearings and linked to the encoder in one side and to the release system on the other side. It is possible with this technique to know the exact angular position for an infinite range. When the center of gravity is not on the axis of symmetry, it is necessary to add a mass to equilibrate the model. Otherwise, the trim position is influenced by the actual position of the center of gravity and do not depend only of the aerodynamic characteristic. The model is made of foam and resin and the reference length is 50mm.

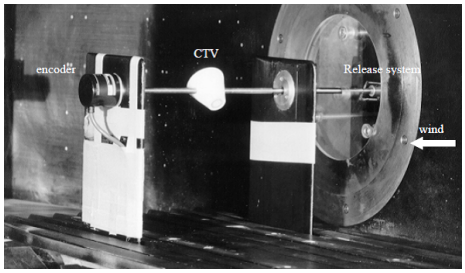

Figure 7: First Set-up for free to tumble test

Second configuration

A new set-up was developed for the VKI S1 wind tunnel to support a model by a transversal rod. This rod is linked to a mechanism able to supply an oscillating movement or it is free to tumble. In this last case, an effort was made to limit the friction of the bearing to a minimum level. For this purpose, ceramic ball bearings were used because friction is very low when they are used without lubrication. A magnetic encoder will measure the angular position with high accuracy (4096 step/revolution). In order to adjust the inertia of the model, a mass can be add on the support but the complete system must be as light as possible to reach the lowest value of inertia. For this purpose, particular care will be taken in the choice of material for the oscillating elements.

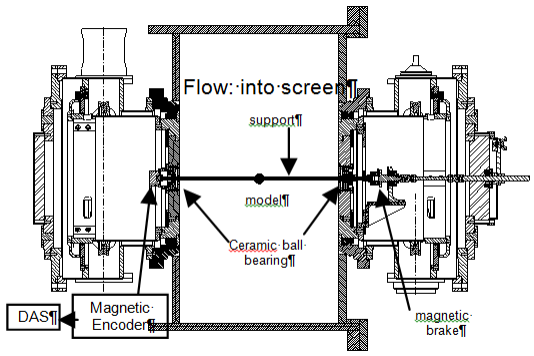

Figure 8: Experimental set-up for free oscillations testing

The previous experience shows problems in releasing system. It was not fast enough and it was difficult to adjust accurately the initial position. A new system was designed to allow fast and accurate angular release position. It is made of a small disk attached to the transversal rod and an electromagnet. This one can be operated by the operator thanks to a secondary axe passing through the wind tunnel.

New configuration

Like for the static efforts, when using a transversal support, the support disturbs the flow topology and produce significant error on the pitching moment measurement. The new set-up was designed in order to produce the oscillations of the capsule through a sting. Since the aim of the study is to measure the forces applied on the capsule while oscillating the set-up is rather complicated (figure 9, 10 and 11):

- A big electrical motor is fixed outside the wind tunnel. It drives the model with the required fre-

quency and amplitude.

- The rotation of the motor is transformed into oscillations thanks to an eccentric system.
- A secondary sting is then animated of periodic forward / backward translation movement inside of the main sting.
- The diameter of the main sting is selected to avoid excessive flexion during the tests campaign.
- Inside of the model, a static piece supports the encoder and the axis of the model.
- This axis is oscillating thanks to a crankshaft system and the balances are fixed on the axis.
- Interfaces between the balances and the model are adjusted together and should give a perfect trim position of the model.
- One optical encoder is fixed inside the model.
- For these dynamic measurements, the center of gravity is very important. It means that the center of rotation of the capsule should correspond to the center of gravity.

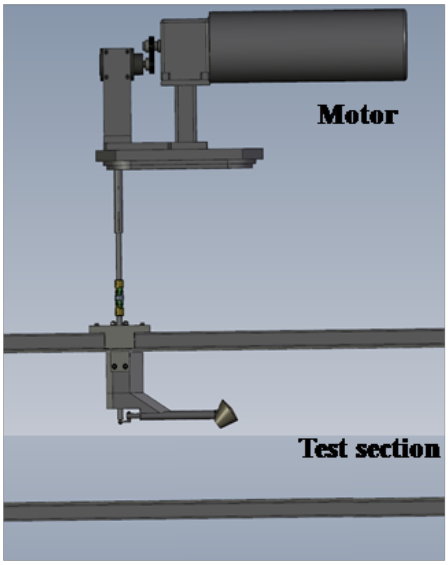

Figure 9: Overview of the dynamic set up

The model is constructed in several parts which are then assembled on the balances which are fixed on the axis. The figure 11 gives a view of the different pieces composing the model.

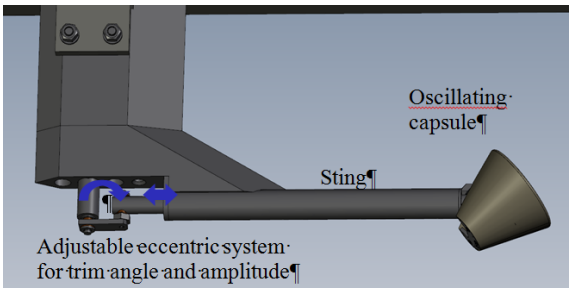

Figure 10: Zoom in on the oscillating system

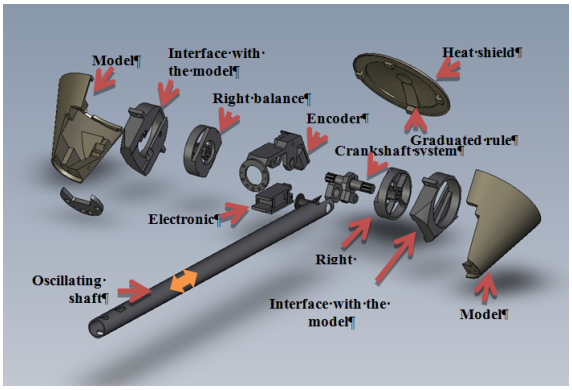

Figure 11: different pieces constituting the model

To obtain the forces applied on the model during the experiments, an aerodynamic balance was designed (balance VKI3822). Two of them are placed inside the model for a better symmetry and so, a higher accuracy.

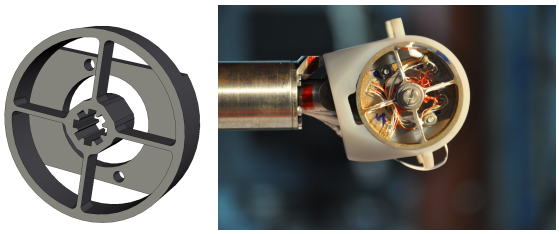

Figure 12: Dynamic balance

The four arms of the balance behave like four beams. The arm distortions are followed by the different distortion gauges stuck at different places on each arm. The center of reduction of the balance is located on the axis of rotation. The balance allows also the measurement of the axial and normal force in order to compensate for interferences.

6. Models manufacturing

As mentioned before, the model has to be light whatever the technique used. In case of free to tumble model, the model is light in order to respect the similitude and when the forced oscillation technique is used, the mass is reduced as much as possible in order to decrease the inertial part of the moment and increase the accuracy. Over the years, the technique used to build the model has changed. The first models were built from foam and resin and the shape was obtained by casting. The problem of the casting was the accuracy of the shape of the model. Then, SLA prototyping was used because of the complexity of the model but this technique does not allow controlling the shape of the model and the location of the CG. The last improvement consists in mixing the SLA for the complexity and the classical machining for the quality. It is the more precise way to build a model but improvements are still needed to decrease the uncertainty in CG location.

7. Results

Many results have been obtained over the years. This part gives typical results obtained with the CTV model.

7.1. Static tests

During the first campaign, the moment can be measured over a large range of angle of attack and the model is supported by a transversal rod. The results are given in the figure 13. The figure 14 shows the same measurement with the new set-up. The range of angle of attack is limited to 15°. The slope is similar but the trim angle is very different ($\alpha \approx -40°$ for the first campaign and $\alpha \approx -17°$ for the second). These last measurements have been compared with literature data and good agreement is found (see figure 15). It clearly indicated the strong influence of the support for this kind of measurement.

7.2. Dynamic tests

The dynamic test carry out during the first campaign consisted in qualitative measurement. The purpose of the tests was to measure the trim angle (figure 15) and to estimate the range of angle of attack for which the model is dynamically stable (see figure 16 and table 2). It can be remark that the dynamic trim angle is the same than the static one. The support was the same and produces the same effect. The phase diagram indicates clearly if the model is stable or not

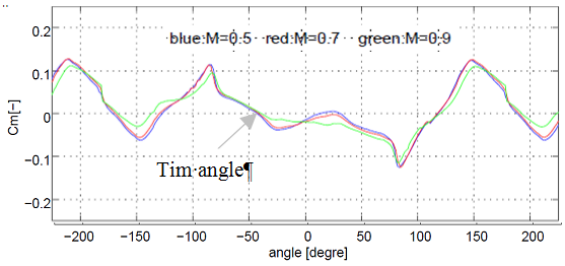

Figure 13: Pitching moment on CTV in transonic regime (first Set-up)

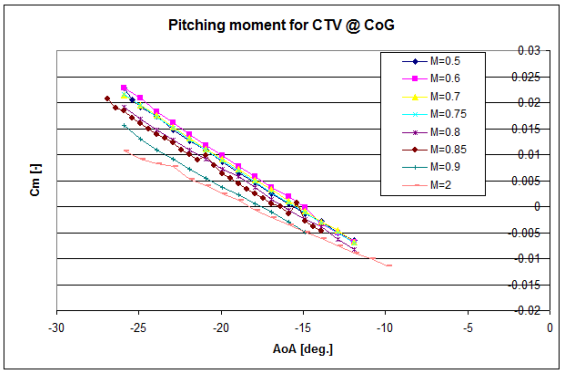

Figure 14: Pitching moment coefficient on the CTV capsule (new set-up)

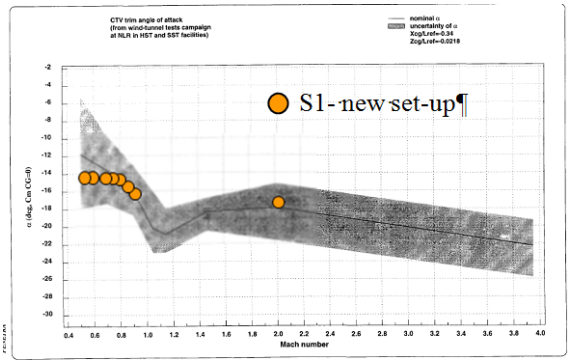

Figure 15: Trim angle of the CTV capsule (new set-up versus literature)

and it can be compared with static result. The trim points found by static experiments are confirmed with the dynamic set-up and each of these points is stable.

model Mach # release angle	CTV Heavy 0.5 final angle	0.7 final angle	0.9 final angle
10	42.2 / 42.4	42.3 / 42.4	39.8 / 39.9
55	42.5 / 42.3 / 42.4	42.4	39.9
80	42.4	42.5	40.1
100	42.8 / 42.4 / 42.5	42.5 / -30.7	40.1 / 40.2
130	42.4 / 42.5 / LO / >>	42.6 / -30.7	40.2
155	42.4	42.5 / 42.4 / -30.7 / LO / >>	170.7
180	42.4 / LO / >>	171.4	40.3 / 40.4
200	42.4 / -34 / LO / >>	42.5 / -31.1 / LO / >>	40.3
225	>>	>>	>>
245	>>	>>	40 / 39.9 / LO / >>
270	43.6 / -34 / -33.8	42.5 / -31.1	40.2 / 38.9
310	42.3 / 42.4 / -33.8	42.5	40.1 / 40.2
330	-33.9 / -33.8	-31	40.3 / 40.2 / 39.6
0			

>> full rotation
LO : continuous Large Oscillation

Table 2: Final position of the CTV Capsule

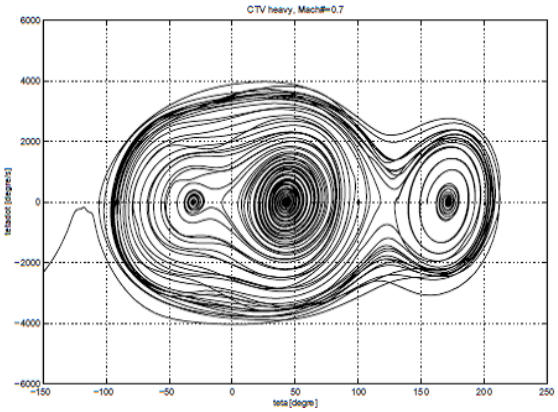

Figure 16: Phase diagram of the CTV capsule at Mach=0.7

The more recent dynamic experiments were performed with the forced oscillating mechanism supported by a sting. Experiments are carried out for various frequency of oscillation in order to assess the sensitivity of this parameter. The damping parameter is computed using the energy method described before. For the CTV, the results are given in the figure 17. It shows the domain of similitude between 0.002 and 0.003. In this range, $C_{mq} + C_{m\dot{\alpha}} \approx +0.7$. That means the vehicle is dynamically unstable. It is remark that for higher Strouhal number, the damping parameter is suddenly increasing. It happens for Strouhal =0.003 at Mach number of 0.9 and for Strouhal =0.006 at Mach number of 0.5.

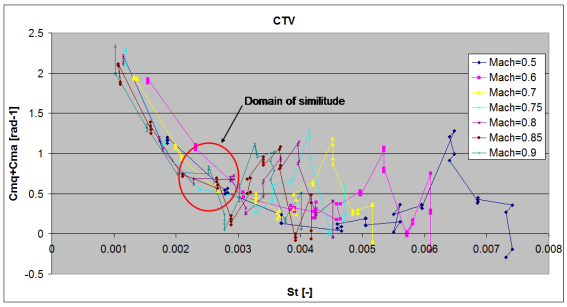

Figure 17: Damping parameter for the CTV capsule in subsonic regime

Dynamic results are given in the figure 18 for supersonic flow. For the CTV capsule, in the range of similitude, the damping parameter is clearly negative indicating stable behavior. A stable capsule in supersonic regime becoming unstable in subsonic is usual and not surprising. The phase diagram (only available for the subsonic regime) was showing opposite behavior, the vehicle was stable between Mach =0.5 and Mach=0.9

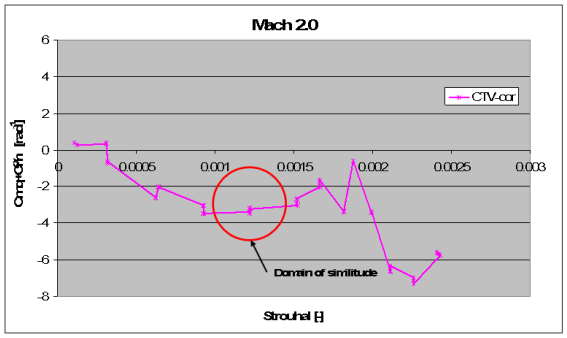

Figure 18: Damping parameter for the CTV capsule in supersonic regime

8. Error analysis

It is now clear that the transversal support introduced error. The recent experiment, carried out with a sting seems to give results of higher quality. Many aspect of the uncertainty have been studied. The error due to the balance is proportional to the one on the damping coefficient (2.3%). The repeatability is good and the flow properties are very accurate. The more critical sources of uncertainty are coming from the CoG location, the balance stiffness, and the support effect. Many efforts have been done to respect the CoG and error is expected to be relatively small

(err<0.1mm). For the balance stiffness, a small shift in angle can happen between angle deduced from the rotation of the main driving shaft and the real angle. Under the maximum load of the balance, its flexure does not exceed 0.07° which corresponds to a shift on the main shaft of a bit less than 1°. The associated error on the damping parameter is deduced to be less than 35 %. It is not possible to quantify the effect of the support because the reference value is not known.

9. Lesson learnt

During this project, models were designed and machined for static and dynamic experiments. In the last campaign, the static model was supported from the base through a balance. Due to the high sensitivity of the CoG location, very special care has to be taken to locate the center of reduction of the balance on the CG. An error of positioning of 0.1mm in the y direction produces a significant error on the trim angle. The model for the dynamic testing was much more complex as it must include the oscillating mechanism, two balances and the encoder. The fast prototyping technique allows producing light model with complex shape but results in not extremely accurate model. For this project, the outer shape of the model was further machined after assembly of all the elements with classical machining. At the end of this second step, some errors are still present in the positioning and it is suggested to investigate more on the way to produce the model for future campaign.

The forced oscillation mechanism allows adjusting the amplitude and the frequency of the model up to the required frequency to respect the similitude. The main difficulty came from gaps between pieces. The bronze bearing should be replace by ball bearing or needle bearing in order to guaranty the movement with minimum friction and minimum gap for every couple of piece. The sting itself was big compare to the capsule. A significant part of the base of the model was removed to allow the passage of the sting. It is known that the sting introduce error in the force measurement but it should be minimize as much as possible. The design was made with such big sting to avoid the flexion. Our experience from this campaign let us believe that the diameter can be further reduced.

The instrumentation for the static measurement is limited to the balance and the encoders used to measure the angle of attack. The balance should of course be correctly calibrated and special measurement must be taken in order to define precisely the location of the center of reduction. As explained before the definition of the trim angle of attack is very sensitive to the location of the center of reduction. For the dynamic experiment, two balances are used. The purpose of using two balances was to keep a good symmetry in the efforts, so that the interferences are limited. Possible improvements for the balance are the size and the stiffness. It is evident that the space in the capsule being limited, a smaller balance would help in the integration phase. Due to the strong oscillations during experiment and the gap between pieces, the balance must withstand high angular acceleration and deflection can be observed. A possibility is to increase the stiffness of the balance or to take it into account in the post-processing. The measurement of the angle of attack during the oscillating tests was initially expected to be measured by an encoder inside the model. It was finaly decide to use an encoder outside the wind tunnel on the driving mechanism but the gaps between pieces introduce significant error and should be corrected by a correct modelisation of all the interfaces. If possible, the angle of attack should be measured as close as possible of the capsule in order to avoid the multiple corrections.

The results for the static effort are in agreement with reference data for CTV. When compared to the measurement performed in the past at VKI with a transversal support, a large deviation is observed on the trim angle of attack. The transversal support is suspected to induce perturbation in the wake and to influence the measurement. Difference on the trim angle was about 20°. In the field of another ESA contract, same kind of conclusion was done for the EXPERT vehicle. Both static and dynamic results are different depending the support used (sting or transversal).

The CTV was already tested in the past with the transversal support and with the free to tumble technique. First of all, as already mentioned before, the trim angle was very different from the one obtained in the present campaign. Secondly, the dynamic behavior of the capsule was clearly stable over a large range of angle while it is now unstable. It is difficult to give a clear conclusion at that point about this difference. Possible source of error was discussed in the section 8. The support is one of the sources of uncertainty but the error cannot be assessed in the field of the present experiment.

The interference of the support on the flow has been shown by comparison between the present results and a previous campaign on CTV. This problem has also been demonstrated with the Expert vehicle by comparing the results from VKI and result from ITAM and

SibNIA [17] on the same geometry but with a different supporting device. In both case the difference is significant for the static and dynamic testing. More investigation should be done to assess the support effect. As it is not possible to make experiment in wind tunnel without any support, it is proposed to investigate this effect with numerical tools. The first step consists in static computation in order to assess the effect of the supports and how they can affect the flow. In a second step, unsteady computation should be done on a static model. Comparison with existing experimental results should help in a better understanding the support effect and the topology of the flow. The final objective is to perform unsteady CFD on an oscillating capsule. Damping parameters can then be calculated with the same technique than the one used in wind tunnel.

10. Future work

Many results have been obtained with different experimental techniques. These results can be very different from one technique to another one and need to be properly validated. That will be the last part of this work. The purpose is to impose on the model a damping perfectly known when forced oscillations are applied. The method to deduce the damping parameter can then be used and results can be compared with the reference. Eddy current break was selected to impose a well-known damping. The advantage is to be able to vary the coefficient and eventually to impose a damping function of the angle of attack. This validation will give more confidence into the method used to found the dynamic derivative. As explained before, the support plays an important role in the results. CFD tools will be used to assess the effect of the support. Better understanding of the flow around the model and the sting should help in choosing the best configuration to be used in wind tunnel to found the dynamic derivative.

11. References

[1] S. Paris and J.M. Charbonnier, "Aerodynamic force and moment measurements and dynamic characterization of an Apollo capsule in the VKI S-1 wind tunnel", VKI, Internal note, 1997

[2] O. Karatekin, "Aerodynamics of a planetary entry capsule at low speeds", VKI, PhD report, 2002

[3] J. Yunis, "Analysis of forced oscillation, sting and tare force tests of subsonic and supersonic reentry vehicles", VKI, Stagiaire report, 2007 [4] E.S. Hanff, "Direct forced oscillation techniques for the determination of stability derivatives in wind tunnels", AGARD lecture series n°114 "Dynamic stability parameters", 1981

[5] G.E. Burt and J.C. Uselton, "Effect of sting oscillations on the measurement of dynamic stability derivatives", Journal of aircraft, Vol.13 n°3, 1976 [6] "Experimental determination of dynamic stability parameters", VKI, Lecture series 2008-02 , 2008

[7] R. Fail, "Experimental determination of stability and control aerodynamic characteristics", VKI, Lecture series 80 "Aircraft stability and control", 1975

[8] D.M. Tang and E.H. Dowell, "Experimental investigation of three dimensional dynamic stall model oscillating in pitch", Journal of aircraft, Vol.32 n°5, 1995

[9] S. Paris, J. Ouvrard and B. Torgler, "Free and forced oscillation testing of Apollo, Pares and Expert capsules", VKI, Contract report, 2008

[10] D.I. Greenwell, "Frequency effects on dynamic stability obtained from small amplitude oscillatory testing", Journal of aircraft, Vol.35 n°5, 1998

[11] F.Y. Wang, O. Karatekin and J.M. Charbonnier, "Low speed aerodynamics of a planetary entry capsule", Journal of spacecraft and rockets, Vol.36 n°5, 1999

[12] E.S. Hanff and C.O. O'Leary, "Oscillatory test techniques", AGARD report n°776 "Special course on aircraft dynamics at high angles of attack: experiments and modelling", 1991

[13] L.E. Ericsson and J.P. Reding, "Review of support interference in dynamic tests", AIAA Journal, Vol.21 n°12, 1983

[14] K. Orlik-Rckemann, "Review of techniques for determination of dynamic stability parameters in wind tunnels", AGARD lecture series n°114 "Dynamic stability parameters", 1981

[15] B.L. Uselton and F.B. Cyran, "Sting interference effects as determined by measurements of dynamic stability derivatives, surface pressure, and base pressure for Mach numbers 2 through 8", AEDC-TR-79-89, 1980

[16] L.E. Ericsson, "Support interference", AGARD lecture series *n*°114 "Dynamic stability parameters", 1981

[17] S.Paris, A. Karitonov, J. Ouvrard SR 4000-VKI. Tool for the study of dynamic stability of reentry vehicle in the transonic/supersonic regime. Determination of aerodynamic damping coefficient of the Expert vehicle in transonic regime. Sept. 2010.

FIRST YEAR DOCTORAL SUMMARIES

Innovative airframe noise reduction techniques

Leandro Dantas de Santana

Aeronautics and Aerospace Department, leandro.santana@vki.ac.be

Supervisor: Christophe Schram

Assistant Professor, Aeronautics and Aerospace Department, von Karman Institute for Fluid Dynamics, Belgium, chazot@vki.ac.be

Promotor: Wim Desmet

Professor, Department of Mechanical Engineering - Katholieke Universiteit Leuven, Wim.Desmet@mech.kuleuven.be

Abstract

This abstract presents a PhD research proposal on airframe noise reduction. Aviation market forecasts a yearly average air traffic growth of 4.9% along the next 20 years. If confirmed this rate, by 2025 the number of passengers-kilometer air transported will be twice the present. This remarkable air traffic growth brings together critical issues for its sustentation, among them the aircraft external noise as one of the most relevant and challenging [1].

From the fifties to the short past years, noise reduction efforts were mostly concentrated on the engine. The development of high by-pass ratio turbofans and improvements on individual engine parts led to state of art engines with noise levels comparable to the airframe, for landing conditions. As consequence, for modern aircrafts, a global airframe noise reduction is only achievable through concomitant works on engine and airframe.

The main airframe noise sources are in order of importance: the parasite noise; the landing gear; slotted slats; flaps and slats side edges; flap and slats tracks; spoilers and component interaction noise [2]. In order to study these devices analytical methods, CFD and CAA computations and experiments are complementary adopted.

The Computational Aeroacoustics (CAA) is the field of study on simulations of the noise generated aerodynamically. High computational cost techniques, i.e. Direct Numerical Simulation (DNS) might be applicable in case of simple geometry studies, moreover, affordable approaches based on Large Eddy Simulations (LES), or hybrid approaches might be used to mitigate the computational cost and simulate complex geometries applicable for airframe noise studies.

Advanced flow and noise sources identification and quantification methods are adopted on aeroacoustics experiments. Among these techniques, the Particle Image Velocimetry (PIV), and the Beamforming method are especially important tools to raise insights about the noise source generation mechanisms, once the first provides a visualization of the flow pattern around the geometry of interest and the second permits the noise sources localization and quantification.

Airframe noise reduction devices cannot negatively impact the maximum lift. Certification regulations links the maximum aircraft lift with the minimum landing speed. As example, if the aircraft maximum lift is reduced by 10% through a noise reduction technique, which reduces the total airframe noise by 1.5 dB (i.e.), the minimum landing speed increases by 5.4%. Considering that the aircraft noise scales with velocity elevated to powers which varies from 4 to 8, the gain obtained by the noise reduction may easily be counterbalanced by the velocity increase effect [2].

Published solutions for airframe noise reduction include, among others: the adoption of fairings and design reconstruction for landing gears; slat cove fillers and seals; application of flow control and plasma on the slat and flap; brushes or porous flap and slats side edges; slat extended seals; the addition of bulbs and liners for the slat cavity.

The present PhD intends to concentrate on airframe noise reduction studies, focusing on opportunities and issues for high-lift devices (slat and flaps) noise reduction. One of the many issues to be studied is how to scale the model noise with a real size aircraft and what is the behavior of these devices in real flight conditions. For the development of this PhD it is expected an experiments focused approach complemented by convenient numerical simulations and suitable analytical analysis.

References

[1] P. C. de Souza e Silva, Embraer Market Outlook 2010-2029, Tech. rep., EMBRAER Empresa Brasileira de Aeronutica S/A (2010).

[2] W. Dobrzynski, Almost 40 years of airframe noise research: What did we achieve?, JOURNAL OF AIRCRAFT 47 (2) (2010) 353367. doi: 10.2514/1.44457

Uncertainty quantification for material response of ablators in hypersonic flows

Julien de Mûelenaere

Aeronautics and Aerospace Department, julien.demuelenaere@vki.ac.be

Supervisor: Thierry Magin

Assistant Professor, Aeronautics and Aerospace Department, Belgium, magin@vki.ac.be

Keywords: atmospheric entry flows, ablation, porous medium, chemical reactions, multi-physics coupling, moving mesh, approximate Riemann solver for hypersonics, Uncertainty Quantification.

1. Motivation

Although many achievements in rocket science have been made since the Apollo program, the prediction of the heat-flux to the surface of a spacecraft during atmospheric entry still remains an imperfect science. The survivability of the space vehicles is critically dependent on the correct prediction of the heat-flux, since inaccuracies in these predictions can be fatal for the crew or the success of robotic missions.

The design of the heat-shield strongly relies on numerical simulations, such as computational fluid dynamics, due to the impossibility of reproducing all the aspect of atmospheric entry in ground test facilities (aerodynamic forces together with heat loads). But even using numerical tools, predicting an accurate heat-flux is a particularly complex task. The difficulty is due to complex surface chemistry on the thermal protection material, and is enhanced when ablative materials are used instead of reusable materials for the heat-shield. In addition, ablation is strongly coupled to other phenomena, such as radiation, gas chemistry and turbulence, that are potential "mission killers" for which coupled multi-physics effects remain challenging from numerical and physical viewpoints.

As a consequence, the uncertainties in the engineering models for the heating and aerodynamic performance of the spacecraft are large. To avoid failure and ensure the safety of astronauts and payload, engineers resort to "safety factors" to determine the thickness of the heat-shield, at the expense of the mass of embarked payload. Some missions are famous examples of "lucky" heat-shield design due to barely enough safety factor. Proper determination of safety factors relies on Uncertainty Quantification which aims at developing rigorous methods to characterize the impact of "limited knowledge" on the heat-flux. A way to reduce these margins for the following missions is to obtain experimental data on the performance of the system during the entry. These data are to be compared with the preflight predictions in order to evaluate the level of uncertainty and to identify places where the current models require improvement.



Figure 1: ESA Atmospheric Reentry Demonstrator (ARD)

Another critical problem, when designing a Thermal Protection System (TPS) for entry capsules, is the choice of a heat-shield material, and its associated material response model. For high-speed atmospheric entry, the temperature of the flow easily exceeds 10,000 K in the shock layer ahead of the vehi-

cle and wall temperature can reach 4000 K. For these cases, reusable ceramic insulation (such as the one used for the Shuttle orbiter) cannot safely be used, and ablative materials needs to be employed. These ablators are used to protect reentry vehicles from the severe heating of hypersonic flows by the decomposition of thermal protection material allowing heat rejection through various complex physico-chemical mechanisms leading to material removal through pyrolysis and ablation.

A new class of light ablative materials (in opposition to the dense ablators from the Apollo program), made of carbon fiber preform impregnated in phenolic resin (e.g. PICA), have been introduced and validated in flight by the Stardust mission (1999 - 2006). The use of this new class of low density carbon/resin composites is being seriously considered for numerous forthcoming missions. For instance, this material has been selected for the Mars Science Laboratory heat-shield, which mission will provide the largest Entry, Descent and Landing (EDL) dataset ever obtained during a non-Earth entry, and will be precious for validation of models following Uncertainty Quantification methods.

During the Apollo program, many efforts were made in the development of models for the prediction of complex gas surface interaction for TPS. However, these models, developed for dense ablative materials, are not suitable for the new type of low-density porous carbon/resin composites. Thorough understanding of the material response of those composite ablators is crucial to ensure safety of the astronauts and payload for the future space missions. Therefore, an important effort in theoretical, numerical and experimental research is necessary for advancement of the prediction tools used for the TPS design of tomorrow's space vehicles and planetary probes, including a sound definition of the margins.

2. Objectives

We propose to follow a complementary approach for prediction of the material response of an ablator in hypersonic flows, integrating new advanced physico-chemical models and computational methods based on a multidisciplinary approach to create a multi-physics numerical tool for the simulation of atmospheric entries.

The three basic ingredients for predictive science are;

- Physico-chemical models
- Computational tools
- Experimental data

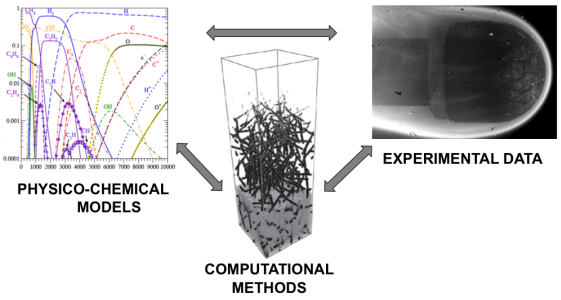

Figure 2: Complementary prediction tools

This work will focus on the development of the hypersonic flow solver based on the OpenFOAM framework. A great deal of the material code module will be provided through collaborations. Experimental data will be crucial for the validation of the physico-chemical models and computational methods developed, following state-of-the-art Uncertainty Quantification methods.

3. State-of-the-art

In this section, we will review some limitations related to the simulation of the material response of ablators in hypersonic flows.

3.1. Physico-chemical models

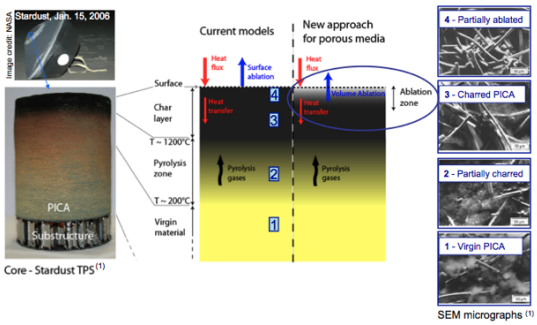

Figure 3: New approach for porous media proposed for the material response of PICA (Phenolic Impregnated Carbon Ablator)

During atmospheric entry, part of the heat is transferred to the material leading to a gradual temperature increase inside the material. When subject to increasing temperature, the virgin material successively transforms following two mechanisms. During the first transformation mechanism, the pyrolysis, the phenolic resin progressively carbonizes and

releases pyrolysis gases, which percolates away, leaving a porous char residue. The second transformation phenomenon is the ablation of this char, combination of heterogeneous chemical reactions, phase changes, and mechanical erosion. These processes will result in mass loss of the char and surface recession that have to be estimated using the material response models.

To characterize the high temperature performance of such materials over a wide range of aero-thermal heating condition and load levels during atmospheric entry, one needs models that predict accurately the ablation rate and the peak temperature at the interface of the TPS.

The new class of low density carbon/resin composites for the heat-shield, rely on models inherited from the 1960s, that rest on major assumptions such as: ablation is described as a surface phenomenon, equilibrium chemistry is considered in a control volume close to the wall, ablation only occurs at the surface, air does not penetrate inside the material, pyrolysis gases are in equilibrium in the pores of the material (overestimation of ablation rates), and pyrolysis gases are transported by convection only. Given the scarcity of the flight data, the physico-chemical models were mainly based on correlations and these models proved to be accurate only for dense materials.

To design properly the low-density composite, a complete analysis and modeling is necessary to describe accurately the following phenomena that have to be addressed in parallel, modeled and coupled: finite-rate chemistry for pyrolysis gas, transport phenomena in porous medium as well as in the boundary layer, and volume ablation with an ablation zone.

In particular, in this work, we will focus on the transports fluxes (diffusion of mass, momentum, and energy) found in the Navier-Stokes equations are related to macroscopic forces by proportionality coefficients called transport properties (diffusion coefficients, thermal diffusion ratios, viscosity, and thermal conductivity). It is difficult to measure those coefficients in high enthalpy flows (such as atmospheric entry plasmas), but they can be interpreted at a microscopic level by studying binary collisions (kinetic theory) among the particles of the gas. Hence, closure of the macroscopic conservation equations is realized at the microscopic level, by determining either the interaction potentials or the cross-sections from experimental measurements. Relevant collision integrals constitute the set of data for the transport properties. Accurate collision integrals are not available for entry with ablation products. The finite rate chemistry will be provided through collaboration.

3.2. *Computational tools*

Ablation is a complex multi-physics problem. The boundary-layer which envelops an ablating heat-shield during super-orbital entry is intimately coupled with the transient ablation processes. The heat material response affects the boundary-layer, and the boundary-layer gradients and transport properties determine the energy and mass fluxes at the surface which in turn control the heat material response. Therefore, the analysis of the transient response of ablative materials requires the modeling of the coupling between the internal heat and mass transfer processes, the surface phenomena, and the boundary-layer.

Hypersonic entry flow solvers are generally based on the discretized Navier-Stokes equations assuming quasi-steady, laminar, chemically reacting flows. The approach used by space agencies for coupling material and flow codes is generally based on a Thin Control Volume model that represent the boundary-layer heat and mass transfer processes by convective/diffusive transfer coefficients while considering detailed chemical interactions and mass and energy balances at the surface of the heat-shield. This method is used to lower the computation time. A strong coupling between the flow solver and the material code would allow to improve the accuracy of the material response prediction.

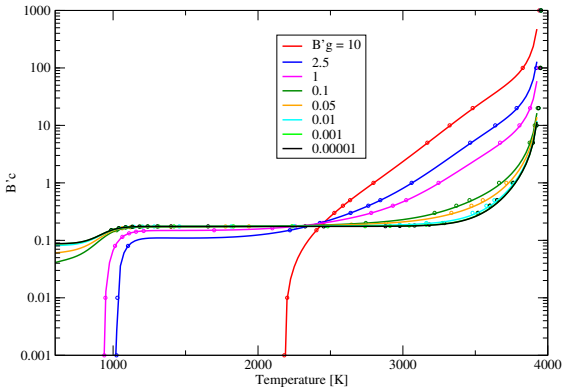

Figure 4: Thin Control Volume approach: $\dot{m}_{ca}$ (ablation rate) over T and $\dot{m}_{pg}$ (gas injection rate); $B'_g = \frac{\dot{m}_{pg}}{\rho_e u_e C_M}$ and $B'_c = \frac{\dot{m}_{ca}}{\rho_e u_e C_M}$

3.3. *Uncertainty Quantification for experimental data integration*

It remains difficult to provide objective confidence levels in quantitative information obtained from numerical predictions. The complexity arises from the amount of uncertainties related to the inputs for such

a complicated system. The uncertainties are naturally associated to the choice of the physical models and to the specifications of the input parameters required for performing the analysis of the system. The quantification of the influence of uncertain parameters on the physical systems, also referred to as Uncertainty Quantification (UQ), is a major issue in order to properly predict the system response to random inputs. Rigorous quantification of uncertainties is required, especially in the area of reliability and safety. UQ is considered by space agencies and industries as a promising tool to define the margins for TPS design.

4. Research methodology

The proposed research methodology is based on a multidisciplinary approach. We will develop advanced physico-chemical models and numerical methods and use state-of-the-art UQ tools developed under the US Predictive Science Academic Alliance Program (PSAAP), to integrate flight and ground experimental data.

4.1. Physico-chemical models

We want to develop a reliable model for low-density carbon/resin composites. A complete analysis and modeling of the following phenomena need to be addressed in parallel, modeled, and coupled.

4.1.1. Thermo-chemistry

Analysis and modeling of the pyrolysis of the phenolic resin will be addressed: identification of the species produced and of their rate of production as a function of the resin temperature (Chemical evolution of the pyrolysis gases inside and outside the material). This part will be provided in collaboration.

4.1.2. Transport

Analysis and modeling of the transport of the pyrolysis gases in the porous material will be addressed as well: collision integral calculation, multi-component diffusion in the transition and rarefied regimes, Darcy-Brinkman transport.

To account for the transport in the boundary-layer: coupling of the chemical evolution of the pyrolysis gases outside the material (reaction of the pyrolysis gases and their products with the air) in a boundary-layer code.

4.2. Computational tools

We want to develop a hypersonic flow solver based on Fortran/OpenFOAM using robust and accurate numerical methods, and couple it to a material response code for ablators.

4.2.1. 0D code

The first step is to approximate the boundary-layer heat and mass transfer processes using convective/diffusive transfer coefficients, and considering equilibrium chemistry and mass and energy balances at the surface.

4.2.2. 1D code

The next step will be to develop a 1D Stagnation line code, based on stagnation line equations derived from the Navier-Stokes equations, in natural variables (no Lees-Dorodnitsyn transformation). This step will allow to deal with sophisticated chemistry (thermo-chemical non-equilibrium of the flow). This will be done in Fortran, then using OpenFOAM.

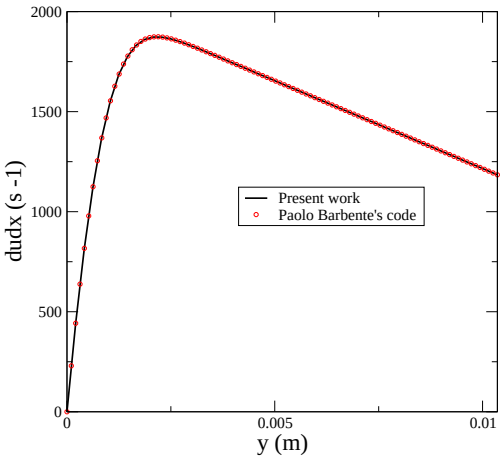

Figure 5: Preliminary result: comparison of $\frac{\partial u}{\partial x}$ along the stagnation line inside the boundary layer between present work and Paolo Barbente's code

A complete 1D model, from above the shock through the inside of the material, will be obtained by coupling the stagnation line code with a 1D material code, which solve for the conservation equation of mass, momentum and energy, (using Darcy's Low for the convection velocity, fitted Arrhenius relations for pyrolysis progress, and Fourrier's heat transfer), and with a viscous shock layer code.

4.2.3. 2D/3D code

Following this step, we will develop an approximate Riemann Flow solver for hypersonics, developping a 3D Entry code, with shock capturing. A 2D Boundary layer code will be considered as an application. From the 1D code, we will be able to grasp enough physics and hence to reduce the complexity of the 3D code. This will be done using OpenFOAM.

Concerning the 3D Material response code, this will be implemented in collaboration. New description of the ablation as a volume phenomenon (the material mass may be depleted in depth) will be implemented: a porous medium approach will be used.

4.2.4. Coupling

We want to integrate the tools developed for advanced physico-chemical models and computational tools into OpenFOAM, and perform the coupling between the material response code and the boundary-layer code. We might also keep in mind possible interactions such as coupling methodology based on conjugate heat transfer.

4.3. Uncertainty Quantification methodology

To have a high-fidelity computational design for this multi-disciplinary design, Uncertainty Quantification tools will be used to asses the methods and their values, based on realistic test cases and flight data.

As we presented above, sources of uncertainty may be due to some unknown or approximated process or mechanism given the complexity of the problem, and due to variability of input and model parameters since the environment is not perfectly known and hardly experimented on Earth.

For those reason, we want to introduce Uncertainty Quantification in the model to evaluate how accurately does the mathematical model describe the true system, how appropriately the numerical methods are used, and how precise are the data information such as initial and boundary conditions and model parameters. The tools developed by the PSAAP project at Stanford will be used.

Several benefits can be obtained from such studies. For example, it allows for realistic safety margins to be introduced, depending on the solution sensitivity to the random inputs. It also allows for the coupling process between several uncertain parameters to be characterized, such as the impact that different parameters have on the heat-flux prediction problem.

We want to apply Uncertainty Quantification first on the 1D tools developed, including both sensitivity analysis (propagation) and inverse methods. Using suitable computer resources, we could imagine applying Uncertainty Quantification on the 2D or even 3D tools.

5. Experimental data to be used

We present here the realistic data that will be used for Uncertainty Quantification.

The Mars Science Laboratory (MSL) is a NASA rover scheduled to be launched in November 2011 and land on Mars in August 2012. It would perform the first ever precision landing on Mars. MSL will assess whether Mars ever was, or is still today, an environment able to support microbial life. The spacecraft will enter the Martian atmosphere at approximately $6km/s$. The aeroshell is much larger and is also much heavier than for previous missions: flow around the spacecraft is expected to become turbulent early during the entry, and resulting heat-flux and shear will be the highest ever encountered on Mars.

The Mars Science Laboratory Entry, Descent, and Landing Instrument (MEDLI) Suite (developed in partnership with NASA Ames Research Center) is the set of engineering sensors designed to measure these data. It will return the largest EDL dataset ever obtained during a non-Earth entry, collecting the atmospheric conditions and performance of the heat-shield during entry and descent. The data collected will be, among others: surface pressure distribution, peak heat-flux and distribution of heating on the vehicle, map of the transition to turbulence, surface and in-depth material performance.

US Air Force and the European Space Agency (ESA) are also currently supporting our ablation activities. Data obtained by ESA flights demonstrators will be used for validation. Only a few Flight experiments are currently available at very high speeds, but several future ESA flight demonstrators are expected to provide additional data, such as Expert.

Data will also be obtained in the VKI facilities. These sources of data will be given by another Ph.D. student, Bernd Helber, working on the experimental part of this project on the Induction Plasmatron of VKI, a worldwide unique facility (most powerful facility of its kind in the world). The quantities to be measured to obtain sufficient understanding of the material response of new generation ablators are: surface and inner temperature distribution of the material (heat-flux), recession rate and mass loss rate, pyrolysis outgassing and boundary-layer interaction, depth of pyrolysis and char layer, degradation of the car-

bonized resin, thinning and ablation of the carbonic fibers.

Development and validation of numerical models will be embedded in this work, in collaboration. Both projects complement one another and provide an ideal base to close the missing link between the physico-chemical models and computational methods by experimental data.

6. Collaborations

Thinking out of the box and basic research are necessary for advancements of the models that will define the environment and requirements for the design and safe operation of tomorrow's space vehicles and planetary probes for the manned space exploration. Space agencies primarily focus on missions and projects, therefore, creative basic research in aerospace science is preferably carried out in universities and research centers. We will strive to continue and strengthen the links established during the master thesis internship at NASA Ames Research Center supervised by Dr. Nagi Mansour and advised by Dr. Jean Lachaud, under a Visiting Researcher Agreement between NASA and the VKI. A strong link exist between the VKI and the European Space Agency that has supported the Plasmastron facility and diagnostics for material testing. A collaboration is envisaged with EADS Astrium to provide new materials to be tested at NASA ARC and the VKI.

7. Acknowledgment

This research work will be sponsored by the European Research Council Starting Grant "*AEROSPACE-PHYS: Multiphysics models and simulations for reacting and plasma flows applied to the space exploration program,*". I also wish to gratefully thank Dr. Nagi N. Mansour and Dr. Jean Lachaud for their support and advises on this project.

References

[1] Kendall, R. M., Barlett, E. P., Rindal, A. R., & Moyer, C. B. 1968 An Analysis of the Chemically Reacting Boundary Layer and Charring Ablator. Part I: Summary Report. *NASA CR-1060*.

[2] Kendall, R. M., Barlett, E. P., Rindal, A. R., & Moyer, C. B. 1968 An Analysis of the Chemically Reacting Boundary Layer and Charring Ablator. Part V: A General Approach to the Thermochemical Solution of Mixed Equilibrium-Nonequilibrium, Homogeneous or Heterogeneous Systems. *NASA CR-1064*.

[3] Lachaud, J., Cozmuta, I., & Mansour, N. N., Multiscale Approach to Ablation Modeling of Phenolic Impregnated Carbon Ablators. *Journal of Spacecraft and Rockets*.

[4] Barbante, P. F. 2001 Accurateand Efficient Modelling of High Temperature Nonequilibrium Air Flows *Ph.D. thesis, Universite Libre de Bruxelles*.

[5] Iaccarina, G. 2008 Quantification of Uncertainty in Flow Simulations Using Probabilistic Methods *VKI Lecture Series*.

[6] Milos, F. S., & Chen, Y.-K. 1997 Comprehensive Model for Multi-Component Ablation Thermochemistry. *AIAA Paper 97-0141*.

[7] Anderson, J. D. 1989 Hypersonic and High Temperature Gas Dynamics *McGraw Hill, New York*.

[8] Cousteix, J. 1997 Aérodynamique - Couche limite laminaire. *Cepadues*.

[9] JANAF Thermochemical Tables Third Edition. M. W. Chase, Jr., C. A. Davies, J. R. Downey, Jr., D. J. Frurip, R. A. McDonald, and A. N. Syverud.

[10] Thermochemical Properties of Individual Substances Fourth Edition. L. V. Gurvich, I.V. Veyts, and C.B. Alcock.

Prediction of natural and forced transition in hypersonic flows - Application to European space vehicles

Guillaume Grossir

Aeronautics and Aerospace Department, grossir@vki.ac.be

Supervisor: Patrick Rambaud

Assistant Professor, Aeronautics and Aerospace Department, Belgium, rambaud@vki.ac.be.

Promoter: Herman Deconinck

Professor, Université Libre de Bruxelles, Avenue Franklin D. Roosevelt 50, B-1050 Bruxelles, Belgium, deconinck@ulb.ac.be

Keywords: Hypersonics, Mach number, Reynolds number, boundary layer, laminar-turbulent transition, heat flux, roughness, linear stability theory, second mode, disturbances, noise levels.

Despite more than 50 years of research on laminar-turbulent transition in hypersonic flows, phenomena are still poorly understood and transition prediction remains a challenge. The large number of influencing parameters and the reduced database available are limiting the current knowledge of phenomena. Further understanding would help, for instance, to design thermal protection systems for space vehicles with a better effectiveness.

In the event of a roughness appearing on the surface of the vehicle, the disturbances applied to the flow might be large enough to destabilize the boundary layer and force transition. The mechanisms involved in this case by-pass the usual paths to turbulence and are not better understood.

For both natural and forced transition cases, consequences are similar and larger wall heat fluxes than the ones encountered for laminar flows are involved. As thermal loads can be twice or up to five times larger, it can be of critical importance for the survivability of the vehicle if it happens about the time of peak heating during the reentry. This project aims at studying the mechanisms responsible for transition particularly at Mach 14 which corresponds to the peak heating occurring during re-entry trajectories of space vehicles such as EXPERT (see Fig. 1).

Over the years, several correlations have been obtained for both natural and forced transition experiments, although their accuracy is fairly limited since they take into account only few parameters. Moreover, their validity is further restricted to geometries and conditions similar to the ones used when they were developed. The main drawback of these correlations is the lack of understanding of the physical phenomena occurring within the flow which would undoubtedly represent a step forward for the prediction of transition in hypersonic.

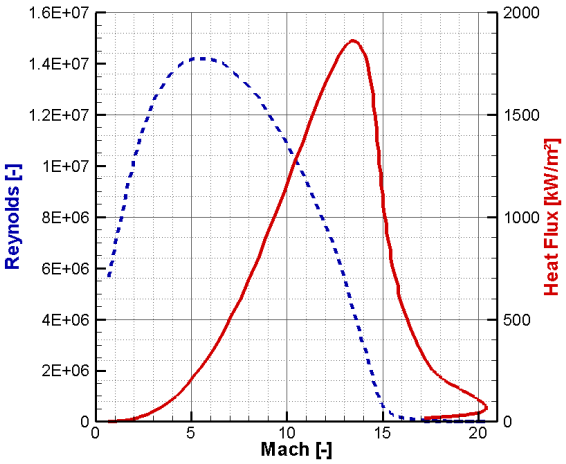

Figure 1: Heat flux and Reynolds number during reentry of EXPERT vehicle

Instead of relying on empirical correlations to predict the onset of transition, a promising alternative technique for a better understanding of flow phenomena is the linear stability theory. It can be used to

predict the damping or the development of boundary layer disturbances which, in the latter case, would lead to a turbulent flow. Computations have shown the importance of the so-called second mode of instabilities. These are high-frequency acoustical-type of disturbances requiring a supersonic flow close to the wall and presenting the largest amplification factors at frequencies of the order of several hundreds of kHz as depicted in Fig. 2.

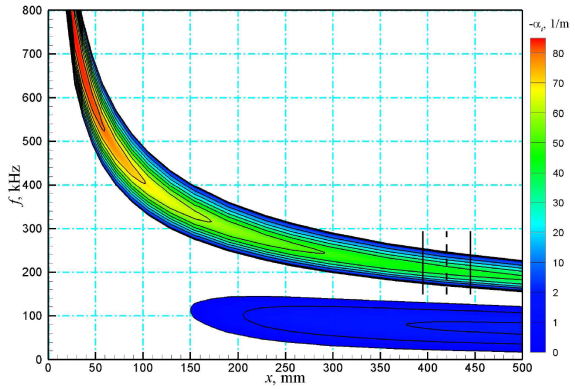

Figure 2: Stability diagram on a 7° angle cone at Mach 6 showing first and second mode of instabilities [1]

Physical measurements of these disturbances have been achieved as presented in Fig. 3 and effectively show their dominant role for transition in hypersonic flows since they are amplified. When the amplitudes of the disturbances are large enough, the boundary layer is destabilized and turns turbulent. Additional measurements and visualizations both at the surface and within the boundary layer are foreseen to provide additional and valuable pieces of information about the destabilizing structures responsible for transition.

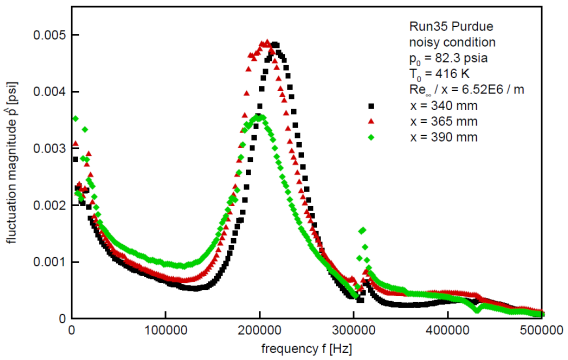

Figure 3: Measurements of pressure fluctuations on a 7° angle cone at Mach 6 [2]

The duplication of flight conditions into wind tunnels is only partial: usually either Mach and Reynolds, or heat fluxes. Important parameters to be taken into account, among the list of parameters influencing transition, are the free-stream conditions and free-stream noise levels. When experiments at high Mach numbers are performed, free-stream noise levels associated can be one or two orders of magnitude larger than for flight. Natural phenomena can be by-passed and the transition Reynolds number is decreased by high noise levels as shown in Fig. 4. Measurements can therefore be fooled by the environment and the conclusions drawn must be taken with great care.

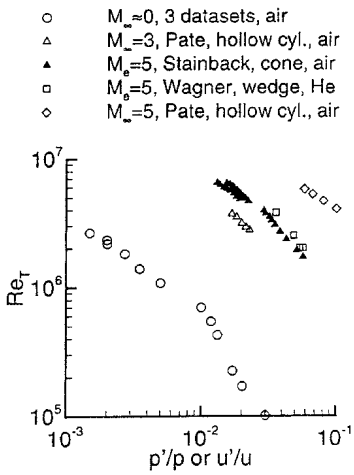

Figure 4: Transition Reynolds number data plotted as a function of the measured disturbance levels [3]

Thus, when studying transition phenomena in wind tunnels, it appears to be of primary importance to have a precise knowledge of the flow conditions at the exit of the nozzle. A better characterization of flow quantities in the free-stream, with both mean values and fluctuations, is required for comparison with data from literature, for understanding of flow phenomena and for extrapolation to flight conditions. This will represent the first part of this doctoral project.

The determination of the free-stream conditions is currently performed using different equations of state for the test gas and assuming an isentropic and adiabatic expansion of the flow through the nozzle. Measurements in the reservoir of the nozzle and at the outlet are required for this procedure. Large uncertainties are introduced by the different assumptions. New rebuilding methods relying on measurements performed only at the exit of the nozzle are under investigation to improve the accuracy.

Fluctuations measurements are presently limited

due to the large amount of particles within in the flow and potentially damaging the instrumentation (for instance pressure sensors or hot wires). Protections can be mounted but decrease the frequency response of the sensors used. The origin of these particles is not yet clearly established but might come from the check valves trapping the compressed gas into the reservoir. The removal of these valves implies to stop the piston at the end of the driven tube and such studies have been initiated over the past years.

Repeatability of the tests conditions is as much important as their accurate determination. They mainly depends on the initial pressure within the driver and driven tube and more accurate measurements of these parameters are foreseen for improvements.

Measurements of boundary layers profiles in the nozzle and of wall heat fluxes are expected to provide valuable pieces of information regarding to the laminar or turbulent state of the boundary layer. For the turbulent case, sound radiations are much more important and will reach the center of the nozzle after a certain distance downstream. Since the Mach numbers involved are large, the radial propagation of these waves might be reduced and there might exist a zone close to the nozzle axis where noise levels remain small. Pressure fluctuations measurements across the nozzle exit are required to assess this possibility. Better simulations of the flow with CFD, taking into account the transition location, could also be obtained and would provide more accurate values of flow conditions at the exit of the nozzle.

Another aspect of the numerical modeling of the facility is the simulation of the facility itself and the trajectory of the piston compressing the test gas in the driven tube. The instrumentation of the piston would provide valuable information for a comparison between its numerical and experimental trajectories.

This entire set of measurements will represent a first basis for the study of transition in hypersonic flows. The precise knowledge of the free-stream conditions, the improved repeatability of the experiments and a better knowledge of the facility will allow future quality experiments to be performed.

Acknowledgments

I gratefully acknowledge FRIA (Fonds pour la formation à la Recherche dans l'Industrie et dans l'Agriculture) for the financial support of this project.

References

[1] T. Roediger, H. Knauss, Hypersonic instability waves measured using fast-response heat flux gauges, in: 46th AIAA Aerospace sciences meeting and exhibit, 2008.

[2] M. Estorf, R. Radespiel, S. P. Schneider, H. B. Johnson, S. Hein, Surface pressure measurements of second mode instability in quiet hypersonic flow, in: 46th AIAA Aerospace sciences meeting and exhibit, 2008.

[3] S. P. Schneider, Effects of high-speed tunnel noise on laminar-turbulent transition, Journal of Spacecraft and Rockets 38 (3) (2001) 323–333.

Comprehensive experimental characterization of the material response of innovative ablators for the space exploration program

Bernd Helber

Aeronautics and Aerospace Department, helber@vki.ac.be

Supervisor: Thierry Magin

Assistant Professor, Aeronautics and Aerospace Department, Belgium, magin@vki.ac.be.

Promotor: Annick Hubin

Professor, Department of Metallurgy, Electrochemistry and Materials Science, Vrije Universiteit Brussel, anhubin@irexchange.vub.ac.be.

Keywords: atmospheric entry, ablation, thermal-protection-system, high enthalpy plasma flows, gas-surface interaction, optical emission spectroscopy, scanning electron microscopy

1. Introduction

After the successful manned missions to the Moon and many probe entries into the atmosphere of outer planets, the next challenges for the space agencies include bringing back samples to Earth and continuing the manned exploration program, which aims to send human beings to Mars and bring them home safely. Following the ExoMars mission of ESA and NASA (2016-2018), whose rover already includes an automatic sample collection system, the next steps will be to identify, develop and qualify required technologies for safely returning Martian samples. The European Space Agency (ESA) is also developing an Advanced Reentry Vehicle (ARV) for crew and cargo transportation from the International Space Station, which will use know-how inherited from the Atmospheric Reentry Demonstrator (ARD, reentry 1998 [1]).

Experimental research at multiscale level is necessary for advancement of the multiphysical prediction tools used for the thermal protection system (TPS) design of tomorrow's space vehicles and planetary probes.

2. Problem statement

For vehicles entering a planet's atmosphere, prediction of the heat flux to the surface of the spacecraft and its TPS remains an imperfect science and inaccuracies in these predictions can be fatal for the crew or the success of robotic missions. To avoid space mission failure and ensure safety of the astronauts and payload, engineers resort to safety factors to determine the spacecraft heat shield thickness, at the expense of reduced mass of embarked payload. Difficulty is enhanced for Earth re-entries at velocities higher than 10km/s, typical of the new missions of ESA and NASA, because radiation becomes a major player and ablative materials are used instead of reusable materials for the heat shield.

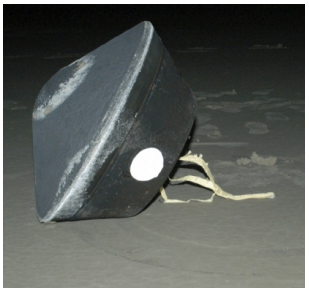

Figure 1: NASA Stardust probe after reentry (Jan. 15, 2006)

In this context, a new class of low density carbon/resin composites, made of a carbon fiber preform impregnated in phenolic resin (PICA), is currently being developed and has already been applied to flight during the Stardust mission [2] (Fig. 1). Those ablators allow heat rejection through various complex mechanisms like phase change, chemical reactions on the surface and inside, leading to material removal through pyrolysis and ablation as shown in Fig. 2.

During pyrolysis, the phenolic resin is progressively carbonized into a low density carbon and loses around 50% of its mass, producing pyrolysis gases by vaporization [3]. The pyrolysis gases are transported out of the material by diffusion and convection through the pores. During this transfer, their chemical composition evolves as their temperature increases and as they mix with air that diffuses into the pores of the material from the boundary layer.

Ablation is the degradation of the char layer, composed of fibrous preform and carbonized resin, promoted by heterogeneous chemical reactions (oxidation, nitridation), phase change (sublimation) and mechanical erosion. During these transformations, charred material is directly removed from the ablator what leads to recession of the surface.

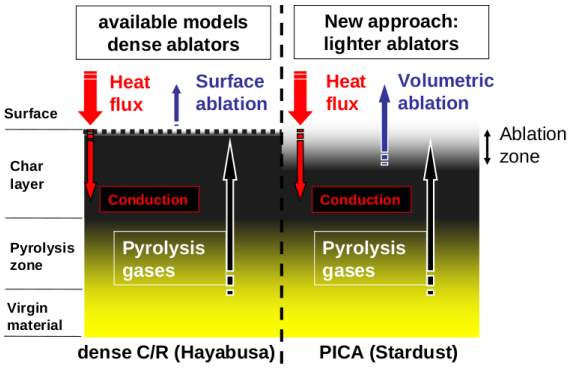

Figure 2: New approach for porous media proposed for the material response of PICA (Phenolic Impregnated Carbon Ablator), following Lachaud [4]

During the Apollo program, strong efforts were invested to develop models for the prediction of complex gas surface interaction for thermal protection materials (TPMs). These models, developed for dense ablative materials, are inspired from Kendall *et al.* published in 1968 [5] and are not suitable for the new type of low-density porous carbon / resin composites. They rest on major assumptions and describe ablation as a surface phenomena occurring on a homogeneous, dense material assuming equilibrium or finite-rate chemistry in a control volume close to the wall [6; 7; 4]. For instance, a well-known issue with current models is the overestimation of ablation rates because equilibrium chemistry is an upper-bound model.

A schematic of current material response models and the approach for new innovative composite ablators is highlighted in Fig. 2, depicting the ablation zone in which a density decrease is assumed to occur due to volumetric ablation if oxygen is able to diffuse into the porous medium.

3. Strategy for ablator response characterization

An important effort in theoretical and experimental investigation is required to understand the complex material response under reentry conditions and its influence on the surrounding flow, as well as for the validation of new material response models [4]. Especially our poor understanding of the coupled mechanisms of **radiation / ablation** leads to the difficulties in heat flux prediction.

For example, the creation of highly radiative emitting atoms and molecules can cause additional thermal radiation which has a not negligible influence on the heat flux at the vehicle surface. Different mechanisms are involved, which give rise to a complex structure of the emission and absorption spectrum [8].

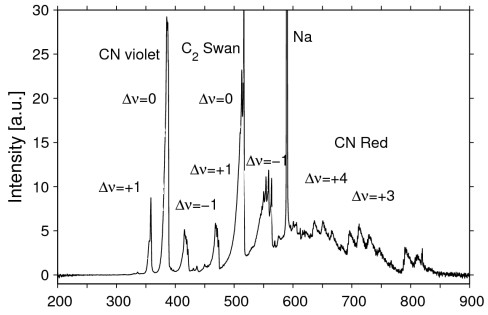

Figure 3: Emission spectrum ahead of ablating carbon resin composite sample in nitrogen test gas [9]

To demonstrate this, an emission spectrum collected during a preliminary campaign in the VKI Plasmatron facility on carbon resin composite ablative samples is shown in Fig. 3 [9] . Nitrogen was used as test gas and it is evident that the spectrum is mainly dominated by the *CN violet* and C_2 *Swan* systems. In contrast, with air as test gas it was found that oxygen is the driving force to provoke reactions as the system undergoes the ablation process, suppressing CN and C_2 formation, leading rather to CO and CO_2 molecules. The mechanism of diffusion of oxygen into the porous material is still poorly understood.

In the next step, going along with a sufficient representation of the physico-chemical processes, material response models should accurately predict the ablation rate through which the charred material is removed. Consequently, the rate of surface recession is an important quantity to be measured and experiments designed for ablation and validation of numerical tools have to account for it. A new technique was

developed [9] and applied to the Plasmatron facility making use of a high speed camera (HSC) to capture the surface recession in-situ. This is presented in Fig. 4 where a contour plot is shown, obtained by applying edge detection filters during post-processing of the HSC images, from which the recession rate can be determined.

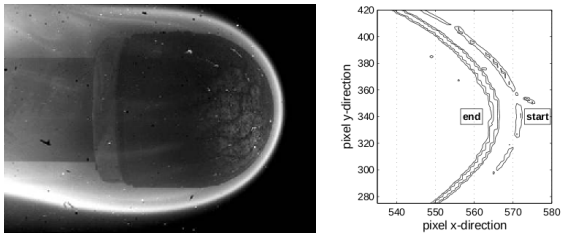

Figure 4: HSC snap-shot during ablation test and contour plot of processed images indicating sample surface at test start and test end for recession analysis [9]

Those two examples illustrate the attempt of experimentally approaching the coupled physico-chemical problems, resulting from the evolution of pyrolysis gases inside and outside the material, their reaction with the gas coming from the freestream and the subsequent process of ablation. They also show the need of additional tools for ablation characterization, such as scanning electron microscopy, to be able to evaluate the state of pyrolysis and the ablation process in depth. Hence, the methodology of this project mainly consists of two parts:

3.1. In-situ measurements

The 1.2 MW Plasmatron facility [10] will be used to carry out all the experiments in high enthalpy flows with a comprehensive setup of intrusive and non-intrusive measurement techniques. It is extensively utilized at the VKI for the simulation of reentry plasma flows for re-usable materials. In-situ measurements of new class, low density ablative samples will be taken for characterization of: **material response** to plasma exposure (temperature, heat transfer, ablation rate) / **flow field** (surrounding gas phase, effect of "blowing" due to outgassing products) / **radiation field** (identification and quantification of molecules and atoms such as C, C_2, CN, CO).

The complete experimental setup applied to the facility for free-stream & in-situ sample observation can be found in Fig. 5 with techniques such as surface and inside temperature recording (two-colour pyrometer, IR-radiation-thermometry and thermocouples), high speed camera imaging (surface recession, surrounding flow field) and optical emission spectroscopy (OES).

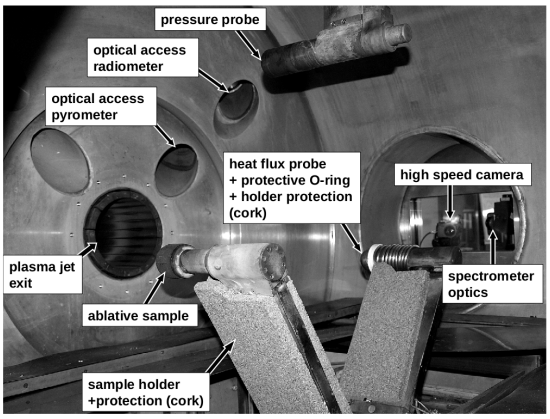

Figure 5: Experimental setup applied to the Plasmatron test chamber with measurement techniques for ablation and free-stream characterization

3.2. Pre- and post-test sample examination

Microscopic and spectroscopic examination will be done at the research group on *Electrochemical and Surface Engineering* (SURF) of the *Vrije Universiteit Brussel* (VUB). Pre- and post-test examination of ablative samples by Scanning Electron Microscopy (SEM) as well as spectroscopic tools, Energy-Dispersive X-ray spectroscopy (EDX) and Auger Electron Spectroscopy (AES), will be used to analyze the ablation phenomena down to the carbon fiber length scale ($\sim 10\,\mu m$) and to evaluate the degradation inside the material.

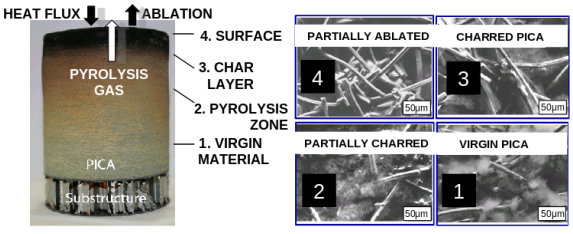

Figure 6: Thermal Protection System core (PICA) with subsequent Scanning Electron Microscopy in four zones of this core (Courtesy NASA [4])

By doing so, a multiscale analysis in macro-, meso−, and microscale is being performed giving information about the depth of pyrolysis and char layer (see Fig. 6). The thinning and erosion of the carbonic fibers is of high interest [4; 11] as this helps in identifying the depth of the ablation zone and the fiber's subject to oxidation.

4. Summary

The experimental data collected within this project will be crucial for the validation and development of physico-chemical models and computational methods being the three basic ingredients for prediction in aerospace science as presented in Fig. 7. A high quality data-set will be provided (pre-test, in-situ, post-test), being the missing link between those numerical tools following state-of-the-art uncertainty quantification methods.

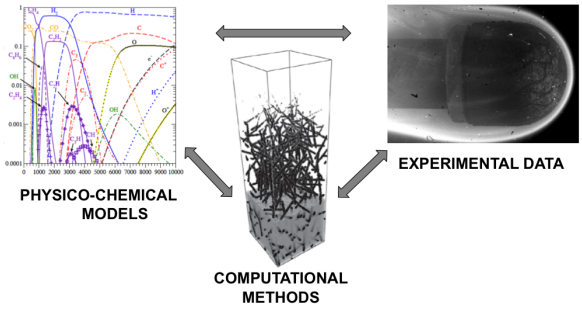

Figure 7: Complementary prediction tools: model for gas composition, code for ablative material response, and TPM testing in Plasmatron

The two research groups involved in this project, the *Aeronautics and Aerospace Department* (*VKI*) and the research group on *Electrochemical and Surface Engineering* of the *VUB*, have complementary experimental tools, high enthalpy facilities and subsequent electron microscopy, that will be used for testing ablative thermal protection materials.

Acknowledgments

The author acknowledges support from the Vrije Universiteit Brussel through a "VUB-Doctoraatsbeurs" fellowship.

References

[1] Ph. Tran, J.C. Paulat and P. Boukhobza, Re-entry Flight Experiments Lessons Learned – The Atmospheric Reentry Demonstrator ARD, in: *Flight Experiments for Hypersonic Vehicle Development* (pp. 10-1 – 10-46), Educational Notes RTO-EN-AVT-130, Paper 10, Neuilly-sur-Seine, 2007.

[2] M. Stackpoole S. Sepka I. Cozmuta and D. Kontinos, Post-Flight Evaluation of Stardust Sample Return Capsule Forebody Heatshield Material, in: AIAA 2008-1202, 2008.

[3] J. Lachaud, Simulation of ablation of carbon-based composites, Ph.D. thesis, Bordeaux 1 University, France (2006).

[4] J. Lachaud, I. Cozmuta, N. N. Mansour, Multiscale approach to ablation modeling of phenolic impregnated carbon ablators, Journal of Spacecraft and Rockets 47 (6) (2010) 910–921.

[5] R. M. Kendall, E. P. Bartlett, R. A. Rindal, and C. B. Moyer, An analysis of the coupled chemically reacting boundary layer and charring ablator: Part I, NASA CR 1060 (1968).

[6] F. S. Milos, Y.-K. Chen, Comprehensive model for multicomponent ablation thermochemistry, in: AIAA paper 1997-0141, 1997.

[7] S. Milos, Y.-K. Chen, Ablation and Thermal Response Property Model Validation for Phenolic Impregnated Carbon Ablator, in: AIAA paper 2009-262, 2009.

[8] M.-Y. Perrin, P. Riviere and A. Soufiani, Radiation database for Earth and Mars entries, in: RTO-EN-AVT-162, Non-equilibrium gas dynamics, from physical models to hypersonic flights, Rhode-Saint- Genese, Belgium, 2008.

[9] B. Helber, Experimental investigation of ablative materials in Plasmatron, PR 2010-16, von Karman Institute for Fluid Dynamics (2010).

[10] B. Bottin, O. Chazot, M. Carbonaro, V. van der Haegen, S. Paris, The VKI Plasmatron Characteristics and Performance, in: *RTO AVT Course on Measurement Techniques for High Enthalpy and Plasma Flows* & published in RTO EN-8, Belgium, 1999.

[11] J. Lachaud, N. N. Mansour, Microscopic scale simulation of the ablation of fibrous materials, in: 48th AIAA Aerospace Sciences Meeting Including the New Horizons Forum and Aerospace Exposition, 4-7 January 2010, Orlando, Florida.

Numerical modeling and experimental investigation of fine particle coagulation and dispersion in dilute flows

Bart Janssens

Turbomachinery and Propulsion Department, bart.janssens@rma.ac.be

Supervisor: Tony Arts

Professor, Turbomachinery and Propulsion Department, von Karman Institute for Fluid Dynamics, Belgium, arts@vki.ac.be.

Promotor: Walter Bosschaerts

Professor, Department of Mechanical Engineering, Royal Military Academy, walter.bosschaerts@rma.ac.be

Promotor: Karim Limam

Professor, Laboratoire d'Étude des Phénomènes de Transfert et de l'Instantanéité, La Rochelle University, France , klimam01@univ-lr.fr

Abstract

In this work, a numerical model will be developed to study the behavior of fine and ultrafine particles under conditions typical for air pollution problems. The particles considered are much heavier than the surrounding fluid, and can have sizes ranging from 5 *nm* to 10 μm. Effects of inter-particle collisions and coagulation will be included in the model.

For the fluid model, the Finite Element Method implemented in COOLFluiD will be used [1], with LES for turbulence modeling. The particle model will use either an Eulerian approach, based on kinetic particle PDF equations, or a Lagrangian approach.

During model development, validation will happen using small-scale experiments and literature data. In a final phase, the developed model will be tested in two industrial problems.

Keywords: Multiphase flow, Disperse flow, coagulation, LES, nanoparticles

1. Introduction

One of the major factors in determining air quality is the level of pollution in the form of particles. In general, particles with an aerodynamic diameter inferior to 10 μm can penetrate into the human body, and constitute a potential health risk [2]. Recently, the additional risks of nanoparticles have received much attention [3], so we will study particles in a range from about 5 *nm* to 10 μm. The goal of the present work is to arrive at a contribution to the numerical modeling of particle-laden flow, where the behavior of ultrafine particles is taken into account, as well as inter-particle collision and coagulation. This will be done in two phases: a model development phase, followed by an application phase. The target applications include flows in confined spaces that can be modeled using CFD. Particle loading should be such that the flow can be considered dilute, i.e. particle dynamics are dominated by the flow rather than inter-particle collisions.

2. Numerical model

The developed model must be able to capture both the flow and the particle behavior. In the class of problems studied here, the instantaneous fluid velocity is a major factor in determining particle behavior, so the accuracy of the fluid model will have a great impact on the results.

2.1. Fluid model

The fluid will be modeled by discretizing the incompressible Navier-Stokes equations using the Finite Element Method, as implemented in COOLFluiD

[1]. The resulting method is of second order accuracy. In order to obtain a reliable velocity input for the particle equations, LES is used for the turbulence modeling. There is some discussion in the literature on the validity of using the LES results as instantaneous velocity input for the particle equation of motion. Some authors suggest that neglecting the small scales of turbulence may influence the results for the particle quantities [4]. They attempt to remedy this by applying an approximate deconvolution method, as described in i.e. [5]. The added complexity of implementing such a method is considered to be beyond the scope of the current work, however, so we will attempt to work with LES solutions that are sufficiently resolved.

2.2. Particle model

When modeling the behavior of the particles, a choice needs to be made between an Eulerian or a Lagrangian approach. Of the many Eulerian methods, the approach presented by Simonin [6] seems most applicable to the current problem, especially since it has been extended to include collision effects [7; 8].

The Lagrangian approach seems more intuitive, as the particle equation of motion is solved directly, while different forces acting upon the particle can be modeled easily. The challenge is that from a computational point of view, it is impossible to track all particles, so statistical methods need to be used. The inclusion of collision effects further complicates matters: since not all particles are tracked directly, collisions can not be deduced directly either. Some approaches to these problems are presented in e.g. [9; 10].

A challenging aspect of the particle model is the inclusion of nanoparticles, which - due to their small size- may need special care in the treatment of the forces acting on the particles. Furthermore, because nanoparticles commonly are produced in very high number concentrations, there is a high probability of inter-particle collisions and particle coagulation [11], which will in turn affect the particle size distribution. This effect can be accounted for by solving a population balance equation. A possible candidate seems to be the method presented by Silva et al. [12], since it is shown to be usable when coupled with CFD simulations.

3. Model validation

During the development of the model, it will be validated against simple test cases, using both literature data and small-scale experiments. As a validation of the fluid model, the classic DNS data for channel flows [13] will of course be used. Channel flow data with dispersed particles is also widely available [14; 15; 16] and can be used for validation of the model including particles.

3.1. Experimental setup

A first experiment that is being developed is designed to measure concentration variations and the effect of particle coagulation in a flow field that should be reproducible using numerical simulation. Flow will enter a cubic chamber through a narrow slot near the top, and exit near the bottom of the opposite wall (see Fig. 1). The particle injection will happen in a short burst near the center of the expected circulation zone.

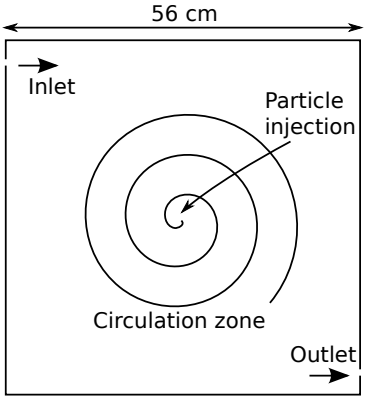

Figure 1: Schematic of the experimental test chamber.

In order to get a reproducible result, the inlet conditions will be controlled using a device similar to the inlet section of a subsonic wind tunnel, as shown in Fig. 2

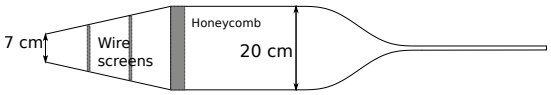

Figure 2: Conditioning of the test chamber inlet.

In a first step, the flow field will be measured using PIV in order to validate the numerical simulation of the flow itself.

It is expected that a circulation zone will appear inside the box, and in a second phase particles will be injected near the center of this zone. The evolution of the particle size distribution will then be monitored over time, and in case of coagulation a shift towards

larger and larger particles should be observed. This evolution will then be compared to predictions made by the particle model.

4. Applications

The final phase of the work consists of an application to industrial problems. Two cases will be considered: the acoustic agglomeration of industrial gases, and the evolution of particles through a turbine.

4.1. Acoustic agglomeration

Acoustic agglomeration is a technique used in the treatment of industrial waste [17], where powerful acoustic waves interact with particulate matter. The particle response to these waves depends on their size, resulting in an enhanced relative motion between particles, and ultimately a higher collision rate. This allows larger particles to "scavenge" smaller particles, making subsequent filtering much easier.

4.2. Turbine

In this application, an attempt will be made to study the behavior of particles downstream the combustion chamber in a gas turbine. This could play a role in the determination of the final properties of the emissions. The effect has previously been studied by Dakhel [18], who concluded that the effect of coagulation is negligible. The study was based on time-scale arguments, however, so it would be interesting to see if it is confirmed by a more detailed simulation.

5. Conclusion

The objective of the current work is to provide a meaningful contribution to the numerical modeling of dispersed phase flow. The inclusion of nanoparticles and coagulation effects constitute new challenges, and should extend the applicability of the method. Areas of application include for example indoor air quality or risk assessment when considering the behavior of chemical or biological agents, as well as the study of pollutant aggregation in close proximity to the source.

References

[1] T. Bányai, D. V. Abeele, H. Deconinck, A fast fully-coupled solution algorithm for the unsteady incompressible Navier-Stokes equations, in: Conference on Modelling Fluid Flow (CMFF'06), Budapest, Hungary, 2006.

[2] C. A. P. III, D. W. Dockery, Health Effects of Fine Particulate Air Pollution: Lines that Connect, J. Air & Waste Manage. Assoc. 56 (2006) 709–742.

[3] G. Oberdörster, E. Oberdörster, J. O. 3, Nanotoxicology: An Emerging Discipline Evolving from Studies of Ultrafine Particles, Environ Health Perspect 113 (2005) 823–839. doi:10.1289/ehp.7339.

[4] J. G. M. Kuerten, Subgrid modeling in particle-laden channel flow, Physics of Fluids 18 (2) (2006) 025108. doi:10.1063/1.2176589.

[5] P. Sagaut, Large Eddy Simulation for Incompressible Flows, Third Edition Edition, Scientific Computation, Springer, 2005.

[6] O. Simonin, Statistical and continuum modelling of turbulent reactive particulate flows, in: Theoretical and experimental modelling of particulate flow, 2000.

[7] L. I. Zaichik, V. M. Alipchenkov, Pair dispersion and preferential concentration of particles in isotropic turbulence, Physics of Fluids 15 (6) (2003) 1776. doi:10.1063/1.1569485.

[8] L. I. Zaichik, O. Simonin, V. M. Alipchenkov, Two statistical models for predicting collision rates of inertial particles in homogeneous isotropic turbulence, Physics of Fluids 15 (10) (2003) 2995. doi:10.1063/1.1608014.

[9] Y. Yamamoto, M. Potthoff, T. Tanaka, T. Kajishima, Y. Tsuji, Large-eddy simulation of turbulent gas–particle flow in a vertical channel: effect of considering inter-particle collisions, Journal of Fluid Mechanics 442. doi:10.1017/S0022112001005092.

[10] A. C. Ho, M. Sommerfeld, Modelling of micro-particle agglomeration in turbulent flows, Chemical Engineering Science 57 (15) (2002) 3073. doi:10.1016/S0009-2509(02)00172-0.

[11] W. W. Nazaroff, Indoor particle dynamics, Indoor Air 14 (s7) (2004) 175–183.

[12] L. Silva, R. Damian, P. Lage, Implementation and analysis of numerical solution of the population balance equation in CFD packages, Computers & Chemical Engineering 32 (12) (2008) 2933. doi:10.1016/j.compchemeng.2008.03.007.

[13] R. D. Moser, J. Kim, N. N. Mansour, Direct numerical simulation of turbulent channel flow up to Re[sub tau] = 590, Physics of Fluids 11 (4) (1999) 943–945. doi:10.1063/1.869966.

[14] C. M., K. K. , M. J. B. , Direct Numerical Simulation of Droplet Collisions in a Turbulent Channel Flow. Part II: collision rates, International Journal of Multiphase Flow 24 (November 1999) 1105–1138.

[15] J. R. Fessler, J. D. Kulick, J. K. Eaton, Preferential concentration of heavy particles in a turbulent channel flow, Physics of Fluids 6 (11) (1994) 3742. doi:10.1063/1.868445.

[16] M. Sommerfeld, Analysis of collision effects for turbulent gas-particle flow in a horizontal channel. Part II. Integral properties and validation, International Journal of Multiphase Flow 29 (4) (2003) 701. doi:10.1016/S0301-9322(03)00033-8.

[17] T. Hoffmann, Environmental implications of acoustic aerosol agglomeration, Ultrasonics 38 (1-8) (2000) 353. doi:10.1016/S0041-624X(99)00184-5.

[18] P. M. Dakhel, S. P. Lukachko, I. A. Waitz, R. C. Miake-Lye, R. C. Brown, Postcombustion Evolution of Soot Properties in an Aircraft Engine, Journal of Propulsion and Power 23 (5) (2007) 942. doi:10.2514/1.26738.

The effect of solidity on compressor performance and stability

Jérôme Sans

Turbomachinery and Propulsion Department, sans@vki.ac.be

Supervisor: Jean-François Brouckaert

Associate Professor, Turbomachinery and Propulsion Department, Belgium, brouckaert@vki.ac.be

Promotor: Tony Arts

Professor, Turbomachinery and Propulsion Department, von Karman Institute for Fluid Dynamics, Belgium, arts@vki.ac.be

Keywords: Compressor, solidity, performance, stability

The solidity is the ratio of the aerodynamic chord over the peripheral distance between two blades also called the pitch. In the last decades, a constant increase of solidity in engine compressors has been noticed (Fig. 1). This can be achieved either by

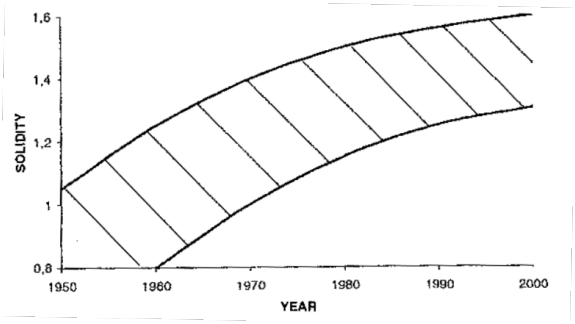

Figure 1: Evolution of the solidity in engine compressors over the last years [1]

decreasing the pitch or by lengthening the chord, i.e. increasing the aspect ratio. For many years, the designers chose to enlarge the aerodynamic chord length since long-chord blades brought experimental evidences of better behavior with respect to secondary flows. This allowed to push back the compressor surge to lower massflow. Today, the axial extension of the engine appears to be a severe constraint which prevents the engineers to keep on this way. New improvements might emerge by studying the blade number effect.

The following PhD proposal aims at investigating numerically and experimentally the effect of the solidity, mainly the blade number effect, on both compressor performance and stability. The compressor which is considered for this investigation is a low-pressure compressor stage studied at VKI within the framework of the DREAM project. The stage has been designed and manufactured by TechSpace Aero and is representative of a state-of-the-art booster. This present study is in line with previous research at VKI on the same compressor stage. The steady performance has been assessed numerically with the CFD software FINE/Turbo^{TM} from Numeca International and experimentally in the VKI R4 facility. The same software and facilities will be used for the present investigation.

After reviewing the literature, the validity of simulating the effect of solidity by CFD must be assessed. The influence of solidity must be analyzed on various two-dimensional profiles of the DREAM rotor and compared to correlations. Then, the same analysis has to be achieved in 3D. Both two- and three-dimensional tests must be related in order to bring out design rules or correlations. Experimental cascade tests must be defined at different solidities in order to build a database and to validate the 2D numerical calculations. Various measurement techniques as hot films or PIV may be used to characterize the blade performance and detect blade separation. The focus must be set on the relation with CFD results but also on the prediction of performance and stability of the three-dimensional rotor. The cascade study

should lead to a final test campaign in the VKI R4 test rig. The performance of a 3D stage with optimum solidity must be assessed at design and off-design conditions. These results are then related to the reference design of the DREAM booster. Efforts will be concentrated on the effect of the solidity variation and the accuracy of the performance prediction.

References

[1] T. Obrecht, HP compressor preliminary design, in: Advances in axial compressor aerodynamics, von Karman Institute for Fluid Dynamics Lecture Series, Belgium, 2006.